

Copyright is owned by the Author of the thesis. Permission is given for a copy to be downloaded by an individual for the purpose of research and private study only. The thesis may not be reproduced elsewhere without the permission of the Author.

Catalysts Derived from Metal-Organic Frameworks

A thesis presented in partial fulfilment of the requirements of the degree of

Doctor of Philosophy

in

Chemistry

at Massey University, Manawatu, New Zealand

W.R.L. Nisansala Bandara

[2021]

To my husband Lahiru,

*for putting his life on hold and following me to New Zealand,
so I could pursue my PhD.*

Abstract

The synthesis of atomic-scale catalysts is a blooming field, and these replace the conventional nanocatalysts due to their high atom utilization, selectivity, and unique catalytic activity. Metal-organic frameworks (MOFs) serve as promising precursors for the synthesis of single-atom catalysts (SACs). This study focused on the synthesis of SACs on nitrogen-doped hollow carbon by using MOFs and MOF composites followed by pyrolysis. The synthesis of two SACs namely rhodium SACs (Rh SACs) and cobalt SACs (Co SACs) by different methods, their characterization, and catalysis was explored. Rh SAC synthesized in this work hydrogenates nitroarenes with high consumption and high selectivity. Moreover, Co SAC did little or no hydrogenation of the nitroarenes. Further applications of these SACs were explored by employing them in oxygen reduction reaction (ORR), NO abatement, and Fenton-like catalysis.

Moreover, the synthesis of two types of hollow nanoboxes (HNB) namely HNB-1 and HNB-2; using MOFs and MOF composites, their characterization and applications were also investigated. HNB-1 was used to make electrode supercapacitors and it showed comparable activity to activated carbon. Further attempts were made to use HNB-2 as a fluorescence sensor. Finally, several ideas on synthesising SACs and HNBs were proposed as a part of future work.

Contributions

All the work in this thesis was completed by W.R.L. Nisansala Bandara

Except:

- Manawatu Microscopy and Imaging Centre (MMIC) provided the facility and the training for optical microscope, SEM, EDX and TEM.
- STEM images of Chapter 2 were taken by Prof. Yihan Zhu at the Center of Electron Microscopy, State Key Laboratory Breeding Base of Green Chemistry Synthesis Technology and Collage of Chemical Engineering, Zhejiang University of Technology, China.
- Raman spectroscopy was collected and analysed by Sam Brook and André Buzas Stowers-Hull at Massey University.
- XPS measurements in Chapters 2 and 3 were performed by Dr. Wanting Chen and Dr. Colin Doyle at the Research Center for Surface and Material Science, University of Auckland
- XPS analysis in Chapters 2 was performed by Dr. Wanting Chen and Prof. Geoffrey Waterhouse at the University of Auckland.
- Dr. Wanting Chen assisted with the XAS analysis in Chapter 3.
- NEXAFS measurements in Chapters 2, 3, and 6 were performed by Nisansala Bandara and Dr. Wanting Chen at the Australian Synchrotron.
- NEXAFS analysis in Chapters 2, 3, and 6 were done by Dr. Wanting Chen and Prof. Geoffrey Waterhouse.
- XAS measurements in Chapter 2 were performed by Nisansala Bandara, Dr. John Clements and Dr. Wanting Chen at the Australian Synchrotron.
- XAS measurements in Chapter 3 were performed by Dr. John Clements and Shikeale Harris at the Australian synchrotron.
- XAS analysis and EXAFS fittings in Chapters 2 and 3 were performed by Dr. Wanting Chen and Prof. Geoffrey Waterhouse.
- David Lun assisted to establish HPLC conditions for the catalysis study.
- ORR experiments in Chapter 5 were conducted by Dr. Lu Shang and Prof. Tierui Zhang who are collaborating with Prof. Geoffrey Waterhouse at the Technical Institute of Physics and Chemistry, Chinese Academy of Sciences.
- NO abatement experiments in Chapter 5 were carried out by our collaborator Dr. Zongli Xie at CSIRO, Australia.

- Joel Cornelio assisted with the fluorescence measurements and analysis presented in Chapter 6.
- Electrochemical measurements in Chapter 6 were performed by our collaborator Dr. Zifeng Lin at the College of Material Science and Engineering, Sichuan University, China.

Acknowledgments

I would like to thank my supervisor, Prof. Shane Telfer, for offering me the opportunity and scholarship to work towards this PhD. Thank you for your guidance and encouragement throughout this journey. I am grateful to you for entrusting me with this opportunity, for training me and for pushing me beyond any limits I ever thought I had.

Thank you to my co-supervisor, Associate Prof. Mark Waterland, for your direction and encouragement throughout this PhD. To Dr. Wanting Chen, who trained me on XPS, NEXAFS, and XAS analysis. To Prof. Geoff Waterhouse, for providing me with many opportunities to visit Synchrotron. To Dr. John Clements, for writing proposals and securing beam time. To the scientists at Australian Synchrotron, for your support and helpful discussions. To all the collaborators who contributed in numerous ways towards this work. I am eternally grateful.

A special thank you goes to my colleagues, Dr. Heather Jameson, Dr. David Perl, and Dr. Joel Cornelio, for untangling my brain and relieving my stresses over the many coffees we have shared. To all my group members, Dr. Tian-You Zhou, Dr. Adil Alkas, Dr. Omid Taheri, Dr. Ben Yin, Shikeale Harris, Tim Craig, Yiming Zhang, Dr. Jose Quinsa, Victoria-Jayne Reid, Bernhard Auer, Dr. Maulik Mungalpara, Dr. Seok June Lee, and all other past group members, for scientific discussions and technical assistance. To Dave Lun, for training me on HPLC. To the technical staff and the people at IFS who helped me in numerous ways over the last three years. I am indebted to you all.

I would like to acknowledge the financial support of MBIE. To McDiarmid Institute, for providing additional funding and opportunities for workshops and symposiums. To the administration of SFS, for paying my tuition fees for the fourth year. Thank you.

To my previous supervisors, Profs. Nalin and Rohini de Silva, for sparking my interest in chemistry. To Prof. Gehan Amarathunga, for giving me the opportunity to work at SLINTEC and improve my theoretical and practical knowledge before I came to New Zealand. To my previous colleagues at SLINTEC, especially Shana, Samantha and Kulathepan for being with me and bringing joy and laughter to my life. I will never forget the memories.

A huge thank you to my childhood friends, Shashi and Dulmini, for keeping me sane over the last few years.

I am blessed to have the love and reassurance of my parents, sister, grandma and cousins. I am sorry I could not visit you because of this pandemic. I thank my mum and dad, Dhammika and Somarathna, for showing me the value of a good education. Your unconditional love, care, and concern have made me the person I am today. I can never thank you enough for the sacrifices you have made for my well-being. What I have done, I have done to make you proud.

Publications and thesis structure

Additional publications

1. Lahiru A. Wijenayaka, Ruchira N. Wijesena, Nadeeka D. Tissera, **W.R.L. Nisansala Bandara**, Gehan J. Amarathunga, K.M. Nalin de Silva, Infrared absorbing nanoparticle impregnated self-heating fabrics for significantly improved moisture management under ambient conditions, *R. Soc. Open Sci.* **2021**, 8,202222.
2. S.P. Rathnayake, C.S. Sadaruwan, M.M.M.G.P.G. Manthilaka, N. de Silva, U.K. Wanninayake, **W.R.L. Nisansala Bandara**, S. Santhoshkumar, E. Murugan, G.A.J. Amarathunga, K.M. Nalin de Silva, Industrial and environmental significance of photonic zirconia nanoflakes: Influence of boron doping on structure and band states, *J. Ind. Eng. Chem.*, **2021**, 95, 203.
3. Dr. Binbin Tu, Dr. Lisa Diestel, Zhao-Lin Shi, **W. R. L. Nisansala Bandara**, Yi Chen, Weimin Lin, Prof. Dr. Yue-Biao Zhang, Prof. Dr. Shane G. Telfer, Prof. Dr. Qiaowei Li, Harnessing Bottom-Up Self-Assembly To Position Five Distinct Components in an Ordered Porous Framework. *Angew. Chem. Int. Ed.* **2019**, 58, 5348.

Abbreviations

AAS	Atomic Absorption Spectroscopy
ABF	Annular Bright Field
AEY	Auger Electron Yield
BE	Binding Energy
BF	Bright Field
BPA	Bisphenol A
BTC	Benzenetricarboxylate
CMS	Carbonaceous Microsphere
CNT	Carbon Nano Tube
CO ₂ RR	Carbon Dioxide Reduction Reaction
COD	Cyclooctadiene Dimer
COF	Covalent-Organic Framework
CSD	Cambridge Structural Database
CTAB	Cetyl Trimethylammonium Bromide
DCD	Dicyandiamide
DFT	Density-Functional Theory
DI	Deionized
EDX	Energy Dispersive X-ray Analysis
EXAFS	X-ray Absorption Fine Structure
Fg ⁻¹	Farads per gram
FT	Fourier Transformed
FTIR	Fourier Transform Infrared Spectroscopy
GA	Gallic Acid
GO	Graphene Oxide
GT	Graphene Tube

HAADF	High Angle Annular Dark Filed
HER	Hydrogen Evolution Reaction
HKUST	Hong Kong University of Science and Technology
HNB	Hollow Nanoboxes
HPLC	High-Performance Liquid Chromatography
HR	High Resolution
IR MOF	Isorecticular Metal-Organic Framework
IUPAC	International Union of Pure and Applied Chemistry
KE	Kinetic Energy
KTA	Potassium Tannic Acid
LIB	Lithium-Ion Battery
meso MOF	mesoporous Metal-Organic Framework
MIL	Materials Institute Lavoisier
MOF	Metal-Organic Framework
MUF	Massey University Framework
NC	Nitrogen-doped Carbon
NEXAFS	Near Edge X-ray Absorption Fine Structure
NP	Nanoparticle
NPC	Nanoparticle Catalyst
NRR	Nitrogen Reduction Reaction
NU	Northwestern University
OAc	Acetate
OER	Oxygen Evolution Reaction
ORR	Oxygen Reduction Reaction
PAN	Polyacrylonitrile
PCN	Porous Coordination Network
PCP	Porous Coordination Polymer

Ph	Phenyl group
PMMA	Poly Methyl Methacrylate
PMS	Peroxymonosulfate
POM	Polyoxometalate
PS	Polystyrene
PTFE	Polytetrafluoroethylene
PVP	Polyvinylpyrrolidone
PVPA	Polyvinylphosphonic Acid
RCSR	Reticular Chemistry Structure Resource
RDE	Rotating Disk Electrode
RHE	Reversible Hydrogen Electrode
rpm	Rounds per minute
SA	Single-Atom
SAC	Single-Atom Catalyst
SCR	Selective Catalytic Reduction
SEM	Scanning Electron Microscopy
SNCR	Selective Non-Catalytic Reduction
STEM	Scanning Transmission Electron Microscopy
TA	Tannic Acid
TEM	Transmission Electron Microscopy
TEY	Total Electron Yield
TGA	Thermogravimetric Analysis
TON	Turn Over Number
TPP	Tetra Phenyl Porphyrin
UiO	University of Oslo
UMCM	University of Michigan Crystalline Material
UV	Ultraviolet

Wh	Watt-hours
XANES	X-ray Absorption Near-Edge Structure
XAS	X-ray Absorption Spectroscopy
XPS	X-ray Photoelectron Spectroscopy
XRD	X-ray Diffraction
ZIF	Zeolitic Imidazolate Framework

Table of Contents

Chapter 1- Introduction.....	1
1.1 Introduction to MOFs	1
1.2 Nomenclature of MOFs	1
1.3 History of MOFs	2
1.4 Application of MOFs	5
1.5 Single metal atom catalysts (SACs).....	8
1.6 Synthetic strategies to SACs.....	10
1.7 Synthesis of SACs by pyrolyzing MOFs and MOF composites	14
1.8 Characterization techniques for SACs.....	21
1.9 Catalysis by SACs synthesized by pyrolysis of MOFs and MOF composites	31
1.10 Introduction to hollow nanostructures	31
1.11 Nomenclature of hollow nanostructures	31
1.12 Synthesis strategies of hollow nanostructures	32
1.13 Synthesis of hollow nanostructures from MOFs	36
1.14 Synthesis strategies of hollow nanostructures by pyrolyzing MOFs and MOF composites.....	37
1.15 Application of hollow nanostructures synthesized by pyrolysis of MOF and MOF composites	42
1.16 Aims of the thesis	43
Chapter 2 – Synthesis and Characterization of Rh SAC	45
2.1 Introduction.....	45
2.2 Results and Discussion	47
2.3 Conclusion	71
2.4 Experimental Section.....	72
Chapter 3 – Synthesis and Characterization of Co SAC	89
3.1 Introduction.....	89
3.2 Results and Discussion	90

3.3	Conclusion	119
3.4	Experimental Section	120
Chapter 4 – Hydrogenation of Nitroarenes by Rh SAC and Co SAC		139
4.1	Introduction	139
4.2	Results and Discussion.....	140
4.3	Conclusion	151
4.4	Experimental Section	153
Chapter 5 – Other Reactions Catalysed by Rh SAC and Co SAC.....		163
5.1	Introduction.....	163
5.2	Results and discussion	165
5.3	Conclusion	172
5.4	Experimental section.....	174
Chapter 6 – Synthesis of Hollow Nanoboxes and Applications		179
6.1	Introduction.....	179
6.2	Results and Discussion.....	180
6.3	Conclusion	193
6.4	Experimental Section	194
Chapter 7 – Summary and Perspectives.....		201
7.1	Summary	201
7.2	Future work.....	203
References.....		213
DRC 16 Forms.....		243
Electronic Appendices.....		249
Appendix A for Chapter 1.....		A1
Appendix B for Chapter 6.....		A21

List of Figures

Figure 1.1: Synthesis strategy of MOFs; metal ions - blue, organic ligands - magenta.	1
Figure 1.2: Crystal structure of MOF-5; Zn-Cyan, C-grey, O-red, Void space-yellow sphere and H is not shown for clarity.	2
Figure 1.3: (a) The ligand metal bond in ZIFs and (b) zeolites.	3
Figure 1.4: Structure of ZIF-8/ZIF-67; Zn/Co-purple, N-blue, C-black and hydrogen is not shown for clarity.	4
Figure 1.5: A cartoon presentation of the applications of MOFs.	6
Figure 1.6: Schematic illustrates the change of surface free energy and specific activity with particle size. ...	9
Figure 1.7: Synthesis procedure for isolated single metal atoms stabilized on defective TiO ₂ nanosheet with oxygen vacancies by defective engineering strategy; O-red, Ti-white, single metal atoms- yellow.	10
Figure 1.8: Preparation of single metal atom catalyst by spatial confinement strategy.	11
Figure 1.9: Synthesis strategy of single metal atom catalyst on hollow nitrogen-doped carbon coordination strategy; N-blue, C-grey, metal atoms-purple and hydrogen is not shown for clarity.	12
Figure 1.10: Synthesis of single metal atom catalyst via iced photochemical synthesis; metal atoms- red.	13
Figure 1.11: Synthesis of SACs by mixed metal strategy.	16
Figure 1.12: Synthesis of SACs by top-down strategy.	20
Figure 1.13: The path of the electron beam of STEM.	22
Figure 1.14: The path of the X-ray beam in XPS.	23
Figure 1.15: XAS $\mu(E)$ for a cobalt sample (Co on N doped C), the measured XAS spectrum is shown with the XANES, and EXAFS regions identified.	26
Figure 1.16: Transmission method and electron yield method of recording.	27
Figure 1.17: Schematic potential and the corresponding NEXAFS K-shell spectrum of a diatomic molecule.	29
Figure 1.18: Electronic schematic for the NEXAFS photoabsorption spectrum; figure adapted from reference Ade et al. ¹⁴²	30
Figure 1.19: Schematic presentation of the angular dependence of NEXAFS.	30
Figure 1.20: Different configurations of hollow nanostructures; (a) single-shell, (b) multi-shell, (c) yolk-shell, (d) rattle-type and (e) yolk-multi shell.	32
Figure 1.21: Synthesis of hollow nanostructures by electrospray techniques.	35
Figure 1.22: Synthesis of hollow nanostructures by hard template methods;	37
Figure 1.23: Structure of tannic acid.	39
Figure 1.24: Schematic presentation of interfacial ion exchange of MOFs.	40
Figure 1.25: Schematic presentation of heterogeneous contraction of MOFs.	41
Figure 1.26: Schematic presentation of self-catalytic pyrolysis of MOFs and synthesis of CNT.	42
Figure 2.1: Synthesis of Rh SAC.	47
Figure 2.2: Synthesis of ZIF-8.	47
Figure 2.3: Synthesis of ZIF-8@KTA.	48
Figure 2.4: Optical microscope images of (a) ZIF-8 and (b) ZIF-8@KTA.	48
Figure 2.5: TEM and EDX images of (a,c) ZIF-8 and (b,d) ZIF-8@KTA.	49

Figure 2.6: Rh loading of ZIF-8@RhTA (green) and Rh-NC (red) with ion exchange solution concentrations.	52
Figure 2.7: PXRD patterns of NC and Rh-NC samples.	53
Figure 2.8: TEM images of (a) Rh-NC, (b) Rh-NC-0.05, (c) Rh-NC-0.10, (d) Rh-NC-0.12, (e) Rh-NC-0.14, (f) Rh-NC-0.15, (g) Rh-NC-0.50 and (h) Rh-NC-0.80.	54
Figure 2.9: (a) HAADF STEM and (b) correlated ABF-STEM images of Rh-NC-0.14.	55
Figure 2.10: (a) STEM image and (b-f) elemental mapping of.	56
Figure 2.11: (a) STEM image and (b-f) elemental mapping of.	56
Figure 2.12: (a) STEM image and (b-f) elemental mapping of.	56
Figure 2.13: (a) STEM image and (b-f) elemental mapping of.	56
Figure 2.14: (a) STEM image and (b-f) elemental mapping of.	57
Figure 2.15: (a, b, c) HAADF-STEM images, (d, e, f) correlated ABF-STEM images and (g, h, i) cartoon shapes of Rh-NC-0.14.	57
Figure 2.16: XPS survey spectra of (a) unpyrolyzed and (b) pyrolyzed samples with standards.	58
Figure 2.17: C 1s XPS spectra of (a) unpyrolyzed samples and (b) pyrolyzed samples with standards.	59
Figure 2.18: N 1s spectra of (a) unpyrolyzed samples and (b) pyrolyzed samples with standards.	60
Figure 2.19: Rh 3d XPS spectra of (a) unpyrolysed samples and (b) pyrolyzed samples with standards.	61
Figure 2.20: The structure of Rh(TPP)Cl.	62
Figure 2.21: The structure of [Rh(COD)Cl] ₂	62
Figure 2.22: C K-edge NEXAFS spectra of (a) unpyrolyzed samples and (b) pyrolyzed samples with standards.	63
Figure 2.23: N K-edge NEXAFS spectra of (a) unpyrolyzed samples and (b) pyrolyzed samples with standards.	65
Figure 2.24: Rh K-edge EXAFS spectra for different samples and standards.	66
Figure 2.25: k ² weighted Rh K-edge spectra for different samples and standards.	67
Figure 2.26: r-space plots obtained from Fourier transform on k ² -weighted Rh K-edge EXAFS spectra for different samples and standards.	68
Figure 2.27: A parameterized spectral fit for Rh SAC; fit within the range 1-5 Å.	69
Figure 2.28: The structural depiction of Rh SAC; X represents O ₂ or H ₂ O.	70
Figure 2.29: PXRD patterns of ZIF-8, ZIF-8@KTA and ZIF-8@RhTA.	75
Figure 2.30: (a) FTIR spectra of 2-methylimidazole, ZIF-8, tannic acid, ZIF-8@KTA, ZIF-8@RhTA-0.14, NC, Rh-NC-0.14 and Rh-NC-0.05 and (b) Raman spectra of ZIF-8, ZIF-8@RhTA-0.14 and Rh-NC samples.	76
Figure 2.31: SEM and EDX of NC, Rh-NC-0.05, Rh-NC-0.10 and Rh-NC-0.12; counts in thousands.	77
Figure 2.32: SEM and EDX of Rh-NC-0.14, Rh-NC-0.15, Rh-NC-0.50 and Rh-NC-0.80; counts in thousands.	78
Figure 2.33: TEM images of (a) ZIF-8@RhTA-0.05, (b) ZIF-8@RhTA-0.10, (c) ZIF-8@RhTA-0.12, (d) ZIF-8@RhTA-0.14, (e) ZIF-8@RhTA-0.15, (f) ZIF-8@RhTA-0.50 and (g) ZIF-8@RhTA-0.80.	79
Figure 2.34: O 1s XPS spectra of (a) unpyrolysed samples and (b) pyrolyzed samples with standards.	81

Figure 2.35: EXAFS fittings for Rh-N/Rh-O for (a) Rh-NC-0.05, (b) Rh-NC-0.10, (c) Rh-NC-0.12 and (d) Rh-NC-0.14 samples; On the top panel individual contributions of Rh-NC samples are shown in k -space, while on the bottom panel they are shown in R -space.....	82
Figure 2.36: EXAFS fittings for Rh-N/Rh-O for (a) Rh-NC-0.15, (b) Rh-NC-0.50, (c) Rh-NC-0.80 samples and (d) Rh foil reference sample; On the top panel individual contributions of Rh-NC samples are shown in k -space, while on the bottom panel they are shown in R -space.	83
Figure 2.37: EXAFS fittings for Rh-N/Rh-O for RhCl ₃ and (b) Rh(TPP)Cl; On the top panel individual contributions of the samples are shown in k -space, while on the bottom panel they are shown in R -space....	84
Figure 2.38: EXAFS fittings for Rh-N and Rh-O for Rh-NC-0.14,.....	86
Figure 3.1: Synthesis of (a) Rh SAC by four steps and (b) Co SAC by three steps.	89
Figure 3.2: Synthesis of CoZn ZIF-8.....	90
Figure 3.3: PXRD patterns of ZIF-8, CoZn ZIF-8 and ZIF-67.....	91
Figure 3.4: Optical microscope images of (a) ZIF-8, (b) Co _{0.42} Zn ZIF-8, (c) Co _{2.07} Zn ZIF-8, (d) Co _{2.88} Zn ZIF-8, (e) Co _{3.50} Zn ZIF-8, (f) Co _{8.32} Zn ZIF-8, (g) Co _{10.79} Zn ZIF-8 and	91
Figure 3.5: Synthesis of CoZn ZIF-8@KTA.....	92
Figure 3.6: PXRD patterns of ZIF-8@KTA, CoZn ZIF-8@KTA samples and.....	93
Figure 3.7: Optical microscope images of (a) tannic acid, (b) ZIF-8@KTA,	94
Figure 3.8: Co loading of CoZn ZIF-8 (magenta) and Co-NC-Ar (brown) with molar% of cobalt in the cation mixture.	95
Figure 3.9: PXRD patterns of NC-Ar, Co-NC-Ar samples and Co _{max} -NC-Ar.....	96
Figure 3.10: TEM images of (a) NC-Ar, (b) Co _{0.42} -NC-Ar, (c) Co _{2.07} -NC-Ar,	97
Figure 3.11: PXRD patterns of NC-H ₂ , Co-NC-H ₂ samples and Co _{max} -NC-H ₂	98
Figure 3.12: TEM images of (a) NC- H ₂ , (b) Co _{0.42} -NC- H ₂ , (c) Co _{2.07} -NC- H ₂ ,.....	99
Figure 3.13: XPS survey spectra of (a) CoZn ZIF-8, (b) CoZn ZIF-8@KTA, (c) Co-NC-Ar and (d) Co-NC-H ₂ with reference samples.....	100
Figure 3.14: C 1s XPS spectra of (a) pristine MOFs, (b) Tannic acid coated MOFs,.....	102
Figure 3.15: N 1s XPS spectra of (a) pristine MOFs, (b) Tannic acid coated MOFs,.....	104
Figure 3.16: Co 2p XPS spectra of (a) pristine MOFs, (b) Tannic acid coated MOFs,	106
Figure 3.17: The structure of Co(TPP).....	108
Figure 3.18: C K-edge NEXAFS spectra of (a) pristine MOFs, (b) Tannic acid coated MOFs, (c) Co-NC-Ar samples and (d) Co-NC-H ₂ samples with standards.	109
Figure 3.19: N K-edge NEXAFS spectra of (a) pristine MOFs, (b) Tannic acid coated MOFs, (c) Co-NC-Ar samples and (d) Co-NC-H ₂ samples with standards.	111
Figure 3.20: Co L-edge NEXAFS spectra of (a) pristine MOFs, (b) Tannic acid coated MOFs, (c) Co-NC-Ar samples and (d) Co-NC-H ₂ samples with standards.	113
Figure 3.21: Co K-edge spectra of (a) Co-NC-Ar samples and (b) Co-NC-H ₂ samples with pristine MOFs, KTA coated MOFs and standards.....	115
Figure 3.22: k^2 weighted Co K-edge spectra of (a) Co-NC-Ar samples and (b) Co-NC-H ₂ samples with pristine MOFs, KTA coated MOFs and standards.	116
Figure 3.23: r -space plots obtained from Fourier transform on k^2 -weighted Co K-edge EXAFS spectra (a) Co-NC-Ar samples and (b) Co-NC-H ₂ samples with pristine MOFs, KTA coated MOFs and standards.	117

Figure 3.24: A parameterized spectral fit for $Co_{2.88}NC-Ar$; fit within the range 1-6 Å.	118
Figure 3.25: Structure depiction of Co SAC.	118
Figure 3.26: SEM and EDX of ZIF-8, $Co_{0.42}Zn$ ZIF-8, $Co_{2.07}Zn$ ZIF-8 and $Co_{2.88}Zn$ ZIF-8; counts in thousands.	124
Figure 3.27: SEM and EDX of $Co_{3.50}Zn$ ZIF-8, $Co_{8.32}Zn$ ZIF-8, $Co_{10.79}Zn$ ZIF-8 and ZIF-67; counts in thousands.	125
Figure 3.28: SEM and EDX of ZIF-8@KTA, $Co_{0.42}Zn$ ZIF-8@KTA, $Co_{2.07}Zn$ ZIF-8@KTA and $Co_{2.88}Zn$ ZIF-8@KTA; counts in thousands.	126
Figure 3.29: SEM and EDX of $Co_{3.50}Zn$ ZIF-8@KTA, $Co_{8.32}Zn$ ZIF-8@KTA, $Co_{10.79}Zn$ ZIF-8@KTA and ZIF-67@KTA; counts in thousands.	127
Figure 3.30: SEM and EDX of NC-Ar, $Co_{0.42}NC-Ar$, $Co_{2.07}Co_{0.42}NC-Ar$ and $Co_{2.88}NC-Ar$; counts in thousands.	128
Figure 3.31: SEM and EDX of $Co_{3.50}NC-Ar$, $Co_{8.32}NC-Ar$, $Co_{10.79}NC-Ar$ and $Co_{max}NC-Ar$; counts in thousands.	129
Figure 3.32: SEM and EDX of $Co_{0.42}NC-H_2$, $Co_{2.07}Co_{0.42}NC-H_2$, $Co_{2.88}NC-H_2$ and $Co_{3.50}NC-H_2$; counts in thousands.	130
Figure 3.33: SEM and EDX of $Co_{8.32}NC-H_2$, $Co_{10.79}NC-H_2$ and $Co_{max}NC-H_2$; counts in thousands.	131
Figure 3.34: TEM images of (a) ZIF-8, (b) $Co_{0.42}Zn$ ZIF-8, (c) $Co_{2.07}Zn$ ZIF-8, (d) $Co_{2.88}Zn$ ZIF-8, (e) $Co_{3.50}Zn$ ZIF-8, (f) $Co_{8.32}Zn$ ZIF-8, (g) $Co_{10.79}Zn$ ZIF-8 and (h) ZIF-67; scale bar 50 nm.	132
Figure 3.35: TEM images of (a) ZIF-8@KTA, (b) $Co_{0.42}Zn$ ZIF-8@KTA,	133
Figure 3.36: EXAFS fittings for Co-N for (a) $Co_{0.42}NC-Ar$, (b) $Co_{2.07}NC-Ar$, (c) $Co_{2.88}NC-Ar$, and (d) $Co_{3.50}NC-Ar$ samples;	136
Figure 3.37: EXAFS fittings for Co-N for (a) $Co_{8.32}NC-Ar$, (b) $Co_{10.79}NC-Ar$, (c) $Co_{max}NC-Ar$, and (d) Co(TPP) samples;	137
Figure 4.1: HPLC chromatograms of (a) substrate: 4-nitroacetophenone, (b) reference product: 4-aminoacetophenone; reaction catalysed by (c) Rh SAC, (d) 5% Rh on C, (e) NC, (f) no catalyst and (g) Co SAC.	142
Figure 4.2: HPLC chromatogram of the reaction mixture (a) before the reaction:	145
Figure 4.3: (a) HPLC chromatogram of the reaction mixture after the incomplete reaction (b) the quantification table of the HPLC chromatogram of the incomplete reaction generated by the software, (c) HPLC chromatogram of the reaction mixture after subjecting the incomplete reaction mixture to reaction conditions and (d) the quantification table of the HPLC chromatogram of the reaction mixture after subjecting the incomplete reaction mixture to reaction conditions generated by the software.	146
Figure 4.4: Re-cyclability test of Rh SAC.	147
Figure 4.5: PXRD of (a) Rh SAC before catalysis, (b) Rh SAC after 1 st use and	148
Figure 4.6: SEM and EDX of (a) Rh SAC before catalysis, (b) Rh SAC after 1 st use and (c) Rh SAC after 10 th re-use.	149
Figure 4.7: TEM images of (a, b) Rh SAC before catalysis, (c, d) Rh SAC after 1 st use and (e, f) Rh SAC after 10 th re-use.	150
Figure 4.8: Mechanisms proposed for the hydrogenation of nitroarenes by (a) Haber et al. through direct deoxygenation pathway and (b) Zhang et al. through indirect hydrogen assisted hydrogenation pathway. .	151

Figure 4.9: Proposed mechanism for the hydrogenation of nitroarenes by Rh SAC; rhodium (magenta), nitrogen (blue), oxygen (red) and hydrogen (grey) are shown in the mentioned colours for clarity.....	152
Figure 4.10: HPLC chromatograms of (a) substrate: 1-chloro-4-nitrobenzene, (b) reference product: 4-chloroaniline; reaction catalysed by (c) Rh SAC, (d) 5% Rh on C and (e) Co SAC.....	155
Figure 4.11: HPLC chromatograms of (a) substrate: 1-chloro-2-nitrobenzene, (b) reference product: 2-chloroaniline; reaction catalysed by (c) Rh SAC, (d) 5% Rh on C, (e) NC, (f) no catalyst and (g) Co SAC.	156
Figure 4.12: HPLC chromatograms of (a) substrate: 4-nitroanisole, (b) reference product: 4-aminoanisole; reaction catalysed by (c) Rh SAC, (d) 5% Rh on C and (e) Co SAC.	157
Figure 4.13: HPLC chromatograms of (a) substrate: 4-nitrotoluene, (b) reference product: 4-aminotoluene; reaction catalysed by (c) Rh SAC, (d) 5% Rh on C and (e) Co SAC.	158
Figure 4.14: HPLC chromatograms of (a) substrate: 4-nitrobenzotrile, (b) reference product: 4-aminobenzotrile; reaction catalysed by (c) Rh SAC, (d) 5% Rh on C and (e) Co SAC.	159
Figure 4.15: HPLC chromatograms of (a) substrate: 3-nitrobenzoic acid, (b) reference product: 4-aminobenzoic acid; reaction catalysed by (c) Rh SAC, (d) 5% Rh on C and (e) Co SAC.	160
Figure 5.1: Steady-state ORR polarization plots for various catalysts (0.6 – 1.0 V).....	165
Figure 5.2: Steady-state ORR polarization plots for after potential cycling stability tests (0.6–1.0 V, 5000 cycles) for Rh SAC and Rh NPC.	166
Figure 5.3: Steady-state ORR polarization plots for various catalysts collected in basic medium (0.1 M KOH).	167
Figure 5.4: NO _x conversions by Rh SAC, Rh NPC, Co SAC, NC, 5% Rh on C and Rh on Al ₂ O ₃ catalysts as a function of temperature; feed: 1000 ppm NO, 1000 ppm NH ₃	168
Figure 5.5: Degradation of BPA by PMS activation.....	170
Figure 5.6: Fenton-like catalytic performance by the catalysts for BPA degradation.....	170
Figure 5.7: First-order kinetic model of the Fenton-like reaction catalysed by Rh SAC,.....	171
Figure 5.8: Steady-state ORR polarization plots for various catalysts in acidic medium (top) and derivatives of ORR polarization plots used to determine E _{1/2} (bottom).....	175
Figure 5.9: Steady-state ORR polarization plots for Rh SAC and Rh NPC recycling tests in acidic medium (top) and derivatives of ORR polarization plots used to determine E _{1/2} (bottom).....	175
Figure 5.10: Steady-state ORR polarization plots for various catalysts in basic medium (top) and derivatives of ORR polarization plots used to determine E _{1/2} (bottom).....	176
Figure 6.1: Synthesis of HNB-1.....	179
Figure 6.2: Synthesis of HNB-2.....	179
Figure 6.3: Optical microscope images of (a) ZIF-8, (b) ZIF-8-475, (c) ZIF-8-500,	180
Figure 6.4: PXRD of ZIF-8 and ZIF-8 pyrolyzed at different temperatures.	181
Figure 6.5: TEM and EDX of (a, c) HNB-2-525 and (b, d) HNB-2-550.	182
Figure 6.6: FTIR spectra of 2-methylimidazole, HNB-2, partially pyrolyzed ZIF-8,.....	183
Figure 6.7: C K-edge NEXAFS spectra of HNB-2, partially pyrolyzed ZIF-8, ZIF-8 and carbon tape.....	184
Figure 6.8: O K-edge NEXAFS spectra of HNB-2, partially pyrolyzed ZIF-8, ZIF-8 and carbon tape.	184
Figure 6.9: N K-edge NEXAFS spectra of HNB-2, partially pyrolyzed ZIF-8, ZIF-8.....	185
Figure 6.10: Zn L-edge NEXAFS spectra of HNB-2, partially pyrolyzed ZIF-8, ZIF-8.....	185
Figure 6.11: The assembly of the device made from two HNB-1 electrodes.....	186

Figure 6.12: Electrochemical performance of device made from HNB-1 electrodes using.....	187
Figure 6.13: Electrochemical performance of device made from HNB-1 electrodes using.....	188
Figure 6.14: Electrochemical performance of device made from HNB-1 electrodes using neat EMI-BF ₄ as electrolytes in a two-electrode system. (a) Galvanostatic charge-discharge plots, (b) plot of capacitance vs scan rate and (c) energy density vs scan rate.	189
Figure 6.15: (a) Fluorescence and (b) relative intensity of HNB-2 dispersed in HCl (pH 1) when adding deionized H ₂ O, (c) fluorescence and (d) relative intensity of HNB-2 dispersed in H ₂ SO ₄ (pH 1) when adding (c, d) 0.1 M NaCl.	190
Figure 6.16: Fluorescence of HNB-2 dispersed in HCl (pH 1) and relative intensity when adding (a, b) 0.1 M NaI and (c, d) 0.1 M NaIO ₃	191
Figure 6.17: Relative intensity at the presence of anions.	192
Figure 6.18: Change in relative intensity after adding 200 μ L of solutions.	192
Figure 6.19: Fluorescence of HNB-2 dispersed in H ₂ SO ₄ (pH 1) and relative intensity when adding (a, b) DI H ₂ O and Fluorescence of HNB-2 dispersed in HCl (pH 1) and relative intensity when adding (c, d) 0.1 M NaBr and (e, f) 0.1 M KBr.	196
Figure 6.20: Fluorescence of HNB-2 dispersed in HCl (pH 1) and relative intensity when adding (a, b) 0.1 M NaF, (c, d) 0.1 M NaNO ₃ and (e, f) 0.1 M Na ₂ CO ₃	197
Figure 6.21: Fluorescence of HNB-2 dispersed in HCl (pH 1) and relative intensity when adding (a, b) 0.1 M Na ₂ SO ₄ and (c, d) 0.1 M Na ₃ PO ₄	198
Figure 7.1: A model of Rh(III) assisted CH activation reaction; blue and green circles represent alkyl or aryl groups.	203
Figure 7.2: A model of hydroformylation of alkanes; blue, purple, and green circles represent alkyl or aryl groups.	203
Figure 7.3: Synthesis of SACs with different metals; M can be any transition metal.	205
Figure 7.4: PXRD of Ag-NC samples.....	206
Figure 7.5: TEM images of (a, b) Ag-NC-0.048, (c, d) Ag-NC-0.024 and (e, f) Ag-NC-0.012 samples.	206
Figure 7.6: Illustration of SACs with multiple metal sites: (a) CoRh SAC and (b) CoRhMn SAC; Rh, Co and Mn atoms are presented in green, purple and pink colours.	207
Figure 7.7: (a) SEM, (b)EDX, (c) TEM and (d) PXRD of CoRh SAC.....	208
Figure 7.8: Tuning the size of HNB-1.	209
Figure 7.9: Synthesis of multi-shell HNB-1.	210
Figure 7.10: Tuning the size of HNB-2.	211

List of Tables

Table 2.1: Reactions catalysed by Rh SACs	46
Table 2.2: Rhodium loading in ZIF-8@RhTA and corresponding Rh-NC samples.	50
Table 2.3: Synthesis of ZIF-8@RhTA and Rh-NC.	76
Table 2.4: Summarized chemical composition data for ZIF-8@RhTA, Rh-NC and reference samples (as wt.%).....	80
Table 2.5: EXAFS fitting parameters at Rh K-edge for Rh SAC samples with various Rh loadings and Rh(TPP)Cl.	85
Table 2.6: EXAFS fitting parameters at Rh K-edge for Rh-NC-0.50.....	85
Table 2.7: EXAFS fitting parameters at Rh K-edge for Rh-NC-0.80.....	85
Table 2.8: EXAFS fitting parameters at Rh K-edge for RhCl ₃ ·3H ₂ O.	86
Table 2.9: EXAFS fitting parameters at Rh K-edge for Rh foil.	86
Table 2.10: EXAFS fitting parameters at Rh K-edge for Rh-NC-0.14 for Rh-N bonds.	87
Table 2.11: EXAFS fitting parameters at Rh K-edge for Rh-NC-0.14 for Rh-O and Rh-N bonds.....	87
Table 3.1: Cobalt loading in CoZn ZIF-8 samples and corresponding Co-NC-Ar and Co-NC-H ₂ samples...	95
Table 3.2: Synthesis of ZIF-8, CoZn ZIF-8, ZIF-67; tannic acid coating; pyrolyzing under Ar, 40% H ₂ /Ar and their sample codes.	123
Table 3.3: Summarized chemical composition data for CoZn ZIF-8, CoZn ZIF-8@KTA and reference samples (as wt.%)	134
Table 3.4: Summarized chemical composition data for CoZn ZIF-8, CoZn ZIF-8@KTA and reference samples (as wt.%)	135
Table 3.5: EXAFS fitting parameters at Co K-edge for Co-NC-Ar samples with various Co loadings, Co(TPP) and metallic Co	138
Table 4.1: Hydrogenation of nitroarenes catalysed by Rh SAC and Co SAC.	141
Table 4.2: Peak areas of the standard reference samples and the reaction mixtures obtained from the HPLC chromatogram.....	154
Table 5.1: Comparison of the ORR performance for catalysts in acidic medium.	165
Table 5.2: Stability testing of Rh catalysts in acidic medium.	166
Table 5.3: Comparison of the ORR performance for catalysts in basic medium.....	167
Table 6.1: Partial pyrolysis of ZIF-8 at different temperatures.	195
Table 6.2: Weights of electrodes, weights of NPC in the electrodes and NPC areal loading in the electrodes in aqueous, organic and ionic liquid medium.....	199
Table 7.1: Synthesis of ZIF-8@AgTA and Ag-NC.....	205

Chapter 1- Introduction

1.1 Introduction to MOFs

Metal-organic frameworks (MOFs) are crystalline materials that have high porosity and high surface area. They have coordination bonds between the metal ions and organic linkers. The pore size of MOFs can be controlled from angstroms to nanometres by changing the length of the organic linker. The pore walls of the MOFs can be functionalized by modifying the organic linker. Because of the high surface area and the high porosity, these MOFs have extensive applications. The synthetic strategy to typical MOFs is illustrated in Figure 1.1.

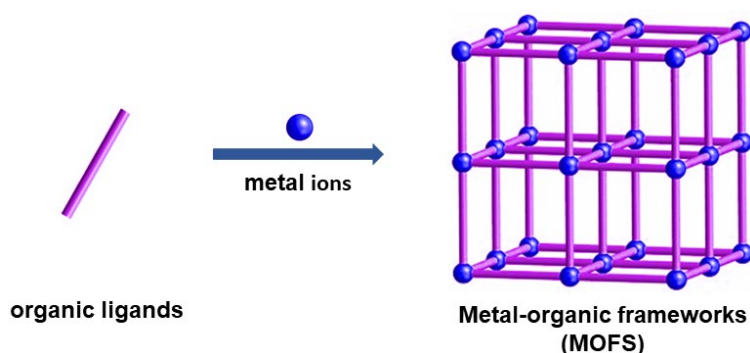


Figure 1.1: Synthesis strategy of MOFs; metal ions - blue, organic ligands - magenta.

1.2 Nomenclature of MOFs

Researchers have given several names to these crystalline materials over three decades due to the lack of a generally accepted definition. Some of those names are based on the chemical structure of the MOFs: such as porous coordination polymers (PCP),¹ porous coordinated networks (PCN),² zeolitic imidazolate frameworks (ZIF)³ and mesoporous metal-organic frameworks (meso MOF)⁴ Another way of naming MOFs is using the name of the university or lab where the MOF is synthesized. Materials Institute Lavoisier (MIL),⁵ Hong Kong University of Science and Technology (HKUST),⁶ and Massey University Framework (MUF)⁷ are a few examples. Using the empirical formula of MOFs which exhibits the stoichiometric ratios of metal and ligand in the MOF is another technique of nomenclature. Examples for such MOFs are $\text{Sc}_2(\text{BDC-NH}_2)_3$,⁸ $\text{Co}(\text{bdp})$,⁹ and $(\text{Co})_3(\text{OH})_2(\text{btca})_2$.¹⁰ Moreover, O’Keeffe and co-workers¹¹ have developed a system of symbols for the identification of MOF networks (topologies). In this nomenclature, they have developed reticular chemistry structure resource (RCSR) symbols. Every structure in the RCSR has a unique symbol. The IUPAC task group is currently revising the IUPAC 1984 recommendations for the nomenclature of MOFs.¹²

1.3 History of MOFs

In 1990 Robson proposed the self-assembly of metal nodes and the linear organic linkers could potentially form highly crystalline and porous materials. This work opened the doors to the world of MOFs.¹³ MOFs came to the light after the independent work performed by Kitagawa (in 1997) and Yaghi (in 1999).¹⁴⁻¹⁵ Synthesis of MOF-5 (Figure 1.2) from ZnO_4 metal clusters and 1,4-benzene dicarboxylate ligand led to the synthesis of thousands of MOFs, opening doors to a new pathway in the field of science.¹⁵ About 70 000 MOF materials had been reported to the Cambridge structural database (CSD), and the number is growing daily.¹⁶ MOFs have become a fast-growing field in chemistry due to their structural and functional tunability.

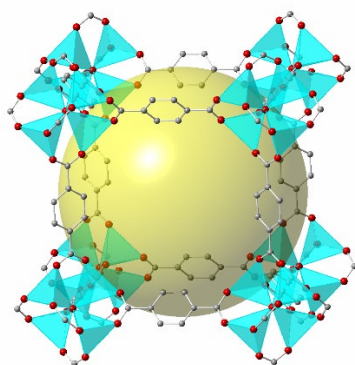


Figure 1.2: Crystal structure of MOF-5; Zn-Cyan, C-grey, O-red, Void space-yellow sphere and H is not shown for clarity.

After the synthesis of MOF-5, a series of MOFs was synthesized based on the skeleton of MOF-5, substituting the ligand with dicarboxylate linear linkers which had different lengths and different functional groups.¹⁷ These different linkers resulted in different pore sizes, surface areas, and chemical properties. As this new class of MOFs had a similar network topology as MOF-5, they were named isorecticular metal-organic frameworks (IR MOFs). This development led to the synthesis of a variety of MOFs by modifying the materials to fine-tune the properties of MOFs based on the applications such as gas separation, gas purification, gas storage, and catalysis.

1.3.1 Zeolitic imidazolate frameworks

Zeolitic imidazolate frameworks (ZIFs) are a sub-class of MOFs that are topologically isomorphic with zeolites. ZIFs are porous crystalline materials which composed of tetrahedral transition metal ions (eg: Zn (II), Co (II)) coordinated to imidazolate ligands.^{3, 18-19} The metal centers of ZIFs are coordinated with nitrogen atoms of imidazole ligands at 1,3 positions, making metal-ligand-metal bonds with a bond angle of 145° (Figure 1.3). This topology is very similar to Si-O-Si in zeolites.²⁰ The metal-imidazole bond length of ZIF is longer than the Si-O bond length of zeolites, making them more porous than zeolites.

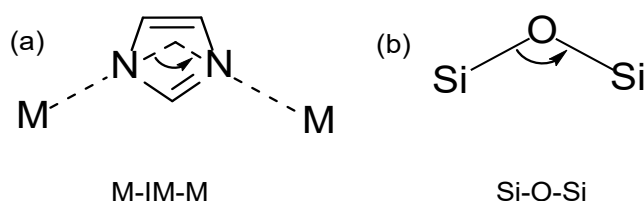


Figure 1.3: (a) The ligand metal bond in ZIFs and (b) zeolites.

A great structural diversity of ZIFs can be achieved by using functionalized imidazole ligands.²⁰ The structure of a ZIF primarily depends on the type of imidazole ligand, metal ion and the solvent used in the synthesis. By using different transition metals and different imidazole ligands a variety of ZIFs have been synthesized that exhibit many common zeolites topologies.^{19, 21} Yaghi and co-workers developed a high throughput protocol for the synthesis of ZIFs and by this method, 25 new ZIF structures were synthesized.²² Roughly 105 ZIFs are recorded in the literature by 2010.²¹

The most common method of preparing ZIFs is solvothermal/hydrothermal synthesis.²³ There are alternative synthesis methods such as microwave synthesis,²⁴ sonochemical synthesis,²⁵ mechanochemical synthesis,²⁶ oxide/hydroxide based solvent-free synthesis,²⁷ dry-gel conversion,²⁸ microfluidic synthesis,²⁹ and electrochemical synthesis.³⁰ Among the ZIFs which have been synthesized using different methods, so far ZIF-8 has been widely used for a variety of applications.

1.3.2 ZIF-8 and ZIF-67

ZIF-8 is composed of tetrahedral Zn(II) nodes which are coordinated with 2-methyl imidazole. ZIF-8 has a sodalite topology. When Co(II) is used instead of Zn(II) in the synthesis process it bridges with 2-methyl imidazole and the resulting ZIF is named ZIF-67. ZIF-8 and ZIF-67 have iso-reticular structures and they have similar lattice parameters. In ZIF-8/ZIF-67, each $\text{Zn}^{2+}/\text{Co}^{2+}$ ion is connected to four 2-methyl imidazole ligands and each ligand is connected to two metal ions (Figure 1.4). The $\text{ZnN}_4/\text{CoN}_4$ tetrahedra are connected through imidazole linkers resulting in cages 11.6 Å in diameter, which are connected through narrow six ring windows 3.4 Å in size.³

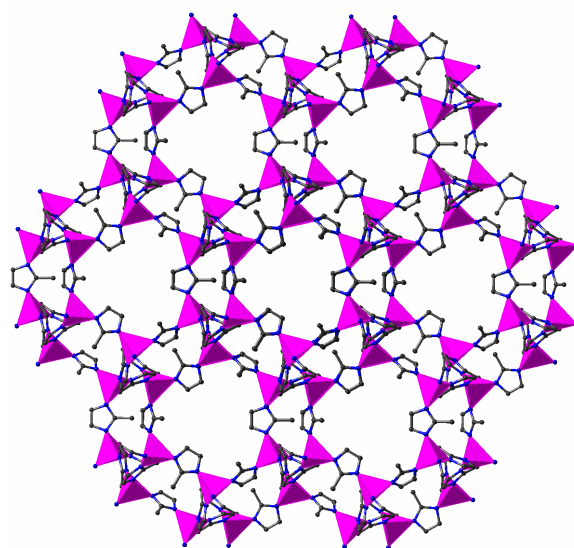


Figure 1.4: Structure of ZIF-8/ZIF-67; Zn/Co-purple, N-blue, C-black and hydrogen is not shown for clarity.

One of the features of these two iso-reticular ZIFs is that Zn(II) can be substituted by Co(II) without changing its topology. This can be achieved by one-pot synthesis by doping Co(II) in the synthesis of ZIF-8.³¹ Compared to other reported MOFs, ZIF-8/ZIF-67 have high thermal stability, high surface area, and can be synthesized easily with high purity at a low cost. Due to these excellent properties, they have been employed in numerous applications such as gas separation,³² sensing,³³⁻³⁴ and catalysis.³⁵

1.4 Application of MOFs

MOFs are mainly studied for gas storage,³⁶⁻³⁸ gas separation, and purification³⁹⁻⁴⁰ due to their high porosity. They are also applied as catalysis,⁴¹⁻⁴³ and in sensing⁴⁴⁻⁴⁶ applications (Figure 1.5). The gas storing MOFs have high porosity and high internal surface areas exceeding $5000 \text{ m}^2\text{g}^{-1}$ in many materials.⁴⁷⁻⁴⁸ The maximum porosity of MOFs is not always accessible due to the inability of complete removal of guest molecules, impurities, and defects in the crystalline structure. The examples for highly porous MOFs are NU-109E ($7000 \text{ m}^2\text{g}^{-1}$),⁴⁹ UMCM-2 ($6000 \text{ m}^2\text{g}^{-1}$),⁵⁰ MIL-101 ($5900 \text{ m}^2\text{g}^{-1}$),⁵ and MOF-177 ($5640 \text{ m}^2\text{g}^{-1}$).⁵¹

Hydrogen is considered a clean energy carrier due to its zero-emission. The first hydrogen adsorption MOF was recorded in 2003 by Yaghi.⁵² Since then, extensive studies are being carried out on the hydrogen storage of MOFs. Many studies have investigated hydrogen storage in MOF-5,⁵³ MIL-101,⁵⁴ UMCM-2,⁵⁰ and PCN-6⁵⁵. It has been found that the high surface area is the most important factor for hydrogen storage MOFs.

Using MOFs for the storage of natural gases such as methane is a smarter way. A methane adsorbing MOF was reported in 1997 by Kitagawa.¹⁴ Since then, the development of MOFs for the storage of methane has been abundant. However, there is no fast development as in hydrogen storing MOFs. HKUST-1 is reported as the highest methane storage MOF.⁵⁶

Carbon dioxide is a greenhouse gas that is contributing to global warming. Yaghi did pioneering work for CO_2 storage in MOFs (MOF177).⁵⁷ NH_4F treated MIL-101 has also emerged as a comparable one to MOF-177 for CO_2 storage.⁵⁸ By using amine-based ligands,⁵⁹ and post-synthetic modifications in MOFs,⁶⁰ the CO_2 uptake can be increased. MOFs are superior to conventional zeolites and activated carbon in gas storage applications.⁵⁸

Gas separation is another attractive application for MOFs. Compared to traditional gas separation materials such as zeolites and activated carbons, MOFs are different due to their variability in functional groups, pore size, pore shape, high surface area, and topology.^{39, 61} Depending on the metal nodes and the organic linkers the affinity to the gas changes. Modifications can be made to the functional groups of the organic linker to make the MOF tuneable to specific gases.

MOFs are employed in a variety of catalysis applications such as catalysis of organic reactions, CO oxidation, CO_2 conversion, hydrogen production, pollution remediation, electrocatalysis, and photocatalysis.⁶²⁻⁶⁴

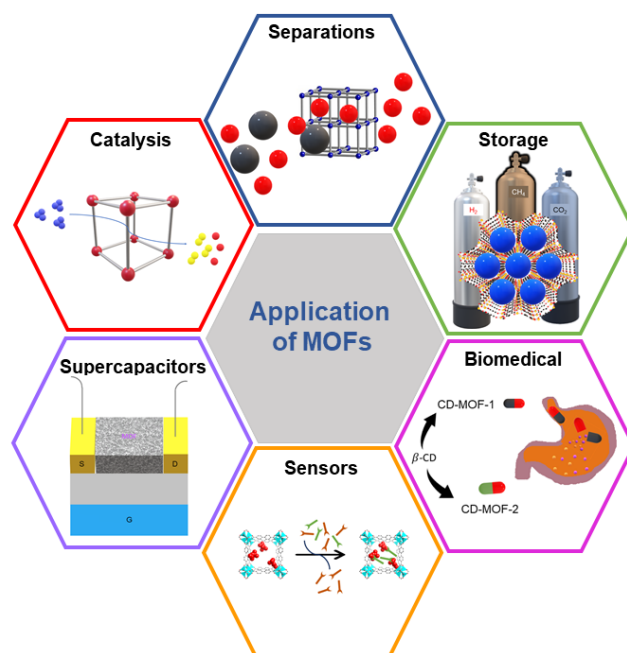


Figure 1.5: A cartoon presentation of the applications of MOFs.

i. Catalysis on open metal sites

In this strategy, the metal nodes of the MOFs act as catalysts. The MOFs like MIL-101 and HKUST-1 have coordinatively unsaturated metal clusters making them strong Lewis acid sites. Such metal clusters can strongly bind to the substrates. For example efficiency of catalytic decomposition of ozone by MIL-100(Fe) is higher than MIL-100(Cr) since the concentration of Lewis acid is higher in MIL-100(Fe) material.⁶⁵ Nikseresht et al. have reported using [Cu₃(BTC)₂] MOF as a catalyst in a Friedländer reaction to synthesize tacrine analogues.⁶⁶ The result of this research shows that the reaction is catalysed by Cu clusters and the role of the organic ligand in the MOF is negligible.

ii. Catalysis at defects:

Defects in MOFs are generated by the removal of either a linker or a cluster or a coordinated solvent from the parent structure. The level of defects can be tuned which will be discussed further in the coming sections. Although defect sites can act as a good platform for catalysis, their controlled synthesis is extremely challenging. Further, it is arduous to obtain the detailed structural information of these defected MOFs.

UiO-66 has been extensively used for defect-based catalysis. The catalytic activity of UiO-66 can be increased tremendously by introducing defects as they can make a huge impact on the structure, porosity, and Lewis/Brønsted acidities.⁶⁷ Using defective UiO-66 for catalysis of Fischer esterification of carboxylic acids in methanol,⁶⁸ and hydrogenation transfer reaction of biomass-derived levulinic acid⁶⁹ are reported. Moreover, defective UiO-

66 and UiO-67 have been used for ethanol dehydration,⁷⁰ and aerobic oxidation of alcohols.⁷¹ Use of defective MIL-101(Cr) is reported for the oxidation of indene.⁷² For cycloaddition of CO₂ and propylene oxide Epp et al. have synthesized three defective MOFs as MOF-525, PCN-222, and PCN-224.⁷³ Using defective ZIF-8 has also been reported to catalyse ring-opening of L-lactide.⁶³

iii. Catalysis on functionalized MOFs:

Introducing additional functionalities to the ligand or the metal sites of the MOF improves its catalytic activity. This can be achieved by post-synthetic modification or one-pot synthesis. The Telfer group changed the microenvironment around the site of catalysis in MUF-77 by introducing functional groups to the organic linkers.⁷⁴ This enhanced both the reactivity and the stereochemical selectivity for aldol reaction which would not be achieved by pristine MUF-77.

Post synthetically modified MOFs have been widely used for the catalysis of CO₂ epoxide coupling. For example, chloro-functionalized ZIF-95 has been used to solvent-free cycloaddition of CO₂ with epoxides.⁷⁵ An et al. reported a molecular iridium complex immobilized UiO-type MOF to enhance the catalytic hydrogenation of CO₂ to form formic acid.⁷⁶

iv. Catalysis on encapsulated species in MOFs:

The MOFs can host a variety of guest species due to their porous nature. There are four well-established strategies in encapsulating the guests in the MOFs namely; ship-in-bottle, bottle-around-ship, sandwich assembly, and in situ encapsulation.⁷⁷ The MOF offers stability for the encapsulated catalyst, and it acts as a selective barrier for the substrates too. Encapsulating metal nanoparticles,⁷⁸⁻⁸⁰ quantum dots,⁸¹ porphyrins,⁸² transition metal complexes,⁸³ polymers,⁸⁴ polyoxometalates,⁸⁵ ionic liquids,⁸⁶ carbon nanostructures, and dyes⁸⁷ in the MOF have been reported.

v. Catalysis by species supported on MOFs:

MOFs provide the anchoring support for catalytic species such as nanoparticles. Long et al.⁸⁸ reported dispersing Au and Pd bimetallic alloy on the surface of MIL-101 by simple a colloidal method for aerobic oxidation of cyclohexane. The bimetallic alloy supported on the surface of the MOF showed superiority in the catalysis over its pure metal counterparts and the mixture.

The catalytic activity and the selectivity of the guest species attached to the MOF can be enhanced by the modification of the surface hydrophobicity or hydrophilicity of the MOF.

This will increase the interaction of the substrate to the catalyst and stabilize the catalyst on the MOF support. The coating of polydimethylsiloxane on Pd nanoparticles/UiO-66 to increase the hydrophobicity has been reported.⁸⁹ This resulted in significant improvement in the catalytic activity compared to pristine Pd nanoparticle/UiO-66.

1.4.1 Limitations of MOFs as catalysts

There are some properties of MOFs that can limit their superiority in the catalysts. e.g. thermal and chemical stability. Although some robust MOFs are reported, many catalytically active MOFs are sensitive to air and moisture. As a result, they undergo hydrolysis, phase transformation, and amorphization even at room temperature.⁹⁰ There is a limitation in the reaction medium when using MOFs as catalysts. High acidic or basic media will degrade many MOFs.^{7, 74, 91} Not only the catalytic activity of a MOF is medium dependent; but also many MOFs are not even stable in water. So that the choice of the medium for the catalysis gets narrower when using MOFs as catalysts. Thus, it is challenging to employ MOFs in catalysis as the scope of the reaction conditions is limited.

The large-scale synthesis of MOFs is also challenging. The transport effects in the catalysis within the MOFs pores are yet to be studied in detail.⁹² So, there is a need for better and stable catalysts other than MOFs which still show the superior properties of MOFs. As a result, MOF-derived catalyst came into the picture to overcome the above limitations. Among them, single-atom catalysts derived from MOFs are a blooming field.

1.5 Single metal atom catalysts (SACs)

A catalyst provides an alternative route to a reaction, lowering the activation energy required for the reactants to reach the transition state. The classification of catalysts depends on the phase in which the catalysts and the reactants are present; homogeneous and heterogeneous catalysis are the two main forms. In homogeneous catalysis, the catalysts are in the same phase as reactants. Whereas in heterogeneous catalysis, the phase of the catalyst is different from the phase of the reactants or product. Thus, the separation of the catalysts from the reaction mixture is easier in heterogeneous catalysis.

Single metal atom catalysts are a new frontier in heterogeneous catalysis.⁹³⁻⁹⁴ In SAC the single metal atoms are distributed over a support. SACs maximise the efficiency of utilization of the expensive metals, cutting down the cost of catalysis. Supported single metal atoms have unique chemical and physical properties. The local chemical environment of the SACs is different from the conventionally supported nanoparticles (NPs) and metal catalysis. SACs have isolated metal atoms anchored by surrounding coordinating atoms on the solid support. Tailoring the local environment of SACs can optimize the geometric and electronic

properties of SACs which influences their reactivity. SACs can have a higher uniformity in the distribution of active sites in heterogeneous catalysis when compared to NPs. The spatially isolated metal sites of SACs inhibit the side reactions which occur in NPs. For example in the non-oxidative conversion of methane to ethylene, iron single-atom sites avoided the surface reaction between the radicals.⁹⁵ Thus, SACs have higher selectivity and a tuneable activity compared to conventional nanoparticles or metal catalysts.⁹⁶ The spatial interaction of single-atoms with the substrate of SACs is similar to the spatial interaction of homogeneous catalysts. Therefore, SACs bridge the gap between homogeneous and heterogeneous catalysis.⁹⁷

When decreasing the size of the particles, the surface free energy of the particles increases, positively influencing the specific activity which promotes aggregation (Figure 1.6).⁹⁸ To avoid aggregation, single metal atoms can be anchored on appropriate support that strongly interacts with the metal atoms. This stabilization will avoid aggregation during the reactions. SACs can be synthesised by a variety of methods.

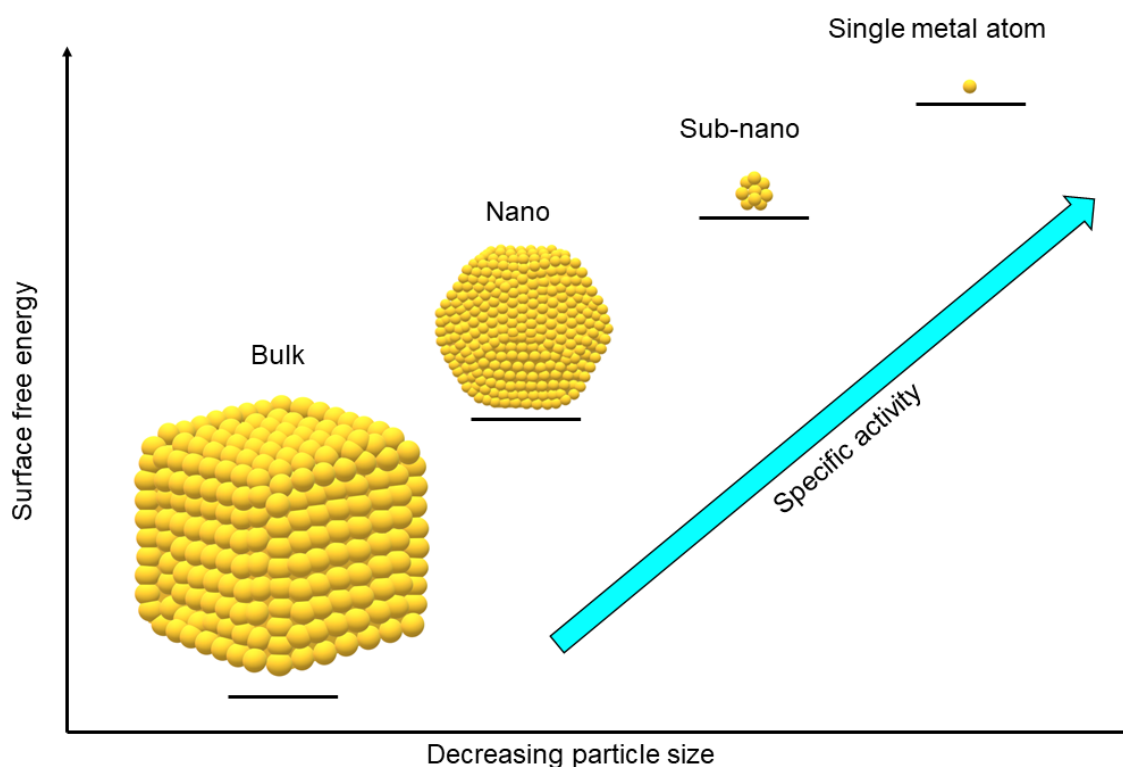


Figure 1.6: Schematic illustrates the change of surface free energy and specific activity with particle size.

1.6 Synthetic strategies to SACs

The approaches of synthesizing SACs can be categorized into a few strategies; defect energy strategy, spatial confinement strategy, coordination design strategy, and other strategies⁹⁹ such as photochemical synthesis,¹⁰⁰ iced photochemical synthesis,¹⁰¹ atomic layer desorption,¹⁰² and co-precipitation.¹⁰³

1.6.1 Defect engineering strategy

Defects on the catalyst support are designed to enhance the capturing and stabilising of the single metal atoms on the catalyst support. These defects can alter the coordination environment and surrounding electronic structure giving rise to vacancies and unsaturated coordination sites. These defective sites can trap the metal ions and anchor metal atoms during the post-treatment. The interaction between the metal atoms and coordinatively unsaturated sites enhances the stability of the single metal atom sites. Defective TiO₂ nanosheets with oxygen vacancies that stabilize single Au atoms can be given as an example for defective catalyst support (Figure 1.7).¹⁰⁴ The defect engineering mechanism uses the defects to trap metal precursors in the defects and stabilize the anchored single metal atoms.

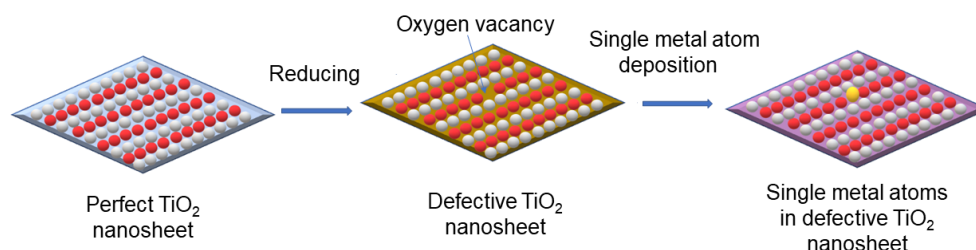


Figure 1.7: Synthesis procedure for isolated single metal atoms stabilized on defective TiO₂ nanosheet with oxygen vacancies by defective engineering strategy; O-red, Ti-white, single metal atoms- yellow.

1.6.2 Spatial confinement strategy

The spatial confinement strategy is achieved by spatially confining single metal ions/atoms into molecular cages such as zeolites, MOFs, and covalent organic frameworks (COFs). Stabilizing the single metal atoms and trapping them can be achieved by post-treatment of these synthesized materials to remove ligands of the precursors.

When zeolites are used as catalyst supports, the metal precursors can be confined by the pores of zeolites by ion exchange. This process is followed by a post-treatment to stabilise the single metal atoms by the neighbouring oxygen sites. An example is; the synthesis of Au single metal sites in zeolites supports.¹⁰⁵ For this Au(CH₃)₂(acac) was mixed with calcined zeolite and was stirred in dry n-pentane. After the removal of the solvent, the resultant powder has Au single-atom sites on zeolite support. Another approach to confine single

metal atoms on zeolite supports is in-situ encapsulation of metal precursors in the synthesis process of zeolites.¹⁰⁶

The pores of MOFs host uniform spatial confinement for metal precursors. For this, the molecular diameter of the metal precursors should be in between the pore diameter and the cage diameter of the MOFs. Thus, depending on the metal ion, a suitable MOF should be selected, encapsulating ferric acetate in the pores of ZIF-8 can be given as an example (Figure 1.8).¹⁰⁷ The pyrolysis process stabilizes the single Fe atoms, by the surrounding nitrogen species formed. Another approach to stabilize the metal precursors by MOFs is to confine the metals by coordinating with the organic linkers of MOFs,¹⁰⁸ followed by pyrolysis through which the attached metal ions can be stabilized.

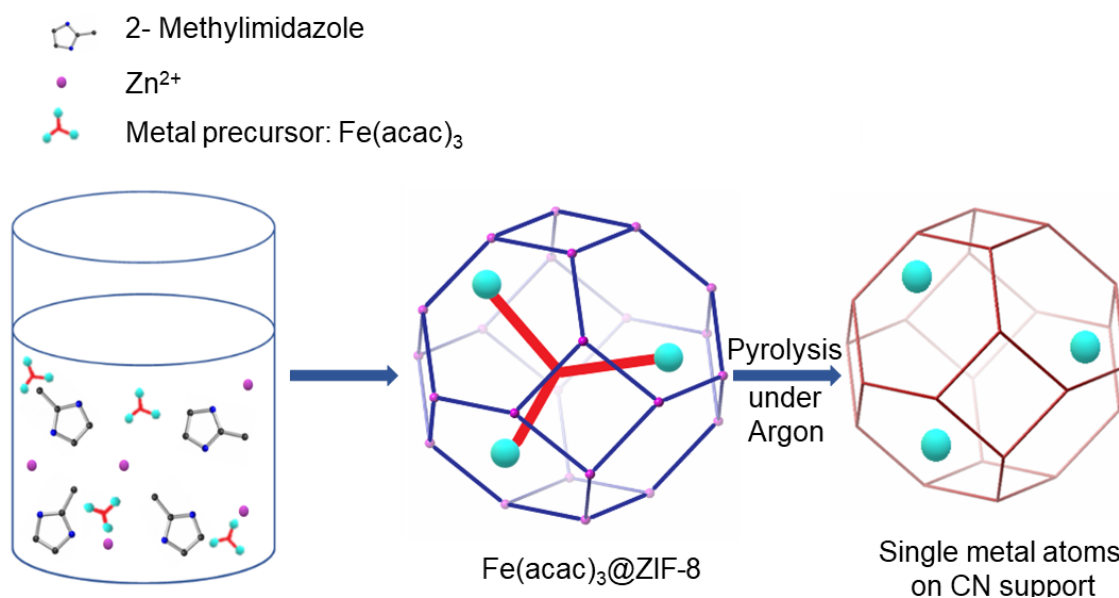


Figure 1.8: Preparation of single metal atom catalyst by spatial confinement strategy.

COFs also provide desirable microenvironments for metal precursors for confinement.¹⁰⁸ The uniform pore sizes and homogenous distribution of pores over the designable MOFs and COFs make them promising supports for single metal atom catalysts. The spatial confinement approach restricts the movement and agglomeration of the metal ions making the catalysts more durable for harsh conditions.

1.6.3 Coordination design strategy

The coordination design strategy is based on the concept of adsorbing and binding the metal precursors/atoms by coordination sites to prevent the migration of metal precursors/atoms (Figure 1.9). The resulting strong interactions of the metal species with the coordination atoms, such as N, O, P, and S occurring from the lone pairs of electrons act as strong anchoring spots.¹⁰⁸⁻¹⁰⁹ A coordination support with high a surface area and a higher

number of functional sites would allow high loading of single-atom sites. Using nitrogen-doped carbon materials as coordination materials is another perspective of coordination design strategy.¹¹⁰ Apart from that doping nitrogen or sulfur coordination sites into the substrates is another way of stabilizing the single metal atoms on the catalyst support.¹¹¹ When designing coordination sites it is important to consider the interactions between the metal atoms and the coordination sites and select them accordingly to maximise the interaction. The uniform distribution of the coordination supports on the catalyst is also a very important factor in the homogeneous distribution of single metal sites. The synthesis conditions such as pH and solvent type which affect the metal atom binding to the coordinated sites are the disadvantages in this strategy. Thus, careful consideration of these factors is necessary when selecting a synthesis method.

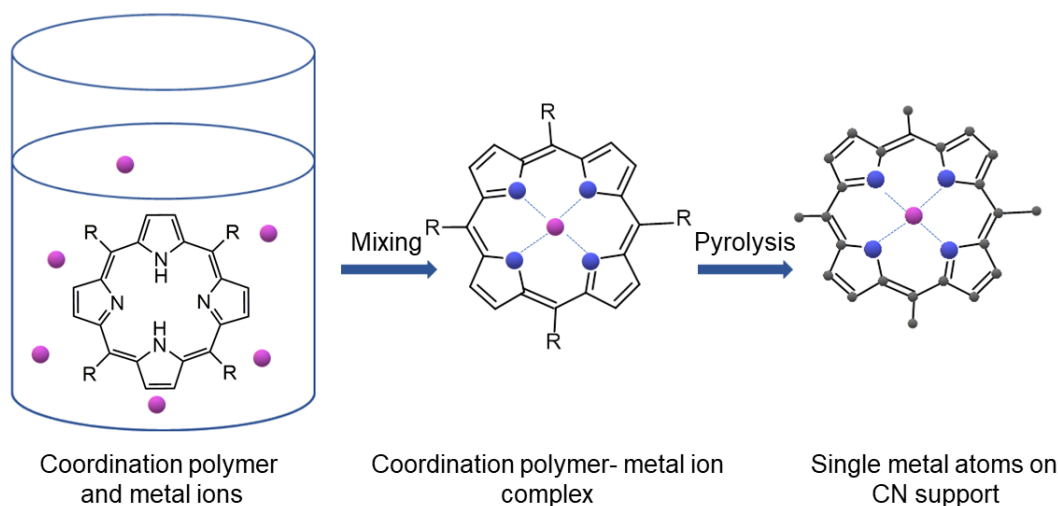


Figure 1.9: Synthesis strategy of single metal atom catalyst on hollow nitrogen-doped carbon coordination strategy; N-blue, C-grey, metal atoms-purple and hydrogen is not shown for clarity.

Other strategies

- **Galvanic replacement:** Galvanic replacement method is an electrochemical method, where the sacrificial template acts as the oxidising agent, and the other metal acts as the reducing agent; when they are exposed to each other in the same solution. The sacrificial metal will be oxidized and dissolved into the solution while the other metal will be reduced and deposited on the template surface.¹¹²
- **Photochemical synthesis:** In the photochemical synthesis of single metal atom catalysts, the metal ions are dispersed in an appropriate medium, and it is irradiated with UV light. The substrate in the medium generates free radicals under UV light and they play a key role in producing and stabilising single metal

atoms at a relatively high loading (1.5%).¹⁰⁰ The produced single metal atoms make coordination bonds with the substrate in the medium resulting in single metal atom catalysts.

- **Iced photochemical synthesis:** Iced photochemical synthesis is a one-step advanced process for the photochemical synthesis of single metal atom catalysts. In iced photochemical synthesis, the solution that contains the metal ions is frozen rapidly with liquid nitrogen before being exposed to UV radiation to restrict the thermal motion of the metal atoms (Figure 1.10).⁷⁷

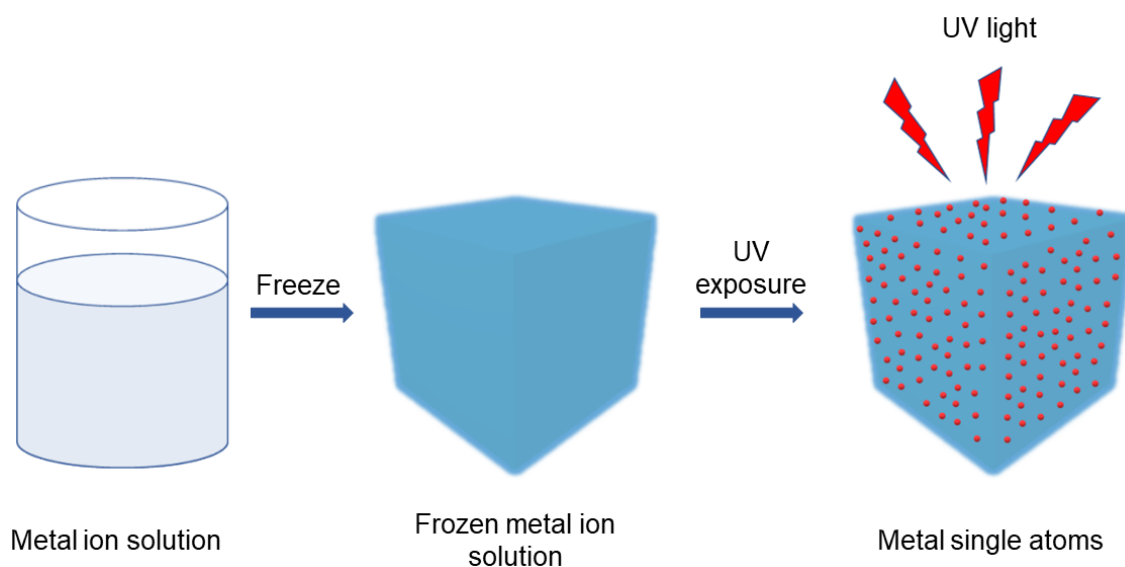


Figure 1.10: Synthesis of single metal atom catalyst via iced photochemical synthesis; metal atoms- red.

- **Atomic layer deposition:** Atomic layer deposition provides a powerful approach to produce single metal atom catalysts. This is a gas phase chemical process, where the metal precursor acts as the high vapor pressure material, and it is reacted with the active sites of the substrate. This is the first half of the reaction. Then the precursor flow is stopped. After that, the excess precursor and the reaction byproducts are removed by an inert gas or vacuum. In the second half of the reaction, the metal precursors are reduced to single metal atoms by a reducing agent. And also, removing of remaining ligands of the metal precursor also takes place. This cycle can be repeated until the desired layer thickness is achieved.¹¹³
- **Atom trapping:** In this method, the metal precursors are mixed with the substrate and heated to a higher temperature in the air. The metal atoms are evaporated and trapped in the substrate as single metal atoms. For this to happen, it is necessary to select a metal and a substrate that have high interaction capabilities.

1.7 Synthesis of SACs by pyrolyzing MOFs and MOF composites

MOFs are not only catalysts by themselves, but also, they can serve as precursors to develop highly stable SACs. The metal nodes and the organic ligands of MOFs serve as precursors for the synthesis of SACs. There are several strategies to make SACs from MOFs and MOF composites. By coordinating introduced metal sites in the position of metal nodes, organic ligands, and pores of the MOF, single metal atom sites can be introduced. There are two types of MOF-based SACs: MOF-supported SACs, which retain the MOF structure, and MOF-derived SACs, which are obtained by chemical or thermal decomposition of MOFs.

The main constraint of using MOFs as supports for single atoms is their low chemical and thermal stability. To overcome this drawback, after introducing single metal sites to the MOF, it can be pyrolyzed. In this technique, MOFs act as sacrificial templates. The MOFs will be partially or completely carbonized depending on the pyrolysis temperature and the inert conditions. Based on the thermal stability of the metal nodes of the MOF, they will be evaporated or will remain in the support. The remaining unwanted metals of the pyrolyzed MOF can be removed by post-treatment. During the pyrolysis process, the metal precursors are reduced to single metal atoms. The pyrolysis temperature, inert gas, and the dopant metal concentration of the guest metal play a key role in making SAC. One or more of the mentioned factors should be optimized to obtain single metal atoms on the carbon support. Otherwise, it will give rise to metal nanoparticles. In the pyrolysis process, the N and O atoms (also the other atoms like P and S) of the organic linkers coordinate with the single-atoms increasing the stability of highly mobile single-atoms.

Synthesis strategies of SACs by pyrolyzing MOFs and MOF composites

In recent years several MOF-based strategies have been invented to synthesize SACs. Mainly these strategies can be divided into two parts: pyrolysis of pristine MOFs and pyrolysis of MOF composites. In this section, these strategies will be discussed in detail with examples.

Pyrolysis of pristine MOFS

1.7.1 Single metal strategy

MOFs have homogeneously dispersed metal nodes connected by organic ligands. Direct pyrolysis of pristine MOFs is one way of preparing SACs. During the pyrolysis, the organic ligands of the MOF transform into carbon support attaching in situ reduced metal nodes into single metal atoms. ZIF-8 is a commonly used precursor to synthesize Zn SACs. Yang et al.¹¹⁵ reported a Zn SAC derived from hollow porous ZIF-8 based on the template growth

followed by pyrolysis. This catalyst was used to catalyse CO₂ cycloaddition with epoxides. By direct pyrolysis of Ni-MOF, a Ni SAC had been synthesized to catalyse hydrogen evolution reaction (HER).¹¹⁶ Another example of a SAC synthesized single metal strategy is Mn SAC synthesized by direct pyrolysis of Mn-based MOF for oxygen reduction reaction (ORR).¹¹⁷ The synthesis of these catalysts was followed by an acid wash to remove the metal nanoparticles/ metal oxides generated during the pyrolysis process.

The drawback in this strategy is during the pyrolysis process two or more metal nodes can be agglomerated giving rise to metal NPs. These NPs can be removed by post-treatment like acid washing followed by another heat treatment to repair the damage carbon support, increase the structural stability and catalytic activity.

1.7.2 Mixed metal strategy

The metal nodes in a MOF can be replaced by the desired metal ions. It is possible to introduce two or more guest metals in this strategy. This can be achieved by one-pot synthesis or post-treatment. The introduced metals replace the nodes of the MOF with homogeneous distribution in the MOF. So far, Zn-based MOFs are frequently used to make bimetallic MOFs. This is due to the convenient removal capability of Zn in the MOF as it poses a low boiling point (907 °C) compared to other transition metals. Among the Zn MOFs, ZIF-8 is considered the most promising MOF for this strategy. The Zn nodes in the ZIF-8 can be replaced by bivalent metals of similar size. In the pyrolysis process, the Zn nodes will be evaporated at high temperatures and the introduced metal ions will turn into SAs making strong coordination bonds with N and C.

Zhang et al.¹¹⁸ reported Fe SAC was synthesized via doping Fe³⁺ ions in the synthesis of ZIF-8 and pyrolyzing it. As ZIF-8 and ZIF-67 are isostructural, synthesis of Co SACs by pyrolyzing Co-doped ZIF-8 is a popular method (Figure 1.11). Co SACs prepared by this method, have been used in catalysing reactions such as hydrogenation of nitroarenes¹¹⁹, selective dehydrogenation of formic acid,¹²⁰ and ORR.¹²¹

In the mixed metal strategy, the nodes of the MOF act as fences to expand the distance between the dopant metal atoms. The doping of the guest metal should be optimized to obtain single atoms after the pyrolysis. The drawback in this method is, not all the metal ions can coordinate with the ligand of the MOF replacing the nodes to form the bimetallic MOF. Mixed metal MOFs can be obtained if the doping metals can give isostructural MOFs.¹²² Selecting a guest metal that does not match the size and the charge of the metal node of the MOF can lead to defects in the pristine MOF. Wrongly selected guest metals can lead to the formation of crystal structures that are different from the original MOF. Thus, the dopant

metal should be selected carefully in the mixed metal strategy. Noble metals have been rarely dispersed in MOFs using this strategy.

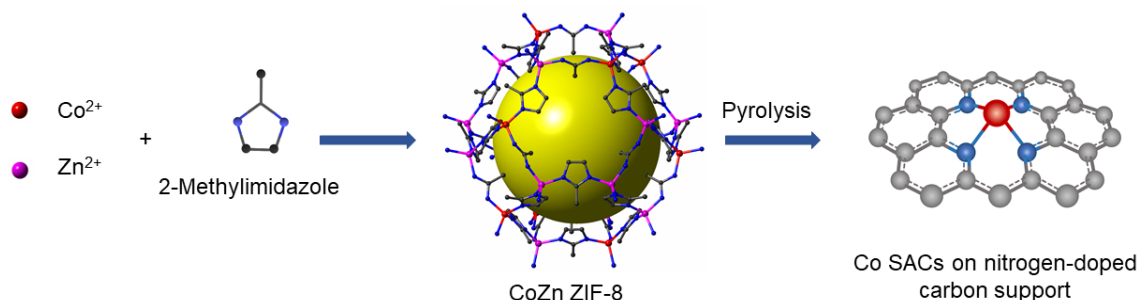


Figure 1.11: Synthesis of SACs by mixed metal strategy.

1.7.3 Metal coordinating ligand strategy

In this strategy, the guest metals will form coordinate bonds with the organic linkers of the pristine MOFs without replacing the nodes of the pristine MOF. These ligands have additional coordination sites to coordinate with the guest metal ions. The organic ligands of the MOF can also be designed in a way to increase the interaction with the single atoms of interest to strongly anchor them and stabilize on the skeleton of the MOF. Functionalized organic ligands in MOFs are a great approach to anchor noble metals to the MOFs, which have difficulties with mixed metal strategy. In the pyrolysis process, the guest metals will make coordination bonds with N and C in the carbonized support.

For example, UiO-66-NH₂ has Zr-based nodes that have coordination bonds with the carboxylate groups. The ligand of this MOF has an NH₂ group that is not coordinated with the metal nodes of the MOF, giving additional coordination sites. Wang et al.¹⁰⁸ has anchored Ru sites on the uncoordinated amine groups of UiO-66-NH₂ and synthesized Ru SACs. Due to the strong interactions between the empty d orbital of Ru atoms and lone pair electron of N (NH₂) the migration and diffusion of Ru atoms are limited during the pyrolysis process. Thus, it avoids aggregations and forming Ru nanoparticles. A tungsten SAC has also been synthesized by a similar method; and performs as a good catalyst for hydrogen evolution reaction (HER).¹²³

Another way of synthesizing SACs by this method is using a porphyrin ligand for the synthesis of MOFs and incorporation of single metal sites to the porphyrin. He et al. reported Zr-based porphyrinic MOF hollow nanotubes. A series of noble metals such as Ir, Pt, Ru, Au, and Pd ions could be immobilized in the ligand center of this porphyrinic MOF by solvothermal method and SACs can be obtained after the pyrolysis.

The drawback in this method is the chemical etching should be done after the pyrolysis to remove the metal atoms/oxides generated by the nodes of the pristine MOF. If the distance of the organic linkers which attach the ions of interest are close to each other, it will lead to aggregations of the single metal atoms. Thus, organic linkers and metal ions should be carefully chosen in this strategy to avoid aggregation of the SAs in the pyrolysis process.

1.7.4 Metal coordinating mixed ligand strategy

This strategy is similar to the metal coordinating ligand strategy but uses two types of ligands to construct MOFs. Here one type of ligand has additional coordination sites while the other ligand does not have any additional coordination sites to host the guest metal. The MOF synthesized using the mixed ligands has the same topology and crystallinity as the pristine MOF. By changing the ratio of the ligands, the distance between adjacent metallated ligands can be adjusted. Thus, the SAs resulting from the pyrolysis process will be separated enough to avoid agglomerations and not result in any nanoparticles. Controlling the ratio of the metallated and pristine ligands to make SACs is similar to controlling the doping metal amount in the mixed metal strategy.

For instance, Jiao et al.¹²⁴ synthesized a Zr MOF with 20% of Fe-TPP and 80% of H₂-TPP porphyrin ligands. The resulting Zr-MOF was pyrolyzed to reduce Fe centers to Fe SACs. The resultant Fe SAC demonstrated excellent performance in catalysing ORR. Ni SAC has been synthesized by pyrolyzing a Zn-based MOF which has 2-methyl imidazole and Ni-porphyrin as organic linkers.¹²⁵ This has been used for electrocatalysis of triiodide reduction in hybrid photovoltaics. The drawbacks of this strategy are the same as the metal coordination ligand strategy. But this strategy has the advantage of the controlled spatial arrangement of the guest metals in the MOF over the other strategy.

Pyrolysis of MOF composites

1.7.5 Micropore confinement strategy

In this strategy, the metal ions of interest are trapped in the uniform pores of MOFs as their ion precursors and pyrolyzed to obtain SACs. The pores of the MOF will act as cages for the metal precursors preventing the migration of the metal precursors in the pyrolysis process and avoiding agglomeration of single-metal atoms. Metal precursors can be trapped in the MOF cages by one-pot synthesis or post-synthesis. By changing the length of the ligand of the MOF, the pore size of MOFs can be increased or decreased to tailor the size of the guest metal precursors. The tailorable porosity of MOFs makes them an excellent host to encapsulate the metal precursors.

For example, Fe SAC has been synthesized by this strategy to catalyse ORR.¹⁰⁷ Li's group has encapsulated Fe(III) acetylacetonate precursors in the cages of ZIF-8 which has a cavity diameter of 11.6 Å and a pore diameter of 3.4 Å. The molecular diameter of the metal precursors is 9.7 Å. Thus, one metal precursor is trapped in one cavity of ZIF-8. In the pyrolysis process, the metal precursors are reduced to single metal atoms anchored on N-doped carbon support. Wang. et al. reported a Fe SAC synthesized by the same method for the catalysis of ORR.¹²⁶ Ni(NO₃)₂ has been trapped in the small hexagonal windows of ZIF-8 and pyrolyzed to obtain Ni SAC for the catalysis of electro reduction of CO₂.¹²⁷ ZIF-8 is extensively being used to trap the metal precursors as it is easy to get rid of Zn by the thermal treatment.

The size of the precursors should be smaller than the size of the cavities of the MOF to trap them inside the cavities. If a cavity of a MOF host has more than one metal precursor, in the pyrolysis process the precursors will reduce to their single-atom and agglomerate forming nanoparticles. To prevent this, the size of the precursors should be bigger than the half size of the MOF cavity, so that two metal precursors will not be trapped in one cavity. Therefore, metal precursors with large ligands are commonly used. And also, the metal precursors should not make any other MOFs with the ligand or the nodes of the pristine MOF. In this strategy, the removal of metal species generated from the nodes of the MOF is done by acid washing. Thus, to prepare SACs by this method, MOFs and precursors should be carefully selected.

1.7.6 Composites of MOFs with other functional materials strategy

The use of functional materials such as graphene, graphene oxides, polymers, surfactants, or other sources with additional coordination atoms with MOFs is a promising strategy to form SACs with controlled morphology. Other functional materials can be added by the one-pot method or post-synthesis method. These functional materials are confining the guest metal ions inside the MOF; so that it avoids aggregation of SAs during the pyrolysis process. Also, these functional materials provide extra coordination sites other than the ligands of the MOFs to coordinate SAs during the pyrolysis and strongly establish them in the carbon support.

For instance, in the synthesis of ZIF-8, NiCl₂ and dicyandiamide (DCD) were added as the guest metal and the additional functional material.¹²⁸ Ni ions and DCD either attached or absorbed to ZIF-8. Pyrolysis of this material is resulting in Ni SACs with rich N content in the carbon support. Apart from the N sites of the ligand of the ZIF-8, N sites of DCD also

act as anchoring supports to Ni SAs which resulted in the pyrolysis process. This Ni SAC has been used for the catalysis of electrochemical CO₂ reduction.

Bulky functional materials can also be used to disperse the MOFs and take the advantage of the additional coordination atoms in the functional material in the process of pyrolysis. So, depending on the requirement, the functional materials should be selected. Liu et al.¹²⁹ reported using graphene oxide (GO) to disperse Fe-doped ZIF-8. In the pyrolysis process, the MOF was melted on the graphene sheet with Fe SACs on the N-doped carbon layer. This Fe SAC had a higher surface area and was used to catalyse ORR. Another example of this strategy is a synthesis of Cu SAC by pyrolyzing Cu-doped ZIF-8 mixed with polyacrylonitrile (PAN) for the catalysis of CO₂ electroreduction to methanol.¹³⁰

The MOFs can be coated with functional material and then pyrolyzed to enhance the surface areas and the pore volumes of the resulting SAC. Hou et al.¹³¹ reported the synthesis of Fe SAC by pyrolysis of SiO₂ coated ZIF-8 with encapsulated Fe precursors. The formed core-shell Fe SAC was acid washed to remove silicon dioxide coating. The role of the coating here is to make the overhang-eave-like structure of the catalyst. This Fe SAC was used to catalyse ORR. Similarly, Fe SAC was synthesized by coating a polymer that contains N, P, and S.¹³² This polymer coating was decomposed during the pyrolysis making N and P rich carbon support for single Fe sites which enhanced the catalytic performance in ORR.

The functional materials should not make any coordination bonds with the nodes of the MOF or ligands of the MOF. It is preferred that the functional material is smaller than the cavities of the MOF if the spatial distribution of the guest metal is expected to be achieved by the addition of the functional material. Hence, it can be homogeneously dispersed in the cavities of the MOF. The ideal situation would be the trapping of each metal precursor and functional material in one cage of the MOF. The functional material should not be competitive with the metal precursor in the encapsulation process. When using bulky functional materials to increase the surface area of SACs, it should be made sure that the MOFs are attached to the bulk materials before the pyrolysis. Otherwise, homogeneous distribution of the SAs could not be achieved by this method. For the coatings, it is convenient to use a functional material that decomposes in the pyrolysis process, so that additional treatment will not have to be done to remove it.

1.7.7 Synthesis of SAC by bulk metals: top-down strategy

All the above strategies prevent the formation of NPs and stabilize the SAs on the nitrogen-doped carbon support. In this strategy, SACs are synthesized using NPs or bulk metals as the precursors by employing the strong metal-support interaction to establish

single-atoms on the support. According to DFT calculations, at relatively low temperatures (300 -900 °C) sintering is dominant, whereas atomization is dominant in higher temperatures (900 -1000 °C).¹³³ Thus, at higher temperatures, the bulk metals are atomized, and these atomized metals are stabilized by N sites in the C support. Compared to metal-metal bonds, metal-N bonds have more stable coordination at higher temperatures to provide the driving force to atomization.

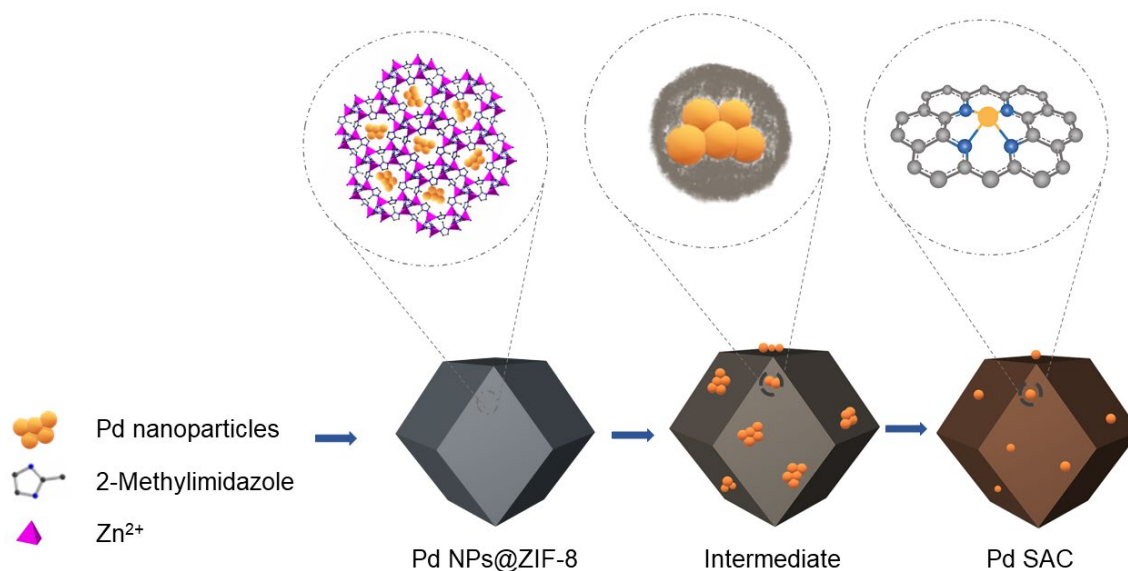


Figure 1.12: Synthesis of SACs by top-down strategy.

For example, Yang et. al¹³⁴ loaded Ni nanoparticles on the surface of NC support prepared by simple pyrolysis of ZIF-8. Then this was pyrolyzed at a higher temperature and resulted in Ni SAC. Ni NPs can break surface C-C bonds in the C support and enter the C support at high temperatures. When Ni NPs are exposed to N sites of the C support, Ni-N bonds are made by stabilizing Ni SAs. The fabrication of catalyst support from SAs by cheap and available bulk material is also reported.¹³⁵ Using this method a Cu SAC has also been synthesized by placing ZIF-8 and Cu foam separately in a tube furnace and pyrolyzing under NH_3 gas.¹³⁵ In this way bulk Cu has directly transformed to Cu SAC on N doped C support with the help of NH_3 to haul the Cu atoms from the Cu foam. Another method of making SACs by this strategy is coating NPs with a MOF and pyrolyzing to a high temperature to obtain SACs. In one pot synthesis, ZIF-8 was synthesized around Pd NPs and the pyrolysis of this material resulted in Pd SACs (Figure 1.12) which exhibited better catalytic activity in semi hydrogenation of acetylene.¹³³

1.8 Characterization techniques for SACs

Characterization of SACs to understand their structure is challenging. It is important to identify the SAs, their spatial distribution, and coordination in the catalyst support. Apart from powder XRD, SEM, TEM, TGA, FTIR, Raman spectroscopy the following techniques are used: aberration-corrected high angle annular dark-field scanning transmission electron microscopy (HAADF-STEM), X-ray photoelectron spectroscopy (XPS), X-ray absorption spectroscopy (XAS) including X-ray absorption fine structure (EXAFS) and X-ray absorption near edge structure (XANES). The atomic structure of SAs on the catalyst support cannot be observed with just one technique. A combination of these characterization techniques helps to understand the atomic configuration of SACs. In this section, these high-end techniques will be discussed in detail.

1.8.1 Aberration-corrected high angle annular dark-field scanning transmission electron microscopy (HAADF-STEM)

With the rapid development of microscopy techniques, STEM combines the principles of SEM and TEM. It can directly take the images of single metal atoms which are dispersed over the catalyst support. Therefore, the spatial distribution of SAs can be determined by this characterization method.

In the STEM, an electron beam is accelerated through a vacuum using a high voltage and focused on the sample by a set of magnetic lenses (Figure 1.13). This small electron probe scans through the sample. When the incident electron beam hits the specimen, the electrons are transmitted through the sample. There are several detectors to detect these beams resulting from the sample. The higher the atomic number (Z) of the elements in the sample, the more of the electrons of the incident electron beam are scattered to higher angles due to higher electrostatic interactions between the nucleus of the elements and the electron beam, called Rutherford scattering. High angle annular dark-field detectors (HAADF) collect the electrons scattered to high angles.¹³⁶ Thus, atoms/clusters of the elements of the sample with high Z values are visible as bright spots in HAADF STEM images. The intensity of these bright spots created by the Rutherford scattering is approximately proportional to the square of the atomic number (Z^2) of the scattering atom. Many SAs of SACs have high atomic numbers and they are dispersed on NC supports that have low atomic values. Consequently, in the HAADF STEM image of these SAs, due to their higher atomic number, SAs appear as bright spots on a dark background created by the low atomic number of the atoms that make the catalyst support.

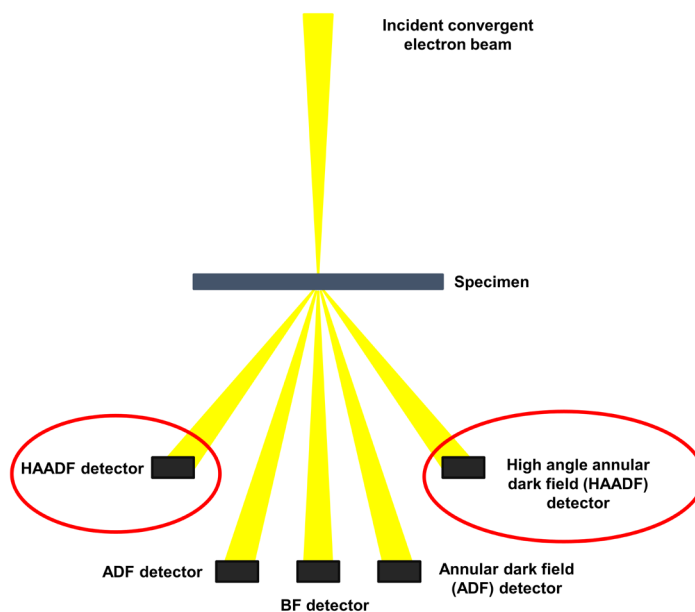


Figure 1.13: The path of the electron beam of STEM.

Bright-field (BF) detectors are located on the path of the incident electron beam. The elements that have smaller Z values will scatter the incident electron beam to lower angles due to smaller electrostatic interactions between the nucleus of the element and the electron beam. These electrons will be detected by the BF detector. Thus, the BF STEM images of lower Z elements will be brighter due to the higher electrons detected and higher Z elements will result in dark spots in the image. Thus, in a STEM image of SAC, the SAs will be visible as bright spots in the dark background in the HAADF STEM image. In the complementary BF STEM image, the SAs will be visible as dark spots in the bright background.

HAADF-STEM and BF-STEM can provide details about the spatial distribution of the SAs on the catalyst support. The tomography can provide details of the geometric distribution of the catalyst. In 3D tomography, the electron beam is focused at one point of the sample and the sample is tilted in the microscope from $+70^\circ$ to -70° increasing the scattered angle from 1° . The electrons scattered by the high angles are detected by the HAADF detector. These images are processed by algorithms and by powerful software such as Imaris, Amira, and Auto Quant to reconstruct the 3D image. This is a very time-consuming process.

1.8.2 X-ray Photoelectron Spectroscopy (XPS)

XPS is a surface-sensitive and element-specific technique. This gives information about the composition and oxidation state of the elements in a sample. XPS was developed by K. Siegbahn group in mid-1960. He was awarded the Nobel prize for physics in 1981 for this discovery.¹³⁷ This concept is based on the photoelectric effect outlined by Einstein in 1905; the ejection of an electron from a surface when a photon strike it.

In XPS, photons of specific energy are incident on the sample causing electrons of the elements which are near the surface of the sample to escape (Figure 1.14). These electrons are detected by a hemispherical analyzer. Photoelectrons originating from more than 10 nm below the surface do not have sufficient energy to be detected due to the inelastic collisions thus giving rise to the background signal. The kinetic energy (KE) of the photoelectrons depends on the photon energy and the binding energy (BE) of the electron. The binding energies of the electrons are like the fingerprints of the elements. Thus, knowing the photon energy ($h\nu$) and the KE of the escaped electron, the BE of the electron can be calculated. BE of the solids is measured with respect to the Fermi level of the solid. So, the work function should also be considered when calculating the BE. The BE depends on the element, orbital and the chemical environment of the atom from which the electron is emitted from Eq. 1.1).

$$KE = h\nu - (BE + \phi) \quad \text{Eq. 1.1}$$

Here, KE is the kinetic energy of the escaped electron. $h\nu$ is the energy of the photoelectron. BE is the binding energy of the photoelectron, and Φ is the work function.

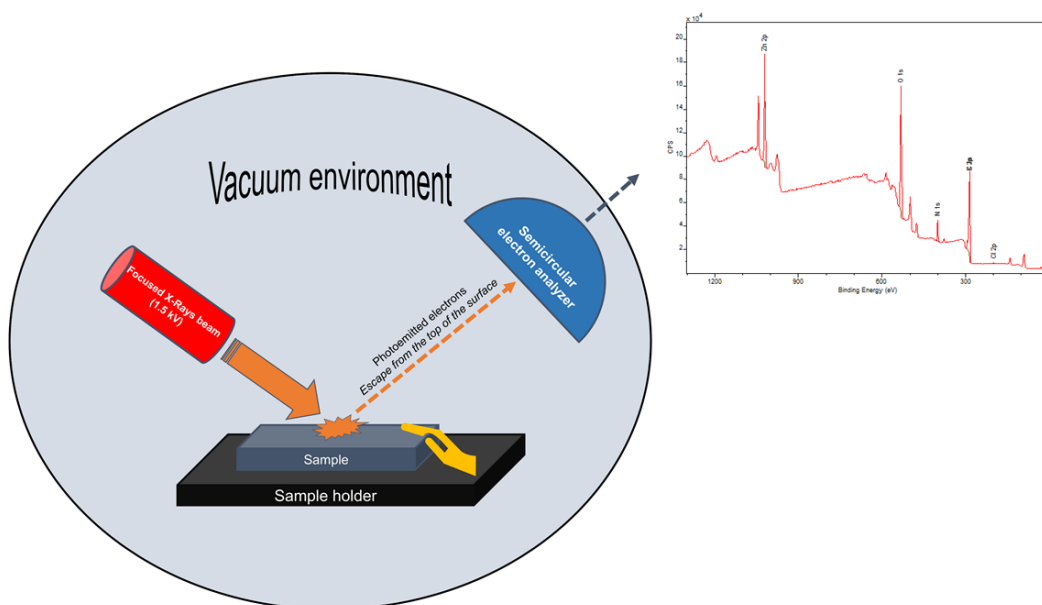


Figure 1.14: The path of the X-ray beam in XPS.

XPS is a quantitative technique. The survey scan gives information about the elements present in the sample, with BE ranging from 0 to 1400 eV. The number of photoelectrons recorded for given binding energy is proportional to the number of specific atoms on the surface. The elemental composition of a sample is determined by the intensities of the particular element.

The narrow scan of XPS focuses on a specific element of the sample. The peaks in the narrow scan are originating from the photoelectrons escaping from the orbitals of the atoms in the sample. The number of peaks resulting in the narrow scan is orbital dependent. If a photoelectron escape from a s orbital it gives rise to one peak whereas p, d, and f orbital result in closely spaced doublets due to the spin-orbital coupling in the final state. For spin-orbital coupling either LS (Russel-Saunders) coupling approximation model or the j-j coupling approximation model is used. The relative intensities of the doublets are determined by Eq. 1.2 and Eq. 1.3. Using equation 1.2 permitted j values are calculated. Then the j values are used in the Eq. 1.3 to calculate the relative intensities. Angular quantum number (l) describes the shape of the orbital. For s, p, d, and f orbitals l is 0, 1, 2, and 3 respectively. Spin angular momentum (s) can be +1/2 or -1/2.

$$j = l \pm s \quad \text{Eq. 1.2}$$

$$ratio = (2j_1 + 1) : (2j_2 + 1) \quad \text{Eq. 1.3}$$

The spin-orbit splitting is not evident with s orbitals. The j values for the spin-orbital doublets are as follows; p orbital: 1/2 and 3/2, d orbital: 3/2, and 5/2, and f orbital: 5/2 and 7/2. The relative intensity of these doublets determines the probability of transition to the state during photoionization. So, the relative intensities of the doublets in p, d, and f orbitals are 1:2, 2:3, and 3:4.

The high-resolution scans give the corresponding binding energies of a specific element. By this, the oxidation number of the element can be determined. Further, based on the binding energies of the high-resolution peaks of a particular element of the functionality the element can be determined, eg: carbonyl C, C-OH, and graphitic C.

1.8.3 X-ray Absorption Spectroscopy (XAS)

X-ray absorption spectra are measured using synchrotron sources, which provide full range X-ray wavelengths, and a monochromator to select specific energy. There are two regimes in the XAS spectrum: X-ray absorption near-edge spectroscopy (XANES) and extended X-ray absorption fine structure (EXAFS). XANES has an energy range beyond the absorption edge by 30 to 50 eV. EXAFS has an energy range above the absorption edge from 50 to 1000 eV or more. XANES is applied to determine oxidation state and geometry, while EXAFS is used to determine coordination number, neighbouring atoms, and bond distances.

In XAS, an X-ray photon with an energy more than the binding energy is absorbed by a core level electron (such as 1s or 2p) and the excess energy is transferred to the photoelectron which is ejected from the atom. (Albert Einstein received the Nobel prize for describing this effect.) When the energy of the X-ray has an energy equal to the binding energy of the electron in the core level, there is a sharp rise in the absorption. This is called the absorption edge. The intensity of the absorption coefficient is measured as a function of X-ray energy which is above the binding energy of a known core-level atom. The core-level electrons of every atom have well-defined binding energies. So, based on the element the energy of the X-ray can be tuned to an appropriate absorption edge.

Once the photoelectron is emitted, the atom will be in an excited state with a core hole. The excited atom will decay within a few femtoseconds either by fluorescence or the Auger effect. In fluorescence decay, a higher energy electron fills the core hole. The excess energy is emitted as a photon. This characteristic fluorescence energies can be used to identify the atoms and quantify them. In the Auger effect also, a higher energy electron from the core level fills the core hole. But here the excess energy is transferred to another electron and a secondary electron is emitted. The energy of this Auger electron is characteristic of the atom, and it can be used to identify and quantify the atoms. The fluorescence effect dominates in the hard X-ray regime (>2 keV). The Auger effect is dominated in the lower X-ray regime (<2 keV). Either of these processes can be used to measure the change in absorption coefficient as a function of X-ray energy (Eq. 1.4 and Eq. 1.5). However, the fluorescence mode is the more common practice. The energy change in the absorption coefficient can be measured either in transmission or fluorescent geometries.

$$\mu(E) = \log(I_0/I) \quad \text{In transmission} \quad \text{Eq. 1.4}$$

$$\mu(E) \propto I_f/I_0 \quad \text{In fluorescence (or Auger emission)} \quad \text{Eq. 1.5}$$

Where $\mu(E)$ is the absorption coefficient. I_0 is the intensity of the X-ray passing through the sample. I is the intensity of the X-ray beam after transmitting through the sample and I_f is the monitored intensity of the fluorescence line.

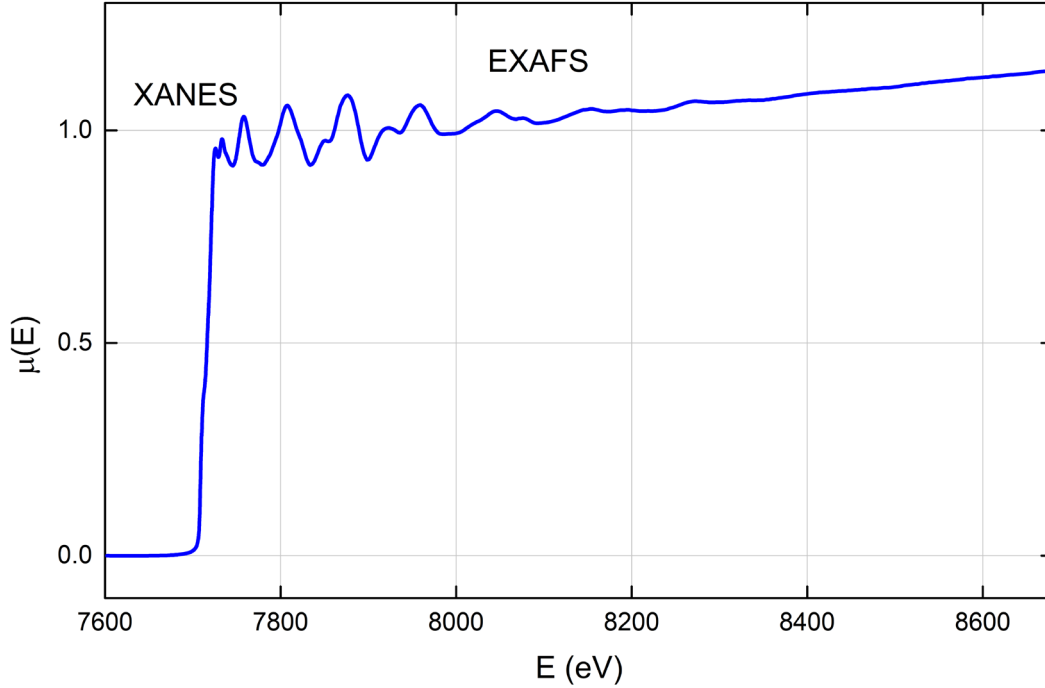


Figure 1.15: XAS $\mu(E)$ for a cobalt sample (Co on N doped C), the measured XAS spectrum is shown with the XANES, and EXAFS regions identified.

Figure 1.15 shows the XAS spectrum of cobalt. The sharp rise in $\mu(E)$ in the spectra is due to the loss of 1s electron from Co atom; XANES. The oscillations in $\mu(E)$ above 30 eV of the main absorption edge are EXAFS. Although the basic physical description of XANES and EXAFS is the same, with some approximations and limits, EXAFS spectra can be interpreted quantitatively. EXAFS function $\chi(E)$ can be defined as follows (Eq. 1.6).

$$\chi(E) = \frac{\mu(E) - \mu_0(E)}{\Delta\mu_0(E)} \quad \text{Eq. 1.6}$$

Where $\mu(E)$ is the measured absorption coefficient. $\mu_0(E)$ is a smooth background function that represents the absorption of an isolated atom and $\Delta\mu_0$ is the increment in the absorption $\mu(E)$ at the threshold energy E .

EXAFS can be understood well when studying the wave behaviour of the photoelectron. When X-ray energy is converted to the wavenumber of the photon, k which has dimensions of 1/distance is defined as follows (Eq. 1.7).

$$k = \frac{\sqrt{2m(E-E_0)}}{h^2} \quad \text{Eq. 1.7}$$

Here E_0 is the absorption edge energy, E is the absorption threshold energy, m is the electron mass and h is the Planck's constant ($6.62607004 \times 10^{-34} \text{ m}^2 \text{ kg/s}$). EXAFS is oscillatory and it decays quickly with the wavenumber of the photoelectron, k . To emphasize these oscillations $\chi(k)$, k is usually multiplied by the power of k e.g.: k^2 or k^3 . The different frequencies visible in the oscillations in $\chi(k)$ are related to different near neighbour coordination shells. This can be described and modeled according to the following EXAFS equation (Eq. 1.8).

$$\chi(k) = \sum_j \frac{N_j f_j(k) e^{-2k^2 \sigma_j^2}}{k R_j^2} \sin [2kR_j + \delta_i(k)] \quad \text{Eq. 1.8}$$

Where $f(k)$ is the scattering amplitude of the neighbouring atoms, $\delta(k)$ is the phase shift of the neighbouring atoms, N is the number of neighbouring atoms, R is the distance to the neighbouring atom and σ^2 is the disorder in the position of the neighbouring distance. When $f(k)$ and $\delta(k)$, the scattering properties of the neighbouring atoms of the excited atom are known, using the EXAFS equation N , R and σ^2 can be determined.

1.8.4 Near Edge X-ray Absorption Fine Structure (NEXAFS)

NEXAFS, sometimes called XANES, measures the absorption fine structure about 50 eV above the absorption edge. In this region, the X-ray absorption coefficient has large variations dominated by intense and narrow resonances. The most common practices are measuring the transmission and electron yield (Figure 1.16 a, Eq. 1.9). The fluorescence effect for lower Z elements is lower compared to electron yield. NEXAFS of thin films is measured in transmission method while electron yield method is applied for other samples (Figure 1.16 b and Eq. 1.10). The electron yield method is often called total electron yield detection (TEY) which is a well-established method of measuring NEXAFS spectra.

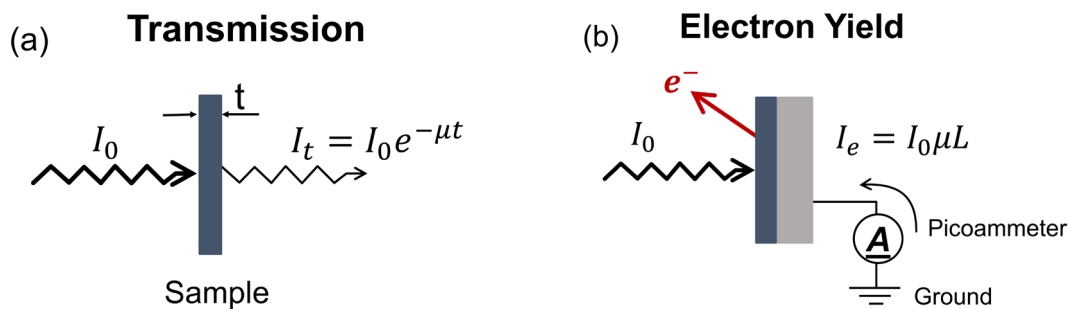


Figure 1.16: Transmission method and electron yield method of recording NEXAFS spectra.

$$I_t = I_0 \exp[-\mu t] \quad \text{transmission mode} \quad \text{Eq. 1.9}$$

$$I_e = I_0 \mu L \quad \text{electron yield mode} \quad \text{Eq. 1.10}$$

Where I_0 is the incident intensity of the X-ray, I_t is the detected intensity of the transmitted X-ray, I_e is the detected intensity of the X-ray in the electron yield mode, μ is the absorption coefficient, t is the sample thickness and L is the sampling depth.

The intensity of the absorbed X-rays is not directly measured in TEY measurements. The energy of the photoelectrons created by absorbed X-rays is measured. The photoelectrons are created by absorbing the incident X-ray by core-level electrons; usually the k edge which is the deepest core shell (Figure 1.17). Then these photoelectrons are excited to empty states above the vacuum or fermi level creating a hole in the core level. This core hole is filled by a higher energy electron transferring the excess energy to another electron resulting in secondary electron emission. The intensity of the primary Auger electron is used in Auger electron yield measurements (AEY) and that is a direct measure of the X-ray absorption process. When the primary Auger electron leaves the sample, it creates a scattered secondary electron that dominates the intensity of TEY. Secondary electrons scattered deeper in the sample lose too much energy and do not possess enough energy to overcome the work function of the sample. Thus, they do not contribute to TEY. The sample depth for TEY is a few nanometres and for AEY it is less than 1 nm. In TEY, the emitted electrons from the sample surface are measured by measuring the drain current. When the electrical decoupling of the sample from the grounded experimental chamber is not possible, the electrons can be collected by a channeltron detector placed near the irradiated area of the sample.¹³⁸

In NEXAFS a series of fine structures are superimposed on the absorption edge near the K shell absorption threshold. The resonance below ionization potential correlates to the excitation of a core electron to a bound orbital such as π^* , Rydberg or σ^* . The resonances above the ionization potential are responsible for the excitation of a core level electron to an unbound orbital of σ^* and double excitation which are usually broad. Resonances at ionization potential show a step-like increase from the onset of the core edge.¹³⁹⁻¹⁴¹

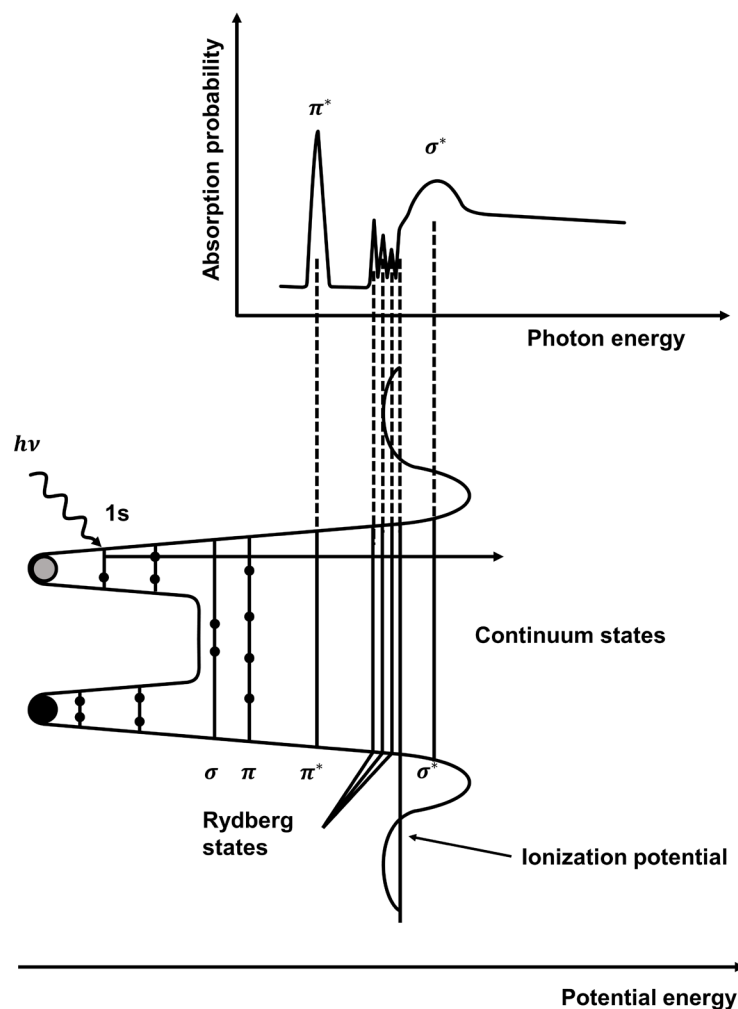


Figure 1.17: Schematic potential and the corresponding NEXAFS K-shell spectrum of a diatomic molecule.

NEXAFS spectroscopy gives qualitative information about a sample. As each element has its specific binding energy (for example C 1s ~ 285 eV, N 1s ~ 410 eV, and O 1s ~ 543 eV); the elements in a sample can be identified. Moreover, NEXAFS is sensitive to the bonding with different functional groups too. For example, C 1s \rightarrow π^* transition of C \equiv N occurs at 287 eV while C 1s \rightarrow π^* transition of C=C occurs at 285 eV (Figure 1.18). The energy difference in the core level \rightarrow π^* transitions in different functional groups is due to the differences in the unoccupied orbital energy and 1s core level. NEXAFs spectroscopy is also sensitive to electron delocalization. For example, the energy shifts of C 1s \rightarrow π^* transition of C=O and C 1s \rightarrow π^* transition of C=C can be observed when changing the nature of the sample.

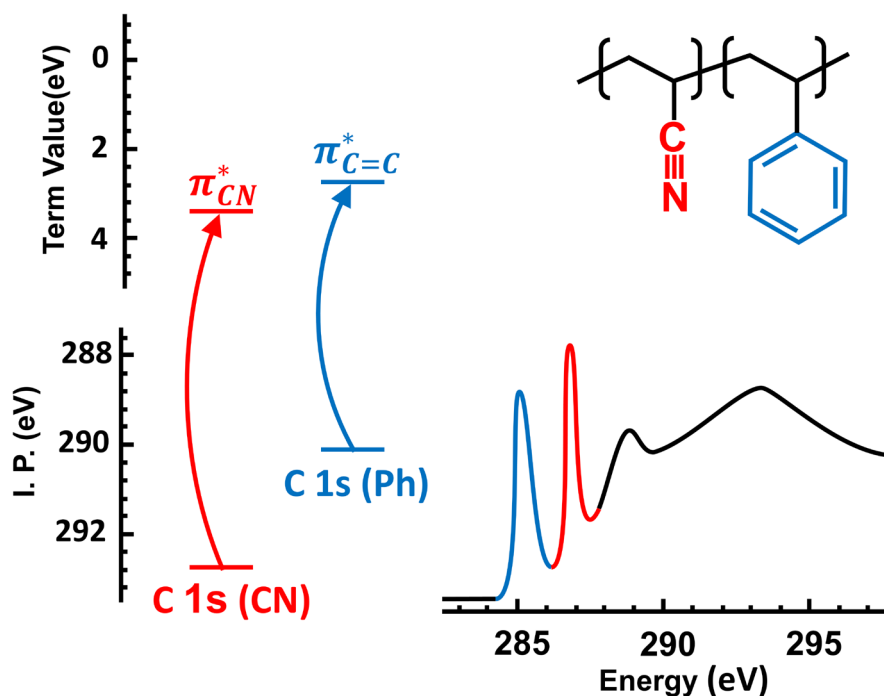


Figure 1.18: Electronic schematic for the NEXAFS photoabsorption spectrum; figure adapted from reference Ade *et al.*¹⁴²

Furthermore, NEXAFS spectroscopy can be used to determine the spatial orientation of the molecular orbitals (Figure 1.19). For this, the polarized X-ray beam of the synchrotron is used to do the NEXAFS measurement at two or more angles of incidence of X-rays. The angular dependence of NEXAFS for a π bonded diatomic molecule is due to the different overlap between the dielectric field and the final state of the orbitals. The π^* resonance is maximized at normal incidence and σ^* resonance is maximized at grazing incident.¹³⁹⁻¹⁴¹

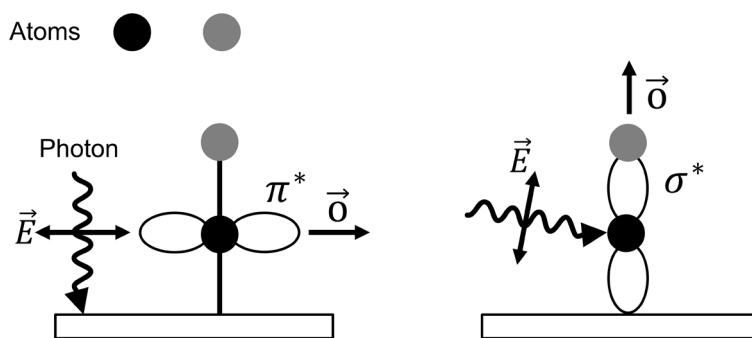


Figure 1.19: Schematic presentation of the angular dependence of NEXAFS.

1.9 Catalysis by SACs synthesized by pyrolysis of MOFs and MOF composites

The reported SACs synthesized by pyrolysis of MOFs and MOF composites catalyse a variety of reactions (Appendix A). The oxygen reduction reaction (ORR), the carbon dioxide reduction reaction (CO₂RR), the nitrogen reduction reaction (NRR), and the hydrogen evolution reaction (HER) are the main electrolysis reactions. Oxidation, hydrogenation, and dimerization are typical chemical processes that have been catalysed by SAC materials.

1.10 Introduction to hollow nanostructures

Hollow nanostructures have become a hot topic over the past two decades. They have a hollow void that is confined in the nanostructures. The chemical synthesis of the hollow nanostructures allows better control of the size and the shape of the particles.¹⁴³⁻¹⁴⁵ Moreover, a tailored hollowness can also be achieved. Thus, these hollow nanostructures have internal cavities with well-defined boundaries and uniform morphology.¹⁴⁶ The density of hollow nanostructures is lower than their dense solid. The surface area of hollow nanostructures is significantly high due to the internal cavities. Owing to the internal cavities, these materials have a high pore volume and large loading capacity, which makes them ideal materials in storage applications.¹⁴⁷⁻¹⁴⁹ Not only that; but also the hollow nano boxes are used in lithium-air batteries,¹⁵⁰⁻¹⁵¹ catalysis,¹⁵²⁻¹⁵³ drug delivery,¹⁵⁴⁻¹⁵⁶ sensor applications,¹⁵⁷⁻¹⁵⁹ nanoreactors,¹⁶⁰⁻¹⁶² water treatment,¹⁶³⁻¹⁶⁵ dye-sensitized solar cells,¹⁶⁶⁻¹⁶⁷ fuel cells,¹⁶⁸⁻¹⁷⁰ and supercapacitor applications.¹⁷¹⁻¹⁷³

1.11 Nomenclature of hollow nanostructures

The nomenclature of hollow nanostructures varies based on the number of shells and the arrangement. Usually, hollow nanostructures exist in different shapes such as spheres, tubes, fibers, and boxes. Based on their structural complexity hollow nanostructures can be simple or complex. Depending on the number of outer shells in these materials these can be termed as single, double, and multi-shell hollow nanostructures (Figure 1.20). Single hollow nanostructures have a single cavity encapsulated with a boundary, whereas double and multiple hollow nanostructures have two or more interior cavities with multiple boundaries. Compared to simple hollow nanostructures, the synthesis of multiple hollow nanostructures is challenging due to their complex structures.

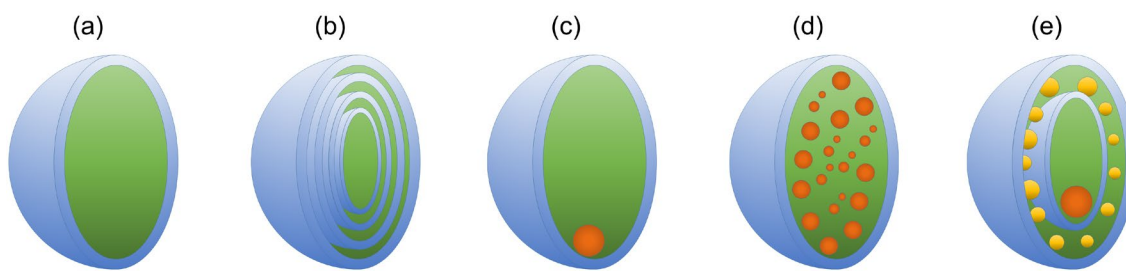


Figure 1.20: Different configurations of hollow nanostructures; (a) single-shell, (b) multi-shell, (c) yolk-shell, (d) rattle-type and (e) yolk-multi shell.

The hollow nanostructures can also encapsulate particles in the void space. When a single-shell hollow nanostructure encapsulates a particle inside the hollow space, it is named a yolk-shell structure. When there are multiple particles inside the hollow space of the single-shell hollow nanostructure, it is named a rattle type structure. A multi-shell hollow nanostructure can have a particle in the central cavity and that is called a yolk-multi shell hollow structure. The more complex structures of hollow nanostructures combine single-yolk shells encapsulated in a rattle-type structure.

1.12 Synthesis strategies of hollow nanostructures

The synthesis strategies of hollow nanostructures can be mainly grouped into three categories: hard templating strategy, soft templating strategy, and self-templating strategy.^{145, 174-176} In the hard templating method polymer, silica, and carbon-based templates are used. In the soft templating method, emulsion-based templates, micelles or vesicle-based templates, gas bubble method, and electrospray methods are employed. Ostwald ripening and etching methods are used in the self-templating method. This thesis will focus on the synthesis of hollow nanostructures by pyrolyzing MOFs and MOF composites.

1.12.1 Hard templating strategies

The hard templating method is an easy method for the synthesis of hollow nanostructures. First, the hard template is synthesized, and then chemical modifications are done to the template surface. After coating the template and making the hollow nanostructure the template is finally removed in resulting the hollow nanostructure. One of the drawbacks of this method is the challenge in the synthesis of nonspherical hollow nanostructures by the hard templating method as it is hard to find suitable nonspherical templates. Even if there are nonspherical templates, it is challenging to achieve the uniform coating and get the sharp edges and corners with such templates. There are a variety of hard templates employed in this method.

- **Polymer templates**

In polymer template-based methods, a sacrificial template such as polystyrene (PS) or polymethyl methacrylate (PMMA) is used. This template is removed by dissolving it in an organic solvent. Yang. *et al.* reported the synthesis of a double-shell TiO₂ hollow structure by using polystyrene as the sacrificial template.¹⁷⁷ They have synthesized sandwich-type TiO₂@PS@TiO₂ hollow structures and then removed the PS. The TiO₂ double-shell hollow spheres were formed after calcination.

- **Silica templates**

Amorphous silica is used as hard templates due to its uniform and tenable particle size and low cost. Synthesis of TiO₂ hollow structures has been achieved by utilizing silica as hard templates. It had been coated TiO₂ and SiO₂ layers alternatively on the SiO₂ spheres and obtained SiO₂@TiO₂ multi-layer shell spheres. Then TiO₂ hollow spheres were obtained after the calcination and removing SiO₂ by etching with NaOH. The drawback of using silica as hard templates is that it requires the removal of silica which is followed by an acid or base etching.

- **Carbon-based templates**

Using carbon spheres as hard templates has the advantages of easy and complete removal of the template and the low cost. Carbonaceous microspheres (CMS) synthesized by hydrothermal carbonization¹⁷⁸ are usually used as hard templates. CMS have pores that enable the penetration of metal cations to produce hollow spheres. Xu et al. reported the synthesis of CuO yolk-shell demonstrating the influence of the carbon source used to produce CMS on the composition of the hollow spheres.¹⁷⁹ When using sucrose as the carbon source, it resulted in CuO yolk-shells whereas glucose CMS produced Cu₂O yolk-shells.

1.12.2 Soft templating strategies

Soft templating methods use fluid or gas templates for the synthesis of hollow structures. The drawback of this method is there is less control over the particle shape. The following methods are the widely used soft templating methods.

- **Emulsion based templating**

Emulsion templates are made of two or more immiscible liquids. For example, Pan et al. synthesized magnetic hollow doubled shell polymers by Pickering emulsion polymerization.¹⁸⁰ In this work oil in water emulsion was made and

attapulgite particles (a hydrated magnesium aluminum silica mineral) were used to stabilize the emulsion. Hydrophilic Fe_3O_4 nanoparticles were in the water phase whereas functional polymeric monomers were present in the oil phase. The magnetic hollow double-shelled imprinted polymers were synthesized after radical polymerization. Then the emulsion stabilizer, attapulgite particles, were removed by hydrofluoric acid treatment. The drawback of using emulsions is that they are not stable in harsh conditions. A good control should be maintained over the pH, temperature, ionic strength as well as the solvents, organic/inorganic additives should be chosen carefully to not to destroy the emulsion.

- **Micelle or vesicle-based templating**

Hollow nanostructures can be obtained by using micelles or vesicles as templates. The formation of micelles happens when an amphiphilic molecule in a single-phase solvent exceeds the critical micelle concentration. Surfactants such as CTAB and polyoxometalate (POM) are used to make the micelles. By changing the concentration of the surfactants, ionic strength, temperature, and pH of the solution, various shapes of micelles and vesicles can be synthesized. Thus, hollow nanostructures of various shapes can be synthesized. For instance, hollow double wall Cu_2O spheres have been synthesized by CTAB vesicles-assisted growth mechanism.¹⁸¹

- **Gas bubble-based templates**

The gas bubble emulsions are made in the liquid phase by sonication, gas blowing or chemical reactions. The surface of the gas bubbles serves as templates for the formation of hollow nanospheres. The synthesis of CaCO_3 hollow spheres by bubble template method by bubbling CO_2 and N_2 mixed gas into CaCl_2 solution; has been reported. Herein, CO_2 dissolves in the solution and precipitates CaCO_3 on the surface of the bubbles. Hollow CaCO_3 was obtained after filtering and drying the resultant solid.¹⁸² The gas bubble templates are affected by several factors such as the temperature of the solvent, surface charge, and particle size of the materials making hollow nanostructures. Therefore, these parameters should be carefully controlled to synthesize hollow nanostructures by this method.

- **Electrospray techniques**

In this method, liquid precursors are injected as droplets under an electric field. The morphology of the hollow structure can be tuned by controlling the voltage of the electric field, precursor concentration, the flow rate of the precursors, and the temperature of the collecting substrate. The hollow structure forms after the

evaporation of the solvent in the hollow space. For example, a solution containing CaCl_2 and chitosan was electro sprayed into a phosphate solution. This formed a hydroxyapatite shell in the sprayed droplets (Figure 1.21). By changing the electro-spray conditions a variety of morphologies such as spherical, elongated, and hanging bell-like structures could be obtained.¹⁸³ The precursor mixture should be conductive to employ the electro-spray method.

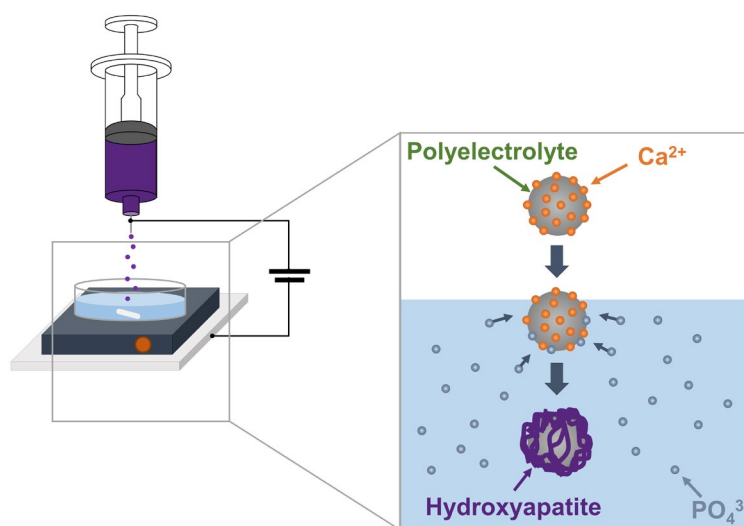


Figure 1.21: Synthesis of hollow nanostructures by electro-spray techniques.

1.12.3 Self-templating methods

In this method, the nanostructure is synthesized first and then it is converted into a hollow nanostructure. The advantage of this method is that it has fewer steps and consumes less time compared to other methods. Subsequently, it reduces the production cost making it more desirable for large-scale synthesis. Etching and Ostwald ripening are the main approaches of self-templating methods.

- **Etching**

The core of the nanostructures is removed to make hollow structures in etching. In the surface protected etching, a protective layer is coated and then the core is etched by an etching agent. The advantage of using a protective agent is that it helps to keep the morphology of the particles unchanged. For example, Zhang et al. synthesized MnFe_2O_4 spheres and soaked them in D-galactose solution to coat them. Then $\text{MnFe}_2\text{O}_4@D\text{-galactose}$ was carbonized to obtain $\text{MnFe}_2\text{O}_4@C$. Then these nanospheres with a protective C layer were put into an acid solution. The acid penetrates the C layer and gets into the core of the spheres etching the core resulting in the hollow nanospheres of $\text{MnFe}_2\text{O}_4\text{-C}$.¹⁸⁴

- **Ostwald ripening**

Ostwald ripening is a phenomenon that changes the homogeneous structure of solid solutions or liquid solutions over time. Small crystal or solution particles dissolve and redeposit into larger particles as it is thermodynamically favourable. This occurs because larger particles have lower surface energy compared the smaller particles. This mechanism is used for the synthesis of complex hollow structures such as multi-shell and yolk-shell structures.¹⁴⁶ Zhang reported the synthesis of hollow Cu₂O spheres by Ostwald ripening. First, they synthesized the colloidal Cu₂O initiated by hydrazine. Then the solution was stirred under ambient conditions for Ostwald ripening until the formation of single-shell Cu₂O spheres. Introducing more hydrazine to the single-shell Cu₂O spheres to initiate the shell growth and stirring it for a longer time for the Ostwald ripening resulted in double-shell Cu₂O spheres.¹⁸⁵

- **Kirkendall effect**

Kirkendall effect occurs due to the difference in the diffusion rate of two metal atoms. As a result that, the motion of the interface between two metals occurs to balance the series of vacancies. The hollow structures are formed when the ratio of vacancies exceeds the saturation value. Son et al. reported the synthesis of hollow Si oxide nanotubes. They mixed Si nanoparticles and nanotubes and heated them to introduce a Si oxide layer. Hydrothermal heating of these templates for a few days resulted in hollow Si oxide nanostructures.¹⁸⁶

1.13 Synthesis of hollow nanostructures from MOFs

Synthesis of hollow nanostructures from MOFs also follows template-guided methods and self-templating methods same as the conventional methods. The MOF-derived hollow nanostructures can be categorized into two groups. One is the synthesis of hollow MOFs followed by pyrolysis and the other the is the conversion of synthesized MOFs into hollow structures. As discussed in the SACs section 1.4.1, there are drawbacks in using pristine MOFs in the applications due to their low thermal and chemical stability. The exceptional stability in harsh conditions of hollow nanostructures can be achieved by pyrolyzing the material. Thus, in this thesis, the tailorable MOFs are converted into robust hollow nanostructures by pyrolysis.

1.14 Synthesis strategies of hollow nanostructures by pyrolyzing MOFs and MOF composites

In the synthesis of hollow nanostructures by pyrolyzing MOFs and MOF composites, the pyrolysis process is done after the synthesis of the MOF. One method is the synthesis of the hollow MOF and then do the pyrolysis. The other way is to do the pyrolysis of the MOF to obtain the hollowness.¹⁷⁶ The advantage of making the hollow nanostructures by the pyrolysis of MOFs and MOF composites is that it permanently establishes the morphology for the structure, which will not change even in harsh conditions. Although the catalytic ability decays with the re-use of the structure, the morphology will not change. If there is nitrogen in the organic ligands of the MOFs, the resulting structure will give nitrogen-doped carbon which is an added advantage for the hollow nanostructures. The synthesis of hollow nanostructures by pyrolyzing MOFs and MOF composites also follow the same synthesis strategies as the conventional synthesis.

1.14.1 Hard templating strategies

The synthesis of hollow nanostructures by MOFs also follows hard templating and soft templating methods as in the conventional synthesis. In the hard template methods, MOF-based synthesis also employs polystyrene (PS),¹⁸⁷ silica,¹⁸⁸ and metal oxides¹⁸⁹ as hard templates. The synthesis of the MOF takes place around the hard template and surface modifications to the hard templates are done to interact with metal nodes and initiate the MOF formation (Figure 1.22). Pre-modification of the hard template is an important factor to consider when using hard templating methods for the synthesis of hollow MOFs. Otherwise, the MOFs will grow away instead of over the hard template. The hard template is removed by etching same as in the conventional synthesis. The use of polyvinylpyrrolidone (PVP) coated (PVP)MoO₃ nanorods for the synthesis of hollow nano ZIFs has been reported.¹⁸⁹

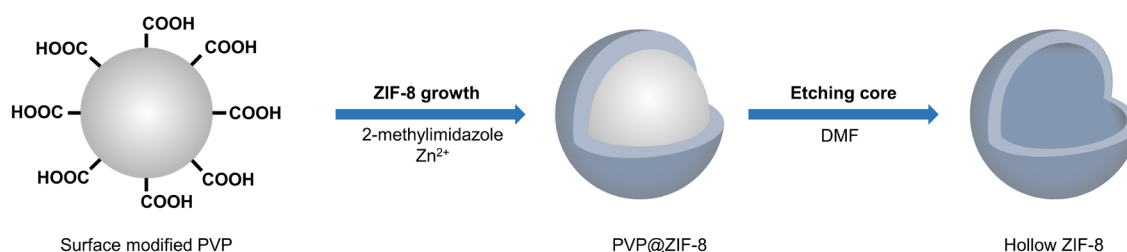


Figure 1.22: Synthesis of hollow nanostructures by hard template methods; MOF-based synthesis using polyvinylpyrrolidone as hard a template.

1.14.2 Soft templating strategies

The MOF-based hollow nanostructure synthesis can also use soft template guided methods same as in the conventional synthesis. Apart from emulsion-based templating, micelle or vesicle-based templating, and spray techniques used in the conventional synthesis the MOF-based synthesis uses metal-based templates such as pure metals, metal oxides, metal hydroxides, and metal carbonates as soft templates.

- **Emulsion-based templates**

This strategy is used in the same way as in the conventional synthesis. In the MOF-based synthesis, the metal ions (in deionized water) are in the emulsion added into an immiscible solvent with the organic linkers (in octanol). The formation of the MOF layer takes place in the interface of two immiscible liquids. For instance, the synthesis of hollow ZIF-8 spheres is reported by using Zn^{2+} emulsions.¹⁹⁰

- **Micelle or vesicle-based templates**

MOF-based synthesis of hollow nanostructures also uses the micelle or vesicle-based templates as conventional synthesis. The synthesis of hollow prism shape ZIF-67 by CTAB micelles assemblies under electrostatic interactions has been reported.¹⁹¹

- **Metal-based templates**

Normally, MOF precursors are synthesized by mixing metal and ligand solutions as homogeneous solutions. In the metal-based soft template approach of synthesizing hollow nanostructures, the metal precursors such as metal oxides, hydroxides, carbonates, etc. themselves act as templates. Metal precursors are added to an organic solvent containing the organic linkers in which they are insoluble. They react slowly with the organic ligands on the solid-liquid interface and form hollow MOFs. The synthesis of cobalt hydroxide prism for the fabrication of hollow ZIF-67 prisms can be denoted as an example.¹⁹²

- **Spray dry technique**

In this method, microdroplets of MOF precursors are sprayed onto a solid surface. Then a gas treatment is followed by heating until the solvent inside the droplet starts to evaporate. So, the MOF precursors are radially diffused onto the surface of the droplet, forming the hollow MOF. The synthesis of hollow nano HKUST-1 by this method has been reported.¹⁹³

1.14.3 Self-templating strategies

The self-templating methods, in the synthesis of MOF-based hollow nanostructures, are the same as in section 1.12.3.

- **Etching**

Unlike in the conventional synthesis, MOFs themselves can undergo etching and produce hollow nanostructures without even having a coating over them. This happens due to the inhomogeneous nature of the MOF external surface and core. The inner core of the MOFs synthesized hydrothermally usually has to found defects due to the surface energy-driven crystallization. Thus, this inner core is etched first, keeping the external surface when this type of MOF is dipped in an appropriate solvent. A multi-shell MIL-100 has been synthesized by repeating MOF growth and etching process.¹⁹⁴

As most of the MOFs have homogeneous structures and compositions the previous method can't be employed for all the MOFs. Thus, the same as in the conventional synthesis of the hollow nanostructures, surface-protected etching is done. PVP, polyvinylphosphonic acid (PVPA), and polyphenols such as tannic acid (TA), and gallic acid (GA) are used for the shielding of the outer surface of MOFs. PVP covers bind to the surface of the MOF by weak coordination bonds. The synthesis of ZIF-8@PVA hollow nanostructures has been reported.¹⁹⁵ Unlike PVP, the polyphenols strongly adsorbed to the MOF surface due to their chelating ability with the metal nodes of the MOFs. The H⁺ ions released by polyphenols do the etching of the inner core. Thus, after the coating of the polyphenolic layer, there is no additional etching step. TA coating on MOFs will be further discussed in the coming chapters.

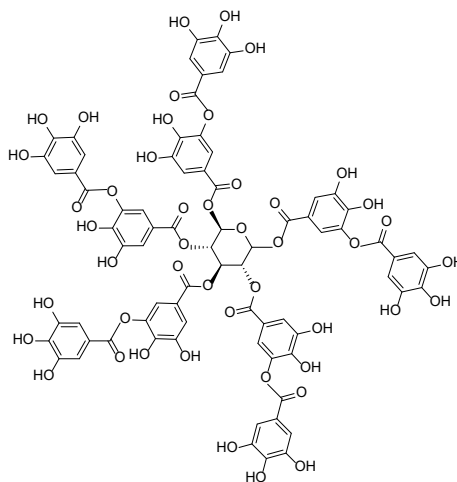


Figure 1.23: Structure of tannic acid.

- **Ostwald ripening**

The phenomenon of Ostwald ripening is used in the MOF-based synthesis of hollow nano boxes as well in the conventional synthesis. Here, highly concentrated small ligands and metal ions are mixed for the crystallization of a large amount of polymer nucleus. Due to the high concentration of the precursors, the MOFs aggregate into larger spherical particles until the concentration of the precursors decreases below a critical level. Subsequently, the outer layer of the MOF continues growing at a slower rate. When the reaction proceeds, less compact solid aggregates of the inner core dissolve and escape to the solution from the core. Due to the low concentration of the precursors, the escaped precursors grow on the outer surface of the MOFs, resulting in hollow nano MOFs. The synthesis of hollow Zn-BTC MOF nanospheres by this method has been reported.¹⁹⁶

1.14.4 Interfacial ion exchange

In this method MOFs are dispersed in an anionic solution such as OH^- , S^{2-} , VO_4^{2-} , Se^- , etc. On the outer surface of the MOF, a thin layer of the anions forms a shield by making bonds with the metal nodes. Usually, the ionic radius of the metal ions is smaller than the ionic radius of the anions. Hence, the metal ions from the core of the MOFs come out breaking the coordination bonds, while the introduced anions of the solution remain there giving rise to a hollow MOF. For example, the synthesis of single-shell Zn/Ni/Cu-Co-S MOFs by single interfacial ion exchange with thioacetamide has been reported.¹⁹⁷ By changing the anions in the MOFs dispersion solution multi-shell structures can be obtained. To achieve this, multiple anions are used in the solution. Synthesis of CoO-MoO₂ multi-shell structures by doing surface ion exchange of ZIF-67 with Na₂MoO₄ (Figure 1.24) was reported by Lyu et al.¹⁹⁸ This method can only work with MOFs, not with the conventional synthesis.

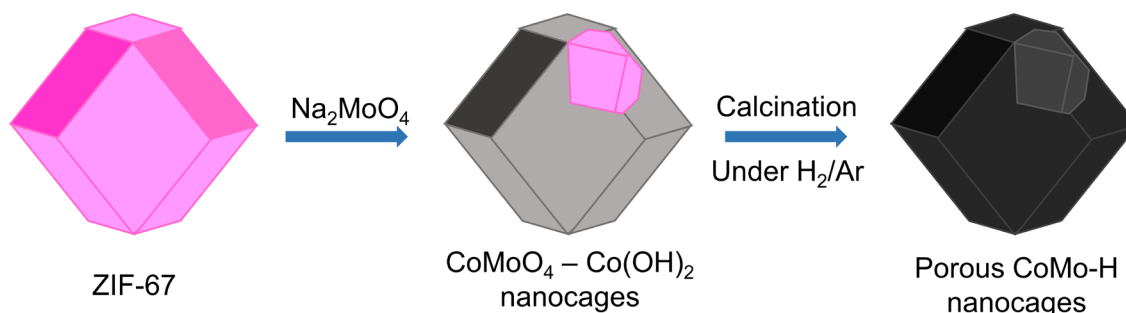


Figure 1.24: Schematic presentation of interfacial ion exchange of MOFs.

1.14.5 Heterogeneous contraction

Heterogeneous contraction is a simple and convenient method, of synthesizing hollow structures by heat treatment. In this method, thermal decomposition of the outer surface of MOF is done by heating the MOF to high temperature at a high heating rate. This forms a dense shell over the MOF keeping the crystalline stuff in the core. When the contraction force exerted by the dense outer shell is greater than the adhesion force of the inner crystalline shell, the separation of the outer shell and the inner core happens. By continuously heating the MOF as described multi-shell structures can be obtained. Synthesis of $\text{Ni}_x\text{Co}_{3-x}\text{O}_4$ spherical multi-shell is reported by the heterogeneous NiCo-BTC MOF (Figure 1.25).¹⁹⁹ The success of this strategy depends on the composition and crystallinity of the MOF. Thus, for some MOFs external coating by materials such as SiO_2 is done to increase the contraction force and make this method successful.²⁰⁰

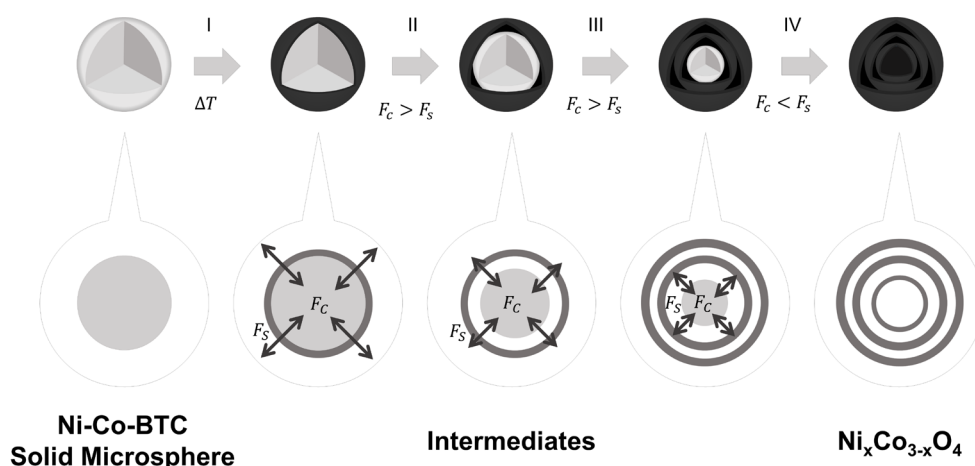


Figure 1.25: Schematic presentation of heterogeneous contraction of MOFs.

1.14.6 Self-catalytic process

Pyrolysis of some MOFs and MOF composites results in carbon nanotubes (CNT) and graphene tubes (GT), which is an emerging hot topic. Synthesis of CNTs and GTs using this method has additional advantages. For example, doping the metal ions and elements in the MOF precursors, such as nitrogen, broadens its applications. Moreover, compared to the conventional methods of synthesis of CNTs and GTs MOF based synthesis is environmentally friendly, convenient, and gives a high yield. Slow temperature pyrolysis is done in the self-catalytic pyrolysis of MOFs. The metal ions in the MOFs form nanoparticles and, due to the slow pyrolysis, they do not aggregate into large colloquial. These nanoparticles near the surface control the catalytic growth and direction of the hollow nanotubes.

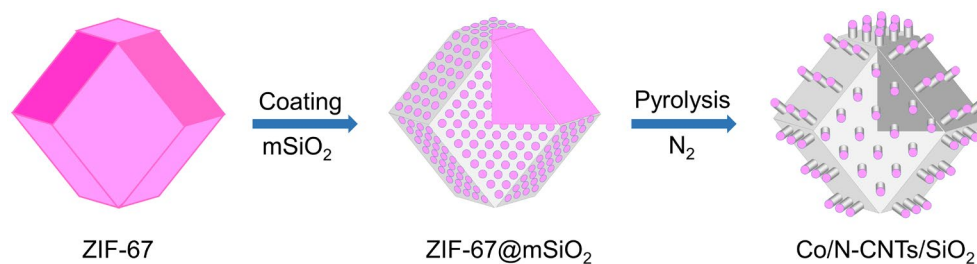


Figure 1.26: Schematic presentation of self-catalytic pyrolysis of MOFs and synthesis of CNT.

Sometimes the self-catalytic pyrolysis of pristine MOFs will not produce CNTs or GTs. The surface modification of MOFs²⁰¹ or introducing guest molecules²⁰² to the MOFs will induce the formation of the nanotubes. For example, the pyrolysis of ZIF-67@SiO₂ has resulted in Co-doped CNT (Figure 1.26).²⁰¹

1.15 Application of hollow nanostructures synthesized by pyrolysis of MOFs and MOF composites

Hollow nanostructures have been applied in lithium-ion batteries, supercapacitors, and electrocatalysis such as HER, OER, and ORR. LIBs play a significant role in electrochemical energy storage (Appendix A). The characteristic features of the hollow nanostructures such as the high surface area, low density, robust structure, and fast interaction with the Li⁺ ions, make them ideal electrode materials for the LIBs. Supercapacitors are energy storage devices with ultrafast energy storage rates. The specific features of hollow nanostructures, such as high surface area, porosity, and a high number of active sites, make them ideal materials for supercapacitors. Because these help supercapacitors to obtain high capacitance and excellent performance. The hollow nanostructures are also used in the electrolysis of HER, OER, and ORR like the SACs.

1.16 Aims of the thesis

This thesis is divided into two main sectors. One part focuses on the synthesis and characterization of SACs by pyrolyzing MOFs and MOF composites (chapters 2 and 3). These SACs are used in hydrogenation reactions and catalysis in chapters 4 and 5. The other part focuses on hollow nanostructures synthesized by pyrolyzing MOFs and MOF composites and their applications as supercapacitors and sensors (chapter 6). This thesis addresses the following questions.

- a) How to synthesize Rh SACs on hollow nitrogen-doped carbon support with a maximum loading of rhodium.
- b) If ZIF-8 is doped with cobalt in the synthesis, then coated with tannic acid, and finally pyrolyzed, will the different synthesis methods or different pyrolysis environments affect the final structure and the bonding environment of the single-atom materials?
- c) Are Rh SAC and Co SAC effective catalysts for the hydrogenation of nitroarenes?
- d) How do Rh SAC and Co SAC materials perform in ORR, N₂O reduction, and BPA degradation reactions?
- e) How to synthesize hollow nanoboxes from pristine MOFs and MOF composites?
- f) What are the applications of hollow nanoboxes?

Chapter 2 – Synthesis and Characterization of Rh SAC

2.1 Introduction

Rhodium is a rare and expensive 4d transition metal that has diverse applications in industrial reactions such as methane conversion to syngas²⁰³⁻²⁰⁵, hydrogen generation,²⁰⁶⁻²⁰⁷ and olefin hydroformylation.²⁰⁸⁻²¹⁰ Furthermore, C-H functionalization²¹¹⁻²¹², hydrogen evolution, oxygen evolution, alcohol oxidation, carbon monoxide oxidation, hydrogen generation, and organic reactions can also be catalysed by rhodium.²¹³ Single-atom catalysts (SACs) can be used in these catalysis applications to maximize the efficiency of utilization of the expensive metals. SACs have isolated metal atoms hosted by solid support.²¹⁴⁻²¹⁶ Compared to nanoparticles single metal atoms have higher surface energy leading to higher reactivity. Apart from the high selectivity of SACs, they have high activity on a per-metal-atom basis so they are less expensive and require lower loading of precious metals compared to nanoparticles or conventional metal catalysts, which make them excellent in catalytic applications.⁹⁶ Hence, synthesizing rhodium SACs may generate sustainably and cost-effective catalysts.

The use of Rh SACs in the catalysis of different reactions has been reported in the literature (Table 2.1). These Rh SAs are immobilized on metal oxide supports such as MgO, CeO₂ nanowires, TiO₂, VO₂ nanorods, and ZnO nanowires, MoS₂, zeolite, aluminosilicates, polymers, and metal alloys have also been used as catalyst supports to anchor Rh single atoms. In most of these Rh SACs, the weight percentage of rhodium amounts to less than 1%. Moreover, most of the reported Rh SACs have metal supports. Although they do not belong to a precious metal category, using metal support is an expensive option.²¹⁷ When using these SACs with metal supports in the catalysis applications, the metal support can also actively participate in the catalysis leading to side products, reducing the selectivity of Rh SACs. Thus, the synthesis of metal catalysts on nitrogen-doped carbon support is a powerful approach in the synthesis of catalysts.²¹⁸

This chapter aims to synthesize a Rh SAC on a nitrogen-doped hollow carbon support. Such catalysts had not been reported in the literature at the time this work was initiated. This research was focused on obtaining SACs, with a maximum loading of rhodium while avoiding any rhodium nanoparticles. The Rh SACs synthesized in this chapter are unique due to the combination of excellent properties of SACs and the exceptional properties of

hollow nanoboxes. This is the first Rh SAC reported on a nitrogen-doped hollow carbon support.

In addition to the uniqueness of the Rh SAC, another aim of this research was to study the structural changes of the material during its synthesis. Although there are some single-atom catalysts reported in the literature, not all the publications do the high-end characterizations of the catalysts or report the coordination environment of the single-atoms of the catalysts. In this research, the process of catalyst synthesis is well characterized. Another aim of the synthesis of Rh SAC is to use it in catalysis applications which are further discussed in chapter four.

Table 2.1: Reactions catalysed by Rh SACs

Entry	Catalyst support	Reaction catalysed	Rh %	Ref.
1	MgO	Acetylene trimerization	u/a	219
2	CeO ₂	Olefin isomerization	u/a	220
3	CeO ₂	CO oxidation	0.04%	221
4	CeO ₂ nanowires	Methane conversion to oxygenates	0.3%	222
5	MgO and CeO ₂	Hydroformylation	u/a	223
6	TiO ₂	Water-gas shift reaction	0.37%	217
7	ZrO ₂	Selective activation of methane	0.3%	224
8	VO ₂ nanowires	Ammonia-borane hydrolysis	0.5%	225
9	ZnO nanowires	CO oxidation	0.007%	226
10	ZnO nanowires	Hydroformylation of olefins	0.3%	227
11	MoS ₂	Crotanaldehyde hydrogenation	0.27%	228
12	Zeolite	Hydrogenation of nitroarenes	0.71%	229
13	Zeolite	Oxidation of methane	0.5%	230
14	Aluminosilicates	Transformation of methane	0.10%	231
15	γ -Al ₂ O ₃	O ₂ activation and CO oxidation	u/a	232
16	Silica nanospheres	Reduction of 4-nitrophenol	4.3%	233
17	PPh ₃ polymers	Hydroformylation of olefins	0.125%	234
18	Phosphotungstic	Co oxidation	0.2%	235
19	CuO nanowires	Water splitting	6.8 %	236
	N-doped C	Formic acid oxidation	0.92%	237

u/a: % of rhodium is not reported.

2.2 Results and Discussion

Rh SAC was synthesized by adaptation of our previously reported method²³⁸⁻²³⁹ involving pyrolysis of tannic acid coated ZIF-8

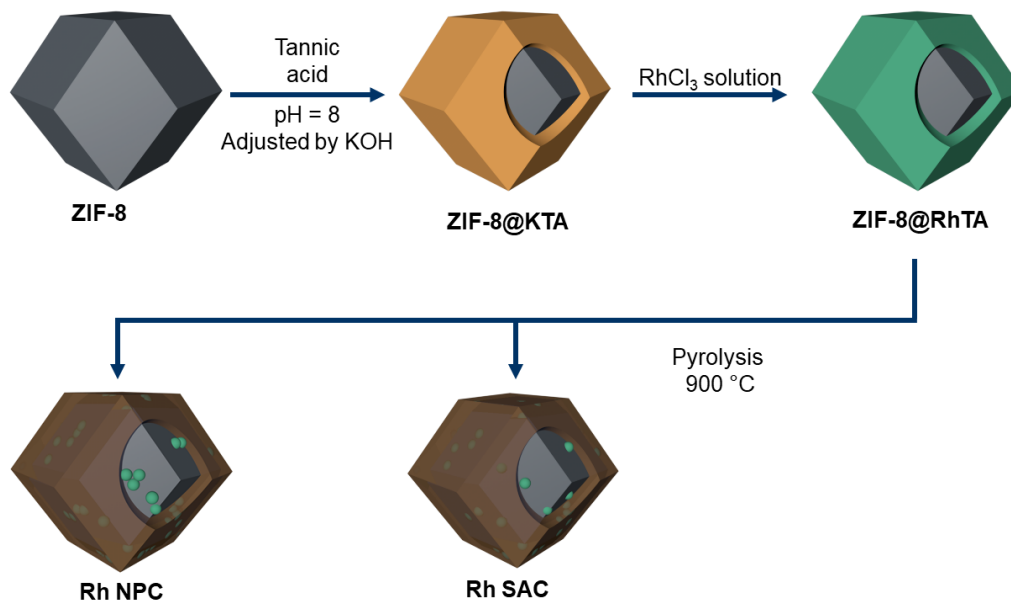


Figure 2.1: Synthesis of Rh SAC.

2.2.1 Synthesis and characterization of ZIF-8

Methanolic room temperature synthesis of ZIF-8 was carried out by using Zn²⁺ and 2-methylimidazole as the precursors (Figure 2.2). The size of the synthesized ZIF-8 crystals was around 200 nm and showed a uniform size distribution. The PXRD of the synthesized ZIF-8 matched with the simulated PXRD pattern of ZIF-8. The sharp edges of the ZIF-8 can be observed under the TEM (Figure 2.5).

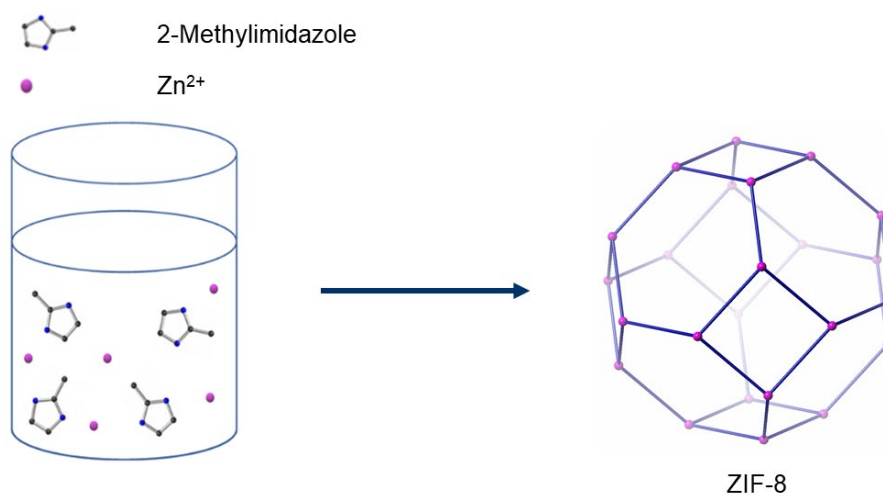


Figure 2.2: Synthesis of ZIF-8.

2.2.2 Synthesis and characterization of ZIF-8@KTA

To coat the ZIF-8 crystals with a coordination polymer of potassium ions and tannic acid (KTA), ZIF-8 crystals were dispersed in deionized (DI) water and added to a TA solution in which the pH was adjusted to 8 by KOH. After stirring for 5 mins, the coated ZIF-8 (termed ZIF-8@KTA) was obtained (Figure 2.3). TA is a polyphenol that has high acidity. If ZIF-8 is added to a tannic acid solution before adjusting the pH upwards, it will dissolve. Hence, the pH of the TA was adjusted to 8 with KOH before adding the ZIF-8. Owing to the chelating ability of TA,²⁴⁰ it forms a coordination polymer on the outer surface of the ZIF-8 crystals in conjunction with potassium ions. As TA molecules are larger than the pores of ZIF-8, KTA does not enter the void spaces of the ZIF-8 crystals.

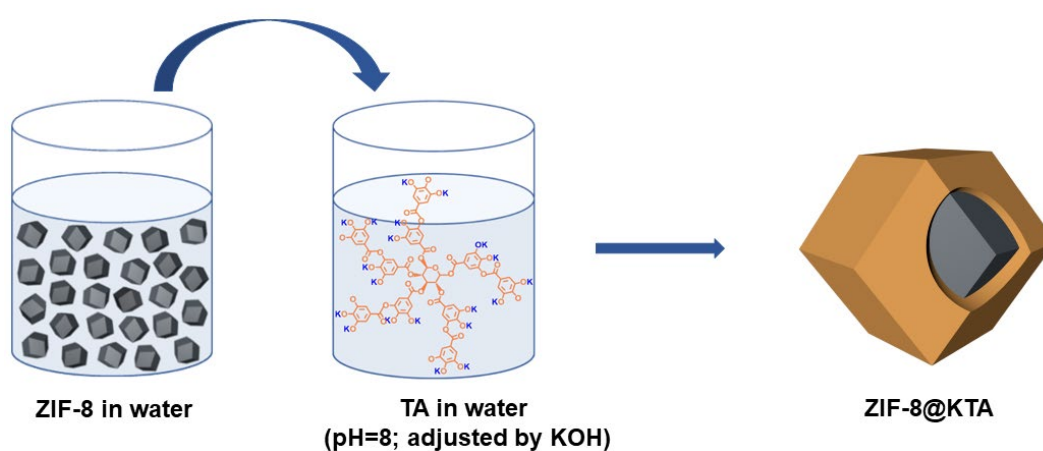


Figure 2.3: Synthesis of ZIF-8@KTA.

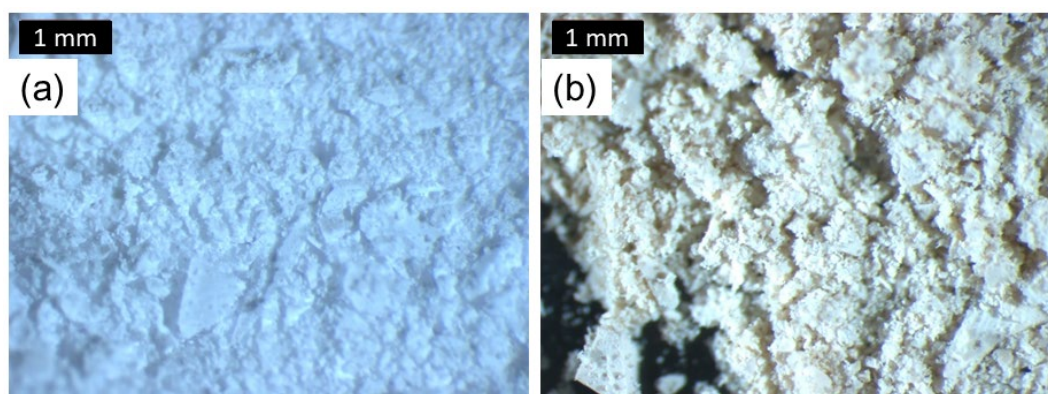


Figure 2.4: Optical microscope images of (a) ZIF-8 and (b) ZIF-8@KTA.

The white colour of ZIF-8 turns to light brown colour after the KTA coating (Figure 2.4). Since KTA is amorphous, the PXRD pattern of ZIF-8@KTA does not show any additional peaks (Experimental section, Figure 2.29). This implies that the crystallinity of the ZIF-8 core in ZIF-8@KTA is retained even after the coating with KTA.

In the EDX of ZIF-8@KTA, the appearance of a K peak can be observed which does not appear in the EDX of ZIF-8 itself (Figure 2.5 c and d). This confirms that the ZIF-8 is coated with KTA. This can be further confirmed by comparing the TEM images of ZIF-8 and ZIF-8@KTA (Figure 2.5 a and b). Sharp edges of ZIF-8 can be observed in its TEM image. But thin, rough, and low-density layers are observed for ZIF-8@KTA. Moreover, the FTIR spectrum of ZIF-8@KTA shows peaks attributable to ZIF-8 and KTA (Experimental section, Figure 2.30 a).

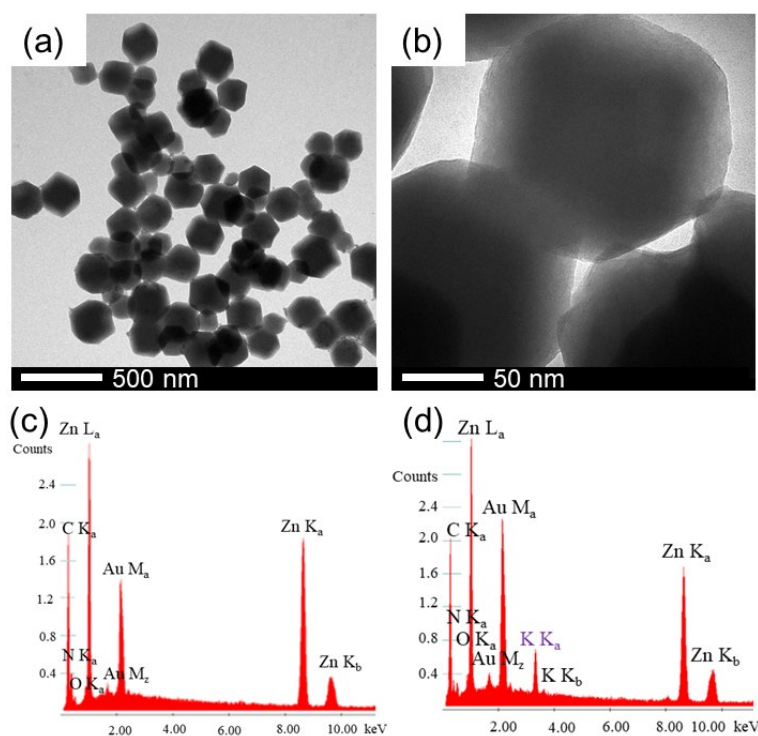


Figure 2.5: TEM and EDX images of (a,c) ZIF-8 and (b,d) ZIF-8@KTA.

2.2.3 Synthesis and characterization of ZIF-8@RhTA

To introduce rhodium ions, ZIF-8@KTA was suspended in methanolic solutions with various concentrations of RhCl₃ (Figure 2.1). The rhodium loading in these samples was quantified by AAS. Rh incorporation increases with the increasing concentration of the RhCl₃ solution (Table 2.2).

EDX spectra of the ZIF-8@RhTA samples show the emergence of the Rh peak and the disappearance of the K peak. This confirms that potassium ions were displaced by rhodium ions, as desired (Experimental section, Figure 2.31). Even the RhCl₃ solution with the lowest concentration reduces the intensity of the K peak significantly. The intensity of the rhodium peak in the EDX spectra of ZIF-8@RhTA increases with the increasing rhodium concentration in the ion exchange solution. By the TEM, the average size of ZIF-8@RhTA was about 200 nm and the shape of the ZIF-8@KTA remained unchanged even after the ion exchange with rhodium ions. Furthermore, there is no impact on the structure of ZIF-8 by the ion exchange process as the PXRD patterns of ZIF-8@RhTA samples matched with the PXRD pattern of ZIF-8 (Experimental section, Figure 2.29)

Table 2.2: Rhodium loading in ZIF-8@RhTA and corresponding Rh-NC samples.

Before pyrolysis			After pyrolysis	
ZIF-8@RhTA code	RhCl ₃ conc. (mM)	Rh loading % w/w	Rh-NC sample code	Rh loading % w/w
ZIF-8@KTA-0	0	0	NC	0
ZIF-8@KTA-0.05	0.05	1.07	Rh-NC-0.05	3.21
ZIF-8@KTA-0.10	0.10	1.39	Rh-NC-0.10	4.14
ZIF-8@KTA-0.12	0.12	1.78	Rh-NC-0.12	5.34
ZIF-8@KTA-0.14	0.14	1.88	Rh-NC-0.14	5.64
ZIF-8@KTA-0.15	0.15	2.30	Rh-NC-0.15	6.90
ZIF-8@KTA-0.50	0.50	3.01	Rh-NC-0.50	9.03
ZIF-8@KTA-0.80	0.80	3.22	Rh-NC-0.80	9.66

A control experiment was performed, whereby uncoated ZIF-8 was exposed to 0.10 mM, 0.14 mM and 0.50 mM methanolic RhCl₃ solutions. An increase in rhodium loading with increasing concentration was observed by atomic absorption spectroscopy. Thus, with the increasing concentration of ion exchange solution, rhodium ions could have been loaded to ZIF-8@RhTA in two ways. First, rhodium(III) ions displace K⁺ in the KTA layer by Rh³⁺. Second, additional Rh³⁺ is incorporated by one of two possible pathways. Either RhCl₃ solution is trapped in the pores of ZIF-8 or rhodium(III) replaced zinc(II) nodes of ZIF-8. For charge balance, an additional chloride ion would also coordinate to the rhodium center.

2.2.4 Synthesis and characterization of Rh SAC

The ZIF-8@RhTA materials were then pyrolyzed. Their differing Rh content allows us to find the maximum loading that would produce Rh SAs without Rh NPs (Table 2.2). As a control, treatment with a 0 mM solution (no ion exchange) was also conducted. After pyrolysis, the rhodium is supported on nitrogen-doped carbon (NC), which arises the thermal decomposition of the ZIF-8 ligands and tannic acid.

Pyrolysis of ZIF-8@RhTA samples at 900 °C under an argon flow for two hours resulted in material termed Rh-NC-X where X is the concentration of the methanolic RhCl₃ solution in the earlier ion exchange step (Table 2.2). In the pyrolysis process, the carbon shell derived from the tannic acid layer acts as a substrate to nucleate nitrogen and carbon from the ZIF-8 core and produce a hollow nanostructure of nitrogen-doped carbon.^{238-239, 241} The rhodium ions become embedded in the nitrogen-doped carbon as either single-atom or nanoparticles. This results in hollow nitrogen-doped carbon nanoboxes with integrated rhodium.

The zinc (II) ions from ZIF-8 are reduced to zerovalent zinc during pyrolysis and mostly vaporized and escaped from the material. Traces of zinc did remain; however, they were detected by EDX (Experimental section, Figure 2.31 and Figure 2.32). Presumably, the zinc is trapped in the nitrogen-doped carbon support. All the zinc from the catalysts could have been evaporated if the ZIF-8@RhTA was pyrolyzed for a longer time.²³⁸

Raman spectra of the Rh-NC samples (Experimental section, Figure 2.30 b), demonstrate transitions predominantly due to graphitic carbon upon the pyrolysis by the presence of G band (1579 cm⁻¹) and D band (1357 cm⁻¹).

When a low concentration rhodium solution was used to prepare ZIF-8@RhTA, pyrolysis resulted in Rh SACs (Figure 2.1). On the other hand, with a highly concentrated rhodium solution, the higher rhodium loading resulted in rhodium nanoparticle catalysts (Rh NPCs) upon pyrolysis (Figure 2.1). In the formation of Rh SAC, the rhodium atoms should

be separated enough to prevent the agglomeration, hindering the formation of rhodium NPs. But when the rhodium loading was higher in ZIF-8@RhTA, the rhodium atoms which were close to each other could agglomerate resulting in Rh NPs on the catalyst support. Thus, in Rh NPC a combination of Rh SAs and Rh NPs are expected. When increasing the concentration of rhodium solution further, greater agglomeration leads to bigger particle formation.

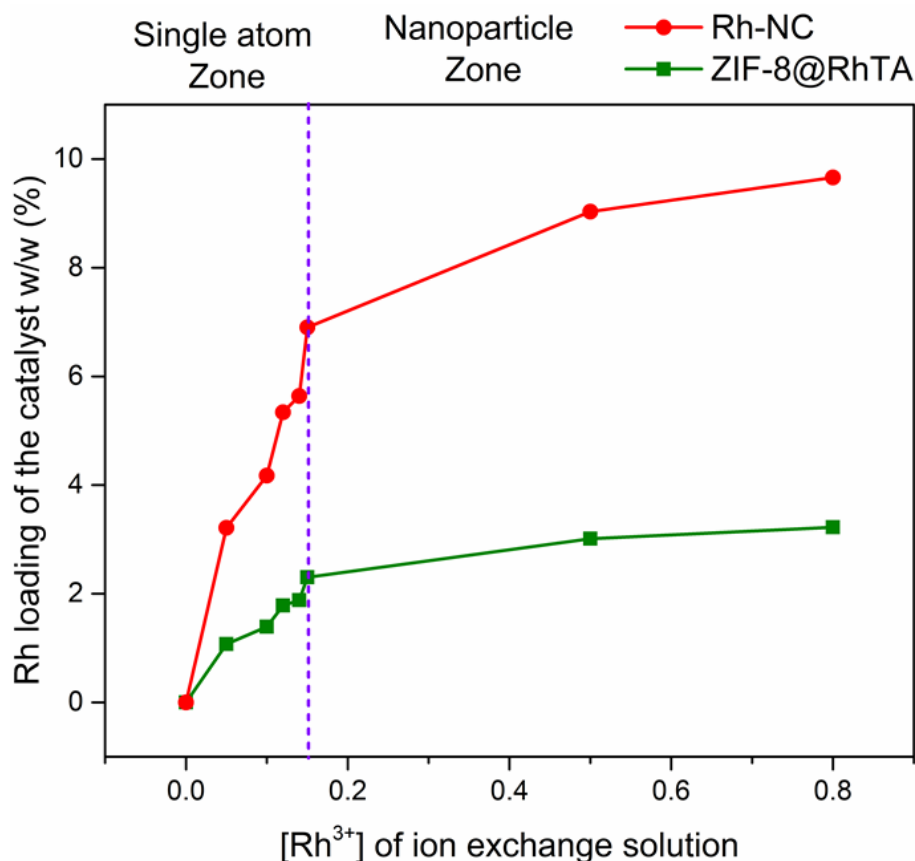


Figure 2.6: Rh loading of ZIF-8@RhTA (green) and Rh-NC (red) with ion exchange solution concentrations.

We can determine the exact point at which the amount of rhodium led to the appearance of nanoparticles in addition to the single-atom sites (Figure 2.6). The Rh NPs were detected using PXRD and TEM. In the PXRD of Rh-NC samples peaks at 41.1° and 47.8° 2θ Cu K_α , are expected for Rh NPs. No such peaks can be observed for Rh-NC-0.05, Rh-NC-0.10, Rh-NC-0.12, Rh-NC-0.14, and Rh-NC-0.15, while they are clear for Rh-NC-0.50 and Rh-NC-0.80 (Figure 2.7).

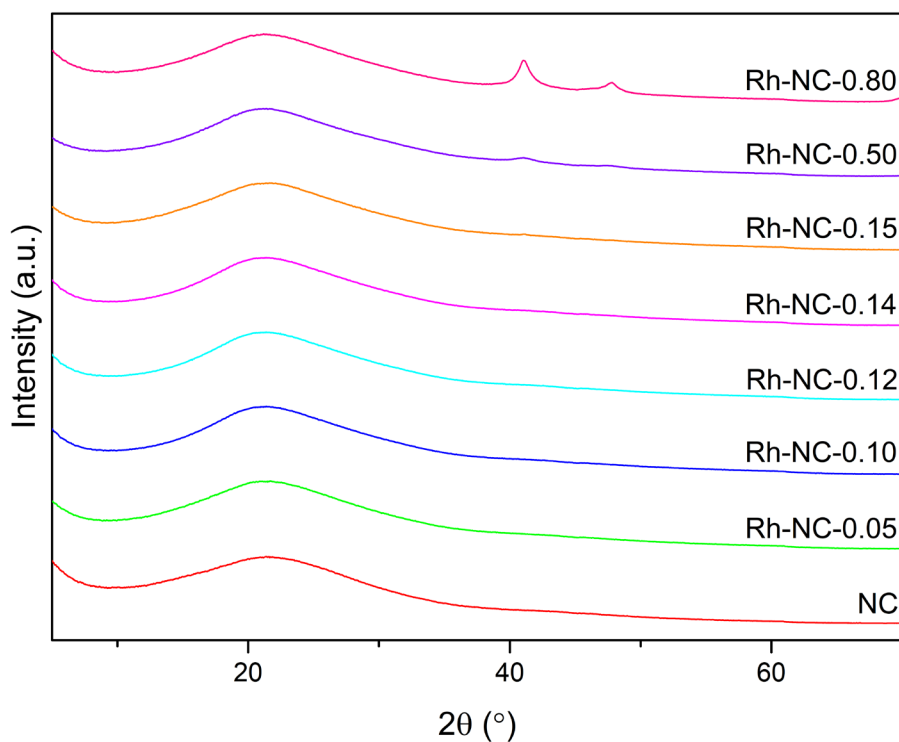


Figure 2.7: PXR D patterns of NC and Rh-NC samples.

NPs were absent from the TEM images of Rh-NC-0.05, Rh-NC-0.10, Rh-NC-0.12, and Rh-NC-0.14. Thus, the rhodium in these samples is present as rhodium single-atoms (SAs). To visualize the single-atoms in these samples HAADF-STEM was conducted (see later). Although the rhodium peaks were absent from the PXR D pattern of Rh-NC-0.15, one rhodium nanoparticle could be found as a dark spot in the sample when carefully observing the TEM grid (Figure 2.8). Thus, the Rh-NC-0.15 sample signals the onset of nanoparticle formation.

The Rh NPs in Rh-NC-0.50 and Rh-NC-0.80 were observed as dark spots in the TEM images (Figure 2.8). As expected, there are more Rh NPS in Rh-NC-0.80 than in the Rh-NC-0.50 sample. Accordingly, in the EDX, the intensity of the Rh peak of Rh-NC-0.80 is higher than the intensity of Rh-NC-0.50 (Experimental section, Figure 2.32).

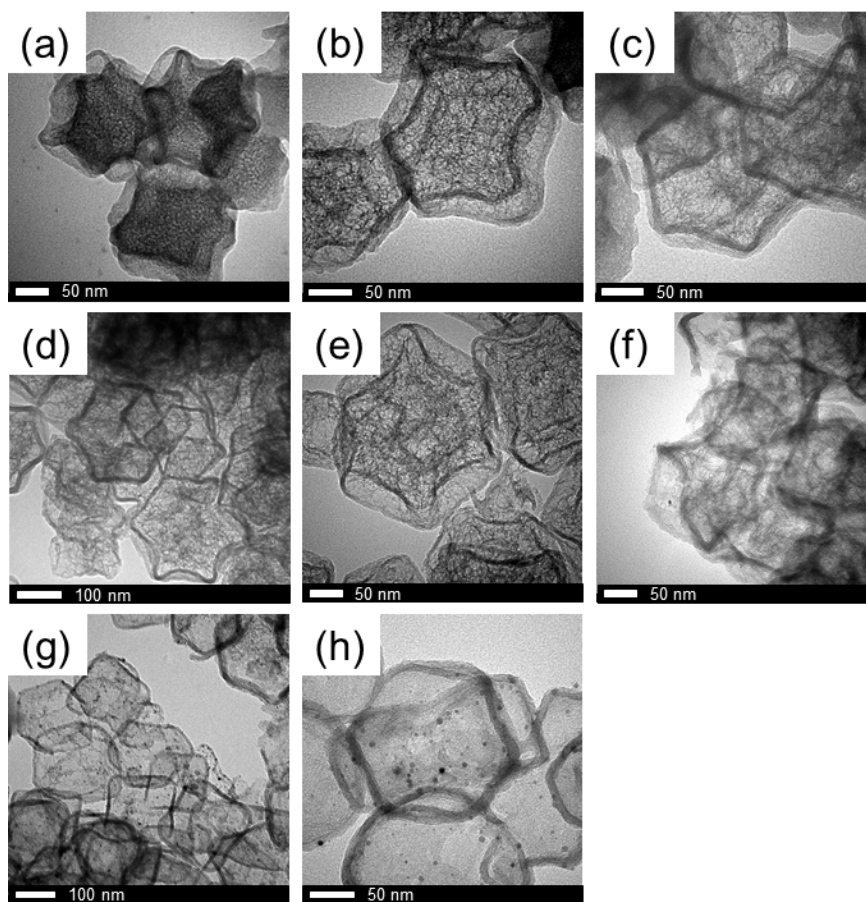


Figure 2.8: TEM images of (a) Rh-NC, (b) Rh-NC-0.05, (c) Rh-NC-0.10, (d) Rh-NC-0.12, (e) Rh-NC-0.14, (f) Rh-NC-0.15, (g) Rh-NC-0.50 and (h) Rh-NC-0.80.

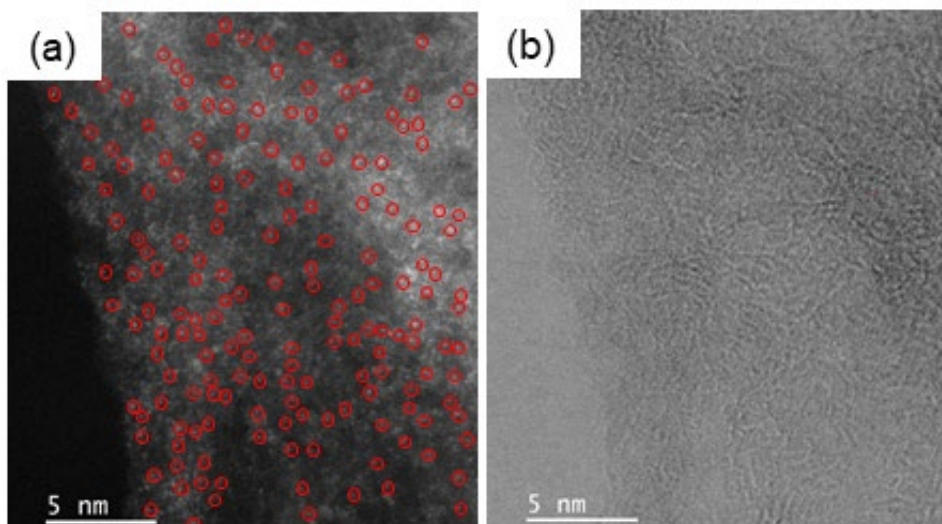


Figure 2.9: (a) HAADF STEM and (b) correlated ABF-STEM images of Rh-NC-0.14.

Unlike in the TEM in STEM, the HAADF detector detects dense areas and the heavy metals as bright spots whereas in ABF-STEM images heavy atoms are imaged as dark spots. In the HAADF-STEM image (Figure 2.9a) of Rh-NC-0.14, Rh SAs are visible as bright spots, whereas the dark spots of the corresponding ABF-STEM (Figure 2.9b) are Rh SAs. The Rh SAs are uniformly distributed over the surface of the material. As seen by Rh elemental mapping Rh SAs are distributed homogeneously throughout the Rh-NC-0.05, Rh-NC-0.10, and Rh-NC-0.14 (Figure 2.10, Figure 2.11, and Figure 2.12). The elemental maps of Rh-NC-0.50 and Rh-NC-0.80 (Figure 2.13 and Figure 2.14) show Rh NPs as larger clusters together with Rh SACs as smaller specks. Moreover, in the elemental map of all the Rh-NC samples, the residual zinc trapped in the nitrogen-doped carbon layer and oxygen which forms part of the catalyst support; can be identified and is consistent with the EDX analysis.

ZIF-8 crystals take on the form of orthorhombic dodecahedra. By using ZIF-8 as the starting material for the synthesis of Rh-NC, it is interesting to observe the final geometric distribution of the synthesized catalyst after being subjected to high-temperature pyrolysis. HAADF-STEM and ABF-STEM tomography of Rh-NC-0.14 confirms that it also has the hollow orthorhombic dodecahedra distribution (Figure 2.15).

The Rh-NC-0.14 material reported has the highest known Rh SAC loading except for the Rh SACs on Cu nanowires described by Sun *et al.*, which has a 6.8% rhodium loading.²²⁹ The Rh SAC materials reported here are the second Rh SACs on nitrogen-doped carbon synthesized by the pyrolysis of MOF composites; the first being reported in 2020.²³⁷ However, Rh-NC-0.14 has a five-fold higher Rh loading.

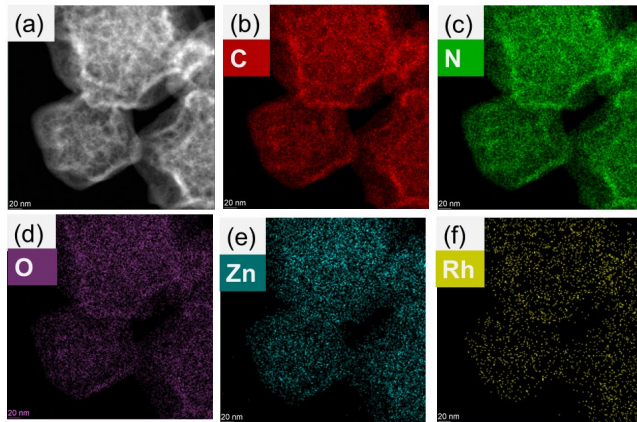


Figure 2.10: (a) STEM image and (b-f) elemental mapping of Rh-NC-0.05 (scale bar 20 nm).

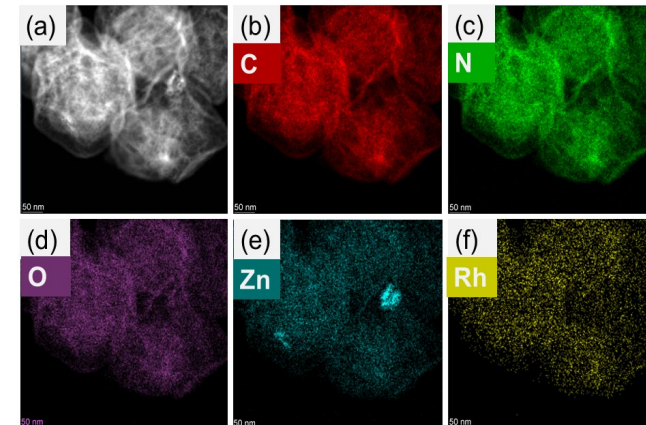


Figure 2.11: (a) STEM image and (b-f) elemental mapping of Rh-NC-0.10 (scale bar 50 nm).

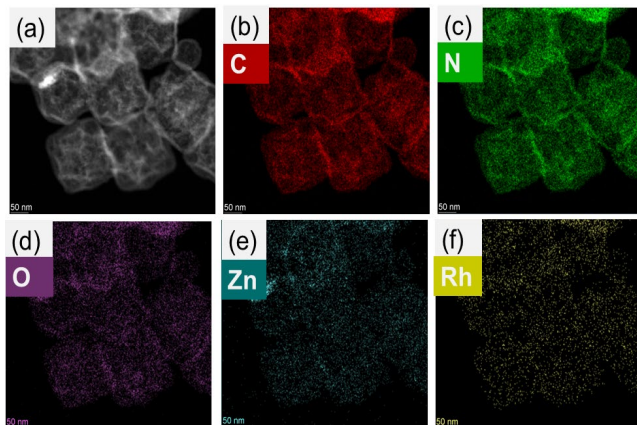


Figure 2.12: (a) STEM image and (b-f) elemental mapping of Rh-NC-0.14 (scale bar 50 nm).

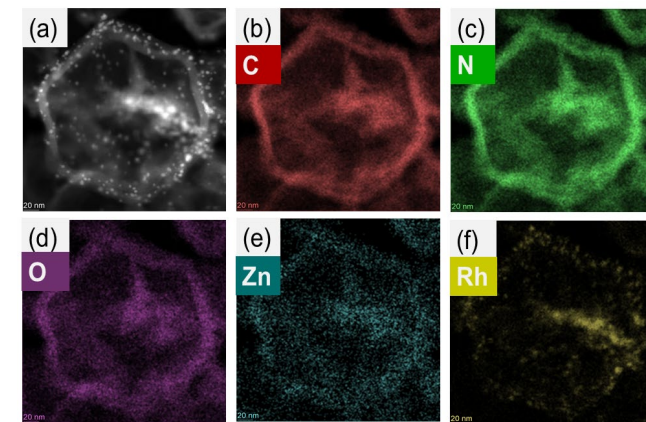


Figure 2.13: (a) STEM image and (b-f) elemental mapping of Rh-NC-0.50 (scale bar 20 nm).

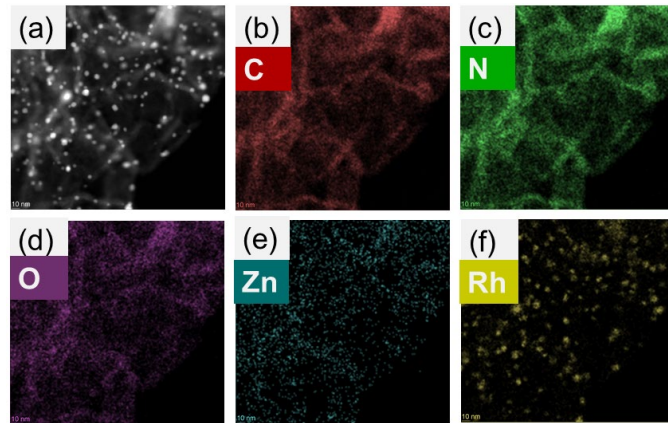


Figure 2.14: (a) STEM image and (b-f) elemental mapping of Rh-NC-0.80 (scale bar 10 nm).

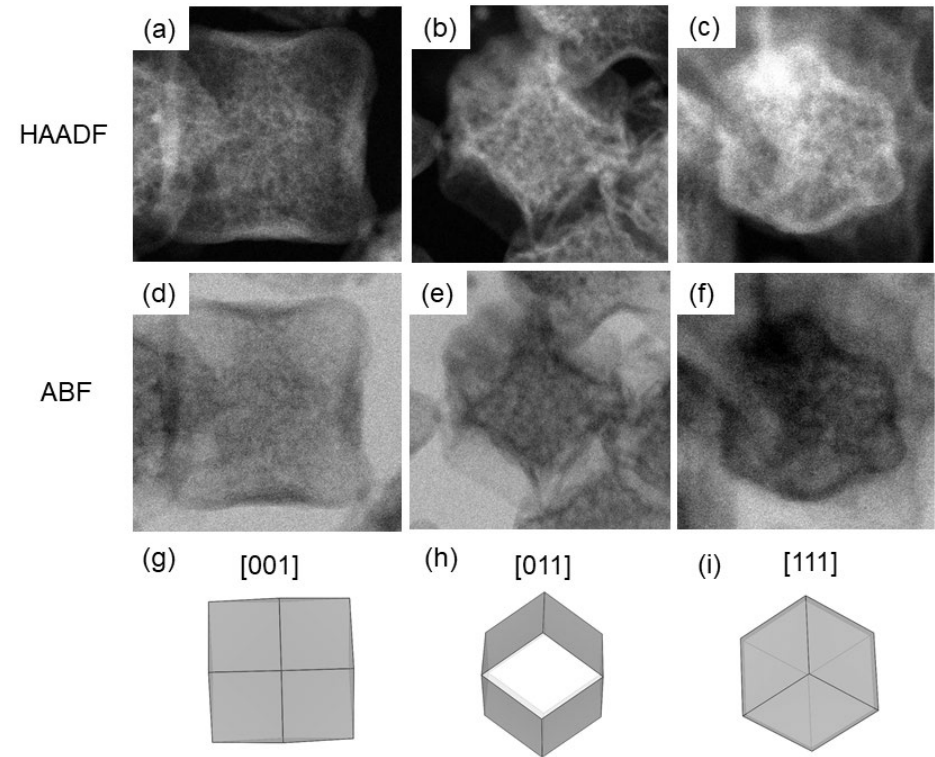


Figure 2.15: (a, b, c) HAADF-STEM images, (d, e, f) correlated ABF-STEM images and (g, h, i) cartoon shapes of Rh-NC-0.14.

2.2.5 X-ray Photoelectron Spectroscopy (XPS) characterization

After the successful synthesis of Rh-NC catalysts, we sought to determine the oxidation state and local environment of the rhodium atoms. The unpyrolyzed (ZIF-8@RhTA) and pyrolyzed (Rh-NC) materials were characterized by XPS. Survey and narrow scan XPS spectra were collected for all samples and compared against reference standards [Rh(TPP)Cl], [Rh(COD)Cl]₂, RhCl₃, and commercial 5% Rh on C (Figure 2.16). In the survey spectra of unpyrolyzed and pyrolyzed materials C, N, O, Zn, and Rh were detected, as expected. Moreover, Cl was also identified in all the samples except in ZIF-8@KTA, suggesting the RhCl₃ used to introduce rhodium is a source of Cl. Quantification was performed using peak areas for the C 1s, N 1s, O 1s, Zn 2p, K 2s, Cl 2p, and Rh 3d regions (Experimental section, Table 2.4). The relative ratios of different C, N and Rh species in the various Rh-NC samples and reference materials were determined from the narrow spectra.

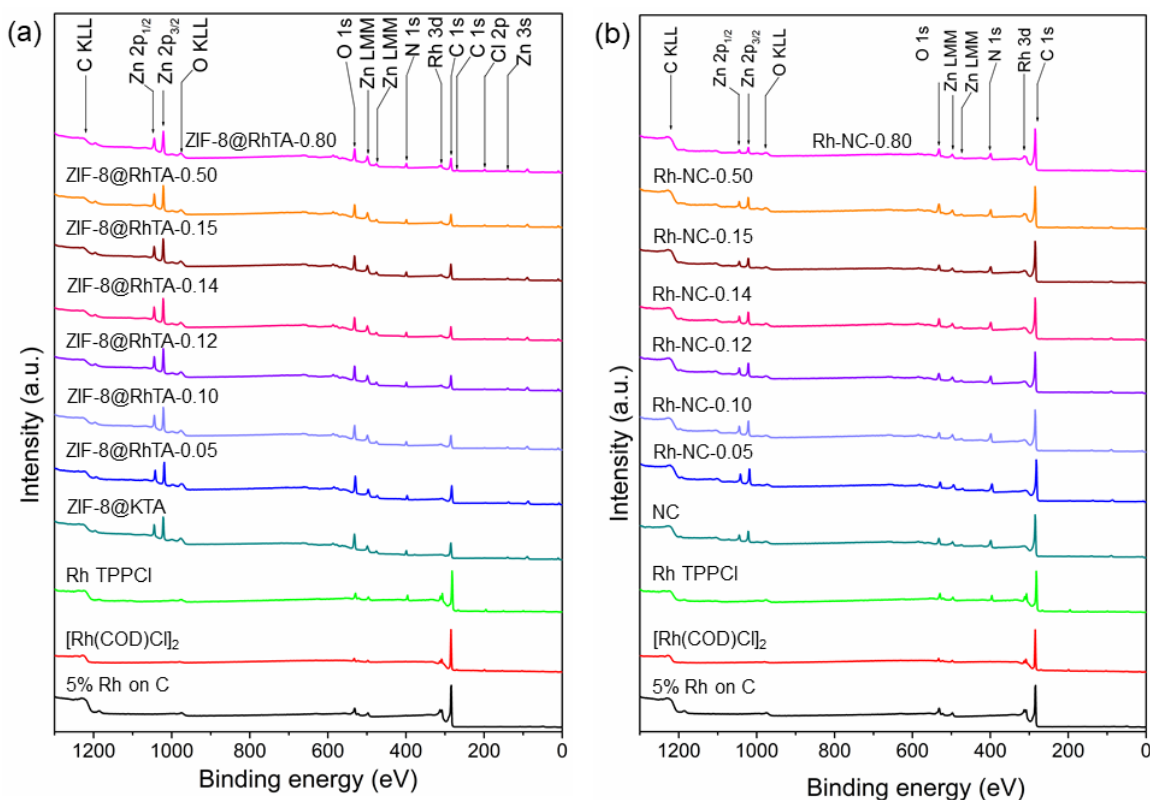


Figure 2.16: XPS survey spectra of (a) unpyrolyzed and (b) pyrolyzed samples with standards.

In the ZIF-8@MTA samples, potassium was only detected in the sample which had not been subjected to ion exchange with Rh^{3+} ions. In ZIF-8@RhTA samples potassium was not detectable, suggesting the incorporation of Rh^{3+} ions in the TA layer (thickness of the TA layer ~ 30 nm) and displacement of K^+ ions, as expected. These results are consistent with increasing rhodium loading as a function of the exchange solution concentration. The weight percentage of Zn in the pyrolyzed samples was reduced after the pyrolysis. This result is consistent with the thermal treatment at 900°C removing most of Zn^{2+} from the precursors by Zn^0 sublimation. The residual Zn sites which also appeared in the EDX of Rh-NC samples; may arise due to the zinc which could not escape the material during the evaporation because of trapping in the nitrogen-doped carbon support. As observed in the TEM images, nanoparticles form in the Rh-NC-0.15, Rh-NC-0.50, and Rh-NC-0.80 samples at the ion exchange concentrations ≥ 0.15 mM, the Rh content increases during the pyrolysis whilst the amounts of the other elements decrease at high temperature. In the survey spectra (Figure 2.16) oxygen content in the sample decreased appreciably after the pyrolysis due to oxygen escape via volatiles such as CO_2 and CO . To obtain further information about C, N and Rh present in the samples those elements were further analysed by narrow XPS scan.

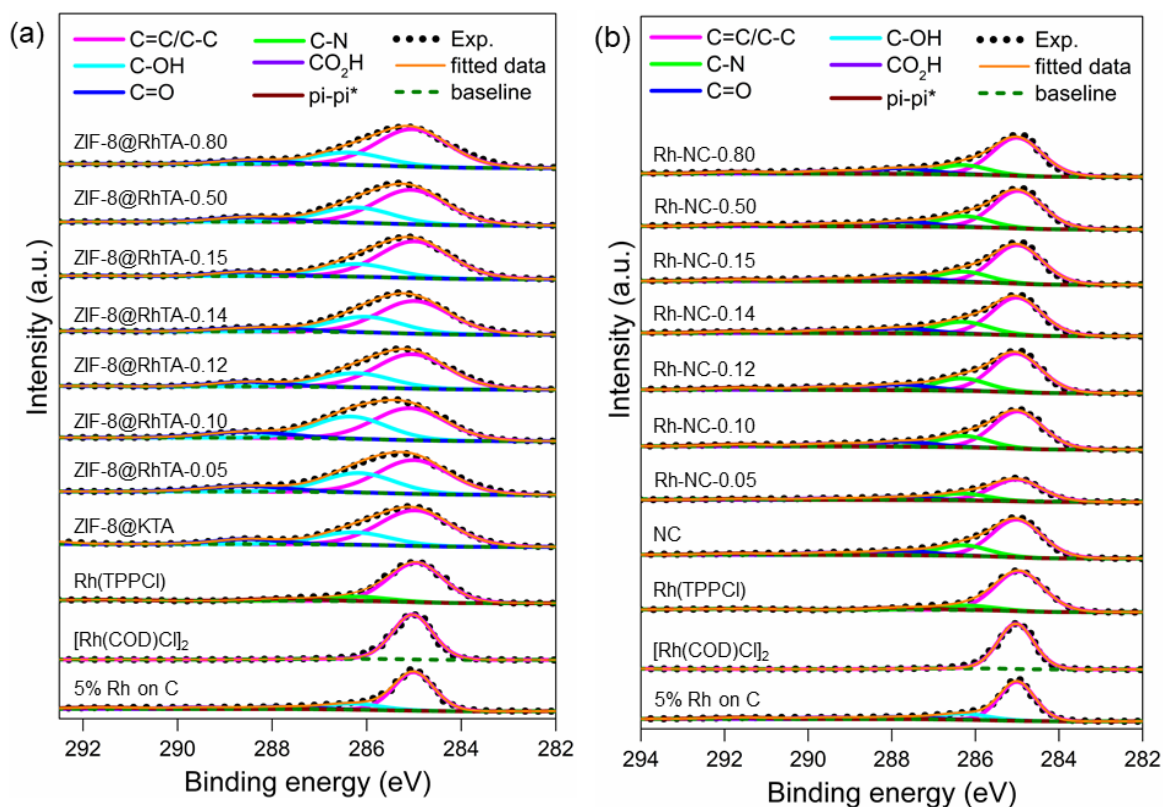


Figure 2.17: C 1s XPS spectra of (a) unpyrolyzed samples and (b) pyrolyzed samples with standards.

The carbon 1s spectra of ZIF-8@KTA and ZIF-8@RhTA samples (Figure 2.17a) show peaks at 284.6, 285.9, and 287.4 eV which can be assigned to C=C/C-C, C-N, and C=O, respectively.²⁴²⁻²⁴⁴ In these samples the $\pi-\pi^*$ peak was absent due to the amorphous nature of the TA polymer. Moreover, a peak at 286.1 eV was observed in ZIF-8@KTA and ZIF-8@RhTA samples which could be attributed to the C-OH of the tannic acid coating.²⁴⁵ These data are consistent with the FTIR peak of tannic acid (Experimental section, Figure 2.30) which comes around 3300 cm^{-1} due to -OH stretching vibrations.²⁴⁶ Also in the C 1s spectra of Rh-NC samples, C=C/C-C, C-N, and C=O peaks could be observed along with additional peaks at 289.1 and 291.2 eV (Figure 2.17b), which can be assigned to $-\text{CO}_2\text{H}$ and $\pi-\pi^*$ respectively.²⁴³⁻²⁴⁴ XPS analysis of Rh-NC samples shows that the carbon substrate of the catalyst support is quite heavily populated with oxygen-containing functional groups: C=O and $-\text{CO}_2\text{H}$; which is consistent with the presence of oxygen in the elemental mapping of STEM analysis (Figure 2.13 and Figure 2.14).

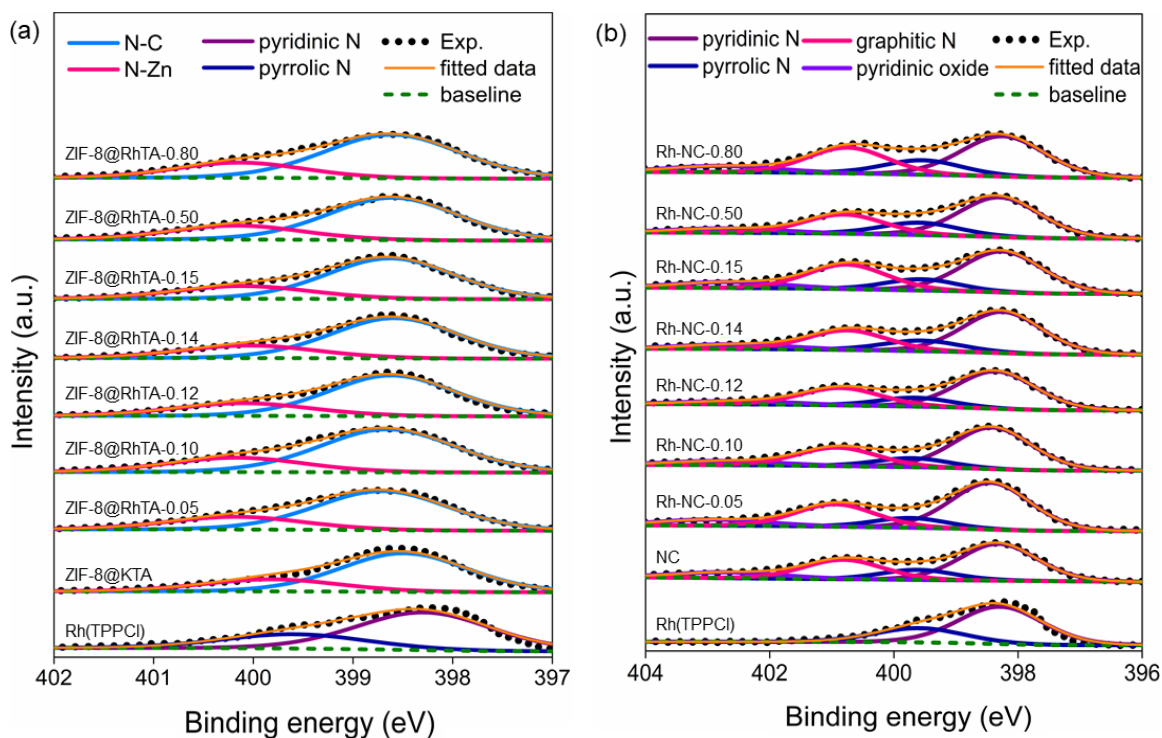


Figure 2.18: N 1s spectra of (a) unpyrolyzed samples and (b) pyrolyzed samples with standards.

The N 1s spectra for the ZIF-8@KTA and ZIF-8@RhTA samples (Figure 2.18a) showed peaks at 398.7 and 400.1 eV, which can be assigned to N-C and N-Zn of the encapsulated ZIF-8 crystals respectively.²⁴⁵ In ZIF-8@KTA and ZIF-8@RhTA, all of the nitrogen is associated with 2-methylimidazole of ZIF-8. Nitrogen 1s spectra of XPS for Rh-NC samples

(Figure 2.18b) showed peaks at 398.4, 399.7, 400.9, and 402.6 eV, which can be assigned to pyridinic N, pyrrolic N, graphitic N, N-C, and pyridinic oxide (N-O) respectively.^{242, 244-245, 247-250} Thus, the nitrogen in the catalyst support of Rh-NC is in the form of pyridinic, pyrrolic, and graphitic N.

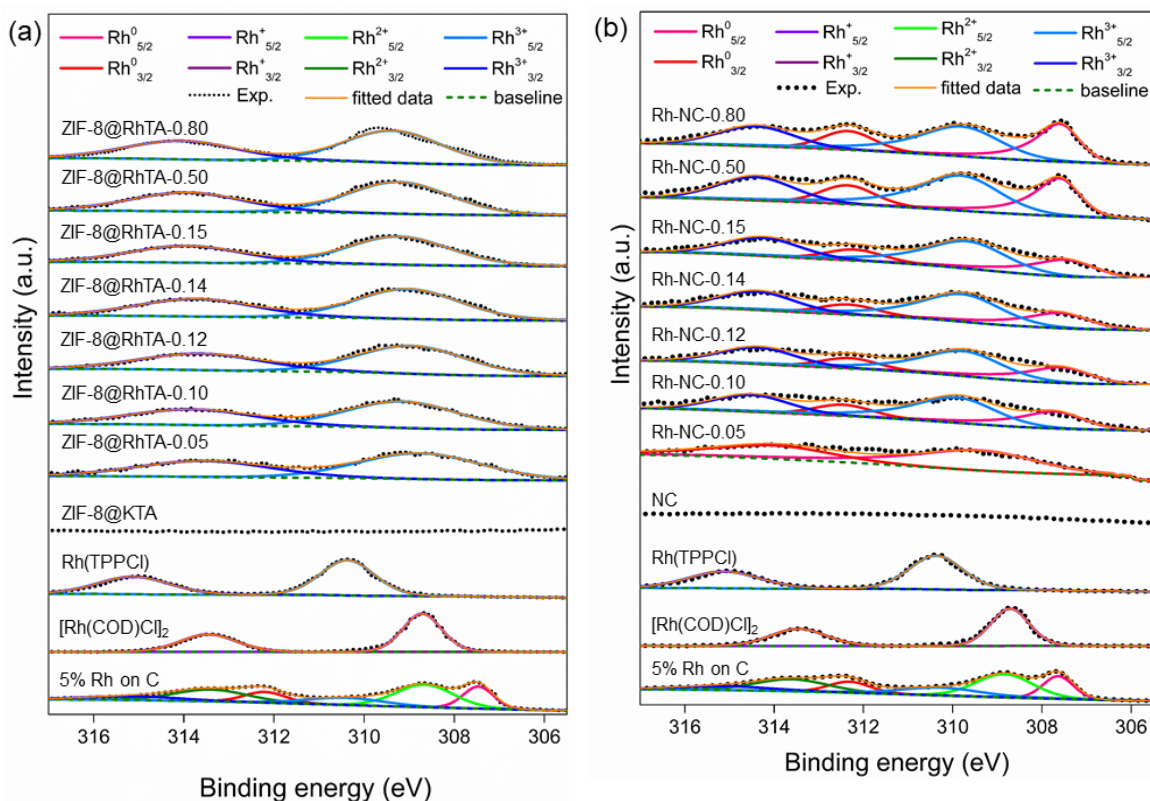


Figure 2.19: Rh 3d XPS spectra of (a) unpyrolysed samples and (b) pyrolyzed samples with standards.

The Rh 3d XPS spectra of all the unpyrolyzed and pyrolyzed samples were measured to compare the possible changes in the oxidation state of rhodium upon the pyrolysis. To compare the Rh 3d spectra of the samples; the narrow scan of the reference samples was also carried out. The rhodium oxidation state of the reference samples is Rh^{3+} for $\text{Rh}(\text{TPP})\text{Cl}$ and Rh^{1+} for $[\text{Rh}(\text{COD})\text{Cl}]_2$ (Figure 2.20 and Figure 2.21). The Rh 3d spectra of all ZIF-8@RhTA and Rh-NC samples (Figure 2.19) showed peaks at 309.5 and 314.1 eV in 4:3 area ratio, which are assigned to Rh 3d_{5/2} and Rh 3d_{3/2} peaks of Rh^{3+} respectively.²⁵¹⁻²⁵² $\text{Rh}(\text{TPP})\text{Cl}$ reference sample showed the Rh^{3+} peak at 310.3 and 315.0 eV. The binding energies of Rh^{3+} in $\text{Rh}(\text{TPP})\text{Cl}$ and ZIF-8@RhTA are slightly different as the bonding environment of those samples is not the same. The Rh^{3+} species in the samples are in a porphyrin like environment.²⁵³⁻²⁵⁷

For Rh-NC samples from Rh-NC-0.10 to Rh-NC-0.80, in addition to Rh^{3+} peaks, additional peaks were observed at 307.5 and 312.3 eV, which intensified with rhodium loading and can be assigned to metallic Rh $3d_{5/2}$ and Rh $3d_{3/2}$ respectively.²⁵⁶ The Rh NPs in Rh-NC-0.50 and Rh-NC-0.80 samples represent the metallic rhodium. As there are no Rh NPs in Rh-NC-0.05, Rh-NC-0.10, Rh-NC-0.12, and Rh-NC-0.14 samples (which is further confirmed by XAS in section 2.2.7), the above peaks can be attributed to Rh SAs which are in a Rh^0 oxidation state. For comparison, commercial 5% Rh on C sample was observed to contain three Rh oxidation states, (Rh^0 , Rh^{2+} and Rh^{3+}).²⁴⁷ In $[\text{Rh}(\text{COD})\text{Cl}]_2$ reference sample, two peaks at 308.7 and 313.5 eV can be observed which is characteristic for Rh^+ species.²⁴⁷ No such signals at these energies were observed for Rh-NC samples, confirming the absence of Rh^+ species.

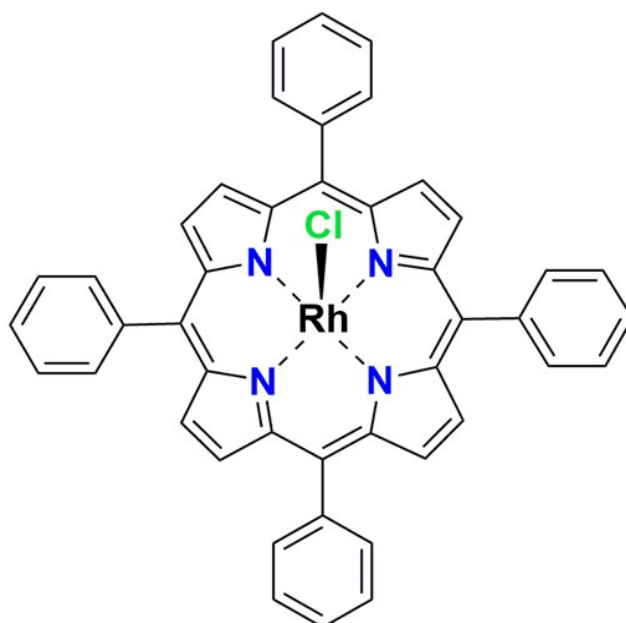


Figure 2.20: The structure of $\text{Rh}(\text{TPP})\text{Cl}$.

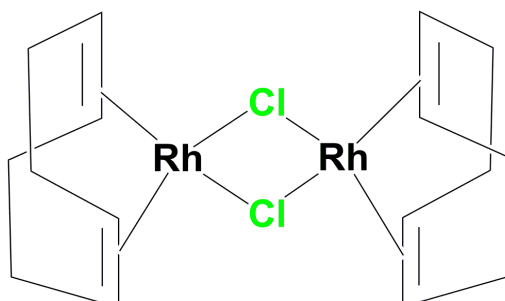


Figure 2.21: The structure of $[\text{Rh}(\text{COD})\text{Cl}]_2$.

2.2.6 Near Edge X-ray Absorption Fine Structure (NEXAFS) characterization

NEXAFS analysis was carried out at the Australian Synchrotron to further investigate the elements and their environments before and after pyrolysis. The measurements of ZIF-8@RhTA, Rh-NC samples and the standard samples were carried out at the carbon and nitrogen K edge. As rhodium has a high atomic number the corresponding measurements could not be done by this soft X-ray technique.

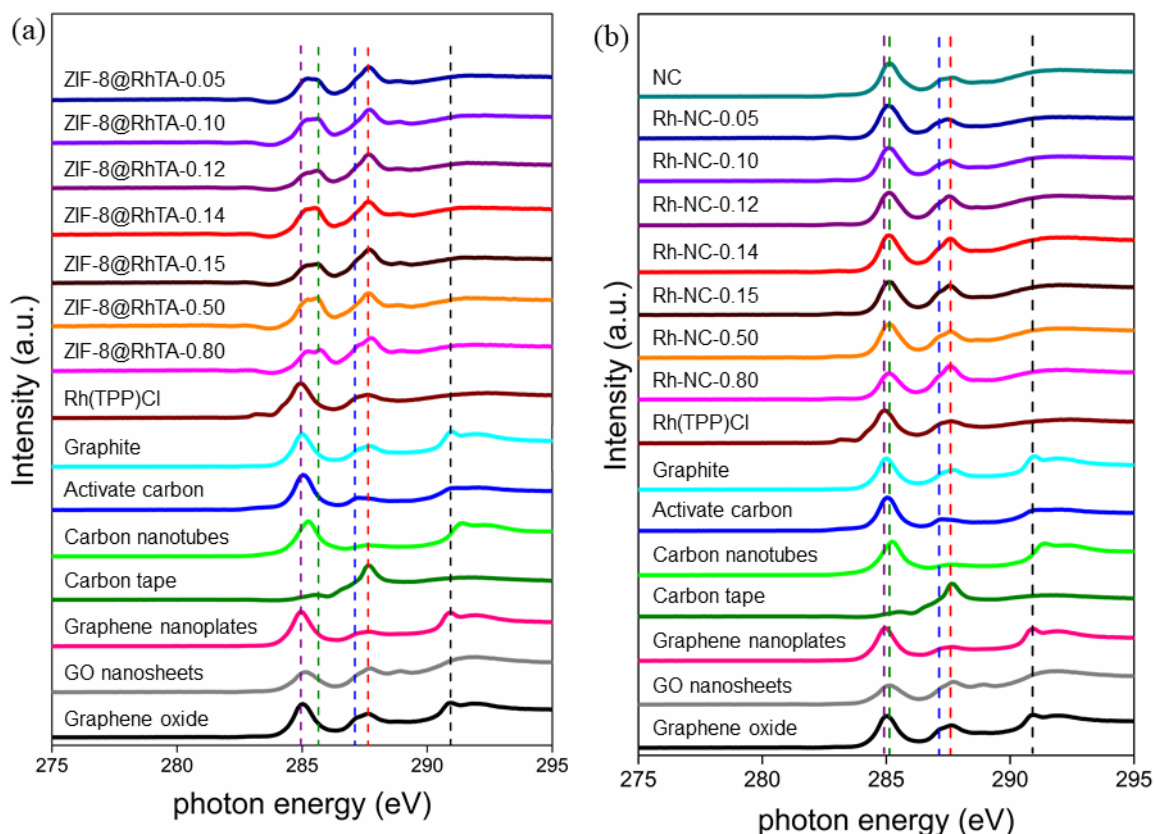


Figure 2.22: C K-edge NEXAFS spectra of (a) unpyrolyzed samples and (b) pyrolyzed samples with standards.

In the carbon K-edge spectra (Figure 2.22), Rh(TPP)Cl has a peak at 284.9 eV (purple dotted line), which can be assigned to C $1s \rightarrow \pi^*$ transitions of the porphyrin.²⁵⁸ This feature can be observed in ZIF-8@RhTA samples as well due to the C $1s \rightarrow \pi^*$ transitions of imidazole ring which is coordinated with Zn^{2+} in ZIF-8. But after the pyrolysis, the resulting Rh-NC samples do not show this peak as the bonding environment of ZIF-8 in ZIF-8@RhTA samples has been changed by the decomposition of the ligands and evaporation of zinc nodes upon the pyrolysis. Both ZIF-8@RhTA and Rh-NC samples show peaks at 285.1 and 285.6 eV (green dotted line), which can be assigned to C $1s \rightarrow \pi^*$ transitions of aromatic C=C.²⁵⁹⁻²⁶¹ In ZIF-8@RhTA samples the imidazole ring of ZIF-8 should be responsible for this peak. Moreover, aromatic C=C peak is prominent in Rh-NC samples, confirming the aromatic

nature of the carbon support which could arise from pyridinic, pyrrolic and graphitic carbon identified in the XPS analysis.

The peak at 287.1 eV (blue dotted line) can be assigned to C 1s $\rightarrow \pi^*$ transitions of C-N and C=C-N in N substituted aromatic carbon.²⁶¹⁻²⁶² This feature can be observed in Rh(TPP)Cl, ZIF-8@RhTA and Rh-NC samples. In ZIF-8@RhTA samples C-N and C=N of 2-methylimidazole is the source for this peak. The appearance of this peak even after the pyrolysis confirms the nature of aromatic nitrogen-doped carbon as N-C and N=C in Rh-NC samples.

In ZIF-8@RhTA samples, a peak at 287.6 eV (red dotted line) is observed. This can be attributed to C 1s $\rightarrow \pi^*$ transitions of C=O.²⁶⁰ This peak is observed in all the samples, as C=O is appearing in the carbon tape which is used to mount the samples during the measurements. But in ZIF-8@RhTA samples from ZIF-8@RhTA-0.05 to ZIF-8@RhTA-0.80, the intensity and the appearance of this peak is the same suggesting this peak is present due to the C=O of tannic acid coating. After the pyrolysis, this peak appeared in Rh-NC samples as well. But compared to the unpyrolyzed analogous material, the intensity of this peak is reduced. That is because during the pyrolysis process the bonded oxygen is removed in the form of gas. Interestingly, when increasing the Rh loading of the Rh-NC samples, the intensity of the C=O peak is increasing, suggesting the reduction of Rh³⁺ of the sample to Rh⁰ by oxidation of phenolic oxygen groups of tannic acid coating to C=O. In both ZIF-8@RhTA and Rh-NC samples, a broad peak around 291 eV is observed (black dotted line) due to C 1s $\rightarrow \sigma^*$ transitions of C-C.²⁵⁹

In the nitrogen K-edge spectra (Figure 2.23), Rh(TPP)Cl showed peaks at 398.8 eV (red dotted line) and 399.7 eV (purple dotted line) can be assigned to N 1s $\rightarrow \pi^*$ transitions of porphyrin N,²⁶³⁻²⁶⁴ and pyrrolic N.²⁶⁵⁻²⁶⁶ These peaks are not visible in ZIF-8@RhTA samples. After the pyrolysis these peaks appeared in Rh-NC samples, suggesting the nature of nitrogen-doped carbon in the catalyst support. Additionally in Rh-NC samples, a peak at 398.3 eV (blue dotted line) was detected which appeared neither in Rh(TPP)Cl nor ZIF-8@RhTA samples. This peak can be assigned to N 1s $\rightarrow \pi^*$ transitions of pyridinic nitrogen.²⁶⁶⁻²⁶⁸ The absence of pyridinic nitrogen in the ZIF-8@RhTA samples and presence in Rh-NC samples are in agreement with XPS data.

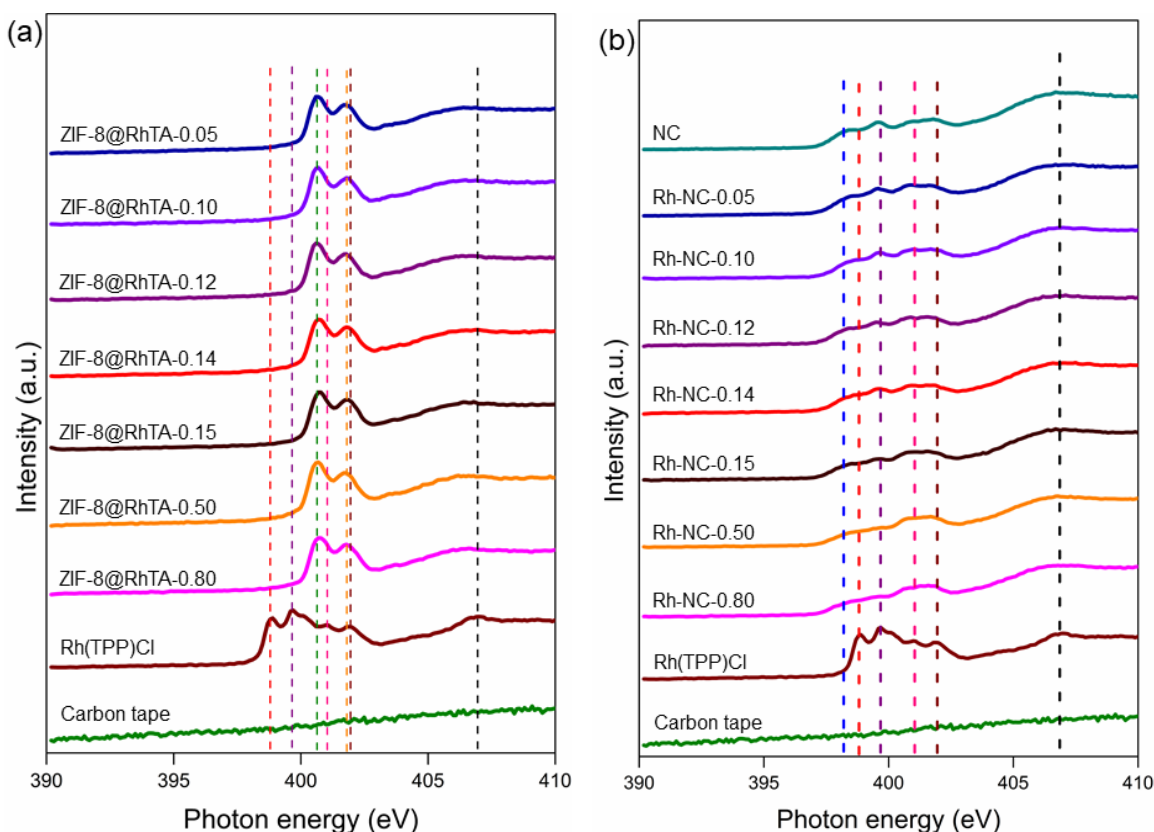


Figure 2.23: N K-edge NEXAFS spectra of (a) unpyrolyzed samples and (b) pyrolyzed samples with standards.

In N K-edge spectra of ZIF-8@RhTA samples (Figure 2.23a) a peak appeared at 400.5 eV (green line) which can be assigned to $N\ 1s \rightarrow \pi^*$ transitions of terminal C-N-H bond.²⁶⁵ This peak should come from terminal N-H of terminating 2-methylimidazole in ZIF-8 which is absent in Rh(TPP)Cl or Rh-NC samples. The peak at 401.7 eV (orange dotted line) in ZIF-8@RhTA samples is possibly due to the $1s \rightarrow \pi^*$ transitions in the C=N bonds.²⁶⁵

Rh(TPP)Cl has peaks at 400.9 eV (pink dotted line) and 401.9 eV (brown dotted line) which can be assigned to $N\ 1s \rightarrow \pi^*$ transitions of N=C and graphitic moieties.²⁶⁸ Both the peaks are absent in ZIF-8@RhTA samples, while in Rh-NC samples both peaks are present. In all the samples the broad peak around 407 eV (black dotted line) appeared due to $N\ 1s \rightarrow \sigma^*$ transitions of C-N.²⁶⁵ The N K-edge spectra of Rh-NC samples show all the peaks of Rh(TPP)Cl suggesting the porphyrin nature of the Rh-NC catalysts.

2.2.7 Extended X-ray Absorption Fine Structure (XAFS) characterization

XAFS measurements were carried out to determine the oxidation state and coordination environment of the rhodium atoms. XAFS measurements of the samples were performed in conjunction with a series of standards.

EXAFS data that were normalized in energy show that in Rh NPCs; Rh-NC-0.50 and Rh-NC-0.80, which had elevated metal loadings, the spectra more closely resemble that of 5% Rh on C and Rh foil with features at 23242, 23252 and 23265 eV (Figure 2.24).

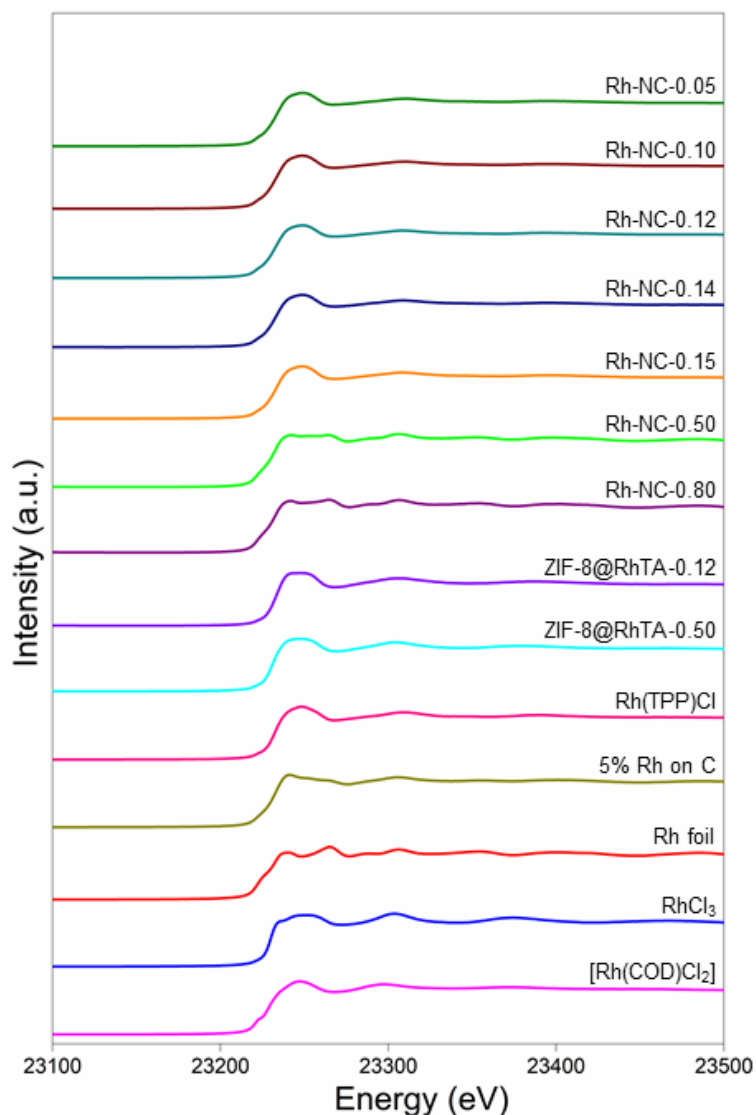


Figure 2.24: Rh K-edge EXAFS spectra for different samples and standards.

These observations are consistent with the presence of metallic Rh⁰ nanoparticles, in Rh-NC-0.50 and Rh-NC-0.80, which is in accord with the conclusion drawn from the XPS, PXRD and microscopy data. For samples within and just outside the single-atom zone; Rh-NC-0.05 to Rh-NC-0.15, only a single feature at 23250 eV is present in the spectra (Figure 2.24). This feature is comparable to the unpyrolyzed ZIF-8@RhTA sample, Rh(TPP)Cl and RhCl₃, inferring that the rhodium is found in the Rh³⁺ oxidation state in the single-atom materials.

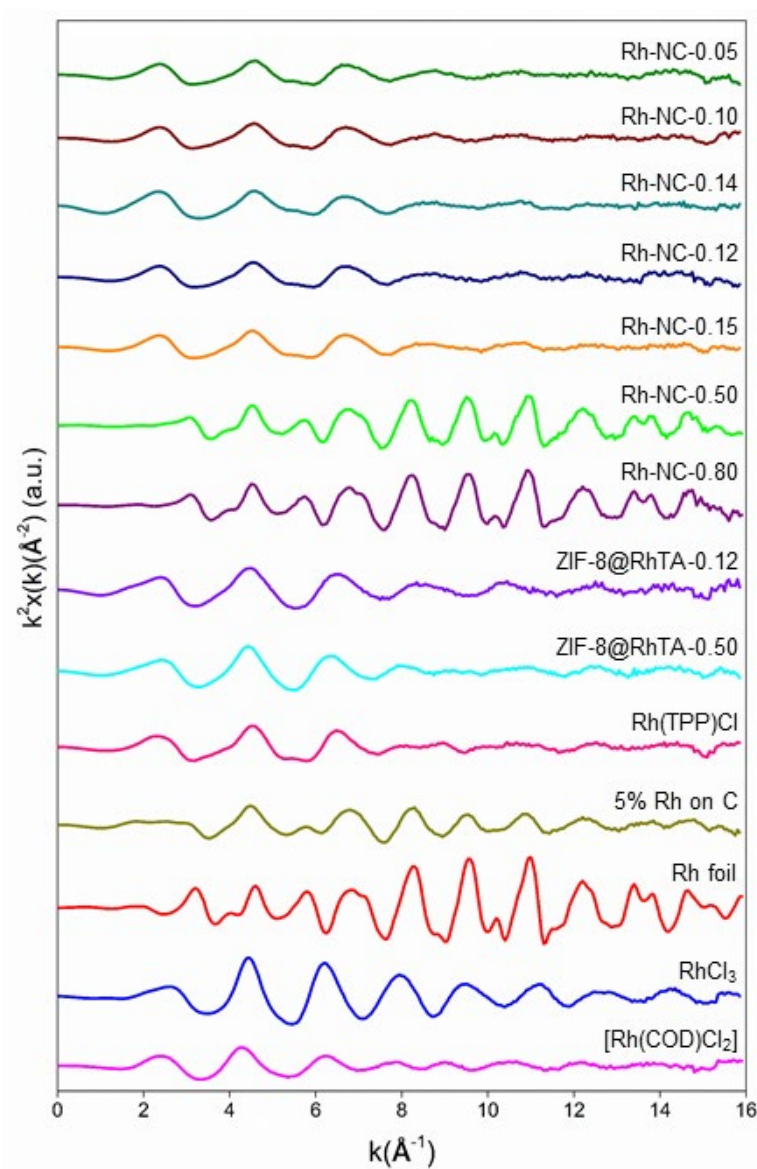


Figure 2.25: k^2 weighted Rh K-edge spectra for different samples and standards.

Turning the attention to the EXAFS region of the spectra, similar oscillations were observed between Rh foil and 5% Rh on C and Rh NPC samples, Rh-NC-0.50 and Rh-NC-0.80 (Figure 2.25). Whereas the remaining samples with lower Rh loading had markedly altered features that rapidly dropped off with increasing k . This observation is consistent with the lack of periodicity in the extended materials. The oscillations of Rh SAC samples Rh-NC-0.05 to Rh-NC-0.14, including Rh-NC-0.15, samples look alike as the chemical environment of those samples are similar. These oscillations are different from the Rh-NC-0.50, Rh-NC-0.80, Rh foil, and 5% Rh on C confirming the different chemical environment of Rh SAC samples compared to the Rh NPC samples. Moreover, ZIF-8@RhTA-0.12 and ZIF-8@RhTA-0.50 samples show similar oscillations as they have similar chemical environments. Those oscillations are different from the Rh SACs and Rh NPCs.

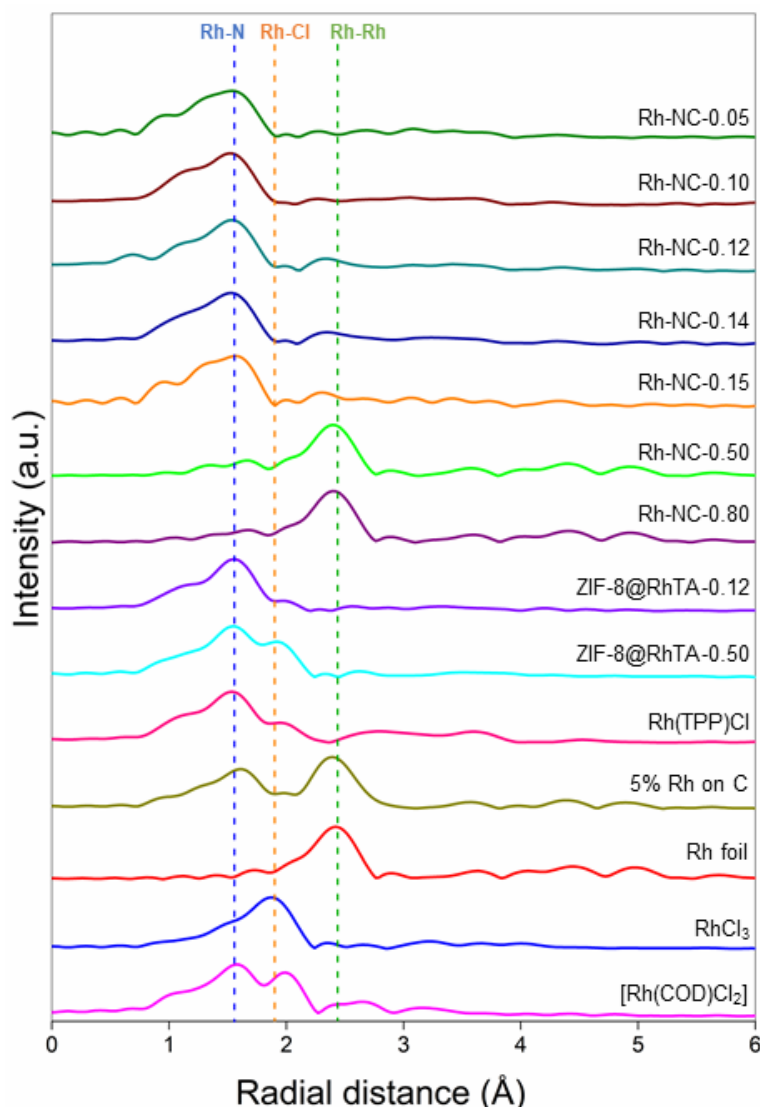


Figure 2.26: r-space plots obtained from Fourier transform on k^2 -weighted Rh K-edge EXAFS spectra for different samples and standards.

Fourier transformed (FT) k-weighted EXAFS curves of the spectra (Figure 2.26) demonstrate a prominent peak at 2.42 Å in R-space in reference to metallic rhodium foil which corresponds to Rh-Rh bonds. This peak is not present in ZIF-8@RhTA samples. Rh-Rh bonds can be observed in Rh-NC-0.50 and Rh-NC-0.80 samples, consistent with metallic nanoparticle formation during thermal treatment. Moreover, in 5% Rh on C, this peak can be observed. Indeed, the lack of metallic Rh-Rh peak with reduced metal loading levels confirms the single-atom nature of Rh-NC-0.05, Rh-NC-0.10, Rh-NC-0.12, and Rh-NC-0.14 samples, complementing earlier conclusions based on other analytical techniques.

The peak at 1.96 Å in R- space corresponds to Rh-Cl, similar to Rh(TPP)Cl and RhCl₃·3H₂O. The Rh-Cl peak was observed in ZIF-8@RhTA samples. Post-pyrolysis this peak is almost lost, likely due to the displacement of chloride capping ligands in Rh³⁺ sites during the carbonization of the material.

The main peak at 1.5 Å corresponding to Rh-N_x coordination can be observed in Rh(TPP)Cl, ZIF-8@RhTA and Rh SAC samples. This peak is not present in Rh NPC samples. With regards to the coordination environment of the single Rh atom sites in the Rh SAC materials, remaining sample peaks at short radial distances were similar to the porphyrin standard Rh(TPP)Cl as evidenced by EXAFS (Figure 2.26) and parameterized fit for this peak (Figure 2.27) to the EXAFS equation based on the crystallographic data of Rh(TPP)Cl.

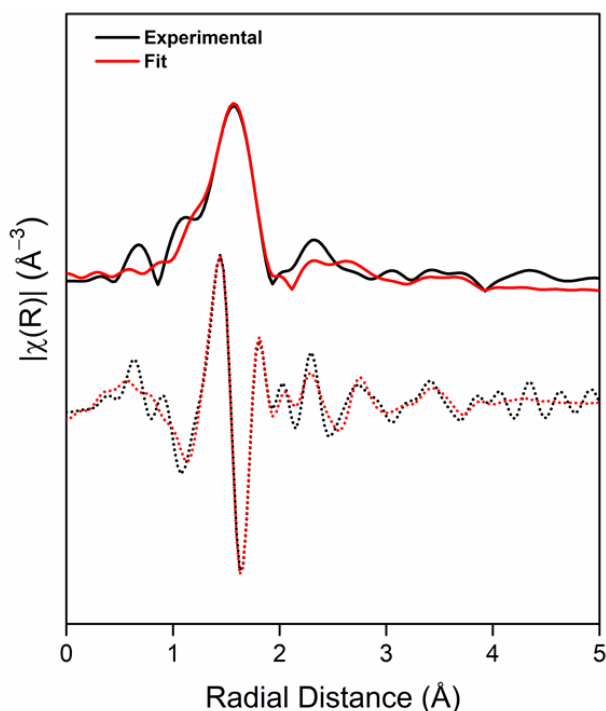


Figure 2.27: A parameterized spectral fit for Rh SAC; fit within the range 1-5 Å.

EXAFS fittings were done to find the coordination number of rhodium in Rh-NC samples and its bonding to the neighbouring atoms. Rh(TPP)Cl and all Rh SAC samples were fitted with Rh-N bond (Experimental section, Figure 2.35 - Figure 2.37). The coordination number of Rh SAC was found as 6 with Rh-N fittings (Experimental section, Table 2.10). The radial distance of Rh-N and Rh-O are 1.98 Å and 2.02 Å respectively. These values are very similar; and almost impossible to distinguish them (Figure 2.38). Therefore, the Rh SAs in Rh SAC has a coordination number of 6 and they could have bonded with nitrogen and oxygen. The fittings of Rh SAC for Rh-N and Rh-O suggest the presence of four Rh-N in the graphitic layer and two axial Rh-O bonds (possibly in the form of H₂O) (Table 2.11).

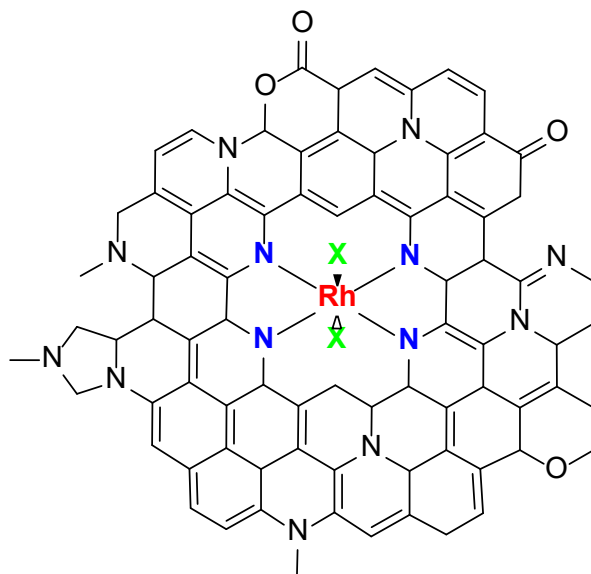


Figure 2.28: The structural depiction of Rh SAC; X represents O₂ or H₂O.

2.3 Conclusion

In conclusion, the synthesis of Rh SAC was carried out in four steps. First ZIF-8 was synthesized and then it was coated with KTA coordination polymer. Subsequently, rhodium was introduced via a rhodium chloride solution. Finally, Rh-NC materials were obtained by pyrolysis. When high rhodium concentrations were used, it resulted in Rh NPCs while low concentrations lead to Rh SACs upon the pyrolysis.

In the pyrolysis process, ZIF-8@RhTA decomposes and the resulting Rh-NC catalysts consist of pyridinic, pyrrolic and graphitic nitrogen-doped carbon. The tannic acid layer acts as a host to nucleate the nitrogen and carbon in ZIF-8 during the decomposition process and results in hollow nitrogen-doped carbon support. The rhodium atoms of Rh SAC are attached to the outer layer of the support. The Rh SAC has 5.64 wt% of rhodium, which is embedded as single atoms in hollow nitrogen-doped carbon supports. Rhodium single-atoms in Rh SAC are in Rh^{3+} and Rh^0 oxidation states in which Rh^{3+} are prominent. When increasing the amount of rhodium, nanoparticles were formed, and the oxidation state of Rh NPCs is Rh^{3+} (corresponding to single-atom sites) and Rh^0 (corresponding to nanoparticles) in which the Rh^0 oxidation state was prominent. In Rh NPCs, Rh-Rh bonds can be detected due to the nanoparticle nature of the samples. In contrast, there were no Rh-Rh bonds detected in Rh SAC confirming the single-atom nature of this material. Rh SAC has six coordinated Rh-N and Rh-O; probably four Rh-N and two Rh-O bonds.

2.4 Experimental Section

2.4.1 General procedures

All starting materials and solvents were used as received from commercial sources without further purification unless otherwise noted. X-ray diffraction data were collected using either of two methods: (a) Rigaku Spider diffractometer equipped with a Micromax MM007 rotating anode generator with Cu K α radiation (wavelength = 1.54180 Å.), high flux Osmic multilayer mirror optics, and a curved image plate detector, and finally processed into 1-D diffractograms using 2DP, (b) Bruker D8 Venture diffractometer with Cu K α radiation (wavelength = 1.54180 Å.), with a diamond microfocus X-ray source and Photon III detector. For PXRD the collected 1D diffractograms were processed using APEX3.

Atomic absorption spectroscopy analysis (AAS) was performed using GBC Scientific Equipment XplorAA series AAS using oxyacetylene flame for the atomization of the metals. Fourier transform infrared spectroscopy (FTIR) data were collected by a Thermo Scientific NICOLET is5 iD7 ATR in ATR mode.

Raman spectra were recorded under ambient conditions with a custom-built Raman microscope. A 532 nm excitation (Laser Quantum Torus 532) was focused onto the silver nanoparticle/analyte aggregate via an N.A. = 0.65 (40 \times magnification) microscope objective. The laser power at the sample was <1 mW. Back-scattered Raman and Rayleigh scattered light was collected by the same objective, and the Rayleigh component was rejected by a 532 nm Raman edge filter (Iridian Spectral Technologies) and focused onto the entrance slit of a Teledyne (Princeton) Instruments Isoplan81 (FERGIE) spectrograph. Spectral data were acquired using LightField 6.1 software. No background removal was applied during data collection. The detector exposure time was 20 – 90 and 5 exposures (data frames) were captured and 2 frames per spectra were collected, which were averaged before data analysis.

For scanning electron microscopy (SEM) images and energy-dispersive X-ray (EDX) analysis, samples are mounted on aluminum stubs and sputter-coated with gold (Baltic SCD 050 sputter coater) and viewed in the FEI Quanta 200 Environmental Scanning Electron Microscope at an accelerating voltage of 15kV – 25kV. EDX data were collected and analysed using EDAX Genesis V.51 software. Transmission electron microscopy (TEM) samples were viewed and imaged with an FEI Tecnai G2 Spirit BioTWIN (Czech Republic) (Camera: Veleta, Olympus SIS Germany). Optical microscope images were taken by Zeiss high-resolution MicroPublisher 6 colour camera.

High-resolution scanning transmission electron microscopy (HRTEM) images were taken using a probe corrected FEI Titan 60-300 electron microscope operated under 300 kV and equipped with an annular dark-field (ADF) detector and an energy dispersive X-ray (EDX) detector. The images are acquired using a convergence angle of 21.4 mrad and collection angle 70-200 mrad.

X-ray photoelectron spectroscopy (XPS) was acquired on a Kratos Axis UltraDLD X-ray photoelectron spectrometer, equipped with a monochromatized Al-K α X-ray source (1486.69 eV). XPS peak fitting was performed using CASSA software.

C K-edge and N K-edge NEXAFS spectra were collected on the soft X-ray spectroscopy beamline at the Australian Synchrotron. For the analyses, the samples were deposited onto double-sided carbon tape. The NEXAFS data were taken in the total electron yield (TEY) mode at an analysis chamber pressure of 1×10^{-10} Torr. The TEY data were normalized against a current measured simultaneously on a gold mesh in the beamline to eliminate potential spectral artifacts caused by fluctuations in the beam intensity whilst scanning. The measurements were carried out in high-resolution (HR) mode by increasing the photon energies in steps of 0.05 or 0.1 eV.

Rh K-edge X-ray XAFS and EXAFS spectra were collected in fluorescence mode on the X-ray absorption spectroscopy beamline at the Australian Synchrotron (200 mA, 3.0 GeV). The powder samples were homogeneously mixed with cellulose to obtain a Rh concentration of around 1000 ppm. A Si (111) single crystal was used to monochromatize the X-ray beam. The raw XAFS data were processed (background subtraction, normalization and Fourier transformation) using standard procedures within the Athena module of the IFEFFIT software package.

Rh K-edge EXAFS data were extracted from the absorption spectra above the threshold energy (E_0). All data were initially fitted with simultaneous k-weighting of 1, 2, and 3, then finalized with k^3 -weighting in R-space. Fit windows in k-space were determined based on the lowest quality data collected, and all data sets were from 0 - 6 \AA^{-1} . Fit windows in R-space were determined on a case-by-case basis, based on the features apparent in the spectrum and the energy shift of the photoelectron (ΔE_0) were global parameters. Independent structural parameters determined by the fits included the change in the scattering half path length (R) and the relative mean square displacement of the scattering element (σ^2). For each fit, the number of variables was not permitted to exceed 2/3 the number of independent points, in keeping with the Nyquist criterion. EXAFS fittings were performed by the Artemis module, following the EXAFS equation below.

$$\chi(k) = \sum_j \frac{N_j S_0^2 F_j(k)}{k R_j^2} \exp[-2K^2 \sigma_j^2] \exp \left[\frac{-2R_j}{\lambda(k)} \right] \sin [2kR_j + \phi_j(k)] \quad \text{Eq. 2.1}$$

Where, S_0^2 is the amplitude reduction factor, $F_j(k)$ is the effective curved-wave backscattering amplitude, N_j is the number of neighbours in the j^{th} atomic shell, R is the distance between the X-ray absorbing central atom and the atoms in the j^{th} atomic shell, λ is the mean free path in Å, $\phi_j(k)$ is the phase shift, σ_j^2 is the Debye-Waller parameter of the j^{th} atomic shell (variation distances around the average R_j).

2.4.2 Synthesis of ZIF-8

Nanocrystalline ZIF-8 was first synthesized by methanolic room temperature synthesis.²³⁸ 2-methylimidazole (4.00 g, 48.72 mmol) was dissolved in 40 mL of methanol. To this, a solution of $\text{Zn}(\text{NO}_3)_2 \cdot 6\text{H}_2\text{O}$ (1.69 g, 5.68 mmol) in 20 mL of methanol was added. The resulting solution was stirred for 1 hr and then was incubated at room temperature for 24 hours without stirring. The solution was centrifuged at 4000 rpm for 15 min to separate the crystalline product, which was then subjected to three washing cycles with methanol (centrifugation at 5000 rpm for 5 min) and then dried *in vacuo* for 24 hours.

2.4.3 Synthesis of ZIF-8@KTA

ZIF-8 (200 mg) was dispersed in deionized water (10 mL) which was then added to a tannic acid solution (5 mL, 24 mM) in which pH was adjusted to 8 with aqueous KOH (6M) prior to adding and stirred for 5 min. The mixture was collected in a centrifuge tube, dispersed in methanol (15 mL) and centrifuged at 5000 rpm for 5 min to separate the precipitate. The precipitate was subjected to three washing cycles with methanol (centrifugation at 5000 rpm for 5 min) and then dried *in vacuo* for 24 hours.

2.4.4 Bulk synthesis of ZIF-8@KTA

ZIF-8 (6.6 g) was dispersed in deionized water (330 mL). This was then added to a tannic acid solution (165 mL, 6.7 g) in which pH was adjusted to 8 with aqueous KOH (6M) prior to adding and stirred for 5 min. The mixture was dispersed in methanol (250 mL) and centrifuged at 5000 rpm for 5 min to separate the product, which was subjected to three washing cycles with methanol (centrifugation at 5000 rpm for 5 min) and then dried *in vacuo* for 24 hours.

2.4.5 Synthesis of ZIF-8@RhTA

ZIF-8@KTA (75 mg) was soaked in a methanolic solution of $\text{RhCl}_3 \cdot 3\text{H}_2\text{O}$. The solution was stirred for 2 hrs. Then it was centrifuged to separate the product (5000 rpm for 5 min). The product was subjected to three washing cycles with methanol (centrifugation at 5000 rpm for 5 min) and then dried *in vacuo* for 24 hours.

2.4.6 Bulk synthesis of ZIF-8@RhTA

ZIF-8@KTA (375 mg) was soaked in a methanolic solution (500 mL) of $\text{RhCl}_3 \cdot 3\text{H}_2\text{O}$. The solution was stirred for 2 hrs. Then it was centrifuged to separate the product (5000 rpm for 5 min). The product was subjected to three washing cycles with methanol (centrifugation at 5000 rpm for 5 min) and then dried *in vacuo* for 24 hours.

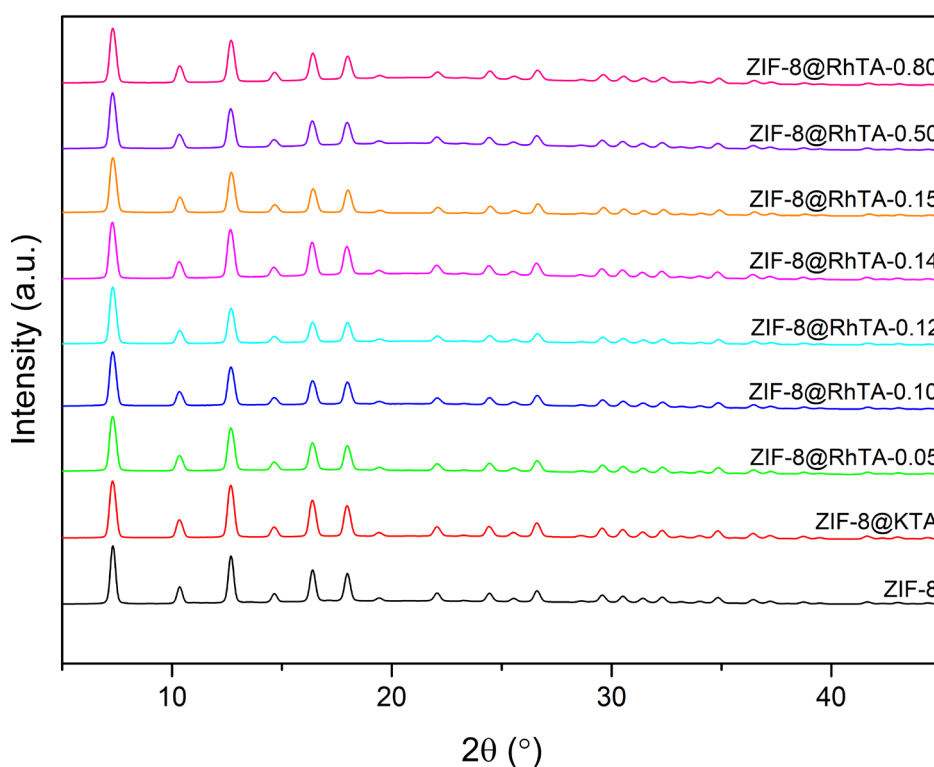


Figure 2.29: PXRD patterns of ZIF-8, ZIF-8@KTA and ZIF-8@RhTA.

2.4.7 Synthesis of Rh-NC

ZIF-8@RhTA (70 mg) was placed on a ceramic boat in a tube furnace which was then purged for 1 hour with argon at a flow rate of 10 ml/min. The samples were set to carbonize at 900 °C for 2 hours at a heating rate of 1 °C/min under the same flow of argon.

Table 2.3: Synthesis of ZIF-8@RhTA and Rh-NC.

ZIF-8@RhTA code	ZIF-8@KTA	[RhCl ₃]	Rh-NC sample code
ZIF-8@KTA-0	375 mg	0 mM	NC
ZIF-8@KTA-0.05	375 mg	0.05 mM	Rh-NC-0.05
ZIF-8@KTA-0.10	375 mg	0.10 mM	Rh-NC-0.10
ZIF-8@KTA-0.12	375 mg	0.12 mM	Rh-NC-0.12
ZIF-8@KTA-0.14	375 mg	0.14 mM	Rh-NC-0.14
ZIF-8@KTA-0.15	375 mg	0.15 mM	Rh-NC-0.15
ZIF-8@KTA-0.50	375 mg	0.50 mM	Rh-NC-0.50
ZIF-8@KTA-0.80	375 mg	0.80 mM	Rh-NC-0.80

2.4.8 FTIR and Raman spectra

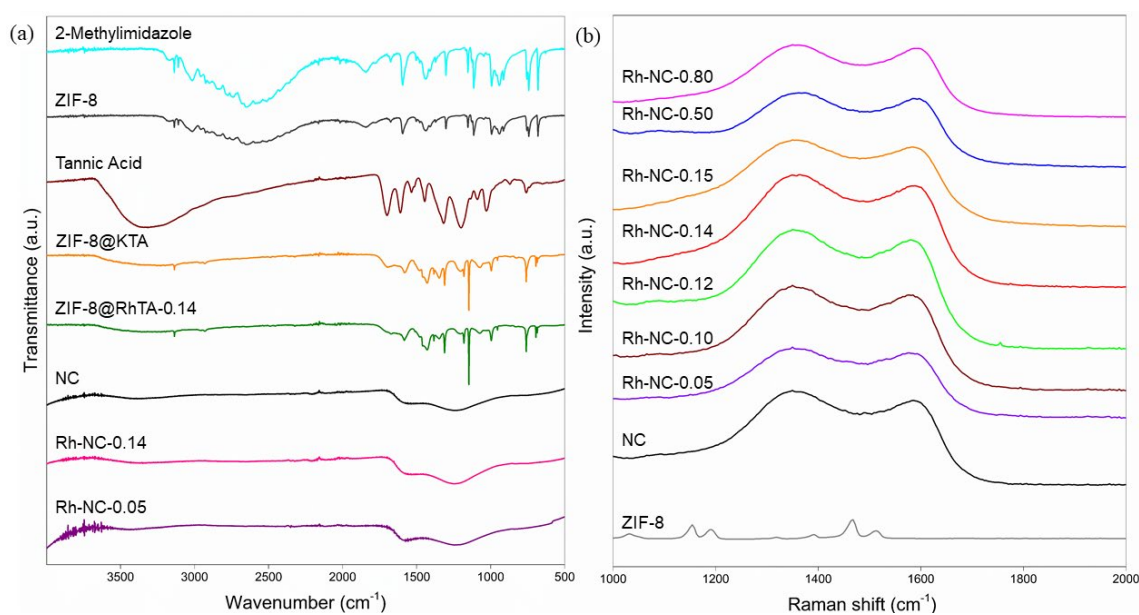


Figure 2.30: (a) FTIR spectra of 2-methylimidazole, ZIF-8, tannic acid, ZIF-8@KTA, ZIF-8@RhTA-0.14, NC, Rh-NC-0.14 and Rh-NC-0.05 and (b) Raman spectra of ZIF-8, ZIF-8@RhTA-0.14 and Rh-NC samples.

2.4.9 SEM and EDX analysis

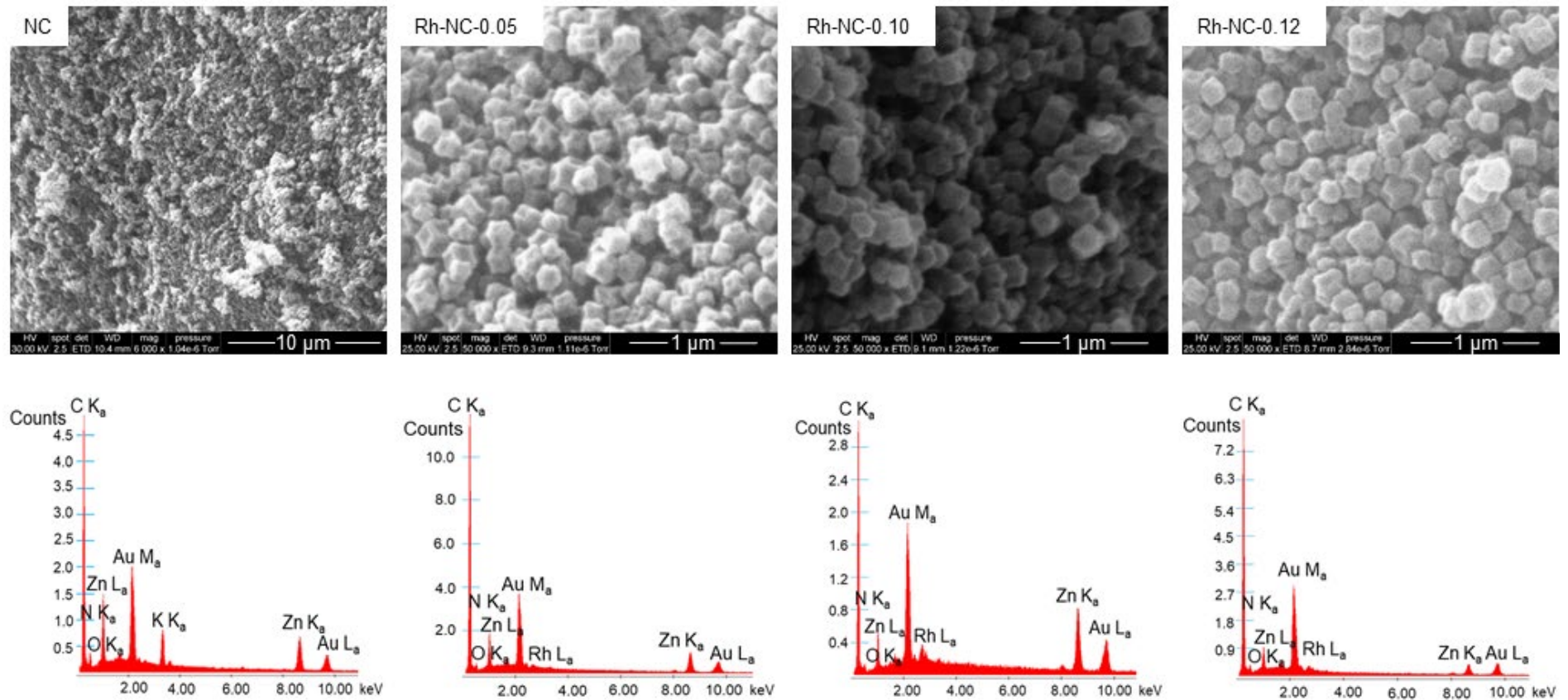


Figure 2.31: SEM and EDX of NC, Rh-NC-0.05, Rh-NC-0.10 and Rh-NC-0.12; counts in thousands.

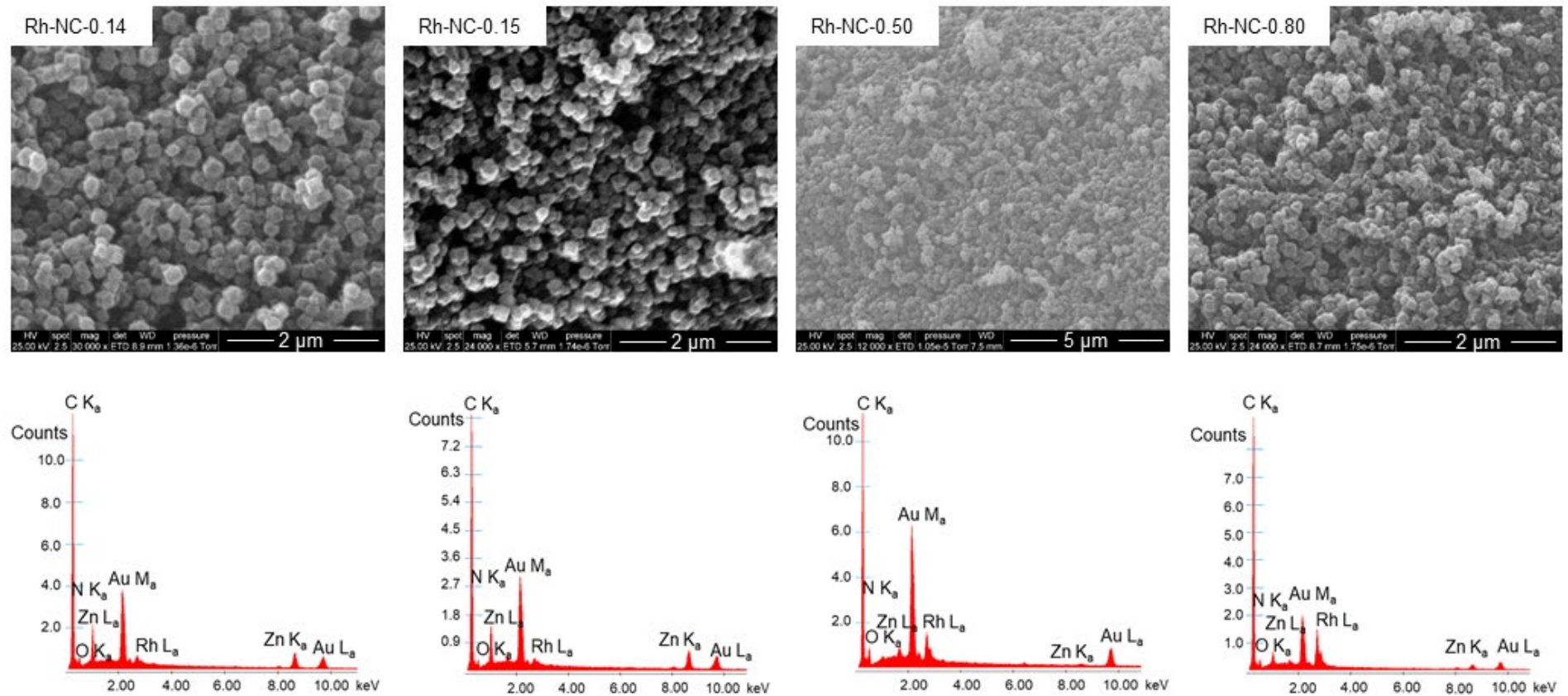


Figure 2.32: SEM and EDX of Rh-NC-0.14, Rh-NC-0.15, Rh-NC-0.50 and Rh-NC-0.80; counts in thousands.

2.4.10 TEM images

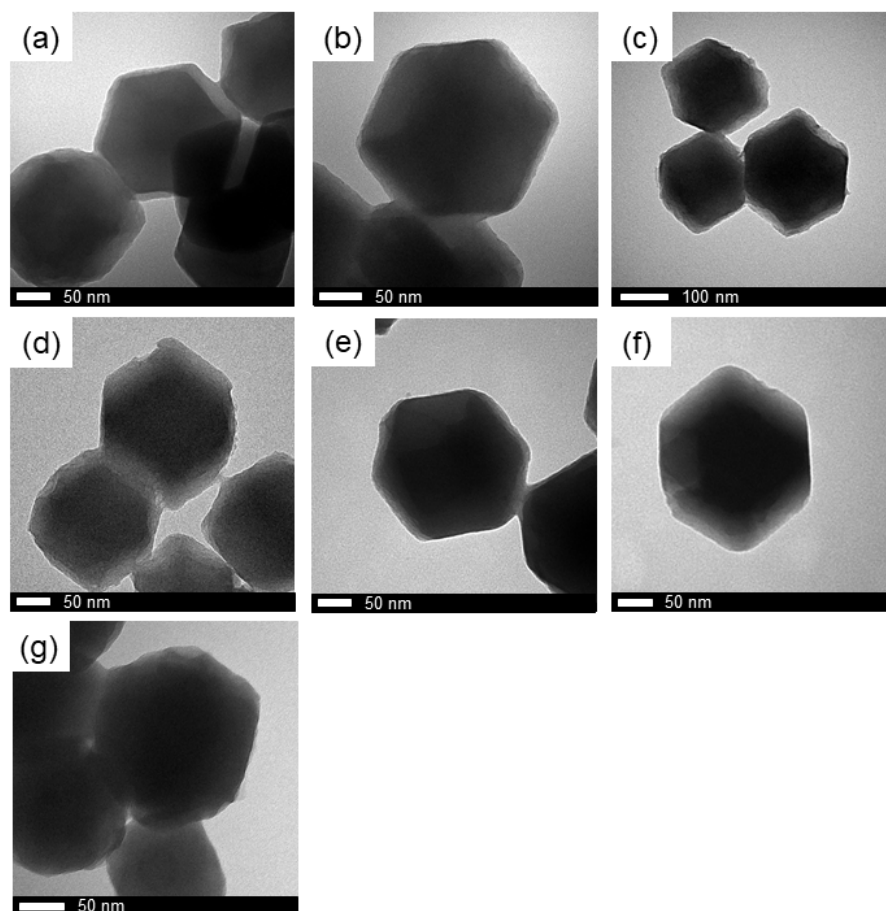


Figure 2.33: TEM images of (a) ZIF-8@RhTA-0.05, (b) ZIF-8@RhTA-0.10, (c) ZIF-8@RhTA-0.12, (d) ZIF-8@RhTA-0.14, (e) ZIF-8@RhTA-0.15, (f) ZIF-8@RhTA-0.50 and (g) ZIF-8@RhTA-0.80.

2.4.11 XPS analysis

Table 2.4: Summarized chemical composition data for ZIF-8@RhTA, Rh-NC and reference samples (as wt.%).

Sample description	Wt. % by survey XPS						
	C	N	O	Zn	Cl	Rh	K
ZIF-8@KTA	47.3	7.9	22.0	20.4	-	-	2.4
ZIF-8@RhTA-0.05	52.2	6.0	20.1	17.6	0.7	2.6	-
ZIF-8@RhTA-0.10	45.0	7.1	19.6	22.8	1.9	3.7	-
ZIF-8@RhTA-0.12	45.1	7.4	18.7	22.4	2.3	4.3	-
ZIF-8@RhTA-0.14	43.2	7.8	18.4	23.8	2.1	4.8	-
ZIF-8@RhTA-0.15	47.5	7.3	18.6	21.0	1.9	3.7	-
ZIF-8@RhTA-0.50	42.6	7.4	17.9	23.6	5.1	3.5	-
ZIF-8@RhTA-0.80	39.7	7.1	15.7	22.0	7.7	7.8	-
NC	78.6	9.9	5.2	5.5	0.8	-	-
Rh-NC-0.05	73.9	10.0	4.9	8.2	0.8	2.3	-
Rh-NC-0.10	72.0	10.6	4.6	8.0	1.0	3.7	-
Rh-NC-0.12	72.3	9.4	5.5	7.5	0.8	4.5	-
Rh-NC-0.14	72.4	9.8	5.9	6.6	0.8	4.5	-
Rh-NC-0.15	73.1	8.4	4.6	5.1	0.8	8.1	-
Rh-NC-0.50	67.6	8.8	7.2	5.4	1.0	10.0	-
Rh-NC-0.80	70.4	7.6	5.9	3.2	0.7	12.2	-
Rh porphyrin	70.0	5.9	4.8	-	4.8	14.7	-
[Rh(COD)Cl] ₂	82.3	2.9	-	-	4.4	10.4	-
5% Rh on C	75.6	-	6.0	-	-	18.3	-

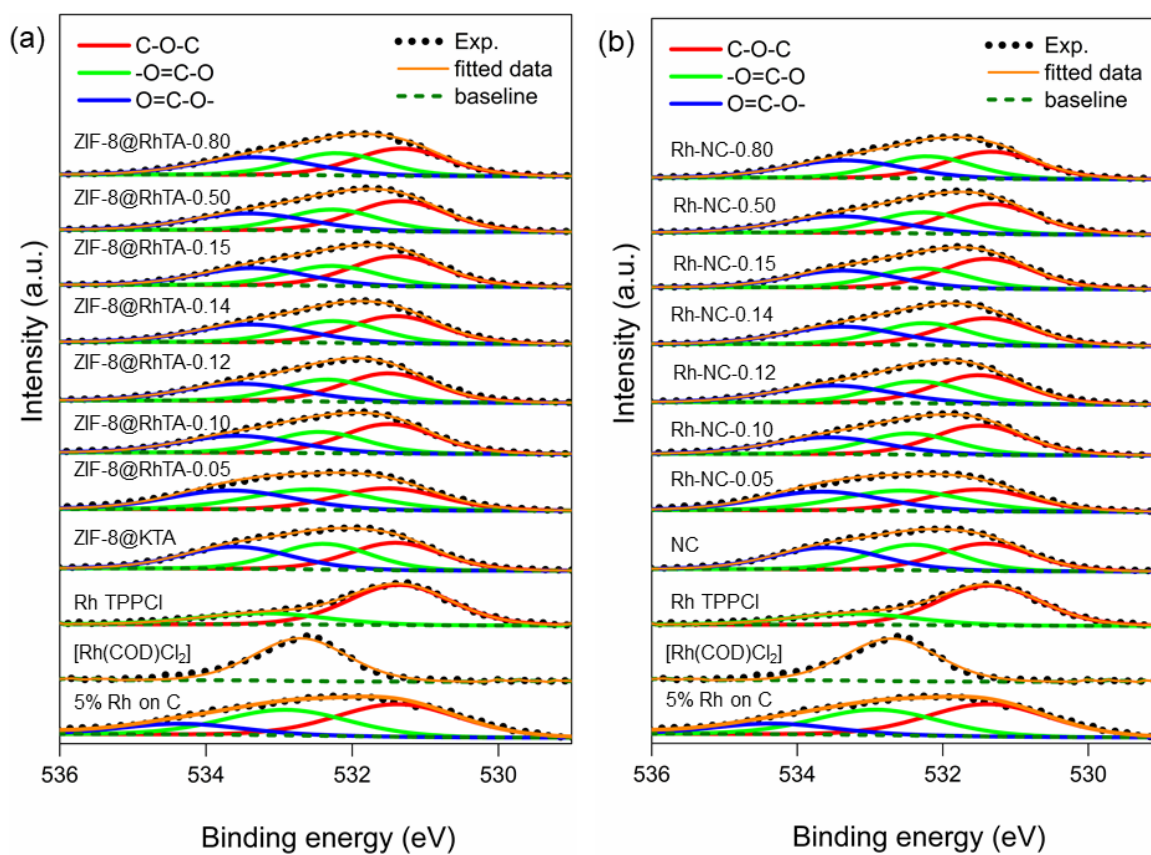


Figure 2.34: O 1s XPS spectra of (a) unpyrolysed samples and (b) pyrolyzed samples with standards.

2.4.12 EXAFS fittings

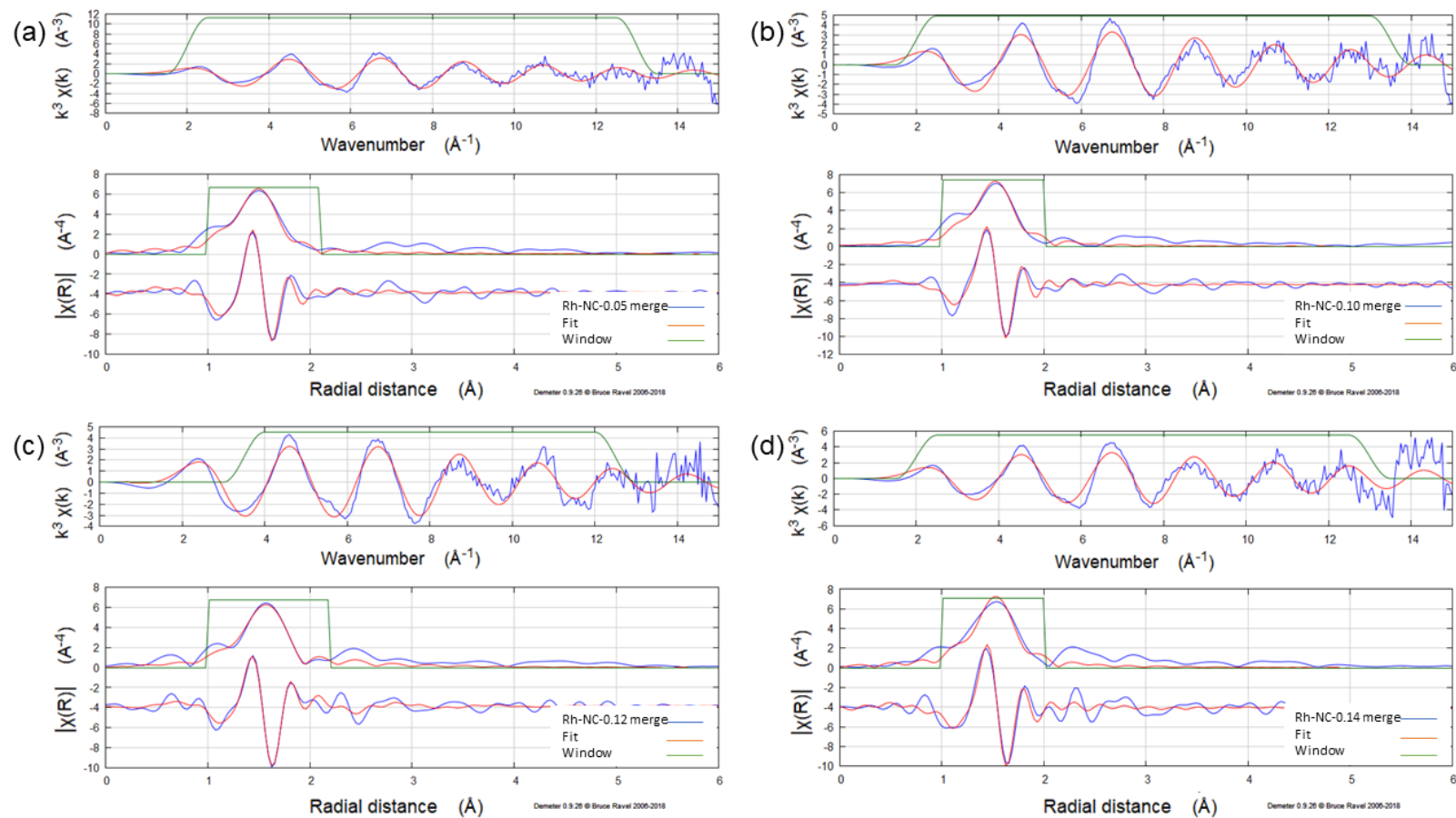


Figure 2.35: EXAFS fittings for Rh-N/Rh-O for (a) Rh-NC-0.05, (b) Rh-NC-0.10, (c) Rh-NC-0.12 and (d) Rh-NC-0.14 samples; On the top panel individual contributions of Rh-NC samples are shown in k-space, while on the bottom panel they are shown in R-space.

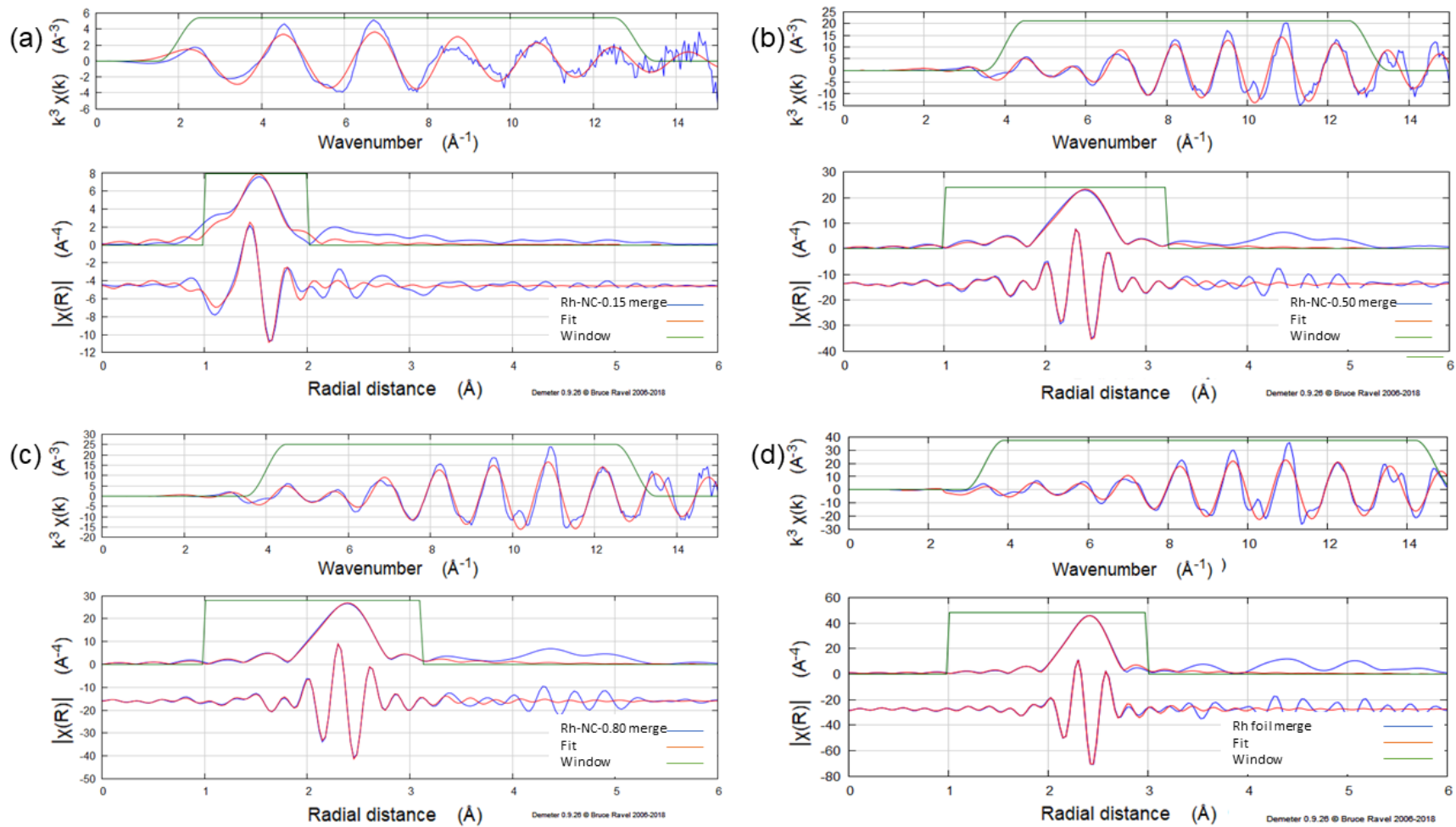


Figure 2.36: EXAFS fittings for Rh-N/Rh-O for (a) Rh-NC-0.15, (b) Rh-NC-0.50, (c) Rh-NC-0.80 samples and (d) Rh foil reference sample; On the top panel individual contributions of Rh-NC samples are shown in k -space, while on the bottom panel they are shown in R -space.

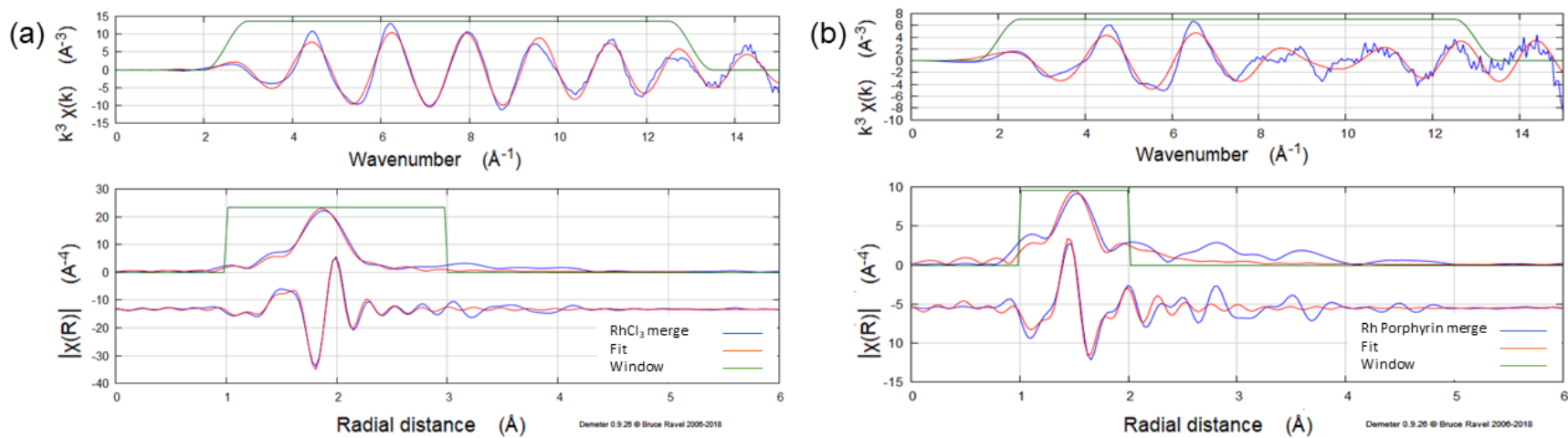


Figure 2.37: EXAFS fittings for Rh-N/Rh-O for RhCl₃ and (b) Rh(TPP)Cl; On the top panel individual contributions of the samples are shown in k-space, while on the bottom panel they are shown in R-space.

Table 2.5: EXAFS fitting parameters at Rh K-edge for Rh SAC samples with various Rh loadings and Rh(TPP)Cl.

Sample	CN	R(Å)	$\sigma^2(\text{Å}^2)$	E_0 (eV)	R factor %
Rh-NC-0.05	6.4	2.002	0.005	-5.689	2.10
Rh-NC-0.10	6.4	2.007	0.004	-2.970	2.48
Rh-NC-0.12	6.5	2.030	0.005	2.110	1.84
Rh-NC-0.14	6.0	2.015	0.004	-1.763	1.77
Rh-NC-0.15	6.5	2.018	0.004	-1.976	1.80
Rh(TPP)Cl	4.6	2.009	0.002	-3.723	1.63

CN: the coordination number; R: interatomic distance between central atoms and surrounding coordination atoms; σ^2 is Debye-Waller factor to measure thermal and static disorder in absorber-scatter distances; ΔE_0 : edge-energy shift (the difference between the zero kinetic energy value of the sample and that of the theoretical model). R factor is used to value the goodness of the fitting. S_0^2 : the amplitude reduction factor; $S_0^2 = 0.76$, S_0^2 is determined from a metallic Rh reference.

Table 2.6: EXAFS fitting parameters at Rh K-edge for Rh-NC-0.50

Rh-N path	CN	R(Å)	$\sigma^2(\text{Å}^2)$	E_0 (eV)	R factor %
Rh-Rh	9.7	2.694	0.005	0.947	0.6
Rh-O	2.0	1.986	0.004		

CN: the coordination number; R: interatomic distance between central atoms and surrounding coordination atoms; σ^2 is Debye-Waller factor to measure thermal and static disorder in absorber-scatter distances; ΔE_0 : edge-energy shift (the difference between the zero kinetic energy value of the sample and that of the theoretical model). R factor is used to value the goodness of the fitting. S_0^2 : the amplitude reduction factor; $S_0^2 = 0.76$, S_0^2 is determined from a metallic Rh reference.

Table 2.7: EXAFS fitting parameters at Rh K-edge for Rh-NC-0.80

Rh-N path	CN	R(Å)	$\sigma^2(\text{Å}^2)$	E_0 (eV)	R factor %
Rh-Rh	10.0	2.691	0.004	1.299	0.26
Rh-O	1.2	1.983	0.002		

CN: the coordination number; R: interatomic distance between central atoms and surrounding coordination atoms; σ^2 is Debye-Waller factor to measure thermal and static disorder in absorber-scatter distances; ΔE_0 : edge-energy shift (the difference between the zero kinetic energy value of the sample and that of the theoretical model). R factor is used to value the goodness of the fitting. S_0^2 : the amplitude reduction factor; $S_0^2 = 0.76$, S_0^2 is determined from a metallic Rh reference.

Table 2.8: EXAFS fitting parameters at Rh K-edge for RhCl₃·3H₂O.

Rh-N path	CN	R(Å)	$\sigma^2(\text{Å}^2)$	E ₀ (eV)	R factor %
Rh-Cl	6.2	2.328	0.003	-0.406	2.05

CN: the coordination number; R: interatomic distance between central atoms and surrounding coordination atoms; σ^2 is Debye-Waller factor to measure thermal and static disorder in absorber-scatterer distances; ΔE_0 : edge-energy shift (the difference between the zero kinetic energy value of the sample and that of the theoretical model). R factor is used to value the goodness of the fitting. S_0^2 : the amplitude reduction factor; $S_0^2 = 0.76$, S_0^2 is determined from a RhCl₃ reference.

Table 2.9: EXAFS fitting parameters at Rh K-edge for Rh foil.

Rh-N path	CN	R(Å)	$\sigma^2(\text{Å}^2)$	E ₀ (eV)	R factor %
Rh-Rh	12.0	2.688	0.004	6.597	0.47

CN: the coordination number; R: interatomic distance between central atoms and surrounding coordination atoms; σ^2 is Debye-Waller factor to measure thermal and static disorder in absorber-scatterer distances; ΔE_0 : edge-energy shift (the difference between the zero kinetic energy value of the sample and that of the theoretical model). R factor is used to value the goodness of the fitting. S_0^2 : the amplitude reduction factor; $S_0^2 = 0.76$, S_0^2 is determined from a metallic Rh reference

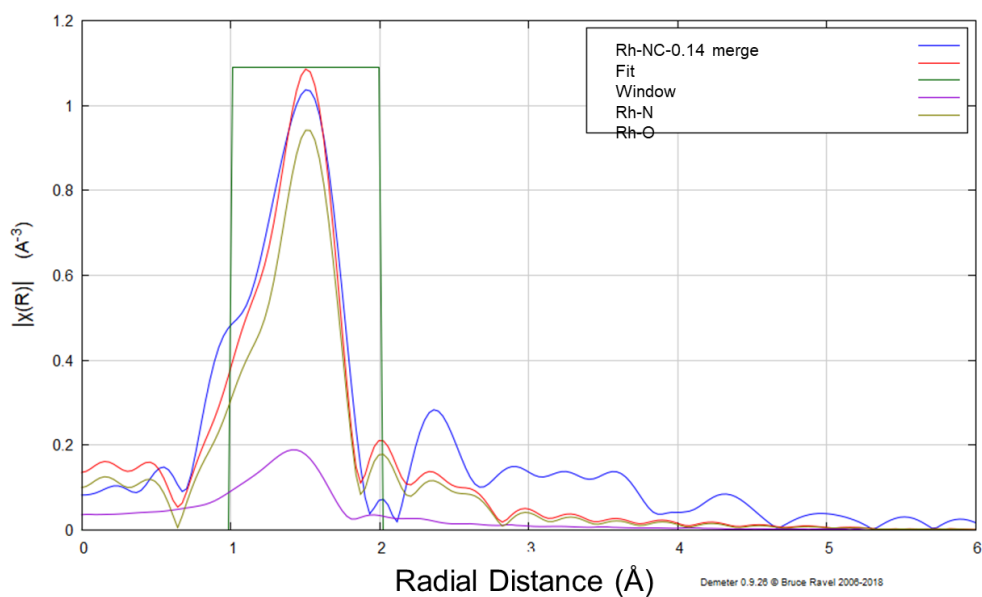


Figure 2.38: EXAFS fittings for Rh-N and Rh-O for Rh-NC-0.14, individual contributions are shown in k-space.

Table 2.10: EXAFS fitting parameters at Rh K-edge for Rh-NC-0.14 for Rh-N bonds.

Rh-N path	CN	R(\AA)	$\sigma^2(\text{\AA}^2)$	E_0 (eV)	R factor %
Rh-N	6.0	2.015	0.004	-1.763	1.77

When the Rh-N bond is fitted, the coordination number of Rh in the sample is ~6

CN: the coordination number; R: interatomic distance between central atoms and surrounding coordination atoms; σ^2 is Debye-Waller factor to measure thermal and static disorder in absorber-scatter distances; ΔE_0 : edge-energy shift (the difference between the zero kinetic energy value of the sample and that of the theoretical model). R factor is used to value the goodness of the fitting. S_0^2 : the amplitude reduction factor; $S_0^2 = 0.76$, S_0^2 is determined from a metallic Rh reference

Table 2.11: EXAFS fitting parameters at Rh K-edge for Rh-NC-0.14 for Rh-O and Rh-N bonds.

Rh-N path	CN	R(\AA)	$\sigma^2(\text{\AA}^2)$	E_0 (eV)	R factor %
Rh-N	4.5	1.982	0.005	-4.073	1.91
Rh-O	1.6	2.024	0.001		

After fitted Rh-O bond, the coordination number of Rh in the sample is ~6

CN: the coordination number; R: interatomic distance between central atoms and surrounding coordination atoms; σ^2 is Debye-Waller factor to measure thermal and static disorder in absorber-scatter distances; ΔE_0 : edge-energy shift (the difference between the zero kinetic energy value of the sample and that of the theoretical model). R factor is used to value the goodness of the fitting. S_0^2 : the amplitude reduction factor; $S_0^2 = 0.76$, S_0^2 is determined from a metallic Rh reference

Chapter 3 – Synthesis and Characterization of Co SAC

3.1 Introduction

In the previous chapter, Rh SAC was synthesized by four steps: (i) synthesis of ZIF-8, (ii) tannic acid coating, (iii) introduction of rhodium (iv) pyrolysis (Figure 3.1 a). The first three steps include washing with methanol and drying the resulting precipitate *in vacuo* for 24 hours. SACs efficiently use expensive metals and may reduce the cost of catalysts. To make the synthesis more efficient and cost-effective, it is convenient to reduce one step of synthesis and bring it down to three steps, saving chemicals and time. Thus, in the synthesis of Co SAC, one step of the above procedure can be reduced by introducing cobalt(II) ions to the framework of ZIF-8. When Co(II) is used in the synthesis of ZIF-8 instead of Zn(II), the resulting ZIF is named ZIF-67 which has an iso-reticular structure to ZIF-8.³ Then the tannic acid coating was carried out to obtain the hollow carbon shell of the catalysts upon pyrolysis (Figure 3.1 b).

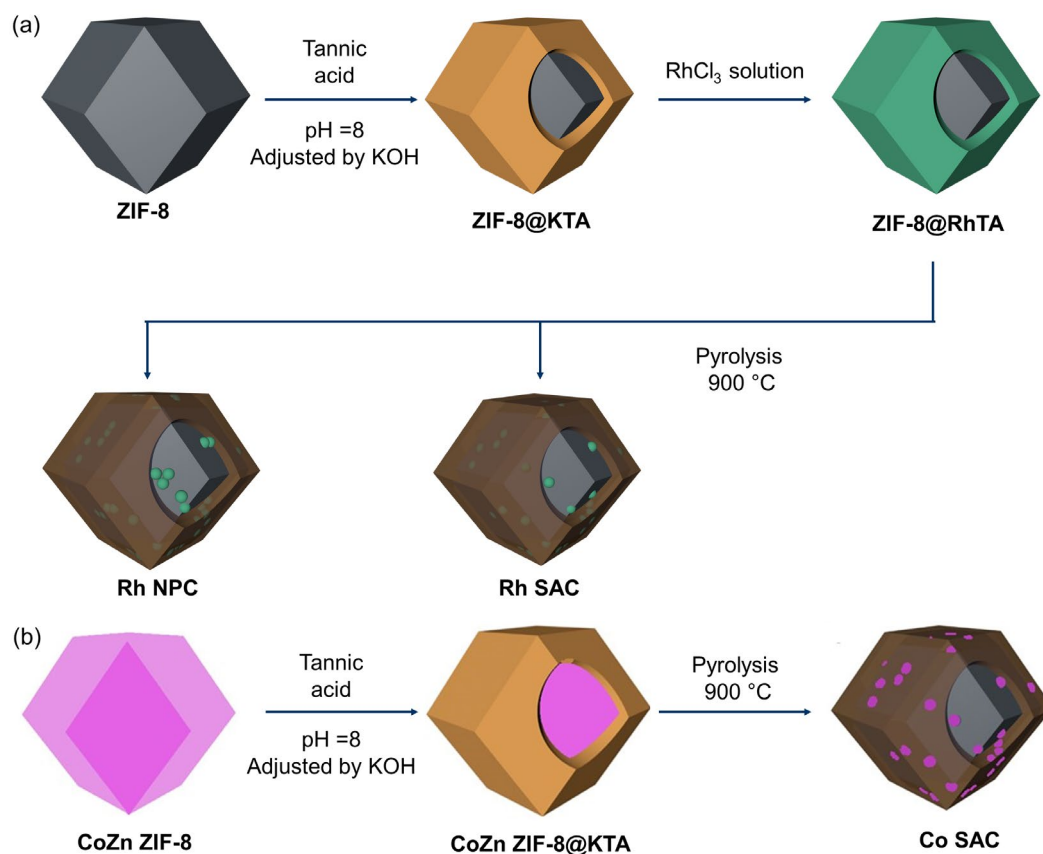


Figure 3.1: Synthesis of (a) Rh SAC by four steps and (b) Co SAC by three steps.

3.2 Results and Discussion

3.2.1 Synthesis and characterization of CoZn ZIF-8

CoZn ZIF-8 was synthesized by mixing cobalt(II) and zinc(II) salts with 2-methylimidazole in the synthesis of ZIF-8 (Figure 3.2). Due to the iso-reticular nature of ZIF-8 and ZIF-67, the zinc and cobalt ions are connected to 2-methylimidazole ligands resulting in CoZn ZIF-8 which showed the same PXRD pattern as ZIF-8/ZIF-67 (Figure 3.3).

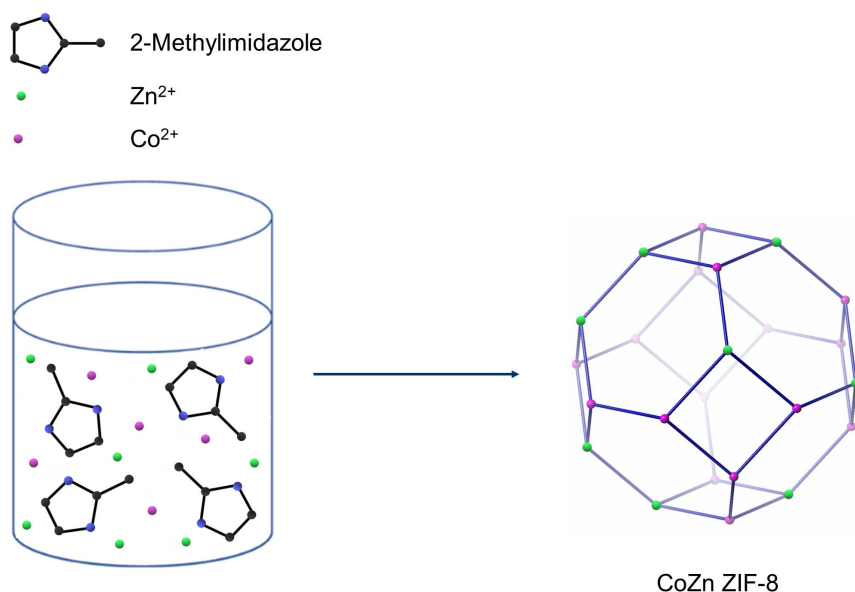


Figure 3.2: Synthesis of CoZn ZIF-8.

Co SAC was synthesized by doing the tannic acid coating over the synthesized CoZn ZIF-8 and pyrolyzing them, which will be discussed later in this chapter. To obtain the maximum amount of cobalt loading in Co SAC, CoZn ZIF-8 samples were synthesized by doping 7, 35, 49, 60, 150, and 200 mg of cobalt in the synthesis of ZIF-8. The size of the resulting CoZn ZIF-8 samples was around 200 nm, and they were named as Co_{0.42}Zn ZIF-8, Co_{2.07}Zn ZIF-8, Co_{2.88}Zn ZIF-8, Co_{3.50}Zn ZIF-8, Co_{8.32}Zn ZIF-8, and Co_{10.79} ZIF-8 respectively, based on the molar percentage of cobalt in the solution used for the synthesis of CoZn ZIF-8 samples (Table 3.2). For this study, ZIF-8 was synthesized as the negative control which did not contain cobalt, and ZIF-67 was synthesized as the positive control which had the highest amount of cobalt loading.

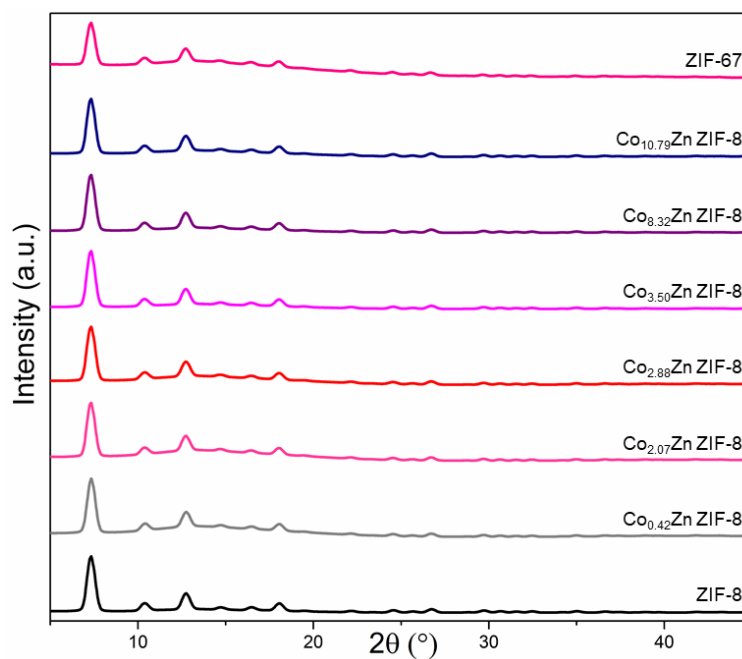


Figure 3.3: PXRD patterns of ZIF-8, CoZn ZIF-8 and ZIF-67.

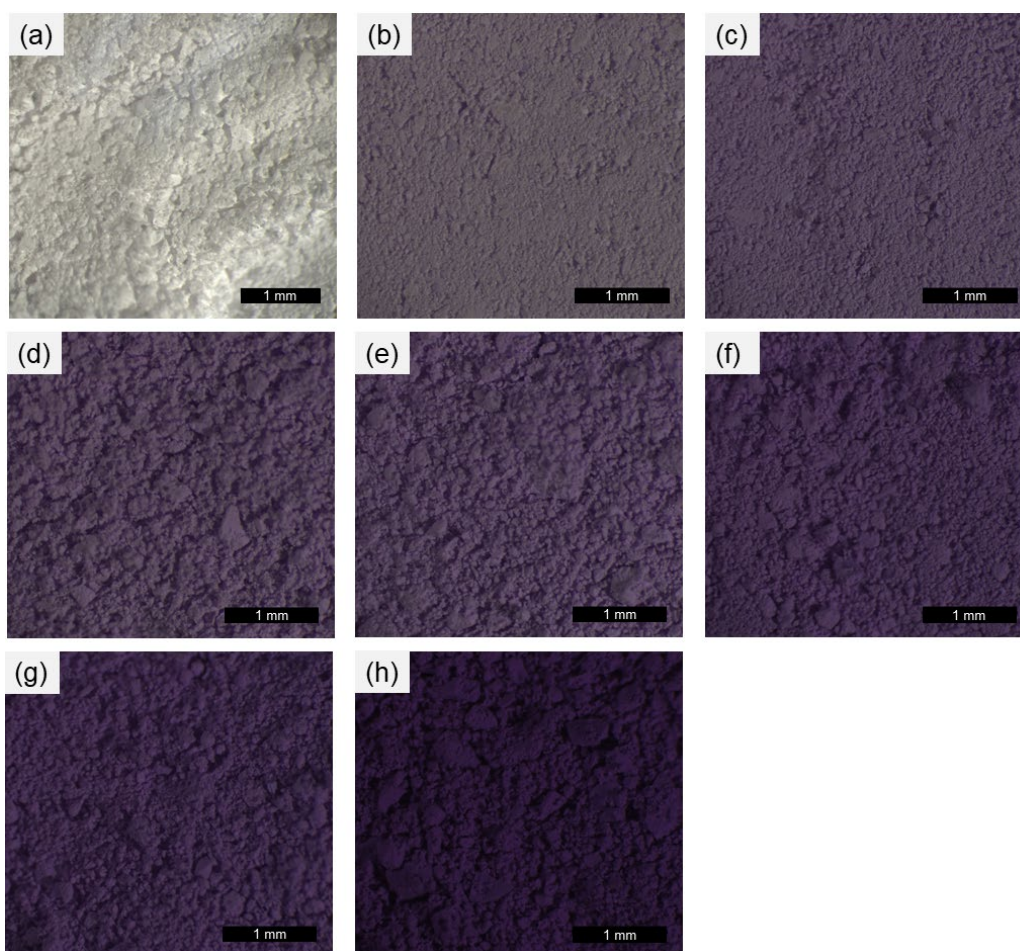


Figure 3.4: Optical microscope images of (a) ZIF-8, (b) Co_{0.42}Zn ZIF-8, (c) Co_{2.07}Zn ZIF-8, (d) Co_{2.88}Zn ZIF-8, (e) Co_{3.50}Zn ZIF-8, (f) Co_{8.32}Zn ZIF-8, (g) Co_{10.79}Zn ZIF-8 and (h) ZIF-67.

The amount of cobalt in the CoZn ZIF-8 samples was increased with the cobalt doping. This can be visualized even by the naked eye, as the colour of CoZn ZIF-8 samples develops from light purple to dark purple when increasing the cobalt doping (Figure 3.4). These samples were quantified by AAS. In agreement with these results, the intensity of cobalt peak in EDX was also increasing when increasing the cobalt doping (Experimental section, Figure 3.26 and Figure 3.27). However, Co_{0.42}Zn ZIF-8 which was the Co Zn ZIF-8 with the lowest cobalt loading did not show any cobalt peak in EDX (Figure 3.26), which is probably due to the low amount of cobalt in the sample.

3.2.2 Synthesis and characterization of CoZn ZIF-8@KTA

The CoZn ZIF-8 samples, ZIF-8 and ZIF-67 crystals were coated with tannic acid (TA) by dispersing them in deionized (DI) water and adding to a TA solution in which the pH was adjusted to 8. After stirring for 5 mins, coated CoZn ZIF-8 samples, ZIF-8 and ZIF-67 (CoZn ZIF-8@KTA, ZIF-8@KTA, ZIF-67@KTA) were obtained (Figure 3.5). Owing to the chelating ability of TA,²⁴⁰ it forms a coordination polymer (termed KTA) on the outer surface of the MOF crystals in conjunction with potassium ions. As TA molecules are larger than the pores of the MOFs, KTA did not enter inside of ZIF-8 through the pores.

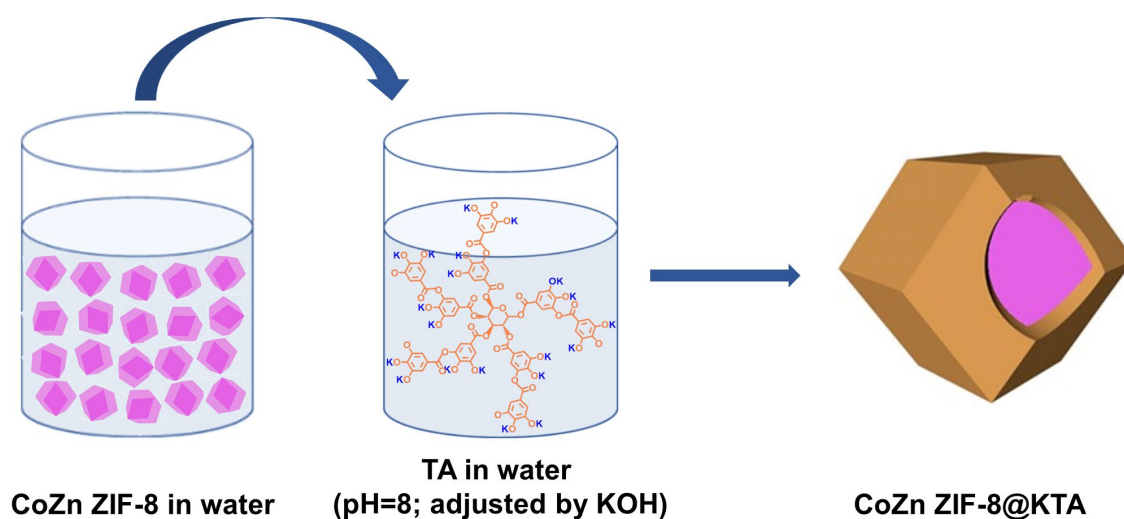


Figure 3.5: Synthesis of CoZn ZIF-8@KTA.

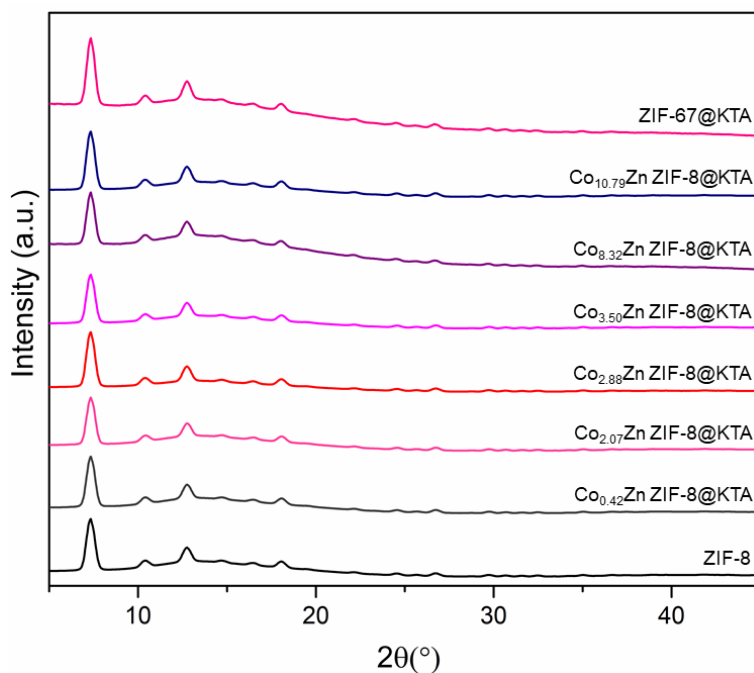


Figure 3.6: PXRD patterns of ZIF-8@KTA, CoZn ZIF-8@KTA samples and ZIF-67@KTA.

The crystallinity of the samples remains unchanged as confirmed by PXRD. Due to the amorphous nature of KTA, it did not introduce any additional peaks to the PXRD of CoZn ZIF-8 samples, ZIF-8@KTA or ZIF-67@KTA upon the coating (Figure 3.6). The appearance of a potassium peak in the EDX spectra confirmed the samples are coated with KTA (Experimental section, Figure 3.28 and Figure 3.29). It was even visible to the naked eye that the samples were coated with KTA, as the bright colour of CoZn ZIF-8 samples faded after the KTA coating (Figure 3.7). This was further confirmed by comparing the TEM images of CoZn ZIF-8 samples and its KTA coated analogues. The sharp edges of CoZn ZIF-8 samples, ZIF-8 and ZIF-67 could be observed under the TEM (Experimental section, Figure 3.34). But after the KTA coating a thin, rough and low-density layer could be observed for CoZn ZIF-8@KTA, ZIF-8@KTA and ZIF-67@KTA samples under TEM (Experimental section, Figure 3.35).

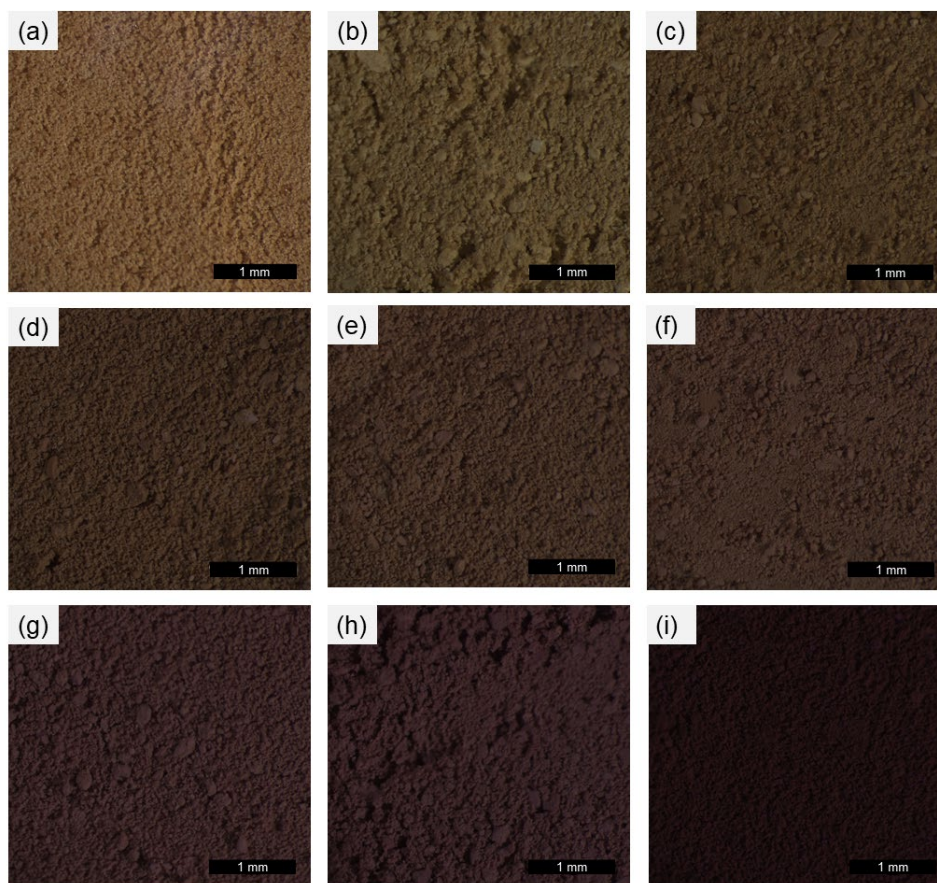


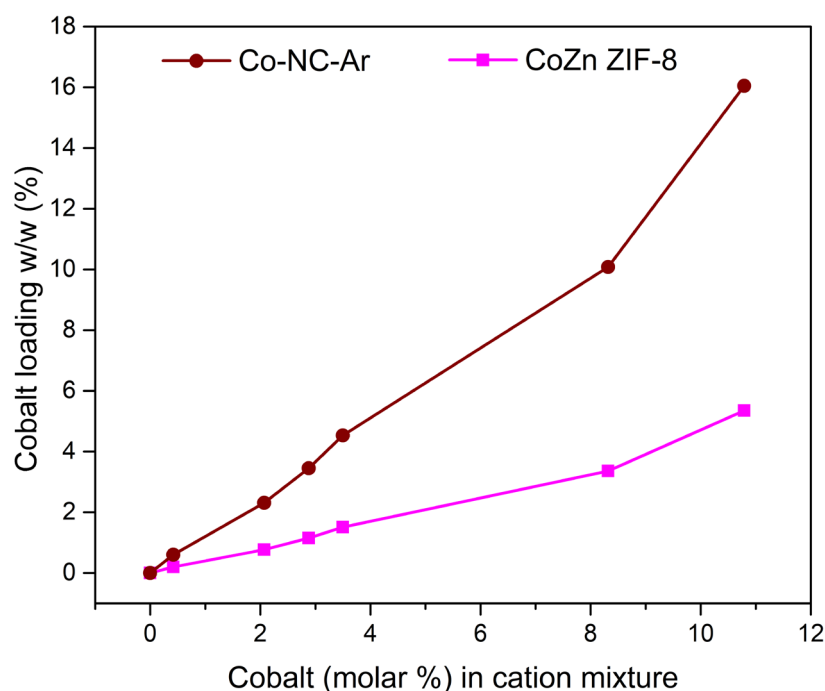
Figure 3.7: Optical microscope images of (a) tannic acid, (b) ZIF-8@KTA, (c) $\text{Co}_{0.42}\text{Zn}$ ZIF-8@KTA, (d) $\text{Co}_{2.07}\text{Zn}$ ZIF-8@KTA, (e) $\text{Co}_{2.88}\text{Zn}$ ZIF-8@KTA, (f) $\text{Co}_{3.50}\text{Zn}$ ZIF-8@KTA (g) $\text{Co}_{8.32}\text{Zn}$ ZIF-8@KTA, (h) $\text{Co}_{10.79}\text{Zn}$ ZIF-8@KTA and (i) ZIF-67@KTA.

3.2.3 Synthesis and characterization of Co-NC

The CoZn ZIF-8 samples were pyrolyzed at 900 °C in a tube furnace. To see the effect of different inert environments in the pyrolysis, these samples were pyrolyzed under Ar and H_2/Ar resulting in materials termed $\text{Co}_x\text{-NC-Ar}$ and $\text{Co}_x\text{-NC-H}_2$ where X is the molar percentage of cobalt in the solution used for the synthesis of CoZn ZIF-8.

Table 3.1: Cobalt loading in CoZn ZIF-8 samples and corresponding Co-NC-Ar and Co-NC-H₂ samples.

CoZn ZIF-8 Code	Co loading % w/w	CoZn ZIF-8@KTA code	Co-NC-Ar sample code	Co loading % w/w	Co-NC-H ₂ sample code
ZIF-8	0	ZIF-8@KTA	NC-Ar	0	NC- H ₂
Co _{0.42} Zn ZIF-8	0.20	Co _{0.42} Zn ZIF8@KTA	Co _{0.42} -NC-Ar	0.06	Co _{0.42} -NC- H ₂
Co _{2.07} Zn ZIF-8	0.77	Co _{2.07} Zn ZIF8@KTA	Co _{2.07} -NC-Ar	2.31	Co _{2.07} -NC- H ₂
Co _{2.88} Zn ZIF-8	1.15	Co _{2.88} Zn ZIF8@KTA	Co _{2.88} -NC-Ar	3.45	Co _{2.88} -NC- H ₂
Co _{3.50} Zn ZIF-8	1.51	Co _{3.50} Zn ZIF8@KTA	Co _{3.50} -NC-Ar	4.53	Co _{3.50} -NC- H ₂
Co _{8.32} Zn ZIF-8	3.36	Co _{8.32} Zn ZIF8@KTA	Co _{8.32} -NC-Ar	10.08	Co _{8.32} -NC- H ₂
Co _{10.79} Zn ZIF-8	5.35	Co _{10.79} Zn ZIF-8@KTA	Co _{10.79} -NC-Ar	16.05	Co _{10.79} -NC- H ₂
ZIF-67	27.57	ZIF-67@KTA	Co _{max} -NC-Ar	82.71	Co _{max} -NC- H ₂

**Figure 3.8:** Co loading of CoZn ZIF-8 (magenta) and Co-NC-Ar (brown) with molar% of cobalt in the cation mixture.

When increasing the cobalt doping in the cation mixture in the synthesis of CoZn ZIF-8 samples, the amount of cobalt in the CoZn ZIF-8 is also increasing accordingly (Figure 3.8). ZIF-67 had the maximum amount of cobalt among these samples. During the pyrolysis process, the KTA layer over the CoZn ZIF-8@KTA forms a carbon shell, which acts as a substrate to nucleate nitrogen-doped carbon and cobalt. The optimization was done by increasing the cobalt doping, to find the precise point at which atomic dispersion of metal sites changed from the single metal atoms to nanoparticles.

In the PXRD of Co-NC-Ar samples peaks at 41.2° and 51.5° 2θ Cu K_α are expected for Co NPs. NC-Ar, Co_{0.42}-NC-Ar, Co_{2.07}-NC-Ar, and Co_{2.88}-NC-Ar samples did not show any Co NP peaks in the PXRD suggesting the single-atom nature of cobalt in these samples (Figure 3.9). Even in the TEM images, there was no sign of dark spots for the Co NPS in these samples, the appearance was the same as the negative control, NC-Ar (Figure 3.10). In the EDX, however, the emergence of cobalt peak confirms the existence of cobalt in these samples (Experimental section, Figure 3.30 and Figure 3.31). The cobalt in NC-Ar, Co_{0.42}-NC-Ar, Co_{2.07}-NC-Ar, and Co_{2.88}-NC-Ar samples should present as single metal atoms.

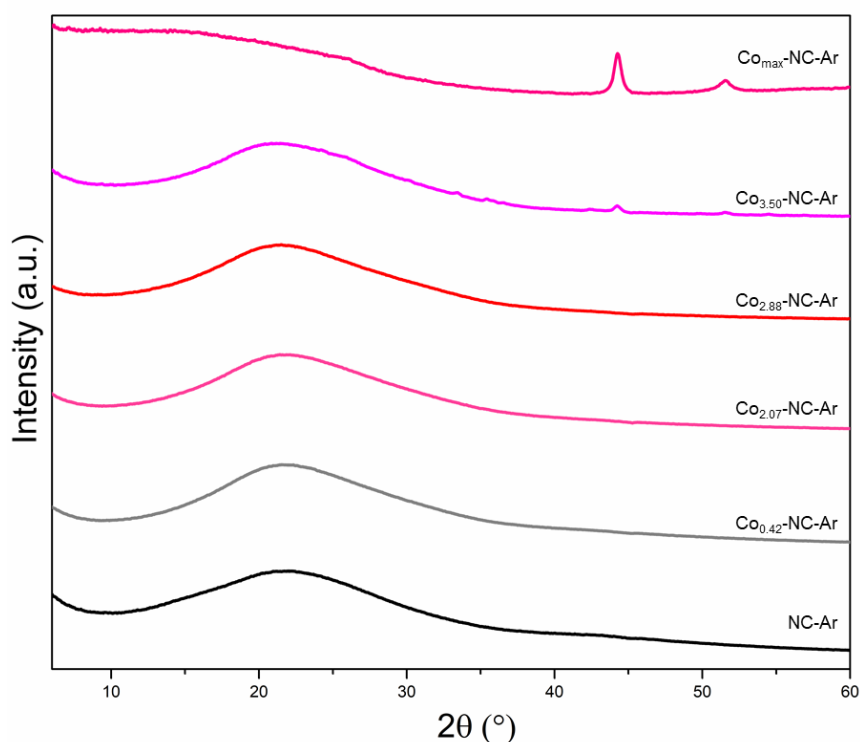


Figure 3.9: PXRD patterns of NC-Ar, Co-NC-Ar samples and Co_{max}-NC-Ar.

When the cobalt doping was increased further, in the $\text{Co}_{3.50}\text{-NC-Ar}$ sample the appearance of Co NP peak in the PXRD was observed (Figure 3.9). For this sample, several Co NPs could be observed in the TEM images as well (Figure 3.10). Hence, the $\text{Co}_{3.50}\text{-NC-Ar}$ sample is the margin of Co SAC and Co NPC. In the $\text{Co}_{\text{max}}\text{-Ar}$ sample which had a maximum cobalt doping, an intense peak for cobalt could be identified in the PXRD suggesting the higher loading of cobalt (Figure 3.9). In agreement with this, in the TEM images, the size and the number of Co NPS in $\text{Co}_{3.50}\text{-NC-Ar}$, $\text{Co}_{8.32}\text{-NC-Ar}$, $\text{Co}_{10.79}\text{-NC-Ar}$, and $\text{Co}_{\text{max}}\text{-NC-Ar}$ were increased with the increased cobalt doping (Figure 3.10).

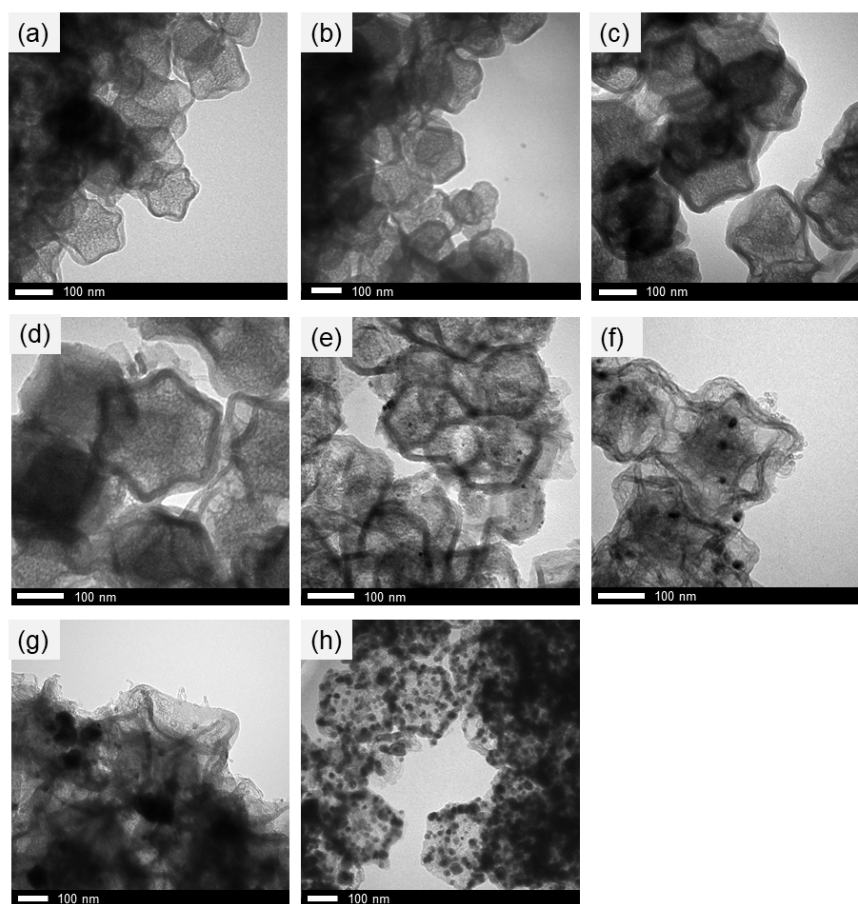


Figure 3.10: TEM images of (a) NC-Ar, (b) $\text{Co}_{0.42}\text{-NC-Ar}$, (c) $\text{Co}_{2.07}\text{-NC-Ar}$, (d) $\text{Co}_{2.88}\text{-NC-Ar}$, (e) $\text{Co}_{3.50}\text{-NC-Ar}$, (f) $\text{Co}_{8.32}\text{-NC-Ar}$, (g) $\text{Co}_{10.79}\text{-NC-Ar}$ and (h) $\text{Co}_{\text{max}}\text{-NC-Ar}$.

This suggests the formation of Co NPs occurs when the Co loading is more than 1.15 %w/w in CoZn ZIF-8. In the pyrolysis process, the Co atoms are attached to the surface of the carbon layer formed by the tannic acid. The Co SAs agglomerate forming Co NPs when the cobalt loading is higher than 1.15 % w/w in CoZn ZIF-8. More Co SAs are forming during the pyrolysis process, causing more agglomerations, forming bigger Co NPS. To

demonstrate the importance of the KTA layer in the formation of Co SACs, $\text{Co}_{2.88}\text{Zn}$ MOF which resulted in $\text{Co}_{2.88}\text{-NC-Ar}$ with a maximum loading of Co SAs in the pyrolysis of its KTA coated analogous; was pyrolyzed under the same conditions. The resultant pyrolyzed material showed a Co NP peak in the PXRD and Co NPs in the TEM micrographs. This suggests that the Co SACs with higher Co loadings could be obtained by pyrolyzing KTA coated CoZn ZIF-8 samples than pyrolyzing pristine CoZn ZIF-8 samples.

To investigate the effect of the inert atmosphere in the formation of Co SACs during the pyrolysis process, all the above KTA coated samples were pyrolyzed under a 3% hydrogen atmosphere. Interestingly, all the CoZn ZIF-8@KTA samples including the sample with the lowest cobalt loading; resulted in Co NPs after the pyrolysis. In the PXRD of $\text{Co}_{0.42}\text{-NC-H}_2$, $\text{Co}_{2.07}\text{-NC-H}_2$, $\text{Co}_{2.88}\text{-NC-H}_2$, $\text{Co}_{3.50}\text{-NC-H}_2$, $\text{Co}_{8.32}\text{-NC-H}_2$, $\text{Co}_{10.79}\text{-NC-H}_2$, and $\text{Co}_{\text{max}}\text{-NC-H}_2$ samples Co NP peak can be observed in which the peak intensity is increased with the cobalt doping (Figure 3.11). In agreement with this, in the EDX the intensity of cobalt peaks was also increased (Experimental section, Figure 3.32 and Figure 3.33). Moreover, under the TEM Co NPs, about 10 nm in size could be observed for the above samples (Figure 3.12).

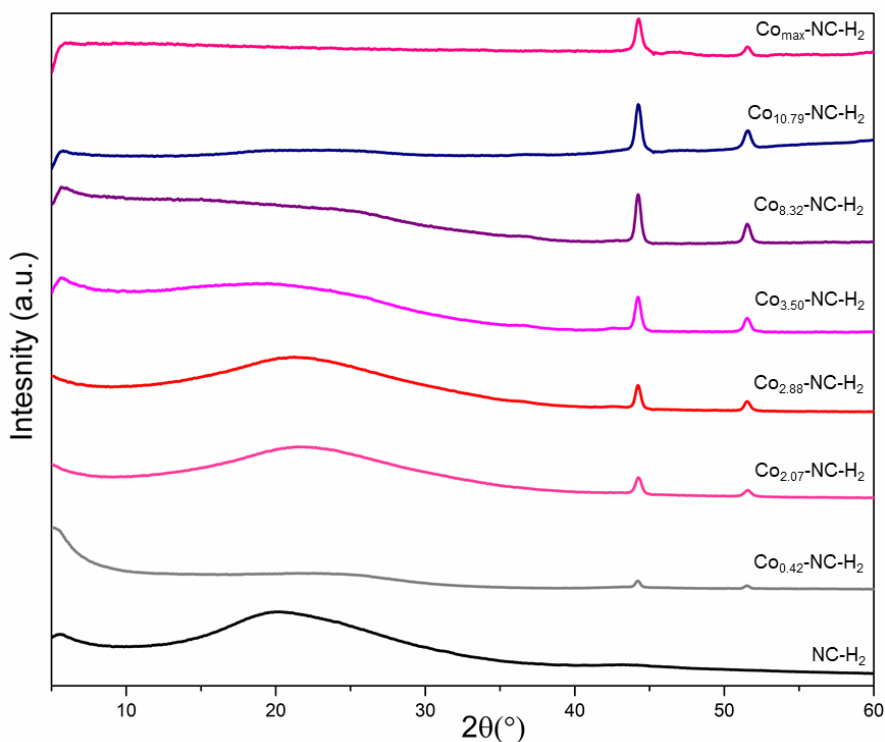


Figure 3.11: PXRD patterns of NC-H_2 , Co-NC-H_2 samples and $\text{Co}_{\text{max}}\text{-NC-H}_2$.

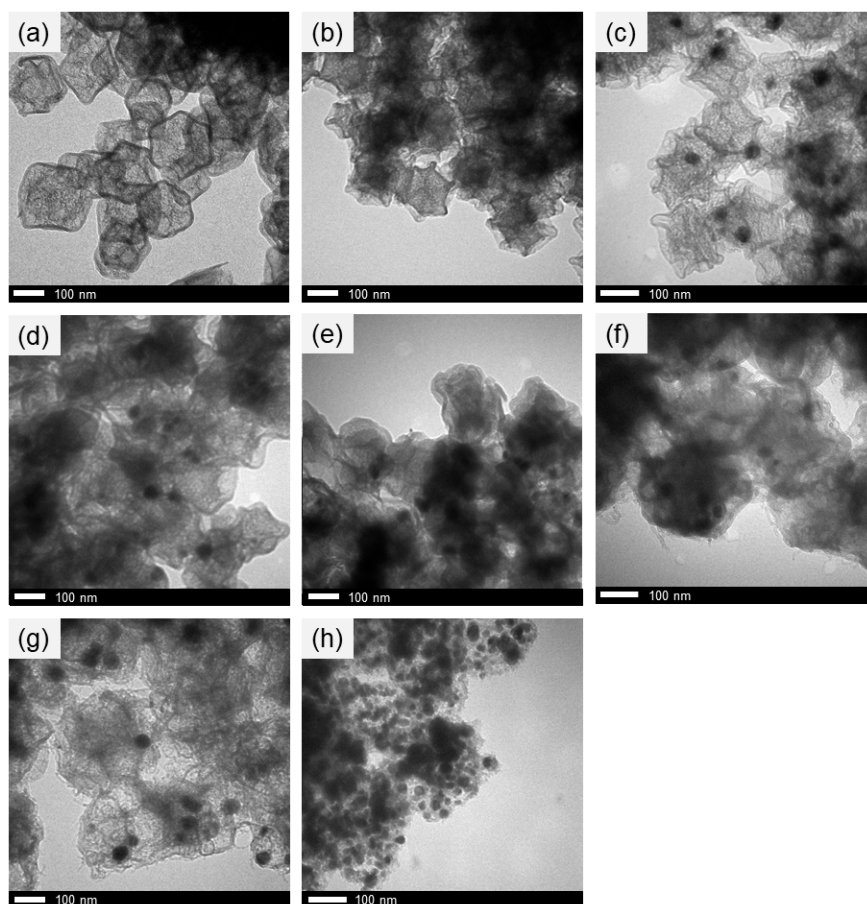


Figure 3.12: TEM images of (a) NC- H₂, (b) Co_{0.42}-NC- H₂, (c) Co_{2.07}-NC- H₂, (d) Co_{2.88}-NC- H₂, (e) Co_{3.50}-NC- H₂, (f) Co_{8.32}-NC- H₂, (g) Co_{10.79}-NC- H₂ and (h) Co_{max}-NC- H₂.

3.2.4 X-ray Photoelectron Spectroscopy (XPS) characterization

After the synthesis of Co-NC-Ar and Co-NC-H₂ catalysts, to further investigate the differences in the oxidation state and the local environment of the cobalt in the pristine MOF.

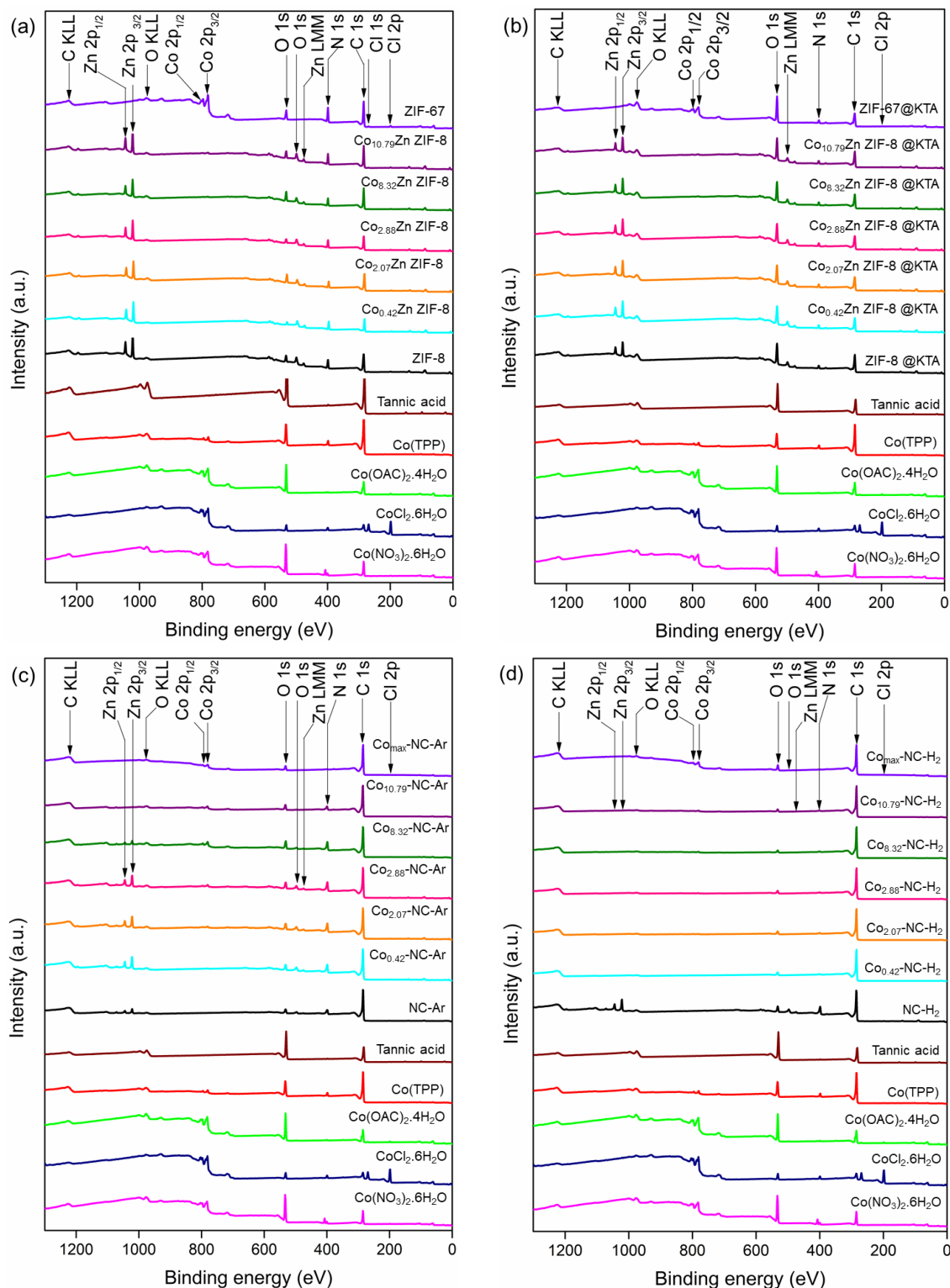


Figure 3.13: XPS survey spectra of (a) CoZn ZIF-8, (b) CoZn ZIF-8@KTA, (c) Co-NC-Ar and (d) Co-NC-H₂ with reference samples.

XPS characterization was carried out on KTA coated MOFs and Co-NC samples synthesized under argon and hydrogen atmospheres. The survey and narrow scan of XPS spectra were collected for all the samples and compared against reference standards; tannic acid, Co(TPP), Co(OAc)₂·4H₂O, CoCl₂·6H₂O, and Co(NO₃)₂·6H₂O. The quantifications were performed using peak areas for the C 1s, N 1s, O 1s, Zn 2p, K 2s, Cl 2p, and Co 2p regions. The relative ratios of C, N and Co species in the various samples, reference materials were determined from the narrow spectra.

In the survey spectra, Zn was detected in ZIF-8 and the CoZn ZIF-8 samples respectively. In ZIF-67 a clear peak for Co could be identified (Figure 3.13 a). After the KTA coating, the intensity of the oxygen peak increased due to the high oxygen content in KTA (Figure 3.13 b). But after the pyrolysis, the oxygen content of those samples was decreased appreciably due to the carbonization. The intensities of N, Co and Zn peaks also decreased in KTA coated samples compared to the pristine MOFs. After the pyrolysis of the samples under argon, the intensity of carbon and nitrogen peaks was increased because of the formation of the nitrogen-doped carbon layer. The intensity of the nitrogen peak in the samples pyrolyzed under hydrogen decreased compared to the samples pyrolyzed under argon (Figure 3.13 c and d). Thus, there is a less amount of nitrogen in the samples which pyrolyzed under hydrogen than in the samples which pyrolyzed under argon.

In the pyrolysis process, the zinc in the MOFs is reduced to Zn⁰ and partly removed by sublimation. Thus, the intensity of zinc is decreased in NC-Ar and Co_{0.42}-NC-Ar to Co_{10.79}-NC-Ar samples that were pyrolyzed under argon, which is in accordance with the EDX data (Experimental section, Figure 3.30 and Figure 3.31). The residual zinc may arise due to the zinc which could not escape the material during the evaporation because of trapping in the nitrogen-doped carbon support.

When it comes to the samples pyrolyzed under hydrogen, the zinc was only detected in the NC-Ar sample. In all the other Co-NC-H₂ samples zinc was not detected in agreement with EDX data (Experimental section, Figure 3.32 and Figure 3.33). Unlike in the pyrolysis under argon, the reduction environment provided by hydrogen could have reduced all the zinc in the sample to Zn⁰ which were then removed by sublimation without trapping in the nitrogen-doped carbon support. Moreover, as discussed above, the lesser amount of nitrogen in Co-NC-H₂ samples than in Co-NC-Ar samples in the catalyst support could be another reason for not trapping residual zinc in Co-NC-H₂ samples. To obtain further information about C, N and Co present in the samples, those elements were further analysed by the narrow scans.

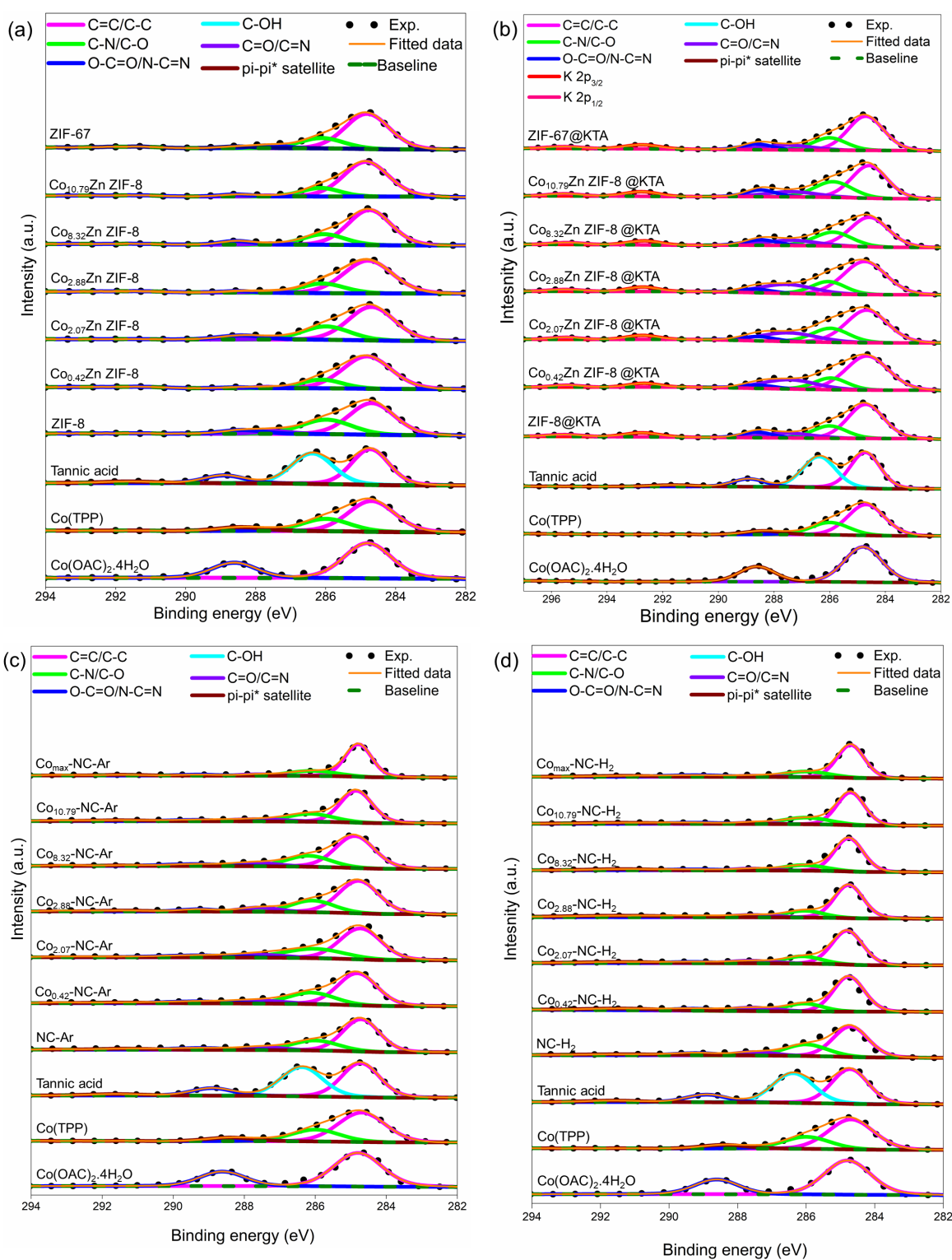


Figure 3.14: C 1s XPS spectra of (a) pristine MOFs, (b) Tannic acid coated MOFs, (c) Co-NC-Ar samples and (d) Co-NC-H₂ samples with standards.

The carbon 1s spectra of XPS for ZIF-8, CoZn ZIF-8 and ZIF-67 samples (Figure 3.14 a and b) show peaks at 284.7, 285.9, 287.4, and 288.6 eV, which can be assigned to C=C/C-C, C-N, C=N, and N-C=N respectively.²⁴²⁻²⁴⁴ In TA and Co(OAC)₂·4H₂O peaks at 288.4 eV can be assigned to O-C=O.²⁶⁹⁻²⁷⁰ In TA peaks at 286.4 eV are appeared due to the O-H groups of polyphenols.²⁴⁵ The π - π^* satellite peak is absent in pristine and TA coated MOFs. Thus, after the KTA coating, the intensity of C-N/C-OH, C=O/C-N, and O-C=O/N-C=N peaks of ZIF-8@KTA, CoZn ZIF-8@KTA and ZIF-67@KTA samples are increased due to the introduction of oxygen groups from KTA. Moreover, the appearance of potassium peaks as K 2p_{3/2} and K 2p_{1/2} at 292.7 and 295.5 eV can be observed due to potassium in KTA coated samples, which is consistent with EDX data.²⁷¹⁻²⁷²

In the XPS carbon 1s spectra of NC-Ar, Co-NC-Ar, NC-H₂ and Co-NC-H₂ samples (Figure 3.14 c and d), all the above peaks observed in KTA coated samples can be observed including π - π^* satellite peak at 291.2 eV.²⁷³ When the samples are pyrolyzed under argon the intensity of C-N/C-O, C=O/C=N and O-C=O/ N-C=N peaks are decreased; under hydrogen, the intensity of these peaks is decreased further. This is due to the pyrolysis process where the C, N and O in the samples exit in the form of gases. Under the hydrogen environment, the removal of these elements in the form of gas is more favourable probably due to the reducing nature of hydrogen.

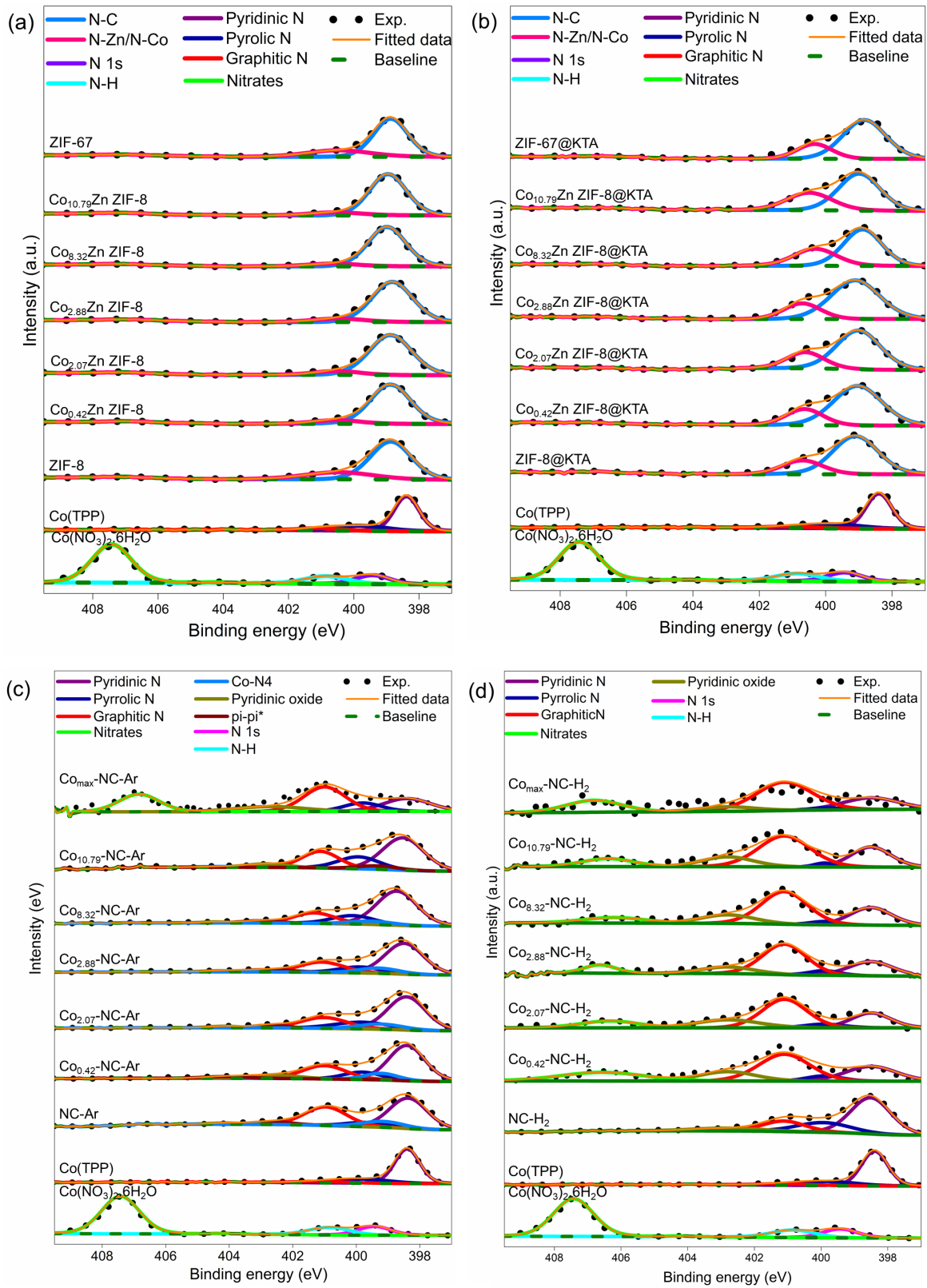


Figure 3.15: N 1s XPS spectra of (a) pristine MOFs, (b) Tannic acid coated MOFs, (c) Co-NC-Ar samples and (d) Co-NC-H₂ samples with standards.

Nitrogen 1s spectra for ZIF-8, CoZn ZIF-8 samples, ZIF-67, ZIF-8@KTA, CoZn ZIF-8@KTA, and ZIF-67@KTA samples (Figure 3.15 a and b) showed peaks at 398.7 and 400.5 eV which can be assigned to N-C and N-Zn/N-Co bonds of the pristine MOFs.²⁴⁵ After the KTA coating the intensity ratio of N-C: N-Zn or N-Co is decreased, probably due to the surface covering of pristine MOFs by KTA leading to a lower intensity signal by N-C, which is in agreement with the survey spectra.

In Co(TPP) reference sample, pyridinic N, pyrrolic N and graphitic N can be observed at 398.4, 399.7 and 400.9 eV.^{242-245, 248} Co(NO₃)₂·6H₂O reference sample showed peaks at 399.4, 400.7 and 407.3 eV which can be attributed to N 1s, N-H and nitrates.²⁷⁴⁻²⁷⁵ Pyridinic N, pyrrolic N and graphitic N can be seen in all the pyrolyzed samples (Figure 3.15 c and d). When increasing the cobalt content of the sample, the intensity of pyridinic N, pyrrolic N and graphitic N is increased from Co_{0.42}-NC-Ar to Co_{10.97}-NC-Ar samples; pyridinic N is the most prominent in these samples including NC-Ar. But the Co_{max}-NC-Ar sample, which has the highest amount of cobalt, does not follow this pattern; graphitic N is the most prominent peak in this sample. Also, in Co-NC-H₂ samples, graphitic N is the most abundant and the intensity of this peak is increasing with the cobalt loading. In contrast with the Co-NC-Ar samples, the intensity of the pyridinic N and pyrrolic N peaks are decreased with the cobalt doping. A peak at 402.7 eV is observed in both samples pyrolyzed under argon and hydrogen, which can be attributed to pyridinic oxide.²⁴⁹⁻²⁵⁰ In Co-NC-Ar samples, this peak is visible only in Co_{10.97}-NC-Ar and Co_{max}-NC-Ar samples which show cobalt nanoparticles. In Co-NC-H₂ samples, the intensity of this peak is higher compared to the Co-NC-Ar samples.

Based on the above analysis, the bonding environment of the Co_{max}-NC-Ar sample and Co-NC-H₂ samples could be similar and different from other Co-NC-Ar samples. In agreement with that, among the samples pyrolyzed under argon, only in the Co_{max}-NC-Ar sample, a peak around 407 eV was observed which can be attributed to nitrates.²⁷⁵ In all the Co-NC-H₂ samples this peak was present. A Co-N₄ peak at 399.3 eV can be observed in NC-Ar and Co-NC-Ar samples except in Co_{max}-NC-Ar and samples pyrolyzed under hydrogen.²⁷⁵⁻²⁷⁶ The intensity of Co-N₄ is decreased when increasing the cobalt doping. This also further confirms the similar nature of the Co_{max}-NC-Ar sample to Co-NC-H₂ samples compared to other Co-NC-Ar samples. Thus, when the nanoparticle nature of the sample is increased, the composition of the sample also changes, which is similar to the samples pyrolyzed under hydrogen.

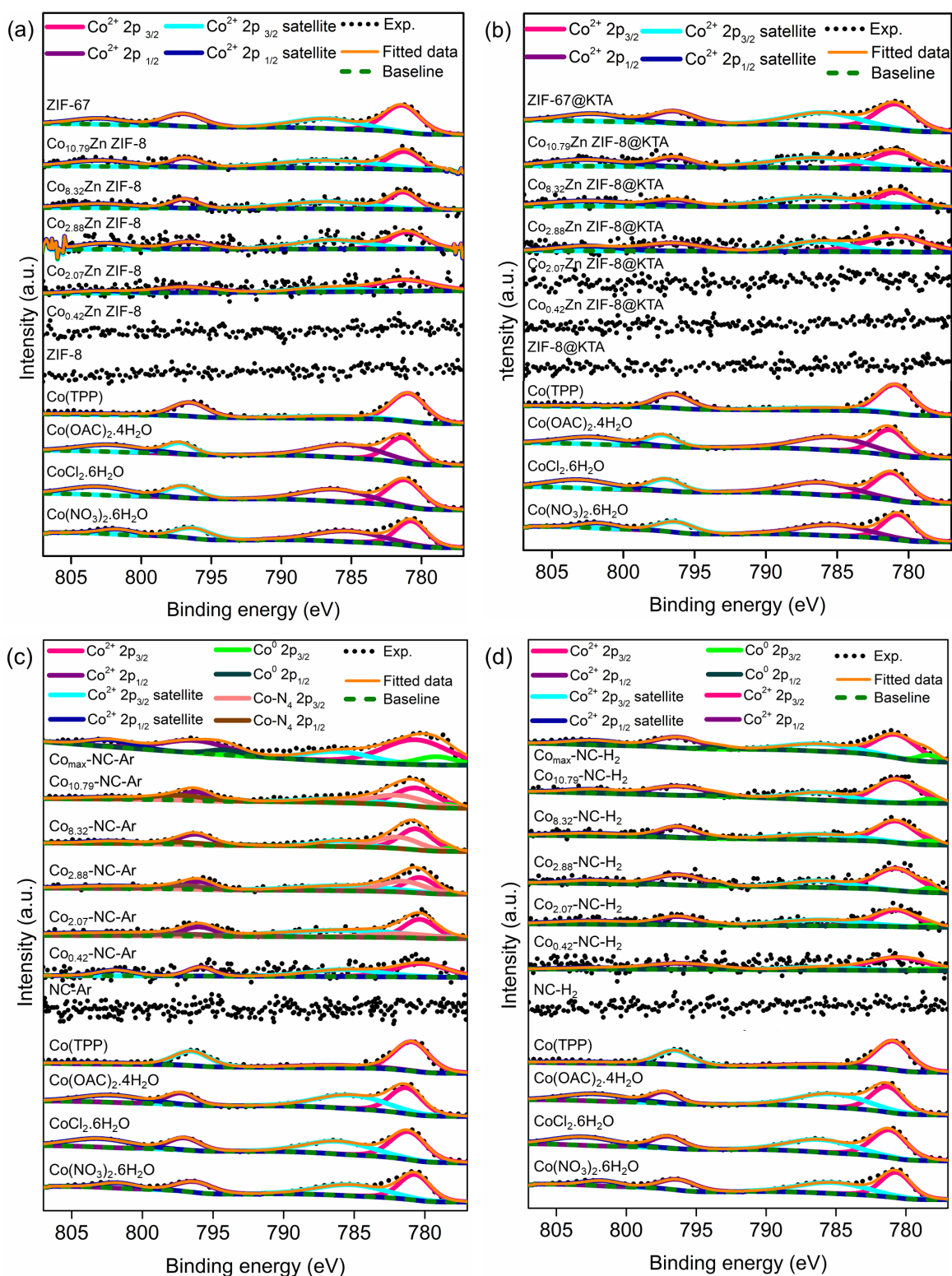


Figure 3.16: Co 2p XPS spectra of (a) pristine MOFs, (b) Tannic acid coated MOFs, (c) Co-NC-Ar samples and (d) Co-NC-H₂ samples with standards.

Co 2p XPS spectra of all the unpyrolyzed and pyrolyzed samples were measured to compare the possible changes in the oxidation state of cobalt upon the pyrolysis under argon and hydrogen environments. To compare the Co 2p spectra of the samples; the narrow scan of the reference samples was also carried out. The reference samples Co(TPP), Co(OAC)₂·4H₂O, CoCl₂·6H₂O, Co(NO₃)₂·6H₂O have a Co²⁺ oxidation state of cobalt.

The Co 2p spectra of pristine MOFs, KTA coated MOFs and reference samples; Co(TPP) (Figure 3.17), Co(OAC)₂·4H₂O, CoCl₂·6H₂O, Co(NO₃)₂·6H₂O (Figure 3.16 a and b) showed peaks at 781.2, 786.6, 798.8, and 802.3 eV which can be assigned to Co²⁺ 2p_{3/2}, Co²⁺ 2p_{3/2} satellite, Co²⁺ 2p_{1/2}, and Co²⁺ 2p_{1/2} satellite peaks; the ratio of the area of 2p_{3/2} and 2p_{1/2} peaks were 1:2.²⁷⁷⁻²⁷⁹ In CoZn ZIF-8 samples and CoZn ZIF-8@KTA samples cobalt was in Co²⁺ state. The oxidation state of cobalt did not change upon the KTA coating. TA and ZIF-8 did not show any signal for cobalt as there was no cobalt in the sample. Co_{0.42}Zn ZIF-8 which had the lowest cobalt loading also did not show cobalt in the narrow scan, probably the surface Co concentration was not enough to overcome the noise and generate a signal. After the KTA coating, Co_{0.42}Zn ZIF-8@KTA and Co_{2.07}Zn ZIF-8@KTA also do not show any signal in Co 2p spectra due to the same reason mentioned above as KTA covers the surface cobalt.

After the pyrolysis Co²⁺ peak was present in both samples pyrolyzed under argon and hydrogen (Figure 3.16 c and d). The intensity of the cobalt peak is increased when the cobalt loading is higher. In Co_{0.42}-NC-Ar, Co_{2.07}-NC-Ar, and Co_{2.88}-NC-Ar samples which have only Co SAs, only Co²⁺ peak could be observed confirming the 2⁺ oxidation state of Co SAs. Additional peaks appeared in the 1:2 ratio at 778.4 and 793.4 eV in Co_{8.32}-NC-Ar, Co_{10.79}-NC-Ar, Co_{max}-NC-Ar, and all the Co-NC-H₂ samples can be assigned to Co⁰ 2p_{3/2} and Co⁰ 2p_{1/2}. Thus, all the samples showed the Co NPs had a Co⁰ peak which increased their intensity with the cobalt doping. As the intensity of the PXRD peak is also increased when increasing the Co doping due to the increment of nanoparticles, Co NPs should be responsible for Co⁰ peak and Co NPs should be in 0 oxidation state. Moreover, at 781.6 and 797.2 eV Co-N₄ 2p_{3/2} and Co-N₄ 2p_{1/2} peaks appear at the 1:2 ratio in Co_{0.42}-NC-Ar, Co_{2.07}-NC-Ar, Co_{2.88}-NC-Ar, and Co_{10.89}-NC-Ar samples.²⁸⁰⁻²⁸¹ These peaks are absent in Co_{max}-NC-Ar and all the Co-NC-H₂ samples, which agrees with the absence of Co-N₄ peak in C 1s XPS spectra.

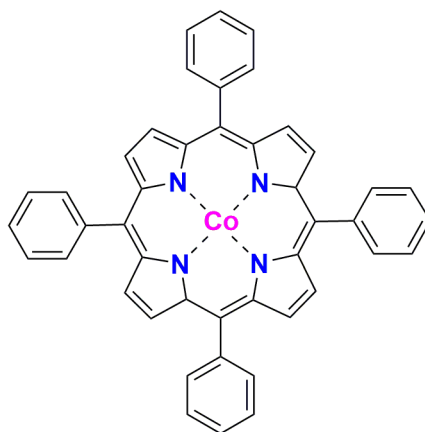


Figure 3.17: The structure of Co(TPP).

3.2.5 Near Edge X-ray Absorption Fine Structure (NEXAFS) characterization

NEXAFS analysis was performed at Australian Synchrotron to further investigate the elements and their environments with different functional groups after the KTA coating and pyrolysis under argon and hydrogen environments.

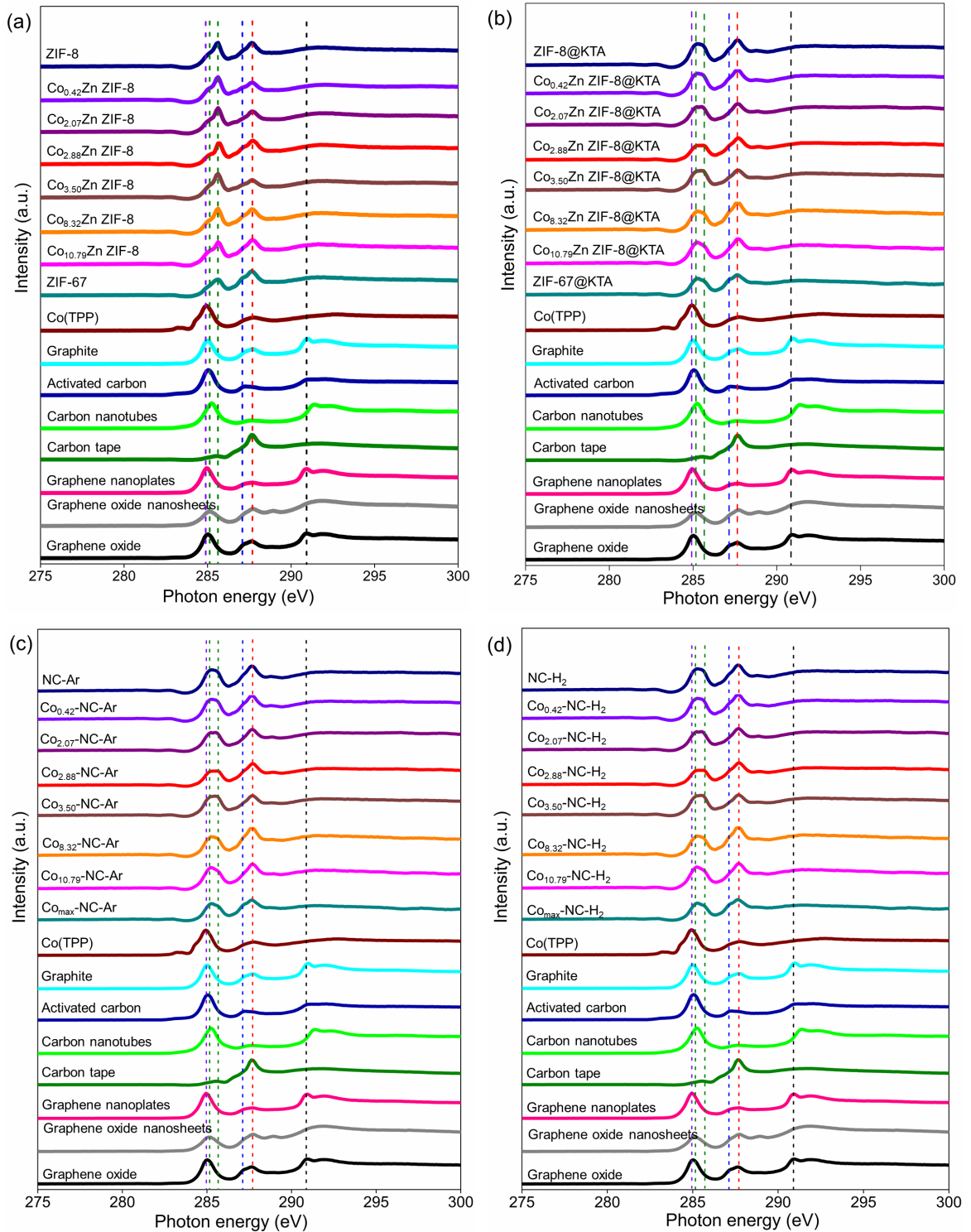


Figure 3.18: C K-edge NEXAFS spectra of (a) pristine MOFs, (b) Tannic acid coated MOFs, (c) Co-NC-Ar samples and (d) Co-NC-H₂ samples with standards.

NEXAFS measurements of pristine MOFs, KTA coated MOFs, samples pyrolyzed under argon and samples pyrolyzed under hydrogen were carried out for C K-edge, N K-edge, and Co L-edge.

In C K-edge spectra of Co(TPP) a peak at 284.9 eV (purple dotted line) can be assigned to $1s \rightarrow \pi^*$ transitions of the porphyrin.²⁵⁸ This feature can be observed in pristine MOF samples as well due to the C $1s \rightarrow \pi^*$ transitions of imidazole ring which is coordinated to Zn^{2+}/Co^{2+} in ZIF-8. But after the pyrolysis, the resulting Co-NC samples do not show this peak as the bonding environment of pristine MOF samples has been changed by the decomposition of the ligands and evaporation of zinc nodes upon the pyrolysis (Figure 3.18).

All these samples showed peaks at 285.1 eV and 285.6 eV (green dotted lines) which can be assigned to C $1s \rightarrow \pi^*$ transitions of aromatic C=C.²⁵⁹⁻²⁶¹ In CoZn ZIF-8 and CoZn ZIF-8@KTA samples imidazole ring of MOFs should be responsible for this peak. In pristine MOFs, the intensity of the latter peak is higher than the intensity of the earlier peak (Figure 3.18 a). After the KTA coating, the intensity of these two peaks is almost similar probably due to the aromatic carbon in TA, contributing to increasing the signal at 281.5 eV (Figure 3.18 b). Moreover, an aromatic C=C peak can be seen in Co-NC samples, confirming the aromatic nature of the carbon support which could arise from pyridinic, pyrrolic and graphitic carbon identified in the XPS analysis.

The peak at 287.1 eV (blue dotted line) can be assigned to C $1s \rightarrow \pi^*$ transitions of C-N and C=C-N in N substituted aromatic carbon (Figure 3.18).²⁶¹⁻²⁶² This feature can be observed in Co(TPP) and all the MOF samples before and after the pyrolysis. In ZIF-8@CoTA samples C-N and C=N of 2-methylimidazole is the source for this peak. The appearance of this peak even after the pyrolysis confirms the nature of aromatic nitrogen-doped carbon as N-C and N=C in Co-NC samples.

The peak at 287.6 eV (red dotted line) observed in all the MOF samples before and after the pyrolysis (Figure 3.18) including Co(TPP) is raised from C $1s \rightarrow \pi^*$ transitions of C=O.²⁶² This peak can be observed in all the samples, as C=O is present in the carbon tape that is used to mount the samples for the measurements. But C=O in TA also contributes to this peak. A broad peak around 291 eV (black dotted line) can be seen in all the samples due to C $1s \rightarrow \sigma^*$ transitions of C-C.²⁵⁹ Doping different amounts of cobalt, tannic acid coating and using argon and hydrogen environments in the pyrolysis does not affect the carbon speciation.

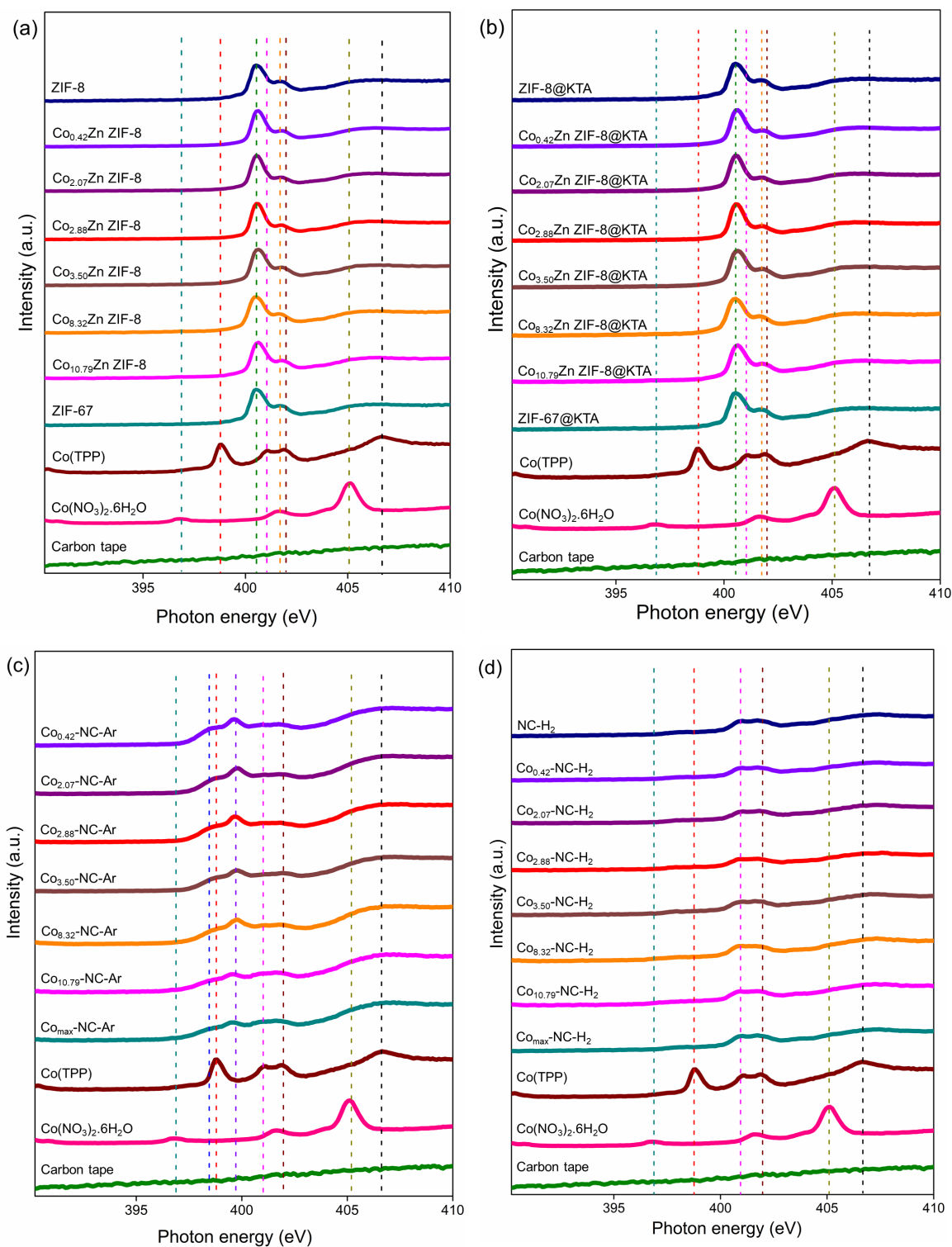


Figure 3.19: N K-edge NEXAFS spectra of (a) pristine MOFs, (b) Tannic acid coated MOFs, (c) Co-NC-Ar samples and (d) Co-NC-H₂ samples with standards.

Co(TPP) showed peaks at 398.8 eV (red dotted line) and 400.9 eV (pink dotted line) which can be assigned to N 1s $\rightarrow \pi^*$ transitions of the porphyrin and N=C.^{263, 282} The N 1s $\rightarrow \pi^*$ transitions of N=C can be identified in all the pyrolyzed samples (Figure 3.19 c and d), while the N 1s $\rightarrow \pi^*$ transitions of porphyrin can only be detected in Co-NC-Ar samples. This clearly shows the different structural arrangements of Co-NC samples when pyrolysis is performed under argon and hydrogen environments. Moreover, Co-NC-Ar samples showed peaks at 398.3 eV (blue dotted line) and 399.7 eV (purple dotted line) which can be attributed to N 1s $\rightarrow \pi^*$ transitions of pyridinic N,²⁶⁶⁻²⁶⁸ and pyrrolic N.²⁶⁵⁻²⁶⁶ In the unpyrolyzed samples and Co-NC-H₂ samples, these peaks could not be detected; even though in N 1s XPS spectra of Co-NC-H₂ samples pyridinic N and pyrrolic N could be identified. The reason might be that pyridinic N and pyrrolic N were not prominent in N 1s XPS spectra of Co-NC-H₂ samples and they were low in intensity; graphitic N was the most abundant type of nitrogen. In agreement with that, in N K-edge spectra of Co-NC-H₂, only graphitic N could be identified at 401.9 eV (brown dotted line) which could also be seen in Co-NC-Ar samples too.²⁶⁸ However, in the pyrolyzed samples the concentration of nitrogen is reduced compared to the unpyrolyzed samples. Based on the intensities of the peaks, Co-NC-H₂ samples have more graphitic N than Co-NC-Ar samples, which agrees with the XPS analysis.

In all of the pyrolyzed and unpyrolyzed samples (Figure 3.19 c and d), the peak at 406.6 eV (black dotted line) appeared due to N 1s $\rightarrow \sigma^*$ transitions of C-N.²⁶⁵ The reference sample Co(NO₃)₂·6H₂O showed two peaks at 396.9 eV (dark cyan dotted line) and 405.1 eV (dark yellow dotted line) which can be assigned to N 1s $\rightarrow \pi^*$ transitions and nitrogen oxide.²⁸³⁻²⁸⁴

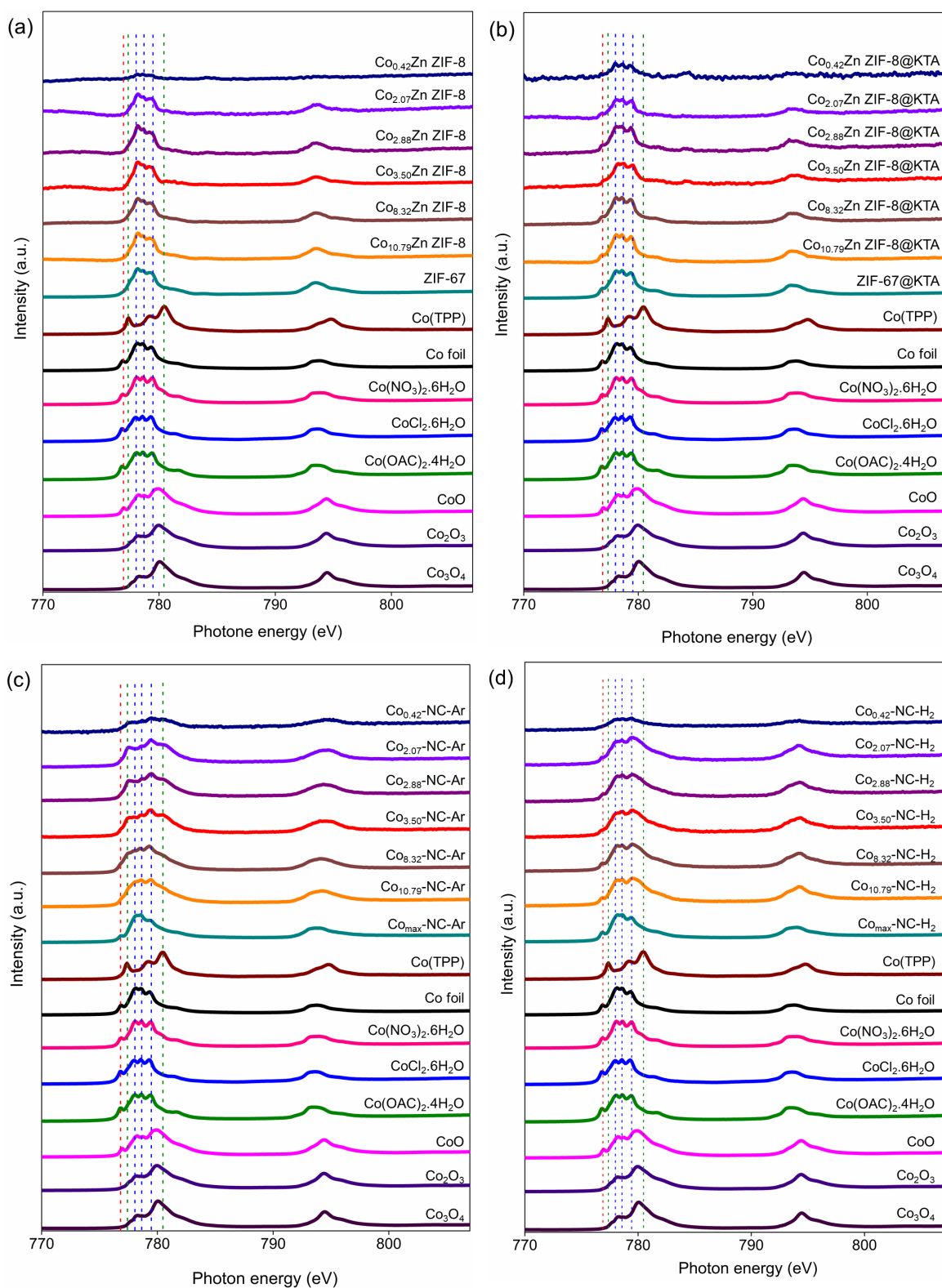


Figure 3.20: Co L-edge NEXAFS spectra of (a) pristine MOFs, (b) Tannic acid coated MOFs, (c) Co-NC-Ar samples and (d) Co-NC-H₂ samples with standards.

The Co L-edge NEXAFS spectra split into two peaks, as a result of core level spin-orbit coupling. The higher energy L_2 peak appeared around 690 eV which resulted from $2p_{3/2} \rightarrow 3d$ transitions.²⁸⁵ The lower energy L_3 peak results from $2p_{3/2} \rightarrow 3d$ transitions which comes around 780 eV. As a result of multiplet structure from electron-electron interaction which implies the local symmetry, L_3 peak is split further.²⁸⁶

Cobalt in CoO , $\text{Co(OAc)}_2 \cdot 4\text{H}_2\text{O}$, $\text{CoCl}_2 \cdot 6\text{H}_2\text{O}$, and $\text{Co(NO}_3)_2 \cdot 6\text{H}_2\text{O}$ reference samples show multiplets at 777.1, 778.7 and 779.4 eV (blue dotted lines) which can be assigned to Co^{2+} ions (Figure 3.20).²⁸⁷ These peaks can be seen in all the unpyrolyzed and pyrolyzed samples confirming the presence of Co^{2+} in all the samples in agreement with XPS analysis. In the above reference samples, the peak at 776.8 eV (red dotted line) was detected due to the octahedrally arranged Co.²⁸⁶ This peak is not observed in the pristine MOF samples. Interestingly, when the pristine MOFs are coated with KTA, the peak at 776.8 eV can be observed, suggesting the octahedral arrangement of the Co^{2+} on the surface of the MOF probably with free oxygen groups in TA. After the pyrolysis, the Co-NC- H_2 samples showed this peak suggesting the octahedral arrangement of cobalt atoms in the catalysts. After pyrolyzing the KTA coated samples under argon, the above peak disappeared from Co-NC-Ar samples except for the Co_{max} -NC-Ar sample, suggesting that only the Co_{max} -Ar sample has the octahedral arrangement of Co atoms. The similar coordination environment of cobalt atoms in Co-NC- H_2 samples and Co_{max} -NC-Ar sample are in agreement with the XPS analysis.

In Co-NC-Ar samples (except Co_{max} -NC-Ar), from $\text{Co}_{0.42}$ -NC-Ar to $\text{Co}_{10.79}$ -NC-Ar, two peaks appeared at 777.4 and 780.4 eV (green dotted lines), which also can be identified in Co(TPP) reference sample²⁸⁸ suggesting the square planar porphyrin like Co^{2+} environment.²⁸⁶ The feature at 777.4 eV is gradually decreased with the increasing cobalt loading.²⁸⁹ This explains the octahedral arrangement of the Co_{max} -NC-Ar sample when increasing the cobalt loading.

3.2.6 Extended X-ray Absorption Fine Structure (XAFS) characterization

XAFS measurements of the samples were performed to determine the oxidation state and coordination environment of cobalt atoms. XAFS measurements of the samples were performed in conjunction with a series of standards.

EXAFS data were normalized in energy (Figure 3.21) and show that all Co-NC-H₂ samples, Co_{max}-NC-Ar and Co_{10.79}-NC-Ar samples, which have Co NPs have a feature at 7711.4 eV. This feature is present in the Co foil while this feature is absent in the Co_{3.50}-NC-Ar sample which is just outside the single-atom zone. These observations are also consistent with the presence of Co⁰ nanoparticles in the above samples, confirmed by XPS, PXRD and microscopic observations. The single feature at 7725.0 eV appears in Co(NO₃)₂·6H₂O and CoCl₂·6H₂O reference sample, can be observed in pristine MOFs, KTA coated MOFs and pyrolyzed samples under argon and hydrogen; consistence with Co²⁺ oxidation state suggests that it does not change upon the pyrolysis which is in agreement with the XPS analysis. Only in the pristine MOFs and KTA coated MOFs, there is a feature at 7708.9 eV that can be observed but which disappears during the pyrolysis.

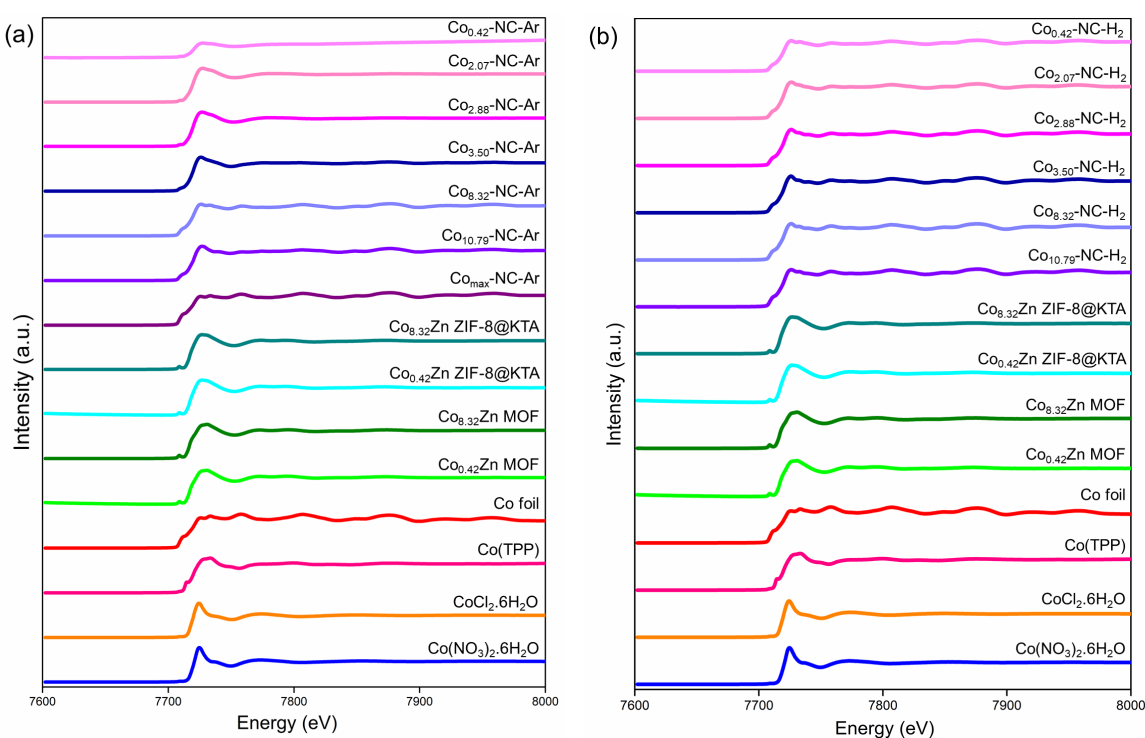


Figure 3.21: Co K-edge spectra of (a) Co-NC-Ar samples and (b) Co-NC-H₂ samples with pristine MOFs, KTA coated MOFs and standards.

The EXAFS region of the spectra (Figure 3.22) shows similar oscillations between Co foil and Co NPC samples; $\text{Co}_{8.32}\text{-NC-Ar}$, $\text{Co}_{10.79}\text{-NC-Ar}$, $\text{Co}_{\text{max}}\text{-NC-Ar}$, and all the Co-NC- H_2 samples. Whereas the Co SAC samples; $\text{Co}_{0.42}\text{-NC-Ar}$, $\text{Co}_{2.07}\text{-NC-Ar}$, and $\text{Co}_{2.88}\text{-NC-Ar}$ had markedly altered features that rapidly dropped off with increasing k . This observation is consistent with the lack of extended structure for these samples, as expected for atomically dispersed single-atom materials. The oscillations of the $\text{Co}_{3.50}\text{-NC-Ar}$ sample which is in the margin of SAs and NPs with traces of NPs; show a combination of oscillations shown by Co SACs and Co NPCs. Moreover, pristine MOF samples ($\text{Co}_{0.42}\text{Zn ZIF-8}$ and $\text{Co}_{8.32}\text{Zn ZIF-8}$) and KTA coated MOF samples ($\text{Co}_{0.42}\text{Zn ZIF-8@KTA}$ and $\text{Co}_{8.32}\text{Zn ZIF-8@KTA}$) show similar oscillations as they have similar chemical environments. Those oscillations are different from the Co SAC and Co NPC samples. But having similarities to oscillations of Co(TPP) suggests that the chemical environment of unpyrolyzed samples has similarities to the porphyrin environment.

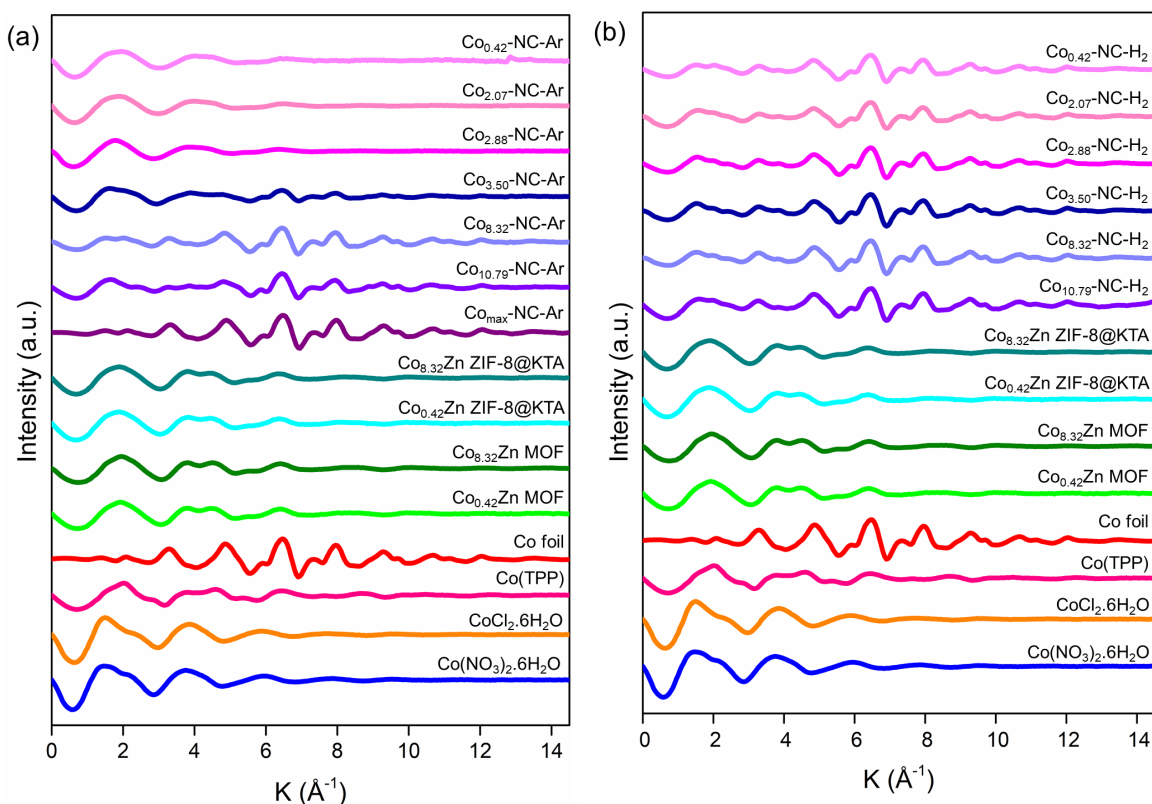


Figure 3.22: k^2 weighted Co K-edge spectra of (a) Co-NC-Ar samples and (b) Co-NC- H_2 samples with pristine MOFs, KTA coated MOFs and standards.

Fourier transformed (FT) k -weighted EXAFS curves of the spectra (Figure 3.23) demonstrate a prominent peak at 2.14 Å in R-space in reference to metallic cobalt foil which is corresponding to Co-Co bonds. This peak is not present in CoZn ZIF-8@KTA samples. Co-Co bond can be observed in Co NPC samples; Co_{0.32}-NC-Ar, Co_{10.79}-NC-Ar, Co_{max}-NC-Ar, and all the Co-NC-H₂ samples. The metallic Co-Co peak is absent in pristine MOFs and KTA coated MOFs, consistent with the metallic NP formation during the thermal treatment. Indeed, the lack of metallic Co-Co peak with reduced metal loadings in Co-NC-Ar samples confirms the single-atom nature of Co_{0.42}-NC-Ar, Co_{2.07}-NC-Ar, and Co_{2.88}-NC-Ar samples. The appearance of the Co-Co peak in the Co-NC-H₂ analogous demonstrates the effect of the internal environment in the pyrolysis process for the formation of SACs.

The main peak at 1.53 Å corresponding to Co-N coordination can be observed in Co(TPP) reference, pristine MOFs and KTA coated MOFs. This feature is absent in all the Co-NPC samples suggesting the bonding environment of those samples is not similar to the porphyrin environment which is in the agreement with the absence of Co-N₄ bonds in the XPS analysis.

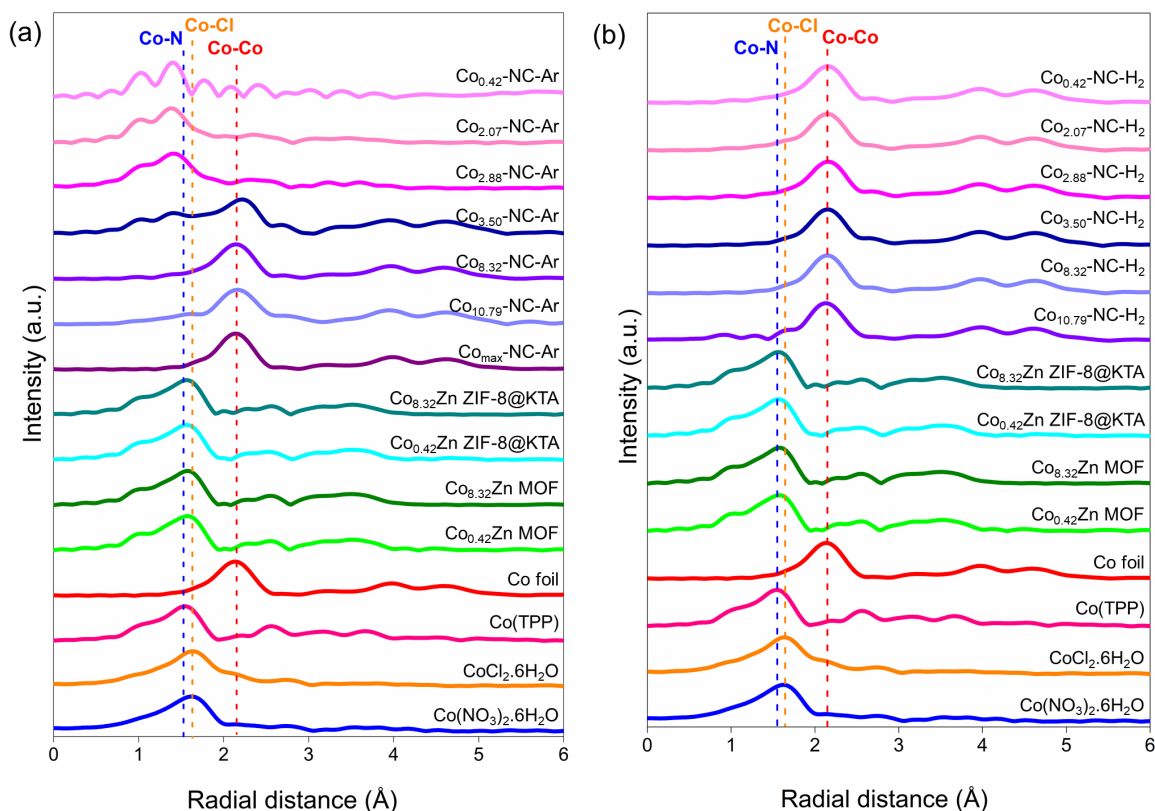


Figure 3.23: r-space plots obtained from Fourier transform on k^2 -weighted Co K-edge EXAFS spectra (a) Co-NC-Ar samples and (b) Co-NC-H₂ samples with pristine MOFs, KTA coated MOFs and standards.

With regards to the coordination of single cobalt atom sites in Co SAC samples, remaining sample peaks at short radial distances were similar to the porphyrin standard Co(TPP) as evidenced by EXAFS (Figure 3.23) and parameterized fit for this peak to the EXAFS equation (Figure 3.24).

EXAFS fittings were done to find the coordination number of cobalt in Co SAC samples and its bonding to the neighbouring atoms. Co(TPP) and all Co-NC-Ar samples were fitted with Co-N bond (Experimental section, Figure 3.36 and Figure 3.37). The coordination number of Co SAC was found as four with four Co-N fittings (Experimental section, Table 3.5) which is in agreement with the Co-N₄ peak as evidenced by XPS and square planar arrangement of Co²⁺ in NEXAFS analysis.

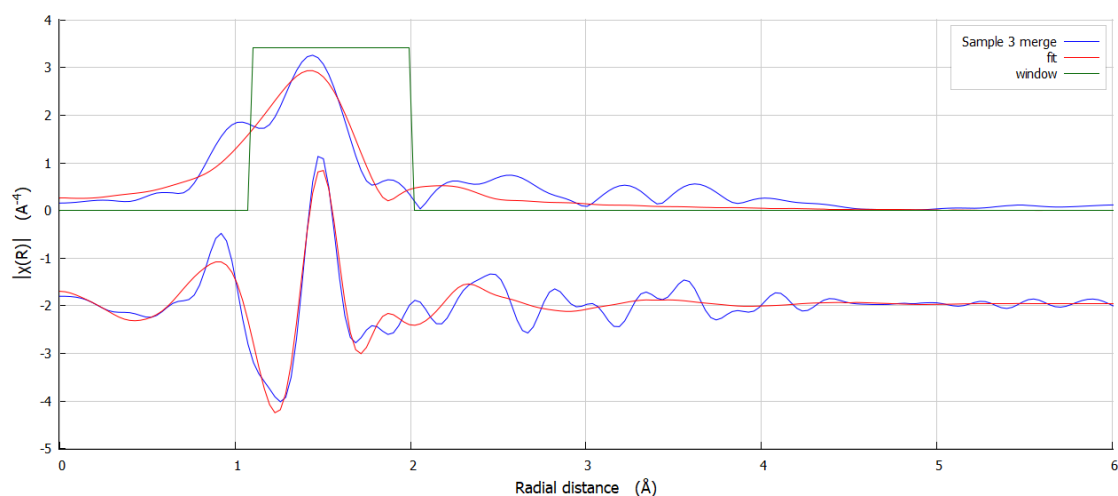


Figure 3.24: A parameterized spectral fit for Co_{2.88}-NC-Ar; fit within the range 1-6 Å.

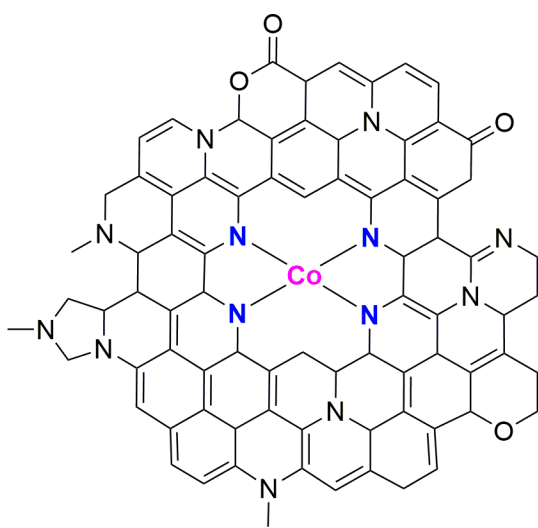


Figure 3.25: Structure depiction of Co SAC.

3.3 Conclusion

Synthesis of cobalt catalysts was done by the pyrolysis of CoZn ZIF-8 in argon and hydrogen environments. When increasing the cobalt doping, cobalt nanoparticles appeared in Co-NC-Ar samples. The Co SAC, Co_{2.88}-NC-Ar had 3.45% of maximum cobalt loading. All the samples pyrolyzed under hydrogen (Co-NC-H₂), resulting in Co NPS. There are fewer C, N, and O in Co-NC-H₂ samples than Co-NC-Ar samples, probably due to the reducing nature of hydrogen. All Co-NC-Ar and Co-NC-H₂ had Co²⁺ while all the samples with Co NPs had had Co⁰ too. Co SACs only had a Co²⁺ oxidation state.

When the nanoparticle nature of the Co-NC-Ar samples is prominent, that showed a similar bonding environment to Co-NC-H₂ samples. Thus, Co_{max}-NC-Ar and Co-NC-H₂ samples have similar bonding environments while other Co-NC-Ar samples have different bonding environments from those. In all the pyrolyzed samples, pyridinic, pyrrolic and graphitic nitrogen could be observed. In Co SAC samples pyridinic and pyrrolic nitrogen is prominent while in all the Co-NC-H₂ samples and Co_{max}-NC-Ar sample graphitic nitrogen is prominent.

Based on the XPS, NEXAFS and XAFS analysis cobalt single-atoms in Co SACs has a Co-N₄ square planar coordination environment. Whereas Co NPCs; all Co-NC-H₂ samples and Co_{max}-NC-Ar sample do not have Co-N₄ coordination and cobalt atoms of those samples have octahedral coordination. This demonstrates the impact of the cobalt loading and pyrolysis environment on the coordination environment of cobalt atoms.

3.4 Experimental Section

3.4.1 General procedures

All starting materials and solvents were used as received from commercial sources without further purification unless otherwise noted. PXRD, AAS, SEM, EDX, TEM, XPS, NEXAFS, and EXAFS measurements were done using the instruments mentioned in Chapter 2.

3.4.2 Synthesis of ZIF-8

Synthesis of ZIF-8 was done following the procedure mentioned in Chapter 2.

3.4.3 Synthesis of ZIF-67

A solution of 2-methylimidazole (4.00 g, 48.72 mmol) was dissolved in 40 mL of methanol. To this, a solution of $\text{Co}(\text{NO}_3)_2 \cdot 6\text{H}_2\text{O}$ (1.65 g, 5.68 mmol) in 20 mL of methanol was added. The resulting solution was stirred for 1 hr and then was incubated at room temperature for 24 hours without stirring. The solution was centrifuged at 4000 rpm for 15 min to separate the crystalline product which was then subjected to three washing cycles with methanol (centrifugation at 5000 rpm for 5 min) and then dried *in vacuo* for 24 hours.

3.4.4 Synthesis of CoZnZIF-8

CoZnZIF-8 was synthesized by doping different amounts of $\text{Co}(\text{NO}_3)_2 \cdot 6\text{H}_2\text{O}$ with the $\text{Zn}(\text{NO}_3)_2 \cdot 6\text{H}_2\text{O}$ when synthesizing ZIF-8. A solution of 2-methylimidazole (4.00 g, 48.73 mmol) was dissolved in 40 mL of methanol. To this, a mixture of $\text{Zn}(\text{NO}_3)_2 \cdot 6\text{H}_2\text{O}$ (1.69 g, 5.68 mmol) and $\text{Co}(\text{NO}_3)_2 \cdot 6\text{H}_2\text{O}$ (amounts are shown in the table) in 20 mL of methanol was added. The resulting solution was stirred for 1 hr and then was incubated at room temperature without stirring. The solution was centrifuged at 4000 rpm for 15 min to separate the crystalline product which was then subjected to three washing cycles with methanol (centrifugation at 5000 rpm for 5 min) and then dried *in vacuo* for 24 hours.

3.4.5 Synthesis of ZIF-8@KTA, ZIF-67@KTA and CoZnZIF-8@KTA

Synthesis of ZIF-8@KTA:

Synthesis of ZIF-8@KTA was performed using the procedure mentioned in Chapter 2.

Synthesis of ZIF-67@KTA:

ZIF-67 (200 mg) was dispersed in deionized water (10 mL) which was then added to a tannic acid solution (5 mL, 24 mM) in which pH was adjusted to 8 with aqueous KOH (6M) prior to adding and stirred for 5 min. The mixture was collected in a centrifuge tube, dispersed in methanol (15 mL) and centrifuged at 5000 rpm for 5 min to separate the precipitate. The precipitate was subjected to three washing cycles with methanol (centrifugation at 5000 rpm for 5 min) and eventually dried *in vacuo* for 24 hours.

Synthesis of CoZnZIF-8@KTA:

CoZnZIF-8 (200 mg) was dispersed in deionized water (10 mL) which was then added to a tannic acid solution (5 mL, 24 mM) in which pH was adjusted to 8 with aqueous KOH (6M) prior to adding and stirred for 5 min. The mixture was collected in a centrifuge tube, dispersed in methanol (15 mL) and centrifuged at 5000 rpm for 5 min to separate the precipitate. The precipitate was subjected to three washing cycles with methanol (centrifugation at 5000 rpm for 5 min) and eventually dried *in vacuo* for 24 hours.

3.4.6 Bulk synthesis of ZIF-8@KTA, ZIF-67@KTA and CoZnZIF-8@KTA

Bulk synthesis of ZIF-8@KTA:

Bulk synthesis of ZIF-8@KTA was performed using the procedure mentioned in Chapter 2.

Bulk synthesis of ZIF-67@KTA:

ZIF-67 (6.6 g) was dispersed in deionized water (330 mL). This was then added to a tannic acid solution (165 mL, 6.7 g) in which pH was adjusted to 8 with aqueous KOH (6M) prior to adding and stirred for 5 min. The mixture was dispersed methanol (250 mL) and centrifuged at 5000 rpm for 5 min. The precipitate was subjected to three washing cycles with methanol (centrifugation at 5000 rpm for 5 min) and eventually dried *in vacuo* for 24 hours.

Bulk synthesis of CoZnZIF-8@KTA:

CoZnZIF-8 (6.6 g) was dispersed in deionized water (330 mL). This was then added to a tannic acid solution (165 mL, 6.7 g) in which pH was adjusted to 8 with aqueous KOH prior to adding and stirred for 5 min. The mixture was dispersed methanol (250 mL) and centrifuged at 5000 rpm for 5 min. The precipitate was subjected to three washing cycles with methanol (centrifugation at 5000 rpm for 5 min) and eventually dried *in vacuo* for 24 hours.

3.4.7 Synthesis of Co-NC-Ar

CoZnZIF-8@KTA/ ZIF-67 (70 mg) was placed in a ceramic boat in a tube furnace which was then purged for 1 hour with argon at a flow rate of 10 ml/min. The samples were set to carbonize at 900 °C for 2 hours at a heating rate of 1 °C/min under the same flow of argon.

3.4.8 Synthesis of Co-NC-H₂

CoZnZIF-8@KTA/ ZIF-67 (70 mg) was placed in a ceramic boat in a tube furnace which was then purged for 1 hour with argon at a flow rate of 12 ml/min. The samples were set to carbonize at 900 °C for 2 hours at a heating rate of 1 °C/min under a gas mixture of argon (flow rate:12 ml/min) and 40% H₂/Ar (flow rate: 2 ml/min)

Table 3.2: Synthesis of ZIF-8, CoZn ZIF-8, ZIF-67; tannic acid coating; pyrolyzing under Ar, 40% H₂/Ar and their sample codes.

MOF Code	Amount of Zn(NO ₃) ₂ ·6H ₂ O	Amount of Co(NO ₃) ₂ ·6H ₂ O	Formula (in terms of molar %)	Sample code after tannic acid coating	Sample code after pyrolysis under Ar	Sample code after pyrolysis under H ₂ /Ar
ZIF-8	1.69 g (5.68 mmol)	0	Co ₀ Zn ₁₀₀	ZIF-8@KTA	NC-Ar	NC-Ar
Co _{0.42} Zn ZIF-8	1.69 g (5.68 mmol)	7 mg (24.05 μmol)	Co _{0.42} Zn _{99.58}	Co _{0.42} Zn ZIF-8@KTA	Co _{0.42} -NC-Ar	Co _{0.42} -NC-H ₂
Co _{2.07} Zn ZIF-8	1.69 g (5.68 mmol)	35 mg (120.26 μmol)	Co _{2.07} Zn _{97.93}	Co _{2.07} Zn ZIF-8@KTA	Co _{2.07} -NC-Ar	Co _{2.07} -NC- H ₂
Co _{2.88} Zn ZIF-8	1.69 g (5.68 mmol)	49 mg (168.36 μmol)	Co _{2.88} Zn _{97.12}	Co _{2.88} Zn ZIF-8@KTA	Co _{2.88} -NC-Ar	Co _{2.88} -NC- H ₂
Co _{3.50} Zn ZIF-8	1.69 g (5.68 mmol)	60 mg (206.22 μmol)	Co _{3.50} Zn _{96.50}	Co _{3.50} Zn ZIF-8@KTA	Co _{3.50} -NC-Ar	Co _{3.50} -NC- H ₂
Co _{8.32} Zn ZIF-8	1.69 g (5.68 mmol)	150 mg (515.41 μmol)	Co _{8.32} Zn _{91.68}	Co _{8.32} Zn ZIF-8@KTA	Co _{8.32} -NC-Ar	Co _{8.32} -NC- H ₂
Co _{10.79} Zn ZIF-8	1.69 g (5.68 mmol)	200 mg (687.21 μmol)	Co _{10.79} Zn _{89.21}	Co _{10.79} Zn ZIF-8@KTA	Co _{10.79} -NC-Ar	Co _{10.79} -NC- H ₂
ZIF-67	0	1.65 g (5.68 mmol)	Co ₁₀₀ Zn ₀	ZIF-67@KTA	Co _{max} -NC-Ar	Co _{max} -NC- H ₂

3.4.9 SEM and EDX analysis

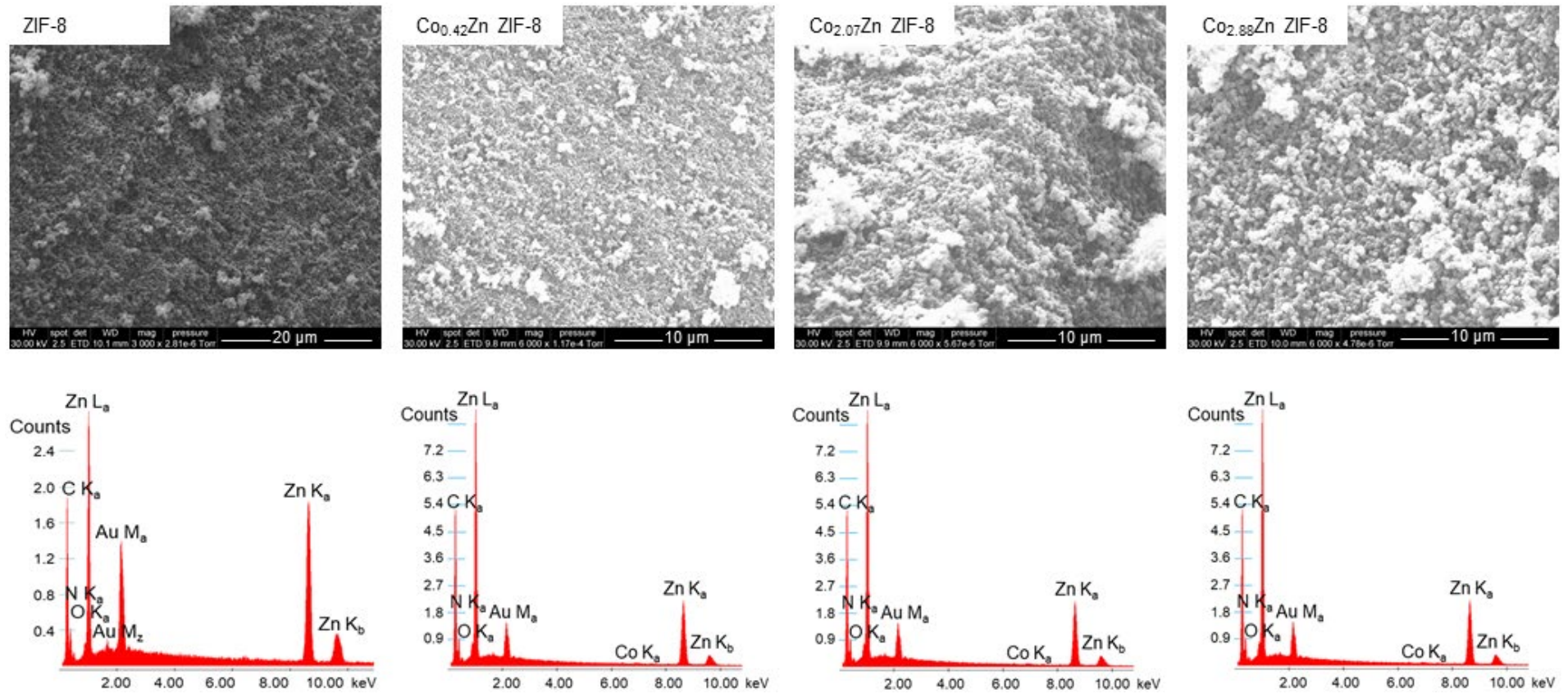


Figure 3.26: SEM and EDX of ZIF-8, $\text{Co}_{0.42}\text{Zn}$ ZIF-8, $\text{Co}_{2.07}\text{Zn}$ ZIF-8 and $\text{Co}_{2.88}\text{Zn}$ ZIF-8; counts in thousands.

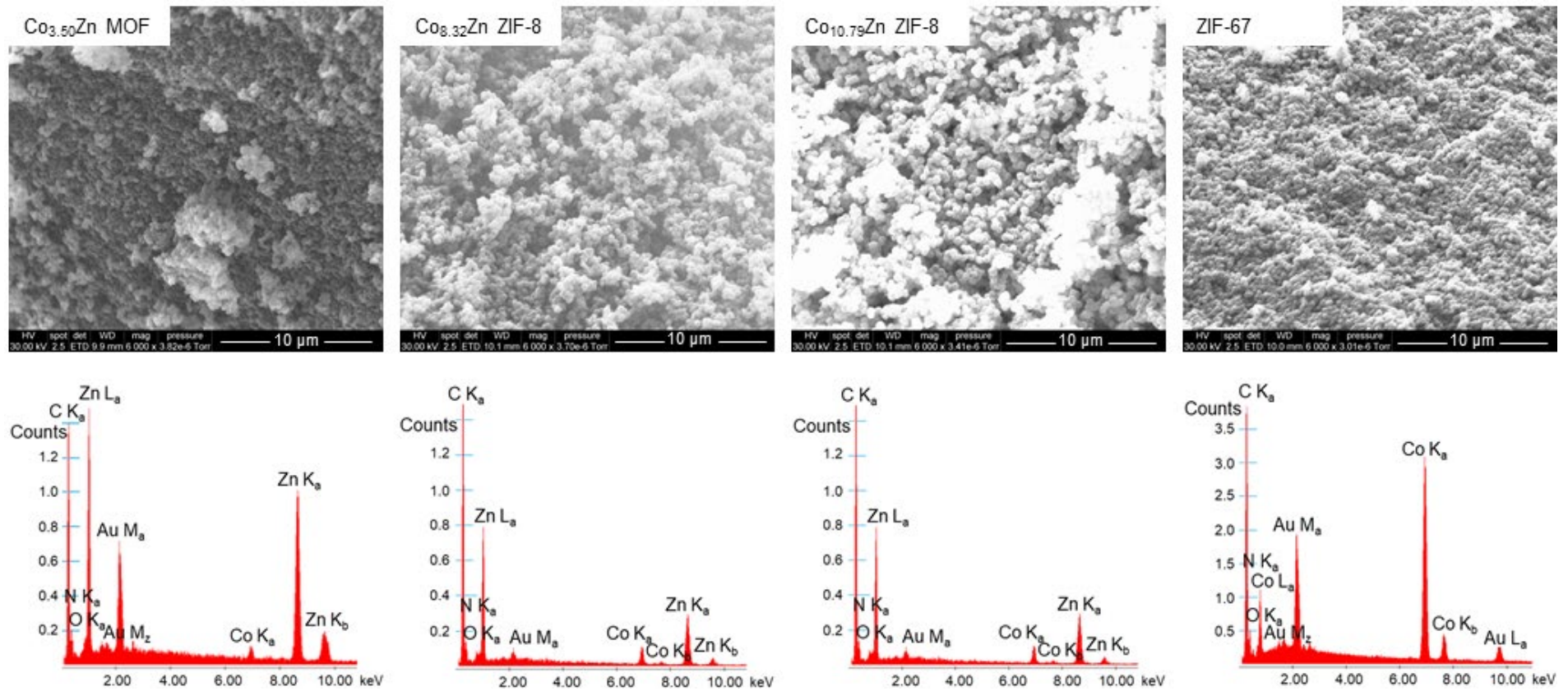


Figure 3.27: SEM and EDX of $\text{Co}_{3.50}\text{Zn}$ ZIF-8, $\text{Co}_{8.32}\text{Zn}$ ZIF-8, $\text{Co}_{10.79}\text{Zn}$ ZIF-8 and ZIF-67; counts in thousands.

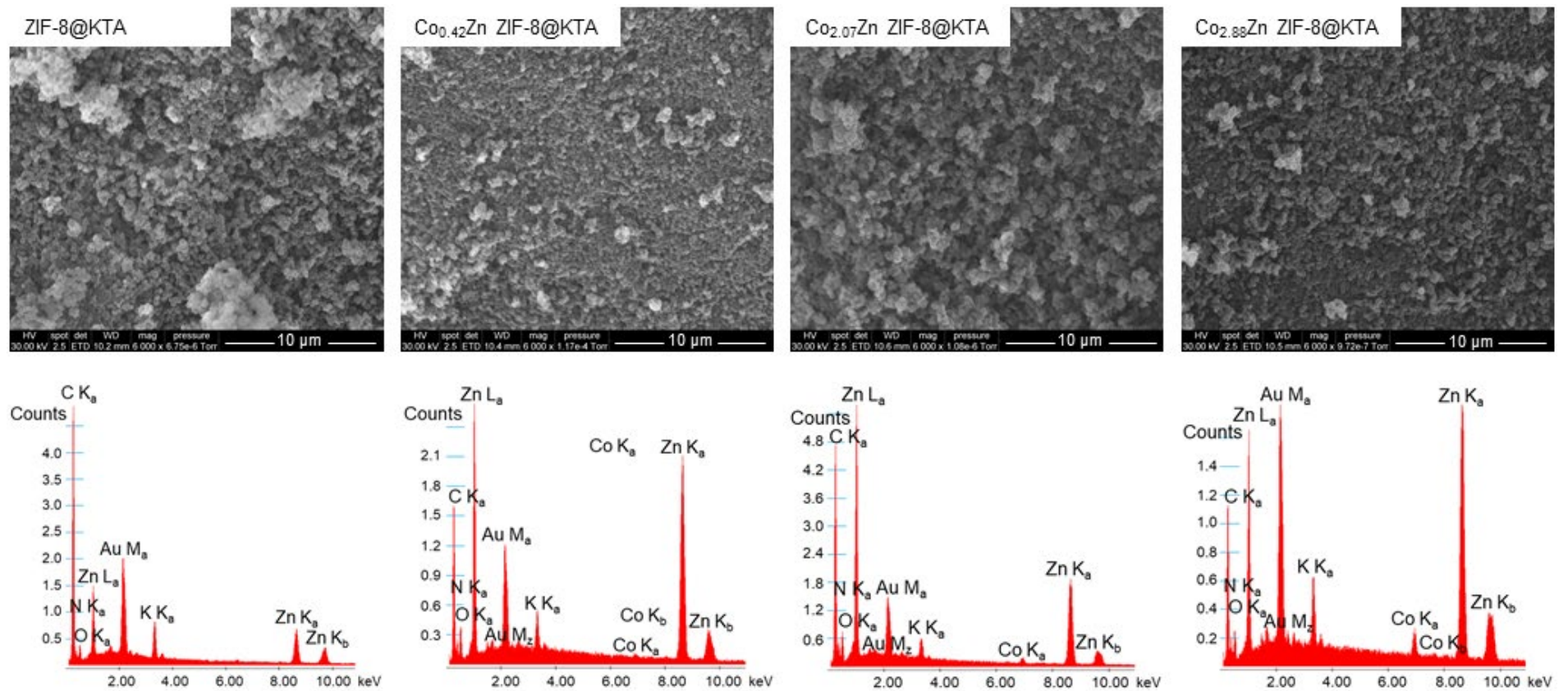


Figure 3.28: SEM and EDX of ZIF-8@KTA, Co_{0.42}Zn ZIF-8@KTA, Co_{2.07}Zn ZIF-8@KTA and Co_{2.88}Zn ZIF-8@KTA; counts in thousands.

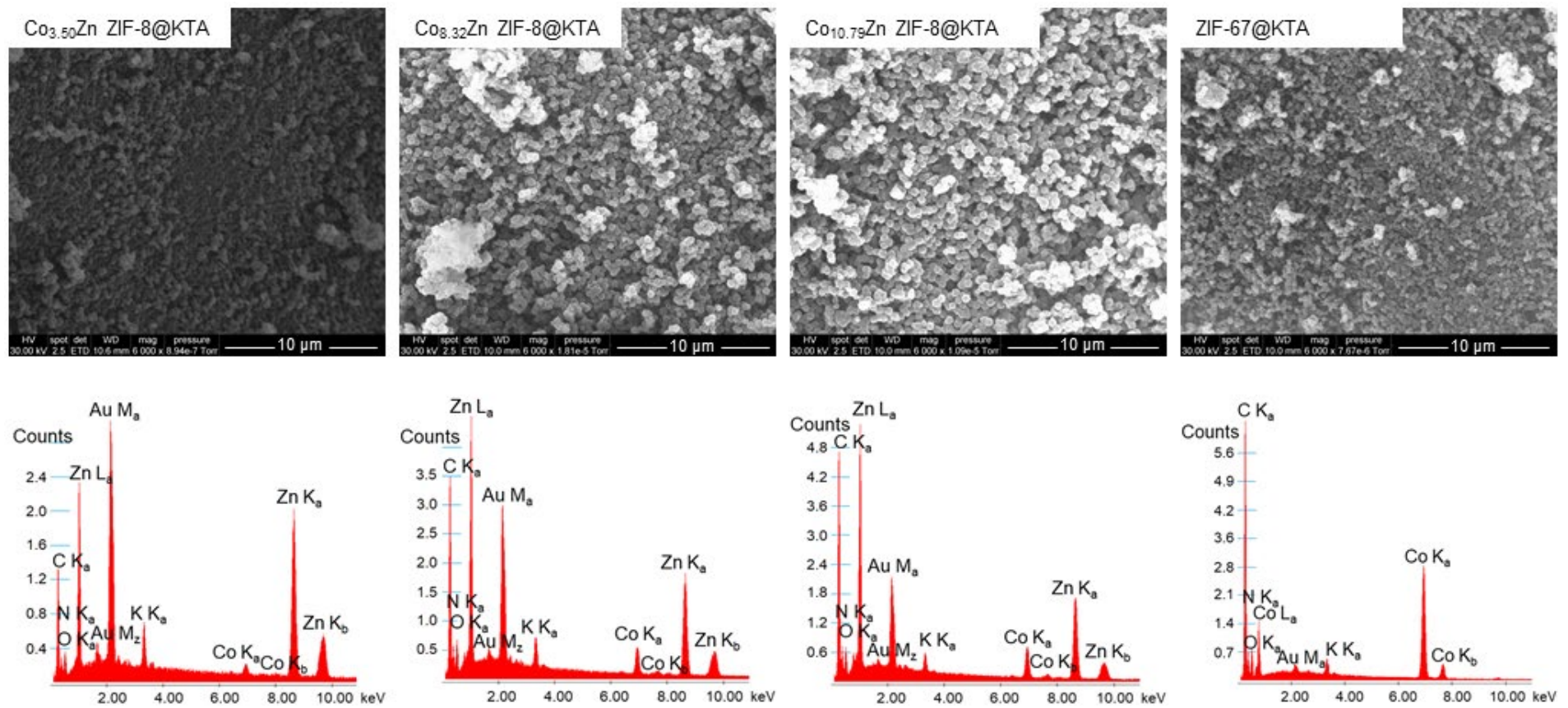


Figure 3.29: SEM and EDX of $\text{Co}_{3.50}\text{Zn ZIF-8@KTA}$, $\text{Co}_{8.32}\text{Zn ZIF-8@KTA}$, $\text{Co}_{10.79}\text{Zn ZIF-8@KTA}$ and ZIF-67@KTA; counts in thousands.

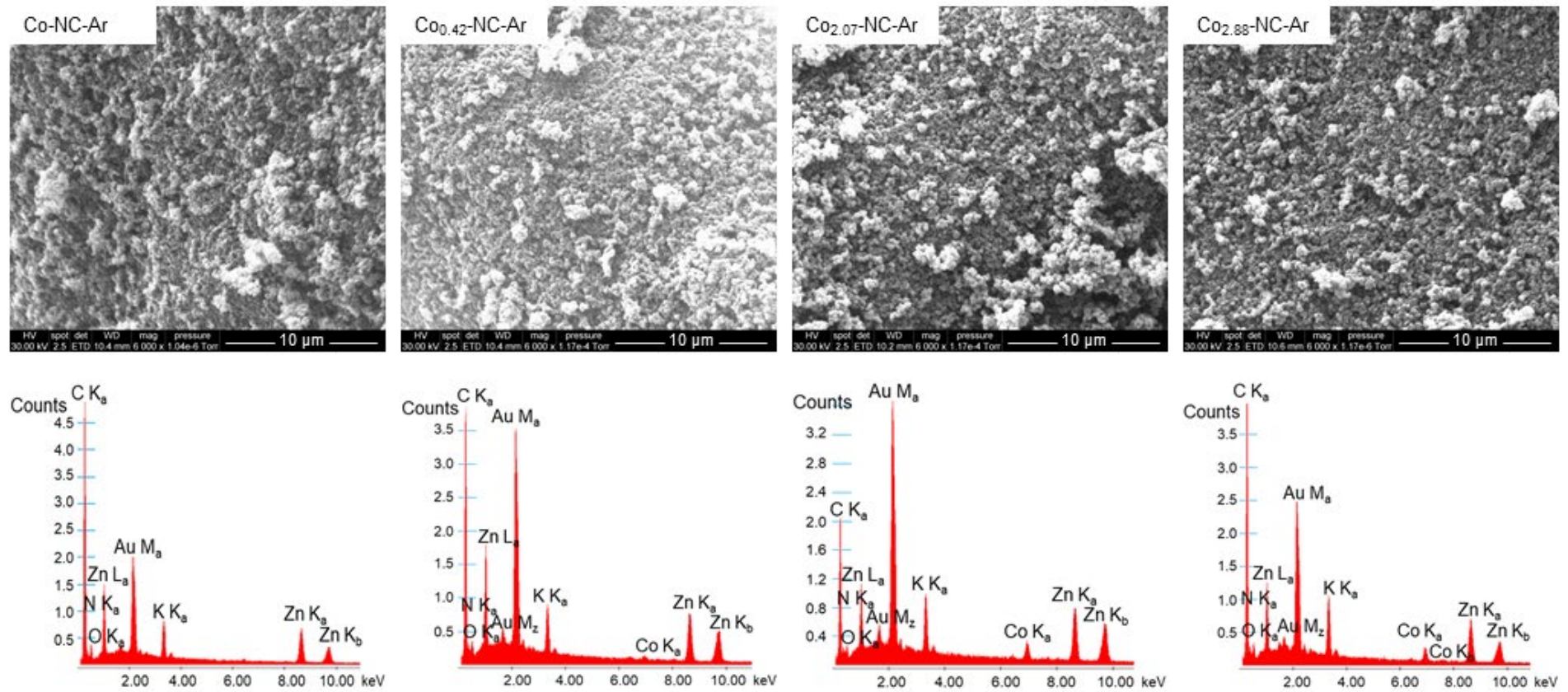


Figure 3.30: SEM and EDX of NC-Ar, Co_{0.42}-NC-Ar, Co_{2.07} Co_{0.42}-NC-Ar and Co_{2.88}-NC-Ar; counts in thousands.

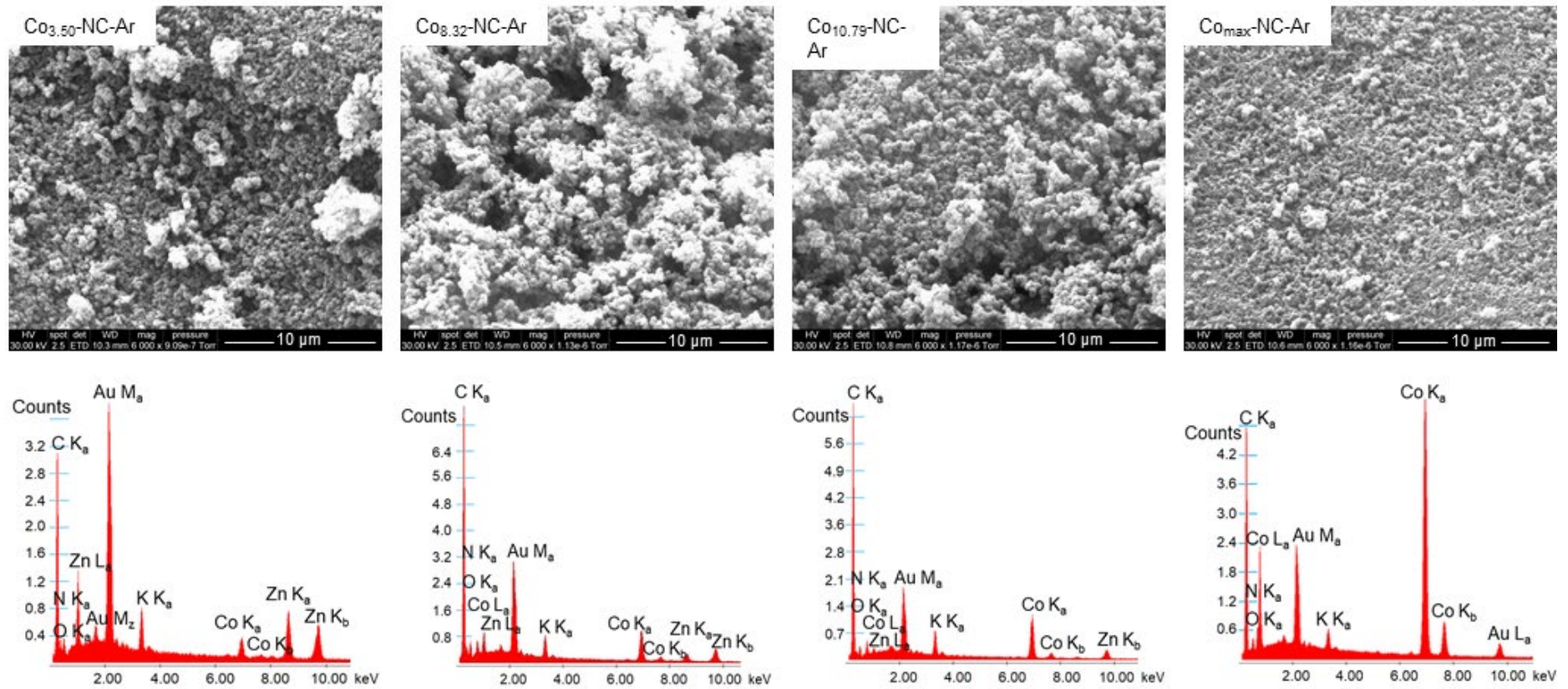


Figure 3.31: SEM and EDX of $\text{Co}_{3.50}\text{-NC-Ar}$, $\text{Co}_{8.32}\text{-NC-Ar}$, $\text{Co}_{10.79}\text{-NC-Ar}$ and $\text{Co}_{\text{max}}\text{-NC-Ar}$; counts in thousands.

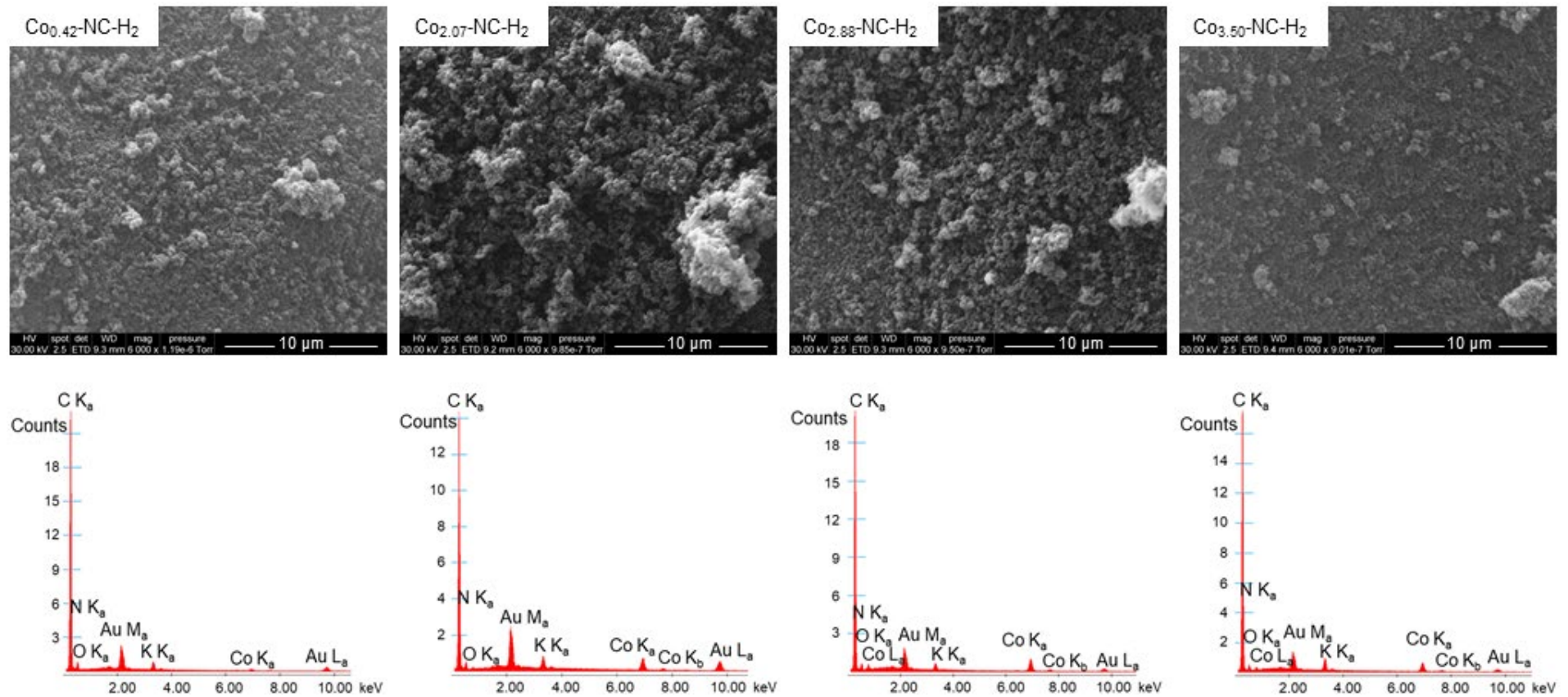


Figure 3.32: SEM and EDX of $\text{Co}_{0.42}\text{-NC-H}_2$, $\text{Co}_{2.07}\text{-NC-H}_2$, $\text{Co}_{2.88}\text{-NC-H}_2$ and $\text{Co}_{3.50}\text{-NC-H}_2$; counts in thousands.

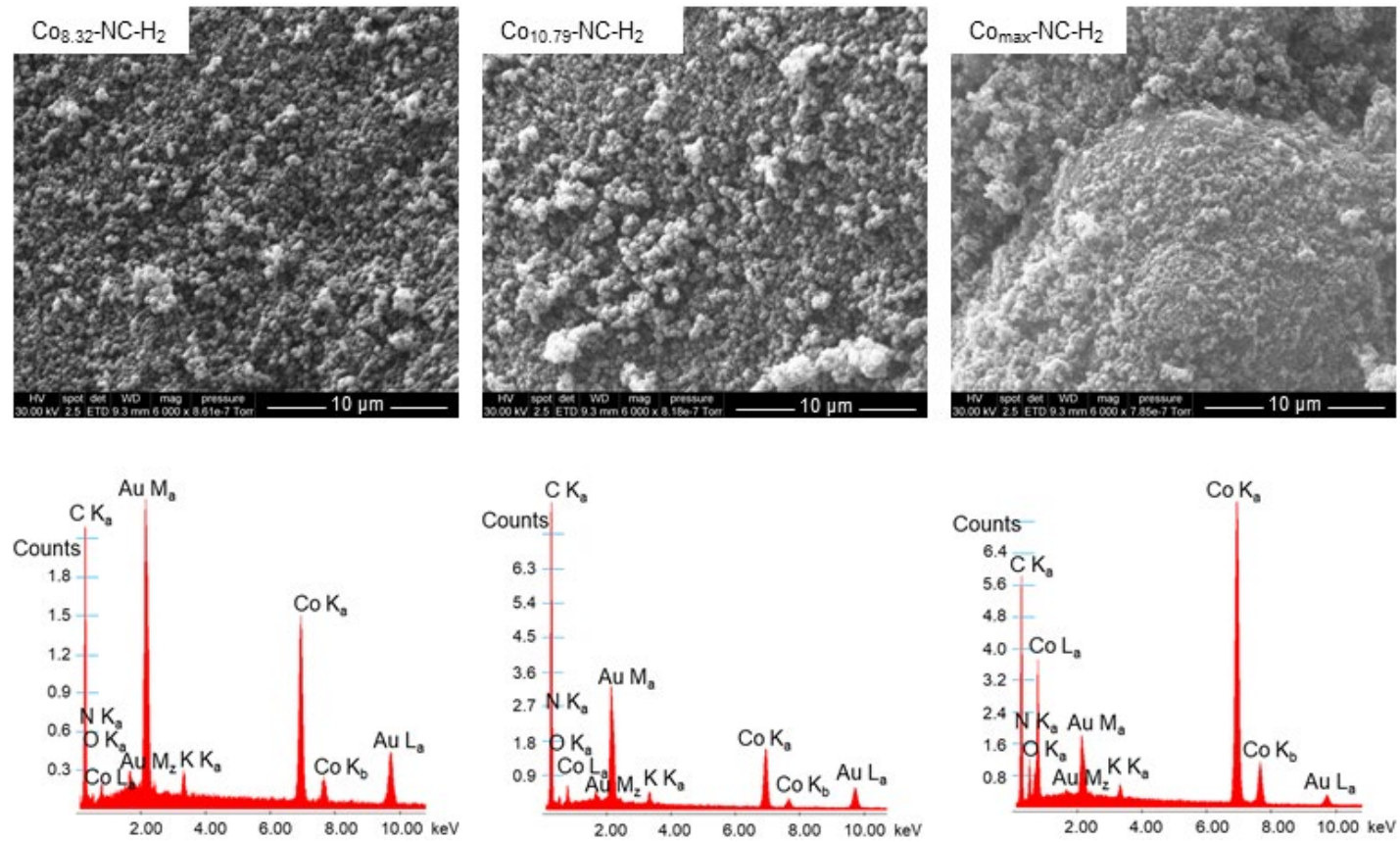


Figure 3.33: SEM and EDX of Co_{0.32}-NC- H₂, Co_{10.79}-NC- H₂ and Co_{max}-NC- H₂; counts in thousands.

3.4.10 TEM images

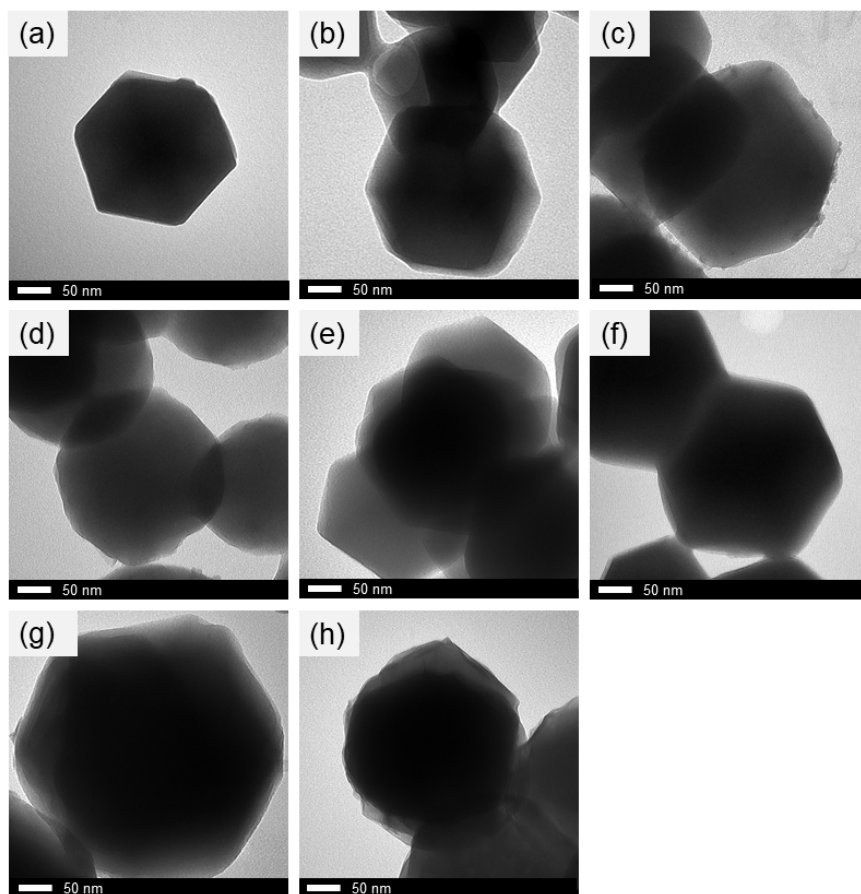


Figure 3.34: TEM images of (a) ZIF-8, (b) $\text{Co}_{0.42}\text{Zn}$ ZIF-8, (c) $\text{Co}_{2.07}\text{Zn}$ ZIF-8, (d) $\text{Co}_{2.88}\text{Zn}$ ZIF-8, (e) $\text{Co}_{3.50}\text{Zn}$ ZIF-8, (f) $\text{Co}_{8.32}\text{Zn}$ ZIF-8, (g) $\text{Co}_{10.79}\text{Zn}$ ZIF-8 and (h) ZIF-67.

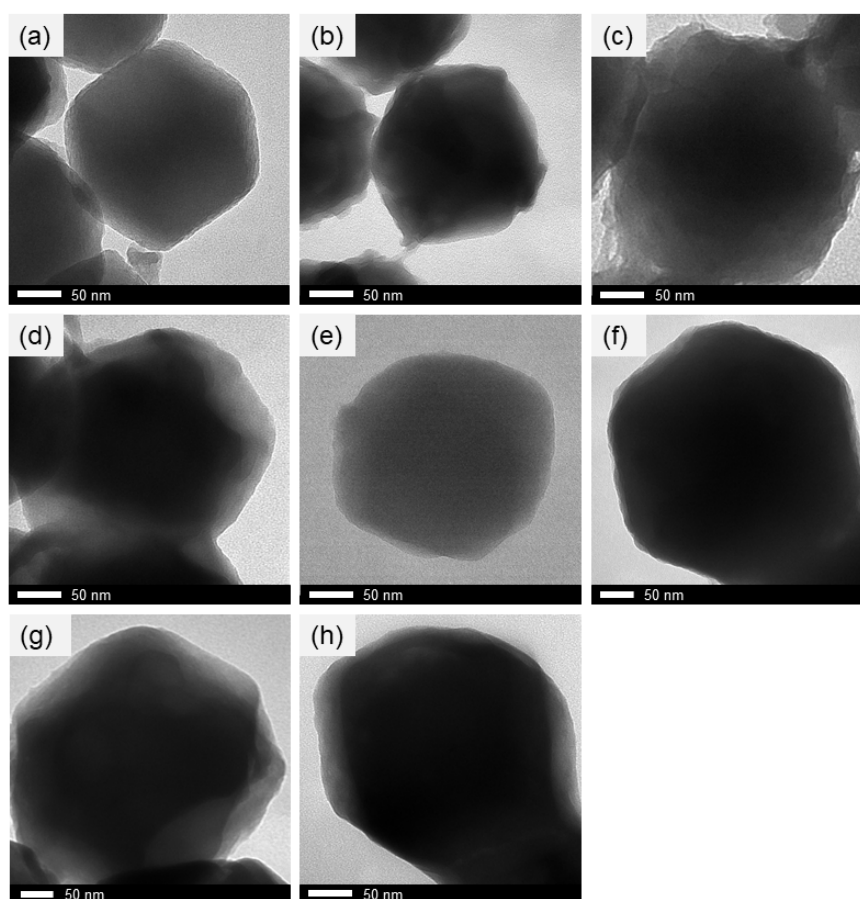


Figure 3.35: TEM images of (a) ZIF-8@KTA, (b) $\text{Co}_{0.42}\text{Zn}$ ZIF-8@KTA, (c) $\text{Co}_{2.07}\text{Zn}$ ZIF-8@KTA (d) $\text{Co}_{2.88}\text{Zn}$ ZIF-8@KTA (e) $\text{Co}_{3.50}\text{Zn}$ ZIF-8@KTA, (f) $\text{Co}_{8.32}\text{Zn}$ ZIF-8@KTA, (g) $\text{Co}_{10.79}\text{Zn}$ ZIF-8@KTA and (h) ZIF-67@KTA.

3.4.11 XPS analysis

Table 3.3: Summarized chemical composition data for CoZn ZIF-8, CoZn ZIF-8@KTA and reference samples (as wt.%).

Sample description	Wt. % by survey XPS						
	C	N	O	Zn	Co	Cl	K
ZIF-8	65.4	12.5	8.4	11.3	-	2.5	-
Co _{0.42} Zn ZIF-8	63.0	15.4	4.5	13.7	-	3.4	-
Co _{2.07} Zn ZIF-8	68.7	9.5	11.0	8.4	-	2.3	-
Co _{2.88} Zn ZIF-8	65.5	13.3	6.5	11.9	0.1	2.6	-
Co _{8.32} Zn ZIF-8	69.5	9.4	11.3	7.9	0.5	1.5	-
Co _{10.79} Zn ZIF-8	64.9	12.9	8.1	10.3	1.2	2.7	-
ZIF-67	61.2	13.5	8.8	-	12.6	3.9	-
ZIF-8@KTA	42.6	2.4	15.9	3.7	-	0.5	34.9
Co _{0.42} Zn ZIF-8@KTA	40.1	3.5	17.5	5.3	-	0.7	32.9
Co _{2.07} Zn ZIF-8@KTA	41.1	3.0	16.7	4.9	-	0.7	33.7
Co _{2.88} Zn ZIF-8@KTA	40.0	3.2	17.8	5.3	-	0.7	32.9
Co _{8.32} Zn ZIF-8@KTA	41.2	2.9	16.9	4.4	0.3	0.5	33.8
Co _{10.79} ZnZIF-8@KTA	40.9	2.8	17.7	4.1	0.4	0.6	33.6
ZIF-67@KTA	39.0	2.6	19.8	-	6.0	0.6	32
Co(NO ₃) ₆ ·6H ₂ O	81.0	3.4	13.9	-	1.7	-	-
CoCl ₂ ·6H ₂ O	-	-	8.2	-	22.4	69.4	-
Co(OAC) ₂ ·4H ₂ O	52.4	-	29.5	-	18.1	-	-
Co(TPP)	81.0	3.4	13.9	-	1.7	-	-
Tannic acid	66.7	-	33.3	-	-	-	-

Table 3.4: Summarized chemical composition data for CoZn ZIF-8, CoZn ZIF-8@KTA and reference samples (as wt.%).

Sample description	Wt. % by survey XPS						
	C	N	O	Zn	Co	Cl	K
Co-NC-Ar	50.7	4.1	2.4	0.9	-	0.2	41.6
Co _{0.42} -NC-Ar	48.4	6.3	3.0	2.3	0.1	0.3	39.7
Co _{2.07} -NC-Ar	47.9	6.7	3.2	2.1	0.4	0.3	39.3
Co _{2.88} -NC-Ar	47.5	7.0	3.3	2.1	0.7	0.5	39.0
Co _{8.32} -NC-Ar	47.6	6.6	4.1	0.6	1.8	0.2	39.1
Co _{10.79} -NC-Ar	50.8	3.2	3.1	-	1.2	0.1	41.7
Co _{max} -NC-Ar	51.3	0.3	3.0	-	1.7	0.1	42.8
Co-NC-H ₂	48.5	6.2	3.0	2.2	-	0.3	39.8
Co _{0.42} -NC-H ₂	53.5	0.6	1.9	-	0.1	0.1	43.8
Co _{2.07} -NC-H ₂	53.3	1.0	1.9	-	0.1	0.1	43.7
Co _{2.88} -NC-H ₂	53.5	0.6	1.8	-	0.2	-	43.9
Co _{8.32} -NC-H ₂	53.5	0.7	1.6	-	0.3	0.1	43.8
Co _{10.79} -NC-H ₂	55.6	0.5	1.6	-	0.4	0.3	43.9
Co _{max} -NC-H ₂	51.5	0.2	3.2	-	2.6	0.3	42.2
Co(NO ₃) ₆ ·6H ₂ O	81.0	3.4	13.9	-	1.7	-	-
CoCl ₂ ·6H ₂ O	-	-	8.2	-	22.4	69.4	-
Co(OAC) ₂ ·4H ₂ O	52.4	-	29.5	-	18.1	-	-
Co(TPP)	81.0	3.4	13.9	-	1.7	-	-
Tannic acid	66.7	-	33.3	-	-	-	-

3.4.12 EXAFS fittings

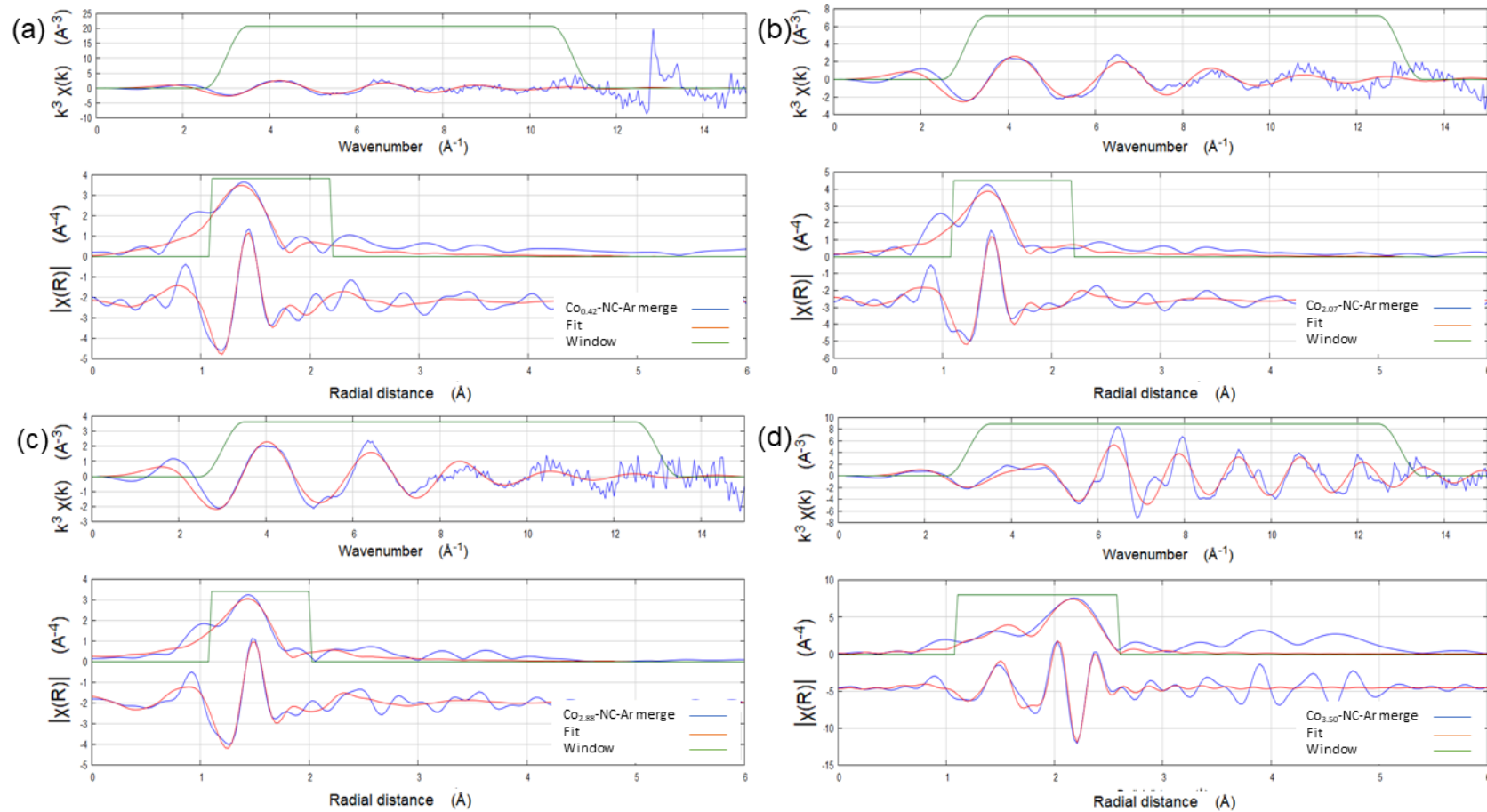


Figure 3.36: EXAFS fittings for Co-N for (a) Co_{0.42}-NC-Ar, (b) Co_{2.07}-NC-Ar, (c) Co_{2.88}-NC-Ar, and (d) Co_{3.50}-NC-Ar samples; On the top panel individual contributions of Co-NC samples are shown in k-space, while on the bottom panel they are shown in R-space.

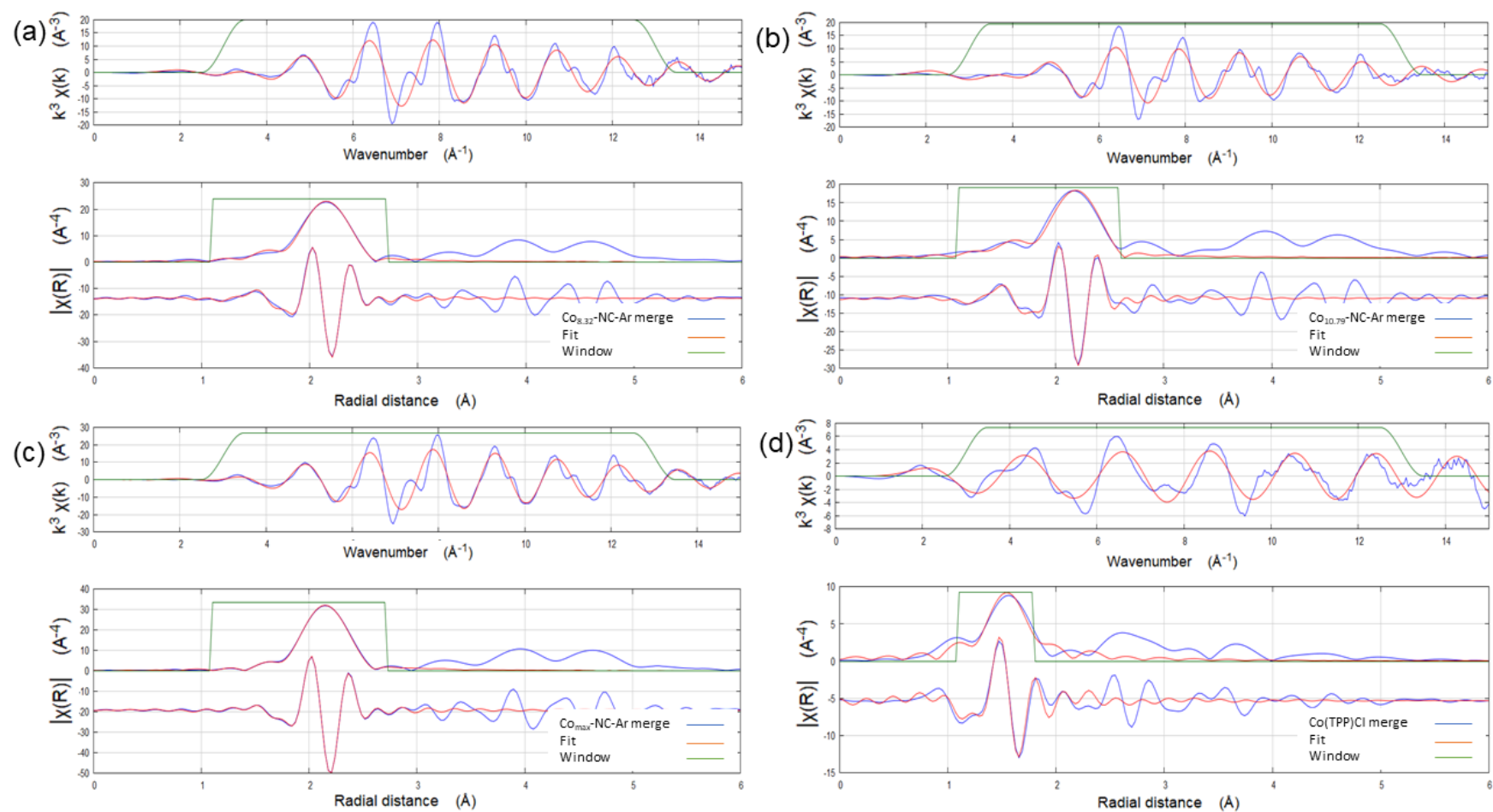


Figure 3.37: EXAFS fittings for Co-N for (a) $\text{Co}_{0.32}\text{-NC-Ar}$, (b) $\text{Co}_{10.79}\text{-NC-Ar}$, (c) $\text{Co}_{\text{max}}\text{-NC-Ar}$, and (d) Co(TPP)Cl samples; On the top panel individual contributions of Co-NC samples are shown in k-space, while on the bottom panel they are shown in R-space.

Table 3.5: EXAFS fitting parameters at Co K-edge for Co-NC-Ar samples with various Co loadings, Co(TPP) and metallic Co for Co-N and Co-Co bond.

Sample	Path	CN	R(Å)	$\sigma^2(\text{Å}^2)$	Path	CN	R(Å)	$\sigma^2(\text{Å}^2)$	E_0 (eV)	R factor %
Co _{0.42} -NC-Ar	Co-N	4.4	1.969	0.0140	Co-Co	-	-	-	-9.5	
Co _{2.07} -NC-Ar	Co-N	4.2	1.983	0.0125	Co-Co	-	-	-	-9.6	
Co _{2.88} -NC-Ar	Co-N	4.1	1.987	0.0131	Co-Co	-	-	-	-9.7	
Co _{3.50} -NC-Ar	Co-N	4.5	1.973	0.0107	Co-Co	2.3	2.499	0.0050	-1.8	
Co _{8.32} -NC-Ar	Co-N	3.7	1.988	0.0107	Co-Co	5.8	2.514	0.0055	2.0	
Co _{10.79} -NC-Ar	Co-N	2.2	1.971	0.0108	Co-Co	7.1	2.497	0.0054	-1.0	
Co _{max} -NC-Ar	Co-N	-	-	-	Co-Co	9.4	2.491	0.0052	-0.5	
Co(TPP)	Co-N	4.0	1.941	0.0009	Co-Co	-	-	-	-1.1	
Metallic Co	Co-N	-	-	-	Co-Co	12.0	2.051	0.0064	-1.3	

CN: the coordination number; R: interatomic distance between central atoms and surrounding coordination atoms; σ^2 is Debye-Waller factor to measure thermal and static disorder in absorber-scatter distances; ΔE_0 : edge-energy shift (the difference between the zero kinetic energy value of the sample and that of the theoretical model). R factor is used to value the goodness of the fitting. S_0^2 : the amplitude reduction factor; $S_0^2 = 0.76367$, S_0^2 is determined from a metallic Co reference.

Chapter 4 – Hydrogenation of Nitroarenes by Rh SAC and Co SAC

4.1 Introduction

The reduction of aromatic nitro groups is a widely used process in the chemical industry to produce aromatic amines. These aromatic amines are used as starting materials and intermediates for the synthesis of a variety of products such as pharmaceuticals, agrochemical products, polymer surfactants, dyestuffs, photographic chemicals, rubber, and chelating agents.²⁹⁰⁻²⁹³ There is a variety of methods for the hydrogenation of nitroarenes such as gold nanoparticle catalysed reduction of nitrophenol.²⁹⁴ Catalytic hydrogenation of nitroarenes with hydrogen and a metal catalyst is the most widely used method in the industry due to minimal production of side products.²⁹⁵⁻²⁹⁶ The hydrogenation of nitroarenes produces more than one million metric tons per year of products such as aniline and toluene diamines.²⁹⁷ High volume of these products is used for the polyurethane industry. For the catalysis of these reactions, palladium on alumina (Bayer), nickel on kieselguhr, copper on silica (BASF), platinum, and ion catalysts on carbon black (DuPont) are used. Moreover, for hydrogenation of nitroarenes containing halide functionalities, the resulting haloanilines are used in the chemical industry to produce pesticides, rubber chemicals, dyes pigments, and pharmaceuticals. Pt on C and activated Ni are used as catalysts in the hydrogenation process. The most important aspect in the catalysis of halonitroarenes is the hydrogenation of the nitro group without de-halogenating the halogen attached to the benzene ring. Furthermore, the selective hydrogenation of the aromatic nitro group to anilines without hydrogenating or reducing the functional group substituted to the aromatic group such as C=C, C≡C, C=N, and C=O is also performed. For this type of catalysis platinum on carbon modified with hypo phosphorus acid and vanadium are used.²⁹⁷

The selective hydrogenation of a nitro group is challenging in the catalytic hydrogenation of nitroarenes in the presence of other functional groups. Another problem is the financial cost of the catalyst employed in the catalysis of hydrogenation. Hence the single-atom catalysts (SACs) may present a solution to both of those problems due to their high selectivity and maximum utilization of the metal. Moreover, these heterogeneous catalysts can also be recycled thus reducing the cost of the catalytic process. Therefore, the Rh SAC and Co SAC synthesized in this research (Chapter 2 and 3) are tested for the hydrogenation of nitroarenes.

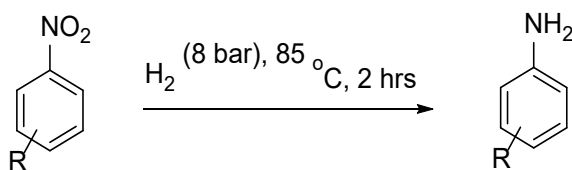
4.2 Results and Discussion

4.2.1 Hydrogenation of nitroarenes

The Rh SAC (Rh-NC-0.14) and Co SAC (Co_{2.88}-NC-Ar) which had the maximum loading of single-atoms, were used for the catalysis of hydrogenation of nitroarenes. Rh SAC consists of 5.64% w/w rhodium and Co SAC had 3.45% w/w cobalt. In the catalytic experiments, 2.5 mg of each catalyst was used: this equates to 1.37 μmol of rhodium and 1.46 μmol of cobalt. Thus, the amount of rhodium and cobalt used in the catalysis is almost the same and the catalytic activity of Rh SAC and Co SAC is comparable. The performance of Rh SAC was compared with the commercially available rhodium catalyst; 5% Rh on C. Control reactions were also performed under the same experimental conditions with the catalyst support (NC) to confirm that it does not catalyse the reaction. After running the reactions with the above catalysts, the reaction mixtures were analysed by reverse-phase HPLC. The expected products in the reactions were identified by comparison of their retention times with the commercially available reference standards. The % consumption and % selectivity of the reactions were calculated based on the peak areas of the HPLC chromatogram (experimental section, Eq. 4.1 and Eq. 4.2).

To investigate the catalytic activity of Rh SAC and Co SAC, the hydrogenation of 4-nitroacetophenone was performed first. 4-Nitroacetophenone has three functional groups that can be hydrogenated in principle. That is the carbonyl group, the nitro group, and the benzene ring. The desired product of this reaction is 4-aminoacetophenone, which entails selective hydrogenation of the nitro group. Rh SAC catalysed the hydrogenation of 4-nitroacetophenone to 4-aminoacetophenone with >99% consumption and >99% selectivity without reducing the carbonyl group (Table 4.1 entry 1; experimental section, Figure 4.1 c).

On the other hand, when using the commercial catalyst 5% Rh on C, 99 % consumption of the substrate was achieved but did not show any 4-aminoacetophenone peaks in the HPLC chromatogram. Instead, no peaks could be identified in the HPLC chromatogram (Table 4.1 entry 2; experimental section, Figure 4.1 d) in the range of 256 nm to 320 nm UV range suggesting that there were not any UV active products. Thus, the commercial catalyst 5% Rh on C could have over hydrogenated the phenyl ring to give a saturated product.

Table 4.1: Hydrogenation of nitroarenes catalysed by Rh SAC and Co SAC.

Entry	Catalyst	R	Consumption (%)	Selectivity (%)
1	Rh SAC	4-COCH ₃	>99	>99
2	5% Rh on C		>99	0
3	NC		0	0
4	No catalyst		0	0
5	Co SAC		0	0
6	Rh SAC	4-Cl	>99	>99
7	5% Rh on C		>99	0
8	Co SAC		0	0
9	Rh SAC	2-Cl	>99	>99
10	5% Rh on C		>99	0
11	NC		0	0
12	No catalyst		0	0
13	Co SAC		8	>99
14	Rh SAC	4-OCH ₃	>99	>99
15	5% Rh on C		>99	0
16	Co SAC		0	0
17	Rh SAC	4-CH ₃	>99	>99
18	5% Rh on C		>99	0
19	Co SAC		0	0
20	Rh SAC	4-CN	>99	93
21	5% Rh on C		>99	0
22	Co SAC		39	30
23	Rh SAC	3-COOH	95	97
24	5% Rh on C		>99	0
25	Co SAC		29	58

Reaction conditions: 85 °C, 2 hrs; 2.5 mg of the catalyst; H₂ 800 kPa; 10 μmol of the substrate in 10 mL of methanol. Consumption and selectivity were calculated based on the peak areas (experimental section, Table 4.2) of the HPLC chromatograms.

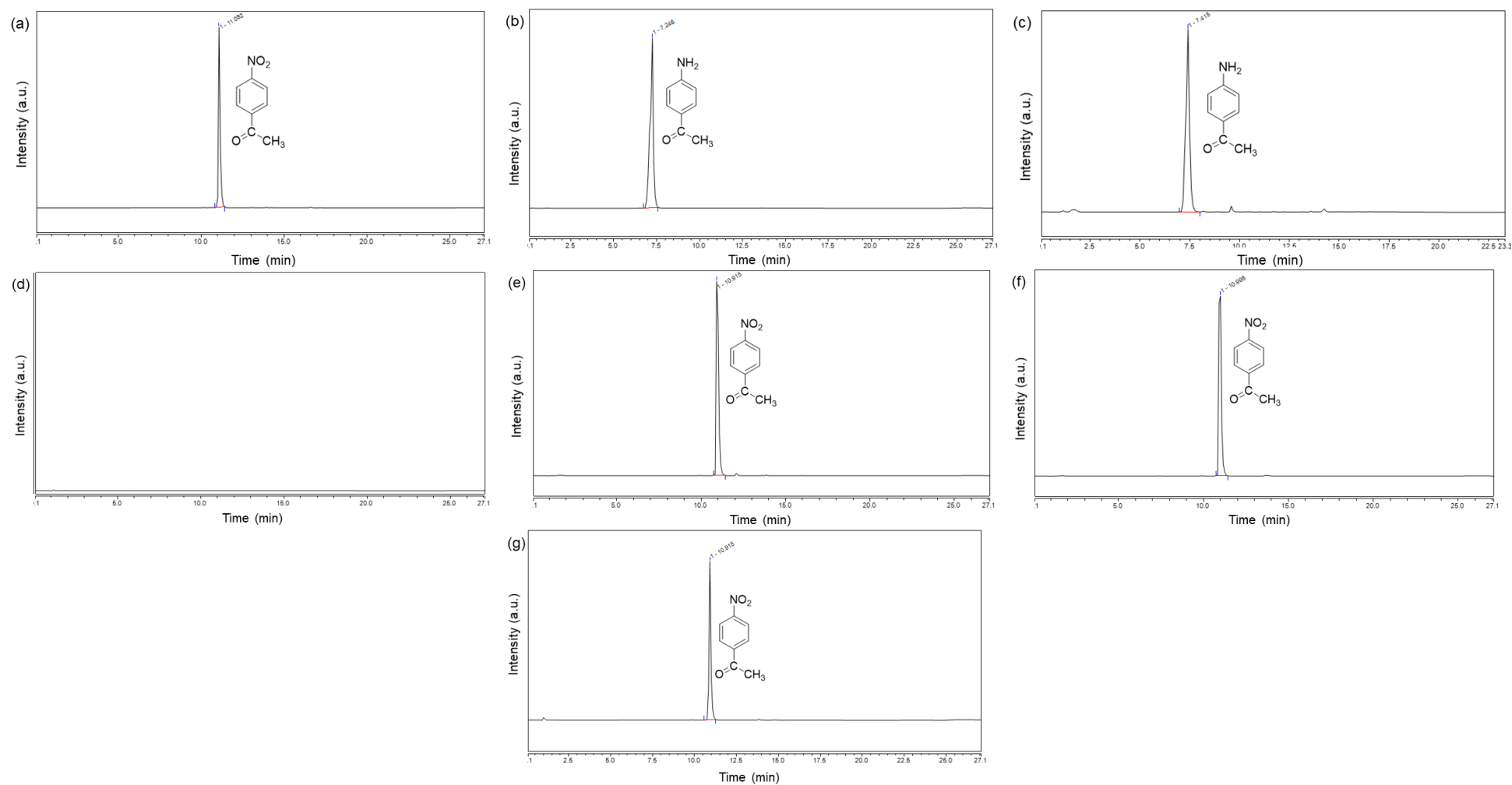


Figure 4.1: HPLC chromatograms of (a) substrate: 4-nitroacetophenone, (b) reference product: 4- aminoacetophenone; reaction catalysed by (c) Rh SAC, (d) 5% Rh on C, (e) NC, (f) no catalyst and (g) Co SAC.

This renders Rh SAC superior in terms of selectivity in catalysing the hydrogenation of 4-nitroacetophenone against the commercial catalyst. The reaction with NC did not catalyse hydrogenation, confirming the catalyst support does not catalyse the reaction (Table 4.1; experimental section, Figure 4.1 e). A reaction was conducted without any catalyst to ensure the absence of background reactions (Table 4.1 entry 4; experimental section, Figure 4.1f). The reaction was performed with Co SAC to test its catalytic activity. Surprisingly, Co SAC did not catalyse the reaction (Table 4.1; experimental section, Figure 4.1g).

To investigate the effect of other functional groups in the hydrogenation of nitroarenes, 1-chloro-4-nitrobenzene was used as the substrate. Rh SAC catalysed the consumption of >99% of 1-chloro-4-nitrobenzene to 4-chloroaniline with >99 % selectivity (Table 4.1 entry 6; experimental section, Figure 4.10 e), without dehalogenation of the functional group nor hydrogenation of the benzene ring. On the other hand, Co SAC did not hydrogenate 1-chloro-4-nitrobenzene (Table 4.1 entry 8; experimental section, Figure 4.10 c). As Rh SAC catalysed the hydrogenation of 1-chloro-4-nitrobenzene with high selectivity, to investigate the effect of the position of the functional group on the selectivity of the Rh SAC, the hydrogenation of 1-chloro-2-nitrobenzene was performed. As expected, Rh SAC catalysed the hydrogenation of 1-chloro-2-nitrobenzene to 2-chloroaniline with >99% consumption and >99% selectivity (Table 4.1 entry 9; experimental section, Figure 4.11 c). Implying the impact of the position of the functional group in the hydrogenation of nitroarenes, Co SAC did the hydrogenation of 1-chloro-2-nitrobenzene with 8% consumption and 99% selectivity (Table 4.1 entry 13; experimental section, Figure 4.11 g).

In the above reactions and most of the reactions, 1.37 μmol of rhodium atoms in Rh SAC hydrogenated 10 μmol of the substrate. The ratio of the moles of substrate consumed to moles of rhodium in the catalyst was 7.2 which is called the turnover number (TON). The higher the turnover number, the more substrate molecules are catalysed by a smaller number of catalysts. On the other hand, for most of the reactions catalysed by Co SAC, TON was zero. Co SAC showed a maximum TON of 2.7 for the hydrogenation of 4-aminobenzonitrile. Hence, Rh SAC is a better catalyst for the hydrogenation of nitroarenes than Co SAC.

To further investigate the selectivity of Rh SAC in the presence of functional groups, hydrogenation of 4-nitroanisole was performed. Rh SAC catalysed the hydrogenation of 4-nitroanisole to 4-aminoanisole with >99% consumption and 99% selectivity (Table 4.1 entry 14; experimental section, Figure 4.12 c), without reducing the methoxy group to the corresponding phenol or methane. In comparison, Co SAC did not hydrogenate 4-

nitroanisole (Table 4.1 entry 16; experimental section, Figure 4.12 e). Moreover, Rh SAC hydrogenated 4-nitrotoluene to 4-aminotoluene with high >99% consumption and 99% selectivity (Table 4.1 entry 17; experimental section, Figure 4.13 c). As usual, Co SAC did not hydrogenate 4-nitrotoluene (Table 4.1 entry 19; experimental section, Figure 4.13 e).

To further investigate the selectivity of Rh SAC in hydrogenating nitroarenes, the hydrogenation of 4-nitrobenzotrile was performed. In the hydrogenation of 4-nitrobenzotrile, the nitro group and nitrile group are susceptible to reduction. Rh SAC catalysed the hydrogenation of 4-nitrobenzotrile with 99% consumption resulting in 4-aminobenzotrile with 91% selectivity (Table 4.1 entry 20; experimental section, Figure 4.14 c), which is a reduction of the selectivity achieved by Rh SAC when compared to the other reactions.

In the previous experiments, Rh SAC hydrogenated the nitro group of nitroarene with high selectivity, without hydrogenating the functional groups on the ortho or para positions of the benzene ring. To further investigate the selectivity of Rh SAC, hydrogenation of 3-nitrobenzoic acid was performed. Its nitro and carboxyl groups can potentially be hydrogenated, leading to products such as 3-aminobenzaldehyde and 3-aminobenzylalcohol. Rh SAC catalysed the hydrogenation of 3-nitrobenzoic acid to 3-aminobenzoic acid with >91% consumption and >97% selectivity under the same experimental conditions (Table 4.1 entry 23; experimental section, Figure 4.15 c). In comparison, Co SAC catalysed the hydrogenation of 3-nitrobenzoic acid with 29% consumption and 57% selectivity (Table 4.1 entry 25; experimental section, Figure 4.15 e).

The commercial catalyst 5% Rh on C catalysed >99.9% of all the above nitroarenes but did not produce the corresponding amino product (Table 4.1 entry 2, 7, 10, 15, 18, 21, and 24). Instead, no peaks were identified in the HPLC chromatogram (experimental section, Figure 4.1 d - Figure 4.15 d), probably due to the over hydrogenation of the nitroarenes and resulting non-UV active products. In contrast, only the hydrogenation of 1-chloro-2-nitrobenzene by 5% Rh on C resulted in a UV active product (experimental section, Figure 4.11 c).

4.2.2 Leaching tests

It is also important to make sure that the single metal atoms are not leaching into the reaction mixture while performing the catalysis. Therefore, two types of leaching tests were done to determine whether catalytically active solutions were produced by any leaching of rhodium from the Rh SAC catalyst. In the first test, Rh SAC was subjected to the reaction conditions in the methanol medium without any substrate. If rhodium was leached into the methanol medium from Rh SAC, it might produce a catalytically active solution. 4-Nitroacetophenone was then added, and the mixture was heated under hydrogen using standard conditions. A HPLC chromatogram showed that no reaction occurred (Figure 4.2).

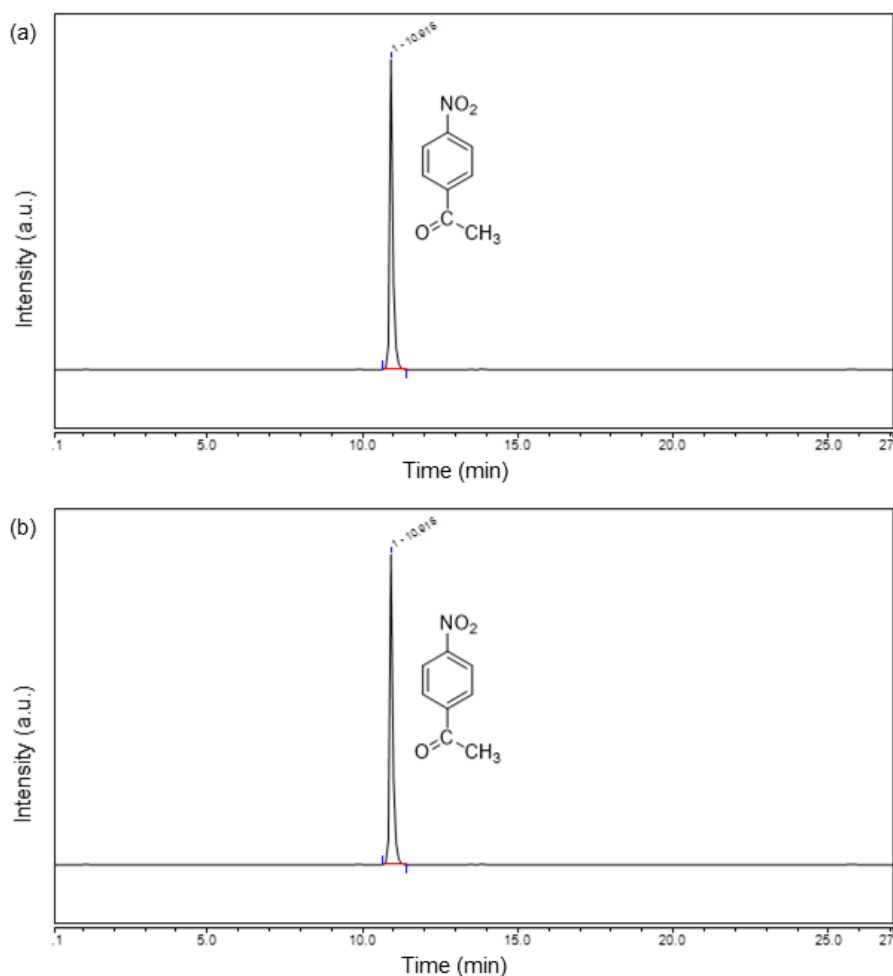


Figure 4.2: HPLC chromatogram of the reaction mixture (a) before the reaction: 0.001 M 4-nitroacetophenone in methanol and (b) after subjecting to reaction conditions; the absence of any product peaks in (b) confirms that the solution is not catalytically active after removing the catalyst.

In a second test, 1-chloro-2-nitrobenzene was partially reduced under the standard conditions. The Rh SAC was then removed from the reaction mixture by filtration. At this point, some consumption of 1-chloro-2-nitrobenzene had been achieved (Figure 4.3). When the reaction mixture was re-subjected to the reaction conditions (without catalyst), no further consumption was detected, (it remained at 8.6%). This indicates that the active catalyst had been successfully removed by the filtration step.

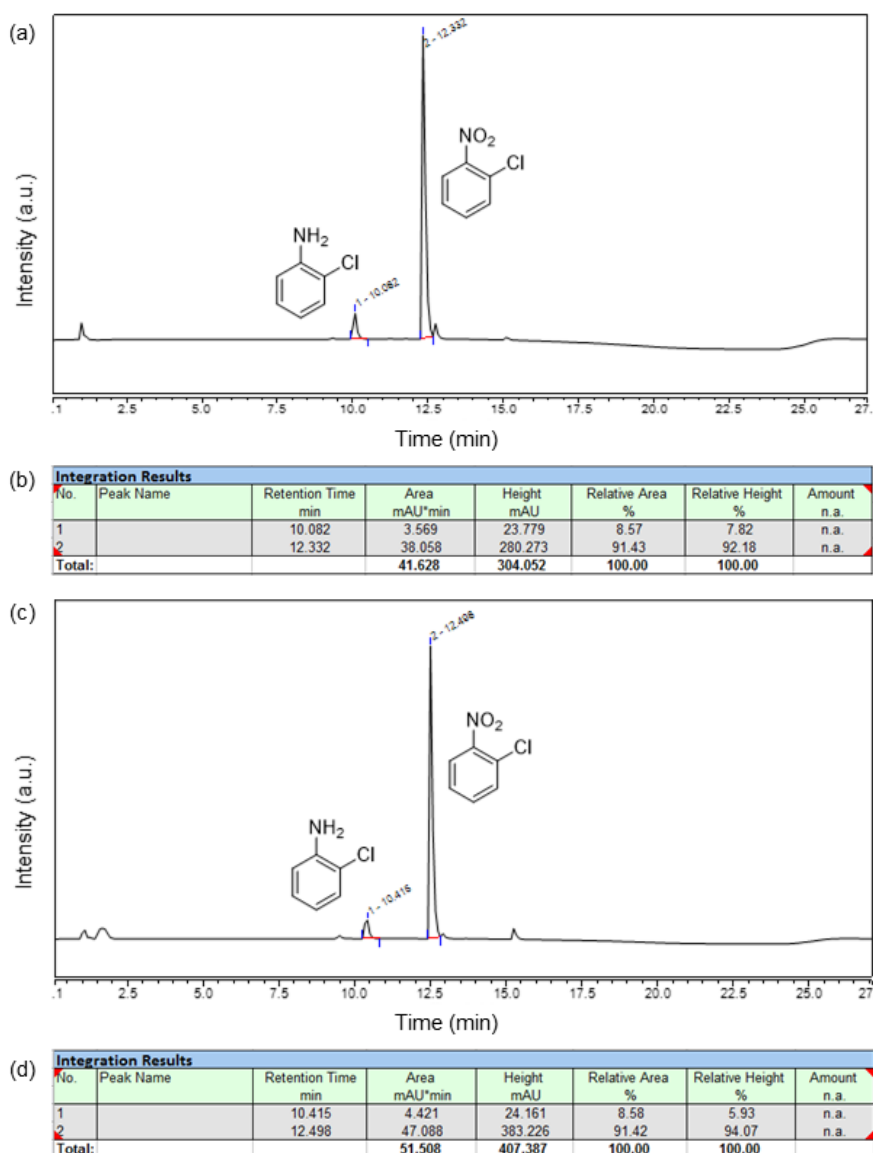


Figure 4.3: (a) HPLC chromatogram of the reaction mixture after the incomplete reaction (b) the quantification table of the HPLC chromatogram of the incomplete reaction generated by the software, (c) HPLC chromatogram of the reaction mixture after subjecting the incomplete reaction mixture to reaction conditions and (d) the quantification table of the HPLC chromatogram of the reaction mixture after subjecting the incomplete reaction mixture to reaction conditions generated by the software.

4.2.3 Re-cyclability of catalyst

Re-cyclability of the catalyst is also important in the catalysis, to use the catalyst effectively thus, reducing the cost of the catalytic process.

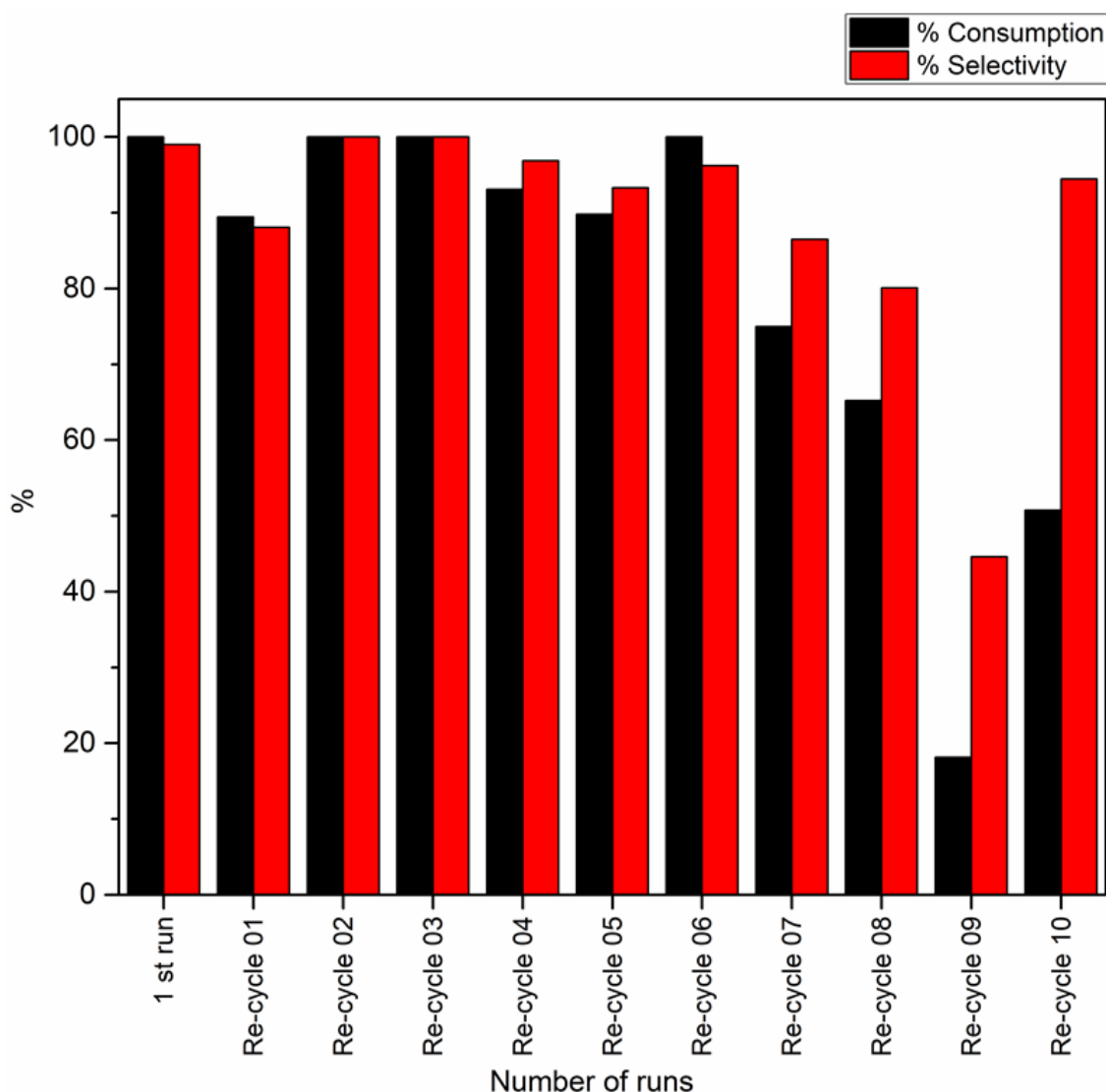


Figure 4.4: Re-cyclability test of Rh SAC.

In the first use of Rh SAC, it hydrogenated the substrate with >99% consumption and 99% selectivity. In the first re-use, Rh SAC lost both selectivity and consumption (about 90% of original activity for both). But in the second and third re-use, it showed >99% consumption and >99% selectivity again. Over six recycling cycles, Rh SAC catalysed the hydrogenation with >90% consumption and >90% selectivity. The consumption and selectivity of Rh SAC decreased significantly in the seventh and eighth re-use cycles. When Rh SAC has recycled for the ninth time a further decrease in the consumption and selectivity could be observed. Surprisingly in the tenth re-usable cycle of Rh SAC, it increases the selectivity >90% although the consumption is low at 50%.

4.2.4 Catalyst characterization after the catalysis

The consumption and selectivity of Rh SAC were reduced upon recycling. It is interesting to investigate the properties of Rh SAC after use as a catalyst by PXRD, SEM, EDX and TEM.

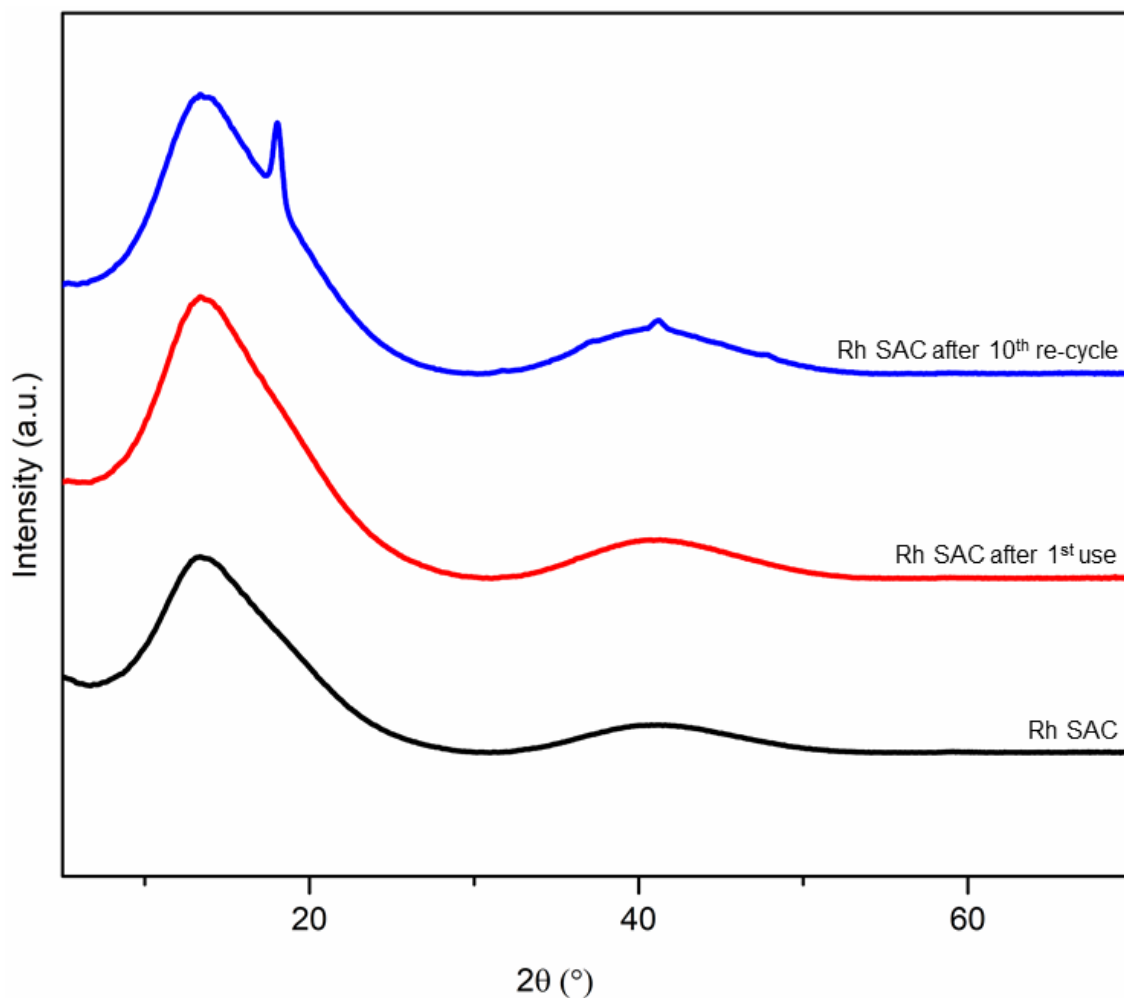


Figure 4.5: PXRD of (a) Rh SAC before catalysis, (b) Rh SAC after 1st use and (c) Rh SAC after 10th re-cycle.

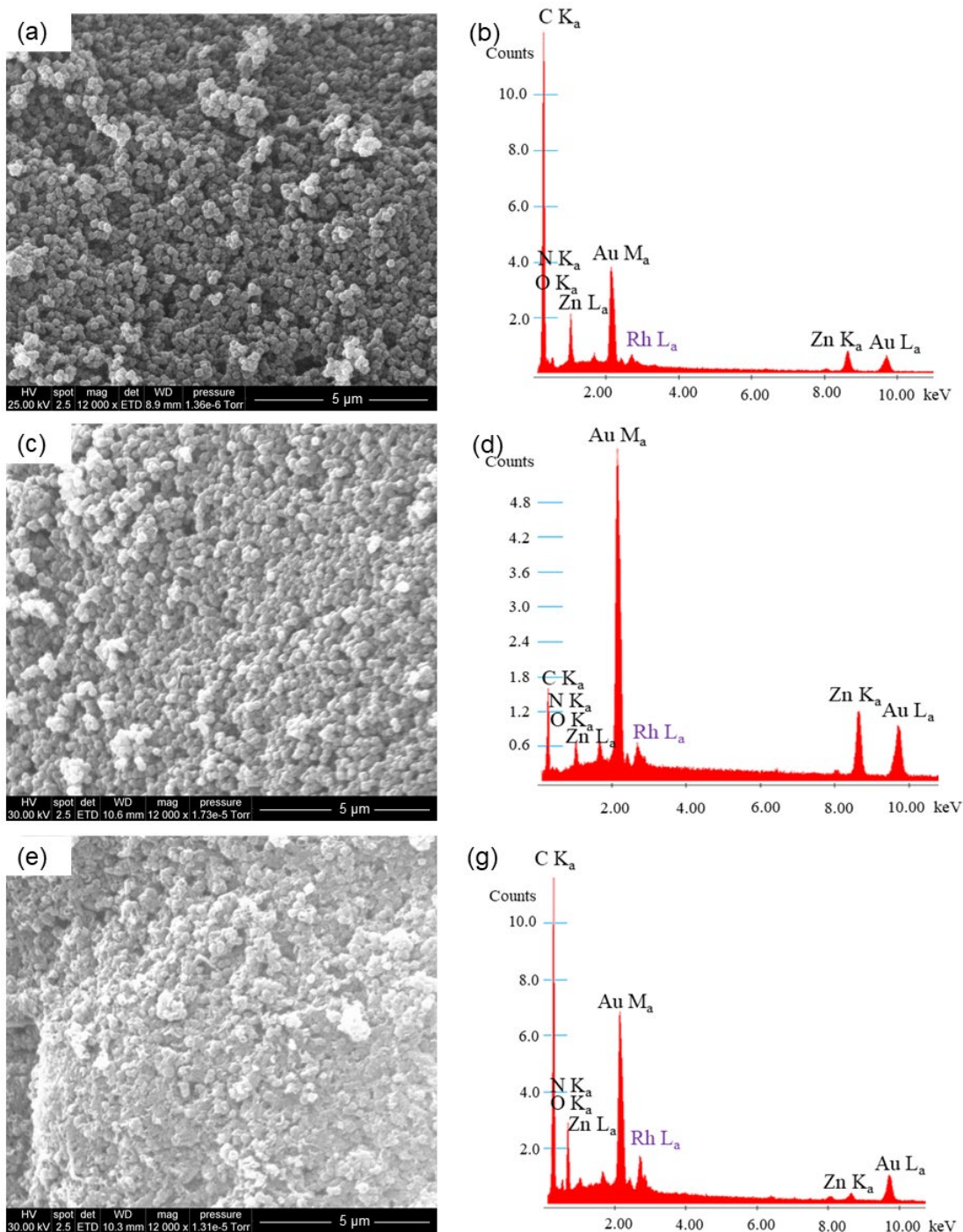


Figure 4.6: SEM and EDX of (a) Rh SAC before catalysis, (b) Rh SAC after 1st use and (c) Rh SAC after 10th re-use.

The PXRD pattern of Rh SAC after the first use matched with the PXRD pattern of fresh Rh SAC (Figure 4.5), which did not show any rhodium nanoparticle peaks and in the corresponding TEM images the presence of nanoparticles was ruled out, confirming its single-atom nature. The PXRD pattern of the catalyst after the tenth re-use (Figure 4.5) showed peaks at 41.1° and 47.8° 2θ Cu $K\alpha$, expected for rhodium nanoparticles (NPs). In the corresponding TEM image (Figure 4.7 c), nanoparticles were observed showing that the single atoms had aggregated into nanoparticles throughout recycling experiments.

Based on these observations, it turns out that the single rhodium atoms in Rh SAC agglomerate over the recycling and produce Rh NPs. That is probably the reason for the reduction in consumption and selectivity with the recycling of the Rh SAC.

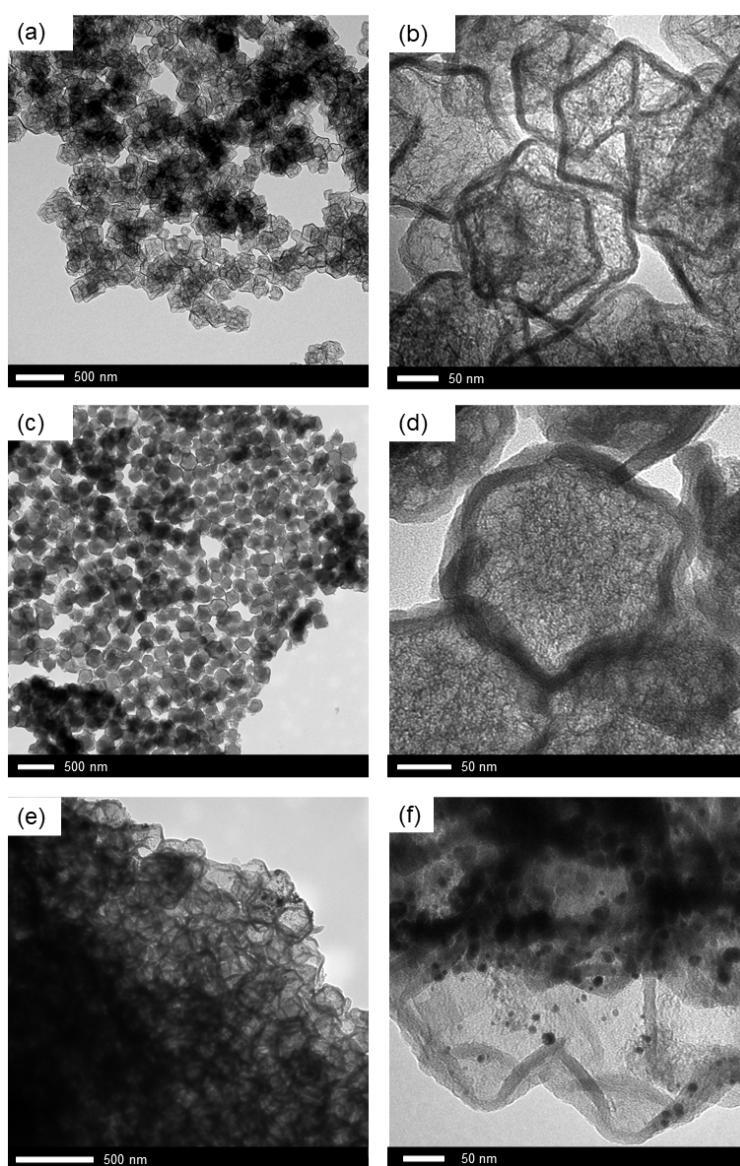


Figure 4.7: TEM images of (a, b) Rh SAC before catalysis, (c, d) Rh SAC after 1st use and (e, f) Rh SAC after 10th re-use.

4.3 Conclusion

Rh SAC catalyses the hydrogenation of nitroarenes with high selectivity and high consumption without reducing other functional groups such as halides, carbonyls, and phenyl rings. According to the characterization of Rh SAC in chapter 2, the single rhodium atoms are coordinated with four nitrogen atoms in the graphitic layer and two axial oxygen atoms (possibly in the form of H₂O). In the catalysis process, one or both oxygen donors detach, resulting in a coordination sphere that allows for the hydrogenation of nitroarenes.

To propose a mechanism for the hydrogenation of nitroarenes by Rh SAC, the widely accepted mechanisms for the hydrogenation of nitroarenes reported in the literature were considered. Haber *et al.* proposed a direct mechanism through a deoxygenation pathway (Figure 4.8 a),²⁹⁸ whereas Zhang *et al.* proposed an indirect hydrogen assisted hydrogenation pathway (Figure 4.8 b).²⁹⁹ Based on these mechanisms and computational modeling Liu *et al.* and Cheong *et al.* proposed a mechanism for the hydrogenation of nitroarenes by iron single-atom catalyst, which is in the form of Fe-N₄.³⁰⁰⁻³⁰¹ An indirect hydrogenation pathway was proposed since it has a lower energy barrier than the direct one.³⁰⁰ Based on the single-atom nature and the coordination environment, we propose Rh SAC also follows a similar mechanism to Fe-N₄ in the hydrogenation of nitroarenes (Figure 4.9).³⁰⁰

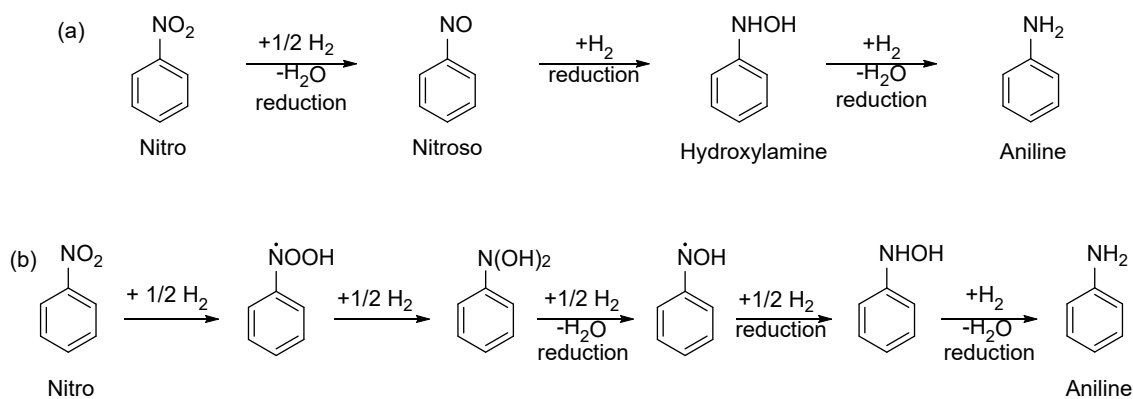


Figure 4.8: Mechanisms proposed for the hydrogenation of nitroarenes by (a) Haber *et al.* through direct deoxygenation pathway and (b) Zhang *et al.* through indirect hydrogen assisted hydrogenation pathway.

For the selective catalysis of hydrogenation of nitroarenes, the nitro group should be strongly adsorbed on Rh SAC. The nitro groups should have more affinity to bind to the rhodium single metal atom hindering the binding of other functional groups of the nitroarenes leading to high selectivity.³⁰² Thus, the first step probably involves the coordination of an O atom of the nitro group to the rhodium (Figure 4.9).

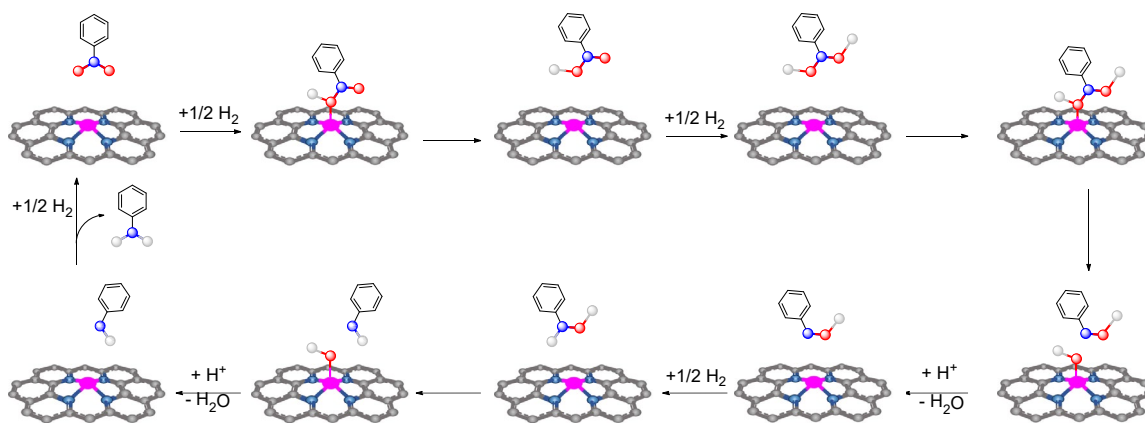


Figure 4.9: Proposed mechanism for the hydrogenation of nitroarenes by Rh SAC; rhodium (magenta), nitrogen (blue), oxygen (red) and hydrogen (grey) are shown in the mentioned colours for clarity.

Subsequently, the second oxygen of the nitro group is hydrogenated, forming the PhN(OH)_2 intermediate. Cleavage of one of the N-O bonds results in PhNOH . Then the hydrogenation of PhNOH to PhNHOH will take place in the next step. The step from PhNHOH to PhNH was considered to be the rate-determining step for the hydrogenation of nitroarenes by the reported Fe- N_4 catalyst.³⁰¹ Finally the hydrogenation of PhNH takes place resulting in PhNH_2 . To confirm this possible reaction mechanism of the Rh SAC during the reaction computational modeling is required.

Hydrogenation of nitroarenes with cobalt is reported in the literature but the Co SAC synthesized in this research was an ineffective catalyst in the hydrogenation of nitroarenes, whereas the reported Co catalysts exhibit excellent consumption and selectivity over the hydrogenation of the nitro group.³⁰³⁻³⁰⁴ In the reported well-characterized cobalt catalysts, hydrogenate nitroarenes Co-O coordination along with Co-N or Co-C coordination could be identified.³⁰³⁻³⁰⁴ It is doubtful the effect of the structure of the catalyst on the catalysis: (i) metallic Co^0 or oxidized CoO_x , (ii) Co sites and (iii) CoN_x species.³⁰⁵ The coordination environment of cobalt single-atoms might influence its catalytic inactivity in the hydrogenation of nitroarenes.

4.4 Experimental Section

4.4.1 General procedures

All starting materials and solvents were used as received from commercial sources without further purification unless otherwise noted. PXRD, SEM, EDX and TEM, measurements were carried out using the instruments detailed in Chapter 2.

High-performance liquid chromatography (HPLC) analysis was used to characterize the product distributions using a reverse-phase Thermo Scientific Accuore C18 column (length 10 mm, internal diameter: 2.1 mm and particle size: 2.6 μm). The following conditions were used for all the reaction mixtures and reference samples except for 3-nitrobenzoic acid and 3-aminobenzoic acid: column temperature: 298 K; flow rate: 0.3 mL/min; gradient: 0-1 min: 100 % DI water, 0-16 min: ramp up to 100 % acetonitrile, 16-21 min: hold 100 % acetonitrile, 21-22 min: ramp up to 100 % DI water, 21-27 min: 100 % DI water; detector: UV light and mass spectrophotometer. For 3-nitrobenzoic acid, 3-aminobenzoic acid and the related reaction mixtures the following conditions were used: column temperature: 298 K; flow rate: 0.3 mL/min; gradient: 0-27 min: 30% acetonitrile; detector: UV light and mass spectrophotometer.

The expected products in the reactions were identified by comparison of their retention times with the commercially available reference standards. The % consumption and % selectivity were calculated based on the peak areas of the chromatograms. For 4-nitroacetophenone, a calibration curve of the substrate and the product was used for the calculation of % consumption and % selectivity. For all the peak area measurements, the average peak area of three HPLC runs was used.

$$\% \text{ Consumption} = \frac{[\text{Substrate}_{\text{initial}} - \text{Substrate}_{\text{final}}]}{\text{Substrate}_{\text{initial}}} \times 100 \quad \text{Eq. 4.1}$$

$$\% \text{ Selectivity} = \frac{\text{desired Product}_{\text{final}}}{\text{desired Product}_{\text{exp}} * \% \text{ consumption}} \times 100 \quad \text{Eq. 4.2}$$

Where $\text{Substrate}_{\text{initial}}$ is the peak area of the substrate before the reaction and $\text{Substrate}_{\text{final}}$ is the peak area of the substrate after the reaction. ($\text{Substrate}_{\text{initial}}$ is determined by running the HPLC of the substrate (0.001 M) before the reaction.) $\text{Product}_{\text{exp}}$ is the expected peak area of the desired product peak if 100% consumption happened with 100% selectivity (a reference standard of the expected concentration (0.001 M) after the reaction was run to determine this value) and $\text{Product}_{\text{final}}$ is the actual peak area of the desired product after the reaction.

Table 4.2: Peak areas of the standard reference samples and the reaction mixtures obtained from the HPLC chromatogram.

Entry	Peak at t (min)	Peak area (mAU*min)						
		Reference standards		Catalyses used for the reaction				
		Substrate (0.001 M)	Product (0.001 M)	Rh SAC	5% Rh on C	Co SAC	NC	No Catalyst
1-5	10.915	164.823	-	-	-	164.823	164.565	167.215
	7.415	-	38.403	39.044	-	-	-	-
6-8	12.748	73.723	-	-	-	75.530	N/A	N/A
	1.665	-	71.900	74.813	-	-	N/A	N/A
9-13	12.582	31.962	-	-	-	29.638	35.887	35.995
	10.415	-	18.306	19.415	-	3.752	-	-
14-16	11.998	184.222	-	-	-	205.801	N/A	N/A
	1.248	-	144.932	146.004	-	-	N/A	N/A
17-19	13.332	164.427	-	-	-	176.393	N/A	N/A
	0.998	-	132.668	157.121	-	-	N/A	N/A
20-22	10.415	137.859	-	-	-	83.928	N/A	N/A
	7.665	-	187.537	174.826	-	21.749	N/A	N/A
23-25	2.249	178.523	-	9.171	-	127.611	N/A	N/A
	1.082	-	140.440	155.602	-	23.824	N/A	N/A

N/A: data not available.

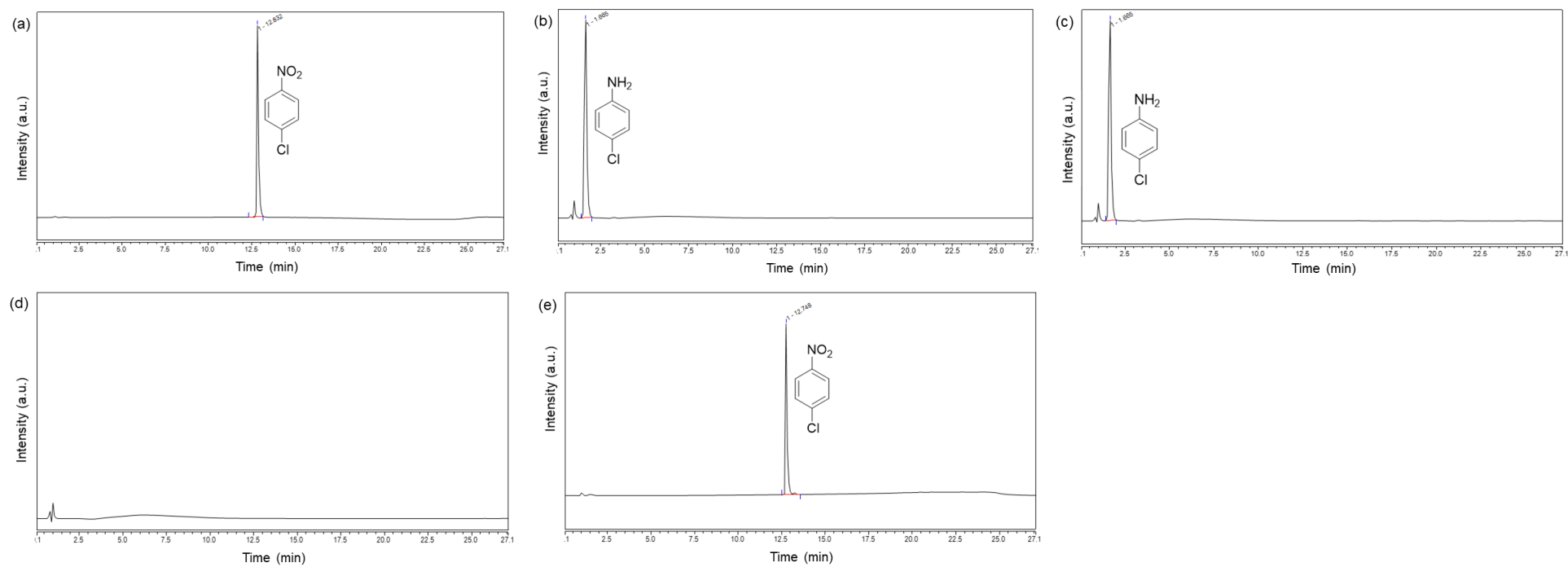


Figure 4.10: HPLC chromatograms of (a) substrate: 1-chloro-4-nitrobenzene, (b) reference product: 4-chloroaniline; reaction catalysed by (c) Rh SAC, (d) 5% Rh on C and (e) Co SAC.

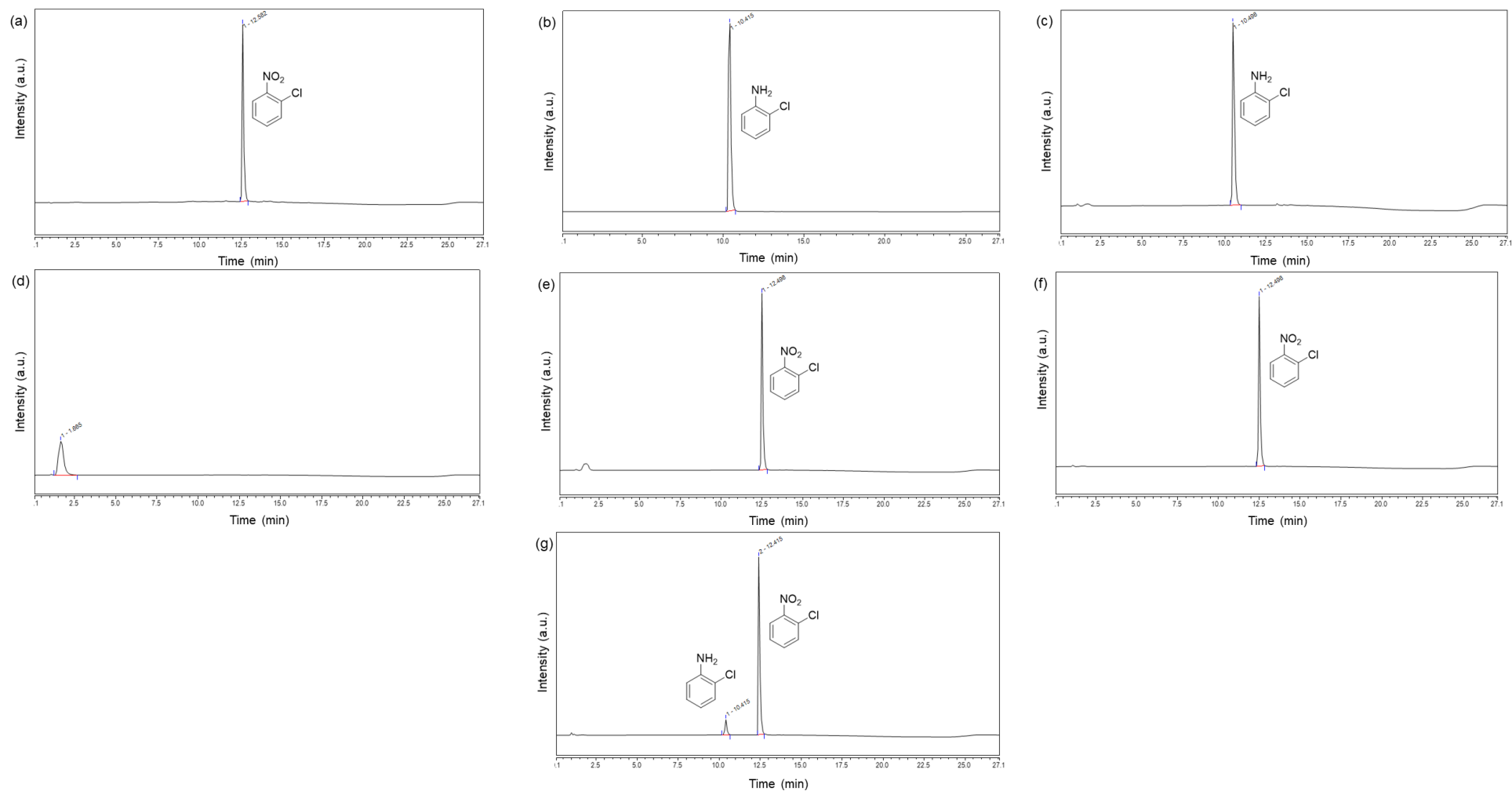


Figure 4.11: HPLC chromatograms of (a) substrate: 1-chloro-2-nitrobenzene, (b) reference product: 2-chloroaniline; reaction catalysed by (c) Rh SAC, (d) 5% Rh on C, (e) NC, (f) no catalyst and (g) Co SAC.

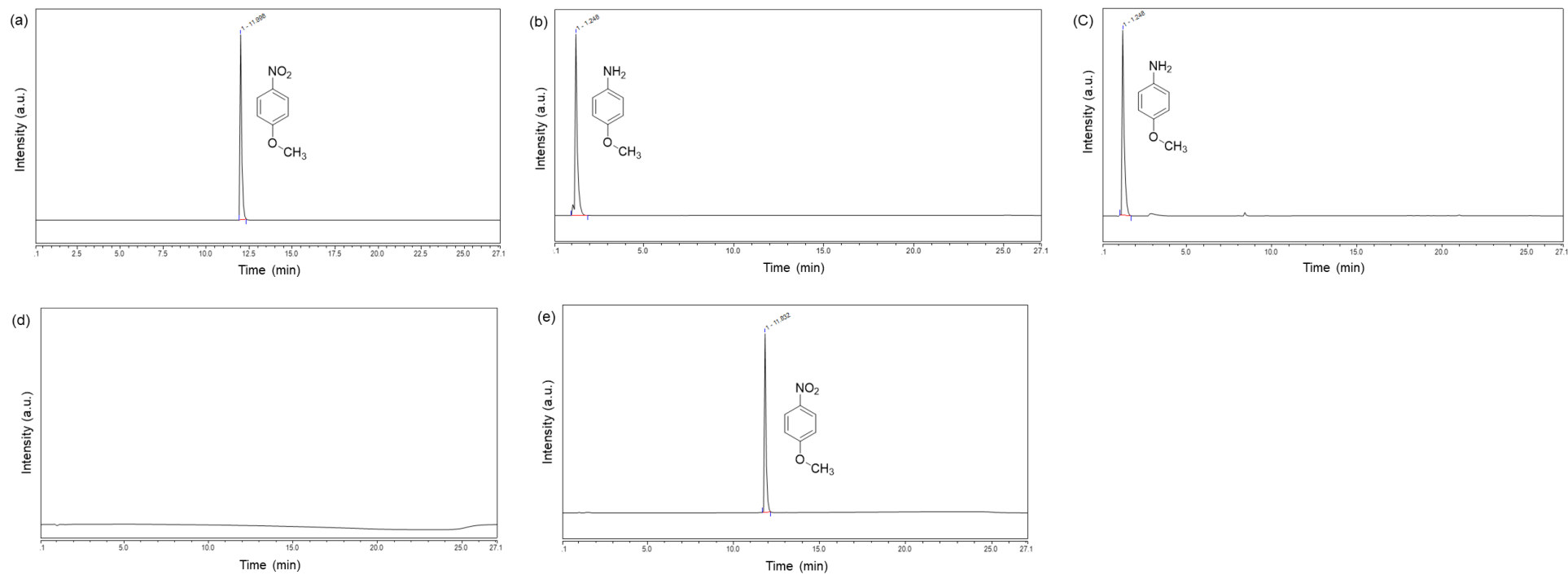


Figure 4.12: HPLC chromatograms of (a) substrate: 4-nitroanisole, (b) reference product: 4-aminoanisole; reaction catalysed by (c) Rh SAC, (d) 5% Rh on C and (e) Co SAC.

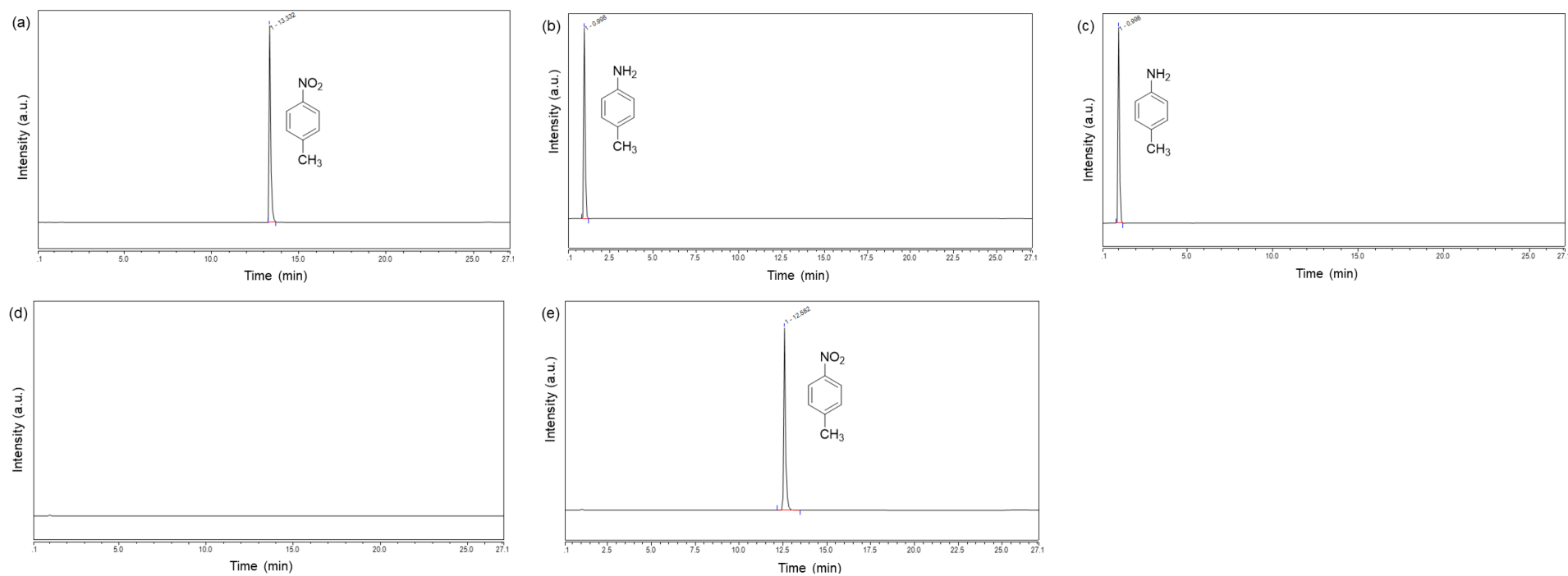


Figure 4.13: HPLC chromatograms of (a) substrate: 4-nitrotoluene, (b) reference product: 4-aminotoluene; reaction catalysed by (c) Rh SAC, (d) 5% Rh on C and (e) Co SAC.

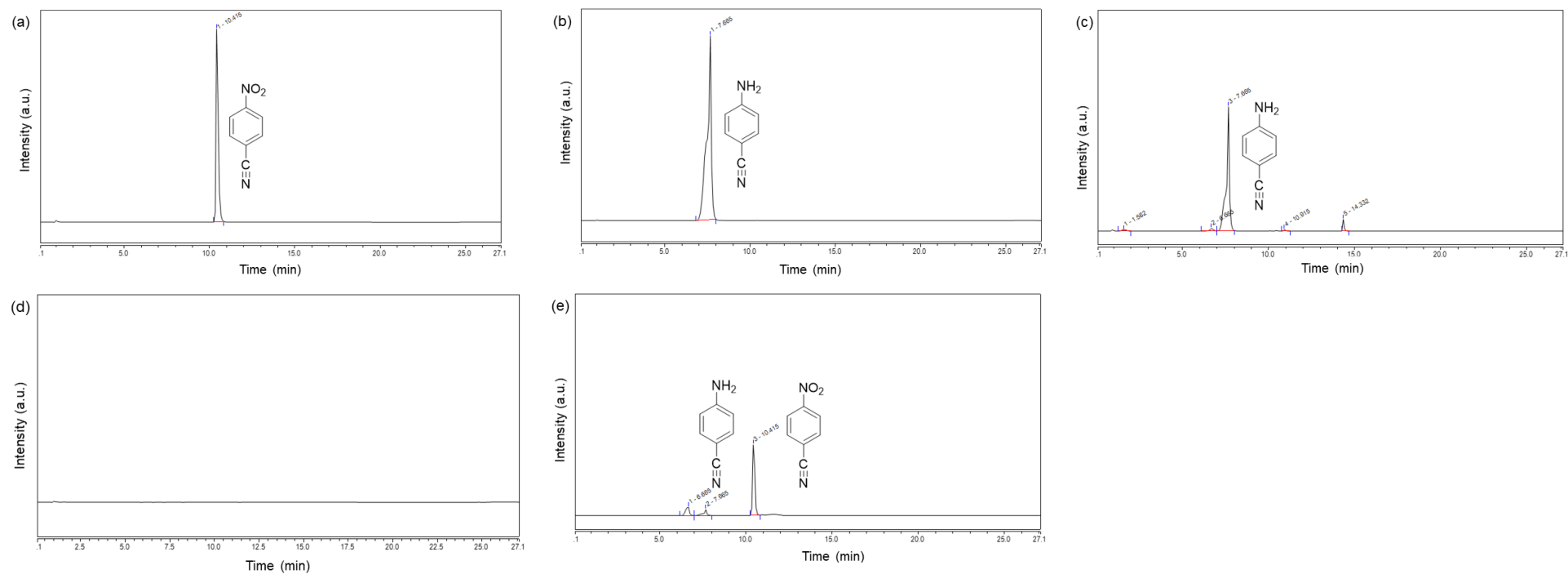


Figure 4.14: HPLC chromatograms of (a) substrate: 4-nitrobenzonitrile, (b) reference product: 4-aminobenzonitrile; reaction catalysed by (c) Rh SAC, (d) 5% Rh on C and (e) Co SAC.

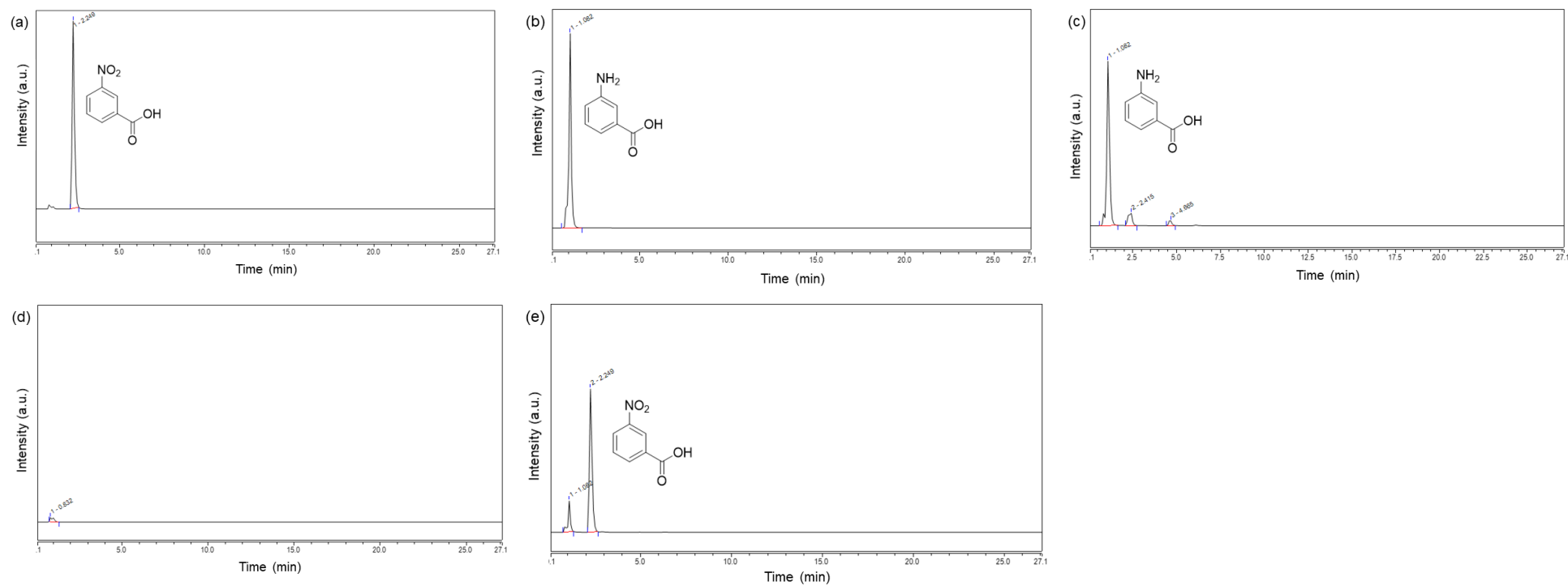


Figure 4.15: HPLC chromatograms of (a) substrate: 3-nitrobenzoic acid, (b) reference product: 4-aminobenzoic acid; reaction catalysed by (c) Rh SAC, (d) 5% Rh on C and (e) Co SAC.

4.4.2 Hydrogenation reactions

Hydrogenation of nitroarenes with SACs

10 mL of 1 mM solution of nitroarene was added to the Parr reactor (50 mL) with 2.5 mg of SAC. The reactor was sealed, and the atmosphere was removed *in vacuo* before pressurizing with H₂ (8 bar). It was then heated to 85 °C within 1 hr and kept for 2 hrs with stirring at 300 rpm. After 2 hrs, the Parr reactor was cooled to room temperature under ambient conditions (within 1.5 hrs). Then the reaction mixture was centrifuged to remove the catalyst. Then, the supernatant was filtered through an elegant syringe filter (PTFE, 0.3 µm) and analysed by HPLC.

Hydrogenation of nitroarenes with catalyst support (NC)

10 mL of 1 mM solution of nitroarene was added to the Parr reactor (50 mL) with 2.5 mg of NC. The reactor was sealed, and the atmosphere was removed *in vacuo* before pressurizing with H₂ (8 bar). It was then heated to 85 °C within 1 hr and kept for 2 hrs with stirring at 300 rpm. After 2 hrs, the Parr reactor was cooled to room temperature under ambient conditions (within 1.5 hrs). Then the reaction mixture was centrifuged to remove the catalyst support. Then, the supernatant was filtered through an elegant syringe filter (PTFE, 0.3µm) and analysed by HPLC.

Hydrogenation of nitroarenes without catalyst

10 mL of 1 mM solution of nitroarene was added to the Parr reactor (50 mL). The reactor was sealed, and the atmosphere was removed *in vacuo* before pressurizing with H₂ (8 bar). It was then heated to 85 °C within 1 hr and kept for 2 hrs with stirring at 300 rpm. After 2 hrs, the Parr reactor was cooled to room temperature under ambient conditions (within 1.5 hrs). Then, the reaction mixture was filtered through an elegant syringe filter (PTFE, 0.3 µm) and was analysed by HPLC.

Leaching test 01

A weight of 2.5 mg of Rh SAC was added into 10 mL of methanol in the Parr reactor vessel (50 mL). The reactor was sealed, and the atmosphere was removed *in vacuo* before pressurizing with H₂ (8 bar). It was then heated to 85 °C within 1 hr and kept for 2 hrs with stirring at 300 rpm. After 2 hrs, the Parr reactor was cooled to room temperature under ambient conditions (within 1.5 hrs). Then the reaction mixture was centrifuged to remove Rh SAC. Finally, methanol was filtered through a syringe filter (PTFE, 0.3 µm). In the filtered methanol medium, 4-nitroacetophenone (1.60 mg, 10 µmol) was dissolved and 100

μL was taken out for HPLC analysis. Then the remaining mixture was sealed in the Parr reactor was sealed and the atmosphere was removed *in vacuo* before pressurizing with H_2 (8 bar). It was then heated to $85\text{ }^\circ\text{C}$ within 1 hr and kept for 2 hrs with stirring at 300 rpm. After 2 hrs, the Parr reactor was cooled to room temperature under ambient conditions (within 1.5 hrs) Finally, the reaction mixture was centrifuged to remove the catalyst. Then, the supernatant was filtered through an elegant syringe filter (PTFE, $0.3\text{ }\mu\text{m}$). The filtrate was analysed by HPLC.

Leaching test 02

The substrate 1-chloro-2-nitrobenzene (0.001 M, 10 mL, in methanol) was added into the Parr reactor vessel (50 mL) with 2.5 mg of Rh SAC. The reactor was sealed, and the atmosphere was removed *in vacuo* before pressurizing with H_2 (3 bar). It was then heated to $85\text{ }^\circ\text{C}$ within 1 hr and kept for 1 hr with stirring at 300 rpm. After 2 hrs, the Parr reactor was cooled to room temperature under ambient conditions (within 1.5 hrs). Then the reaction mixture was centrifuged to remove Rh SAC. From the filtered reaction mixture, $100\text{ }\mu\text{L}$ was taken out for HPLC analysis. Then the reactor was sealed, and the atmosphere was removed *in vacuo* before pressurizing with H_2 (3 bar). It was then heated to $85\text{ }^\circ\text{C}$ within 1 hr and kept for 3 hrs with stirring at 300 rpm. After 2 hrs, the Parr reactor was cooled to room temperature under ambient conditions (within 1.5 hrs). Finally, the supernatant was filtered through an elegant syringe filter (PTFE, $0.3\text{ }\mu\text{m}$). The filtrate was analysed by HPLC.

Recycling of Rh SAC

Hydrogenation of 4-nitroacetophenone was performed in the Par reactor. The reactor was sealed, and the atmosphere was removed *in vacuo* before pressurizing with H_2 (8 bar). It was then heated to $85\text{ }^\circ\text{C}$ within 1 hr and kept for 2 hrs with stirring at 300 rpm. After 2 hrs, the Parr reactor was cooled to room temperature under ambient conditions (within 1.5 hrs). Rh SAC was recovered after the reaction by centrifugation of the reaction mixture (5000 rpm, 5 min) and washing with methanol (15 mL) followed by drying *in vacuo* for 24 hrs. Then, the supernatant was filtered through an elegant syringe filter (PTFE, $0.3\text{ }\mu\text{m}$) and analysed by HPLC. With the recovered Rh SAC, a new reaction with the fresh substrate was set. This cycle was continued up to ten re-usability tests.

Chapter 5 – Other Reactions Catalysed by Rh SAC and Co SAC

5.1 Introduction

The catalytic activity of Rh SAC and Co SAC was tested for hydrogenation of nitroarenes in chapter 4. To further investigate the catalytic activity of Rh SAC and Co SAC they were tested for ORR, N₂O reduction and degradation of bisphenol A (BPA).

5.1.1 Oxygen reduction reaction (ORR)

ORR is an important reaction in the energy conversion and fuel cells and metal-air batteries. So far, Pt on C is the optimal catalyst for this reaction. Oxygen reduction reaction occurs at the cathode, either by two-electron or four-electron pathways. If the two-electron reaction occurs, it will produce hydrogen peroxide. The four-electron pathway will result in water, which is preferable due to its high energy conversion efficiency and it can be applied in fuel cells and metal-air batteries.³⁰⁶ Pt-based catalysts show high catalytic activity toward ORR.³⁰⁷⁻³⁰⁸ The SACs made from transition metal ions show a promising catalytic activity and low cost against the conventional Pt-based catalysts.³⁰⁹⁻³¹⁰ Furthermore, they show promising activities for ORR in acidic (Eq. 5.1 and Eq. 5.2) and alkaline (Eq. 5.3 and Eq. 5.4) medium.



The difficulty of O₂ adsorption on the electrode surface, O-O bond cleavage and oxide removal are the causes of the slow kinetics of ORR.³¹¹ When the catalyst used has a higher half-wave potential (E_{1/2}), a lower overpotential is required to complete ORR. Therefore, the catalysts with high E_{1/2} are preferable for the catalysis of ORR. Using SACs in catalysing ORR is expected to result in high activity due to the high reactivity and unique coordination structure. Moreover, it leads to efficient metal utilization of the catalyst too. Therefore, Rh SAC was tested for ORR.

5.1.2 NO_x abatement

Nitrogen oxides (NO_x) are a mixture of nitric oxide (NO) and nitrogen dioxide (NO₂) generated by burning fossil fuels, coal and natural gases. NO_x is responsible for environmental problems such as photochemical smog, acid rain, tropospheric ozone, and ozone layer depletion which leads to global warming. Moreover, prolonged exposure to NO_x causes health problems such as respiratory problems in humans.³¹² Thus, the removal of NO_x from mobile and stationary sources is important. Although NO_x is thermodynamically unstable it does not decompose due to high activation energy.³¹³ Therefore a catalyst is required to lower the activation energy and enhance the decomposition of NO_x. Selective catalytic reduction (SCR), selective noncatalytic reduction (SNCR) and hybrid method (SCR-SNCR) are commonly used.

Selective catalytic reduction (SCR) of NO_x is the most widely used method for the removal of NO_x.³¹⁴ In the catalytic reduction of NO_x, NH₃ is injected and the catalytic reduction of NH₃ across the selective catalyst reduces NO_x into basic atmosphere elements such as N₂ and H₂O. For SCR the precious metals and transition metals are widely used as catalysts.³¹⁵⁻³¹⁶ Single metal catalysts increase the utilization efficiency of precious metals. Hence, Rh SAC and Co SAC synthesized in this research were tested for NO_x abatement.



5.1.3 Fenton-like catalysis

The Fenton-like process is considered a clean and efficient way to remove environmental pollutants through the generation of oxygen radicals. Fenton's reagent uses hydrogen peroxide (H₂O₂) with iron ions (typically from FeSO₄) to generate highly reactive hydroxyl radicals to degrade organic compounds.³¹⁷⁻³¹⁸ But the narrow pH range (low) and slow reaction kinetics limit the practical applications of the Fenton catalyst.³¹⁹ Using heterogeneous catalysts in Fenton-like reactions is a promising approach to overcome the limitations of using homogeneous catalysts in classical Fenton-like reactions. Employing single-atom catalysts in this reaction will maximize the utilization of precious metals; while overcoming the limitations such as the need for strict pH regulation, sludge generation and the loss of catalyst in the effluent.³²⁰⁻³²² Thus, Rh SAC and Co SAC were tested for their Fenton-like applications such as bisphenol A (BPA) degradation via peroxymonosulfate (PMS) activation.

5.2 Results and discussion

5.2.1 Oxygen Reduction Reaction (ORR)

ORR was performed by the rotating disk electrode (RDE) method which is widely used to screen the catalytic performance of new materials.³²³ The performance of Rh SAC was compared with Rh NPC (Rh-NC-0.50), catalyst support (NC), a commercial rhodium material (5% Rh on C), and the conventional catalyst (20% Pt on C). Rh SAC and Rh NPC showed similar activity ($E_{1/2} = 0.72$ V) for ORR in an acidic medium. Considering the lower rhodium loading of Rh SAC (~5.64% w/w) compared to the Rh NPC (~9.03% w/w), Rh SAC has a better performance than per rhodium. The activity of the catalyst support (NC) was very low ($E_{1/2} = 0.27$ V) confirming that rhodium is responsible for the high catalytic activity. This performance was superior compared to the performance of commercial catalyst 5% Rh on C ($E_{1/2} = 0.49$ V). As expected, 20% Pt on C showed the best performance under acidic conditions ($E_{1/2} = 0.85$ V).

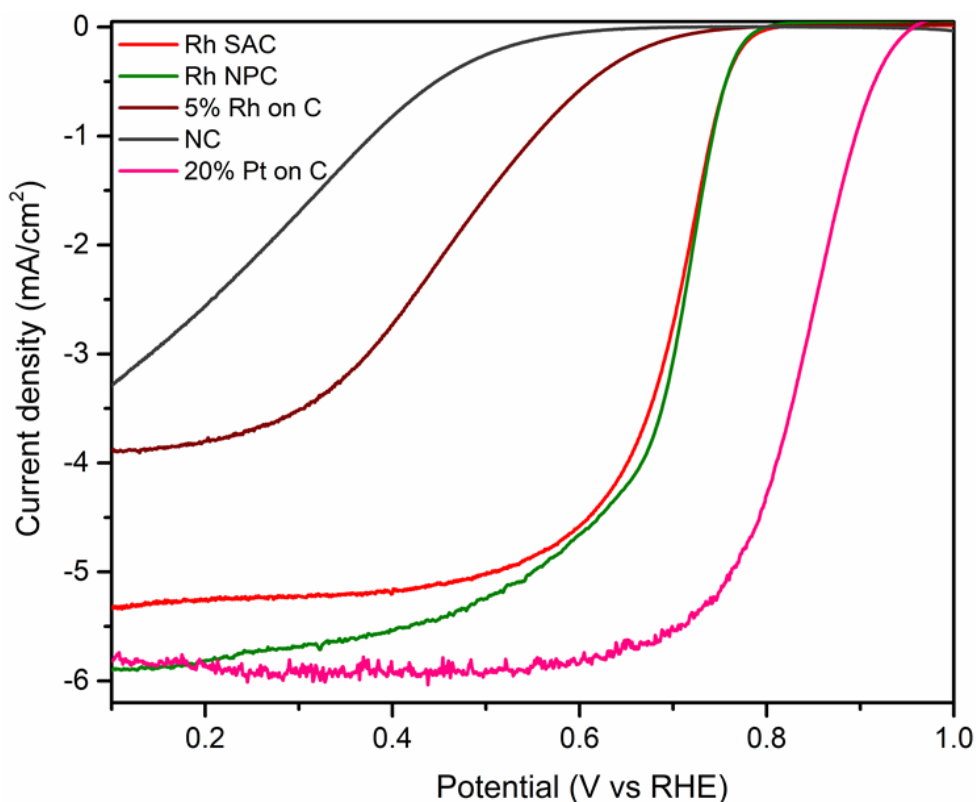


Figure 5.1: Steady-state ORR polarization plots for various catalysts (0.6 – 1.0 V) Rh-based samples were tested in 0.5 M H_2SO_4 electrolytes; whilst Pt/C reference catalyst was tested in 0.1 M HClO_4 .

Table 5.1: Comparison of the ORR performance for catalysts in acidic medium.

Sample	Rh SAC	Rh NPC	NC	5% Rh/C	20% Pt/C
$E_{1/2}$	0.72	0.72	0.27	0.49	0.85

The stability of Rh SAC and Rh NPC in ORR was tested in an acidic medium. Rh SAC lost 20 mV in $E_{1/2}$ after 5000 cycles which is acceptable and negligible. However, there was no obvious decay in $E_{1/2}$ of Rh NPC after 5000 cycles. Thus, Rh NPC was more stable than Rh SAC under ORR testing conditions. Considering the high rhodium loading of Rh NPC, which is nearly double as Rh SAC, Rh SAC has better stability and efficiently uses the precious metals in catalysing ORR.

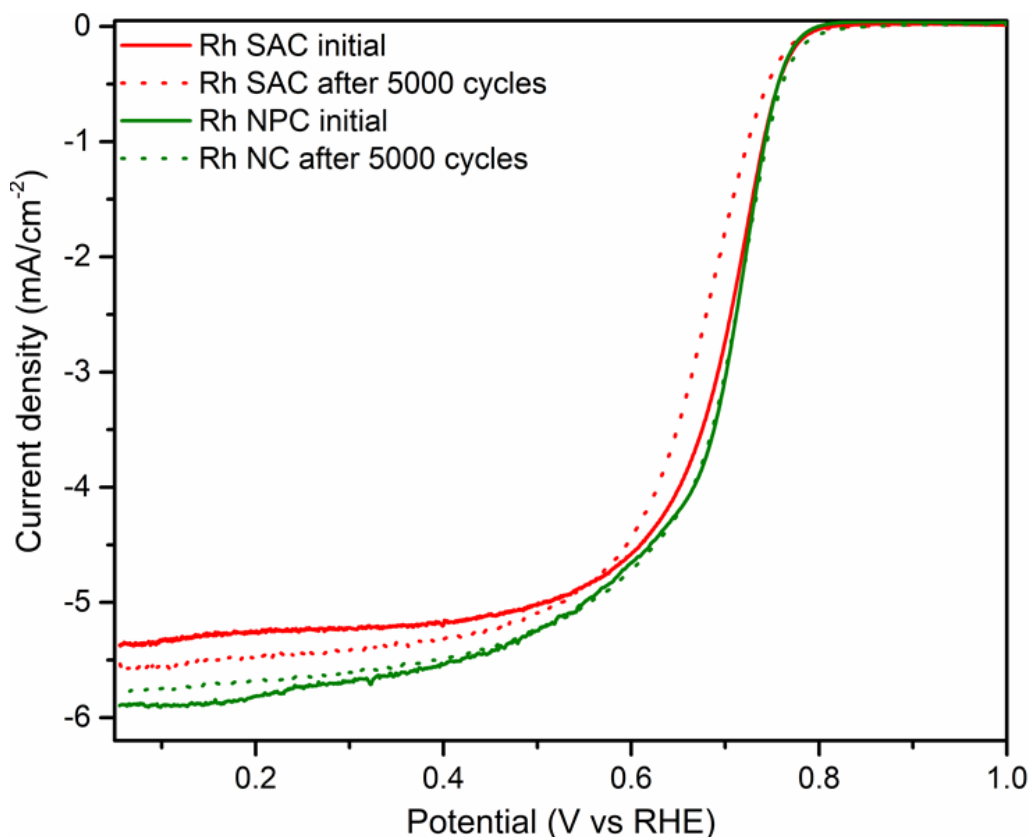


Figure 5.2: Steady-state ORR polarization plots for after potential cycling stability tests (0.6–1.0 V, 5000 cycles) for Rh SAC and Rh NPC.

Table 5.2: Stability testing of Rh catalysts in acidic medium.

Sample	Rh SAC	Rh NPC
$E_{1/2}$ initial	0.72	0.72
$E_{1/2}$ initial after 5000 cycles	0.70	0.72

The performance of Rh SAC, Rh NPC, NC, and 5% Rh on C in ORR was tested in basic conditions along with the standard catalyst 20% Pt on C. It was impressive that Rh SAC showed comparable ORR activity to 20% Pt on C under alkaline conditions. Considering low rhodium loading (~ 5.64 %w/w) in Rh SAC versus high metal loading of Pt on C (20 % w/w), the Rh SAC offers much better precious metal utilization. The catalytic activity of catalysts decreased in the acidic medium more than in the alkaline medium probably due to the corrosion of the carbon support in the acidic medium.

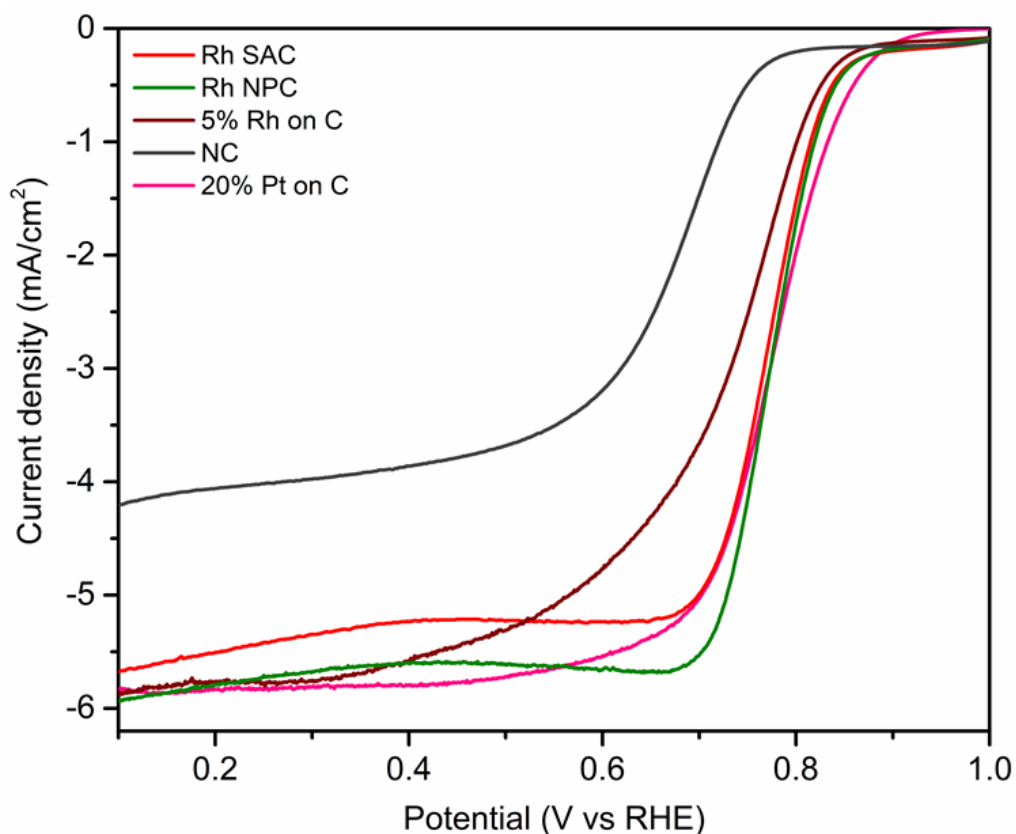


Figure 5.3: Steady-state ORR polarization plots for various catalysts collected in basic medium (0.1 M KOH).

Table 5.3: Comparison of the ORR performance for catalysts in basic medium.

Sample	Rh SAC	Rh NPC	NC	5% Rh/C	20% Pt/C
$E_{1/2}$	0.78	0.77	0.69	0.76	0.78

5.2.2 NO_x abatement

NO_x abatement was performed for Rh SAC, Rh NPC, and Co SAC in a fixed bed reactor using a mixture of NO (1000 ppm), NH₃ (1000 ppm) and O₂ (3%) as the feed gas. The performance of these catalysts was compared against NC and commercially available rhodium catalysts 5% Rh on C and Rh on Al₂O₃. In this process, NH₃ is adsorbed on the catalyst surface and reacts with adsorbed NO or free NO and subsequently decomposes to N₂ and H₂O.³²⁴⁻³²⁵

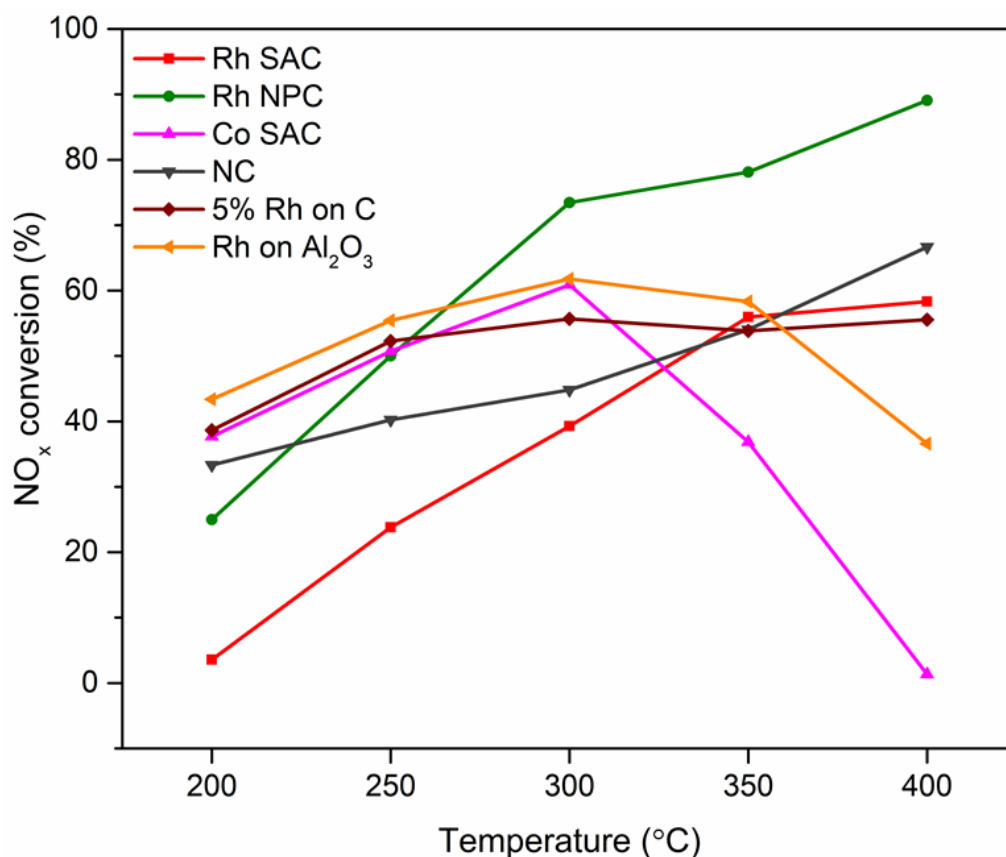


Figure 5.4: NO_x conversions by Rh SAC, Rh NPC, Co SAC, NC, 5% Rh on C and Rh on Al₂O₃ catalysts as a function of temperature; feed: 1000 ppm NO, 1000 ppm NH₃ and 3 vol. % O₂.

In comparison with other catalysts, Rh NPC showed the best performance in NO_x conversion. Rh SAC and Rh NPC showed an increment in NO_x conversion with the increasing temperature. At 400 °C Rh NPC showed 89.0 % conversion while Rh SAC did 58.3 % conversion of NO_x. Surprisingly the catalyst support (NC) did 66.7% conversion at 400 °C which is higher than the conversion done by Rh SAC. Both NC and Rh SAC showed similar NO_x conversion at 350 °C. Thus, the performance of Rh SAC and NC in catalysing NO_x reduction is similar. Probably the rhodium single-atoms in Rh SAC in +3 oxidation state do not catalyse the NO_x reduction.

The commercial catalyst 5% rhodium on carbon demonstrated steady catalytic behaviour with increasing temperature above 300 °C. Whereas the other commercial rhodium catalyst Rh on Al₂O₃ had the maximum performance at 300 °C; when the temperature was further increased the % conversion was reduced. The four rhodium catalysts behaved in different ways in the reduction of NO_x under these experimental conditions. Rh NPC synthesized in this research, which had rhodium nanoparticles in zero oxidation state, showed the best performance in NO_x conversion among the four rhodium catalysts tested.

The Co SAC increased the NO_x conversion with increasing temperature and showed a maximum conversion of 60.9% at 300 °C. When the temperature was increased further the conversion declined probably due to desorption of NO or physical instability of the catalyst at the temperatures greater than 300 °C. The cobalt single-atoms were in a Co⁺² oxidation state, and they had Co-N₄ coordination. Interestingly at 400 °C the catalyst support NC exhibited 66.7% conversion while Co SAC decreased its conversion to 1.3%. Thus, at temperatures greater than 300 °C, Co SAC lost its performance.

When comparing the performance of Rh SAC and Co SAC, Rh SAC increased the % NO_x conversion with increasing temperature whereas the Co SAC started to decrease its performance after reaching a maximum. Thus, the performance of Rh SAC is better than Co SAC in catalysing NO_x reduction. However, the catalyst support NC performed better than both Rh SAC and Co SAC in the reduction of NO_x under the given experimental conditions. The Rh NPC performed better than all the catalysts. Probably the coordination environment or the oxidation states of SACs are not favourable for the NO_x abatement.

5.2.3 Fenton-like catalysis

Catalysis of bisphenol A (BPA) oxidation via activation of peroxymonosulfate (PMS) by Rh SAC, Co SAC and catalyst support (NC) was studied as the Fenton-like catalysis reaction. The degradation of BPA was performed by the singlet oxygen produced from the activation of PMS by the catalysts (Figure 5.5).³²⁶ The concentration of BPA was determined by HPLC analysis. The % degradation of BPA was determined by comparing the existing amount of BPA after the reaction with regards to the stock solution of BPA before the reaction, using the peak areas of the HPL chromatogram. Co SAC catalyst degraded about 68.5% BPA in 15 min while Rh SAC removed 56.5%. Whereas the catalyst support (NC) also removed 32.3% of BPA (Figure 5.6). The control reaction (no catalyst) did not show significant BPA degradation. Li et al. reported the homogeneous Fenton-like catalysis of BPA, using the same concentration of the metal ions as the catalysts, the degradation of BPA was reported as 3 times lower as the heterogeneous catalysts.³²⁶

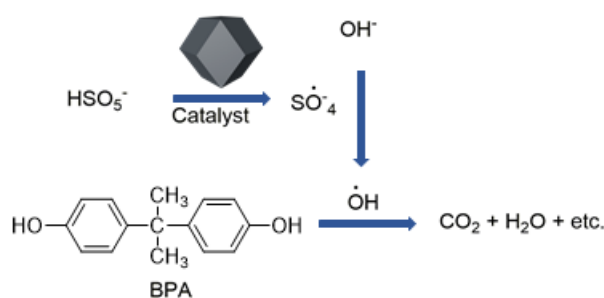


Figure 5.5: Degradation of BPA by PMS activation.

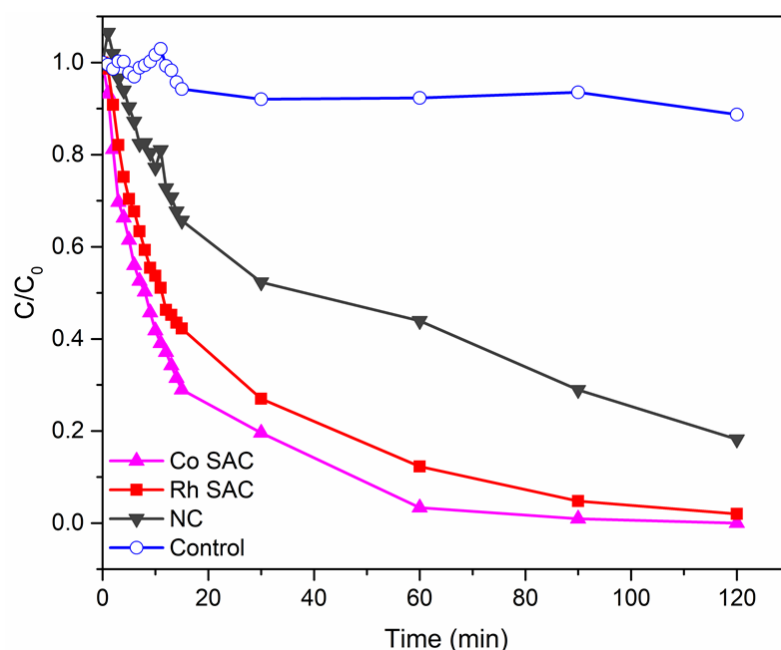


Figure 5.6: Fenton-like catalytic performance by the catalysts for BPA degradation.

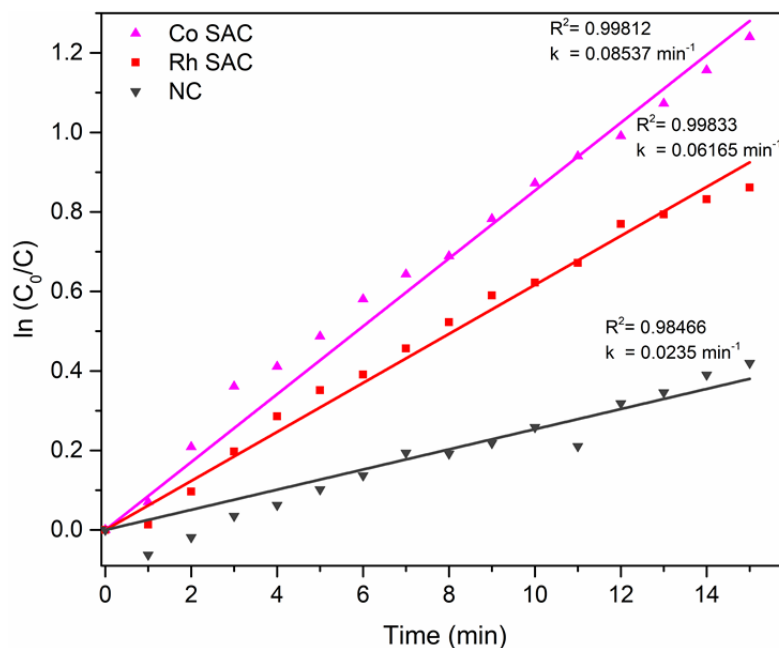


Figure 5.7: First-order kinetic model of the Fenton-like reaction catalysed by Rh SAC, Co SAC, NC and control reaction.

To compare the performance of the catalysts over BPA degradation, BPA removal kinetics was fitted (Experimental section, 5.4.4) and the linear relationship suggests that the reaction is pseudo-first-order. Co SAC showed a higher rate constant for BPA degradation (0.085 min^{-1}) than Rh SAC (0.062 min^{-1}) which is 37% higher than that of Rh SAC. NC showed a BPA degradation rate constant of 0.023 min^{-1} . The rate constants measured for Co SAC and Rh SAC were about 3.7 times and 2.7 times higher than that of catalyst support (Figure 5.7).

After two hours, Co SAC completely degraded BPA while Rh SAC degraded 98%. Although Co SAC demonstrated a higher reaction rate than Rh SAC in the degradation of BPA, after two hours the % degradation was similar by both catalysts. By considering the lower cost of cobalt than rhodium, and the complete degradation of BPA in two hours, Co SAC is the best catalyst among these two for Fenton-like catalysis.

The concentration of BPA was remarkably reduced by the catalyst support (NC) with time which reached 82% after 2 hours. This result is impressive based on the low cost of synthesis due to the non-precious metallic nature of NC; besides the single metal atoms, nitrogen-doped carbon such as graphite N, pyridinic N, pyrrolic N, and traces of zinc might also contribute to the degradation of BPA by the activation of PMS, leading degradation of BPA.³²⁷

5.3 Conclusion

Rh SAC shows better performance in catalysing ORR in acidic (0.72 V) and basic medium (0.78 V) compared to Rh NPC, catalyst support (NC) and commercial catalyst 5% Rh on C. The catalytic activity of Rh NPC does not increase with the increasing metal content. That is probably the Rh SAs in the interior of Rh NPs which are covered by surface atoms are not exposed to the reactants and not actively participating in the catalysis. The catalytic activity of Rh SAC is comparable to the commercial catalyst 20% Pt on C which is used as a benchmark in ORR.

The adsorption of O₂ on the surface of the catalyst is the first step to initiate ORR.³²⁸⁻³²⁹ After that O₂ can either dissociate into two *O atoms or hydrogenate to *OOH. As the energy barrier of O₂ dissociation is high, dissociation of O₂ to two *O is very unlikely to occur.³²⁸⁻³²⁹ On the other hand, it is very likely to occur hydrogenation of O₂ to *OOH due to its lower energy barrier. Then it will break into *O + *OH and further hydrogenate to *OH + *OH and *O + H₂O.

Among all the catalysts tested for NO_x abatement, Rh NPC exhibits the best performance. Adsorption and activation of gases on the catalyst surface are important in NO_x abatement.³³⁰ Due to the non-activated sites of NO, it is difficult to adsorb on the active sites of the catalyst without the presence of O₂.³³¹ Many similar mechanisms are proposed for the NO_x abatement by selective catalytic reduction.³³²⁻³³⁴ Based on the mechanism proposed by Long *et al.* for NO_x abatement by iron-based zeolite catalyst, we propose this mechanism for our catalysts.³³⁵ In NO_x abatement, NO is oxidized to NO₂ by O₂ which is then catalytically reduced by adsorbed NH₃ on the catalyst surface which is transformed to NH₄⁺. The resulting NO₂ forms NO₂(NH₄⁺)₂ intermediate with two neighbouring NH₄⁺ which later react with another NO and produce N₂ and H₂O.

BPA degradation rate by Co SAC was 37% higher than Rh SAC. Based on the cost and high degradation rate of BPA, Co SAC is the best catalyst for Fenton-like catalysis among Rh SAC and Co SAC. In Rh SAC one rhodium atom is coordinated with four nitrogen atoms in the graphitic layer with two axial oxygen atoms (possibly in the form of H₂O) whereas, Co SAC has CoN₄ coordination. Li *et al.* suggest that metal-N₄ coordination is better for PMS activation due to the reduction of adsorption energy and facilitated electron transfer for PMS.^{326, 336} Thus, the presence of metal-N₄ coordination in Co SAC and Rh SAC could be one of the reasons for the catalysts to do in BPA degradation. Moreover, pyrrolic N in N-doped graphene is verified as an adsorption site for BPA by DFT calculations.³²⁶ Probably

the adsorption of BPA on single-atom sites could be followed by donating electrons by pyridinic N and accepting electrons by -OH in BPA.³²⁶

The catalyst support NC also achieved 81.8% degradation of BPA in two hours. Compared to the high cost of single metal catalysts and comparable activity of NC along with the low cost of synthesis due to the non-precious metallic nature makes NC a better catalyst for Fenton-like catalysis. The pyridinic N in NC could act as adsorption sites for BPA. The residual zinc in NC could be activating PMS. Probably the performance of Fenton-like catalysis by NC is lower due to the slow activation of PMS by residual zinc sites.

5.4 Experimental section

5.4.1 General procedures

All starting materials and solvents were used as received from commercial sources without further purification unless otherwise noted. Rh SAC and NC were synthesized as mentioned in Chapter 2. Co SAC was synthesized as mentioned in Chapter 3.

5.4.2 Oxygen reduction reaction (ORR)

An electrochemical workstation (CHI760) equipped with a three-electrode cell was employed to perform electrochemical oxygen reduction reaction (ORR) measurements. A saturated calomel electrode and a Pt foil were used as the reference and counter electrodes, respectively. Catalyst inks were prepared by ultrasonically dispersing 8.0 mg of catalysts in 1 mL of a solution containing 10 μL of Nafion solution (5 wt.%), 495 μL of isopropanol and 495 μL of H_2O . The catalyst inks were drop-casted onto a rotating disk electrode (RDE, 5 mm diameter) and then air-dried at room temperature, to achieve a catalyst loading of 408 $\mu\text{g cm}^{-2}$ for ORR in acid solution or 204 $\mu\text{g cm}^{-2}$ for ORR in alkaline solution.

ORR in acid solution

Linear sweep voltammetry data were collected at a scanning speed of 0.01 mV/s, from 1.0 to 0.1 V versus RHE in O_2 -saturated 0.5 M H_2SO_4 solution at 25 $^\circ\text{C}$. The rotation rate is 1600 rpm. Catalyst stability was studied by cycling potentials from 0.6 to 1.0 V in O_2 -saturated 0.5 M H_2SO_4 at a scanning rate of 50 mV s^{-1} . Data for a commercial Pt/C (20 wt.% Pt) reference catalyst was tested in 0.1 M HClO_4 solution with catalyst layer of a Pt loading of 51 $\mu\text{g cm}^{-2}$ (note: Pt is poisoned by S in aqueous H_2SO_4 , hence the need to collect the ORR data in aqueous HClO_4).

ORR in basic solution

Linear sweep voltammetry data was collected at a scanning speed of 0.01 mV/s, from 1.0 to 0.1 V versus RHE in O_2 -saturated 0.1 M KOH solution at 25 $^\circ\text{C}$. The rotation rate is 1600 rpm. Catalyst stability was studied by cycling potentials from 0.6 to 1.0 V in O_2 -saturated 0.1 M KOH at a scanning rate of 50 mV s^{-1} . Data for a commercial Pt/C (20 wt.% Pt) reference catalyst were obtained in 0.1 M KOH solution with a catalyst layer of a Pt loading of 51 $\mu\text{g cm}^{-2}$.

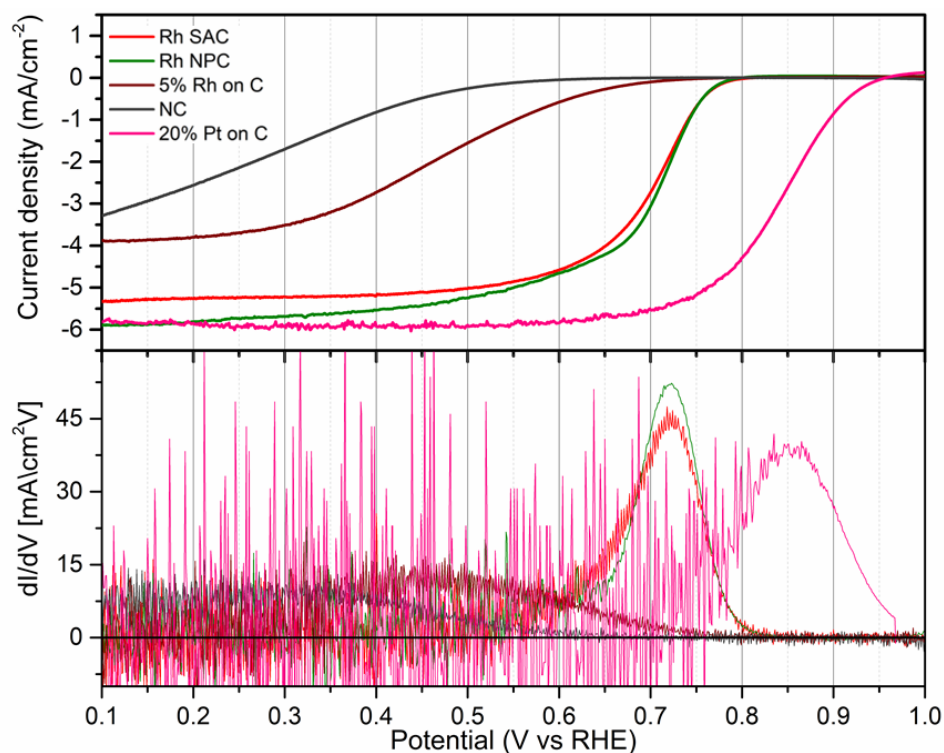


Figure 5.8: Steady-state ORR polarization plots for various catalysts in acidic medium (top) and derivatives of ORR polarization plots used to determine $E_{1/2}$ (bottom).

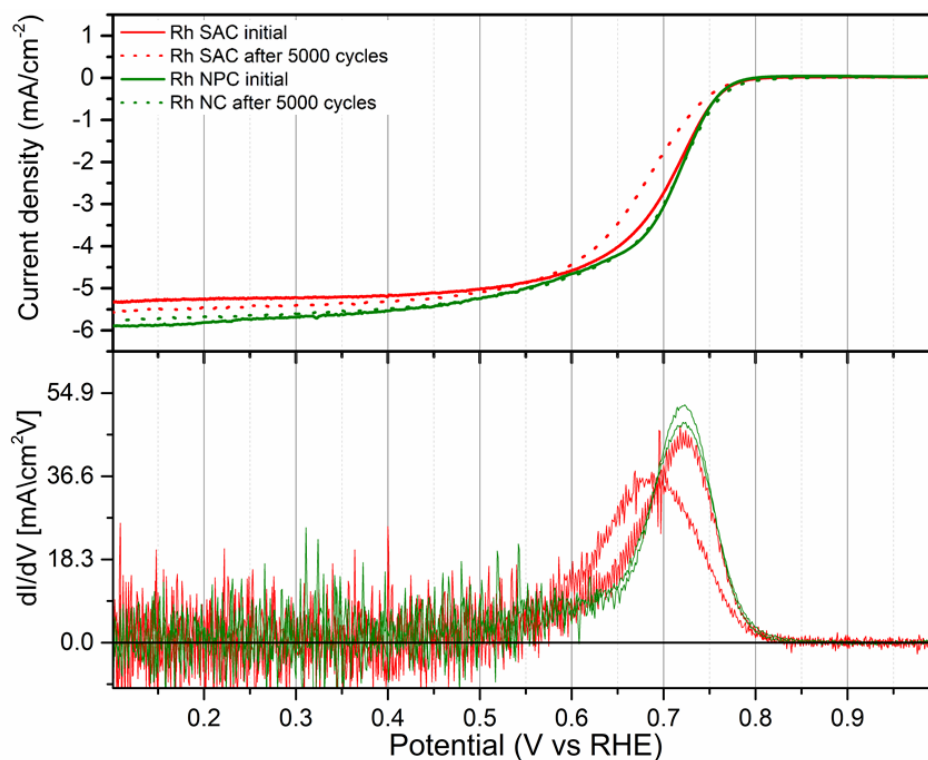


Figure 5.9: Steady-state ORR polarization plots for Rh SAC and Rh NPC recycling tests in acidic medium (top) and derivatives of ORR polarization plots used to determine $E_{1/2}$ (bottom).

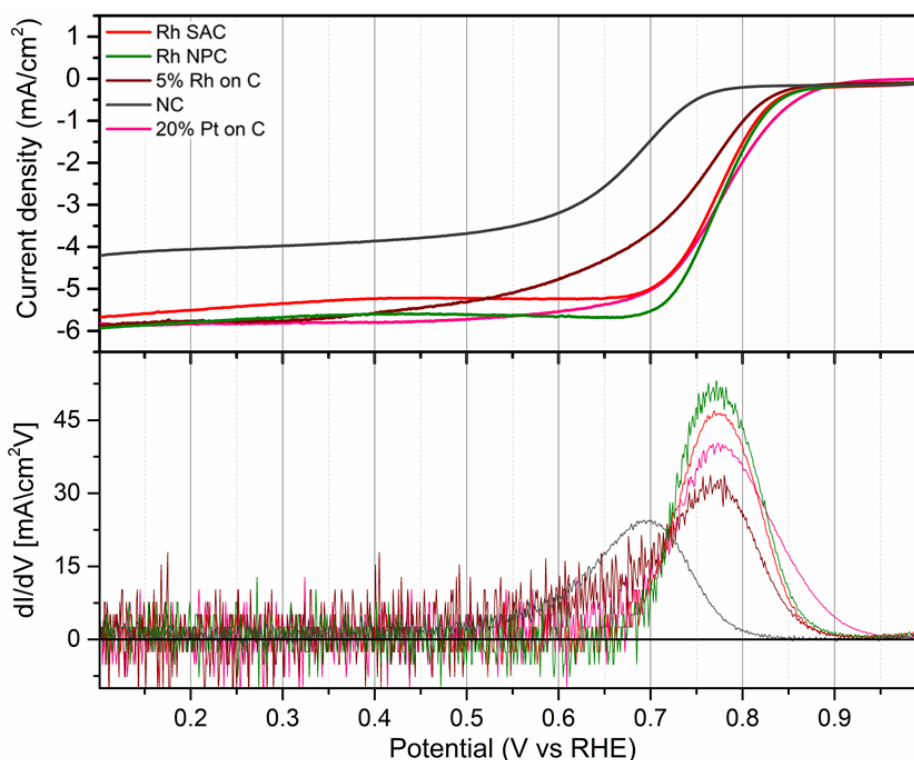


Figure 5.10: Steady-state ORR polarization plots for various catalysts in basic medium (top) and derivatives of ORR polarization plots used to determine $E_{1/2}$ (bottom).

5.4.3 NO_x abatement

The catalytic activities of Rh SAC, Rh NPC, Co SAC, NC, 5% Rh on C, Rh on Al₂O₃ were tested in a fixed bed reactor (inner diameter: 7.7 mm). Each sample was sieved to 88 - 500 μm mesh first and then 50 mg of sample was placed in the middle of the reactor (filled depth: 10 mm). N₂ was used as the carrier gas and the composition of feed gas was NO (1000 ppm), NH₃ (1000 ppm), O₂ (3 vol. %) The gas flow rate was 70 mL/min and the corresponding gas hourly space velocity was (GHSV) was 15,000 h⁻¹ for all the samples except for 5% Rh on C (GHSV= 30,000 h⁻¹). The catalyst samples were stabilized at 200 °C for 1 hr under nitrogen flow before the testing to remove residual species adsorbed on the surface. The temperature was ramped up from 200 °C to 400 °C with an interval of 50 °C. The concentrations of gases at the inlet and outlet were measured and the conversions were recorded when the readings were stable, indicating the equilibrated reactions. The NO_x conversion was calculated as follows.

$$\text{NO}_x \text{ conversion} = \frac{[\text{NO}_x]_{\text{in}} - [\text{NO}_x]_{\text{out}}}{[\text{NO}_x]_{\text{in}}} \times 100\% \quad \text{Eq. 5.6}$$

5.4.4 BPA degradation

The reaction was performed in a 100 mL beaker with BPA (20 mg L^{-1} / 0.0876 M , $\text{pH} = 6.0$) maintaining the temperature at $25 \text{ }^\circ\text{C}$ using a water bath. Catalyst (2.5 mg) was added to BPA solution (25 mL) and stirred for 30 min to establish an adsorption-desorption equilibrium. PMS (0.3 mL) was added to initiate the reaction and 0.5 mL of the reaction mixture was taken out in 1 min intervals from $1\text{-}15 \text{ min}$ and then at 30 min , 60 min , 90 min and 120 min . Then the reaction mixture was quenched with sodium sulfite solution (0.1 M , 0.3 mL). The catalyst was removed by filtering the mixture through an elegant syringe filter (PTFE, $0.3 \text{ }\mu\text{m}$). The filtrate was analysed by HPLC.

The rate of the reaction was evaluated by pseudo-first-order kinetics by the following reaction. Where; C_0 is the initial concentration of BPA, C_t is the concentration of BPA at a certain time, t is the time and k is the reaction rate constant. As HPLC peak area is proportional to the concentration of BPA, for C_0/C_t ratio, the peak areas of respective HPLC chromatograms were used.

$$\ln(C_0/C_t) = kt \quad \text{Eq. 5.7}$$

Chapter 6 – Synthesis of Hollow Nanoboxes and Applications

6.1 Introduction

In this chapter, two types of hollow nanoboxes (HNB) are synthesized using ZIF-8 by a self-templating strategy. HNB-1 was already used as the catalyst support (NC) in the synthesis of Rh SAC and Co SAC in the previous chapters where; ZIF-8 is coated with a potassium tannic acid coordinated polymer (KTA) and pyrolyzed to high temperature. The KTA coating acts as a template in the pyrolysis process hosting a substrate to nucleate nitrogen and carbon of ZIF-8 (Figure 6.1).

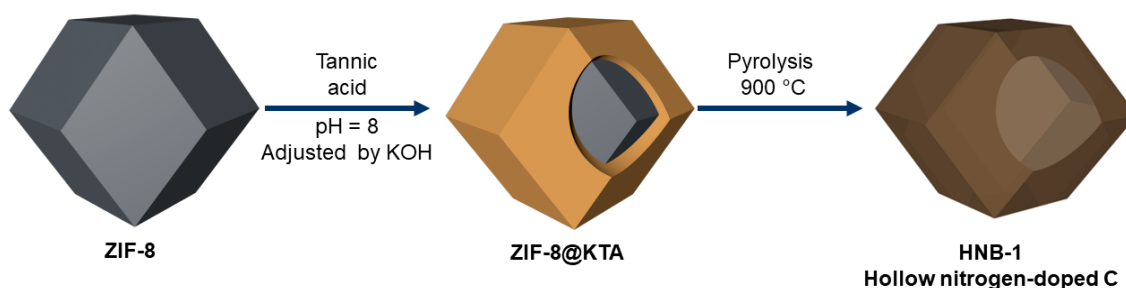


Figure 6.1: Synthesis of HNB-1.

In the synthesis of HNB-2, only ZIF-8 itself was used. The outer layer of ZIF-8 was pyrolyzed while keeping the inner core of the crystal intact. The subsequent removal of crystalline ZIF-8 from the core of the partially pyrolyzed material with an acid wash results in HNB-2 (Figure 6.2). The synthesis and characterization of HNB-2 are described in this chapter. Furthermore, the feasibility of using these HNB synthesized by tannic acid coated ZIF-8 and ZIF-8 itself was tested by employing them in different applications.

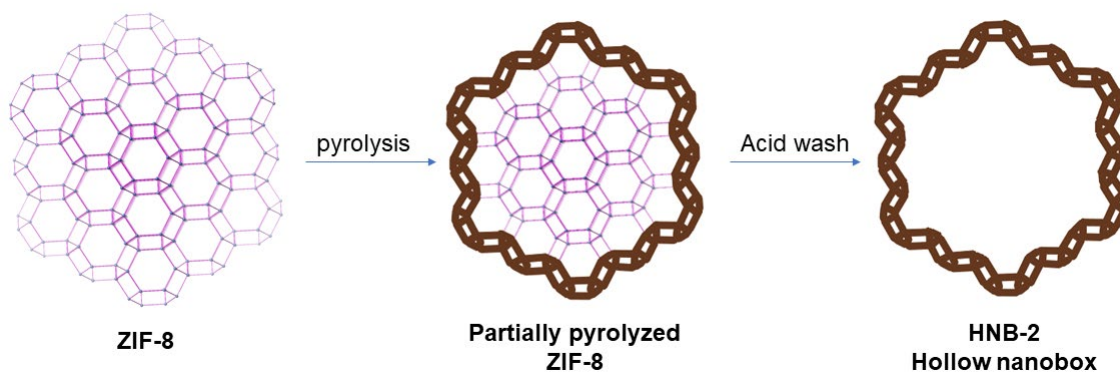


Figure 6.2: Synthesis of HNB-2.

6.2 Results and Discussion

6.2.1 Synthesis and characterization of HNB - 1 by pyrolysis of ZIF-8@KTA

The nitrogen-doped carbon synthesized in chapter 2 by the pyrolysis ZIF-8@KTA was used as HNB-1.

6.2.2 Synthesis and characterization of HNB - 2 by partial pyrolysis of ZIF-8

HNB-2 was synthesized by partial pyrolysis of ZIF-8 followed by chemical etching. ZIF-8 was pyrolyzed at 475 °C, 500 °C, 525 °C, 550 °C, 555 °C, 560 °C, 575 °C, and 600 °C to investigate the optimum temperature that pyrolyzes the outer shell of ZIF-8 keeping the crystallinity of the inner core of ZIF-8. These pyrolyzed samples were labelled as ZIF-8-475, ZIF-8-500, ZIF-8-525, ZIF-8-550, ZIF-8-555, ZIF-8-560, ZIF-8 575, and ZIF-8-600 respectively. The colour of ZIF-8 evolved from white to dark brown with increasing temperature due to the pyrolysis (Figure 6.3). Based on the PXRD patterns of pyrolyzed ZIF-8 at different temperatures, at 550 °C ZIF-8-550 is still crystalline, while at 555 °C the crystallinity of ZIF-8-555 vanished. Thus, below 550 °C ZIF-8 is partially pyrolyzed (Figure 6.4)

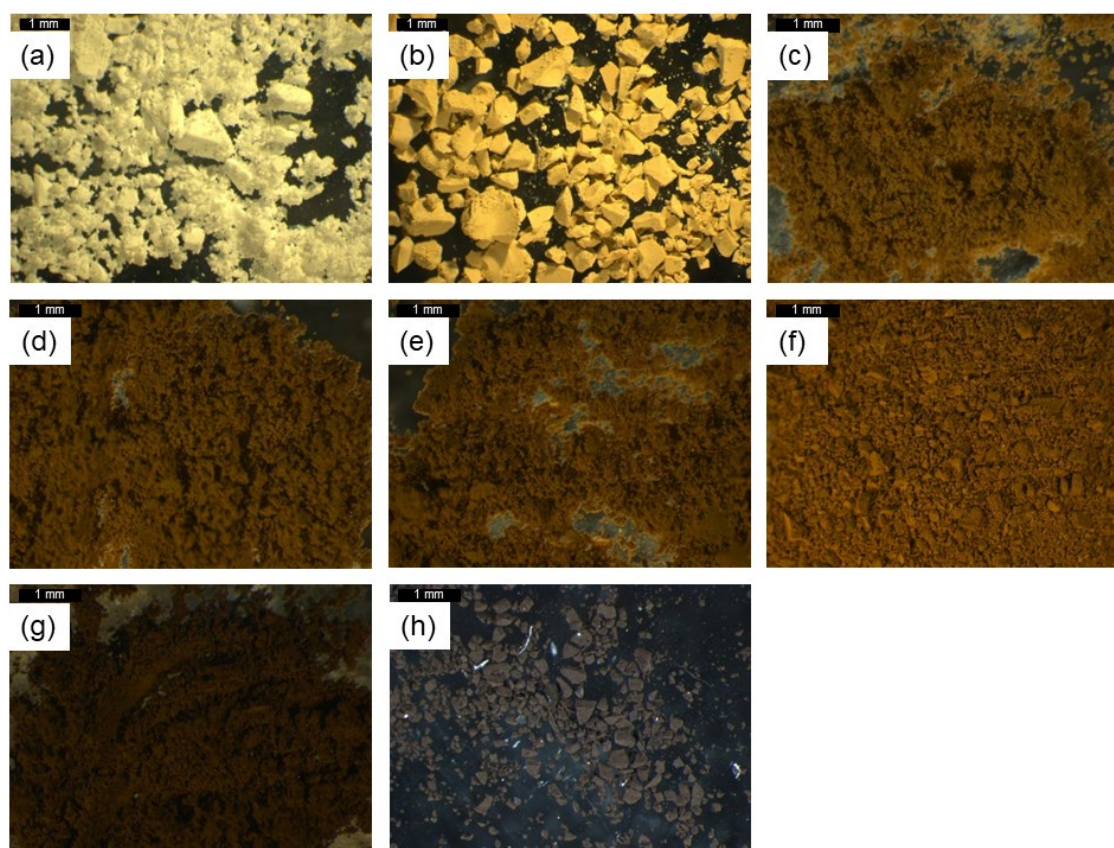


Figure 6.3: Optical microscope images of (a) ZIF-8, (b) ZIF-8-475, (c) ZIF-8-500, (d) ZIF-8-525, (e) ZIF-8 550, (f) ZIF-8 555, (g) ZIF-8- 575 and (h) ZIF-8-600.

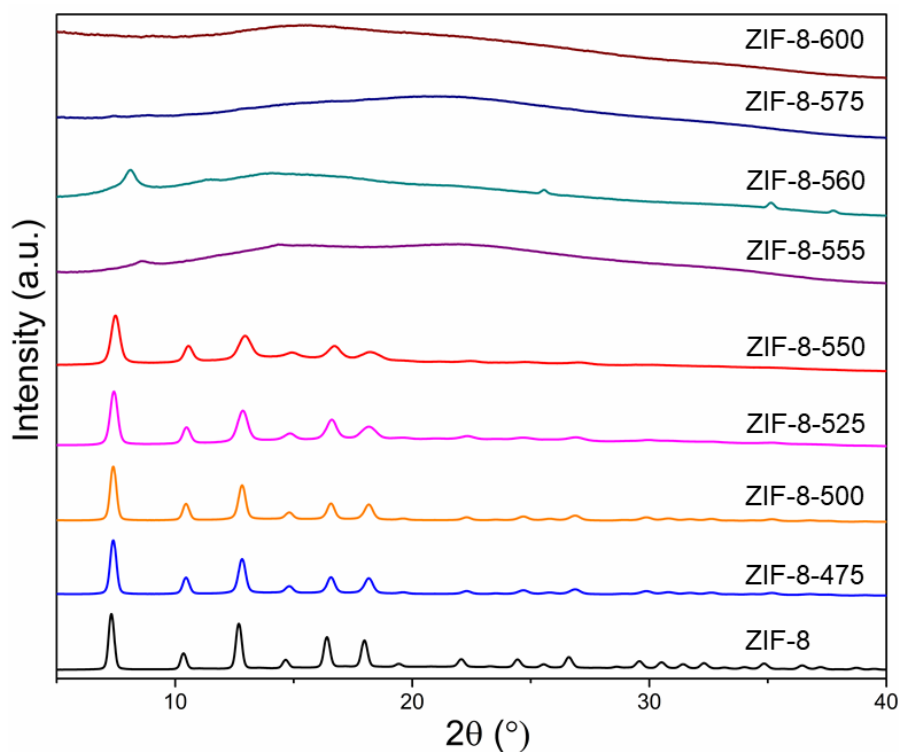


Figure 6.4: PXRD of ZIF-8 and ZIF-8 pyrolyzed at different temperatures.

HNB-2 is obtained by removing the unpyrolyzed core of ZIF-8 in partially pyrolyzed ZIF-8 by acid washing. Thus, the partially pyrolyzed ZIF-8 samples; ZIF-8-475, ZIF-8-500, ZIF-8-525, ZIF-8-550 were dispersed in 2M HCl to dissolve ZIF-8. The partially pyrolyzed samples, ZIF-8-475 and ZIF-8-500 were dissolved in 2M HCl without leaving any precipitate. Thus, at 475 °C and 500 °C; the outer shell of ZIF-8 is not pyrolyzed enough to create a solid nitrogen-doped carbon layer around ZIF-8 crystals. The partially pyrolyzed samples, ZIF-8-525 and ZIF-8-550 left a precipitate after the wash (with 2M HCl) which could be HNB-2. Hence those samples were named HNB-2-525 and HNB-2-550.

In the TEM image of HNB-2-525 (Figure 6.5 a), a hollow nanobox structure could be observed. The edges form a dense margin with a void space in the middle. On the other hand, a dense structure could be observed for HNB-2-550 (Figure 6.5 b). Although both ZIF-8-525 and ZIF-8-550 had ZIF-8 in their core, at 525 °C only the outer ZIF-8 layer is pyrolyzed while at 550 °C almost all of the ZIF-8 crystal is pyrolyzed. Thus, when washing ZIF-8-525 with acid, ZIF-8 in the core can be washed out to make a hollow nanobox. In the EDX spectra of HNB-2-550 and HNB-2-525, carbon and nitrogen and zinc could be observed suggesting the presence of nitrogen-doped carbon with zinc (Figure 6.5 c and d). HNB-2-525 that showed a hollow nanostructure was further characterized and used for the fluorescence study which is referred as to HNB-2.

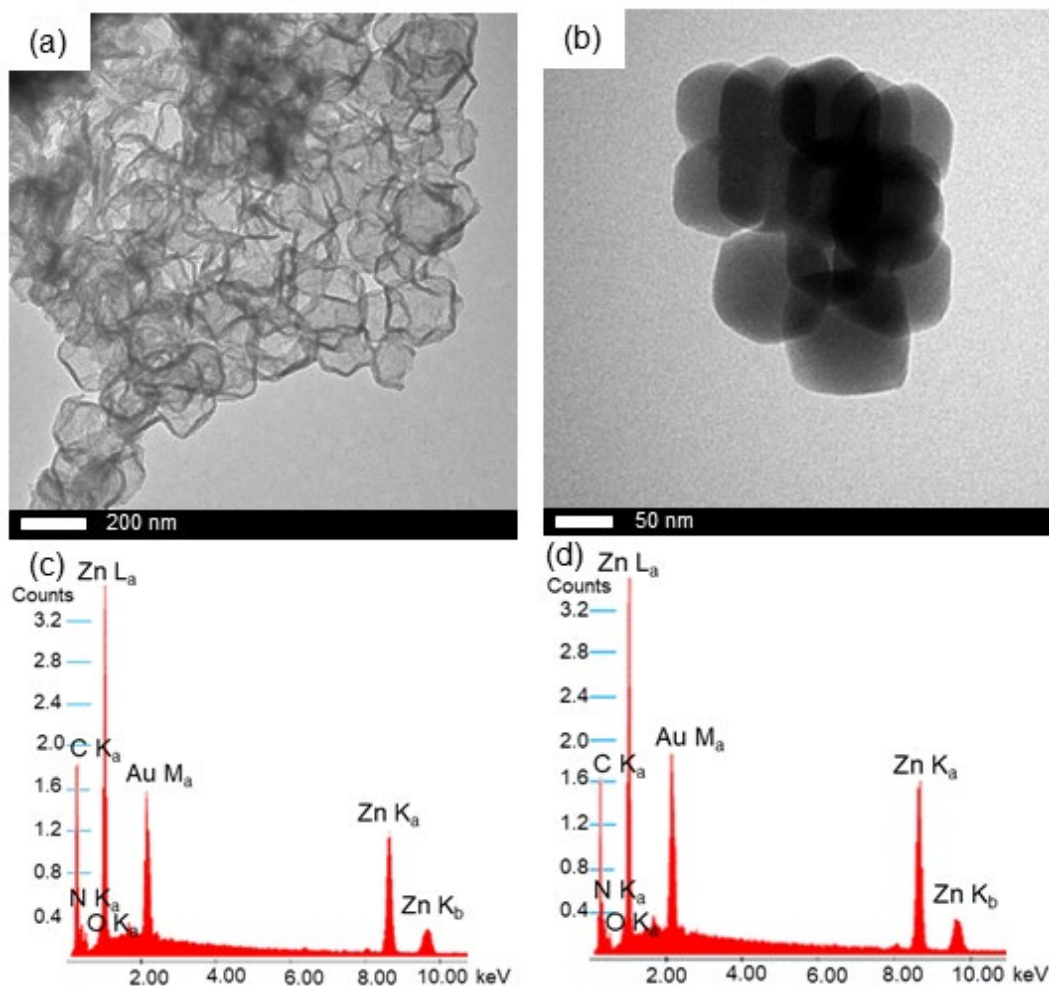


Figure 6.5: TEM and EDX of (a, c) HNB-2-525 and (b, d) HNB-2-550.

The FTIR spectra (Figure 6.6) of ZIF-8 and partially pyrolyzed ZIF-8 looked identical. A peak at 422 cm^{-1} showed the stretching of Zn-N.³³⁷ The significant reduction of the intensity of this peak in HNB-2 confirms that almost all the ZIF-8 was washed with the acid washing and probably there were only traces of ZIF-8 in HNB-2. Moreover, the appearance of zinc in the EDX of HNB-2 suggests that Zn could be trapped in the nitrogen-doped carbon shell of HNB-2. The peaks at 759 cm^{-1} and 994 cm^{-1} could be assigned to C=C in-plane and out-plane bending vibrations of 2-methylimidazole in pristine and partially pyrolyzed ZIF-8.³³⁸ The appearance of a small peak in this position in HNB-2 suggests the presence of C=C in the outer shell of HNB-2 and probably the presence of residual 2-methylimidazole from the traces of ZIF-8. Moreover, in HNB-2, partially pyrolyzed ZIF-8, ZIF-8 and 2-methylimidazole a series of peaks appeared in the range of 1300 cm^{-1} and 1460 cm^{-1} namely at 1308 cm^{-1} , 1427 cm^{-1} and 1459 cm^{-1} which can be assigned to the absorption band of C-N bond.³³⁸ The appearance of small peaks in the range of 2930 cm^{-1} and 3180 cm^{-1} , precisely at 2928 cm^{-1} and 3136 cm^{-1} in HNB-2, partially pyrolyzed ZIF-8 and ZIF-8; confirms the

presence of stretching aliphatic and aromatic C-H bonds. Thus, the presence of C-H bonds in HNB-2 is also possible.

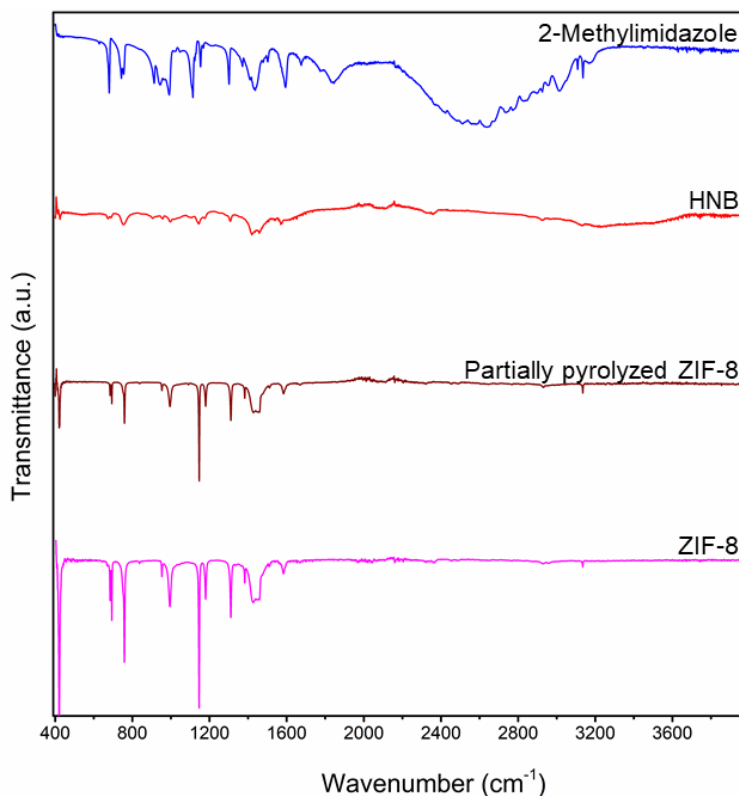


Figure 6.6: FTIR spectra of 2-methylimidazole, HNB-2, partially pyrolyzed ZIF-8, and ZIF-8.

To further investigate the structure of HNB-2, NEXAFS analysis was performed. NEXAFS measurements of ZIF-8, partially pyrolyzed ZIF-8 (ZIF-8-525) and HNB-2 were carried out at the C K-edge, N K-edge, O K-edge, and Zn L-edge. In the C K-edge spectra (Figure 6.7) the peak appearing at 284.9 eV can be assigned to $1s \rightarrow \pi^*$ transitions of aromatic C.²⁵⁸ This peak is visible in ZIF-8, partially pyrolyzed ZIF-8 and HNB-2. In these three samples a peak at 286.5 eV can be identified, which can be assigned to C $1s \rightarrow \pi^*$ transitions of C-OH.²⁴⁵ Moreover, the peak at 287.1 eV can be assigned to C $1s \rightarrow \pi^*$ transitions of C-N and C=C-N in N substituted aromatic carbon.²⁶¹⁻²⁶² This feature can be observed in ZIF-8, partially pyrolyzed ZIF-8 and HNB-2. The C=O peak appearing at 288.5 eV due to the C $1s \rightarrow \pi^*$ transitions of C=O can be observed in the samples as well as the carbon tape. Based on the fact that carbon tape which used to stick the samples showed C=O and the absence of C=O bond in the known structure of ZIF-8, the C=O appearing in the samples could be treated as a signal coming from the carbon tape, not from the samples.

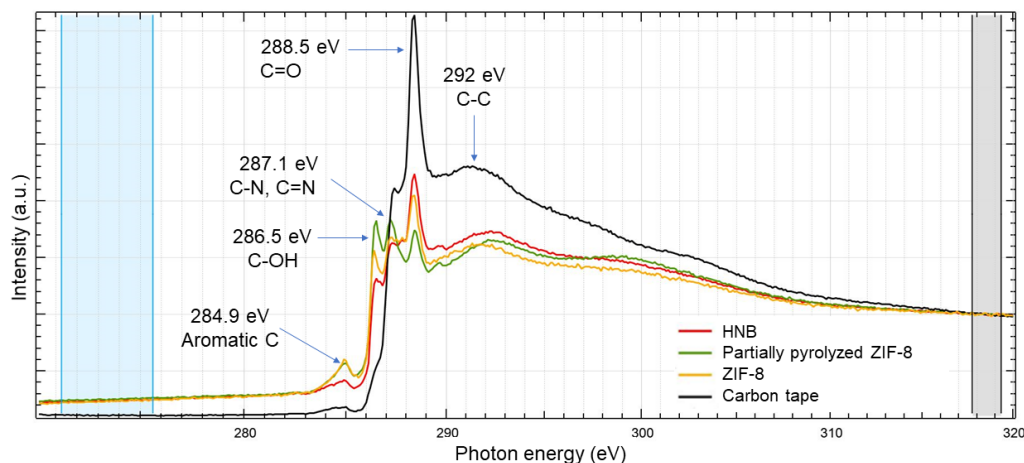


Figure 6.7: C K-edge NEXAFS spectra of HNB-2, partially pyrolyzed ZIF-8, ZIF-8 and carbon tape.

The O K-edge spectra of HNB-2 (Figure 6.8) showed all the peaks which can be observed in the O K-edge spectra of carbon tape; in agreement with the previous suggestion: C=O appearing in HNB-2, pristine and partially pyrolyzed ZIF-8 is arising probably from the carbon tape.

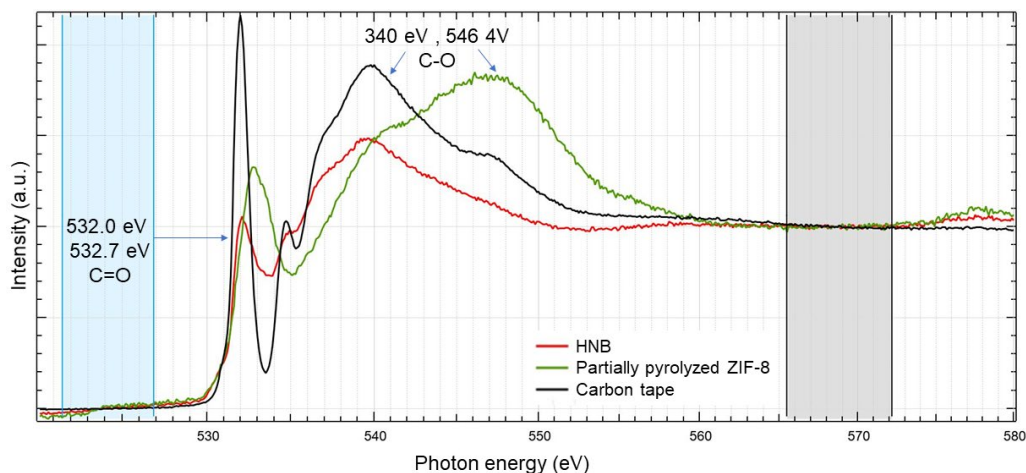


Figure 6.8: O K-edge NEXAFS spectra of HNB-2, partially pyrolyzed ZIF-8, ZIF-8 and carbon tape.

In the N K-edge spectra (Figure 6.9) of HNB-2, partially pyrolyzed ZIF-8 and ZIF-8; a peak at 400.5 eV can be assigned to $N\ 1s \rightarrow \pi^*$ transitions of terminal C-N-H.²⁴⁵ The presence of this bond even in HNB-2 suggests that the outer shell of HNB-2 has C-N-H bonds which are probably arising from 2-methylimidazole in residual ZIF-8. In agreement with this in HNB-2, a peak appeared at 401.7 eV which also appeared in the reference urea sample, partially pyrolyzed and pristine ZIF-8 samples. Based on the bonding environment of urea this peak can be assigned to $N\ 1s \rightarrow \pi^*$ transitions of CN-H_x and N=O. The appearance of this peak in HNB-2 confirms that nitrogen-doped carbon shells also consist of N=O bonds.

The broad peaks around 406 eV and 413 eV which can be detected in all the samples can be assigned to N 1s $\rightarrow \sigma^*$ transitions of C-N.²⁶⁵

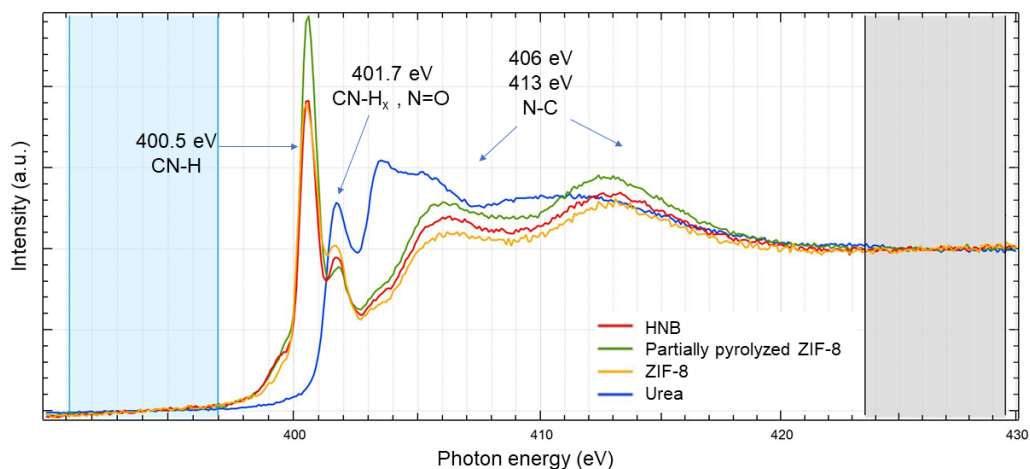


Figure 6.9: N K-edge NEXAFS spectra of HNB-2, partially pyrolyzed ZIF-8, ZIF-8 and urea.

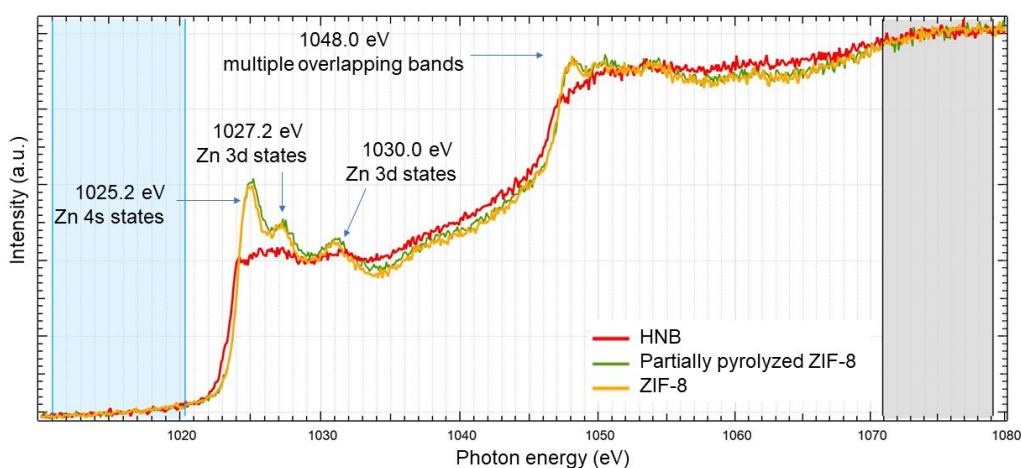


Figure 6.10: Zn L-edge NEXAFS spectra of HNB-2, partially pyrolyzed ZIF-8, ZIF-8.

In Zn L-edge spectra (Figure 6.10) of ZIF-8 and partially pyrolyzed ZIF-8 a prominent peak at 1025.2 eV can be observed which is arising from Zn 4s state.³³⁹⁻³⁴⁰ The peaks at 1027.2 eV and 1030.0 eV can be assigned to 3d transition states.³³⁹⁻³⁴⁰ In HNB-2 Zn 4s transitions and 3d transitions are not clear compared to ZIF-8 and partially pyrolyzed ZIF-8 as most of the ZIF-8 is washed out in the acid washing process. ZIF-8, partially pyrolyzed ZIF-8 and HNB-2 showed a broad peak around 1048 eV, which can be assigned to multiple overlapping bands.³³⁹ Even after the acid washing, a small amount of Zn is remaining in HNB-2. This is likely to be zinc (II) bonded to the nitrogen-doped carbon layer of HNB-2.

6.2.3 Applications of HNBs

Porous carbon is widely used as an electrode material due to its good electronic conductivity, large surface area and high chemical stability. As HNB-1 exhibits high stability, it was tested as a supercapacitor electrode material. HNB-2 was tested as a fluorescence sensor application.

6.2.4 Application of HNB - 1 as supercapacitor electrodes

HNB-1 was used as the working and counter electrode in an electrochemical cell. Positive and negative electrodes made from HNB-1 were studied in two-electrode cell configurations by cyclic voltammetric measurements in aqueous, organic, and ionic liquid media. The measurements were conducted at different voltage sweep rates ranging from 5-1000 mV/s. The results of the test, with current data converted into capacitance, were used to evaluate the performance of the device made with two HNB-1 electrodes.

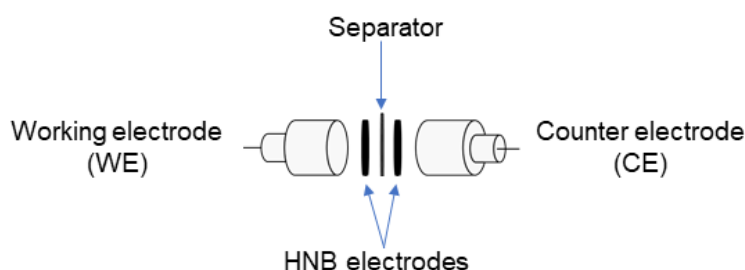


Figure 6.11: The assembly of the device made from two HNB-1 electrodes.

In an aqueous medium, 1 M KOH was used as the solvent in a 0 to 0.7 V potential window. The charge-discharge plots of the device showed nearly symmetrical rectangular shapes at 5, 10, 20, 50, 100, 200, and 500 mV s^{-1} due to the formation of a typical electric double layer showing capacitive behaviour. Even at an increased scan rate of 1000 mV s^{-1} , the device maintained a good rectangular shape, indicating the high performance of the device. (Figure 6.12 a)

When the scan rate increases, the current also increases, but the capacitance decreases. When the scan rate is slow, the electrolyte can penetrate to the pores of the electrode material more thoroughly making good contact with the internal surface of the electrode material. This leads to more charge being stored on the surface of the electrode yielding larger measured capacitance. On the other hand, at higher scan rates, electrode and electrolyte are in contact for a short time and leading to lower charge storage and capacitance.³⁴¹ Figure 6.12 (b) shows the plots of the capacitance of the HNB-1 electrode and the device as a function of the scan rate. With the increasing scan rate, the capacitance of the electrodes and

the device decreases. The maximum capacitance of the device was 25 Fg^{-1} while the capacitance of the HNB-1 electrode was 100 Fg^{-1} in 1 M KOH medium at a 5 mV s^{-1} scan rate. At the same scan rate, the device exhibited a maximum energy density of 1.7 Wh kg^{-1} .

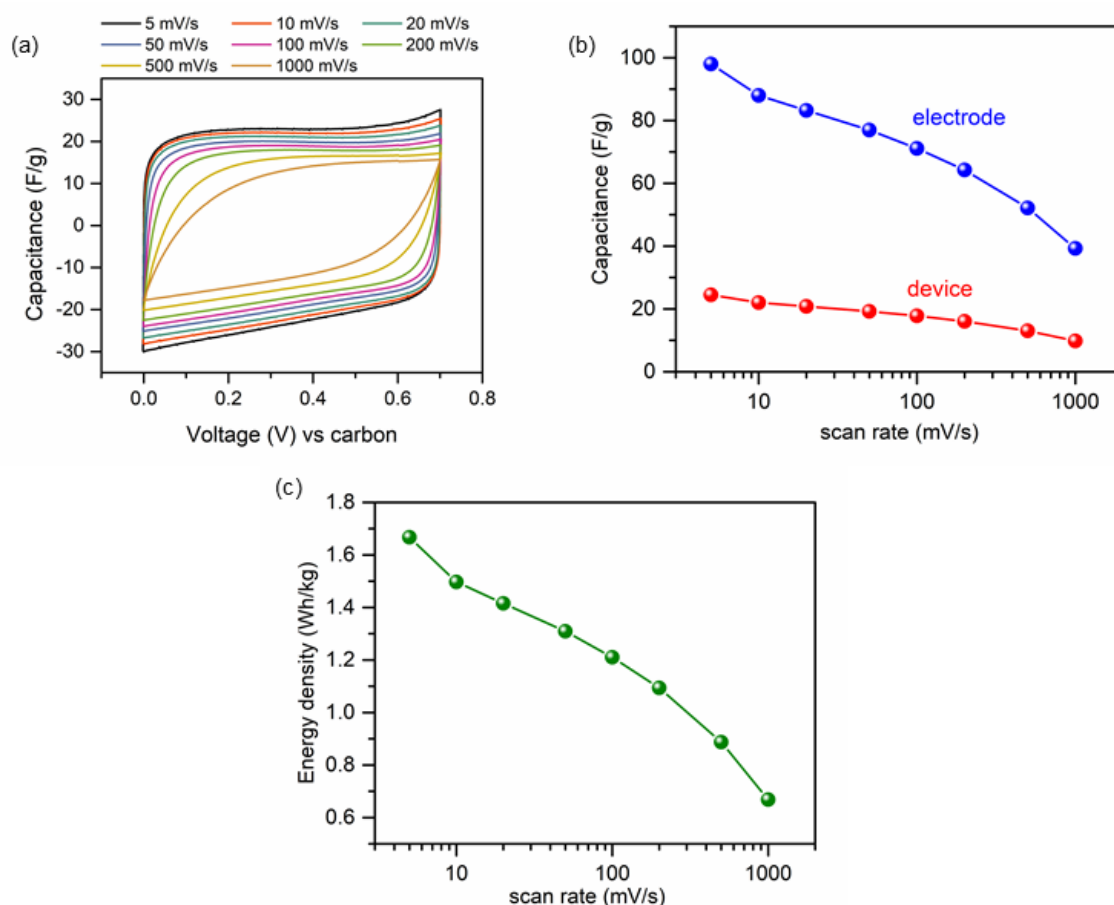


Figure 6.12: Electrochemical performance of device made from HNB-1 electrodes using 1 M KOH as the electrolyte (a) Galvanostatic charge-discharge plots, (b) plot of capacitance vs scan rate and (c) energy density vs scan rate.

To increase the energy density of the device, the HNB-1 supercapacitor was constructed with an organic electrolyte; $1 \text{ M NEt}_4\text{-BF}_4$ (tetraethylammonium cation (NEt_4^+) and tetrafluoroborate anion (BF_4^-)). The device was tested in a broader working voltage window from 0 to 2.2 V . The charge-discharge plots of the device showed nearly symmetrical rectangular shapes in all the scan rates, as in the aqueous medium. The maximum capacitance of the device was 13 Fg^{-1} while the capacitance of the HNB-1 electrode was 42 Fg^{-1} . When using the organic electrolyte, the capacitance of the device decreases compared to the aqueous electrolyte. That is because the organic electrolyte has a low conductivity compared to the aqueous electrolyte hence the device has low capacitance.³⁴² Owing to the wide operational voltage window when using the organic electrolyte, the maximum energy

density was 9.0 Wh kg^{-1} . That was more than five times the maximum energy density when using the aqueous electrolyte.

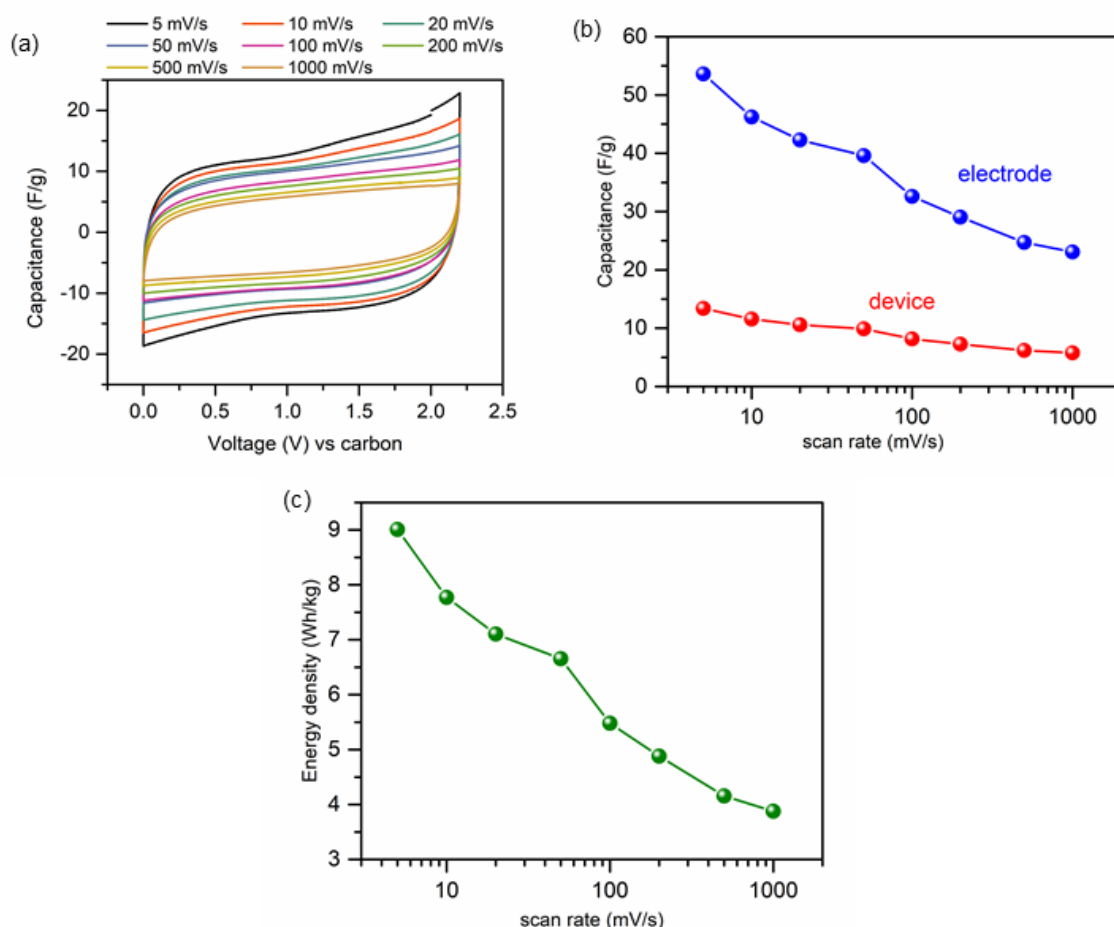


Figure 6.13: Electrochemical performance of device made from HNB-1 electrodes using 1 M $\text{NET}_4\text{-BF}_4$ as electrolytes in a two-electrode system. (a) Galvanostatic charge-discharge plots, (b) plot of capacitance vs scan rate and (c) energy density vs scan rate.

An ionic liquid was also used as an electrolyte. Ionic liquids overcome the disadvantages of aqueous and organic electrolytes as they have high ionic conductivity and wide operating voltage windows.³⁴³ In this research neat EMI-BF_4 (1-ethyl-3-methylimidazolium tetrafluoroborate) was used. The device was tested in a working voltage window from 0 to 2.2 V. The charge-discharge plots of the device showed nearly symmetrical rectangular shapes at all scan rates. The maximum capacitance of the device and the HNB-1 electrode were 11 Fg^{-1} and 44 Fg^{-1} . The device showed the lowest capacitance values when using the ionic liquid compared to the aqueous and organic electrolytes. The maximum energy density is 7.5 Wh kg^{-1} which is more than four times higher than the device which used an aqueous electrolyte but smaller than the device which used organic electrolyte.

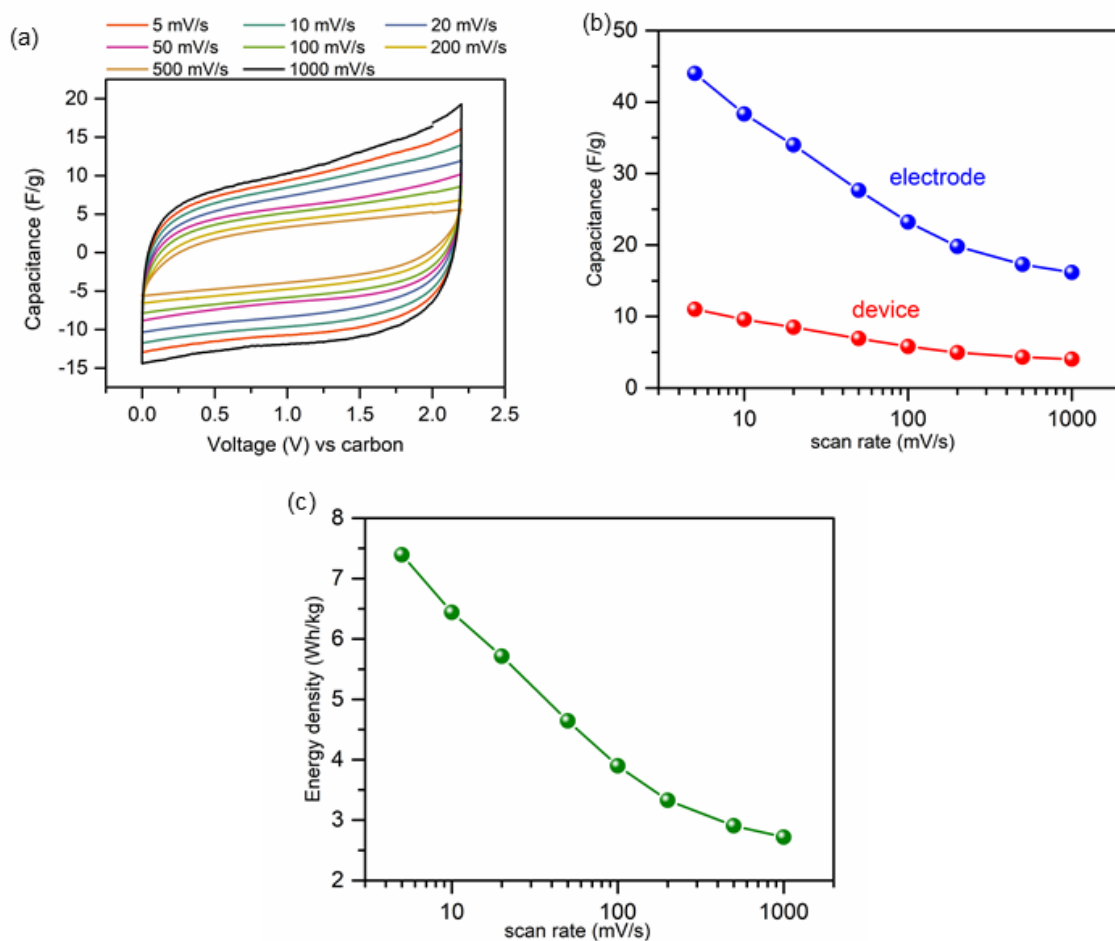


Figure 6.14: Electrochemical performance of device made from HNB-1 electrodes using neat EMI-BF₄ as electrolytes in a two-electrode system. (a) Galvanostatic charge-discharge plots, (b) plot of capacitance vs scan rate and (c) energy density vs scan rate.

6.2.5 Application of HNB - 2 as a fluorescence sensor

Fluorescence spectra of dispersions of HNB-2 were measured in aqueous solutions of various pH (1 to 14) with excitation wavelengths in the range of 340 - 480 nm (Appendix B). While the HNB-2 did not show fluorescence in the range pH 5-12, fluorescence was observed at low pH (1-3) and high pH (13-14) using excitation wavelengths between 340 nm - 380 nm. Thus, pH 1 and a 340 nm excitation wavelength were selected to study the fluorescence behaviour of HNB-2 in the presence of added anions. Dramatic changes in its fluorescence signals would indicate its effectiveness as an anion sensor.

The effect of halide, sulfates, nitrates, carbonates, and phosphates on the fluorescence of HNB-2 was studied. When studying the effect of Cl^- on the fluorescence of HNB-2, aqueous H_2SO_4 was used to disperse HNB-2, instead of HCl to eliminate the effect of Cl^- . For all other anions, HCl was used to disperse the HNB-2.

As an initial control experiment, deionized water was added to HNB-2 dispersions in HCl and H_2SO_4 . The addition of water had little impact on the emission spectra (Figure 6.15).

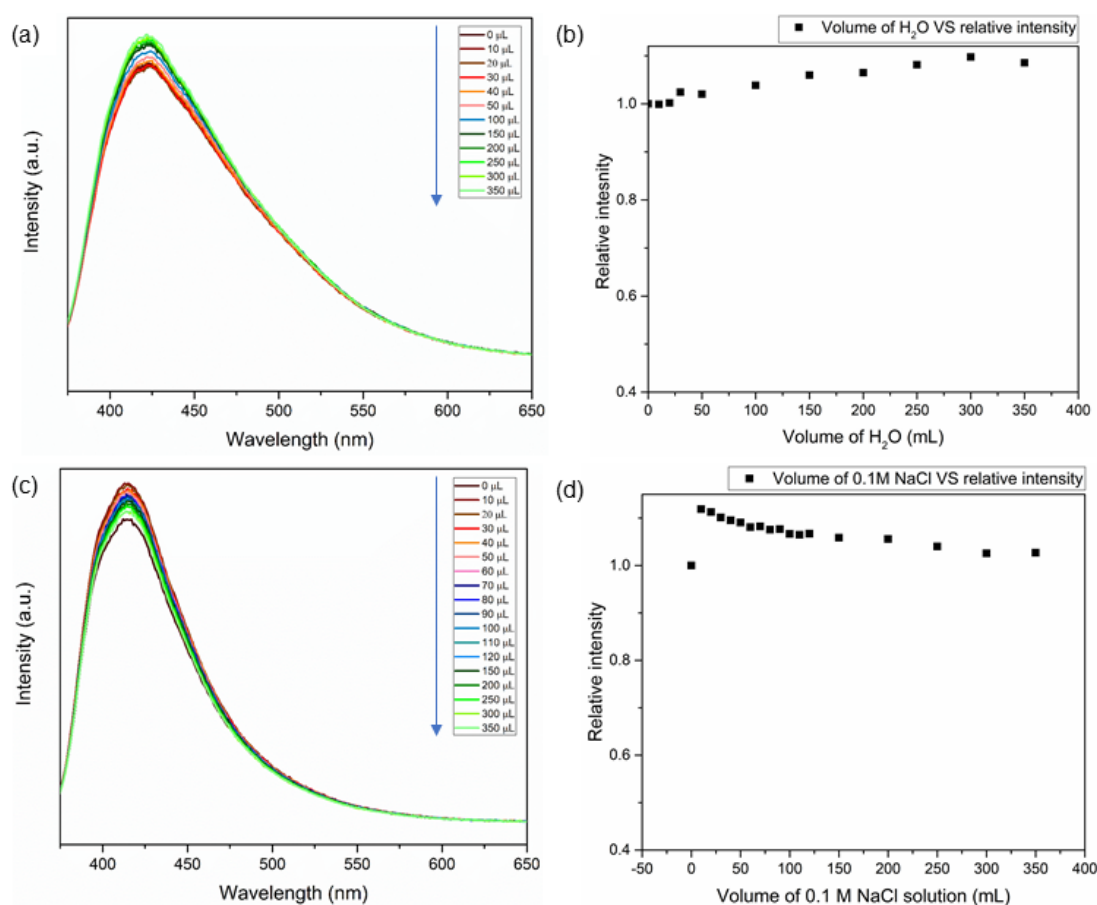


Figure 6.15: (a) Fluorescence and (b) relative intensity of HNB-2 dispersed in HCl (pH 1) when adding deionized H_2O , (c) fluorescence and (d) relative intensity of HNB-2 dispersed in H_2SO_4 (pH 1) when adding (c, d) 0.1 M NaCl.

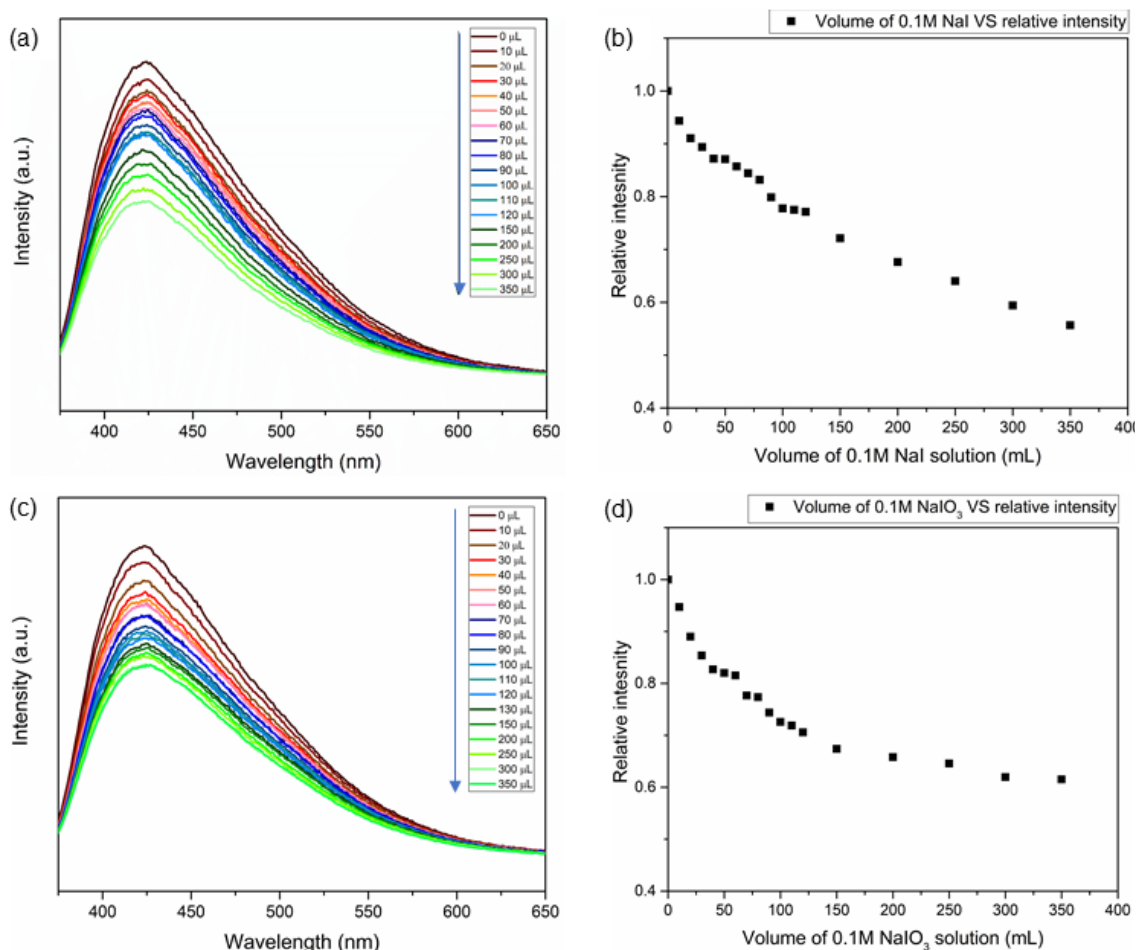


Figure 6.16: Fluorescence of HNB-2 dispersed in HCl (pH 1) and relative intensity when adding (a, b) 0.1 M NaI and (c, d) 0.1 M NaIO₃.

Adding solutions of F⁻, Cl⁻, NO₃⁻, SO₄²⁻, CO₃²⁻, PO₄³⁻ as their sodium salts to HNB -2 dispersions did not quench the fluorescence (Experimental section, Figure 6.20 and Figure 6.21). NaBr, on the other hand, quenched the fluorescence (Experimental section, Figure 6.19 c and d). To see the effect of Na⁺ in the fluorescence quenching, the potassium salt of bromide, KBr, was added to HNB-2 (Experimental section, Figure 6.19 e and f). The fluorescence quenching by both NaBr and KBr was similar, suggesting that Br⁻ is responsible for this effect. The effect of I⁻ and IO₃⁻ was also investigated (Figure 6.16). The quenching effect of I⁻ was greater than Br⁻ and the effect of IO₃⁻ was greater still (Figure 6.17 and Figure 6.18). Hence, HNB-2 has some promise as a sensor for I⁻ and IO₃⁻.

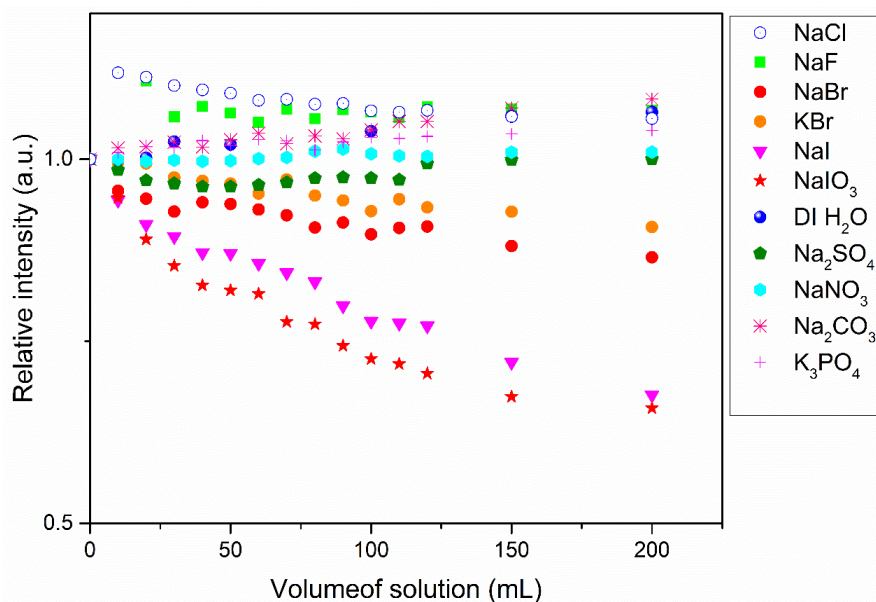


Figure 6.17: Relative intensity at the presence of anions.

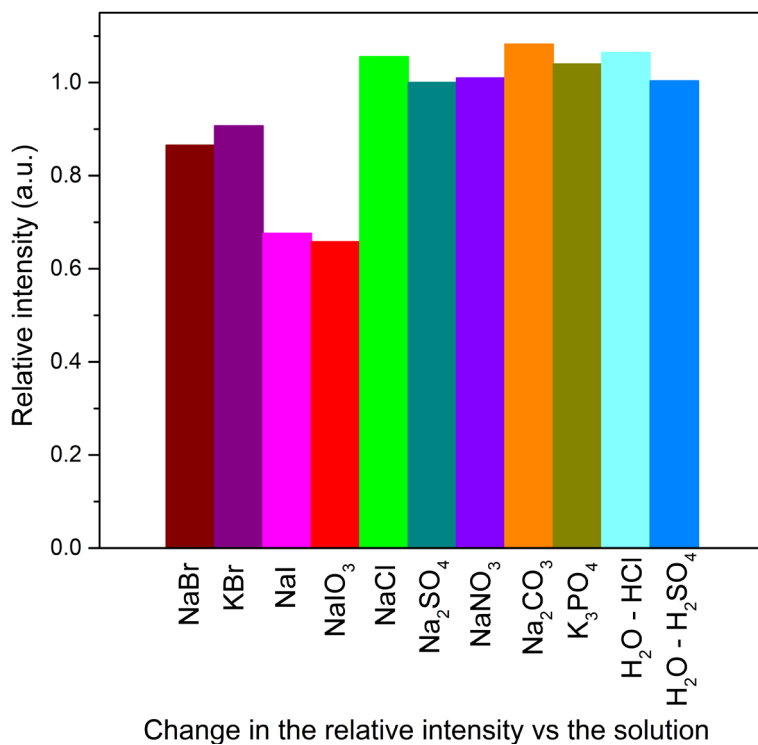


Figure 6.18: Change in relative intensity after adding 200 μ L of solutions.

6.3 Conclusion

The capacitance of the HNB-1 electrode in an aqueous medium was 100 Fg^{-1} which is comparable to the capacitance of the activated carbon electrode.³⁴⁴ The HNB-1 electrodes were stable in all the electrolytes. The energy density of the HNB-1 supercapacitor device is also close to the reported values of devices made from microporous carbon which is in the range of $3 - 5 \text{ Whkg}^{-1}$.³⁴⁵ The macropores of HNB-1 could serve as ion buffering reservoirs to minimize the diffusing distance of the electrolyte which leads to high performance.³⁴⁶ Overall, these results suggest HNB-1 is a good material to be used in electrodes as supercapacitor electrodes.

To produce HNB-2, $525 \text{ }^\circ\text{C}$ is the optimum temperature for the partial pyrolyzation of ZIF-8 followed by acid washing. There are traces of zinc in HNB-2 which were detected by EDX and NEXAFS analysis. The structure of HNB-2 was evaluated further by NEXAFS analysis. HNB-2 comprises nitrogen-doped aromatic carbon. C-OH, C-N, C=N, and C-N-H bonds present in HNB-2 could give rise to the fluorescence in HNB-2 in highly acidic and basic mediums. Due to the conspicuous fluorescence quenching that occurred after the addition of IO_3^- and I^- , HNB-2 could be used as a sensor for IO_3^- and I^- .

6.4 Experimental Section

6.4.1 General procedures

All starting materials and solvents were used as received from commercial sources without further purification unless otherwise noted.

6.4.1.1 Synthesis of HNB-1 by pyrolysis of ZIF-8@KTA

Synthesis of ZIF-8 and ZIF-8@KTA was performed following the procedure mentioned in Chapter 2.

6.4.1.2 Synthesis of HNB-1

ZIF-8@KTA (100 mg) was put into a ceramic boat. The furnace was purged for 1 hour with argon at a flow rate of 10 mL/min. The samples were set to carbonize at 900 °C for 2 hours at a heating rate of 1 °C/min under the same flow of argon.

Synthesis of HNB-2 by partial pyrolysis of ZIF-8

6.4.1.3 Partial pyrolysis of ZIF-8

ZIF-8 nanocrystals (20 mg) were put into a ceramic boat. The furnace was purged for 1 hour with argon at a flow rate of 10 mL/min. The samples of ZIF-8 were pyrolyzed at different temperatures (from 475 °C to 600 °C) for 30 min at a heating rate of 10 °C/min under the same flow of argon (Table 6.1).

6.4.1.4 Synthesis of HNB-2 by partially pyrolyzed ZIF-8

Partially pyrolyzed ZIF-8 (ZIF-8-525, 100 mg) was put in HCl (2M, 15 mL) solution and stirred for 5 min at 300 rpm. Then the HNB-2 was precipitated from the solution by centrifugation (5000 rpm, 5 min). The precipitate was washed with methanol 3 times and dried *in vacuo* for 24 hours.

Table 6.1: Partial pyrolysis of ZIF-8 at different temperatures.

Sample name	Temperature (°C)	Time (min)	Heating rate (°C/min)	Sample code after etching
ZIF-8-475	475	30	10	PP-ZIF-8-475
ZIF-8-500	500	30	10	PP-ZIF-8-500
ZIF-8-525	525	30	10	PP-ZIF-8-525
ZIF-8-550	550	30	10	PP-ZIF-8-550
ZIF-8-555	555	30	10	PP-ZIF-8-555
ZIF-8-560	560	30	10	PP-ZIF-8-560
ZIF-8-575	575	30	10	PP-ZIF-8-575
ZIF-8-600	600	30	10	PP-ZIF-8-600

6.4.2 Fluorescence measurements of HNB-2 at different pH and different excitation wavelengths

A series of solutions ranging from pH 1 to pH 14 was prepared using HCl and NaOH. First, a solution of 1 M HCl was prepared to dilute 8.33 mL of 37% HCL (12 M) to 100 mL using deionized water. Then a serial dilution was performed using deionized water to prepare 0.1 M (pH 1), 0.01 M (pH 2), 0.001 M (pH 3), 0.0001 M (pH 4), 0.00001 M (pH 5), and 0.000001 M (pH 6) HCl solutions. Then a solution of 1 M NaOH was prepared by dissolving 4.0 g of NaOH in deionized water and diluting it to 100 mL. A serial dilution was performed to prepare 0.1 M (pH 13), 0.01 M (pH 12), 0.001 M (pH 11), 0.0001 M (pH 10), 0.00001 M (pH 9), and 0.000001 M (pH 8) NaOH solutions. For pH 7 solution deionized water and a 1:1 mixture of 0.1 M HCl and 0.1 M NaOH were used. After preparing the solutions, a pH meter was used to measure the pH and precisely adjust the pH by using HCl and NaOH. For the fluorescence measurements, HNB-2 (3.5 mg) was suspended in a solution with the desired pH (3.5 mL). The fluorescent measurements were carried out at 340 nm, 360 nm, 380 nm, 400 nm, 420 nm, 440 nm, 460 nm, and 480 nm excitation wavelengths.

6.4.3 Fluorescence measurements of HNB-2 at the presence of different anions

A series of anion solutions, NaBr, KBr, NaI, NaIO₃, NaCl, Na₂SO₄, NaNO₃, Na₂CO₃, and K₃PO₄ was prepared (0.1 M). A particular anion solution was added to the HNB-2 dispersion at pH 1 in 10, 20, 30, 40, 50, 60, 70, 80, 90, 100, 110, 120, 150, 200, 250, 300, and 350 μ L quantities and the fluorescence measurements were performed at 340 nm excitation wavelength.

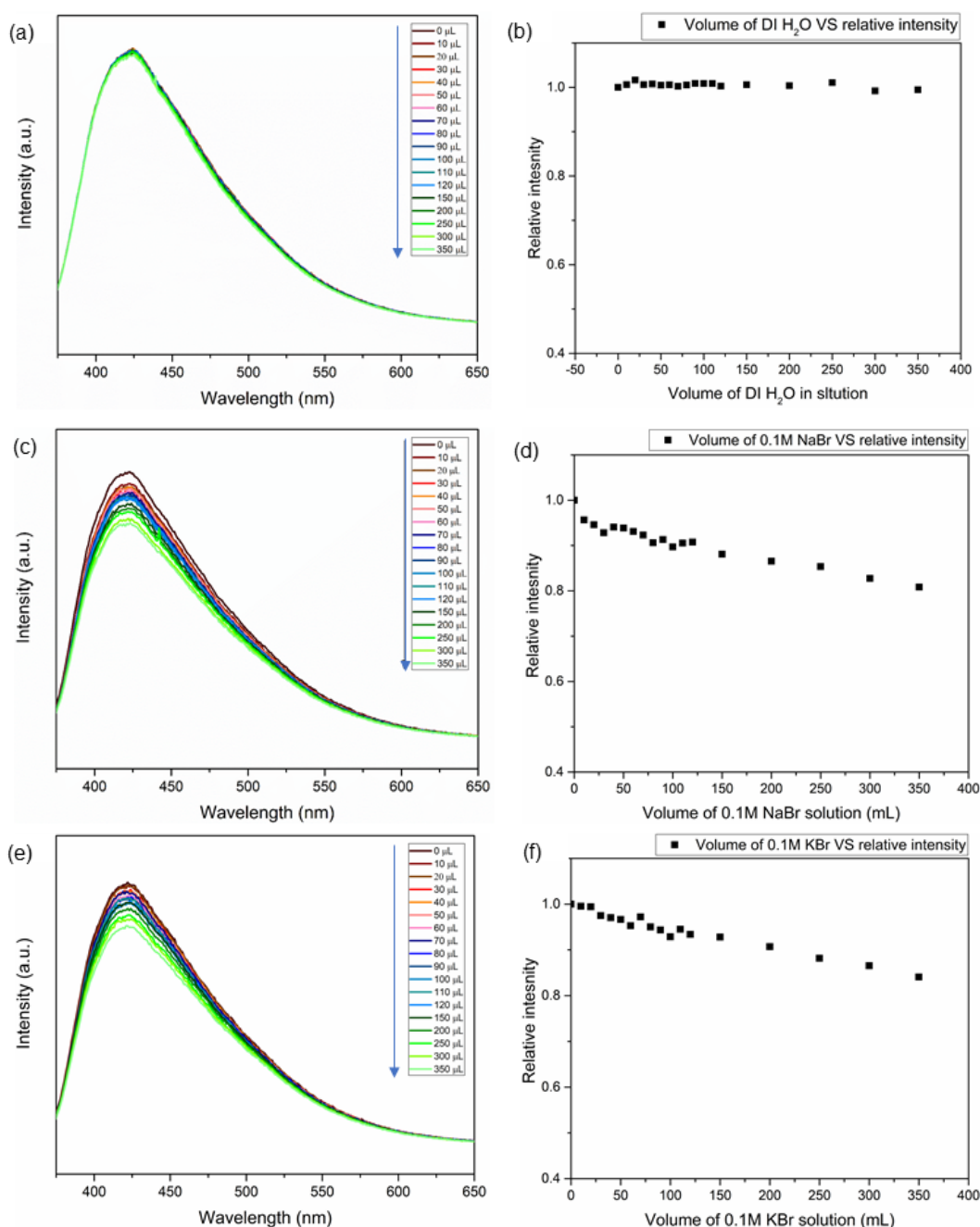


Figure 6.19: Fluorescence of HNB-2 dispersed in H₂SO₄ (pH 1) and relative intensity when adding (a, b) DI H₂O and Fluorescence of HNB-2 dispersed in HCl (pH 1) and relative intensity when adding (c, d) 0.1 M NaBr and (e, f) 0.1 M KBr.

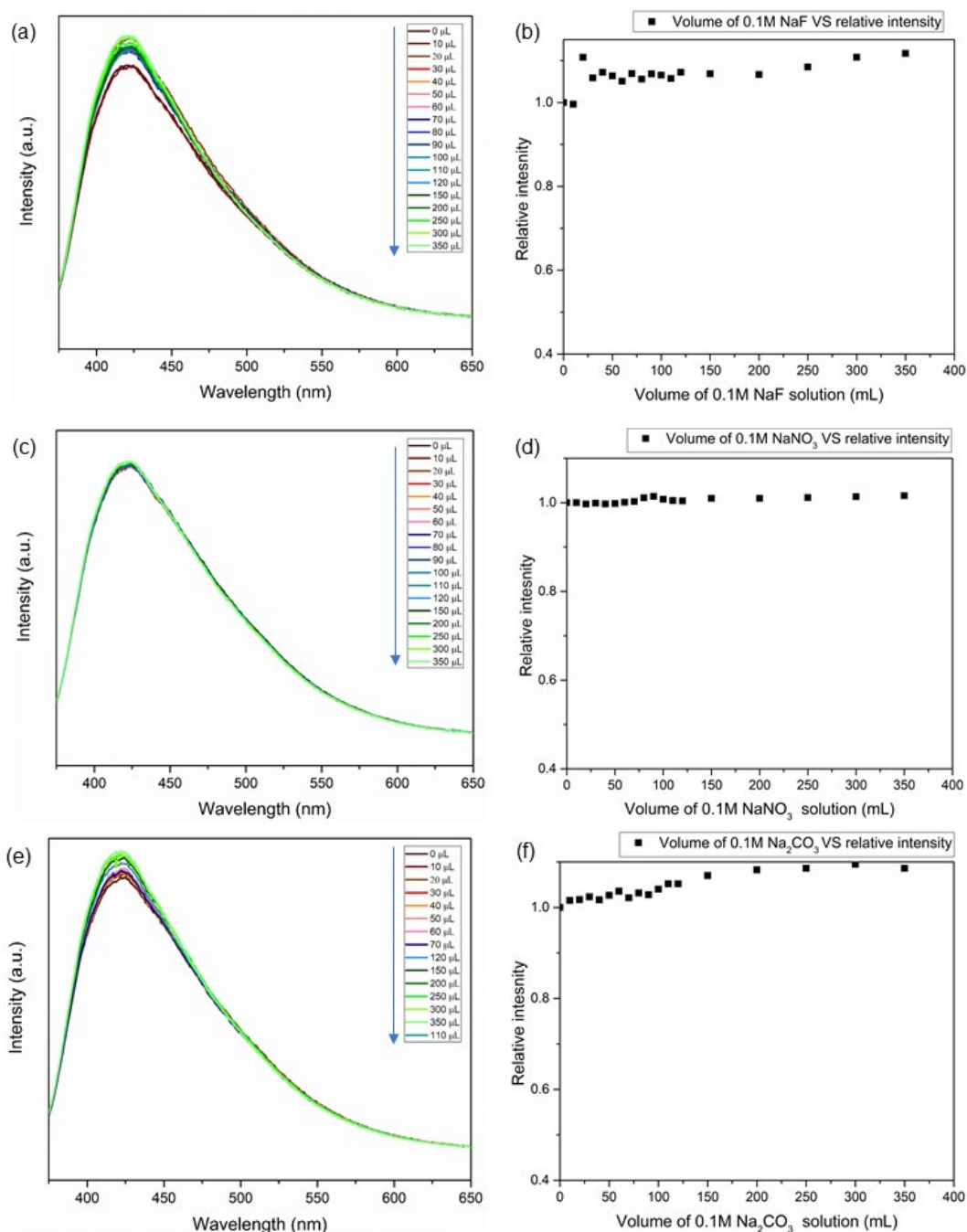


Figure 6.20: Fluorescence of HNB-2 dispersed in HCl (pH 1) and relative intensity when adding (a, b) 0.1 M NaF, (c, d) 0.1 M NaNO_3 and (e, f) 0.1 M Na_2CO_3 .

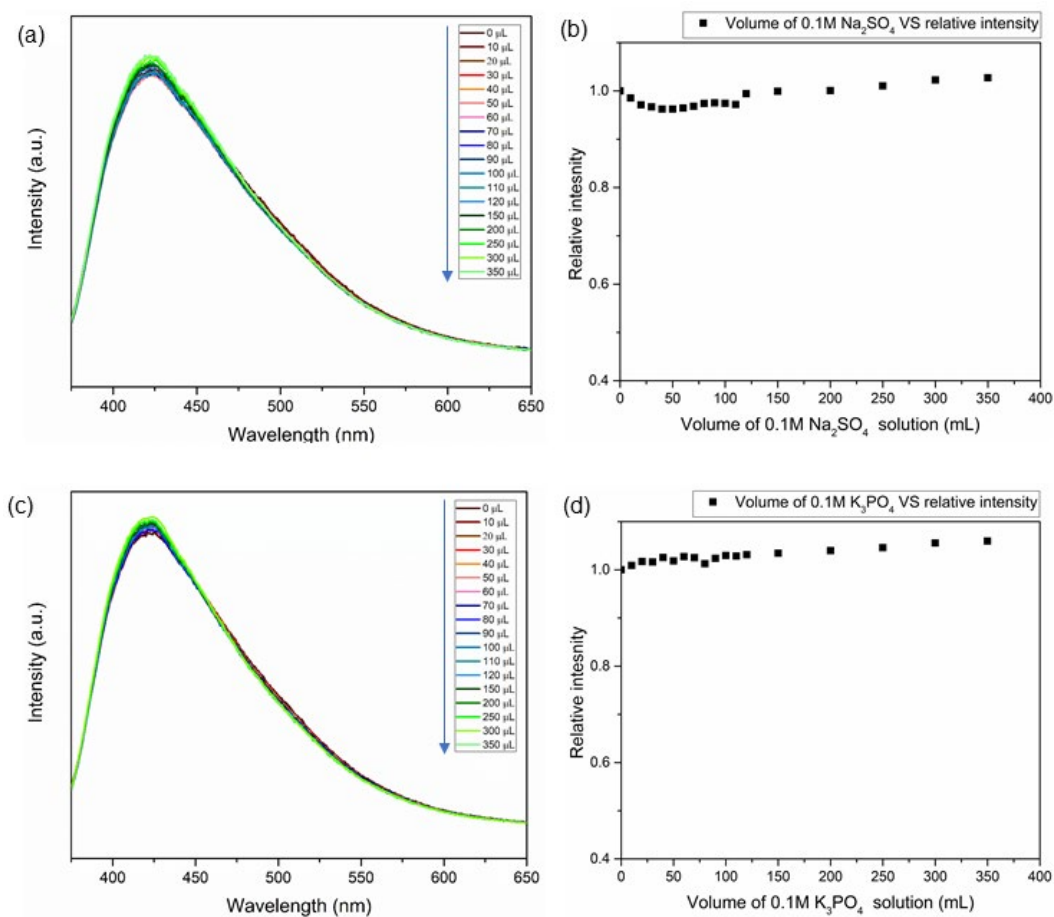


Figure 6.21: Fluorescence of HNB-2 dispersed in HCl (pH 1) and relative intensity when adding (a, b) 0.1 M Na_2SO_4 and (c, d) 0.1 M Na_3PO_4 .

6.4.4 Preparation of electrode

The working electrodes were made with 80 wt.% HNB-1 as active material, 10 wt.% acetylene black as conductive addition, and 10 wt.% PTFE dissolved in alcohol as a binder. The mixed slurry was then made into a free-standing electrode by the way similar to hand-rolling until the alcohol was completely evaporated. The electrodes were cut into 12mm diameter discs by a punching machine and the mass of the electrode is measured by a high precision electronic balance.

6.4.5 Cell assembling

A symmetrical capacitor was assembled using a Swagelok electrochemical cell, using the prepared HNB-1 electrodes as both working and counter electrodes, which were separated by a sheet of borosilicate glass fiber (Whatman GF/B) in 1 M KOH aqueous electrolyte, and Whatman GF/A in 1 M $\text{NEt}_4\text{-BF}_4$ organic electrolyte and neat EMI- BF_4 ionic liquid electrolyte. Platinum plates serve as collectors. In addition, in organic electrolytes and ionic liquids, the whole assembly process was protected by argon atmosphere in the glove box with H_2O and O_2 contents < 0.1 ppm.

Table 6.2: Weights of electrodes, weights of NPC in the electrodes and NPC areal loading in the electrodes in aqueous, organic and ionic liquid medium.

Electrolyte	Electrode weight	NPC weight	NPC loading
1 M KOH	3.82 mg	3.06 mg	2.7 mg/cm ²
	3.9 mg	3.10 mg	
1 M $\text{NEt}_4\text{-BF}_4$	2.75 mg	2.20 mg	2.15 mg/cm ²
	3.10 mg	2.47 mg	
Neat EMI- BF_4	3.80 mg	3.04 mg	2.90 mg/cm ²
	4.20 mg	3.36 mg	

6.4.6 Electrochemical testing

The electrochemical performance was evaluated by cyclic voltammetry tests (Autolab m204) at various scan rates. In a 1 M KOH aqueous electrolyte, the voltage range is 0-0.7 V, and the scan rates change from 5-1000 mV/s. In 1 M NEt₄-BF₄ organic electrolyte and neat EMI-BF₄ ionic liquid electrolytes, the voltage range is 0-2.2 V, and the scan rates change from 5-1000 mV/s.

The total capacitance of the device (C_{cell}) can be calculated from cyclic voltammetric data. Where, I (in A) is the discharge current, m (in g) is the total mass of the active materials in the two electrodes, dV/dt is the slope of the discharge curve.

$$C_{\text{cell}} = I(m \, dV/dt)^{-1} \quad \text{Eq. 6.1}$$

In a symmetrical two-electrode system, the capacitance of a single electrode can be evaluated by the total capacitance of the cell by equation 6.2. Where, C_{cell} is the capacitance of the device for the two-electrode supercapacitor calculated for the CV curve or charge-discharge curve, C_{one} is the capacitance of a single electrode.

$$C_{\text{one}} = 4C_{\text{cell}} \quad \text{Eq. 6.2}$$

The maximum energy (E_{max} , in W h kg^{-1}) of a two-electrode capacitor system can be calculated by Eq. 6.3. Where, C_{cell} is the capacitance of the device and V is the cell voltage.

$$E_{\text{max}} = 1/2 C_{\text{cell}} V^2 \quad \text{Eq. 6.3}$$

Chapter 7 – Summary and Perspectives

7.1 Summary

The work presented in this thesis initially focused on the synthesis of single-atom catalysts on hollow nitrogen-doped carbon supports derived from MOFs and MOF composites. Chapter 2 and Chapter 3 described two methods of synthesizing rhodium and cobalt single-atom catalysts. In Chapter 4 and Chapter 5, these single-atom catalysts have been used in catalysis applications. The use of catalyst support as a hollow nanobox which was synthesized in chapter 2 and synthesis of another hollow nanobox by a different method along with their applications are discussed in Chapter 6.

In Chapter 2, the synthesis of Rh SAC was reported by adaptation of our previously reported method²³⁸⁻²³⁹. The Rh SAC that is reported in this chapter was the first Rh SAC on nitrogen-doped carbon synthesized by the pyrolysis of MOF composites; until Yu *et al.* reported Rh SAC on N-doped C in 2020. However, the Rh loading of the Rh SAC presented in this work is more than 5 times higher than the reported one. Thus, the Rh SAC reported in this chapter depicts the one with the highest rhodium loading on nitrogen-doped carbon support so far. The oxidation state, coordination and bonding environment of rhodium single-atoms were evaluated by XPS, NEXAFS and EXAFS analysis.

In Chapter 3, synthesis of Co SAC was performed by reducing one synthesis step in the Rh SAC synthesis method. Here, cobalt was doped in the synthesis of ZIF-8 and potassium tannic acid coating was done to obtain the hollowness of the catalysts in the pyrolysis process. The impact of the pyrolysis environment on the bonding environment of the single metal atoms was studied by pyrolyzing the tannic acid coated cobalt-doped ZIF-8 in argon and hydrogen environments. The oxidation state and the coordination environment of the cobalt catalysts synthesized in argon and hydrogen environments were evaluated by XPS, NEXAFS and EXAFS analysis.

In Chapter 4, the synthesized Rh SAC and Co SAC in Chapter 2 and Chapter 3 were employed in the hydrogenation of nitroarenes. The control reactions were performed with the catalyst support as well. Rh SAC selectively reduced the nitro group of nitroarenes without affecting the functional groups attached to it with high consumption. Whereas the commercial catalyst 5% Rh on C did not show selectivity in the catalysis although the consumption was high. Moreover, Co SAC did little or no hydrogenation of nitroarenes, hence the catalysts were tested for further applications in the next chapter.

In Chapter 5, Rh SAC was tested for ORR and in the basic medium, the catalytic activity of Rh SAC is comparable to the commercial catalyst 20% Pt on C which is used as a benchmark in ORR. Rh SAC, Rh NPC, and Co SAC were tested for NO abatement. Rh NPC showed the best performance while the catalyst support NC performed better than both Rh SAC and Co SAC probably the coordination environment or the oxidation states of the single-atom catalysts were not favourable for the NO abatement. Rh SAC and Co SAC were further utilized in BPA degradation where Co SAC demonstrated a better performance than Rh SAC. The catalyst support also showed significant activity in the degradation of BPA.

As the catalyst support also showed significant catalysis behaviour in NO_x abatement and BPA degradation, the application of the catalysts supports as a hollow nanobox (HNB-1) was further explored in Chapter 6. HNB-1 was used to make an electrode in supercapacitor electrodes which showed comparable activity to activated carbon. Moreover, in this chapter, the synthesis of another type of hollow nanobox (HNB-2) by a different method was described. HNB-2 was synthesized by partial pyrolysis of ZIF-8 and washing out the remaining ZIF-8 in the core. This novel approach of synthesizing hollow nanoboxes. HNB-2 was used as fluorescence sensors of anions.

7.2 Future work

7.2.1 Further catalytic applications of Rh SAC

In this thesis, the Rh SAC was tested for the catalysis of hydrogenation of nitroarenes, ORR, NO abatement and BPA degradation. In future work, it would be interesting to explore the ability of Rh SAC in catalysing other reactions. Rhodium catalysts have been used over the past decade for C-H functionalization where C-H bond is cleaved and replaced with C-C, C-O or C-N.³⁴⁷⁻³⁴⁸ This is an important reaction in the synthesis of complex structures. It is reported using rhodium (III) catalysts widely for C-H activation due to its high selectivity and reactivity.³⁴⁹⁻³⁵² Thus, the feasibility of Rh SAC, which has rhodium (III) single-atom sites, can be explored for the C-H activation.

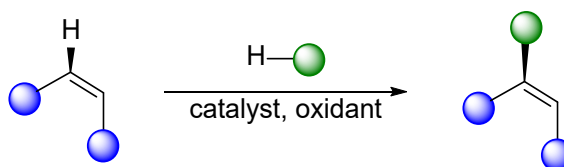


Figure 7.1: A model of Rh(III) assisted CH activation reaction; blue and green circles represent alkyl or aryl groups.

Moreover, rhodium catalysts are widely used in the catalysis of hydroformylation in which formyl group and hydrogen are added to a carbon double bond.³⁵³⁻³⁵⁴ Hydroformylation is an industrial process used for the production of aldehydes from alkenes. Using rhodium (III) for the catalysis of this reaction is reported.³⁵⁵⁻³⁵⁶ Hence, the Rh SAC synthesized in this research can be used as a catalyst for the hydroformylation reactions.

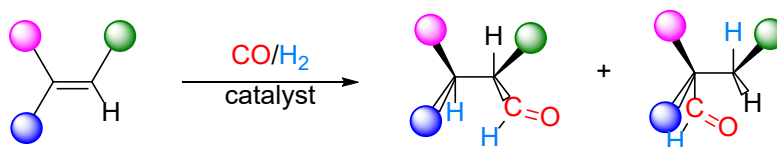


Figure 7.2: A model of hydroformylation of alkenes; blue, purple, and green circles represent alkyl or aryl groups.

7.2.2 Further catalytic applications of Co SAC

Co SAC synthesized in this research was tested for hydrogenation of nitroarenes, NO abatement and BPA degradation. Cobalt is also used as a catalyst for the hydroformylation reaction in the industry.³⁵⁷⁻³⁵⁸ Using cobalt (II) catalyst for this reaction was also reported in the literature.³⁵⁹ Thus, the feasibility of using Co SAC synthesized in this research with cobalt(II) single-atoms for the hydroformylation reaction can be investigated. Moreover, it is reported using Co SACs for ORR in the literature.³⁶⁰⁻³⁶³ The Co SAC synthesized in this research can be tested for ORR.

7.2.3 Synthesis of Rh SACs in different pyrolysis environments

In Chapter 2, the synthesis of Rh SAC was carried out by the ion exchange of ZIF-8@KTA followed by pyrolysis under an argon environment. This study can be extended to investigate the impact of the pyrolysis environment in the formation of catalysts. After the ion exchange, the pyrolysis can be carried out under hydrogen and nitrogen environments. The impact of the pyrolysis environment on the oxidation state and the coordination environment of rhodium can be studied by XPS and EXAFS characterization.

7.2.4 Synthesis of Co SAC by ion-exchange method

In Chapter 3, the synthesis of Co SAC was performed by doping cobalt in the synthesis of ZIF-8 followed by tannic acid coating and pyrolysis. This chapter demonstrated that the different pyrolysis environments impacted the coordination environment of cobalt single-atoms. This study can be continued further by the synthesis of cobalt catalysts by ion exchange of ZIF-8@KTA with cobalt ions and pyrolysis in different environments. The impact of the synthesis method and the pyrolysis environment in the coordination environment can be further studied.

7.2.5 Synthesis of SACs with heteroatom dopants in the catalyst support

In the synthesis of Rh SAC and Co SAC, the metal catalysts were synthesized on a nitrogen-doped carbon support. Most of the single-atom catalysts reported in the literature have nitrogen-doped carbon supports. Still, the synthesis of SACs on boron, phosphorus and sulfur-doped carbon support is not common. The SAs will coordinate with phosphorus and sulfur while boron will substitute carbon in the catalyst support. Some studies suggest boron doping in the catalyst support may boost the catalytic activity of the SACs.³⁶⁴⁻³⁶⁵ The scope is still open for the synthesis of SACs on boron, phosphorus and sulfur-doped carbon supports. Furthermore, the synthesis of SACs on either with a single or combination of boron, nitrogen, phosphorus, and sulfur-doped carbon can also be performed. The study of the

coordination environment of the proposed catalysts and their impact on the catalysis can be studied. But the controlled synthesis of SACs to obtain the desired coordination environment is still challenging.

7.2.6 Synthesis of SACs with different metals

The method used for the synthesis of Rh SAC can be employed for the synthesis of different SACs by simply changing the cation solution used in the ion exchange process with ZIF-8@KTA (Figure 7.3). An attempt was made for the synthesis of Ag SACs by using this method (Table 2.3).

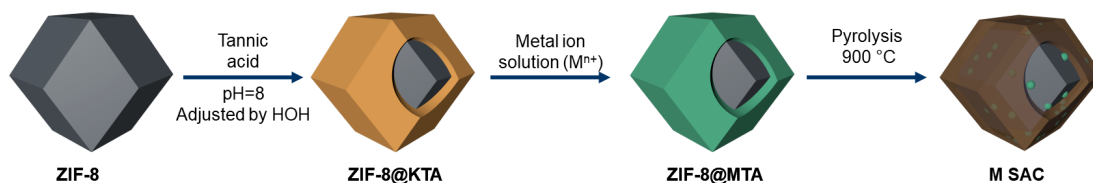


Figure 7.3: Synthesis of SACs with different metals; M can be any transition metal.

Table 7.1: Synthesis of ZIF-8@AgTA and Ag-NC.

ZIF-8@AgTA code	ZIF-8@KTA	[AgNO ₃]	Ag-NC sample code
ZIF-8@AgTA-0.012	75 mg	0.012 mM	Ag-NC-0.012
ZIF-8@AgTA-0.024	75 mg	0.024 mM	Ag-NC-0.024
ZIF-8@AgTA-0.048	75 mg	0.048 mM	Ag-NC-0.048

In the synthesis of Ag SAC, the concentration of the silver ion solution was decreased to obtain only Ag SAs. The above ion-exchange concentrations resulted, in Ag NPS after the pyrolysis in Ag-NC-0.012, 0.024, 0.048 samples. In the PXRD peaks at 28.2, 44.3, 64.4, 77.5, and 81.6 2 θ Cu K α , are as expected for Ag NPs (Figure 7.4). In the TEM images of Ag-NC samples, apart from the Ag NPs, an unexpected feature could be observed with the reduction of silver. In Ag-NC-0.012 sample formation of tube-like structure which elongated outwards from the material could be observed (Figure 7.5). Further studies can be continued for the synthesis of Ag SACs and investigate the formation of tubular-like structures when using silver. The resulting silver catalysts can be employed in electrochemical applications such as HER and CO₂ electro reduction reactions.³⁶⁶⁻³⁶⁷ Moreover, the Ag SACs can be employed in water purification applications owing to their ability to decompose dyes and to their antibacterial activity.³⁶⁸⁻³⁷⁰

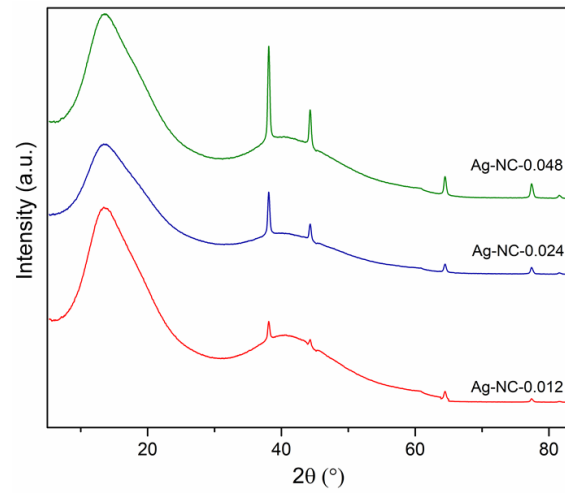


Figure 7.4: PXRD of Ag-NC samples.

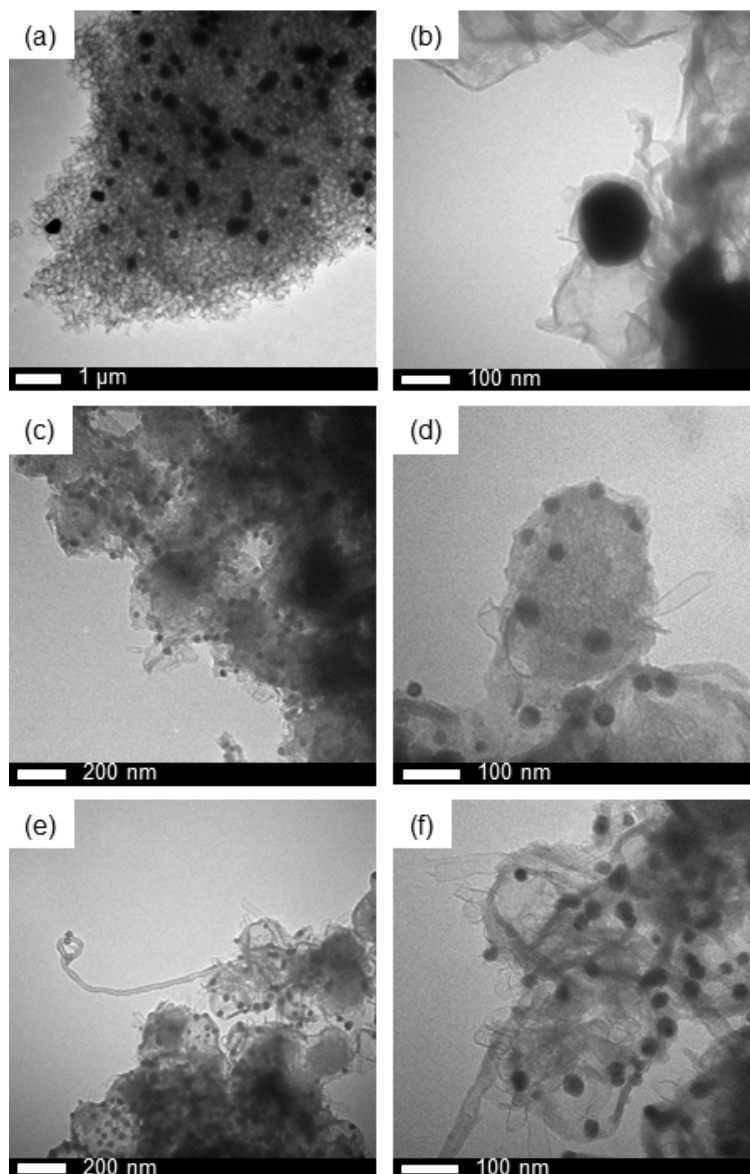


Figure 7.5: TEM images of (a, b) Ag-NC-0.048, (c, d) Ag-NC-0.024 and (e, f) Ag-NC-0.012 samples.

Furthermore, more SACs of transition metals can be synthesized by the above method. As the reactivity of the metals increases when going down through the column of the periodic table, it would be interesting to synthesize Ir SAC following this method and compare the TON of hydrogenation of nitroarenes with Rh SAC.³⁷¹⁻³⁷² Moreover, synthesis of Mn SAC following this method would be another possible study. As manganese has oxidation states from Mn^{2+} to Mn^{7+} , this would be the ideal catalyst to study the impact of the pyrolysis environment on the oxidation state of the catalyst.

7.2.7 Synthesis of SACs with multiple metal sites and cooperative catalysis

Synthesis of SACs with multiple single-atom sites can be carried out using the method used for the synthesis of Rh SAC. Here in the cation mixture, two or three metal ions can be used to introduce them into the tannic acid layer. The multiple metal catalysts can be used in cooperative catalysis. For example, a cationic mixture of rhodium, cobalt and manganese can be used in the ion exchange process and optimized to obtain a SAC with rhodium, cobalt, and manganese single-atom sites (Figure 7.6). The CoRhMn SAC can be used in cooperative catalysis.

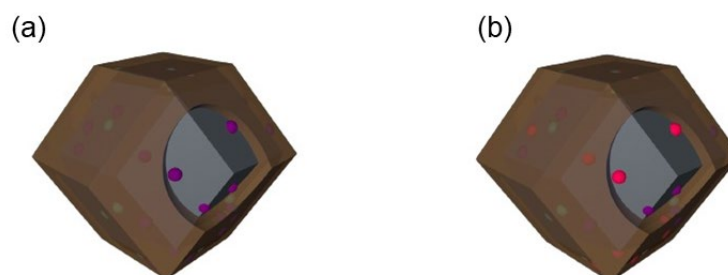


Figure 7.6: Illustration of SACs with multiple metal sites: (a) CoRh SAC and (b) CoRhMn SAC; Rh, Co and Mn atoms are presented in green, purple and pink colours.

Moreover, an attempt was made to synthesize a dual SAC by a combination of the two methods used to synthesize Rh SAC and Co SAC. In this method after the synthesis of Co ZIF-8@KTA, that was subjected to ion exchange with rhodium ions and CoRh-SAC was obtained by the pyrolysis of Co ZIF-8@RhTA. In the initial characterization, EDX showed both peaks for cobalt and rhodium (Figure 7.7 b), while there were no cobalt or rhodium nanoparticle peaks in the PXRD (Figure 7.7 d). Consistent with that, nanoparticles were absent in the TEM image (Figure 7.7 c). Further optimization is required to obtain the maximum cobalt and rhodium loading for this catalyst. This CoRh SAC can be used in cooperative catalysis.

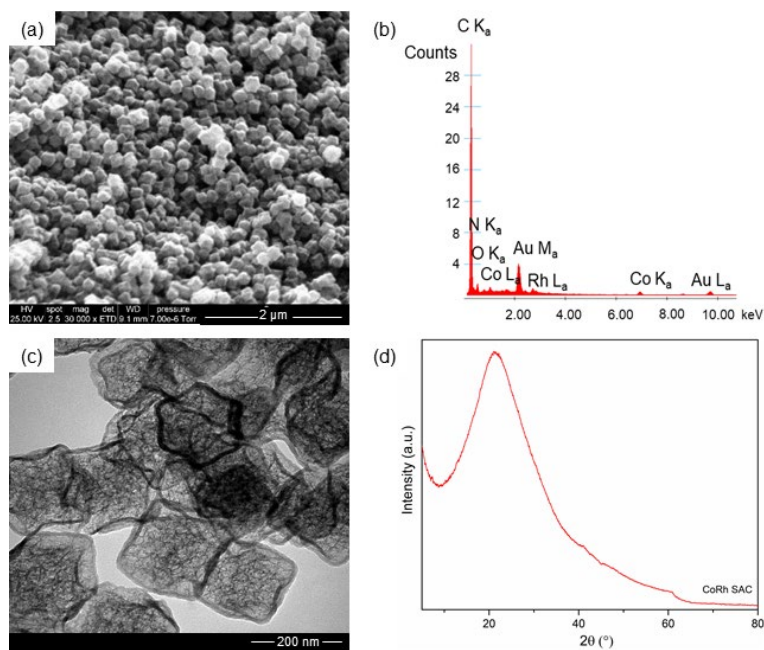


Figure 7.7: (a) SEM, (b)EDX, (c) TEM and (d) PXRD of CoRh SAC.

7.2.8 Investigate the impact of second coordination shell of SACs

Although SACs are an emerging field of research, there is only a handful of research to explore the influence of the second coordination shell of SACs for catalysis.³⁷³⁻³⁷⁴ Thus, the synthesis of SACs with heteroatom dopants and the study of the impact of a second coordination shell for catalysis will be a hot research area in the future. Not having control over the coordination environment of the catalyst during the synthesis is one of the limitations of this kind of study. Moreover, the requirement of high-end characterization techniques, expertise, and limited access to the required resources such as synchrotron facilities are the major constraint.

7.2.9 Computational modeling

Although synthesis and catalysis by SACs are emerging fields, there is a lack of information about the impact of the coordination environment on catalysis. Thus, it will be interesting to synthesize boron-doped, nitrogen-doped, phosphorus-doped, and sulfur-doped single-atom catalysts by pyrolyzing them in different environments and investigating their bonding environment of the first and second coordination shell and how it affects the catalysis in terms of selectivity and consumption. To understand this, computational modeling can be used. But the controlled synthesis of SACs is essential for this type of study, which is very challenging to date. Furthermore, the limited access to high-end facilities such as synchrotrons, specific software and supercomputers are other causes that hinder computational modeling studies.

7.2.10 Tuning the size of HNB-1

HNB-1 is synthesized by pyrolyzing ZIF-8@KTA. By controlling the size of ZIF-8, the size of HNB-1 can be tuned (Figure 7.8).³⁷⁵ In this thesis HNB-1 was used for supercapacitor electrodes. The performance of supercapacitor electrodes can be improved by tuning the pore size to fit the size of electrolyte ions. HNB with optimum pore size can be synthesized by size-controlled synthesis to enhance the performance of supercapacitors.³⁷⁶⁻³⁷⁸ Moreover, the ability to synthesize HNB with narrow pore size distribution with this method is an additional advantage that improves the performance of electrode.³⁷⁸⁻³⁷⁹

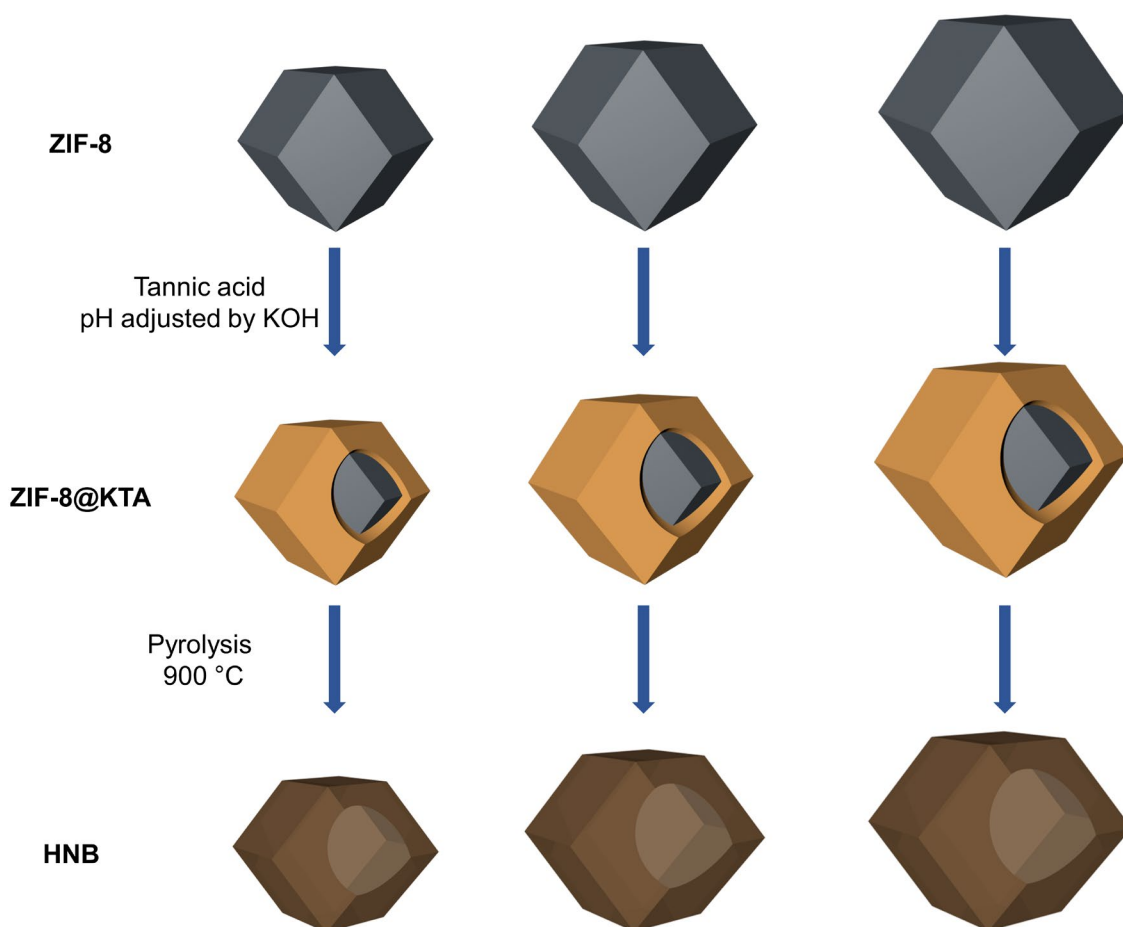


Figure 7.8: Tuning the size of HNB-1.

7.2.11 Synthesis of multi-shell HNB-1

HNB-1 was synthesized by pyrolysis of ZIF-8@KTA. An attempt can be made for the synthesis of multi-shell HNB using this method. After the KTA coating ZIF-8@KTA can be soaked in a zinc ion solution for the introduction of zinc ions to the KTA layer. Then immersing the resulting ZIF-8@ZnTA in a 2-methylimidazole solution will result in another layer of ZIF-8 over the material; ZIF-8@TA@ZIF-8. The KTA coating, introduction of zinc and making ZIF-8 layer by soaking in a solution of 2-methylimidazole can be repeated to obtain a preferred number of layers. The pyrolysis of this material will result in multi-shell hollow nanoboxes (Figure 7.9).

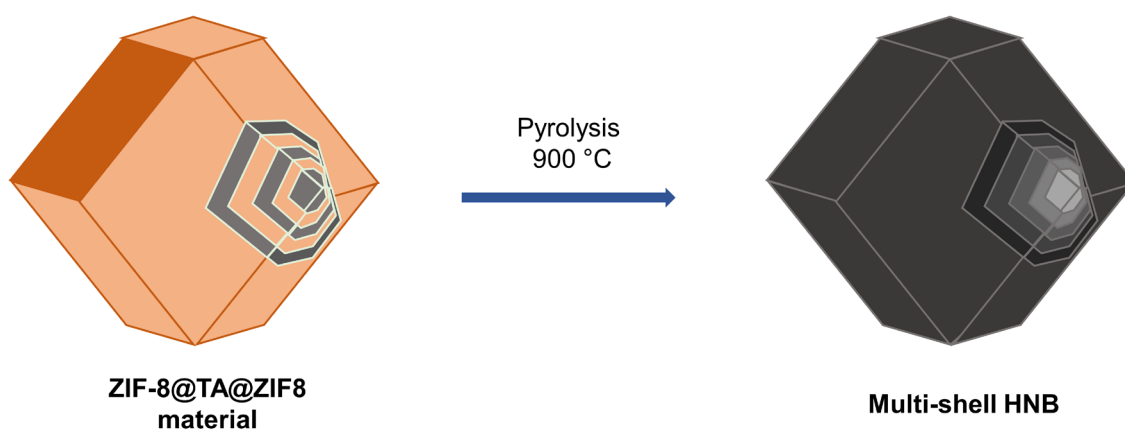


Figure 7.9: Synthesis of multi-shell HNB-1.

7.2.12 Tuning the size of HNB-2

HNB-2 was synthesized by partial pyrolysis of ZIF-8 and washing off the ZIF-8 in the core. Different sizes of HNB-2 can be synthesized by changing the size of ZIF-8 and the potential of using them in sensing applications can be explored (Figure 7.10).³⁸⁰⁻³⁸¹

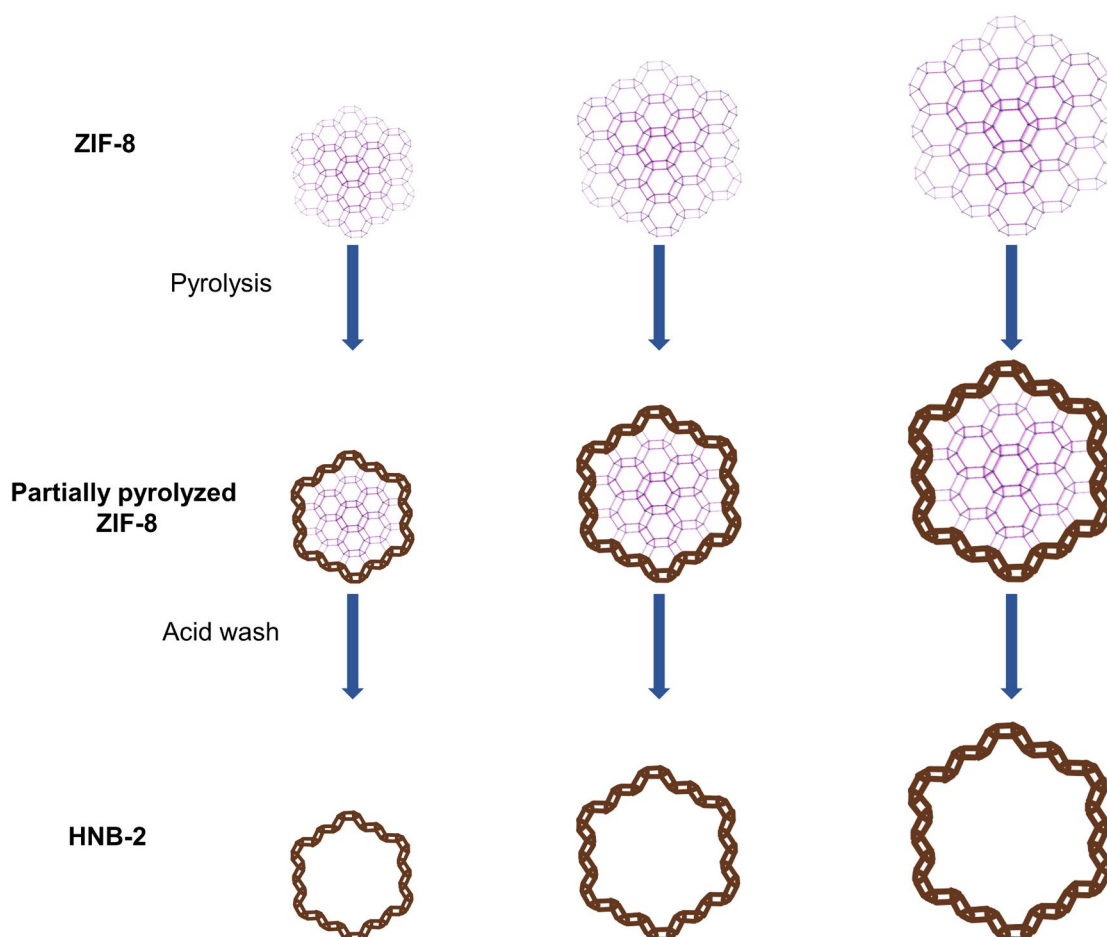


Figure 7.10: Tuning the size of HNB-2.

References

1. Kitagawa, S.; Kitaura, R.; Noro, S. i., Functional porous coordination polymers. *Angew. Chem. Int. Ed.* **2004**, *43*, 2334.
2. Kesanli, B.; Lin, W., Chiral porous coordination networks: rational design and applications in enantioselective processes. *Coord. Chem. Rev.* **2003**, *246*, 305.
3. Park, K. S.; Ni, Z.; Côté, A. P.; Choi, J. Y.; Huang, R.; Uribe-Romo, F. J.; Chae, H. K.; O’Keeffe, M.; Yaghi, O. M., Exceptional chemical and thermal stability of zeolitic imidazolate frameworks. *PANS* **2006**, *103*, 10186.
4. Wang, X.-S.; Ma, S.; Sun, D.; Parkin, S.; Zhou, H.-C., A mesoporous metal–organic framework with permanent porosity. *J. Am. Chem. Soc.* **2006**, *128*, 16474.
5. Férey, G.; Mellot-Draznieks, C.; Serre, C.; Millange, F.; Dutour, J.; Surblé, S.; Margiolaki, I., A chromium terephthalate-based solid with unusually large pore volumes and surface area. *Science* **2005**, *309*, 2040.
6. Chui, S. S.-Y.; Lo, S. M.-F.; Charmant, J. P.; Orpen, A. G.; Williams, I. D., A chemically functionalizable nanoporous material [Cu₃(TMA)₂(H₂O)₃]. *Science* **1999**, *283*, 1148.
7. Liu, L.; Zhou, T.-Y.; Telfer, S. G., Modulating the performance of an asymmetric organocatalyst by tuning its spatial environment in a metal–organic framework. *J. Am. Chem. Soc.* **2017**, *139*, 13936.
8. Greenaway, A.; Gonzalez - Santiago, B.; Donaldson, P. M.; Frogley, M. D.; Cinque, G.; Sotelo, J.; Moggach, S.; Shiko, E.; Brandani, S.; Howe, R. F., In situ Synchrotron IR Microspectroscopy of CO₂ Adsorption on Single Crystals of the Functionalized MOF Sc₂(BDC-NH₂)₃. *Angew. Chem. Int. Ed.* **2014**, *53*, 13483.
9. Taylor, M. K.; Runčevski, T. e.; Oktawiec, J.; Gonzalez, M. I.; Siegelman, R. L.; Mason, J. A.; Ye, J.; Brown, C. M.; Long, J. R., Tuning the adsorption-induced phase change in the flexible metal–organic framework Co (bdp). *J. Am. Chem. Soc.* **2016**, *138*, 15019.
10. Ren, H.-Y.; Zhang, X.-M., Enhanced Selective CO₂ Capture upon Incorporation of Dimethylformamide in the Cobalt Metal–Organic Framework [Co₃(OH)₂(btca)₂]. *Energy Fuels* **2016**, *30*, 526.
11. O’Keeffe, M.; Peskov, M., Ramsden., SJ; Yaghi, OM. *Acc. Chem. Res* **2008**, *41*, 1782.
12. Batten, S. R.; Champness, N. R.; Chen, X.-M.; Garcia-Martinez, J.; Kitagawa, S.; Öhrström, L.; O’Keeffe, M.; Suh, M. P.; Reedijk, J., Terminology of metal–organic frameworks and coordination polymers (IUPAC Recommendations 2013). *Pure Appl. Chem.* **2013**, *85*, 1715.
13. Hoskins, B. F.; Robson, R., Design and construction of a new class of scaffolding-like materials comprising infinite polymeric frameworks of 3D-linked molecular rods. A reappraisal of the zinc cyanide and cadmium cyanide structures and the synthesis and

- structure of the diamond-related frameworks $[N(CH_3)_4][Cu(I)Zn(II)(CN)_4]$ and CuI [4, 4', 4'', 4'''-tetracyanotetraphenylmethane] $BF_4 \cdot xC_6H_5NO_2$. *J. Am. Chem. Soc.* **1990**, *112*, 1546.
14. Kondo, M.; Yoshitomi, T.; Matsuzaka, H.; Kitagawa, S.; Seki, K., Three - Dimensional Framework with Channeling Cavities for Small Molecules: $\{[M_2(4, 4 - bpy)_3(NO_3)_4] \cdot xH_2O\}_n$ (M = Co, Ni, Zn). *Angew. Chem. Int. Ed.* **1997**, *36*, 1725.
 15. Li, H.; Eddaoudi, M.; O'Keeffe, M.; Yaghi, O. M., Design and synthesis of an exceptionally stable and highly porous metal-organic framework. *Nature* **1999**, *402*, 276.
 16. Moghadam, P. Z.; Li, A.; Wiggin, S. B.; Tao, A.; Maloney, A. G.; Wood, P. A.; Ward, S. C.; Fairen-Jimenez, D., Development of a Cambridge Structural Database subset: a collection of metal-organic frameworks for past, present, and future. *Chem. Mater.* **2017**, *29*, 2618.
 17. Eddaoudi, M.; Kim, J.; Rosi, N.; Vodak, D.; Wachter, J.; O'Keeffe, M.; Yaghi, O. M., Systematic design of pore size and functionality in isorecticular MOFs and their application in methane storage. *Science* **2002**, *295*, 469.
 18. Huang, X. C.; Lin, Y. Y.; Zhang, J. P.; Chen, X. M., Ligand - directed strategy for zeolite - type metal - organic frameworks: zinc (II) imidazoles with unusual zeolitic topologies. *Angew. Chem. Int. Ed.* **2006**, *45*, 1557.
 19. Noh, K.; Lee, J.; Kim, J., Compositions and structures of zeolitic imidazolate frameworks. *Isr. J. Chem.* **2018**, *58*, 1075.
 20. Bhattacharjee, S.; Jang, M.-S.; Kwon, H.-J.; Ahn, W.-S., Zeolitic imidazolate frameworks: synthesis, functionalization, and catalytic/adsorption applications. *Catal. Surv. Asia* **2014**, *18*, 101.
 21. Phan, A.; Doonan, C. J.; Uribe-Romo, F. J.; Knobler, C. B.; O'keeffe, M.; Yaghi, O. M., Synthesis, structure, and carbon dioxide capture properties of zeolitic imidazolate frameworks. *Acc. Chem. Res.* **2009**, *43*, 58.
 22. Banerjee, R.; Phan, A.; Wang, B.; Knobler, C.; Furukawa, H.; O'Keeffe, M.; Yaghi, O. M., High-throughput synthesis of zeolitic imidazolate frameworks and application to CO₂ capture. *Science* **2008**, *319*, 939.
 23. Nune, S. K.; Thallapally, P. K.; Dohnalkova, A.; Wang, C.; Liu, J.; Exarhos, G. J., Synthesis and properties of nano zeolitic imidazolate frameworks. *Chem. Commun.* **2010**, *46*, 4878.
 24. Bao, Q.; Lou, Y.; Xing, T.; Chen, J., Rapid synthesis of zeolitic imidazolate framework-8 (ZIF-8) in aqueous solution via microwave irradiation. *Inorg. Chem. Commun.* **2013**, *37*, 170.
 25. Seoane, B.; Zamaro, J. M.; Tellez, C.; Coronas, J., Sonocrystallization of zeolitic imidazolate frameworks (ZIF-7, ZIF-8, ZIF-11 and ZIF-20). *CrystEngComm* **2012**, *14*, 3103.
 26. Tanaka, S.; Kida, K.; Nagaoka, T.; Ota, T.; Miyake, Y., Mechanochemical dry conversion of zinc oxide to zeolitic imidazolate framework. *Chem. Commun.* **2013**, *49*, 7884.

27. Lin, J.-B.; Lin, R.-B.; Cheng, X.-N.; Zhang, J.-P.; Chen, X.-M., Solvent/additive-free synthesis of porous/zeolitic metal azolate frameworks from metal oxide/hydroxide. *Chem. Commun.* **2011**, *47*, 9185.
28. Shi, Q.; Chen, Z.; Song, Z.; Li, J.; Dong, J., Synthesis of ZIF - 8 and ZIF - 67 by steam - assisted conversion and an investigation of their tribological behaviors. *Angew. Chem.* **2011**, *123*, 698.
29. Faustini, M.; Kim, J.; Jeong, G.-Y.; Kim, J. Y.; Moon, H. R.; Ahn, W.-S.; Kim, D.-P., Microfluidic approach toward continuous and ultrafast synthesis of metal–organic framework crystals and hetero structures in confined microdroplets. *J. Am. Chem. Soc.* **2013**, *135*, 14619.
30. Martinez Joaristi, A.; Juan-Alcañiz, J.; Serra-Crespo, P.; Kapteijn, F.; Gascon, J., Electrochemical synthesis of some archetypical Zn²⁺, Cu²⁺, and Al³⁺ metal organic frameworks. *Cryst. Growth Des.* **2012**, *12*, 3489.
31. Taheri, M.; Enge, T. G.; Tsuzuki, T., Water stability of cobalt doped ZIF-8: a quantitative study using optical analyses. *Mater. Today Chem.* **2020**, *16*, 100231.
32. Zeeshan, M.; Keskin, S.; Uzun, A., Enhancing CO₂/CH₄ and CO₂/N₂ separation performances of ZIF-8 by post-synthesis modification with [BMIM][SCN]. *Polyhedron* **2018**, *155*, 485.
33. Ren, G.; Li, Z.; Yang, W.; Faheem, M.; Xing, J.; Zou, X.; Pan, Q.; Zhu, G.; Du, Y., ZnO@ ZIF-8 core-shell microspheres for improved ethanol gas sensing. *Sens. Actuators B Chem.* **2019**, *284*, 421.
34. Bagheri, N.; Khataee, A.; Hassanzadeh, J.; Samaei, L., Highly sensitive chemiluminescence sensing system for organophosphates using mimic LDH supported ZIF-8 nanocomposite. *Sens. Actuators B Chem.* **2019**, *284*, 220.
35. Chizallet, C.; Lazare, S.; Bazer-Bachi, D.; Bonnier, F.; Lecocq, V.; Soyer, E.; Quoineaud, A.-A.; Bats, N., Catalysis of transesterification by a nonfunctionalized metal–organic framework: acido-basicity at the external surface of ZIF-8 probed by FTIR and ab initio calculations. *J. Am. Chem. Soc.* **2010**, *132*, 12365.
36. Hu, Y. H.; Zhang, L., Hydrogen storage in metal–organic frameworks. *Adv. Mater.* **2010**, *22*, E117.
37. Vitillo, J. G.; Regli, L.; Chavan, S.; Ricchiardi, G.; Spoto, G.; Dietzel, P. D.; Bordiga, S.; Zecchina, A., Role of exposed metal sites in hydrogen storage in MOFs. *J. Am. Chem. Soc.* **2008**, *130*, 8386.
38. Yang, J.; Grzech, A.; Mulder, F. M.; Dingemans, T. J., Methyl modified MOF-5: a water stable hydrogen storage material. *Chem. Comm.* **2011**, *47*, 5244.
39. Li, J.-R.; Kuppler, R. J.; Zhou, H.-C., Selective gas adsorption and separation in metal–organic frameworks. *Chem. Soc. Rev.* **2009**, *38*, 1477.
40. Liang, Z.; Marshall, M.; Chaffee, A. L., CO₂ Adsorption-Based Separation by Metal Organic Framework (Cu-BTC) versus Zeolite (13X). *Energy Fuels* **2009**, *23*, 2785.

41. Lee, J.; Farha, O. K.; Roberts, J.; Scheidt, K. A.; Nguyen, S. T.; Hupp, J. T., Metal-organic framework materials as catalysts. *Chem. Soc. Rev.* **2009**, *38*, 1450.
42. Ma, L.; Abney, C.; Lin, W., Enantioselective catalysis with homochiral metal-organic frameworks. *Chem. Soc. Rev.* **2009**, *38*, 1248.
43. Corma, A.; García, H.; Llabrés i Xamena, F. X., Engineering Metal Organic Frameworks for Heterogeneous Catalysis. *Chem. Rev.* **2010**, *110*, 4606.
44. Kumar, P.; Deep, A.; Kim, K.-H., Metal organic frameworks for sensing applications. *Trends Analyt. Chem.* **2015**, *73*, 39.
45. Cui, Y.; Chen, B.; Qian, G., Lanthanide metal-organic frameworks for luminescent sensing and light-emitting applications. *Coordin. Chem. Rev.* **2014**, *273*, 76.
46. Wales, D. J.; Grand, J.; Ting, V. P.; Burke, R. D.; Edler, K. J.; Bowen, C. R.; Mintova, S.; Burrows, A. D., Gas sensing using porous materials for automotive applications. *Chem. Soc. Rev.* **2015**, *44*, 4290.
47. Kepert, C. J., Advanced functional properties in nanoporous coordination framework materials. *Chem. Comm.* **2006**, 695.
48. Rosseinsky, M., Recent developments in metal-organic framework chemistry: design, discovery, permanent porosity and flexibility. *Micropor. Mesopor. Mat.* **2004**, *1*, 15.
49. Farha, O.; Eryazici, I.; Jeong, N.; Hauser, B.; Wilmer, C.; Sarjeant, A., a.; Snurr, RQ; Nguyen, ST; Yazaydin, AO; Hupp, JT. *J. Am. Chem. Soc.* **2012**, *134*, 15016.
50. Koh, K.; Wong-Foy, A. G.; Matzger, A. J., A porous coordination copolymer with over 5000 m²/g BET surface area. *J. Am. Chem. Soc.* **2009**, *131*, 4184.
51. Chae, H. K.; Siberio-Perez, D. Y.; Kim, J.; Go, Y.; Eddaoudi, M.; Matzger, A. J.; O'keeffe, M.; Yaghi, O. M., A route to high surface area, porosity and inclusion of large molecules in crystals. *Nature* **2004**, *427*, 523.
52. Rosi, N. L.; Eckert, J.; Eddaoudi, M.; Vodak, D. T.; Kim, J.; O'keeffe, M.; Yaghi, O. M., Hydrogen storage in microporous metal-organic frameworks. *Science* **2003**, *300*, 1127.
53. Murray, L. J.; Dincă, M.; Long, J. R., Hydrogen storage in metal-organic frameworks. *Chem. Soc. Rev.* **2009**, *38*, 1294.
54. Latroche, M.; Surblé, S.; Serre, C.; Mellot-Draznieks, C.; Llewellyn, P. L.; Lee, J. H.; Chang, J. S.; Jung, S. H.; Férey, G., Hydrogen storage in the giant-pore metal-organic frameworks MIL-100 and MIL-101. *Angew. Chem.* **2006**, *45*, 8227.
55. Ma, S.; Eckert, J.; Forster, P. M.; Yoon, J. W.; Hwang, Y. K.; Chang, J.-S.; Collier, C. D.; Parise, J. B.; Zhou, H.-C., Further investigation of the effect of framework catenation on hydrogen uptake in metal-organic frameworks. *J. Am. Chem. Soc.* **2008**, *130*, 15896.
56. Möllmer, J.; Möller, A.; Dreisbach, F.; Gläser, R.; Staudt, R., High pressure adsorption of hydrogen, nitrogen, carbon dioxide and methane on the metal-organic framework HKUST-1. *Microporous Mesoporous Mater.* **2011**, *138*, 140.

57. Millward, A. R.; Yaghi, O. M., Metal–organic frameworks with exceptionally high capacity for storage of carbon dioxide at room temperature. *J. Am. Chem. Soc.* **2005**, *127*, 17998.
58. Llewellyn, P. L.; Bourrelly, S.; Serre, C.; Vimont, A.; Daturi, M.; Hamon, L.; De Weireld, G.; Chang, J.-S.; Hong, D.-Y.; Kyu Hwang, Y., High uptakes of CO₂ and CH₄ in mesoporous metal–organic frameworks MIL-100 and MIL-101. *Langmuir* **2008**, *24*, 7245.
59. Bae, Y.-S.; Farha, O. K.; Hupp, J. T.; Snurr, R. Q., Enhancement of CO₂/N₂ selectivity in a metal-organic framework by cavity modification. *J. Mater. Chem.* **2009**, *19*, 2131.
60. Wang, Z.; Cohen, S. M., Postsynthetic modification of metal–organic frameworks. *Chem. Soc. Rev.* **2009**, *38*, 1315.
61. Khan, N. A.; Hasan, Z.; Jhung, S. H., Adsorptive removal of hazardous materials using metal-organic frameworks (MOFs): a review. *J. Hazard. Mater.* **2013**, *244*, 444.
62. He, H.; Li, R.; Yang, Z.; Chai, L.; Jin, L.; Alhassan, S. I.; Ren, L.; Wang, H.; Huang, L., Preparation of MOFs and MOFs derived materials and their catalytic application in air pollution: A review. *Catal. Today* **2021**, *375*, 10.
63. Bavykina, A.; Kolobov, N.; Khan, I. S.; Bau, J. A.; Ramirez, A.; Gascon, J., Metal–organic frameworks in heterogeneous catalysis: recent progress, new trends, and future perspectives. *Chem. Rev.* **2020**, *120*, 8468.
64. Sharma, V. K.; Feng, M., Water depollution using metal-organic frameworks-catalyzed advanced oxidation processes: a review. *J. Hazard. Mater.* **2019**, *372*, 3.
65. Wang, H.; Rassa, P.; Wang, X.; Li, H.; Wang, X.; Wang, X.; Feng, X.; Yin, A.; Li, P.; Jin, X., An Iron-Containing Metal–Organic Framework as a Highly Efficient Catalyst for Ozone Decomposition. *Angew. Chem. Int. Ed.* **2018**, *57*, 16416.
66. Nikseresht, A.; Ghasemi, S.; Parak, S., [Cu₃(BTC)₂]: A metal–organic framework as an environment-friendly and economically catalyst for the synthesis of tacrine analogues by Friedländer reaction under conventional and ultrasound irradiation. *Polyhedron* **2018**, *151*, 112.
67. Chakarova, K.; Strauss, I.; Mihaylov, M.; Drenchev, N.; Hadjiivanov, K., Evolution of acid and basic sites in UiO-66 and UiO-66-NH₂ metal-organic frameworks: FTIR study by probe molecules. *Microporous Mesoporous Mater.* **2019**, *281*, 110.
68. Caratelli, C.; Hajek, J.; Cirujano, F. G.; Waroquier, M.; i Xamena, F. X. L.; Van Speybroeck, V., Nature of active sites on UiO-66 and beneficial influence of water in the catalysis of Fischer esterification. *J. Catal.* **2017**, *352*, 401.
69. Kuwahara, Y.; Kango, H.; Yamashita, H., Catalytic transfer hydrogenation of biomass-derived levulinic acid and its esters to γ -valerolactone over sulfonic acid-functionalized UiO-66. *ACS Sustain. Chem. Eng.* **2017**, *5*, 1141.

70. Yang, D.; Ortuño, M. A.; Bernales, V.; Cramer, C. J.; Gagliardi, L.; Gates, B. C., Structure and dynamics of Zr₆O₈ metal–organic framework node surfaces probed with ethanol dehydration as a catalytic test reaction. *J. Am. Chem. Soc.* **2018**, *140*, 3751.
71. Zwoliński, K. M.; Chmielewski, M. J., TEMPO-appended metal–organic frameworks as highly active, selective, and reusable catalysts for mild aerobic oxidation of Alcohols. *ACS Appl. Mater. Interfaces* **2017**, *9*, 33956.
72. Zhao, T.; Dong, M.; Yang, L.; Liu, Y., Synthesis of stable hierarchical MIL-101 (Cr) with enhanced catalytic activity in the oxidation of indene. *Catalysts* **2018**, *8*, 394.
73. Epp, K.; Semrau, A. L.; Cokoja, M.; Fischer, R. A., Dual Site Lewis-Acid Metal–Organic Framework Catalysts for CO₂ Fixation: Counteracting Effects of Node Connectivity, Defects and Linker Metalation. *ChemCatChem* **2018**, *10*, 3506.
74. Zhou, T.-Y.; Auer, B.; Lee, S. J.; Telfer, S. G., Catalysts confined in programmed framework pores enable new transformations and tune reaction efficiency and selectivity. *J. Am. Chem. Soc.* **2019**, *141*, 1577.
75. Bhin, K. M.; Tharun, J.; Roshan, K. R.; Kim, D.-W.; Chung, Y.; Park, D.-W., Catalytic performance of zeolitic imidazolate framework ZIF-95 for the solventless synthesis of cyclic carbonates from CO₂ and epoxides. *J. CO₂ Util.* **2017**, *17*, 112.
76. An, B.; Zeng, L.; Jia, M.; Li, Z.; Lin, Z.; Song, Y.; Zhou, Y.; Cheng, J.; Wang, C.; Lin, W., Molecular iridium complexes in metal–organic frameworks catalyze CO₂ hydrogenation via concerted proton and hydride transfer. *J. Am. Chem. Soc.* **2017**, *139*, 17747.
77. Chen, L.; Luque, R.; Li, Y., Controllable design of tunable nanostructures inside metal–organic frameworks. *Chem. Soc. Rev.* **2017**, *46*, 4614.
78. Yu, J.; Mu, C.; Yan, B.; Qin, X.; Shen, C.; Xue, H.; Pang, H., Nanoparticle/MOF composites: preparations and applications. *Mater. Horiz.* **2017**, *4*, 557.
79. Hu, P.; Morabito, J. V.; Tsung, C.-K., Core–shell catalysts of metal nanoparticle core and metal–organic framework shell. *ACS Catal.* **2014**, *4*, 4409.
80. Xu, D.; Lv, H.; Liu, B., Encapsulation of metal nanoparticle catalysts within mesoporous zeolites and their enhanced catalytic performances: a review. *Front. Chem.* **2018**, *6*, 550.
81. Aguilera-Sigalat, J.; Bradshaw, D., Synthesis and applications of metal-organic framework–quantum dot (QD@ MOF) composites. *Coord. Chem. Rev.* **2016**, *307*, 267.
82. Chen, J.; Zhu, Y.; Kaskel, S., Porphyrin-Based Metal–Organic Frameworks for Biomedical Applications. *Angew. Chem. Int. Ed.* **2021**, *60*, 5010.
83. Li, Z.; Rayder, T. M.; Luo, L.; Byers, J. A.; Tsung, C.-K., Aperture-opening encapsulation of a transition metal catalyst in a metal–organic framework for CO₂ hydrogenation. *J. Am. Chem. Soc.* **2018**, *140*, 8082.
84. Kitao, T.; Zhang, Y.; Kitagawa, S.; Wang, B.; Uemura, T., Hybridization of MOFs and polymers. *Chem. Soc. Rev.* **2017**, *46*, 3108.

85. Samaniyan, M.; Mirzaei, M.; Khajavian, R.; Eshtiagh-Hosseini, H.; Streb, C., Heterogeneous catalysis by polyoxometalates in metal–organic frameworks. *ACS Catal.* **2019**, *9*, 10174.
86. Fujie, K.; Kitagawa, H., Ionic liquid transported into metal–organic frameworks. *Coord. Chem. Rev.* **2016**, *307*, 382.
87. Song, T.; Yu, J.; Cui, Y.; Yang, Y.; Qian, G., Encapsulation of dyes in metal–organic frameworks and their tunable nonlinear optical properties. *Dalton Trans.* **2016**, *45*, 4218.
88. Long, J.; Liu, H.; Wu, S.; Liao, S.; Li, Y., Selective oxidation of saturated hydrocarbons using Au–Pd alloy nanoparticles supported on metal–organic frameworks. *ACS Catal.* **2013**, *3*, 647.
89. Huang, G.; Yang, Q.; Xu, Q.; Yu, S. H.; Jiang, H. L., Polydimethylsiloxane coating for a palladium/MOF composite: highly improved catalytic performance by surface hydrophobization. *Angew. Chem.* **2016**, *128*, 7505.
90. Hausdorf, S.; Wagler, J.R.; Moßig, R.; Mertens, F. O., Proton and water activity-controlled structure formation in zinc carboxylate-based metal organic frameworks. *J. Phys. Chem. A* **2008**, *112*, 7567.
91. Vellingiri, K.; Philip, L.; Kim, K.-H., Metal–organic frameworks as media for the catalytic degradation of chemical warfare agents. *Coord. Chem. Rev.* **2017**, *353*, 159.
92. Johnson, B. A.; Beiler, A. M.; McCarthy, B. D.; Ott, S., Transport Phenomena: Challenges and Opportunities for Molecular Catalysis in Metal–Organic Frameworks. *J. Am. Chem. Soc.* **2020**, *142*, 11941.
93. Yang, X.-F.; Wang, A.; Qiao, B.; Li, J.; Liu, J.; Zhang, T., Single-atom catalysts: a new frontier in heterogeneous catalysis. *Acc. Chem. Res.* **2013**, *46*, 1740.
94. Wang, A.; Li, J.; Zhang, T., Heterogeneous single-atom catalysis. *Nat. Rev. Chem.* **2018**, *1*.
95. Guo, X.; Fang, G.; Li, G.; Ma, H.; Fan, H.; Yu, L.; Ma, C.; Wu, X.; Deng, D.; Wei, M., Direct, nonoxidative conversion of methane to ethylene, aromatics, and hydrogen. *Science* **2014**, *344*, 616.
96. Liang, S.; Hao, C.; Shi, Y., The power of single-atom catalysis. *ChemCatChem* **2015**, *7*, 2559.
97. Cui, X.; Li, W.; Ryabchuk, P.; Junge, K.; Beller, M., Bridging homogeneous and heterogeneous catalysis by heterogeneous single-metal-site catalysts. *Nat. Catal.* **2018**, *1*, 385.
98. Lou, Y.; Xu, J.; Zhang, Y.; Pan, C.; Dong, Y.; Zhu, Y., Metal-support interaction for heterogeneous catalysis: from nanoparticles to single atoms. *Mater. Today Nano* **2020**, 100093.
99. Chen, Y.; Ji, S.; Chen, C.; Peng, Q.; Wang, D.; Li, Y., Single-atom catalysts: Synthetic strategies and electrochemical applications. *Joule* **2018**, *2*, 1242.

100. Liu, P.; Zhao, Y.; Qin, R.; Mo, S.; Chen, G.; Gu, L.; Chevrier, D. M.; Zhang, P.; Guo, Q.; Zang, D., Photochemical route for synthesizing atomically dispersed palladium catalysts. *Science* **2016**, *352*, 797.
101. Wei, H.; Huang, K.; Wang, D.; Zhang, R.; Ge, B.; Ma, J.; Wen, B.; Zhang, S.; Li, Q.; Lei, M., Iced photochemical reduction to synthesize atomically dispersed metals by suppressing nanocrystal growth. *Nat. Commun.* **2017**, *8*, 1490.
102. Yan, H.; Cheng, H.; Yi, H.; Lin, Y.; Yao, T.; Wang, C.; Li, J.; Wei, S.; Lu, J., Single-atom Pd₁/graphene catalyst achieved by atomic layer deposition: remarkable performance in selective hydrogenation of 1,3-butadiene. *J. Am. Chem. Soc.* **2015**, *137*, 10484.
103. Qiao, B.; Wang, A.; Yang, X.; Allard, L. F.; Jiang, Z.; Cui, Y.; Liu, J.; Li, J.; Zhang, T., Single-atom catalysis of CO oxidation using Pt₁/FeO_x. *Nat. Chem.* **2011**, *3*, 634.
104. Wan, J.; Chen, W.; Jia, C.; Zheng, L.; Dong, J.; Zheng, X.; Wang, Y.; Yan, W.; Chen, C.; Peng, Q., Defect effects on TiO₂ nanosheets: stabilizing single atomic site Au and promoting catalytic properties. *Adv. Mater.* **2018**, *30*, 1705369.
105. Lu, J.; Aydin, C.; Browning, N. D.; Gates, B. C., Imaging isolated gold atom catalytic sites in zeolite NaY. *Angew. Chem.* **2012**, *124*, 5944.
106. Wang, N.; Sun, Q.; Bai, R.; Li, X.; Guo, G.; Yu, J., In situ confinement of ultrasmall Pd clusters within nanosized silicalite-1 zeolite for highly efficient catalysis of hydrogen generation. *J. Am. Chem. Soc.* **2016**, *138*, 7484.
107. Chen, Y.; Ji, S.; Wang, Y.; Dong, J.; Chen, W.; Li, Z.; Shen, R.; Zheng, L.; Zhuang, Z.; Wang, D., Isolated single iron atoms anchored on N-doped porous carbon as an efficient electrocatalyst for the oxygen reduction reaction. *Angew. Chem.* **2017**, *56*, 6937.
108. Wang, X.; Chen, W.; Zhang, L.; Yao, T.; Liu, W.; Lin, Y.; Ju, H.; Dong, J.; Zheng, L.; Yan, W., Uncoordinated amine groups of metal-organic frameworks to anchor single Ru sites as chemoselective catalysts toward the hydrogenation of quinoline. *J. Am. Chem. Soc.* **2017**, *139*, 9419.
109. Sa, Y. J.; Seo, D.-J.; Woo, J.; Lim, J. T.; Cheon, J. Y.; Yang, S. Y.; Lee, J. M.; Kang, D.; Shin, T. J.; Shin, H. S., A general approach to preferential formation of active Fe-N x sites in Fe-N/C electrocatalysts for efficient oxygen reduction reaction. *J. Am. Chem. Soc.* **2016**, *138*, 15046.
110. Chen, W.; Pei, J.; He, C. T.; Wan, J.; Ren, H.; Zhu, Y.; Wang, Y.; Dong, J.; Tian, S.; Cheong, W. C., Rational Design of Single Molybdenum Atoms Anchored on N-Doped Carbon for Effective Hydrogen Evolution Reaction. *Angew. Chem.* **2017**, *129*, 16302.
111. Choi, C. H.; Kim, M.; Kwon, H. C.; Cho, S. J.; Yun, S.; Kim, H.-T.; Mayrhofer, K. J.; Kim, H.; Choi, M., Tuning selectivity of electrochemical reactions by atomically dispersed platinum catalyst. *Nat. Commun.* **2016**, *7*, 10922.
112. Lucci, F. R.; Liu, J.; Marcinkowski, M. D.; Yang, M.; Allard, L. F.; Flytzani-Stephanopoulos, M.; Sykes, E. C. H., Selective hydrogenation of 1,3-butadiene on platinum-copper alloys at the single-atom limit. *Nat. Commun.* **2015**, *6*, 8550.

113. O'Neill, B. J.; Jackson, D. H.; Lee, J.; Canlas, C.; Stair, P. C.; Marshall, C. L.; Elam, J. W.; Kuech, T. F.; Dumesic, J. A.; Huber, G. W., Catalyst design with atomic layer deposition. *ACS Catal.* **2015**, *5*, 1804.
114. Jones, J.; Xiong, H.; DeLaRiva, A. T.; Peterson, E. J.; Pham, H.; Challa, S. R.; Qi, G.; Oh, S.; Wiebenga, M. H.; Hernández, X. I. P., Thermally stable single-atom platinum-on-ceria catalysts via atom trapping. *Science* **2016**, *353*, 150.
115. Yang, Q.; Yang, C. C.; Lin, C. H.; Jiang, H. L., Metal–Organic-Framework-Derived Hollow N-Doped Porous Carbon with Ultrahigh Concentrations of Single Zn Atoms for Efficient Carbon Dioxide Conversion. *Angew. Chem. Int. Ed.* **2019**, *58*, 3511.
116. Fan, L.; Liu, P. F.; Yan, X.; Gu, L.; Yang, Z. Z.; Yang, H. G.; Qiu, S.; Yao, X., Atomically isolated nickel species anchored on graphitized carbon for efficient hydrogen evolution electrocatalysis. *Nat. Commun.* **2016**, *7*, 1.
117. Yang, Y.; Mao, K.; Gao, S.; Huang, H.; Xia, G.; Lin, Z.; Jiang, P.; Wang, C.; Wang, H.; Chen, Q., O-, N- atoms-coordinated Mn cofactors within a graphene framework as bioinspired oxygen reduction reaction electrocatalysts. *Adv. Mater.* **2018**, *30*, 1801732.
118. Zhang, H.; Hwang, S.; Wang, M.; Feng, Z.; Karakalos, S.; Luo, L.; Qiao, Z.; Xie, X.; Wang, C.; Su, D., Single atomic iron catalysts for oxygen reduction in acidic media: particle size control and thermal activation. *J. Am. Chem. Soc.* **2017**, *139*, 14143.
119. Wang, H.; Wang, Y.; Li, Y.; Lan, X.; Ali, B.; Wang, T., Highly Efficient Hydrogenation of Nitroarenes by N-Doped Carbon-Supported Cobalt Single-Atom Catalyst in Ethanol/Water Mixed Solvent. *ACS Appl. Mater. Interfaces* **2020**, *12*, 34021.
120. Li, X.; Surkus, A. E.; Rabeah, J.; Anwar, M.; Dastagir, S.; Junge, H.; Brückner, A.; Beller, M., Cobalt Single-Atom Catalysts with High Stability for Selective Dehydrogenation of Formic Acid. *Angew. Chem. Int. Ed.* **2020**, *59*, 15849.
121. Yin, P.; Yao, T.; Wu, Y.; Zheng, L.; Lin, Y.; Liu, W.; Ju, H.; Zhu, J.; Hong, X.; Deng, Z., Single cobalt atoms with precise N-coordination as superior oxygen reduction reaction catalysts. *Angew. Chem.* **2016**, *128*, 10958.
122. Zheng, Y.; Qiao, S.-Z., Metal-organic framework assisted synthesis of single-atom catalysts for energy applications. *Nat. Sci. Rev.* **2018**, *5*, 626.
123. Chen, W.; Pei, J.; He, C. T.; Wan, J.; Ren, H.; Wang, Y.; Dong, J.; Wu, K.; Cheong, W. C.; Mao, J., Single tungsten atoms supported on MOF-derived N-doped carbon for robust electrochemical hydrogen evolution. *Adv. Mater.* **2018**, *30*, 1800396.
124. Jiao, L.; Wan, G.; Zhang, R.; Zhou, H.; Yu, S. H.; Jiang, H. L., From metal–organic frameworks to single - atom Fe implanted N - doped porous carbons: efficient oxygen reduction in both alkaline and acidic media. *Angew. Chem. Int. Ed.* **2018**, *57*, 8525.
125. Lin, D.; Jiang, R.; Ma, P.; Hong, S.; Cheng, Z.; Guo, J.; Xu, R.; Lin, Y.; Zhao, Y.; Yin, X., Nickel-Based Single-Atom Catalyst toward Triiodide Reduction Reaction in Hybrid Photovoltaics. *ACS Sustain. Chem. Eng.* **2021**.

126. Wang, J.; Han, G.; Wang, L.; Du, L.; Chen, G.; Gao, Y.; Ma, Y.; Du, C.; Cheng, X.; Zuo, P., ZIF-8 with ferrocene encapsulated: a promising precursor to single - atom Fe embedded nitrogen - doped carbon as highly efficient catalyst for oxygen electroreduction. *Small* **2018**, *14*, 1704282.
127. Zhao, C.; Dai, X.; Yao, T.; Chen, W.; Wang, X.; Wang, J.; Yang, J.; Wei, S.; Wu, Y.; Li, Y., Ionic exchange of metal–organic frameworks to access single nickel sites for efficient electroreduction of CO₂. *J. Am. Chem. Soc.* **2017**, *139*, 8078.
128. Lu, P.; Yang, Y.; Yao, J.; Wang, M.; Dipazir, S.; Yuan, M.; Zhang, J.; Wang, X.; Xie, Z.; Zhang, G., Facile synthesis of single-nickel-atomic dispersed N-doped carbon framework for efficient electrochemical CO₂ reduction. *App. Catal. B: Environ.* **2019**, *241*, 113.
129. Liu, D.; Li, J. C.; Ding, S.; Lyu, Z.; Feng, S.; Tian, H.; Huyan, C.; Xu, M.; Li, T.; Du, D., 2D Single-Atom Catalyst with Optimized Iron Sites Produced by Thermal Melting of Metal - Organic Frameworks for Oxygen Reduction Reaction. *Small Methods* **2020**, *4*, 1900827.
130. Yang, H.; Wu, Y.; Li, G.; Lin, Q.; Hu, Q.; Zhang, Q.; Liu, J.; He, C., Scalable production of efficient single-atom copper decorated carbon membranes for CO₂ electroreduction to methanol. *J. Am. Chem. Soc.* **2019**, *141*, 12717.
131. Hou, C. C.; Zou, L.; Sun, L.; Zhang, K.; Liu, Z.; Li, Y.; Li, C.; Zou, R.; Yu, J.; Xu, Q., Single-Atom Iron Catalysts on Overhang-Eave Carbon Cages for High-Performance Oxygen Reduction Reaction. *Angew. Chem.* **2020**, *132*, 7454.
132. Chen, Y.; Ji, S.; Zhao, S.; Chen, W.; Dong, J.; Cheong, W.-C.; Shen, R.; Wen, X.; Zheng, L.; Rykov, A. I., Enhanced oxygen reduction with single-atomic-site iron catalysts for a zinc-air battery and hydrogen-air fuel cell. *Nat. Commun.* **2018**, *9*, 1.
133. Wei, S.; Li, A.; Liu, J.-C.; Li, Z.; Chen, W.; Gong, Y.; Zhang, Q.; Cheong, W.-C.; Wang, Y.; Zheng, L., Direct observation of noble metal nanoparticles transforming to thermally stable single atoms. *Nat. Nanotechnol.* **2018**, *13*, 856.
134. Yang, J.; Qiu, Z.; Zhao, C.; Wei, W.; Chen, W.; Li, Z.; Qu, Y.; Dong, J.; Luo, J.; Li, Z., In situ thermal atomization to convert supported nickel nanoparticles into surface-bound nickel single-atom catalysts. *Angew. Chem. Int. Ed.* **2018**, *57*, 14095.
135. Qu, Y.; Li, Z.; Chen, W.; Lin, Y.; Yuan, T.; Yang, Z.; Zhao, C.; Wang, J.; Zhao, C.; Wang, X., Direct transformation of bulk copper into copper single sites via emitting and trapping of atoms. *Nat. Catal.* **2018**, *1*, 781.
136. Pennycook, S.; Jesson, D., High-resolution Z-contrast imaging of crystals. *Ultramicroscopy* **1991**, *37*, 14.
137. Hollander, J. M.; Shirley, D. A.; Stoicheff, B. P., The 1981 nobel prize in physics. *Science* **1981**, *214*, 629.
138. Nefedov, A.; Wöll, C., Advanced applications of NEXAFS spectroscopy for functionalized surfaces. In *Surface Science Techniques*, Springer: 2013; pp 277.

139. Filatova, E.; Sokolov, A., Effect of reflection and refraction on NEXAFS spectra measured in TEY mode. *J. Synchrotron Radiat.* **2018**, *25*, 232.
140. Chen, J. G., NEXAFS investigations of transition metal oxides, nitrides, carbides, sulfides and other interstitial compounds. *Surf. Sci. Rep.* **1997**, *30*, 1.
141. Hähner, G., Near edge X-ray absorption fine structure spectroscopy as a tool to probe electronic and structural properties of thin organic films and liquids. *Chem. Soc. Rev.* **2006**, *35*, 1244.
142. Ade, H.; Kirz, J.; Rarback, H.; Hulbert, S.; Johnson, E.; Kern, D.; Chang, P.; Vladimirsky, Y., Possibilities for a Scanning Photoemission Microscope at the NSLS. In *X-Ray Microscopy II*, Springer: 1988; pp 280.
143. Yu, L.; Yu, X. Y.; Lou, X. W., The Design and Synthesis of Hollow Micro-/Nanostructures: Present and Future Trends. *Adv. Mater.* **2018**, *30*, 1800939.
144. Yu, L.; Hu, H.; Wu, H. B.; Lou, X. W., Complex hollow nanostructures: synthesis and energy-related applications. *Adv. Mater.* **2017**, *29*, 1604563.
145. Soares, S. F.; Fernandes, T.; Daniel-da-Silva, A. L.; Trindade, T., The controlled synthesis of complex hollow nanostructures and prospective applications. *Proc. R. Soc. A* **2019**, *475*, 20180677.
146. Yec, C. C.; Zeng, H. C., Synthesis of complex nanomaterials via Ostwald ripening. *J. Mater. Chem. A* **2014**, *2*, 4843.
147. Gupta, A.; Shervani, S.; Rani, P.; Sivakumar, S.; Balani, K.; Subramaniam, A., Hybrid hollow structures for hydrogen storage. *Int. J. Hydrog. Energy* **2020**, *45*, 24076.
148. Wang, J.; Wang, H.; Li, F.; Xie, S.; Xu, G.; She, Y.; Leung, M. K.; Liu, T., Oxidizing solid Co into hollow Co₃O₄ within electrospun (carbon) nanofibers towards enhanced lithium storage performance. *J. Mater. Chem. A* **2019**, *7*, 3024.
149. Yu, K.; Ling, M.; Liang, J.; Liang, C., Formation of TiO₂ hollow spheres through nanoscale Kirkendall effect and their lithium storage and photocatalytic properties. *Chem. Phys.* **2019**, *517*, 222.
150. Lou, X. W.; Wang, Y.; Yuan, C.; Lee, J. Y.; Archer, L. A., Template-free synthesis of SnO₂ hollow nanostructures with high lithium storage capacity. *Adv. Mater.* **2006**, *18*, 2325.
151. Geng, H.; Guo, Y.; Ding, X.; Wang, H.; Zhang, Y.; Wu, X.; Jiang, J.; Zheng, J.; Yang, Y.; Gu, H., Porous cubes constructed by cobalt oxide nanocrystals with graphene sheet coatings for enhanced lithium storage properties. *Nanoscale* **2016**, *8*, 7688.
152. Lee, J.; Park, J. C.; Song, H., A nanoreactor framework of a Au@ SiO₂ yolk/shell structure for catalytic reduction of *p*-nitrophenol. *Adv. Mater.* **2008**, *20*, 1523.
153. Zhang, Q.; Zhang, T.; Ge, J.; Yin, Y., Permeable silica shell through surface-protected etching. *Nano Lett.* **2008**, *8*, 2867.
154. An, K.; Hyeon, T., Synthesis and biomedical applications of hollow nanostructures. *Nano Today* **2009**, *4*, 359.

155. Mondal, S.; Hoang, G.; Manivasagan, P.; Kim, H.; Oh, J., Nanostructured hollow hydroxyapatite fabrication by carbon templating for enhanced drug delivery and biomedical applications. *Ceram. Int.* **2019**, *45*, 17081.
156. Chen, J.; Li, X.; Sun, Y.; Hu, Y.; Peng, Y.; Li, Y.; Yin, G.; Liu, H.; Xu, J.; Zhong, S., Synthesis of size-tunable hollow polypyrrole nanostructures and their assembly into folate-targeting and pH-responsive anticancer drug-delivery agents. *Chem Eur J* **2017**, *23*, 17279.
157. Lee, J. E.; Lim, C. K.; Park, H. J.; Song, H.; Choi, S.-Y.; Lee, D.-S., ZnO–CuO Core-Hollow Cube Nanostructures for Highly Sensitive Acetone Gas Sensors at the ppb Level. *ACS Appl. Mater. Interfaces* **2020**, *12*, 35688.
158. Graniel, O.; Iatsunskyi, I.; Coy, E.; Humbert, C.; Barbillon, G.; Michel, T.; Maurin, D.; Balme, S.; Miele, P.; Bechelany, M., Au-covered hollow urchin-like ZnO nanostructures for surface-enhanced Raman scattering sensing. *J. Mater. Chem. C* **2019**, *7*, 15066.
159. Joseph, D.; Kwak, C. H.; Huh, Y. S.; Han, Y.-K., Synthesis of AuAg@ Ag core@ shell hollow cubic nanostructures as SERS substrates for attomolar chemical sensing. *Sens. Actuators B Chem.* **2019**, *281*, 471.
160. Li, K.; Yang, C.; Yu, H.; Xiao, T.; Guan, W.; Ding, P.; Yin, H.; Cohen Stuart, M. A.; Wang, J.; Zhou, S., Coordination-Enhanced Synthesis for Hollow Mesoporous Silica Nanoreactors. *Chem. Mater.* **2020**, *32*, 2086.
161. Yan, P.; Tian, P.; Li, K.; Stuart, M. A. C.; Wang, J.; Yu, X.; Zhou, S., Rh nanoclusters encaged in hollow mesoporous silica nanoreactors with enhanced catalytic performance for phenol selective hydrogenation. *Chem. Eng. J.* **2020**, *397*, 125484.
162. Han, F.; Wang, R.; Feng, Y.; Wang, S.; Liu, L.; Li, X.; Han, Y.; Chen, H., On demand synthesis of hollow fullerene nanostructures. *Nat. Commun.* **2019**, *10*, 1.
163. Fei, J.; Cui, Y.; Yan, X.; Qi, W.; Yang, Y.; Wang, K.; He, Q.; Li, J., Controlled preparation of MnO₂ hierarchical hollow nanostructures and their application in water treatment. *Adv. Mater.* **2008**, *20*, 452.
164. Wei, Z.; Xing, R.; Zhang, X.; Liu, S.; Yu, H.; Li, P., Facile template-free fabrication of hollow nestlike α -Fe₂O₃ nanostructures for water treatment. *ACS Appl. Mater. Interfaces* **2013**, *5*, 598.
165. Cao, S.-W.; Zhu, Y.-J., Hierarchically nanostructured α -Fe₂O₃ hollow spheres: preparation, growth mechanism, photocatalytic property, and application in water treatment. *J. Phys. Chem. C* **2008**, *112*, 6253.
166. Wu, X.; Lu, G. Q. M.; Wang, L., Shell-in-shell TiO₂ hollow spheres synthesized by one-pot hydrothermal method for dye-sensitized solar cell application. *Energy Environ. Sci.* **2011**, *4*, 3565.
167. Qian, J.; Liu, P.; Xiao, Y.; Jiang, Y.; Cao, Y.; Ai, X.; Yang, H., TiO₂ - coated multilayered SnO₂ hollow microspheres for dye - sensitized solar cells. *Adv. Mater.* **2009**, *21*, 3663.

168. Zhou, X.; Gan, Y.; Du, J.; Tian, D.; Zhang, R.; Yang, C.; Dai, Z., A review of hollow Pt-based nanocatalysts applied in proton exchange membrane fuel cells. *J. Power Sources* **2013**, *232*, 310.
169. Hu, C.; Guo, Y.; Wang, J.; Yang, L.; Yang, Z.; Bai, Z.; Zhang, J.; Wang, K.; Jiang, K., Additive-free fabrication of spherical hollow palladium/copper alloyed nanostructures for fuel cell application. *ACS Appl. Mater. Interfaces* **2012**, *4*, 4461.
170. Hu, Y.; Jensen, J. O.; Zhang, W.; Martin, S.; Chenitz, R.; Pan, C.; Xing, W.; Bjerrum, N. J.; Li, Q., Fe₃C-based oxygen reduction catalysts: synthesis, hollow spherical structures and applications in fuel cells. *J. Mater. Chem. A* **2015**, *3*, 1752.
171. Sharma, V.; Singh, I.; Chandra, A., Hollow nanostructures of metal oxides as next generation electrode materials for supercapacitors. *Sci. Rep.* **2018**, *8*, 1.
172. Biswas, S.; Sharma, V.; Mandal, D.; Chowdhury, A.; Chakravarty, M.; Priya, S.; Gowda, C. C.; De, P.; Singh, I.; Chandra, A., Hollow nanostructures of metal oxides as emerging electrode materials for high performance supercapacitors. *CrystEngComm* **2020**, *22*, 1633.
173. Fang, J.; Kang, C.; Fu, L.; Li, S.; Liu, Q., Fabrication of hollow bamboo-shaped NiCo₂O₄ with controllable shell morphologies for high performance hybrid supercapacitors. *J. Alloys Compd.* **2020**, *849*, 156317.
174. Wang, X.; Feng, J.; Bai, Y.; Zhang, Q.; Yin, Y., Synthesis, properties, and applications of hollow micro-/nanostructures. *Chem. Rev.* **2016**, *116*, 10983.
175. Qiu, T.; Gao, S.; Liang, Z.; Wang, D. G.; Tabassum, H.; Zhong, R.; Zou, R., Pristine Hollow Metal–Organic Frameworks: Design, Synthesis and Application. *Angew. Chem. Int. Ed.* **2021**.
176. Cai, Z. X.; Wang, Z. L.; Kim, J.; Yamauchi, Y., Hollow functional materials derived from metal–organic frameworks: synthetic strategies, conversion mechanisms, and electrochemical applications. *Adv. Mater.* **2019**, *31*, 1804903.
177. Yang, M.; Ma, J.; Zhang, C.; Yang, Z.; Lu, Y., General synthetic route toward functional hollow spheres with double-shelled structures. *Angew. Chem. Int. Ed.* **2005**, *44*, 6727.
178. Sevilla, M.; Fuertes, A. B., Chemical and structural properties of carbonaceous products obtained by hydrothermal carbonization of saccharides. *Chem. Eur. J.* **2009**, *15*, 4195.
179. Xu, J.; Yao, X.; Wei, W.; Wang, Z.; Yu, R., Multi-shelled copper oxide hollow spheres and their gas sensing properties. *Mater. Res. Bull.* **2017**, *87*, 214.
180. Pan, J.; Li, L.; Hang, H.; Wu, R.; Dai, X.; Shi, W.; Yan, Y., Fabrication and evaluation of magnetic/hollow double-shelled imprinted sorbents formed by Pickering emulsion polymerization. *Langmuir* **2013**, *29*, 8170.
181. Wang, W.; Tu, Y.; Zhang, P.; Zhang, G., Surfactant-assisted synthesis of double-wall Cu₂O hollow spheres. *CrystEngComm* **2011**, *13*, 1838.

182. Han, Y. S.; Hadiko, G.; Fuji, M.; Takahashi, M., A novel approach to synthesize hollow calcium carbonate particles. *Chem. Lett.* **2005**, *34*, 152.
183. Yunoki, A.; Tsuchiya, E.; Fukui, Y.; Fujii, A.; Maruyama, T., Preparation of inorganic/organic polymer hybrid microcapsules with high encapsulation efficiency by an electrospray technique. *ACS Appl. Mater. Interfaces* **2014**, *6*, 11973.
184. Zhang, C.; Jin, C.; Teng, G.; Gu, Y.; Ma, W., Controllable synthesis of hollow MnFe_2O_4 by self-etching and its application in high-performance anode for lithium-ion batteries. *Chem. Eng. J.* **2019**, *365*, 121.
185. Zhang, L.; Wang, H., Interior structural tailoring of Cu_2O shell-in-shell nanostructures through multistep Ostwald ripening. *J. Phys. Chem. C* **2011**, *115*, 18479.
186. Son, Y.; Son, Y.; Choi, M.; Ko, M.; Chae, S.; Park, N.; Cho, J., Hollow silicon nanostructures via the Kirkendall effect. *Nano Lett.* **2015**, *15*, 6914.
187. Lee, H. J.; Cho, W.; Oh, M., Advanced fabrication of metal–organic frameworks: template-directed formation of polystyrene@ ZIF-8 core–shell and hollow ZIF-8 microspheres. *Chem. Commun.* **2012**, *48*, 221.
188. Park, J. U.; Lee, H. J.; Cho, W.; Jo, C.; Oh, M., Facile synthetic route for thickness and composition tunable hollow metal oxide spheres from silica-templated coordination polymers. *Adv. Mater.* **2011**, *23*, 3161.
189. Tian, W.; Hu, H.; Wang, Y.; Li, P.; Liu, J.; Liu, J.; Wang, X.; Xu, X.; Li, Z.; Zhao, Q., Metal–organic frameworks mediated synthesis of one-dimensional molybdenum-based/carbon composites for enhanced lithium storage. *ACS Nano* **2018**, *12*, 1990.
190. Yang, Y.; Wang, F.; Yang, Q.; Hu, Y.; Yan, H.; Chen, Y.-Z.; Liu, H.; Zhang, G.; Lu, J.; Jiang, H.-L., Hollow metal–organic framework nanospheres via emulsion-based interfacial synthesis and their application in size-selective catalysis. *ACS Appl. Mater. Interfaces* **2014**, *6*, 18163.
191. Tan, Y. C.; Zeng, H. C., Self-templating synthesis of hollow spheres of MOFs and their derived nanostructures. *Chem. Commun.* **2016**, *52*, 11591.
192. Yu, L.; Yang, J. F.; Lou, X. W., Formation of CoS_2 nanobubble hollow prisms for highly reversible lithium storage. *Angew. Chem. Int. Ed.* **2016**, *55*, 13422.
193. Carné-Sánchez, A.; Imaz, I.; Cano-Sarabia, M.; Maspocho, D., A spray-drying strategy for synthesis of nanoscale metal–organic frameworks and their assembly into hollow superstructures. *Nat. Chem.* **2013**, *5*, 203.
194. Liu, W.; Huang, J.; Yang, Q.; Wang, S.; Sun, X.; Zhang, W.; Liu, J.; Huo, F., Multi-shelled Hollow Metal–Organic Frameworks. *Angew. Chem. Int. Ed.* **2017**, *56*, 5512.
195. Sen, U.; Erkartal, M.; Kung, C.-W.; Ramani, V.; Hupp, J. T.; Farha, O. K., Proton conducting self-assembled metal–organic framework/polyelectrolyte hollow hybrid nanostructures. *ACS Appl. Mater. Interfaces* **2016**, *8*, 23015.

196. Lee, I.; Choi, S.; Lee, H. J.; Oh, M., Hollow Metal–Organic Framework Microparticles Assembled via a Self-Templated Formation Mechanism. *Cryst. Growth Des.* **2015**, *15*, 5169.
197. Huang, Z.-F.; Song, J.; Li, K.; Tahir, M.; Wang, Y.-T.; Pan, L.; Wang, L.; Zhang, X.; Zou, J.-J., Hollow cobalt-based bimetallic sulfide polyhedra for efficient all-pH-value electrochemical and photocatalytic hydrogen evolution. *J. Am. Chem. Soc.* **2016**, *138*, 1359.
198. Lyu, F.; Bai, Y.; Li, Z.; Xu, W.; Wang, Q.; Mao, J.; Wang, L.; Zhang, X.; Yin, Y., Self-Templated Fabrication of CoO-MoO₂ Nanocages for Enhanced Oxygen Evolution. *Adv. Funct. Mater.* **2017**, *27*, 1702324.
199. Wu, L. L.; Wang, Z.; Long, Y.; Li, J.; Liu, Y.; Wang, Q. S.; Wang, X.; Song, S. Y.; Liu, X.; Zhang, H. J., Multishelled Ni_xCo_{3-x}O₄ Hollow Microspheres Derived from Bimetal - Organic Frameworks as Anode Materials for High - Performance Lithium - Ion Batteries. *Small* **2017**, *13*, 1604270.
200. Liu, C.; Huang, X.; Wang, J.; Song, H.; Yang, Y.; Liu, Y.; Li, J.; Wang, L.; Yu, C., Hollow Mesoporous Carbon Nanocubes: Rigid - Interface - Induced Outward Contraction of Metal - Organic Frameworks. *Adv. Funct. Mater.* **2018**, *28*, 1705253.
201. Zhou, H.; He, D.; Saana, A. I.; Yang, J.; Wang, Z.; Zhang, J.; Liang, Q.; Yuan, S.; Zhu, J.; Mu, S., Mesoporous-silica induced doped carbon nanotube growth from metal–organic frameworks. *Nanoscale* **2018**, *10*, 6147.
202. Li, Q.; Xu, P.; Gao, W.; Ma, S.; Zhang, G.; Cao, R.; Cho, J.; Wang, H. L.; Wu, G., Graphene/graphene - tube nanocomposites templated from cage - containing metal - organic frameworks for oxygen reduction in Li-O₂ batteries. *Adv. Mater.* **2014**, *26*, 1378.
203. Buyevskaya, O.; Wolf, D.; Baerns, M., Rhodium-catalyzed partial oxidation of methane to CO and H₂. Transient studies on its mechanism. *Catal. Lett.* **1994**, *29*, 249.
204. Hou, Y.; Ogasawara, S.; Fukuoka, A.; Kobayashi, H., Zeolite-supported rhodium sub-nano cluster catalyst for low-temperature selective oxidation of methane to syngas. *Catal. Sci. Technol.* **2017**, *7*, 6132.
205. Chen, W.-H.; Chiu, T.-W.; Hung, C.-I.; Lin, M.-R., Hysteresis and reaction characterization of methane catalytic partial oxidation on rhodium catalyst. *J. Power Sources* **2009**, *194*, 467.
206. Celik, D.; Karahan, S.; Zahmakıran, M.; Özkar, S., Hydrogen generation from the hydrolysis of hydrazine-borane catalyzed by rhodium(0) nanoparticles supported on hydroxyapatite. *Int. J. Hydrog. Energy* **2012**, *37*, 5143.
207. Singh, S. K.; Zhang, X.-B.; Xu, Q., Room-temperature hydrogen generation from hydrous hydrazine for chemical hydrogen storage. *J. Am. Chem. Soc.* **2009**, *131*, 9894.
208. Koch, D.; Leitner, W., Rhodium-catalyzed hydroformylation in supercritical carbon dioxide. *J. Am. Chem. Soc.* **1998**, *120*, 13398.

209. Ahn, S. H.; Klein, M. J.; Manthiram, A., 1D Co and N-Doped Hierarchically Porous Carbon Nanotubes Derived from Bimetallic Metal Organic Framework for Efficient Oxygen and Tri - iodide Reduction Reactions. *Adv. Energy Mater.* **2017**, *7*, 1601979.
210. Alsalahi, W.; Trzeciak, A., Rhodium-catalyzed hydroformylation under green conditions: Aqueous/organic biphasic, "on water", solventless and Rh nanoparticle based systems. *Coord. Chem. Rev.* **2021**, *430*, 213732.
211. Kumar, S.; Nunewar, S.; Oluguttula, S.; Nanduri, S.; Kanchupalli, V., Recent advances in Rh(iii)/Ir(iii)-catalyzed C–H functionalization/annulation via carbene migratory insertion. *Org. Biomol. Chem.* **2021**, *19*, 1438.
212. Nunewar, S.; Kumar, S.; Talakola, S.; Nanduri, S.; Kanchupalli, V., Co (III), Rh (III) & Ir (III) - Catalyzed Direct C–H Alkylation/Alkenylation/Arylation with Carbene Precursors. *Chem. Asian J.* **2021**, *16*, 443.
213. Yin, J.; Wang, J.; Ma, Y.; Yu, J.; Zhou, J.; Fan, Z., Recent Advances in the Controlled Synthesis and Catalytic Applications of Two-Dimensional Rhodium Nanomaterials. *ACS Mater. Lett.* **2020**, *3*, 121.
214. Zhang, J.; Liu, C.; Zhang, B., Insights into single-atom metal-support interactions in electrocatalytic water splitting. *Small Methods* **2019**, *3*, 1800481.
215. Ramalingam, V.; Varadhan, P.; Fu, H. C.; Kim, H.; Zhang, D.; Chen, S.; Song, L.; Ma, D.; Wang, Y.; Alshareef, H. N., Heteroatom-mediated interactions between ruthenium single atoms and an MXene support for efficient hydrogen evolution. *Adv. Mater.* **2019**, *31*, 1903841.
216. Kaiser, S. K.; Chen, Z.; Faust Akl, D.; Mitchell, S.; Pérez-Ramírez, J., Single-atom catalysts across the periodic table. *Chem. Rev.* **2020**, *120*, 11703.
217. Guan, H.; Lin, J.; Qiao, B.; Miao, S.; Wang, A. Q.; Wang, X.; Zhang, T., Enhanced performance of Rh₁/TiO₂ catalyst without methanation in water-gas shift reaction. *AIChE J.* **2017**, *63*, 2081.
218. He, L.; Weniger, F.; Neumann, H.; Beller, M., Synthesis, characterization, and application of metal nanoparticles supported on nitrogen-doped carbon: catalysis beyond electrochemistry. *Angew. Chem. Int. Ed.* **2016**, *55*, 12582.
219. Wörz, A. S.; Judai, K.; Abbet, S.; Antonietti, J.-M.; Heiz, U.; Del Vitto, A.; Giordano, L.; Pacchioni, G., Chemistry on single atoms: key factors for the acetylene trimerization on MgO-supported Rh, Pd, and Ag atoms. *Chem. Phys. Lett.* **2004**, *399*, 266.
220. Sarma, B. B.; Kim, J.; Amsler, J.; Agostini, G.; Weidenthaler, C.; Pfänder, N.; Arenal, R.; Concepción, P.; Plessow, P.; Studt, F., One-Pot Cooperation of Single-Atom Rh and Ru Solid Catalysts for a Selective Tandem Olefin Isomerization-Hydrosilylation Process. *Angew. Chem. Int. Ed.* **2020**, *59*, 5806.
221. Han, B.; Li, T.; Zhang, J.; Zeng, C.; Matsumoto, H.; Su, Y.; Qiao, B.; Zhang, T., A highly active Rh₁/CeO₂ single-atom catalyst for low-temperature CO oxidation. *Chem. Commun.* **2020**, *56*, 4870.

222. Bai, S.; Liu, F.; Huang, B.; Li, F.; Lin, H.; Wu, T.; Sun, M.; Wu, J.; Shao, Q.; Xu, Y., High-efficiency direct methane conversion to oxygenates on a cerium dioxide nanowires supported rhodium single-atom catalyst. *Nat. Commun.* **2020**, *11*, 1.
223. Amsler, J.; Sarma, B. B.; Agostini, G.; Prieto, G.; Plessow, P. N.; Studt, F., Prospects of heterogeneous hydroformylation with supported single atom catalysts. *J. Am. Chem. Soc.* **2020**, *142*, 5087.
224. Kwon, Y.; Kim, T. Y.; Kwon, G.; Yi, J.; Lee, H., Selective activation of methane on single-atom catalyst of rhodium dispersed on zirconia for direct conversion. *J. Am. Chem. Soc.* **2017**, *139*, 17694.
225. Wang, L.; Li, H.; Zhang, W.; Zhao, X.; Qiu, J.; Li, A.; Zheng, X.; Hu, Z.; Si, R.; Zeng, J., Supported rhodium catalysts for ammonia–borane hydrolysis: Dependence of the catalytic activity on the highest occupied state of the single rhodium atoms. *Angew. Chem. Int. Ed.* **2017**, *56*, 4712.
226. Han, B.; Lang, R.; Tang, H.; Xu, J.; Gu, X.-K.; Qiao, B.; Liu, J. J., Superior activity of Rh₁/ZnO single-atom catalyst for CO oxidation. *Chinese J. Catal.* **2019**, *40*, 1847.
227. Lang, R.; Li, T.; Matsumura, D.; Miao, S.; Ren, Y.; Cui, Y. T.; Tan, Y.; Qiao, B.; Li, L.; Wang, A., Hydroformylation of olefins by a rhodium single-atom catalyst with activity comparable to RhCl(PPh₃)₃. *Angew. Chem. Int. Ed.* **2016**, *55*, 16054.
228. Lou, Y.; Zheng, Y.; Li, X.; Ta, N.; Xu, J.; Nie, Y.; Cho, K.; Liu, J., Pocketlike active site of Rh₁/MoS₂ single-atom catalyst for selective crotonaldehyde hydrogenation. *J. Am. Chem. Soc.* **2019**, *141*, 19289.
229. Sun, Q.; Wang, N.; Zhang, T.; Bai, R.; Mayoral, A.; Zhang, P.; Zhang, Q.; Terasaki, O.; Yu, J., Zeolite-Encaged Single-Atom Rhodium Catalysts: Highly-Efficient Hydrogen Generation and Shape-Selective Tandem Hydrogenation of Nitroarenes. *Angew. Chem. Int. Ed.* **2019**, *58*, 18570.
230. Shan, J.; Li, M.; Allard, L. F.; Lee, S.; Flytzani-Stephanopoulos, M., Mild oxidation of methane to methanol or acetic acid on supported isolated rhodium catalysts. *Nature* **2017**, *551*, 605.
231. Tang, Y.; Li, Y.; Fung, V.; Jiang, De.-en.; Huang, W.; Zhang, S.; Iwasawa, Y.; Sakata, T.; Nguyen, L.; Zhang, X., Single rhodium atoms anchored in micropores for efficient transformation of methane under mild conditions. *Nat. Commun.* **2018**, *9*, 1.
232. Ghosh, T. K.; Nair, N. N., Rh₁/γ-Al₂O₃ Single-Atom Catalysis of O₂ Activation and CO Oxidation: Mechanism, Effects of Hydration, Oxidation State, and Cluster Size. *ChemCatChem* **2013**, *5*, 1811.
233. Tian, J.; Yang, D.; Wen, J.; Filatov, A. S.; Liu, Y.; Lei, A.; Lin, X.-M., A stable rhodium single-site catalyst encapsulated within dendritic mesoporous nanochannels. *Nanoscale* **2018**, *10*, 1047.

234. Jiang, M.; Yan, L.; Ding, Y.; Sun, Q.; Liu, J.; Zhu, H.; Lin, R.; Xiao, F.; Jiang, Z.; Liu, J., Ultrastable 3V-PPh₃ polymers supported single Rh sites for fixed-bed hydroformylation of olefins. *J. Mol. Catal. A: Chem.* **2015**, *404*, 211.
235. Hülsey, M. J.; Zhang, B.; Ma, Z.; Asakura, H.; Do, D. A.; Chen, W.; Tanaka, T.; Zhang, P.; Wu, Z.; Yan, N., In situ spectroscopy-guided engineering of rhodium single-atom catalysts for CO oxidation. *Nat. Commun.* **2019**, *10*, 1.
236. Xu, H.; Liu, T.; Bai, S.; Li, L.; Zhu, Y.; Wang, J.; Yang, S.; Li, Y.; Shao, Q.; Huang, X., Cation Exchange Strategy to Single-Atom Noble-Metal Doped CuO Nanowire Arrays with Ultralow Overpotential for H₂O Splitting. *Nano Lett.* **2020**, *20*, 5482.
237. Xiong, Y.; Dong, J.; Huang, Z.-Q.; Xin, P.; Chen, W.; Wang, Y.; Li, Z.; Jin, Z.; Xing, W.; Zhuang, Z., Single-atom Rh/N-doped carbon electrocatalyst for formic acid oxidation. *Nat. Nanotechnol.* **2020**, *15*, 390.
238. Yang, H.; Bradley, S. J.; Chan, A.; Waterhouse, G. I.; Nann, T.; Kruger, P. E.; Telfer, S. G., Catalytically active bimetallic nanoparticles supported on porous carbon capsules derived from metal–organic framework composites. *J. Am. Chem. Soc.* **2016**, *138*, 11872.
239. Yang, H.; Chen, X.; Chen, W.-T.; Wang, Q.; Cuello, N. C.; Nafady, A.; Al-Enizi, A. M.; Waterhouse, G. I.; Goenaga, G. A.; Zawodzinski, T. A., Tunable synthesis of hollow metal–nitrogen–carbon capsules for efficient oxygen reduction catalysis in proton exchange membrane fuel cells. *ACS Nano* **2019**, *13*, 8087.
240. Wang, Y.; Chen, S.; Zhao, S.; Chen, Q.; Zhang, J., Interfacial coordination assembly of tannic acid with metal ions on three-dimensional nickel hydroxide nanowalls for efficient water splitting. *J. Mater. Chem. A* **2020**, *8*, 15845.
241. Guo, F.; Yang, H.; Liu, L.; Han, Y.; Al-Enizi, A. M.; Nafady, A.; Kruger, P. E.; Telfer, S. G.; Ma, S., Hollow capsules of doped carbon incorporating metal@ metal sulfide and metal@ metal oxide core–shell nanoparticles derived from metal–organic framework composites for efficient oxygen electrocatalysis. *J. Mater. Chem. A* **2019**, *7*, 3624.
242. Artyushkova, K.; Kiefer, B.; Halevi, B.; Knop-Gericke, A.; Schlögl, R.; Atanassov, P., Density functional theory calculations of XPS binding energy shift for nitrogen-containing graphene-like structures. *Chem. Commun.* **2013**, *49*, 2539.
243. Briggs, D., Book review of handbook of X-ray photoelectron spectroscopy. *Surf. Interface Anal.* **1981**, *3*.
244. Jiang, Z.-J.; Jiang, Z., Interaction induced high catalytic activities of CoO nanoparticles grown on nitrogen-doped hollow graphene microspheres for oxygen reduction and evolution reactions. *Sci. Rep.* **2016**, *6*, 1.
245. Pan, D.; Wang, L.; Li, Z.; Geng, B.; Zhang, C.; Zhan, J.; Yin, L.; Wang, L., Synthesis of graphene quantum dot/metal–organic framework nanocomposites as yellow phosphors for white light-emitting diodes. *New J. Chem.* **2018**, *42*, 5083.

246. Falcão, L.; Araújo, M. E. M., Application of ATR–FTIR spectroscopy to the analysis of tannins in historic leathers: the case study of the upholstery from the 19th century Portuguese Royal Train. *Vib. Spectrosc.* **2014**, *74*, 98.
247. Briggs, D., Handbook of X-ray Photoelectron Spectroscopy CD Wanger, WM Riggs, LE Davis, JF Moulder and GE Muilenberg Perkin-Elmer Corp., Physical Electronics Division, Eden Prairie, Minnesota, USA, 1979. *Surf. Interface Anal.* **1981**, *3*,v.
248. Yuan, X.; Hu, X.-X.; Ding, X.-L.; Kong, H.-C.; Sha, H.-D.; Lin, H.; Wen, W.; Shen, G.; Guo, Z.; Ma, Z.-F., Effects of cobalt precursor on pyrolyzed carbon-supported cobalt-polypyrrole as electrocatalyst toward oxygen reduction reaction. *Nanoscale Res. Lett.* **2013**, *8*, 1.
249. Gorgulho, H. F.; Gonçalves, F.; Pereira, M. F. R.; Figueiredo, J. L., Synthesis and characterization of nitrogen-doped carbon xerogels. *Carbon* **2009**, *47*, 2032.
250. Pylypenko, S.; Mukherjee, S.; Olson, T. S.; Atanassov, P., Non-platinum oxygen reduction electrocatalysts based on pyrolyzed transition metal macrocycles. *Electrochim. Acta* **2008**, *53*, 7875.
251. Talo, A.; Lahtinen, J.; Hautojärvi, P., An XPS study of metallic three-way catalysts: The effect of additives on platinum, rhodium, and cerium. *App. Catalysis B: Environ.* **1995**, *5*, 221.
252. Wang, L.; Sowa, J. R.; Wang, C.; Lu, R. S.; Gassman, P. G.; Flood, T. C., XPS Investigations of (1,4,7-trimethyl-1,4,7-triazacyclononane) RhMe₃ and [1,1,1-tris((dimethylphosphino)methyl)ethane] RhMe₃ and Their Rh–C Cleavage Derivatives. Comparison of Hard-and Soft-Ligated Rhodium Organometallics. *Organometallics* **1996**, *15*, 4240.
253. Li, C.; Liu, J.; Gao, W.; Zhao, Y.; Wei, M., Ce-Promoted Rh/TiO₂ Heterogeneous Catalysts Towards Ethanol Production from Syngas. *Catal. Lett.* **2013**, *143*, 1247.
254. Nguyen, C.-C.; Dinh, C.-T.; Do, T.-O., Hollow Sr/Rh-codoped TiO₂ photocatalyst for efficient sunlight-driven organic compound degradation. *RSC Adv.* **2017**, *7*, 3480.
255. Wang, J.; Yu, Z.; Wang, L.; Wang, B.; Liu, F.; Liang, X.; Sun, P.; Yan, X.; Chuai, X.; Lu, G., Improvement of NO₂ sensing characteristic for mixed potential type gas sensor based on YSZ and Rh/Co₃V₂O₈ sensing electrode. *RSC Adv.* **2017**.
256. Wang, L.; Zhang, W.; Wang, S.; Gao, Z.; Luo, Z.; Wang, X.; Zeng, R.; Li, A.; Li, H.; Wang, M., Atomic-level insights in optimizing reaction paths for hydroformylation reaction over Rh/CoO single-atom catalyst. *Nat. Commun.* **2016**, *7*, 1.
257. Parres-Esclapez, S.; Such-Basañez, I.; Illán-Gómez, M.; De Lecea, C. S.-M.; Bueno-López, A., Study by isotopic gases and in situ spectroscopies (DRIFTS, XPS and Raman) of the N₂O decomposition mechanism on Rh/CeO₂ and Rh/γ-Al₂O₃ catalysts. *J. Catal.* **2010**, *276*, 390.

258. Watcharinyanon, S.; Puglia, C.; Göthelid, E.; Bäckvall, J.-E.; Moons, E.; Johansson, L. S., Molecular orientation of thiol-derivatized tetraphenylporphyrin on gold studied by XPS and NEXAFS. *Surf. Sci.* **2009**, *603*, 1026.
259. Zhong, J.; Deng, J.-J.; Mao, B.-H.; Xie, T.; Sun, X.-H.; Mou, Z.-G.; Hong, C.-H.; Yang, P.; Wang, S.-D., Probing solid state N-doping in graphene by X-ray absorption near-edge structure spectroscopy. *Carbon* **2012**, *50*, 335.
260. Lehmann, J.; Liang, B.; Solomon, D.; Lerotic, M.; Luizão, F.; Kinyangi, J.; Schäfer, T.; Wirick, S.; Jacobsen, C., Near-edge X-ray absorption fine structure (NEXAFS) spectroscopy for mapping nano-scale distribution of organic carbon forms in soil: Application to black carbon particles. *Glob. Biogeochem. Cycles* **2005**, *19*.
261. Singh, B.; Fang, Y.; Cowie, B. C.; Thomsen, L., NEXAFS and XPS characterisation of carbon functional groups of fresh and aged biochars. *Org. Geochem.* **2014**, *77*, 1.
262. Latham, K. G.; Dose, W. M.; Allen, J. A.; Donne, S. W., Nitrogen doped heat treated and activated hydrothermal carbon: NEXAFS examination of the carbon surface at different temperatures. *Carbon* **2018**, *128*, 179.
263. Turner, M.; Vaughan, O. P.; Kyriakou, G.; Watson, D. J.; Scherer, L. J.; Papageorgiou, A. C.; Sanders, J. K.; Lambert, R. M., Deprotection, Tethering, and Activation of a One-Legged Metalloporphyrin on a Chemically Active Metal Surface: NEXAFS, Synchrotron XPS, and STM Study of [SAC] P– Mn (III) Cl on Ag (100). *J. Am. Chem. Soc.* **2009**, *131*, 14913.
264. Zegkinoglou, I.; Ragoussi, M.-E.; Pemmaraju, C.; Johnson, P. S.; Pickup, D. F.; Ortega, J. E.; Prendergast, D.; De la Torre, G.; Himpfel, F., Spectroscopy of Donor– π – Acceptor Porphyrins for Dye-Sensitized Solar Cells. *J. Phys. Chem. C* **2013**, *117*, 13357.
265. Zubavichus, Y.; Shaporenko, A.; Grunze, M.; Zharnikov, M., Innershell absorption spectroscopy of amino acids at all relevant absorption edges. *J. Phys. Chem. A* **2005**, *109*, 6998.
266. Bulusheva, L.; Okotrub, A.; Fedoseeva, Y. V.; Kurennya, A.; Asanov, I.; Vilkov, O.; Koós, A. A.; Grobert, N., Controlling pyridinic, pyrrolic, graphitic, and molecular nitrogen in multi-wall carbon nanotubes using precursors with different N/C ratios in aerosol assisted chemical vapor deposition. *Phys. Chem. Chem. Phys.* **2015**, *17*, 23741.
267. Latham, K. G.; Simone, M. I.; Dose, W. M.; Allen, J. A.; Donne, S. W., Synchrotron based NEXAFS study on nitrogen doped hydrothermal carbon: Insights into surface functionalities and formation mechanisms. *Carbon* **2017**, *114*, 566.
268. Melke, J.; Peter, B.; Habereeder, A.; Ziegler, J.; Fasel, C.; Nefedov, A.; Sezen, H.; Wöll, C.; Ehrenberg, H.; Roth, C., Metal–support interactions of platinum nanoparticles decorated N-doped carbon nanofibers for the oxygen reduction reaction. *ACS Appl. Mater. Interfaces* **2016**, *8*, 82.

269. Kačiulis, S.; Mattogno, G.; Pandolfi, L.; Cavalli, M.; Gnappi, G.; Montenero, A., XPS study of apatite-based coatings prepared by sol-gel technique. *Appl. Surf. Sci.* **1999**, *151*, 1.
270. Cano, E.; Bastidas, J.; Polo, J.; Mora, N., Study of the effect of acetic acid vapor on copper corrosion at 40 and 80% relative humidity. *J. Electrochem. Soc.* **2001**, *148*, B431.
271. Moggia, J.; Milt, V. G.; Ulla, M.; Cornaglia, L. M., Surface characterization of Co, K/La₂O₃ catalysts used for the catalytic combustion of diesel soot. *Surface and Interface Analysis: An International Journal devoted to the development and application of techniques for the analysis of surfaces, interfaces and thin films* **2003**, *35*, 216.
272. Frey, S.; Heister, K.; Zharnikov, M.; Grunze, M., Modification of semifluorinated alkanethiolate monolayers by low energy electron irradiation. *Phys. Chem. Chem. Phys.* **2000**, *2*, 1979.
273. Al-Gaashani, R.; Najjar, A.; Zakaria, Y.; Mansour, S.; Atieh, M., XPS and structural studies of high quality graphene oxide and reduced graphene oxide prepared by different chemical oxidation methods. *Ceram. Int.* **2019**, *45*, 14439.
274. Chan, H. S.; Hor, T. A.; Sim, M.; Tan, K.; Tan, B., X-ray photoelectron spectroscopic studies of polyquinazolones: an assessment of the degree of cyclization. *Polym. J.* **1990**, *22*, 883.
275. Křepelová, A.; Newberg, J.; Huthwelker, T.; Bluhm, H.; Ammann, M., The nature of nitrate at the ice surface studied by XPS and NEXAFS. *Phys. Chem. Chem. Phys.* **2010**, *12*, 8870.
276. Lin, B.; Wang, A.; Guo, Y.; Ding, Y.; Guo, Y.; Wang, L.; Zhan, W.; Gao, F., Ambient temperature NO adsorber derived from pyrolysis of Co-MOF (ZIF-67). *ACS Omega* **2019**, *4*, 9542.
277. Wang, W.-J.; Wang, Y.; Xu, Q.; Ju, H.-X.; Wang, T.; Tao, Z.-J.; Hu, S.-W.; Zhu, J.-F., Interaction of cobalt with ceria thin films and its influence on supported Au nanoparticles. *Chin. Chem. Lett.* **2017**, *28*, 1760.
278. Wei, G.; Yan, L.; Huang, H.; Yan, F.; Liang, X.; Xu, S.; Lan, Z.; Zhou, W.; Guo, J., The hetero-structured nanoarray construction of Co₃O₄ nanowires anchored on nanoflakes as a high-performance electrode for supercapacitors. *Appl. Surf. Sci.* **2021**, *538*, 147932.
279. Wang, Z.; Ren, X.; Shi, X.; Asiri, A. M.; Wang, L.; Li, X.; Sun, X.; Zhang, Q.; Wang, H., A platinum oxide decorated amorphous cobalt oxide hydroxide nanosheet array towards alkaline hydrogen evolution. *J. Mater. Chem. A* **2018**, *6*, 3864.
280. Gao, Z.; Yang, H.; Mao, J.; Wu, J., Construction of α -Fe₂O₃ and Fe/Co-N₄ structures with faceted TiO₂ nanocrystals for highly efficient degradation of sulfathiazole in water. *J. Clean. Prod.* **2019**, *220*, 668.
281. Lei, Z.; Tan, Y.; Zhang, Z.; Wu, W.; Cheng, N.; Chen, R.; Mu, S.; Sun, X., Defects enriched hollow porous Co-N-doped carbons embedded with ultrafine CoFe/Co

nanoparticles as bifunctional oxygen electrocatalyst for rechargeable flexible solid zinc-air batteries. *Nano Research* **2021**, *14*, 868.

282. Bhattacharyya, S.; Lübbe, M.; Bressler, P.; Zahn, D.; Richter, F., Structure of nitrogenated amorphous carbon films from NEXAFS. *Diamond Relat. Mater.* **2002**, *11*, 8.

283. Jin, Y.; Bartlett, R. J., Accurate computation of X-ray absorption spectra with ionization potential optimized global hybrid functional. *J. Chem. Phys.* **2018**, *149*, 064111.

284. Fogarty, R. M.; Matthews, R. P.; Clough, M. T.; Ashworth, C. R.; Brandt-Talbot, A.; Corbett, P. J.; Palgrave, R. G.; Bourne, R. A.; Chamberlain, T. W.; Vander Hoogerstraete, T., NEXAFS spectroscopy of ionic liquids: experiments versus calculations. *Phys. Chem. Chem. Phys.* **2017**, *19*, 31156.

285. Hibberd, A. M.; Doan, H. Q.; Glass, E. N.; De Groot, F. M.; Hill, C. L.; Cuk, T., Co polyoxometalates and a Co₃O₄ thin film investigated by L-edge X-ray absorption spectroscopy. *J. Phys. Chem. C* **2015**, *119*, 4173.

286. Wang, X. X.; Cullen, D. A.; Pan, Y. T.; Hwang, S.; Wang, M.; Feng, Z.; Wang, J.; Engelhard, M. H.; Zhang, H.; He, Y., Nitrogen - coordinated single cobalt atom catalysts for oxygen reduction in proton exchange membrane fuel cells. *Adv. Mater.* **2018**, *30*, 1706758.

287. Mesilov, V.; Galakhov, V.; Gubkin, A.; Sherstobitova, E.; Zakharova, G.; Uimin, M.; Yermakov, A. Y.; Kvashnina, K.; Smirnov, D., X-ray diffraction and X-ray spectroscopy studies of cobalt-doped anatase TiO₂: Co nanopowders. *J. Phys. Chem. C* **2017**, *121*, 24235.

288. Calloni, A.; Jagadeesh, M.; Bussetti, G.; Fratesi, G.; Achilli, S.; Picone, A.; Lodesani, A.; Brambilla, A.; Goletti, C.; Ciccacci, F., Cobalt atoms drive the anchoring of Co-TPP molecules to the oxygen-passivated Fe (0 0 1) surface. *Appl. Surf. Sci.* **2020**, *505*, 144213.

289. Ahad, A.; Shukla, D.; Rahman, F.; Majid, S.; Okram, G.; Sinha, A.; Phase, D., Colossal thermopower, spin states and delocalization effects in single layered La_{2-x}Sr_xCoO₄. *Acta Mater.* **2017**, *135*, 233.

290. Sukhorukov, A. Y., Nitro Compounds as Versatile Building Blocks for the Synthesis of Pharmaceutically Relevant Substances. *Front. Chem.* **2020**, *8*.

291. Downing, R.; Kunkeler, P.; Van Bekkum, H., Catalytic syntheses of aromatic amines. *Catal. Today* **1997**, *37*, 121.

292. Jagadeesh, R. V.; Wienhöfer, G.; Westerhaus, F. A.; Surkus, A.-E.; Pohl, M.-M.; Junge, H.; Junge, K.; Beller, M., Efficient and highly selective iron-catalyzed reduction of nitroarenes. *Chem. Commun.* **2011**, *47*, 10972.

293. Amini, B., Amines, Aromatic, Aniline and Its Derivatives. *Kirk - Othmer Encyclopedia of Chemical Technology* **2000**.

294. Zhang, J.; Chen, G.; Chaker, M.; Rosei, F.; Ma, D., Gold nanoparticle decorated ceria nanotubes with significantly high catalytic activity for the reduction of nitrophenol and mechanism study. *App. Catal. B: Environ.* **2013**, *132*, 107.

295. Song, J.; Huang, Z.-F.; Pan, L.; Li, K.; Zhang, X.; Wang, L.; Zou, J.-J., Review on selective hydrogenation of nitroarene by catalytic, photocatalytic and electrocatalytic reactions. *App. Catal. B: Environ.* **2018**, *227*, 386.
296. Zubar, V.; Dewanji, A.; Rueping, M., Chemoselective Hydrogenation of Nitroarenes Using an Air-Stable Base-Metal Catalyst. *Org. Lett.* **2021**, *23*, 2742.
297. Möbus, K.; Wolf, D.; Benischke, H.; Dittmeier, U.; Simon, K.; Packruhn, U.; Jantke, R.; Weidlich, S.; Weber, C.; Chen, B., Hydrogenation of Aromatic Nitrogroups with Precious metal powder catalysts: Influence of Modifier on Selectivity and Activity. *Top. Catal.* **2010**, *53*, 1126.
298. Haber, F., Gradual electrolytic reduction of nitrobenzene with limited cathode potential. *Elektrochem. Angew. Phys. Chem* **1898**, *22*, 506.
299. Zhang, L.; Shao, Z.-J.; Cao, X.-M.; Hu, P., Insights into Different Products of Nitrosobenzene and Nitrobenzene Hydrogenation on Pd (111) under Realistic Reaction Conditions. *J. Phys. Chem. C* **2018**, *122*, 20337.
300. Cheong, W.-C.; Yang, W.; Zhang, J.; Li, Y.; Zhao, D.; Liu, S.; Wu, K.; Liu, Q.; Zhang, C.; Wang, D., Isolated iron single-atomic site-catalyzed chemoselective transfer hydrogenation of nitroarenes to arylamines. *ACS Appl. Mater. Interfaces* **2019**, *11*, 33819.
301. Liu, Y.; Zhang, W.; Zheng, Y.; Wu, K.; Dong, P.; He, R.; Lu, N.; Mao, J., Single-atom Fe–N₄ site for the hydrogenation of nitrobenzene: theoretical and experimental studies. *Dalton Trans.* **2021**.
302. Blaser, H. U.; Steiner, H.; Studer, M., Selective catalytic hydrogenation of functionalized nitroarenes: an update. *ChemCatChem* **2009**, *1*, 210.
303. Liu, W.; Zhang, L.; Yan, W.; Liu, X.; Yang, X.; Miao, S.; Wang, W.; Wang, A.; Zhang, T., Single-atom dispersed Co–N–C catalyst: structure identification and performance for hydrogenative coupling of nitroarenes. *Chem. Sci.* **2016**, *7*, 5758.
304. Yan, H.; Zhao, X.; Guo, N.; Lyu, Z.; Du, Y.; Xi, S.; Guo, R.; Chen, C.; Chen, Z.; Liu, W., Atomic engineering of high-density isolated Co atoms on graphene with proximal-atom controlled reaction selectivity. *Nat. Commun.* **2018**, *9*, 1.
305. Dai, Y.; Jiang, C.; Xu, M.; Bian, B.; Lu, D.; Yang, Y., Cobalt in N-doped carbon matrix catalyst for chemoselective hydrogenation of nitroarenes. *Appl. Catal. A: Gen* **2019**, *580*, 158.
306. Wang, Y.-J.; Zhao, N.; Fang, B.; Li, H.; Bi, X. T.; Wang, H., Carbon-supported Pt-based alloy electrocatalysts for the oxygen reduction reaction in polymer electrolyte membrane fuel cells: particle size, shape, and composition manipulation and their impact to activity. *Chem. Rev.* **2015**, *115*, 3433.
307. Lin, R.; Cai, X.; Zeng, H.; Yu, Z., Stability of High-Performance Pt-Based Catalysts for Oxygen Reduction Reactions. *Adv. Mater.* **2018**, *30*, 1705332.
308. Liu, M.; Zhao, Z.; Duan, X.; Huang, Y., Nanoscale structure design for high-performance Pt-based ORR catalysts. *Adv. Mater.* **2019**, *31*, 1802234.

309. Zhang, J.; Yang, H.; Liu, B., Coordination Engineering of Single-Atom Catalysts for the Oxygen Reduction Reaction: A Review. *Adv. Energy Mater.* **2021**, *11*, 2002473.
310. Niu, W. J.; He, J. Z.; Gu, B. N.; Liu, M. C.; Chueh, Y. L., Opportunities and Challenges in Precise Synthesis of Transition Metal Single-Atom Supported by 2D Materials as Catalysts toward Oxygen Reduction Reaction. *Adv. Funct. Mater.* **2021**, 2103558.
311. Nie, Y.; Li, L.; Wei, Z., Recent advancements in Pt and Pt-free catalysts for oxygen reduction reaction. *Chem. Soc. Rev.* **2015**, *44*, 2168.
312. Skalska, K.; Miller, J. S.; Ledakowicz, S., Trends in NO_x abatement: A review. *Sci. Total Environ.* **2010**, *408*, 3976.
313. Roy, S.; Hegde, M.; Madras, G., Catalysis for NO_x abatement. *Appl. Energy* **2009**, *86*, 2283.
314. Luck, F.; Roiron, J., Selective catalytic reduction of NO_x emitted by nitric acid plants. *Catal. Today* **1989**, *4*, 205.
315. Macleod, N.; Lambert, R. M., Lean NO_x reduction with CO + H₂ mixtures over Pt/Al₂O₃ and Pd/Al₂O₃ catalysts. *Appl. Catal. B: Environ.* **2002**, *35*, 269.
316. Thirupathi, B.; Smirniotis, P. G., Co-doping a metal (Cr, Fe, Co, Ni, Cu, Zn, Ce, and Zr) on Mn/TiO₂ catalyst and its effect on the selective reduction of NO with NH₃ at low-temperatures. *Appl. Catal. B: Environ.* **2011**, *110*, 195.
317. Haber, F.; Weiss, J., The catalytic decomposition of hydrogen peroxide by iron salts. *Proc. Math. Soc. Phys. Eng.* **1934**, *147*, 332.
318. Pignatello, J. J.; Oliveros, E.; MacKay, A., Advanced oxidation processes for organic contaminant destruction based on the Fenton reaction and related chemistry. *Crit. Rev. Environ. Sci. Technol.* **2006**, *36*, 1.
319. Duesterberg, C. K.; Mylon, S. E.; Waite, T. D., pH effects on iron-catalyzed oxidation using Fenton's reagent. *Environ. Sci. Technol.* **2008**, *42*, 8522.
320. Garrido-Ramírez, E. G.; Theng, B. K.; Mora, M. L., Clays and oxide minerals as catalysts and nanocatalysts in Fenton-like reactions—a review. *Appl. Clay Sci.* **2010**, *47*, 182.
321. Cheng, M.; Lai, C.; Liu, Y.; Zeng, G.; Huang, D.; Zhang, C.; Qin, L.; Hu, L.; Zhou, C.; Xiong, W., Metal-organic frameworks for highly efficient heterogeneous Fenton-like catalysis. *Coord. Chem. Rev.* **2018**, *368*, 80.
322. Chen, F.; Wu, X. L.; Shi, C.; Lin, H.; Chen, J.; Shi, Y.; Wang, S.; Duan, X., Molecular Engineering toward Pyrrolic N-Rich M-N₄ (M= Cr, Mn, Fe, Co, Cu) Single-Atom Sites for Enhanced Heterogeneous Fenton-Like Reaction. *Adv. Funct. Mater.* **2021**, *31*, 2007877.
323. Shao, M.; Chang, Q.; Dodelet, J.-P.; Chenitz, R., Recent advances in electrocatalysts for oxygen reduction reaction. *Chem. Rev.* **2016**, *116*, 3594.
324. Busca, G.; Lietti, L.; Ramis, G.; Berti, F., Chemical and mechanistic aspects of the selective catalytic reduction of NO_x by ammonia over oxide catalysts: a review. *Appl. Catal. B: Environ.* **1998**, *18*, 1.

325. Forzatti, P., Present status and perspectives in de-NO_x SCR catalysis. *Appl. Catal. A: Gen* **2001**, 222, 221.
326. Li, X.; Huang, X.; Xi, S.; Miao, S.; Ding, J.; Cai, W.; Liu, S.; Yang, X.; Yang, H.; Gao, J., Single cobalt atoms anchored on porous N-doped graphene with dual reaction sites for efficient Fenton-like catalysis. *J. Am. Chem. Soc.* **2018**, 140, 12469.
327. Gong, Y.; Zhao, X.; Zhang, H.; Yang, B.; Xiao, K.; Guo, T.; Zhang, J.; Shao, H.; Wang, Y.; Yu, G., MOF-derived nitrogen doped carbon modified g-C₃N₄ heterostructure composite with enhanced photocatalytic activity for bisphenol A degradation with peroxydisulfate under visible light irradiation. *Appl. Catal. B: Environ.* **2018**, 233, 35.
328. Teets, T. S.; Nocera, D. G., Oxygen reduction reactions of monometallic rhodium hydride complexes. *Inorg. Chem.* **2012**, 51, 7192.
329. Meng, Y.; Qu, X.; Li, K.; Yang, Y.; Wang, Y.; Wu, Z., Rhodium and nitrogen codoped graphene as a bifunctional electrocatalyst for the oxygen reduction reaction and CO₂ reduction reaction: mechanism insights. *J. Phys. Chem. C* **2019**, 123, 5176.
330. Qingya, L.; Zhenyu, L.; Chengyue, L., Adsorption and activation of NH₃ during selective catalytic reduction of NO by NH₃. *Chinese J. Catal.* **2006**, 27, 636.
331. Kijlstra, W. S.; Brands, D. S.; Smit, H. I.; Poels, E. K.; Bliiek, A., Mechanism of the Selective Catalytic Reduction of NO with NH₃ over MnO_x/Al₂O₃. *J. Catal.* **1997**, 171, 219.
332. Busca, G.; Larrubia, M. A.; Arrighi, L.; Ramis, G., Catalytic abatement of NO_x: chemical and mechanistic aspects. *Catal. Today* **2005**, 107, 139.
333. Han, L.; Cai, S.; Gao, M.; Hasegawa, J.-y.; Wang, P.; Zhang, J.; Shi, L.; Zhang, D., Selective catalytic reduction of NO_x with NH₃ by using novel catalysts: State of the art and future prospects. *Chem. Rev.* **2019**, 119, 10916.
334. Gao, F.; Tang, X.; Yi, H.; Zhao, S.; Li, C.; Li, J.; Shi, Y.; Meng, X., A review on selective catalytic reduction of NO_x by NH₃ over Mn-based catalysts at low temperatures: catalysts, mechanisms, kinetics and DFT calculations. *Catalysts* **2017**, 7, 199.
335. Long, R.; Yang, R., Reaction mechanism of selective catalytic reduction of NO with NH₃ over Fe-ZSM-5 catalyst. *J. Catal.* **2002**, 207, 224.
336. Li, X.; Ao, Z.; Liu, J.; Sun, H.; Rykov, A. I.; Wang, J., Topotactic transformation of metal-organic frameworks to graphene-encapsulated transition-metal nitrides as efficient Fenton-like catalysts. *ACS Nano* **2016**, 10, 11532.
337. Gadipelli, S.; Travis, W.; Zhou, W.; Guo, Z., A thermally derived and optimized structure from ZIF-8 with giant enhancement in CO₂ uptake. *Energy Environ. Sci.* **2014**, 7, 2232.
338. Binaeian, E.; Maleki, S.; Motaghedi, N.; Arjmandi, M., Study on the performance of Cd²⁺ sorption using dimethylethylenediamine-modified zinc-based MOF (ZIF-8-mmen): optimization of the process by RSM technique. *Sep. Sci. Technol.* **2020**, 55, 2713.

339. Bhardwaj, R.; Bharti, A.; Singh, J. P.; Chae, K. H.; Goyal, N.; Gautam, S., Structural and electronic investigation of ZnO nanostructures synthesized under different environments. *Heliyon* **2018**, *4*, e00594.
340. Chiou, J.; Kumar, K. K.; Jan, J.; Tsai, H.; Bao, C.; Pong, W.-F.; Chien, F.; Tsai, M.-H.; Hong, I.-H.; Klauser, R., Diameter dependence of the electronic structure of ZnO nanorods determined by X-ray absorption spectroscopy and scanning photoelectron microscopy. *Appl. Phys. Lett.* **2004**, *85*, 3220.
341. Mishra, N.; Shinde, S.; Vishwakarma, R.; Kadam, S.; Sharon, M.; Sharon, M. In *MWCNTs synthesized from waste polypropylene plastics and its application in supercapacitors*, AIP Conference Proceedings, American Institute of Physics: 2013; pp 228.
342. Zhong, C.; Deng, Y.; Hu, W.; Qiao, J.; Zhang, L.; Zhang, J., A review of electrolyte materials and compositions for electrochemical supercapacitors. *Chem. Soc. Rev.* **2015**, *44*, 7484.
343. Yu, L.; Chen, G. Z., Ionic liquid-based electrolytes for supercapacitor and supercapattery. *Front. Chem.* **2019**, *7*, 272.
344. Iro, Z. S.; Subramani, C.; Dash, S., A brief review on electrode materials for supercapacitor. *Int. J. Electrochem. Sci* **2016**, *11*, 10628.
345. Burke, A., Ultracapacitors: why, how, and where is the technology. *J. Power Sources* **2000**, *91*, 37.
346. Zhang, Y.; Yu, S.; Lou, G.; Shen, Y.; Chen, H.; Shen, Z.; Zhao, S.; Zhang, J.; Chai, S.; Zou, Q., Review of macroporous materials as electrochemical supercapacitor electrodes. *J. Mater. Sci.* **2017**, *52*, 11201.
347. Colby, D. A.; Bergman, R. G.; Ellman, J. A., Rhodium-catalyzed C–C bond formation via heteroatom-directed C–H bond activation. *Chem. Rev.* **2010**, *110*, 624.
348. Qi, X.; Li, Y.; Bai, R.; Lan, Y., Mechanism of rhodium-catalyzed C–H functionalization: advances in theoretical investigation. *Acc. Chem. Res.* **2017**, *50*, 2799.
349. Slugovc, C.; Padilla-Martínez, I.; Sirol, S.; Carmona, E., Rhodium- and iridium-trispyrazolylborate complexes: C–H activation and coordination chemistry. *Coord. Chem. Rev.* **2001**, *213*, 129.
350. Li, S.-S.; Qin, L.; Dong, L., Rhodium-catalyzed C–C coupling reactions via double C–H activation. *Org. Biomol. Chem.* **2016**, *14*, 4554.
351. Song, G.; Wang, F.; Li, X., C–C, C–O and C–N bond formation via rhodium (iii)-catalyzed oxidative C–H activation. *Chem. Soc. Rev.* **2012**, *41*, 3651.
352. Ackermann, L., Metalla-electrocatalyzed C–H activation by earth-abundant 3d metals and beyond. *Acc. Chem. Res.* **2019**, *53*, 84.
353. Franke, R.; Selent, D.; Börner, A., Applied hydroformylation. *Chem. Rev.* **2012**, *112*, 5675.


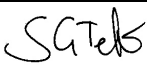
354. Yu, S.; Zhang, X.; Yan, Y.; Cai, C.; Dai, L.; Zhang, X., Synthesis and Application of Tetrphosphane Ligands in Rhodium - Catalyzed Hydroformylation of Terminal Olefins: High Regioselectivity at High Temperature. *Chem. Eur. J.* **2010**, *16*, 4938.
355. El Ali, B.; Tijani, J.; Fettouhi, M.; El-Faer, M.; Al-Arfaj, A., Rhodium (I) and rhodium (III)-heteropolyacids supported on MCM-41 for the catalytic hydroformylation of styrene derivatives. *Appl. Catal. A: Gen* **2005**, *283*, 185.
356. Kläui, W.; Schramm, D.; Schramm, G., Tripodal oxygen and tripodal nitrogen ligands in hydroformylation reactions: formation of novel rhodium (III) carbonyl bis (acyl) complexes. *Inorg. Chim. Acta* **2004**, *357*, 1642.
357. De, C.; Saha, R.; Ghosh, S. K.; Ghosh, A.; Mukherjee, K.; Bhattacharyya, S. S.; Saha, B., A review of biphasic hydroformylation for long chain substrates. *Res. Chem. Intermed.* **2013**, *39*, 3463.
358. Hertrich, M. F.; Scharnagl, F. K.; Pews - Davtyan, A.; Kreyenschulte, C. R.; Lund, H.; Bartling, S.; Jackstell, R.; Beller, M., Supported cobalt nanoparticles for hydroformylation reactions. *Chem. Eur. J.* **2019**, *25*, 5534.
359. Hood, D. M.; Johnson, R. A.; Carpenter, A. E.; Younker, J. M.; Vinyard, D. J.; Stanley, G. G., Highly active cationic cobalt (II) hydroformylation catalysts. *Science* **2020**, *367*, 542.
360. Long, Z.; Ao, C.; Huang, L.; Zhang, W.; Liu, C.; Zhang, L.; He, W.; Wang, S.; Pan, Y.; Sun, Z., Unique Coordination Structure of Cobalt Single-Atom Catalyst Supported on Dopant-Free Carbon. *J. Phys. Chem. C* **2021**, *125*, 6735.
361. Wan, G.; Yu, P.; Chen, H.; Wen, J.; Sun, C. j.; Zhou, H.; Zhang, N.; Li, Q.; Zhao, W.; Xie, B., Engineering single-atom cobalt catalysts toward improved electrocatalysis. *Small* **2018**, *14*, 1704319.
362. Wan, C.; Duan, X.; Huang, Y., Molecular Design of Single-Atom Catalysts for Oxygen Reduction Reaction. *Adv. Energy Mater.* **2020**, *10*, 1903815.
363. Han, X.; Ling, X.; Wang, Y.; Ma, T.; Zhong, C.; Hu, W.; Deng, Y., Generation of nanoparticle, atomic-cluster, and single-atom cobalt catalysts from zeolitic imidazole frameworks by spatial isolation and their use in zinc-air batteries. *Angew. Chem.* **2019**, *131*, 5413.
364. Sun, H.; Wang, M.; Du, X.; Jiao, Y.; Liu, S.; Qian, T.; Yan, Y.; Liu, C.; Liao, M.; Zhang, Q., Modulating the d-band center of boron doped single-atom sites to boost the oxygen reduction reaction. *J. Mater. Chem. A* **2019**, *7*, 20952.
365. Peng, L.; Shang, L.; Zhang, T.; Waterhouse, G. I., Recent Advances in the Development of Single-Atom Catalysts for Oxygen Electrocatalysis and Zinc-Air Batteries. *Adv. Energy Mater.* **2020**, *10*, 2003018.
366. Jiang, X. H.; Zhang, L. S.; Liu, H. Y.; Wu, D. S.; Wu, F. Y.; Tian, L.; Liu, L. L.; Zou, J. P.; Luo, S. L.; Chen, B. B., Silver single atom in carbon nitride catalyst for highly efficient photocatalytic hydrogen evolution. *Angew. Chem. Int. Ed.* **2020**, *59*, 23112.

367. Zhang, N.; Zhang, X.; Tao, L.; Jiang, P.; Ye, C.; Lin, R.; Huang, Z.; Li, A.; Pang, D.; Yan, H., Silver single - atom catalyst for efficient electrochemical CO₂ reduction synthesized from thermal transformation and surface reconstruction. *Angew. Chem. Int. Ed.* **2021**, *60*, 6170.
368. Gadkari, R. R.; Ali, S. W.; Alagirusamy, R.; Das, A., Silver nanoparticles in water purification: opportunities and challenges. *Modern age environmental problems and their remediation* **2018**, 229.
369. Das, S. K.; Khan, M. M. R.; Guha, A. K.; Das, A. R.; Mandal, A. B., Silver-nano biohybride material: synthesis, characterization and application in water purification. *Bioresour. Technol.* **2012**, *124*, 495.
370. Che, W.; Xiao, Z.; Wang, Z.; Li, J.; Wang, H.; Wang, Y.; Xie, Y., Wood-based mesoporous filter decorated with silver nanoparticles for water purification. *ACS Sustain. Chem. Eng.* **2019**, *7*, 5134.
371. Wang, C.-Y.; Fu, C.-F.; Liu, Y.-H.; Peng, S.-M.; Liu, S.-T., Synthesis of iridium pyridinyl N-heterocyclic carbene complexes and their catalytic activities on reduction of nitroarenes. *Inorg. Chem.* **2007**, *46*, 5779.
372. Chen, S.; Lu, G.; Cai, C., Iridium-catalyzed transfer hydrogenation of nitroarenes to anilines. *New J. Chem.* **2015**, *39*, 5360.
373. Huang, X.; Yan, H.; Huang, L.; Zhang, X.; Lin, Y.; Li, J.; Xia, Y.; Ma, Y.; Sun, Z.; Wei, S., Toward understanding of the support effect on Pd₁ single-atom-catalyzed hydrogenation reactions. *J. Phys. Chem. C* **2018**, *123*, 7922.
374. Tang, C.; Chen, L.; Li, H.; Li, L.; Jiao, Y.; Zheng, Y.; Xu, H.; Davey, K.; Qiao, S.-Z., Tailoring Acidic Oxygen Reduction Selectivity on Single-Atom Catalysts via Modification of First and Second Coordination Spheres. *J. Am. Chem. Soc.* **2021**, 10.1021/jacs.1c03135.
375. Polyzoidis, A.; Altenburg, T.; Schwarzer, M.; Loebbecke, S.; Kaskel, S., Continuous microreactor synthesis of ZIF-8 with high space–time–yield and tunable particle size. *Chem. Eng. J.* **2016**, *283*, 971.
376. Simon, P.; Gogotsi, Y., Materials for electrochemical capacitors. *Nanoscience and technology: a collection of reviews from Nature journals* **2010**, 320.
377. Zhang, L. L.; Zhao, X., Carbon-based materials as supercapacitor electrodes. *Chem. Soc. Rev.* **2009**, *38*, 2520.
378. Endo, M.; Takeda, T.; Kim, Y.; Koshiba, K.; Ishii, K., High power electric double layer capacitor (EDLC's); from operating principle to pore size control in advanced activated carbons. *Carbon lett.* **2001**, *1*, 117.
379. Wang, Y.; Zhang, L.; Hou, H.; Xu, W.; Duan, G.; He, S.; Liu, K.; Jiang, S., Recent progress in carbon-based materials for supercapacitor electrodes: a review. *J. Mater. Sci.* **2021**, *56*, 173.

380. Zhao, Q.; Gao, Y.; Bai, X.; Wu, C.; Xie, Y., Facile synthesis of SnO₂ hollow nanospheres and applications in gas sensors and electrocatalysts. *Eur J. Inorg. Chem.* **2006**, 1643.
381. Park, J.; Shen, X.; Wang, G., Solvothermal synthesis and gas-sensing performance of Co₃O₄ hollow nanospheres. *Sens. Actuators B Chem.* **2009**, 136, 494.

STATEMENT OF CONTRIBUTION DOCTORATE WITH PUBLICATIONS/MANUSCRIPTS

We, the candidate and the candidate's Primary Supervisor, certify that all co-authors have consented to their work being included in the thesis and they have accepted the candidate's contribution as indicated below in the *Statement of Originality*.

Name of candidate:	
Name/title of Primary Supervisor:	
In which chapter is the manuscript /published work:	
<p>Please select one of the following three options:</p> <p>The manuscript/published work is published or in press</p> <ul style="list-style-type: none"> • Please provide the full reference of the Research Output: <p>The manuscript is currently under review for publication – please indicate:</p> <ul style="list-style-type: none"> • The name of the journal: • The percentage of the manuscript/published work that was contributed by the candidate: • Describe the contribution that the candidate has made to the manuscript/published work: <p style="text-align: center;">It is intended that the manuscript will be published, but it has not yet been submitted to a journal</p>	
Candidate's Signature:	 Nisansala <small>Digitally signed by Nisansala Date: 2021.08.30 09:46:34 +12'00'</small>
Date:	
Primary Supervisor's Signature:	 2021.08.30 10:42:56 +12'00'
Date:	


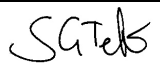
This form should appear at the end of each thesis chapter/section/appendix submitted as a manuscript/ publication or collected as an appendix at the end of the thesis.



GRADUATE
RESEARCH
SCHOOL

STATEMENT OF CONTRIBUTION DOCTORATE WITH PUBLICATIONS/MANUSCRIPTS

We, the candidate and the candidate's Primary Supervisor, certify that all co-authors have consented to their work being included in the thesis and they have accepted the candidate's contribution as indicated below in the *Statement of Originality*.

Name of candidate:	
Name/title of Primary Supervisor:	
In which chapter is the manuscript /published work:	
<p>Please select one of the following three options:</p> <p>The manuscript/published work is published or in press</p> <ul style="list-style-type: none"> • Please provide the full reference of the Research Output: <p>The manuscript is currently under review for publication – please indicate:</p> <ul style="list-style-type: none"> • The name of the journal: • The percentage of the manuscript/published work that was contributed by the candidate: • Describe the contribution that the candidate has made to the manuscript/published work: <p style="text-align: center;">It is intended that the manuscript will be published, but it has not yet been submitted to a journal</p>	
Candidate's Signature:	 Nisansala <small>Digitally signed by Nisansala Date: 2021.08.30 09:50:18 +12'00'</small>
Date:	
Primary Supervisor's Signature:	 2021.08.30 10:42:45 +12'00'
Date:	

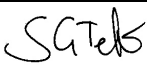
This form should appear at the end of each thesis chapter/section/appendix submitted as a manuscript/ publication or collected as an appendix at the end of the thesis.



GRADUATE
RESEARCH
SCHOOL

STATEMENT OF CONTRIBUTION DOCTORATE WITH PUBLICATIONS/MANUSCRIPTS

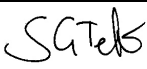
We, the candidate and the candidate's Primary Supervisor, certify that all co-authors have consented to their work being included in the thesis and they have accepted the candidate's contribution as indicated below in the *Statement of Originality*.

Name of candidate:	
Name/title of Primary Supervisor:	
In which chapter is the manuscript /published work:	
<p>Please select one of the following three options:</p> <p>The manuscript/published work is published or in press</p> <ul style="list-style-type: none"> • Please provide the full reference of the Research Output: <p>The manuscript is currently under review for publication – please indicate:</p> <ul style="list-style-type: none"> • The name of the journal: • The percentage of the manuscript/published work that was contributed by the candidate: • Describe the contribution that the candidate has made to the manuscript/published work: <p style="text-align: center;">It is intended that the manuscript will be published, but it has not yet been submitted to a journal</p>	
Candidate's Signature:	Nisansala <small>Digitally signed by Nisansala Date: 2021.08.30 09:51:44 +12'00'</small>
Date:	
Primary Supervisor's Signature:	 2021.08.30 10:42:25 +12'00'
Date:	

This form should appear at the end of each thesis chapter/section/appendix submitted as a manuscript/publication or collected as an appendix at the end of the thesis.

STATEMENT OF CONTRIBUTION DOCTORATE WITH PUBLICATIONS/MANUSCRIPTS

We, the candidate and the candidate's Primary Supervisor, certify that all co-authors have consented to their work being included in the thesis and they have accepted the candidate's contribution as indicated below in the *Statement of Originality*.

Name of candidate:	
Name/title of Primary Supervisor:	
In which chapter is the manuscript /published work:	
<p>Please select one of the following three options:</p> <p>The manuscript/published work is published or in press</p> <ul style="list-style-type: none"> • Please provide the full reference of the Research Output: <p>The manuscript is currently under review for publication – please indicate:</p> <ul style="list-style-type: none"> • The name of the journal: • The percentage of the manuscript/published work that was contributed by the candidate: • Describe the contribution that the candidate has made to the manuscript/published work: <p style="text-align: center;">It is intended that the manuscript will be published, but it has not yet been submitted to a journal</p>	
Candidate's Signature:	Nisansala <small>Digitally signed by Nisansala Date: 2021.08.30 09:54:10 +12'00'</small>
Date:	
Primary Supervisor's Signature:	 2021.08.30 10:42:04 +12'00'
Date:	

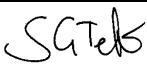
This form should appear at the end of each thesis chapter/section/appendix submitted as a manuscript/ publication or collected as an appendix at the end of the thesis.



GRADUATE
RESEARCH
SCHOOL

STATEMENT OF CONTRIBUTION DOCTORATE WITH PUBLICATIONS/MANUSCRIPTS

We, the candidate and the candidate's Primary Supervisor, certify that all co-authors have consented to their work being included in the thesis and they have accepted the candidate's contribution as indicated below in the *Statement of Originality*.

Name of candidate:	
Name/title of Primary Supervisor:	
In which chapter is the manuscript /published work:	
<p>Please select one of the following three options:</p> <p>The manuscript/published work is published or in press</p> <ul style="list-style-type: none"> • Please provide the full reference of the Research Output: <p>The manuscript is currently under review for publication – please indicate:</p> <ul style="list-style-type: none"> • The name of the journal: • The percentage of the manuscript/published work that was contributed by the candidate: • Describe the contribution that the candidate has made to the manuscript/published work: <p style="text-align: center;">It is intended that the manuscript will be published, but it has not yet been submitted to a journal</p>	
Candidate's Signature:	Nisansala <small>Digitally signed by Nisansala Date: 2021.08.30 09:55:13 +12'00'</small>
Date:	
Primary Supervisor's Signature:	 <small>2021.08.30 10:43:14 +12'00'</small>
Date:	

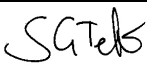
This form should appear at the end of each thesis chapter/section/appendix submitted as a manuscript/ publication or collected as an appendix at the end of the thesis.



GRADUATE
RESEARCH
SCHOOL

STATEMENT OF CONTRIBUTION DOCTORATE WITH PUBLICATIONS/MANUSCRIPTS

We, the candidate and the candidate's Primary Supervisor, certify that all co-authors have consented to their work being included in the thesis and they have accepted the candidate's contribution as indicated below in the *Statement of Originality*.

Name of candidate:	
Name/title of Primary Supervisor:	
In which chapter is the manuscript /published work:	
<p>Please select one of the following three options:</p> <p>The manuscript/published work is published or in press</p> <ul style="list-style-type: none"> • Please provide the full reference of the Research Output: <p>The manuscript is currently under review for publication – please indicate:</p> <ul style="list-style-type: none"> • The name of the journal: • The percentage of the manuscript/published work that was contributed by the candidate: • Describe the contribution that the candidate has made to the manuscript/published work: <p style="text-align: center;">It is intended that the manuscript will be published, but it has not yet been submitted to a journal</p>	
Candidate's Signature:	Nisansala <small>Digitally signed by Nisansala Date: 2021.08.30 09:57:36 +12'00'</small>
Date:	
Primary Supervisor's Signature:	 2021.08.30 10:43:05 +12'00'
Date:	

This form should appear at the end of each thesis chapter/section/appendix submitted as a manuscript/ publication or collected as an appendix at the end of the thesis.

Catalysts Derived from Metal-Organic Frameworks

Electronic Appendices

Contents

Appendix A

Table A 1: SACs derived by pyrolysis MOFs and MOF composites which catalysis ORR.....	1
Table A 2: SACs derived by pyrolysis MOFs and MOF composites which catalysis CO ₂ RR.....	4
Table A 3: SACs derived by pyrolysis MOFs and MOF composites which catalysis N ₂ RR.	6
Table A 4: SACs derived by pyrolysis MOFs and MOF composites which catalysis HER.....	7
Table A 5: SACs derived by pyrolysis MOFs and MOF composites which catalysis oxidation, hydrogenation, dimerization and other reactions.	8
Table A 6: hollow nanostructures synthesized by pyrolysis MOFs and MOF composites and their applications.	9
References.....	12

Appendix B

Figure B 1: Fluorescence of HNB-2 at (a) pH 1, (b) pH 2, (c) pH 3 and pH 4.....	21
Figure B 2: Fluorescence of HNB-2 at (a) pH 5, (b) pH 6, (c) pH 7 and pH 8.....	22
Figure B 3: Fluorescence of HNB-2 at (a) pH 9, (b) pH 10, (c) pH 11 and pH 12.....	23
Figure B 4: Fluorescence of HNB-2 at (a) pH 13 and (b) pH 14.....	24
Figure B 5: Fluorescence of HNB-2 at (a) 340 nm, (b) 360 nm, (c) 380 nm and (d) 400 nm excitation wavelengths.....	25
Figure B 6: Fluorescence of HNB-2 at (a) 420 nm, (b) 440nm, (c) 460 nm and (d) 480 nm excitation wavelength.	26

Appendix A for Chapter 1

Table A 1: SACs derived by pyrolysis MOFs and MOF composites which catalysis ORR.

MOF precursor	Supported metal	Metal content wt %	Performance vs RHE	Stability	Ref.
Fe doped ZIF-8	Fe	0.15	$E_{1/2} = 0.92$ V in 0.1 M KOH	No obvious decay in $E_{1/2}$ after 20000 s	1
Fe doped ZIF-8	Fe	0.45	$E_{1/2} = 0.85$ V in 0.5 M H ₂ SO ₄	Loss of 20 mV in $E_{1/2}$ after 10000 cycles	2
Fe(acac) ₃ @ZIF-8	Fe	2.16	$E_{1/2} = 0.90$ V in 0.1 M KOH	No obvious decay in $E_{1/2}$ after 5000 cycles	3
Fc@ZIF-8	Fe	0.43	$E_{1/2} = 0.904$ V in 0.1 M KOH	No obvious decay in $E_{1/2}$ after 10000 cycles	4
ZIF-8/Fe@PZS	Fe	1.54	$E_{1/2} = 0.912$ V in 0.1 M KOH	No obvious decay in $E_{1/2}$ after 5000 cycles	5
FePc-x@ZIF-8	Fe	0.2	$E_{1/2} = 0.909$ V in 0.1 M KOH	No obvious decay in $E_{1/2}$ after 10000 cycles	6
Fe-ZIF-8	Fe	N/A	$E_{1/2} = 0.90$ V in 0.1 M KOH	Loss of 16 mV in $E_{1/2}$ after 10000 cycles	7
Fe/Zn ZIF	Fe	4.58	$E_{1/2} = 0.89$ V in 0.1 M KOH	No obvious decay in $E_{1/2}$ after 5000 cycles	8
Fe-ZIF-8	Fe	5	$E_{1/2} = 0.735$ V in 0.1 M KOH	N/A	9
ZIF-8@FeTA	Fe	1.27	$E_{1/2} = 0.77$ V in 0.1 M KOH	N/A	10
Fe-ZIF-8	Fe	3	$E_{1/2} = 0.871$ V in 0.1 M KOH	98.2 % current retention after 10000 s	11
F-Phen@ZIF-8	Fe	0.81	$E_{1/2} = 0.91$ V in 0.1 M KOH	99 % current retention after 15 hrs	12
Fe-ZIF-7	Fe	0.37	$E_{1/2} = 0.82$ V in 0.1 M KOH	Loss of 8 mV in $E_{1/2}$ after 10000 cycles	13
Fe-TPI-ZIF	Fe	1.14	$E_{1/2} = 0.78$ V in 0.1 M HClO ₄	No obvious decay in $E_{1/2}$ after 10000 cycles	14

Uio(bpdC)-FeCl ₃	Fe	1.5	$E_{1/2} = 0.89$ V in 0.1 M KOH	No obvious decay in $E_{1/2}$ after 5000 cycles	15
Fe-PCN-222	Fe	1.76	$E_{1/2} = 0.89$ V in 0.1 M KOH	No obvious decay in $E_{1/2}$ after 5000 cycles	16
FeD@MIL-101-NH ₂	Fe	1.1	$E_{1/2} = 0.84$ V in 0.1 M KOH	95 % current retention after 20000 s	17
Zn/Co ZIF	Co	0.34	$E_{1/2} = 0.80$ V in 0.1 M HClO ₄	Loss of 30 mV in $E_{1/2}$ after 10000 cycles	18
Zn/Co ZIF	Co	0.4	$E_{1/2} = 0.87$ V in 0.1 M KOH	97 % current retention after 24 hrs	19
Zn/Co ZIF	Co	0.9	$E_{1/2} = 0.84$ V in 0.1 M H ₂ SO ₄	Loss of 40 mV in $E_{1/2}$ after 30000 cycles	20
Zn/Co ZIF	Co	1.7	$E_{1/2} = 0.82$ V in 0.1 M KOH	94.4 % current retention after 22.5 hrs	21
Zn/Co ZIF@C Cloth	Co	2.3	$E_{1/2} = 0.81$ V in 0.1 M KOH	89.2 % current retention after 80 hrs	22
Zn/Co ZIF	Co	4	$E_{1/2} = 0.881$ V in 0.1 M KOH	No obvious decay in $E_{1/2}$ after 5000 cycles	23
Zn/Co ZIF	Co	4.3	$E_{1/2} = 0.79$ V in 0.1 M HClO ₄	Loss of 12 mV in $E_{1/2}$ after 20000 cycles	24
ZIF-67@C cloth	Co	1.84	$E_{1/2} = 0.87$ V in 0.1 M KOH	2500 min, 125 cycles in Zn air battery	25
ZIF-67@KCl	Co	15.3	$E_{1/2} = 0.91$ V in 0.1 M KOH	95 % current retention after 20000 s	26
PCN-244-Fe&Co	Fe	0.43	$E_{1/2} = 0.87$ V in 0.1 M KOH	Loss of 84 mV in $E_{1/2}$ after 10000 cycles	27
	Co	0.37			
FeCl ₃ @Zn/Co ZIF	Fe	0.93	$E_{1/2} = 0.863$ V in 0.1 M HClO ₄	No obvious decay in $E_{1/2}$ after 100 hrs	28
	Co	1.17	$E_{1/2} = 0.954$ V in 0.1 M KOH	No obvious decay in $E_{1/2}$ after 10000 cycles	
CrCl ₃ @ZIF-8	Cr	0.62	$E_{1/2} = 0.773$ V in HClO ₄	Loss of 15 mV in $E_{1/2}$ after 20000 cycles	29

Mn(ac) ₃ @ZIF-8	Mn	3.03	$E_{1/2} = 0.80$ V in 0.5 M H ₂ SO ₄	Loss of 17 mV in $E_{1/2}$ after 30000 cycles	30
Cu foam & ZIF-8	Cu	0.54	$E_{1/2} = 0.895$ V in 0.1 M KOH	No obvious decay in $E_{1/2}$ after 5000 cycles	31
Ir(acac) ₃ ZIF-8	Ir	0.2	$E_{1/2} = 0.864$ V in HClO ₄	No obvious decay in $E_{1/2}$ after 5000 cycles	32

N/A: Information not reported.

Table A 2: SACs derived by pyrolysis MOFs and MOF composites which catalysis CO₂RR.

MOF precursor	Supported metal	Metal content wt%	Products	Performance: % (Faradic Efficiency)	Stability	Ref.
Zn/Co ZIF	Co	0.25	CO	94	No obvious decay in FE and current in 60 hrs	33
Zn/Co ZIF	Co	0.60	CO	82	No obvious decay in FE and current in 10 hrs	34
Co/PAN@ZIF-8	Co	0.7	CO	97	No obvious decay in FE and current in 50 hrs	35
ZnO@Zn/Co ZIF	Co	3.4	Syngas	100	No obvious decay in FE and current in 24 hrs	36
Fe MOF	Fe	1.08	CO	99.6	No obvious decay in FE and current in 24 hrs	37
Fe-ZIF-8	Fe	2.8	CO	95	No obvious decay in FE and current in 12 hrs	38
Zn/Fe ZIF	Fe	2.6	CO	90	No obvious decay in FE after 12 hrs	38
Zn/Fe ZIF	Fe	4.58	CO	86.9	No obvious decay in FE after 12 hrs	8
AFC@ZIF-8	Fe	0.69	CO	89.1	Not mentioned	39
ZIF-Fe-CNT-FA	Fe	2.7	CO	100	Higher than 98% FE after 10 hrs	40
Fe@ZIF-8	Fe	0.1	CO	93	Higher than 93% FE after 24 hrs	41
Co@ZIF-8	Co	0.1		45		
Fe/ZIF-8@CoPC	Fe	1.04	CO	98	No obvious decay in FE after 20 hrs	42
	Co	0.65				
Fe/Ni ZIF	Fe	0.97	CO	90	No obvious decay in FE after 30 hrs	43

	Ni	0.34				
ZnNi ZIF-8	Ni	5.44	CO	92	No obvious decay in FE after 30 hrs	44
Ni ZIF	Ni	0.16	CO	96	No obvious decay in FE in 10 hrs	45
Ni ZIF	Ni	6.63	CO	97	Higher than 90% FE after 30 hrs	46
Ni(NO ₃) ₂ @ZIF-8	Ni	1.53	CO	71.9	No obvious decay in FE after 60 hrs	47
Ni MOF	Ni	8.2	CO	99	No obvious decay in FE after 3 hrs	48
ZnO@ZIF-NiZn	Ni	0.46	CO	~ 100	No obvious decay in FE and current in 20 hrs	49
Ni/PAN@ZIF-8	Ni	1.3	CO	95	No obvious decay in FE in 120 hrs	50
NiNPs@NC	Ni	N/A	CO	88	No obvious decay in FE after 60 hrs	51
MgNi-MOF-74	Ni	0.9	CO	98	No obvious decay in FE after 10 hrs	52
Bi-MOF	Bi	0.2	CO	97	No obvious decay in FE after 4 hrs	53
Cu@ZIF-8	Cu	1.3	Methanol	44	No obvious decay in current in 50 hrs	54
CuCl ₂ /ZIF-8	Cu	1.4	Ethanol	55	No obvious decay in current in 60 mins	55
Cu(BTC) MOF	Cu	2.4	C ₂ H ₄	38.6	No obvious decay in current in 10 hrs	56
Cu ZIF-8	Cu	0.59	Acetone	36.7	No obvious decay in FE after 5 cycles	57
Y-ZIF-8	Y	0.38	CO	88.3	No obvious decay in current in 12 hrs	58
Sc-ZIF-8	Sc	1.24	CO	81.3	No obvious decay in current in 12 hrs	58

Table A 3: SACs derived by pyrolysis MOFs and MOF composites which catalysis N₂RR.

MOF precursor	Supported metal	Metal content wt%	NH ₃ yield	Performance: % (Faradic Efficiency)	Stability	Ref.
Zn/Co ZIF	Co	1.4	0.86 $\mu\text{mol cm}^{-2}\text{h}^{-1}$	10.5	No obvious decay in FE in 6 cycles	59
Fe-ZIF	Fe	4.2	62.9 $\mu\text{g mg}^{-1}\text{h}^{-1}$	18.6	No apparent deactivation after 24 hrs	60
Fe-ZIF-8-CNT	Fe	0.5	34.83 $\mu\text{g mg}^{-1}\text{h}^{-1}$	9.28	No obvious decay after 48 hrs	61
PCN-222(Fe)	Fe	1.71	1.56x10 ⁻¹¹ mol cm ⁻² s ⁻¹	4.51	No obvious decay in 5 cycles	62
Ru(acac) ₃ @ZIF-8	Ru	0.18	102.9 $\mu\text{g mg}^{-1}\text{h}^{-1}$	29.6	Less than 7% decay of yield after 12 hrs	63
ZrO ₂ /Ru@UiO-66	Ru		3.6 mg mg ⁻¹ h ⁻¹	21	No obvious decay in FE in 6 cycles	64
Y-ZIF-8	Y	0.38	21.8 $\mu\text{g cm}^{-2}\text{h}^{-1}$	12.1	FE decreases in 1.2% after 12 hrs	58
Sc-ZIF-8	Sc	1.24	19.2 $\mu\text{g cm}^{-2}\text{h}^{-1}$	11.2	FE decreases in 3.1% after 12 hrs	58

Table A 4: SACs derived by pyrolysis MOFs and MOF composites which catalysis HER.

MOF precursor	Supported metal	Metal content wt %	Performance vs RHE	Stability	Ref.
Zn/Co MOF	Co	4.05	260 mV at 10 mA cm ⁻² in 0.5 M H ₂ SO ₄	No obvious decay after 2000 cycles	65
Ni-MOF	Ni	1.5	34 mV at 10 mA cm ⁻² in 0.5 M H ₂ SO ₄	No apparent deactivation after 25 hrs	66
WCl ₅ /UiO-66-NH ₂	W	1.21	85 mV at 10 mA cm ⁻² in 0.1 M KOH	No obvious decay after 10000 CV cycles	67

Table A 5: SACs derived by pyrolysis MOFs and MOF composites which catalysis oxidation, hydrogenation, dimerization and other reactions.

MOF precursor	Supported metal	Metal content wt%	Reaction catalysed	Performance	Stability	Ref.
Ru(CO) ₁₂ @ZIF-8	Ru	0.1	Oxidation of alcohols	Conversion > 99%, TOF – 4320 h ⁻¹	Not mentioned	68
ZIF-8	Zn	3.12	Oxidation of 3,3',5,5'-tertramethylbenzidine	Not mentioned	Stable from pH 2-11 and 0 °C to 90 0 °C	69
Rh/ZIF-8	Rh	0.92	Formic acid oxidation	Activity-16.1 A mg ⁻¹	No obvious decay in 50000 s	70
Co/Zn ZIF	Co	3.5	Hydrogenation of nitroarenes	Conversion – 34%	Conversion decreases to 6% after 4 cycles	71
Zn ₂₄ Co ₁ BMOF	Co	1.33	Hydrogenation of nitroarenes	Conversion – ~100 Selectivity – 40 %	No obvious decay after 49 hrs	72
ZnNi-ZIF	Ni		Hydrogenation of acetylene	Yield – 90%	No obvious decay in 20 hrs	73
RuCl ₃ @UiO-66-NH ₂	Ru	0.3	Hydrogenation of quinoline	Conversion > 99%	No obvious decay after 5 cycles	74
Pd@ZIF-67	Pd	1.81	Dimerization of terminal aryl acetylenes	Yield – 80%	No obvious decay after 6 cycles	75
PS@ZIF-8	Zn	11.3	CO ₂ cycloaddition	Yield – 94%	No obvious decay after 3 cycles	
CoPC@Zn MOF	Co	0.14	O-silylation of alcohols	Conversion > 99%	No obvious decay after 5 cycles	76

Table A 6: hollow nanostructures synthesized by pyrolysis MOFs and MOF composites and their applications.

MOF precursor	MOF derived hollow structure	Application	Performance	Stability	Ref.
Tubular ZIF-67	CNT/ Co ₃ O ₄	LIBs	Initial charge/discharge capacities: 1840 and 1281 mAh g ⁻¹ at 0.1 A g ⁻¹	No obvious decay in the reversible capacity after 200 cycles	77
Tubular ZIF-67	CoS ₂ hollow prisms	LIBs	Initial charge/discharge capacities: 1542 and 861 mAh g ⁻¹ at 0.2 A g ⁻¹	Reversible capacity 737 mAh g ⁻¹ after 600 cycles	78
ZIF-67/ZIF-8 @ZIF-67	ZnCoS@Co ₉ S ₈ /NC Hollow structures	LIBs	Reversible capacity 2182 mAh g ⁻¹ at 0.1 A g ⁻¹	Reversible capacity 1814 mAh g ⁻¹ after 500 cycles	79
MIL-88B@ZIF-67	Fe ₂ O ₃ nano tubes@Co ₃ O ₄ composite	LIBs	Initial charge/discharge capacities: 709.8 and 921.9 mAh g ⁻¹ at 0.5 A g ⁻¹	No obvious decay in the reversible capacity after 80 cycles	80
MoO ₃ @BMZIF	MoO ₂ / C nanotube	LIBs	Reversible capacity: 1142 mAh g ⁻¹ at 0.1 A g ⁻¹	Reversible capacity remains 810 mAh g ⁻¹ after 600 cycles	81
Yolk shell Ni-Zn MOF	Ni/ZnO hollow sphere	Supercapacitors	Reversible capacity: 497 Fg ⁻¹ at 13.1 A g ⁻¹	Reversible capacity remains 478 Fg ⁻¹ at 5.2 A g ⁻¹ after 2000 cycles	82
Ni-Co-BPA	NiS nanoframes	Supercapacitors	Specific capacitance: 711Fg ⁻¹ at 5 A g ⁻¹	Specific capacity remains at 1290 Fg ⁻¹ at 4 A g ⁻¹ after 4000 cycles	83

Co based MOF	Hollow NiCo ₂ O ₄	Supercapacitors	Capacitance: 89.7 Fg ⁻¹ and 76.8 Fg ⁻¹ at 5 mA cm ⁻²	Initial capacity remains for 20000 cycles at 5 mA cm ⁻²	84
ZIF-8@ZIF-67	CoP NPs embedded N doped C nanotube	HER	140 mV overpotential at 10 mA cm ⁻² in 1 M KOH	No obvious decay after 36 hrs	85
ZnCo-ZIF polyhedra	Hollow Zn _{0.3} Co _{2.7} S ₄ polyhedra	HER	80 mV overpotential at 10 mA cm ⁻² in 0.5 M H ₂ SO ₄	No obvious change in the activity and morphology after 60 hrs	86
Mo based POM - Ni MOF	Ni decorated MoC _x hollow structures	HER	123 mV overpotential at 10 mA cm ⁻² in 0.1 M KOH	No obvious decay after 7000 s	87
Ni-Co-BPA	Ni-Co-MoS ₂ nanocubes	HER	155 mV overpotential at 10 mA cm ⁻² in 0.1 M KOH	Negligible decay after 1000 cycles	88
ZIF-67 polyhedrons	Hollow Co ₃ S ₄ @MOS ₂	HER	210 mV overpotential at 10 mA cm ⁻² in 1 M KOH	Slight reduction in current density after 500 cycles	89
		OER	330 mV overpotential at 10 mA cm ⁻¹ in 1 M KOH	Slight reduction change in the current density after 500 cycles	
Hollow ZIF-67	Hollow Cu/Co ₃ O ₄ spheres	OER	361 mV over potential at 10 mA cm ⁻¹ ¹ in 0.1 M KOH	Not mentioned	90
Ni-Co-BPA	Ni-Co mixed oxide nanocages	OER	380 mV over potential at 10 mA cm ⁻¹ ¹ in 0.1 M NaOH	No obvious change in the current density after 10 hrs	91
ZIF-67	NiCo ₂ O ₄ /N-CNT	Zn-Air batteries	ORR E _{1/2} = 0.862 V vs RHE OER E _{j10} = 339 mV at 10 mA in 0.1 M KOH	No obvious change in the current density after 10000 cycles	92

ZIF-8@ZIF-67	NC@Co-NGC Nano cages	ORR	$E_{1/2} = 0.82$ V vs RHE in 0.1 M KOH	90.1% retain in the normalized current after 20000 s	93
		OER	$E_{j10} = 1.64$ V vs RHE 10 mA cm ⁻¹ in 0.5 M H ₂ SO ₄	No obvious change in the current density after 30000 s	
ZIF-67	N doped CNT	ORR	$E_{1/2} = 0.87$ V vs RHE in 0.1 M KOH	96% of the original current retained after 10000 s	94
		OER	$E_{j10} = 1.6$ V vs RHE 10 mA cm ⁻¹ in 1 M KOH	No obvious change in the current after 4000 s	
ZIF-67	N doped CNT	ORR	$E_{1/2} = 0.85$ V vs RHE in 0.1 M KOH	95% current retention after 40000 s	95
MIL-100(Fe)	Bamboo Pt/N GTs	ORR	$E_{1/2} = 0.88$ V vs RHE in 0.1 M KOH	No significant loss in $E_{1/2}$ after 5000 cycles	96
N-Fe-MOF	N doped GT	ORR	$E_{1/2} = 0.88$ V vs RHE in 0.1 M KOH	27% capacity loss after 50 cycles	97
ZIF-8@FeOOH/ ZIF-67	Fe-Co alloy N doped C cage	ORR	$E_{1/2} = 0.88$ V vs RHE in 0.1M KOH	89.2% retain in the current density after 24 hrs	98
ZIF8@TA/BDBA	B/N doped hollow C	ORR	-0.12 V onset potential vs Ag/AgCl in 0.1 M KOH	No obvious decay in onset potential after 10000 cycles	99
PS@ZIF-67	Signe shell Co/N doped C spheres	ORR	$E_{1/2} = 0.87$ V vs RHE in 0.1M KOH	No obvious decay in potential after 24 hrs	100

References

1. Fu, S.; Zhu, C.; Su, D.; Song, J.; Yao, S.; Feng, S.; Engelhard, M. H.; Du, D.; Lin, Y., Porous Carbon-Hosted Atomically Dispersed Iron-Nitrogen Moiety as Enhanced Electrocatalysts for Oxygen Reduction Reaction in a Wide Range of pH. *Small* **2018**, *14*, 1703118.
2. Zhang, H.; Hwang, S.; Wang, M.; Feng, Z.; Karakalos, S.; Luo, L.; Qiao, Z.; Xie, X.; Wang, C.; Su, D., Single atomic iron catalysts for oxygen reduction in acidic media: particle size control and thermal activation. *J. Am. Chem. Soc.* **2017**, *139*, 14143.
3. Chen, Y.; Ji, S.; Wang, Y.; Dong, J.; Chen, W.; Li, Z.; Shen, R.; Zheng, L.; Zhuang, Z.; Wang, D., Isolated single iron atoms anchored on N-doped porous carbon as an efficient electrocatalyst for the oxygen reduction reaction. *Angew. Chem. Int. Ed.* **2017**, *56*, 6937.
4. Wang, J.; Han, G.; Wang, L.; Du, L.; Chen, G.; Gao, Y.; Ma, Y.; Du, C.; Cheng, X.; Zuo, P., ZIF-8 with ferrocene encapsulated: a promising precursor to single-atom Fe embedded nitrogen-doped carbon as highly efficient catalyst for oxygen electroreduction. *Small* **2018**, *14*, 1704282.
5. Chen, Y.; Ji, S.; Zhao, S.; Chen, W.; Dong, J.; Cheong, W.-C.; Shen, R.; Wen, X.; Zheng, L.; Rykov, A. I., Enhanced oxygen reduction with single-atomic-site iron catalysts for a zinc-air battery and hydrogen-air fuel cell. *Nat. Commun.* **2018**, *9*, 1.
6. Jiang, R.; Li, L.; Sheng, T.; Hu, G.; Chen, Y.; Wang, L., Edge-site engineering of atomically dispersed Fe-N₄ by selective C-N bond cleavage for enhanced oxygen reduction reaction activities. *J. Am. Chem. Soc.* **2018**, *140*, 11594.
7. Xiao, F.; Xu, G.-L.; Sun, C.-J.; Xu, M.; Wen, W.; Wang, Q.; Gu, M.; Zhu, S.; Li, Y.; Wei, Z., Nitrogen-coordinated single iron atom catalysts derived from metal organic frameworks for oxygen reduction reaction. *Nano Energy* **2019**, *61*, 60.
8. Chen, X.; Ma, D.-D.; Chen, B.; Zhang, K.; Zou, R.; Wu, X.-T.; Zhu, Q.-L., Metal-organic framework-derived mesoporous carbon nanoframes embedded with atomically dispersed Fe-N_x active sites for efficient bifunctional oxygen and carbon dioxide electroreduction. *Appl. Catal. B: Environ.* **2020**, *267*, 118720.
9. Lai, Q.; Zheng, L.; Liang, Y.; He, J.; Zhao, J.; Chen, J., Metal-organic-framework-derived Fe-N/C electrocatalyst with five-coordinated Fe-N_x sites for advanced oxygen reduction in acid media. *ACS Catal.* **2017**, *7*, 1655.
10. Yang, H.; Chen, X.; Chen, W.-T.; Wang, Q.; Cuello, N. C.; Nafady, A.; Al-Enizi, A. M.; Waterhouse, G. I.; Goenaga, G. A.; Zawodzinski, T. A., Tunable Synthesis of Hollow Metal-Nitrogen-Carbon Capsules for Efficient Oxygen Reduction Catalysis in Proton Exchange Membrane Fuel Cells. *ACS Nano* **2019**, *13*, 8087.
11. Liu, Q.; Liu, X.; Zheng, L.; Shui, J., The Solid - Phase Synthesis of an Fe-N-C Electrocatalyst for High-Power Proton-Exchange Membrane Fuel Cells. *Angew. Chem.* **2018**, *130*, 1218.

12. Han, J.; Meng, X.; Lu, L.; Bian, J.; Li, Z.; Sun, C., Single - Atom Fe - N_x - C as an Efficient Electrocatalyst for Zinc - Air Batteries. *Adv. Funct. Mater.* **2019**, *29*, 1808872.
13. Ye, Y.; Li, H.; Cai, F.; Yan, C.; Si, R.; Miao, S.; Li, Y.; Wang, G.; Bao, X., Two-dimensional mesoporous carbon doped with Fe-N active sites for efficient oxygen Reduction. *ACS Catal.* **2017**, *7*, 7638.
14. Zhao, D.; Shui, J. L.; Grabstanowicz, L. R.; Chen, C.; Commet, S. M.; Xu, T.; Lu, J.; Liu, D. J., Highly efficient non-precious metal electrocatalysts prepared from one - pot synthesized zeolitic imidazolate frameworks. *Adv. Mater.* **2014**, *26*, 1093.
15. Lin, Y.; Liu, P.; Velasco, E.; Yao, G.; Tian, Z.; Zhang, L.; Chen, L., Fabricating Single-Atom Catalysts from Chelating Metal in Open Frameworks. *Adv. Mater.* **2019**, *31*, 1808193.
16. Jiao, L.; Wan, G.; Zhang, R.; Zhou, H.; Yu, S. H.; Jiang, H. L., From metal - organic frameworks to single-atom Fe implanted N-doped porous carbons: efficient oxygen reduction in both alkaline and acidic media. *Angew. Chem. Int. Ed.* **2018**, *57*, 8525.
17. Zhu, Q.-L.; Xia, W.; Zheng, L.-R.; Zou, R.; Liu, Z.; Xu, Q., Atomically dispersed Fe/N-doped hierarchical carbon architectures derived from a metal-organic framework composite for extremely efficient electrocatalysis. *ACS Energy Lett.* **2017**, *2*, 504.
18. Wang, X. X.; Cullen, D. A.; Pan, Y. T.; Hwang, S.; Wang, M.; Feng, Z.; Wang, J.; Engelhard, M. H.; Zhang, H.; He, Y., Nitrogen-coordinated single cobalt atom catalysts for oxygen reduction in proton exchange membrane fuel cells. *Adv. Mater.* **2018**, *30*, 1706758.
19. Ahn, S. H.; Klein, M. J.; Manthiram, A., 1D Co-and N-Doped Hierarchically Porous Carbon Nanotubes Derived from Bimetallic Metal Organic Framework for Efficient Oxygen and Tri-iodide Reduction Reactions. *Adv. Energy Mater.* **2017**, *7*, 1601979.
20. He, Y.; Hwang, S.; Cullen, D. A.; Uddin, M. A.; Langhorst, L.; Li, B.; Karakalos, S.; Kropf, A. J.; Wegener, E. C.; Sokolowski, J., Highly active atomically dispersed CoN₄ fuel cell cathode catalysts derived from surfactant-assisted MOFs: carbon-shell confinement strategy. *Energy Environ. Sci.* **2019**, *12*, 250.
21. Han, X.; Ling, X.; Wang, Y.; Ma, T.; Zhong, C.; Hu, W.; Deng, Y., Generation of nanoparticle, atomic-cluster, and single-atom cobalt catalysts from zeolitic imidazole frameworks by spatial isolation and their use in zinc-air batteries. *Angew. Chem. Int. Ed.* **2019**, *58*, 5359.
22. Xie, W.; Song, Y.; Li, S.; Li, J.; Yang, Y.; Liu, W.; Shao, M.; Wei, M., Single-Atomic-Co Electrocatalysts with Self-Supported Architecture toward Oxygen-Involved Reaction. *Adv. Funct. Mater.* **2019**, *29*, 1906477.
23. Yin, P.; Yao, T.; Wu, Y.; Zheng, L.; Lin, Y.; Liu, W.; Ju, H.; Zhu, J.; Hong, X.; Deng, Z., Single cobalt atoms with precise N-coordination as superior oxygen reduction reaction catalysts. *Angew. Chem.* **2016**, *128*, 10958.
24. Xiao, M.; Zhang, H.; Chen, Y.; Zhu, J.; Gao, L.; Jin, Z.; Ge, J.; Jiang, Z.; Chen, S.; Liu, C., Identification of binuclear Co₂N₅ active sites for oxygen reduction reaction with

more than one magnitude higher activity than single atom CoN₄ site. *Nano Energy* **2018**, *46*, 396.

25. Zang, W.; Sumboja, A.; Ma, Y.; Zhang, H.; Wu, Y.; Wu, S.; Wu, H.; Liu, Z.; Guan, C.; Wang, J., Single Co atoms anchored in porous N-doped carbon for efficient zinc- air battery cathodes. *ACS Catal.* **2018**, *8*, 8961.

26. Wu, J.; Zhou, H.; Li, Q.; Chen, M.; Wan, J.; Zhang, N.; Xiong, L.; Li, S.; Xia, B. Y.; Feng, G., Densely Populated Isolated Single Co- N Site for Efficient Oxygen Electrocatalysis. *Adv. Energy Mater.* **2019**, *9*, 1900149.

27. Zhang, D.; Chen, W.; Li, Z.; Chen, Y.; Zheng, L.; Gong, Y.; Li, Q.; Shen, R.; Han, Y.; Cheong, W.-C., Isolated Fe and Co dual active sites on nitrogen-doped carbon for a highly efficient oxygen reduction reaction. *Chem. Commun.* **2018**, *54*, 4274.

28. Wang, J.; Huang, Z.; Liu, W.; Chang, C.; Tang, H.; Li, Z.; Chen, W.; Jia, C.; Yao, T.; Wei, S., Design of N-coordinated dual-metal sites: a stable and active Pt-free catalyst for acidic oxygen reduction reaction. *J. Am. Chem. Soc.* **2017**, *139*, 17281.

29. Luo, E.; Zhang, H.; Wang, X.; Gao, L.; Gong, L.; Zhao, T.; Jin, Z.; Ge, J.; Jiang, Z.; Liu, C., Single-Atom Cr-N₄ Sites Designed for Durable Oxygen Reduction Catalysis in Acid Media. *Angew. Chem. Int. Ed.* **2019**, *58*, 12469.

30. Li, J.; Chen, M.; Cullen, D. A.; Hwang, S.; Wang, M.; Li, B.; Liu, K.; Karakalos, S.; Lucero, M.; Zhang, H., Atomically dispersed manganese catalysts for oxygen reduction in proton-exchange membrane fuel cells. *Nat. Catal.* **2018**, *1*, 935.

31. Qu, Y.; Li, Z.; Chen, W.; Lin, Y.; Yuan, T.; Yang, Z.; Zhao, C.; Wang, J.; Zhao, C.; Wang, X., Direct transformation of bulk copper into copper single sites via emitting and trapping of atoms. *Nat. Catal.* **2018**, *1*, 781.

32. Xiao, M.; Zhu, J.; Li, G.; Li, N.; Li, S.; Cano, Z. P.; Ma, L.; Cui, P.; Xu, P.; Jiang, G., A single-atom iridium heterogeneous catalyst in oxygen reduction reaction. *Angew. Chem.* **2019**, *131*, 9742.

33. Wang, X.; Chen, Z.; Zhao, X.; Yao, T.; Chen, W.; You, R.; Zhao, C.; Wu, G.; Wang, J.; Huang, W., Regulation of coordination number over single Co sites: triggering the efficient electroreduction of CO₂. *Angew. Chem.* **2018**, *130*, 1962.

34. Geng, Z.; Cao, Y.; Chen, W.; Kong, X.; Liu, Y.; Yao, T.; Lin, Y., Regulating the coordination environment of Co single atoms for achieving efficient electrocatalytic activity in CO₂ reduction. *App. Catal. B: Environ.* **2019**, *240*, 234.

35. Yang, H.; Lin, Q.; Wu, Y.; Li, G.; Hu, Q.; Chai, X.; Ren, X.; Zhang, Q.; Liu, J.; He, C., Highly efficient utilization of single atoms via constructing 3D and free-standing electrodes for CO₂ reduction with ultrahigh current density. *Nano Energy* **2020**, *70*, 104454.

36. Song, X.; Zhang, H.; Yang, Y.; Zhang, B.; Zuo, M.; Cao, X.; Sun, J.; Lin, C.; Li, X.; Jiang, Z., Bifunctional nitrogen and cobalt codoped hollow carbon for electrochemical syngas production. *Adv. Sci.* **2018**, *5*, 1800177.

37. Quan, F.; Zhan, G.; Shang, H.; Huang, Y.; Jia, F.; Zhang, L.; Ai, Z., Highly efficient electrochemical conversion of CO₂ and NaCl to CO and NaClO. *Green Chem.* **2019**, *21*, 3256.
38. Gu, J.; Hsu, C.-S.; Bai, L.; Chen, H. M.; Hu, X., Atomically dispersed Fe³⁺ sites catalyze efficient CO₂ electroreduction to CO. *Science* **2019**, *364*, 1091.
39. Ye, Y.; Cai, F.; Li, H.; Wu, H.; Wang, G.; Li, Y.; Miao, S.; Xie, S.; Si, R.; Wang, J., Surface functionalization of ZIF-8 with ammonium ferric citrate toward high exposure of Fe-N active sites for efficient oxygen and carbon dioxide electroreduction. *Nano Energy* **2017**, *38*, 281.
40. Guo, Y.; Yang, H.; Zhou, X.; Liu, K.; Zhang, C.; Zhou, Z.; Wang, C.; Lin, W., Electrocatalytic reduction of CO₂ to CO with 100% faradaic efficiency by using pyrolyzed zeolitic imidazolate frameworks supported on carbon nanotube networks. *J. Mater. Chem. A* **2017**, *5*, 24867.
41. Pan, F.; Zhang, H.; Liu, K.; Cullen, D.; More, K.; Wang, M.; Feng, Z.; Wang, G.; Wu, G.; Li, Y., Unveiling active sites of CO₂ reduction on nitrogen-coordinated and atomically dispersed iron and cobalt catalysts. *ACS Catal.* **2018**, *8*, 3116.
42. Lin, L.; Li, H.; Yan, C.; Li, H.; Si, R.; Li, M.; Xiao, J.; Wang, G.; Bao, X., Synergistic Catalysis over Iron-Nitrogen Sites Anchored with Cobalt Phthalocyanine for Efficient CO₂ Electroreduction. *Adv. Mater.* **2019**, *31*, 1903470.
43. Ren, W.; Tan, X.; Yang, W.; Jia, C.; Xu, S.; Wang, K.; Smith, S. C.; Zhao, C., Isolated diatomic Ni-Fe metal-nitrogen sites for synergistic electroreduction of CO₂. *Angew. Chem. Int. Ed.* **2019**, *58*, 6972.
44. Yan, C.; Li, H.; Ye, Y.; Wu, H.; Cai, F.; Si, R.; Xiao, J.; Miao, S.; Xie, S.; Yang, F., Coordinatively unsaturated nickel-nitrogen sites towards selective and high-rate CO₂ electroreduction. *Energy Environ. Sci.* **2018**, *11*, 1204.
45. Pan, F.; Zhang, H.; Liu, Z.; Cullen, D.; Liu, K.; More, K.; Wu, G.; Wang, G.; Li, Y., Atomic-level active sites of efficient imidazolate framework-derived nickel catalysts for CO₂ reduction. *J. Mater. Chem. A* **2019**, *7*, 26231.
46. Lu, P.; Yang, Y.; Yao, J.; Wang, M.; Dipazir, S.; Yuan, M.; Zhang, J.; Wang, X.; Xie, Z.; Zhang, G., Facile synthesis of single-nickel-atomic dispersed N-doped carbon framework for efficient electrochemical CO₂ reduction. *App. Catal. B: Environ.* **2019**, *241*, 113.
47. Zhao, C.; Dai, X.; Yao, T.; Chen, W.; Wang, X.; Wang, J.; Yang, J.; Wei, S.; Wu, Y.; Li, Y., Ionic exchange of metal-organic frameworks to access single nickel sites for efficient electroreduction of CO₂. *J. Am. Chem. Soc.* **2017**, *139*, 8078.
48. Wen, C. F.; Mao, F.; Liu, Y.; Zhang, X. Y.; Fu, H. Q.; Zheng, L. R.; Liu, P. F.; Yang, H. G., Nitrogen-Stabilized Low-Valent Ni Motifs for Efficient CO₂ Electrocatalysis. *ACS Catal.* **2019**, *10*, 1086.

49. Hou, Y.; Liang, Y.-L.; Shi, P.-C.; Huang, Y.-B.; Cao, R., Atomically dispersed Ni species on N-doped carbon nanotubes for electroreduction of CO₂ with nearly 100% CO selectivity. *App. Catal. B: Environ.* **2020**, *271*, 118929.
50. Yang, H.; Lin, Q.; Zhang, C.; Yu, X.; Cheng, Z.; Li, G.; Hu, Q.; Ren, X.; Zhang, Q.; Liu, J., Carbon dioxide electroreduction on single-atom nickel decorated carbon membranes with industry compatible current densities. *Nat. Commun.* **2020**, *11*, 1.
51. Yang, J.; Qiu, Z.; Zhao, C.; Wei, W.; Chen, W.; Li, Z.; Qu, Y.; Dong, J.; Luo, J.; Li, Z., In situ thermal atomization to convert supported nickel nanoparticles into surface - bound nickel single-atom catalysts. *Angew. Chem. Int. Ed.* **2018**, *57*, 14095.
52. Gong, Y. N.; Jiao, L.; Qian, Y.; Pan, C. Y.; Zheng, L.; Cai, X.; Liu, B.; Yu, S. H.; Jiang, H. L., Regulating the Coordination Environment of MOF-Templated Single-Atom Nickel Electrocatalysts for Boosting CO₂ Reduction. *Angew. Chem. Int. Ed.* **2020**, *59*, 2705.
53. Zhang, E.; Wang, T.; Yu, K.; Liu, J.; Chen, W.; Li, A.; Rong, H.; Lin, R.; Ji, S.; Zheng, X., Bismuth single atoms resulting from transformation of metal-organic frameworks and their use as electrocatalysts for CO₂ reduction. *J. Am. Chem. Soc.* **2019**, *141*, 16569.
54. Yang, H.; Wu, Y.; Li, G.; Lin, Q.; Hu, Q.; Zhang, Q.; Liu, J.; He, C., Scalable production of efficient single-atom copper decorated carbon membranes for CO₂ electroreduction to methanol. *J. Am. Chem. Soc.* **2019**, *141*, 12717.
55. Karapinar, D.; Huan, N. T.; Ranjbar Sahraie, N.; Li, J.; Wakerley, D.; Touati, N.; Zanna, S.; Taverna, D.; Galvão Tizei, L. H.; Zitolo, A., Electroreduction of CO₂ on single - site copper-nitrogen-doped carbon material: selective formation of ethanol and reversible restructuring of the metal sites. *Angew. Chem. Int. Ed.* **2019**, *58*, 15098.
56. Guan, A.; Chen, Z.; Quan, Y.; Peng, C.; Wang, Z.; Sham, T.-K.; Yang, C.; Ji, Y.; Qian, L.; Xu, X., Boosting CO₂ electroreduction to CH₄ via tuning neighboring single-copper sites. *ACS Energy Lett.* **2020**, *5*, 1044.
57. Zhao, K.; Nie, X.; Wang, H.; Chen, S.; Quan, X.; Yu, H.; Choi, W.; Zhang, G.; Kim, B.; Chen, J. G., Selective electroreduction of CO₂ to acetone by single copper atoms anchored on N-doped porous carbon. *Nat. Commun.* **2020**, *11*, 1.
58. Liu, J.; Kong, X.; Zheng, L.; Guo, X.; Liu, X.; Shui, J., Rare earth single-atom catalysts for nitrogen and carbon dioxide reduction. *ACS Nano* **2020**, *14*, 1093.
59. Liu, Y.; Xu, Q.; Fan, X.; Quan, X.; Su, Y.; Chen, S.; Yu, H.; Cai, Z., Electrochemical reduction of N₂ to ammonia on Co single atom embedded N-doped porous carbon under ambient conditions. *J. Mater. Chem. A* **2019**, *7*, 26358.
60. Lü, F.; Zhao, S.; Guo, R.; He, J.; Peng, X.; Bao, H.; Fu, J.; Han, L.; Qi, G.; Luo, J., Nitrogen-coordinated single Fe sites for efficient electrocatalytic N₂ fixation in neutral media. *Nano Energy* **2019**, *61*, 420.
61. Wang, Y.; Cui, X.; Zhao, J.; Jia, G.; Gu, L.; Zhang, Q.; Meng, L.; Shi, Z.; Zheng, L.; Wang, C., Rational design of Fe-N/C hybrid for enhanced nitrogen reduction electrocatalysis under ambient conditions in aqueous solution. *ACS Catal.* **2018**, *9*, 336.

62. Zhang, R.; Jiao, L.; Yang, W.; Wan, G.; Jiang, H.-L., Single-atom catalysts templated by metal–organic frameworks for electrochemical nitrogen reduction. *J. Mater. Chem. A* **2019**, *7*, 26371.
63. Geng, Z.; Liu, Y.; Kong, X.; Li, P.; Li, K.; Liu, Z.; Du, J.; Shu, M.; Si, R.; Zeng, J., Achieving a Record-High Yield Rate of 120.9 for N₂ Electrochemical Reduction over Ru Single-Atom Catalysts. *Adv. Mater.* **2018**, *30*, 1803498.
64. Tao, H.; Choi, C.; Ding, L.-X.; Jiang, Z.; Han, Z.; Jia, M.; Fan, Q.; Gao, Y.; Wang, H.; Robertson, A. W., Nitrogen fixation by Ru single-atom electrocatalytic reduction. *Chem* **2019**, *5*, 204.
65. Zhao, W.; Wan, G.; Peng, C.; Sheng, H.; Wen, J.; Chen, H., Key single-atom electrocatalysis in metal-organic framework (MOF)-derived bifunctional catalysts. *ChemSusChem* **2018**, *11*, 3473.
66. Fan, L.; Liu, P. F.; Yan, X.; Gu, L.; Yang, Z. Z.; Yang, H. G.; Qiu, S.; Yao, X., Atomically isolated nickel species anchored on graphitized carbon for efficient hydrogen evolution electrocatalysis. *Nat. Commun.* **2016**, *7*, 1.
67. Chen, W.; Pei, J.; He, C. T.; Wan, J.; Ren, H.; Wang, Y.; Dong, J.; Wu, K.; Cheong, W. C.; Mao, J., Single tungsten atoms supported on MOF-derived N-doped carbon for robust electrochemical hydrogen evolution. *Adv. Mater.* **2018**, *30*, 1800396.
68. Ji, S.; Chen, Y.; Fu, Q.; Chen, Y.; Dong, J.; Chen, W.; Li, Z.; Wang, Y.; Gu, L.; He, W., Confined pyrolysis within metal–organic frameworks to form uniform Ru₃ clusters for efficient oxidation of alcohols. *J. Am. Chem. Soc.* **2017**, *139*, 9795.
69. Xu, B.; Wang, H.; Wang, W.; Gao, L.; Li, S.; Pan, X.; Wang, H.; Yang, H.; Meng, X.; Wu, Q., A Single - Atom Nanozyme for Wound Disinfection Applications. *Angew. Chem.* **2019**, *131*, 4965.
70. Xiong, Y.; Dong, J.; Huang, Z.-Q.; Xin, P.; Chen, W.; Wang, Y.; Li, Z.; Jin, Z.; Xing, W.; Zhuang, Z., Single-atom Rh/N-doped carbon electrocatalyst for formic acid oxidation. *Nat. Nanotechnol.* **2020**, *15*, 390.
71. Sun, X.; Olivos-Suarez, A. I.; Osadchii, D.; Romero, M. J. V.; Kapteijn, F.; Gascon, J., Single cobalt sites in mesoporous N-doped carbon matrix for selective catalytic hydrogenation of nitroarenes. *J. Catal.* **2018**, *357*, 20.
72. Wang, H.; Wang, Y.; Li, Y.; Lan, X.; Ali, B.; Wang, T., Highly Efficient Hydrogenation of Nitroarenes by N-Doped Carbon-Supported Cobalt Single-Atom Catalyst in Ethanol/Water Mixed Solvent. *ACS Appl. Mater. Interfaces* **2020**, *12*, 34021.
73. Dai, X.; Chen, Z.; Yao, T.; Zheng, L.; Lin, Y.; Liu, W.; Ju, H.; Zhu, J.; Hong, X.; Wei, S., Single Ni sites distributed on N-doped carbon for selective hydrogenation of acetylene. *Chem. Commun.* **2017**, *53*, 11568.
74. Wang, X.; Chen, W.; Zhang, L.; Yao, T.; Liu, W.; Lin, Y.; Ju, H.; Dong, J.; Zheng, L.; Yan, W., Uncoordinated amine groups of metal–organic frameworks to anchor single Ru sites as chemoselective catalysts toward the hydrogenation of quinoline. *J. Am. Chem. Soc.* **2017**, *139*, 9419.

75. Zhao, C.; Yu, H.; Wang, J.; Che, W.; Li, Z.; Yao, T.; Yan, W.; Chen, M.; Yang, J.; Wei, S., A single palladium site catalyst as a bridge for converting homogeneous to heterogeneous in dimerization of terminal aryl acetylenes. *Mat. Chem. Front.* **2018**, *2*, 1317.
76. Wang, X.; Li, P.; Li, Z.; Chen, W.; Zhou, H.; Zhao, Y.; Wang, X.; Zheng, L.; Dong, J.; Lin, Y., 2D MOF induced accessible and exclusive Co single sites for an efficient O-silylation of alcohols with silanes. *Chem. Commun.* **2019**, *55*, 6563.
77. Chen, Y. M.; Yu, L.; Lou, X. W., Hierarchical tubular structures composed of Co₃O₄ hollow nanoparticles and carbon nanotubes for lithium storage. *Angew. Chem. Int. Ed.* **2016**, *55*, 5990.
78. Yu, L.; Yang, J. F.; Lou, X. W., Formation of CoS₂ nanobubble hollow prisms for highly reversible lithium storage. *Angew. Chem. Int. Ed.* **2016**, *55*, 13422.
79. Aslam, M. K.; Shah, S. S. A.; Li, S.; Chen, C., Kinetically controlled synthesis of MOF nanostructures: single-holed hollow core-shell ZnCoS@Co₉S₈/NC for ultra-high performance lithium-ion batteries. *J. Mater. Chem. A* **2018**, *6*, 14083.
80. Zhang, S. L.; Guan, B. Y.; Wu, H. B.; Lou, X. W. D., Metal-organic framework-assisted synthesis of compact Fe₂O₃ nanotubes in Co₃O₄ host with enhanced lithium storage properties. *Nano-micro Lett.* **2018**, *10*, 1.
81. Tian, W.; Hu, H.; Wang, Y.; Li, P.; Liu, J.; Liu, J.; Wang, X.; Xu, X.; Li, Z.; Zhao, Q., Metal-organic frameworks mediated synthesis of one-dimensional molybdenum-based/carbon composites for enhanced lithium storage. *ACS Nano* **2018**, *12*, 1990.
82. Li, G.-C.; Liu, P.-F.; Liu, R.; Liu, M.; Tao, K.; Zhu, S.-R.; Wu, M.-K.; Yi, F.-Y.; Han, L., MOF-derived hierarchical double-shelled NiO/ZnO hollow spheres for high-performance supercapacitors. *Dalton Trans.* **2016**, *45*, 13311.
83. Yu, X. Y.; Yu, L.; Wu, H. B.; Lou, X. W., Formation of nickel sulfide nanoframes from metal-organic frameworks with enhanced pseudocapacitive and electrocatalytic properties. *Angew. Chem.* **2015**, *127*, 5421.
84. Guan, C.; Liu, X.; Ren, W.; Li, X.; Cheng, C.; Wang, J., Rational design of metal-organic framework derived hollow NiCo₂O₄ arrays for flexible supercapacitor and electrocatalysis. *Adv. Energy Mater.* **2017**, *7*, 1602391.
85. Pan, Y.; Sun, K.; Liu, S.; Cao, X.; Wu, K.; Cheong, W.-C.; Chen, Z.; Wang, Y.; Li, Y.; Liu, Y., Core-shell ZIF-8@ ZIF-67-derived CoP nanoparticle-embedded N-doped carbon nanotube hollow polyhedron for efficient overall water splitting. *J. Am. Chem. Soc.* **2018**, *140*, 2610.
86. Huang, Z.-F.; Song, J.; Li, K.; Tahir, M.; Wang, Y.-T.; Pan, L.; Wang, L.; Zhang, X.; Zou, J.-J., Hollow cobalt-based bimetallic sulfide polyhedra for efficient all-pH-value electrochemical and photocatalytic hydrogen evolution. *J. Am. Chem. Soc.* **2016**, *138*, 1359.
87. Xu, X.; Nosheen, F.; Wang, X., Ni-decorated molybdenum carbide hollow structure derived from carbon-coated metal-organic framework for electrocatalytic hydrogen evolution reaction. *Chem. Mater.* **2016**, *28*, 6313.

88. Yu, X. Y.; Feng, Y.; Jeon, Y.; Guan, B.; Lou, X. W.; Paik, U., Formation of Ni–Co–MoS₂ nanoboxes with enhanced electrocatalytic activity for hydrogen evolution. *Adv. Mater.* **2016**, *28*, 9006.
89. Guo, Y.; Tang, J.; Qian, H.; Wang, Z.; Yamauchi, Y., One-pot synthesis of zeolitic imidazolate framework 67-derived hollow Co₃S₄@MoS₂ heterostructures as efficient bifunctional catalysts. *Chem. Mater.* **2017**, *29*, 5566.
90. Tan, Y. C.; Zeng, H. C., Self-templating synthesis of hollow spheres of MOFs and their derived nanostructures. *Chem. Commun.* **2016**, *52*, 11591.
91. Han, L.; Yu, X. Y.; Lou, X. W., Formation of prussian-blue-analog nanocages via a direct etching method and their conversion into Ni-Co-mixed oxide for enhanced oxygen evolution. *Adv. Mater.* **2016**, *28*, 4601.
92. Li, J.; Lu, S.; Huang, H.; Liu, D.; Zhuang, Z.; Zhong, C., ZIF-67 as continuous self-sacrifice template derived NiCo₂O₄/Co, N-CNTs nanocages as efficient bifunctional electrocatalysts for rechargeable Zn–air batteries. *ACS Sustain. Chem. Eng.* **2018**, *6*, 10021.
93. Liu, S.; Wang, Z.; Zhou, S.; Yu, F.; Yu, M.; Chiang, C. Y.; Zhou, W.; Zhao, J.; Qiu, J., Metal-organic-framework-derived hybrid carbon nanocages as a bifunctional electrocatalyst for oxygen reduction and evolution. *Adv. Mater.* **2017**, *29*, 1700874.
94. Xia, B. Y.; Yan, Y.; Li, N.; Wu, H. B.; Lou, X. W. D.; Wang, X., A metal–organic framework-derived bifunctional oxygen electrocatalyst. *Nature energy* **2016**, *1*, 1.
95. Meng, J.; Niu, C.; Xu, L.; Li, J.; Liu, X.; Wang, X.; Wu, Y.; Xu, X.; Chen, W.; Li, Q., General oriented formation of carbon nanotubes from metal–organic frameworks. *J. Am. Chem. Soc.* **2017**, *139*, 8212.
96. Li, Q.; Pan, H.; Higgins, D.; Cao, R.; Zhang, G.; Lv, H.; Wu, K.; Cho, J.; Wu, G., Metal-Organic Framework-Derived Bamboo-like Nitrogen-Doped Graphene Tubes as an Active Matrix for Hybrid Oxygen - Reduction Electrocatalysts. *Small* **2015**, *11*, 1443.
97. Li, Q.; Xu, P.; Gao, W.; Ma, S.; Zhang, G.; Cao, R.; Cho, J.; Wang, H. L.; Wu, G., Graphene/graphene - tube nanocomposites templated from cage - containing metal - organic frameworks for oxygen reduction in Li–O₂ batteries. *Adv. Mater.* **2014**, *26*, 1378.
98. Guan, B. Y.; Lu, Y.; Wang, Y.; Wu, M.; Lou, X. W., Porous iron-cobalt alloy/nitrogen-doped carbon cages synthesized via pyrolysis of complex metal-organic framework hybrids for oxygen reduction. *Adv. Funct. Mater.* **2018**, *28*, 1706738.
99. Wu, M.; Li, C.; Zhao, J.; Ling, Y.; Liu, R., Tannic acid-mediated synthesis of dual-heteroatom-doped hollow carbon from a metal–organic framework for efficient oxygen reduction reaction. *Dalton Trans.* **2018**, *47*, 7812.
100. Guan, B. Y.; Yu, L.; Lou, X. W., Formation of single-holed cobalt/N-doped carbon hollow particles with enhanced electrocatalytic activity toward oxygen reduction reaction in alkaline media. *Adv. Sci.* **2017**, *4*, 1700247.

Appendix B for Chapter 6

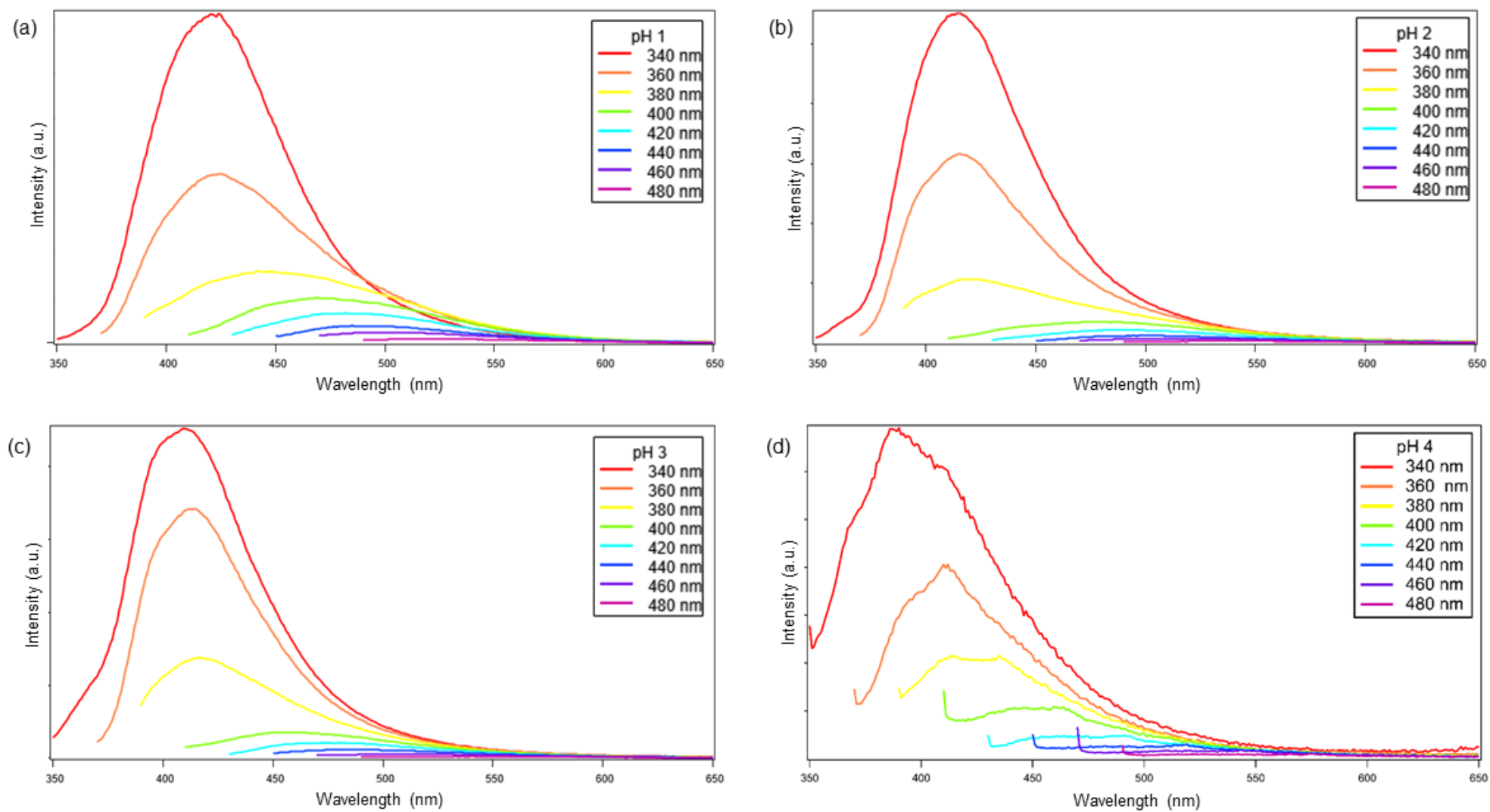


Figure B 1: Fluorescence of HNB-2 at (a) pH 1, (b) pH 2, (c) pH 3 and pH 4.

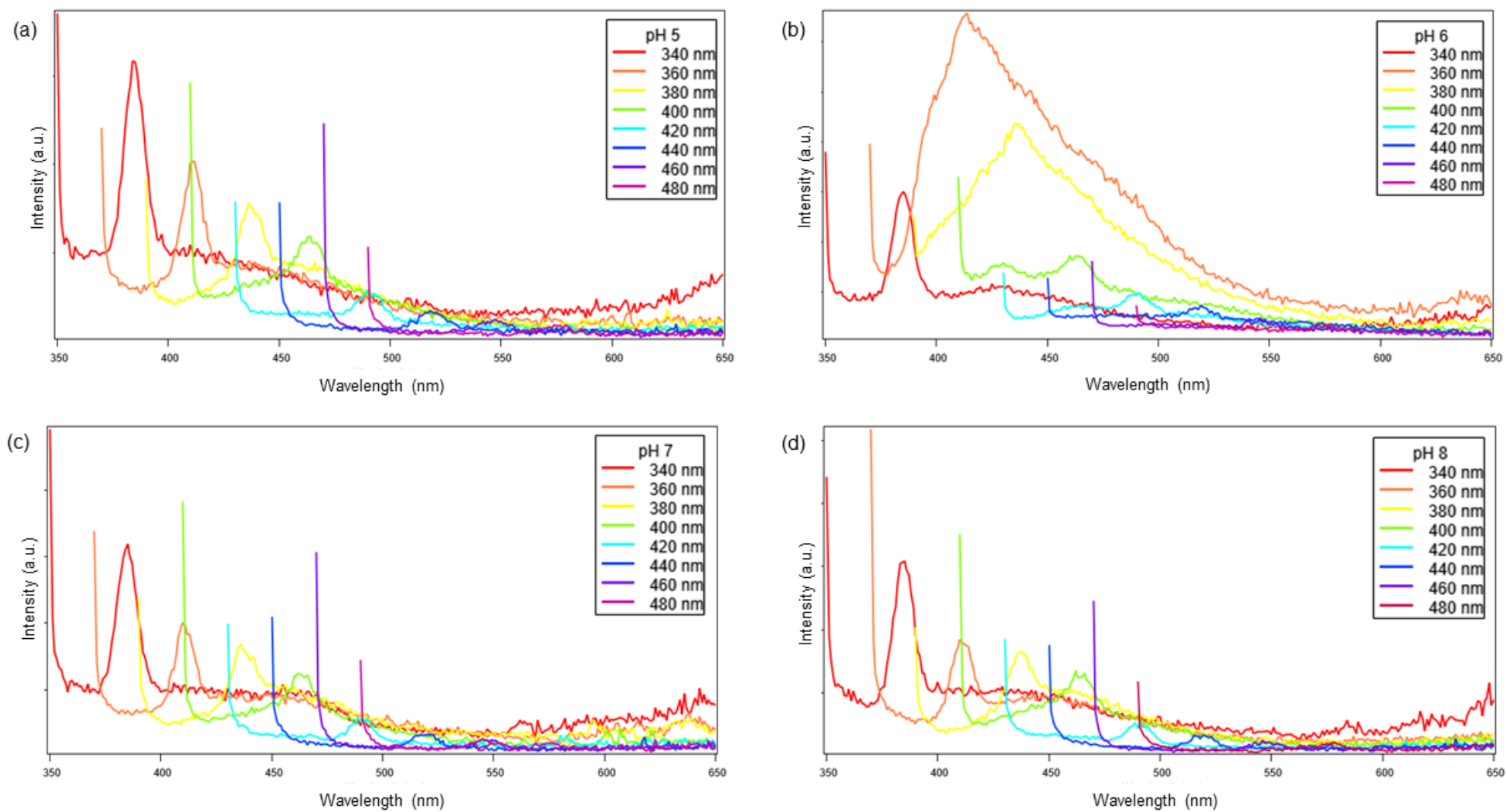


Figure B 2: Fluorescence of HNB-2 at (a) pH 5, (b) pH 6, (c) pH 7 and pH 8.

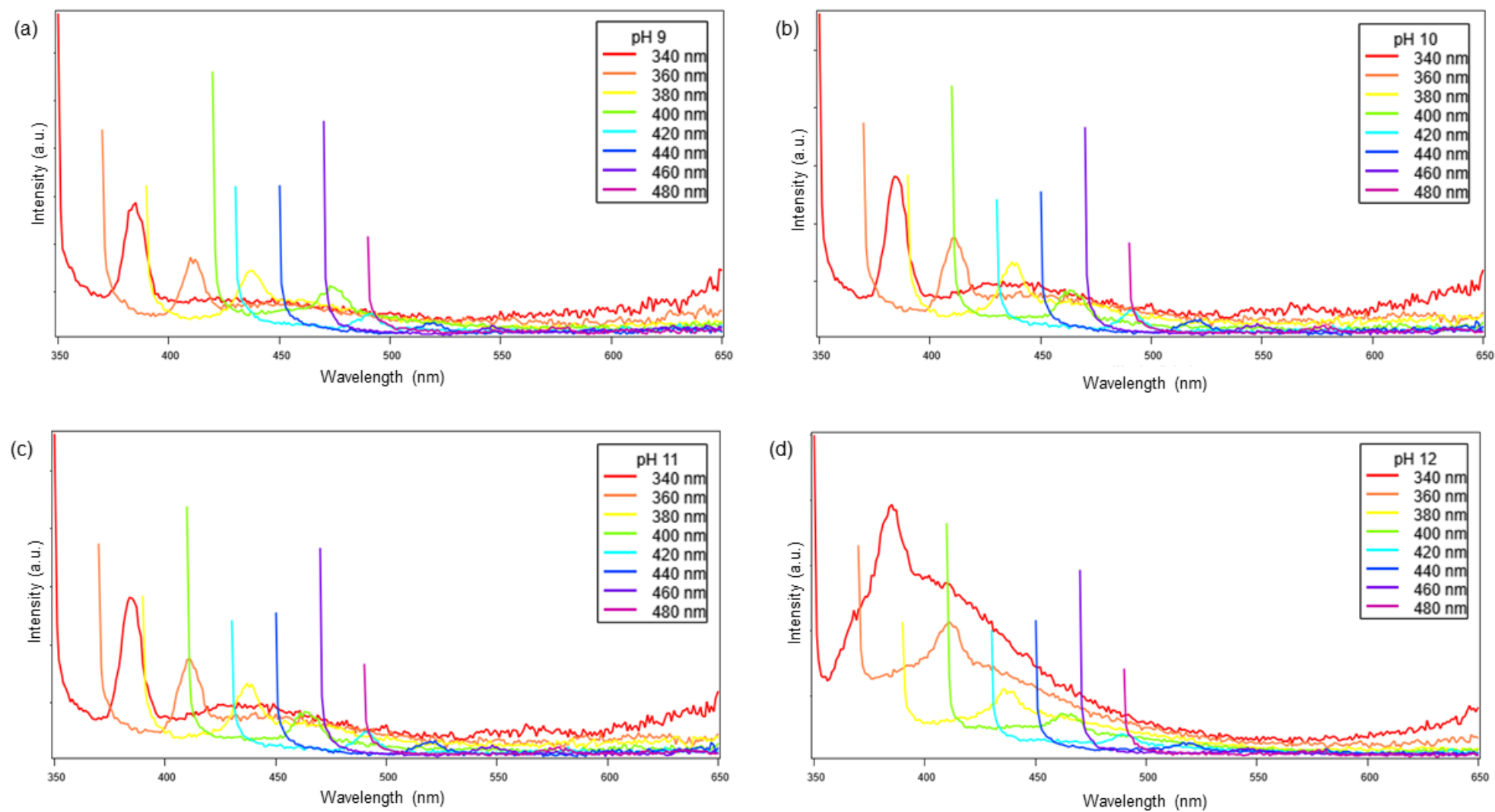


Figure B 3: Fluorescence of HNB-2 at (a) pH 9, (b) pH 10, (c) pH 11 and pH 12.

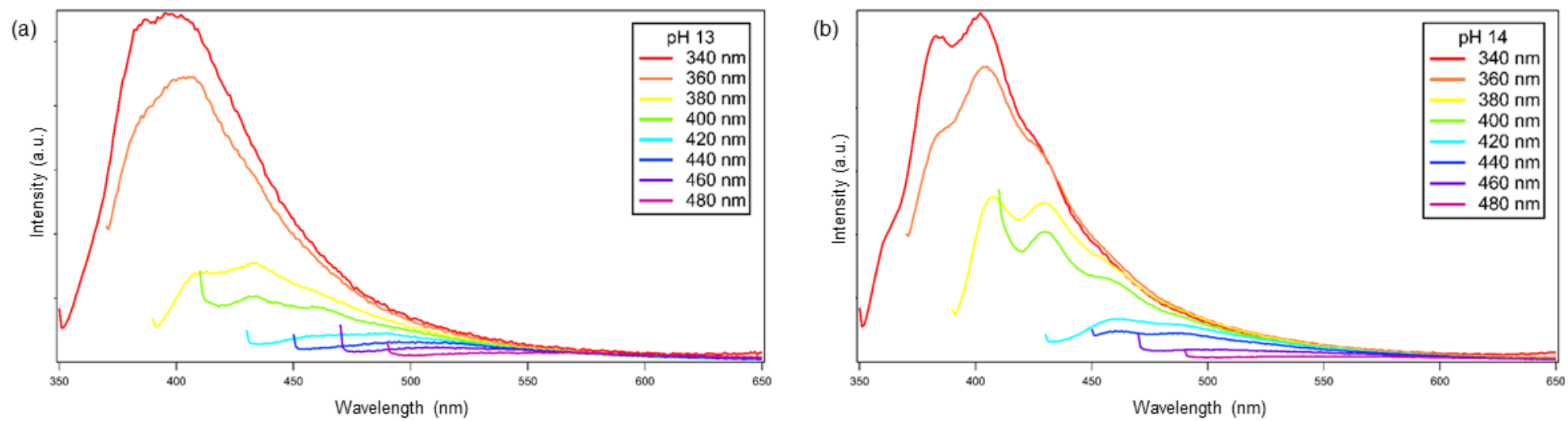


Figure B 4: Fluorescence of HNB-2 at (a) pH 13 and (b) pH 14.

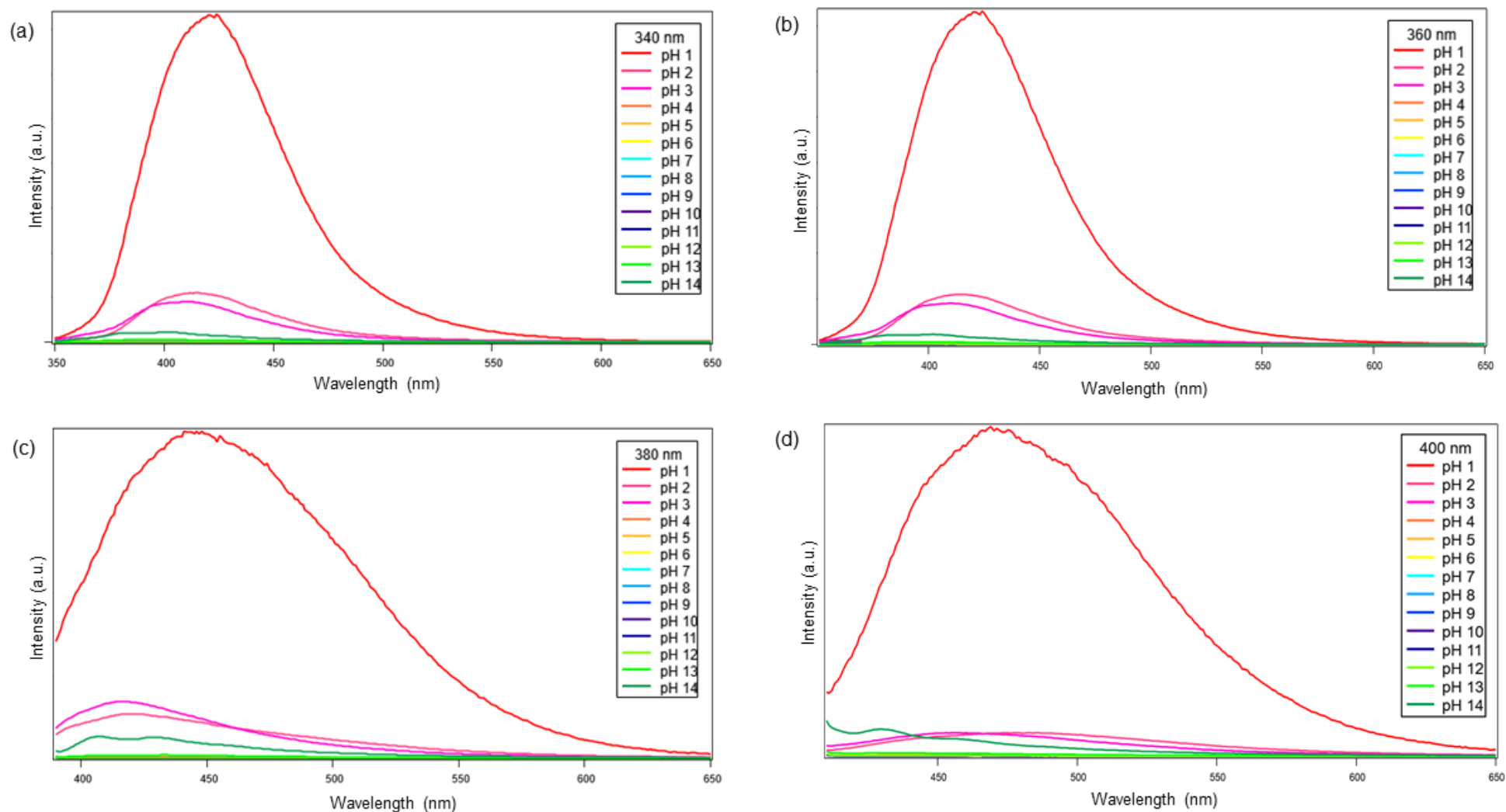


Figure B 5: Fluorescence of HNB-2 at (a) 340 nm, (b) 360 nm, (c) 380 nm and (d) 400 nm excitation wavelengths.

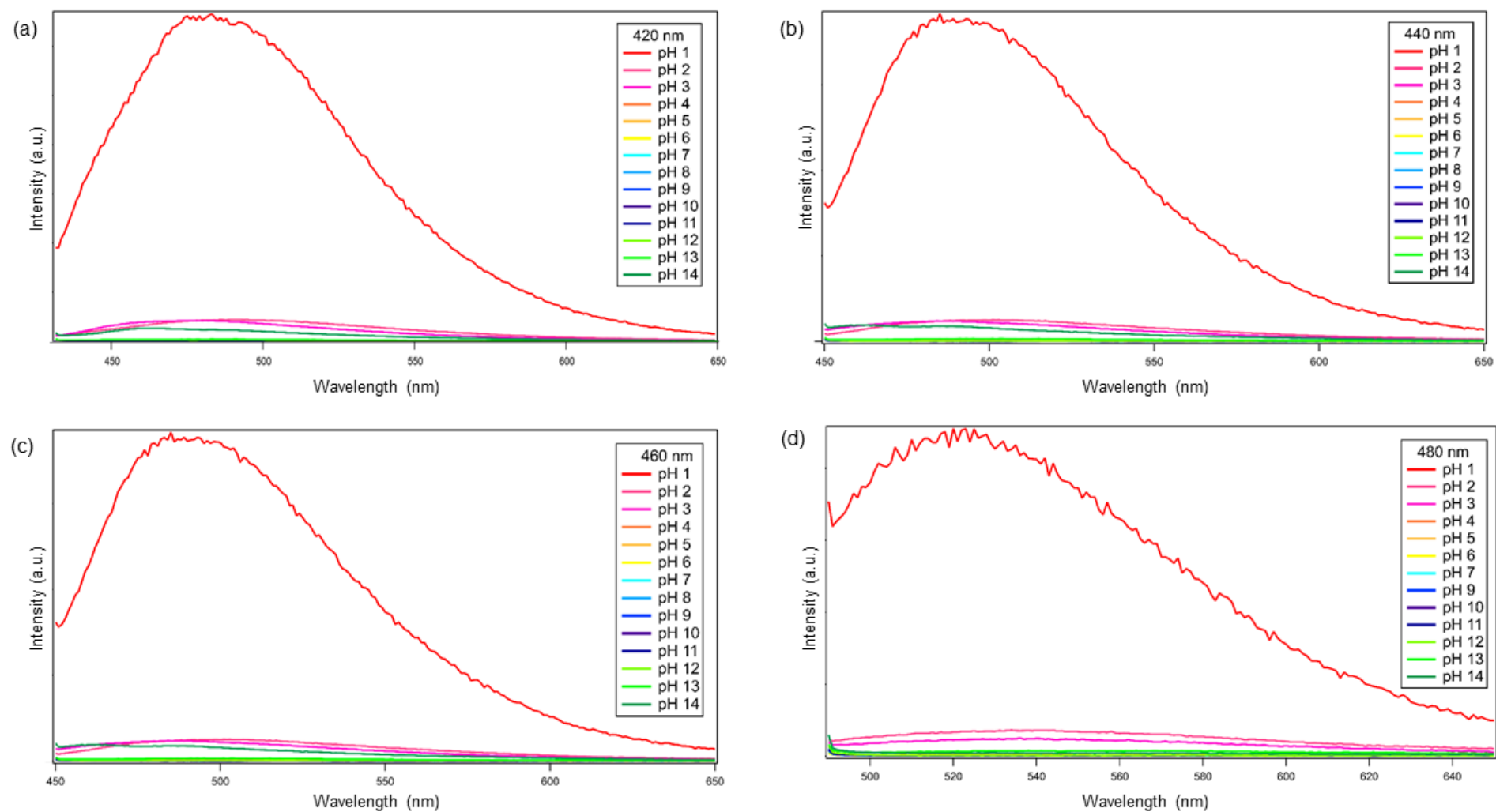


Figure B 6: Fluorescence of HNB-2 at (a) 420 nm, (b) 440nm, (c) 460 nm and (d) 480 nm excitation wavelength.

